Proc. 30th Symposium on Celestial Mechanics

会学天第集研体30録究力回

第30回天体力学研究会集録

平成10年3月4日～3月6日

総合研究大学院大学葉山キャンパス

Proceedings of the 30th Symposium on Celestial Mechanics

Held in Hayama, Kanagawa, Japan, March 4–6, 1998.

Toshio Fukushima, Takashi Ito, Tetsuharu Fuse and Hiroaki Umehara (editors)

Editors/世話人

福島登志夫 (Toshio Fukushima)
国立天文台位置天文天体力学研究系宇宙計量研究部門
Division of Astrometry and Celestial Mechanics, National Astronomical Observatory
E-mail: toshio@nao.ac.jp

伊藤孝士 (Takashi Ito)
国立天文台天文学データ解析計算センター
Astronomical Data Analysis Center, National Astronomical Observatory
E-mail: tito@cc.nao.ac.jp

布施哲治 (Tetsuharu Fuse)
総合研究大学院大学数物科学研究科天文科学専攻博士課程
Department of Astronomical Science, Graduate University of Advanced Studies
E-mail: tetsu@pluto.mtk.nao.ac.jp

梅原広明 (Hiroaki Umehara)
通信総合研究所鹿島宇宙センター宇宙制御技術研究室
Kashima Space Center, Communication Research Laboratory
E-mail: umehara@milano.mtk.nao.ac.jp

PREFACE ～まえがきにかえて

時の経つのは早いもので、天体力学研究会も今回で30回目を迎えることができました。とはいっても今回の世話人一同は三十年前の発足当時のことについてまったく不案内なので、古在先生に特別講演をお願いしていままでの長い歴史とか発足当時の雰囲気などをご紹介していただきました。また、これまでの研究会のプログラム等については布施さんの講演の集録をご覧ください。

ここのところ開催地が同じ国立天文台三鷹ばかりでしたので、今回は雰囲気を変えるために総合研究大学院大学の葉山本部で合宿形式で行いました。また、ポスター発表形式も導入してみました。この試みの結果を踏まえて今後の研究会の開催形式を検討していきたいと思っております。

最後に、慣れない世話人ばかりで不手際も多かったと思います。この場を借りてお詫びいたします。

平成10年3月20日
第30回天体力学研究会世話人代表
福島登志夫

Program/プログラム

[3月4日]

13:25～13:30	
世話人挨拶	福島登志夫
事務連絡	世話人
13:30～15:30 (惑星形成など, 座長：吉川真)	
原始惑星系の安定性	伊藤孝士
The stability of protoplanet systems	吉永恵子
The legend of CH Cygni ～伝説のはじまり～	谷川清隆
15:30～ (ポスター短発表 150秒/枚)＋ポスター議論	
Sweeping resonanceによるアステロイドの軌道進化	長沢真樹子
静止衛星の軌道解析に関する一考察	河合雅司
潮汐力による地殻の水平変動について	河合雅司
ガウスのケプラー方程式の高速解法	福島登志夫
天文学者からの質問190	谷川清隆
目次で見る天体力学研究会の30年	布施哲治
16:30～18:30 (数値計算法, 座長：福島登志夫)	
対称線形多段法再考	福島登志夫
NEW TIME-SYMMETRIC INTEGRATORS FOR PLANETARY DYNAMICS	小久保英一郎
非可積分系のシンプレクティック積分: ステップサイズ零への極限近傍に見る複雑なステップサイズ依存性	梅野健

[3月5日]

09:10～11:50 (太陽系天体1, 座長：布施哲治)	
改良型MVSIと小天体の力学への応用	布施哲治
小惑星ネレウスの運動 －そのカオス的性質と軌道運動予測－	吉川真
(休憩)	
木曽シュミット望遠鏡による木星外衛星の位置観測精度	中村士
スバル望遠鏡による外部衛星の探査	中村士
13:30～16:10 (力学系理論, 座長：梅原広明)	
The isolated saddle-node bifurcation inside the horseshoe	桐木紳
Standard Mappingにおける不変曲線の構造変化	山口喜博
(休憩)	
Numerical Examples of Triple Collision Orbits and Near Triple Collision Orbits	中村健
自由落下三体問題のblow-up解析	梅原広明
16:30～17:50 (太陽系天体2, 座長：伊藤孝士)	
SELENEに働く摂動力	仙石新
水星中間軌道の有効性	井上猛
17:50～ (ポスター短発表 150秒/枚)	
SELENE計画の月周回衛星とリレー衛星に対する非重力効果について	久保岡俊宏
小惑星探査のための超多数回フライバイ軌道	吉川真
主成分解析法によるHenon-Heiles系の再現	湯浅学
自由度３ハミルトン系カオスの諸概念と技法	黒崎暁
非退化条件を破るハミルトン系のカオスへの遷移機構	篠原晋
Research announcements of the high dimensional H\'enon map	桐木紳

[3月6日]

09:10～12:00 (太陽系天体3, 座長：中井宏)	
65cm屈折望遠鏡による写真位置観測: 土星の衛星・二重星など	畑中至純
座標系の違いによる見掛けの離心率の変化	中井宏
(休憩)	
古在メカニズムの抑制と崩壊	木下宙
天体力学研究会の30年	古在由秀
12:00～12:10	
事務連絡	世話人
世話人挨拶	福島登志夫

Table of Contents

Planetary Formation and Resonances

Our Solar System

Artificial Satellites and Gravitational Field

Theory of Dynamical Systems

Numerical Techniques and Coordinate Systems

History and General Topics

Stability and instability of the terrestrial protoplanet system and their possible roles in the final stage of planet formation

TAKASHI ITO and KIYOTAKA TANIKAWA
National Astronomical Observatory, Mitaka, Tokyo 181, Japan
tito@cc.nao.ac.jp

A working scenario for the final stage of planet formation through the accumulation of protoplanets into planets is proposed. The basic idea is that the dynamical structure of the terrestrial and jovian planet regions are different, represented by the separation normalized by the Hill radius: jovian planets are dynamically independent whereas terrestrial planets are dependent on jovian planets. The adequacy of the hypothesis is checked numerically and theoretically in some aspects, especially notifying the instability time of the terrestrial protoplanet system. It is likely that the instability of the terrestrial protoplanet system was accelerated by perturbation by outer giant planets, which progress the evolution of protoplanet system into the present configuration of the planets. Secular resonance with Jupiter, though suppressed much by the mutual interaction among the protoplanets, enhances the eccentricities of protoplanets and increases the probability of close encounters. Even only Jupiter exists without Saturn, secular perturbation is effective on the terrestrial protoplanet system. Due to the effect of secular perturbation by jovian planets, instability time of the terrestrial protoplanet system is limited to 10^6 years, at most 10^7 years, depending on the degree of mass variation among protoplanets. Timescale of instability also depends much on the initial velocity dispersion. Large random velocities and large mass distribution reduce the instability time and may accelerate the evolution. But too large velocity dispersion is not convenient to form the present nearly circular and planar orbits of Venus or the Earth. Although the full-detailed N-body simulations are necessary, it can be said that the perturbation from jovian planets on the terrestrial region has played a significant role in the final stage of planet formation.

1 Introduction

The origin of the present configuration of the solar system planets — mass, number, and separation — is not well understood. The problem of the separations among planets which are much sparser in the terrestrial planetary subsystem than in the jovian planetary subsystem, is particularly interesting in the viewpoint of planet formation theory and the stability of the planetary system. When we measure the planet separations by the mutual Hill radii R_H, separations in the terrestrial region are more than $25R_H$ whereas those in the jovian region are about $15R_H$ or less (Table I). The wide separation of planets may have kept them stable in quite a long period, maybe the age of the solar system (Laskar 1994) although the motion of the planets shows chaotic behavior with positive Lyapunov exponents (Sussman and Wisdom 1988, 1992, Laskar 1990). Notification on the relationship between the instability time and the Lyapunov time has been reported (Lecar *et al.* 1992, Morbidelli and Froeschlé 1996). There are some ideas to explain the separation by the dynamical evolution after the planetary system has been formed (e.g. Laskar 1997), but it will be more natural to consider that the origin of the planetary separation is ascribed to the formation process of the planets.

Table I

Recently the size of simulations on the planet accretion becomes larger, and more realistic owing to the development of special-purpose hardware (Sugimoto *et al.* 1990, Ebisuzaki *et al.*

1993, Makino *et al.* 1997) and software algorithms (Makino 1991, Makino and Aarseth 1992). According to the latest results, a number of medium-sized protoplanets would be formed having nearly equal separations with low eccentric orbits in the final stage of planet accretion through the runaway growth in the swarm of planetesimals (Kokubo and Ida 1998). Typical mass of the protoplanets is $0.1M_\oplus \sim 0.2M_\oplus$ at $a = 1$AU, where $M_\oplus$ is the mass of the Earth and a is the semimajor axis. Typical separation between the protoplanets is around $8R_H$ such as $0.02\text{AU} \sim 0.04\text{AU}$ at $a = 1$AU (Note that the description "10 Hill radius ($10r_H$) of separation" in Kokubo and Ida (1998) is nearly equal to $8R_H$ when measured by the mutual Hill radius. See Appendix). Orbits of protoplanets are nearly circular due to the equi-partition of energy (dynamical friction), and the growth of protoplanets slows down along with the decrease of the number of planetesimals around each protoplanet. It makes the system quite stable, and the timescale of evolution becomes longer after the stage of runaway growth of protoplanets. The stability of equal-mass, equal-separated self-organized protoplanet system has been investigated by Chambers *et al.* (1996). The system can be approximated by a Hamiltonian system since the frequency of physical collision among particles becomes less. Hence it is meaningful to consider the late stage of planet formation which consists of medium sized protoplanets as a Hamiltonian system, and to analyze it by the traditional method of celestial mechanics. It will be beneficial because the Hamiltonian dynamics can be handled for very long timespan with high accuracy.

In this paper our target is the final stage of planet formation. We investigate the motion of protoplanets under the perturbation by the jovian planets using the numerical integration and the secular perturbation theory. Though there are some former researches which considered the formation stage of the terrestrial planets from the protoplanets (e.g. Lecar and Aarseth 1986), our approach has its novelty taking the effect of the secular perturbation from outside the terrestrial region. We confirmed that the secular perturbation by jovian planets, especially Jupiter and Saturn, can accelerates the instability of the terrestrial protoplanet system. Standing on the results of Kokubo and Ida (1998), Chambers *et al.* (1996) and our calculation, we propose a possible working hypothesis for the late stage of planet formation divided in three parts. (1) Runaway and slow-down of growth of protoplanets. (2) Drastic increase of mass of the jovian planets (Jupiter and Saturn) by rapid gas capture. (3) Instability of terrestrial protoplanet system due to the secular perturbation from the jovian planets. Difference of separations between the terrestrial planets and the jovian planets may be explained by the difference of formation process in the late stage we notice here.

In Section 2 we give a brief summary on the previous researches of the planet accretion and their problems. Section 3 is devoted to show our results of calculation on the instability in the terrestrial protoplanet systems. Some more discussion is given in Section 4 on the secular perturbation by jovian planets. Section 5 goes on the discussion, implication and problems on the results.

2 Late stage of planet formation in the terrestrial zone

Here we review the late stage of planet formation through two phases: runaway growth of planetesimals into protoplanets, rapid gas capture of jovian protoplanets. Instability of the

terrestrial protoplanet system by the perturbation from jovian planets is suggested.

Runaway growth of planetesimals into protoplanets. Runaway growth of protoplanets in the swarm of planetesimals are recently well investigated by the gravitational N-body numerical simulations. As a result, protoplanets of nearly equal masses ($0.1M_\oplus \sim 0.2M_\oplus$ at 1AU) with equal separations ($\sim 8R_H$) are expected to form. First we give a brief summary of the previous researches following Kokubo and Ida (1995, 1996, 1998) concerning the runaway growth of planetesimals into protoplanets.

It is generally accepted that terrestrial planets and the cores of jovian planets are formed through the accretion of planetesimals. Wetherill and Stewart (1989) found that the growth of planetesimals is dominated by the positive feedback called runaway growth by studying the coagulation equation of planetesimals. The theory has been reinforced by the statistical approach and direct gravitational N-body simulations. Beginning from the homogeneous distribution of planetesimals, runaway planetesimals called protoplanets break the homogeneity by their strong gravitational perturbation (Ida and Makino 1993). Neighboring protoplanets grow keeping their orbital separation about several R_H with low eccentricities by the orbital repulsion mechanism. Increase of their mass makes them close gravitationally, and the protoplanets scatter each other. It leads to the increase of eccentricities and orbital separation. Then, the dynamical friction among the planetesimals reduces the eccentricities of protoplanets while the orbital separations or semimajor axes remain almost the same. Typical separation of two neighboring protoplanets is about $8R_H$ (or $10r_H$) with weak dependence on the semimajor axes, masses, and the surface number density of the planetesimals. Typical mass of the protoplanets is about $0.2M_\oplus$ with the typical separation about 0.07AU at 1AU, and $17M_\oplus$ with the typical separation 8AU at 25AU when all the planetesimals are accumulated into protoplanets. In the case of terrestrial planets, the estimated mass and the orbital separation are still smaller than the present values. Some kind of instability had to make the protoplanets system unstable and collide with each other, and make them grow compellingly. Growth timescale of protoplanets becomes longer in the more distant region from the Sun. Protoplanets at near 1AU reach the typical sizes and separations by around $10^4 \sim 10^5$ years, whereas the cores of jovian protoplanets, especially those of Jupiter and Saturn, take $10^6 \sim 10^7$ years.

Protoplanet system thus formed is quite stable since the orbits of protoplanets are nearly planar and circular. In this stage the number of planetesimals is decreased, which leads to the slow-down of growth of the planetesimals. On the stability of such protoplanet system, an intensive numerical study of Chambers, Wetherill and Boss (1996, hereafter called CWB) based on the detailed study of two-planet systems by Gladman (1993) gave an answer. They placed the equal-mass protoplanets ("planetary embryos" they call) with equal normalized separation in the planar orbits, and integrated them numerically. They measured the instability time which is defined by the time till the occurrence of the first close encounter (close approach within the mutual Hill radius). Then, the relationship between the logarithm of instability time T_I and initial separation normalized by the mutual Hill radius is well approximated by the linear function. For example, consider the case when the twenty bodies with masses $1.0 \times 10^{-7}M_\odot$ ($M_\odot$ is the solar mass) locate initially having the equal separation of about $10R_H$ in circular orbits. It corresponds to the situation in the terrestrial region described in Kokubo and Ida

(1998). In this case, results of CWB show that the instability time can be extrapolated up to $10^6 \sim 10^7$ years with uncertainty of one order of magnitude due to the difference of initial distribution of longitudes. Actual three dimensional orbits may lengthen the instability time more. It may suggest that the terrestrial protoplanet system might keep global stability till the end of the formation of the cores of Jupiter and Saturn within $10^6 \sim 10^7$ years, though local instability might occur.

Rapid gas capture of jovian protoplanets. Unlike terrestrial planets, jovian planets have been formed from significant quantity of the gas of the solar nebula around the solid core accumulated from the planetesimals. When the mass of the jovian cores exceeds a limit, the gas around the planets begins to fall in due to their strong gravitational attraction (Mizuno *et al.* 1978, Mizuno 1980). This limit of mass is called the critical core mass. Bodenheimer and Pollack (1986) carried out an evolutionary calculation of the core instability model. They showed that the accretion rate gets much larger than that of planetesimals when the mass of the core exceeds the critical core mass. This instability is considered to be the cause of the formation of atmosphere of the jovian planets. Calculations of the runaway growth of protoplanets indicate that the estimated mass and the orbital separation of the protoplanets in the jovian region may be consistent with the present configuration: the sizes of protoplanets in the jovian region is of the same order with the critical mass of the cores of Jupiter and Saturn, and with total mass of Uranus and Neptune with less gas envelope. Upper limit of the timescales of rapid gas capture is considered to be $10^6 \sim 10^7$ years according to the numerical calculations (Pollack *et al.* 1996, Tajima 1998).

Instability in the terrestrial protoplanet system. Separation, number and mass of the protoplanets in the terrestrial region which are quite different from the present configuration give us a problem, not easily solved; their sizes and normalized separation must become larger, and their number becomes less toward the present state. Evolutionary timescale may be too long to form the terrestrial planets within a realistic period as implied by the research of CWB. It is necessary to introduce some kinds of instability mechanism. We expect that rapid increase of mass of Jupiter and Saturn by gas capture enables their secular perturbation to be effective in the terrestrial region. In the next section we investigate how stable or unstable the terrestrial protoplanet system is, and measure the instability time, extending the numerical experiments of CWB.

3 Stability of the terrestrial protoplanet system

Two kinds of systems are investigated: autonomous protoplanet systems without perturbation from outside, and protoplanet systems perturbed by jovian planets. We consider two cases as perturbed protoplanet systems. One is perturbed by both Jupiter and Saturn, and the other is perturbed only by Jupiter. Effect of initial velocity dispersion and mass distribution are also included.

3.1 Models and methods

We place ten to twenty protoplanets whose total mass is about $2M_\oplus$ (close to the total mass of the present terrestrial planets) in the region of terrestrial planets, beginning at $a_1 = 0.25$AU to 0.5AU with equal separation $\Delta \times R_H$. a_1 is the semimajor axis of the innermost protoplanet, and a parameter Δ controls the planetary separation. Semimajor axis of the $i+1$-th protoplanet is determined by an implicit relationship $a_{i+1} = a_i + \Delta \times R_H^{i,i+1}$. See Appendix for definition of $R_H^{i,i+1}$. Spatial distributions of protoplanets differ from model to model. a_1 is adjusted from model to model so that the spatial distribution of the protoplanet does not overlap the zone of mean motion resonance with Jupiter, especially 5:1 resonance at near $a = 1.8$AU. Number of protoplanets is denoted by N.

Integration is continued until the first close encounter happens somewhere in the system. We define that a system experiences a close encounter when either two bodies approach one another within the size of the larger activity sphere (the sphere of influence), $(m/M_\odot)^{\frac{2}{5}} d$ where d is the heliocentric distance (Danby 1992). Within the activity sphere, it may be dynamically natural to consider a protoplanet as moving in an orbit around another protoplanet, instead of the Sun. The quantitative results are not largely affected if we change the critical distance from the radius of the activity sphere to the Hill radius, $(m/3M_\odot)^{\frac{1}{3}} d$. All celestial bodies are handled as point masses. No consideration for relativity, tidal forces, gas drag, and other non-gravitational or dissipative effects are taken into. When the system does not experience any close encounters, integration is terminated after 5×10^7 years.

We utilized the second order symplectic mapping as the integration method (Wisdom and Holman 1991, Kinoshita *et al.* 1991) with a special start-up procedure to reduce the truncation error of angle variables, "warm start"(Saha and Tremaine 1992, 1994). Symplectic mapping with warm start is quite a fast and accurate tool for numerical integration of perturbed dynamical systems. We used fixed stepsizes from five to ten days, depending on a_1. The integration seems to be accurate enough until the first close encounter occurs: for example, the averaged relative errors of total energy ($\langle \delta E/E_0 \rangle \sim 10^{-9}$ where δE is the maximum change of the total energy and E_0 is its initial value) and of total angular momentum ($\langle \delta L/L_0 \rangle \sim 10^{-14}$ where δL is the maximum change of angular momentum and L_0 is its initial value) are kept nearly constant until the first close encounter. Warm start reduces the averaged relative error of the total energy by one order of magnitude or more in this case compared with the symplectic mapping without it.

It is difficult to apply the symplectic mapping to the situations with a lot of close encounters among celestial bodies in general. Although several methods are proposed to handle close encounters (Levison and Duncan 1994, Mikkola 1997), we did not adopt them here since we concentrate on measuring the instability time defined by the period till the first close encounter as the typical timescale of the evolution of the system. Calculation of instability time or making a CWB-type diagram is only equivalent to draw a snapshot of the protoplanet evolution. However, though accurate calculations which handle scattering and collision of protoplanets under the effect of jovian planets is absolutely necessary, we consider that it is possible to make a successive story on the late stage of planet formation by inspecting the numerical results on the instability times for various dynamical models.

3.2 Initial conditions

The velocity dispersion of protoplanets formed through the runaway accretion of planetesimals is one of the key parameters for the instability time. The initial distribution of eccentricities e and inclinations I of planetesimals is reasonably represented by the Rayleigh distribution with the probability density function (Ida and Makino 1992)

$$f(e)de^2 = \frac{1}{\langle e^2 \rangle} \exp\left(-\frac{e^2}{\langle e^2 \rangle}\right) de^2, \quad f(I)dI^2 = \frac{1}{\langle I^2 \rangle} \exp\left(-\frac{I^2}{\langle I^2 \rangle}\right) dI^2. \tag{1}$$

with dispersions $\langle e^2 \rangle^{\frac{1}{2}}$ and $\langle I^2 \rangle^{\frac{1}{2}}$, respectively. We assume that the protoplanets formed through the runaway growth of planetesimals also obey the Rayleigh-type distribution, and satisfy $\langle e^2 \rangle^{\frac{1}{2}} = 2\langle I^2 \rangle^{\frac{1}{2}}$. According to the results of numerical N-body simulations (Kokubo and Ida 1998), $\langle e^2 \rangle^{\frac{1}{2}}$ is less than 0.005. In the terrestrial protoplanet system, $\langle e^2 \rangle^{\frac{1}{2}} = 2\langle I^2 \rangle^{\frac{1}{2}} = 0.005$ is nearly equal to $1h$ where $h \equiv r_H/d = (m/3M_\odot)^{\frac{1}{3}}$ is the reduced Hill radius. When $m = 0.1M_\oplus = 3 \times 10^{-7} M_\odot$, we have $h = (3 \times 10^{-7}/3)^{\frac{1}{3}} = 0.0046$.

The initial values of the mean anomaly are selected randomly from a uniform distribution subject to the constraint that the longitudes of bodies on adjacent orbits differ by at least 20°. The initial values of the longitude of perihelion ϖ, the longitude of ascending node Ω are randomly selected from 0° to 360°.

Dependence of the instability time on the initial orbital elements $(e_0, \varpi_0, I_0, \Omega_0, l_0)$ becomes larger when the velocity dispersion increases compared with the case with initially planar and circular orbits. In the case of $\langle e^2 \rangle^{\frac{1}{2}} = 2\langle I^2 \rangle^{\frac{1}{2}} = 0.005$, variation range of the instability time is of one to two orders of magnitude depending on the initial coordinate (Fig. 1(a)). We have FIG. 1
to perform several integrations and get average of the results for quantitative discussion. Note that we have adopted the logarithmic averaging since the data show nearly uniform distribution on the log-scale graph. We hereafter call the diagram of $(\Delta, \log T_I)$ the CWB diagram.

Logarithmic average of the instability times seems to converge to a unique value when the number of repetition for the random initial orbits increases. We can see that five to ten times of repetition produce nearly the same averaged values in Fig. 2. So we plot the CWB diagrams FIG. 2
using four to five initial conditions in the following sections. In some region of large Δ which needs quite a long time for calculation we have plotted two or three points and averaged them. We also consider the mass distribution of the protoplanets for two cases: small or no variation of mass, and large variation of mass. We consider the uniform distribution of protoplanet masses. For example, one of the cases of small mass variation corresponds to $2.5 \times 10^{-7} M_\odot < m < 3.5 \times 10^{-7} M_\odot$ with the average mass $\langle m \rangle = 3.0 \times 10^{-7} M_\odot$. A case of large mass variation corresponds to $2.0 \times 10^{-7} M_\odot < m < 8.0 \times 10^{-7} M_\odot$ with the average mass $\langle m \rangle = 5.0 \times 10^{-7} M_\odot$. Distribution function of protoplanet mass is one of the key factors to determine the evolutionary timescale of protoplanets into planets, and future individual researches are needed.

3.3 Autonomous protoplanet systems

Autonomous systems here denote the protoplanet systems without any perturbation from outer giant planets. On the stability of the autonomous protoplanet systems, detailed investigations have been done in CWB in the case of planar and initially circular orbits. Since the

present separation of the terrestrial planets is larger than $25R_H$ (Table I), we extended the CWB diagram up to $\Delta = 17$ of the autonomous systems. Extension to the three-dimensional case does not change the qualitative feature of $\log T_I \propto \Delta$ (Fig. 3(a)). The instability time seems to become limitlessly longer when Δ increases. FIG. 3

We can list two major causes of the instability of autonomous protoplanet systems: the velocity dispersion (random velocities coming from $\langle e \rangle$ and $\langle I \rangle$) of the protoplanets, and the mass distribution of the protoplanet. Dependence of the instability time on the initial velocity dispersion is large. Figure 1(b) shows the averaged CWB diagram of $\langle e^2 \rangle^{\frac{1}{2}} = 2\langle I^2 \rangle^{\frac{1}{2}} = 0.005, 0.010, 0.015,$ and 0.020 for $4 < \Delta < 10$. The lines denote the logarithmic average of the results of ten integrations for each set of initial velocity dispersion. In the case of $\langle e^2 \rangle^{\frac{1}{2}} = 2\langle I^2 \rangle^{\frac{1}{2}} = 0.015 = 3.26h$, instability time is reduced by one order of magnitude or more compared with the case of $\langle e^2 \rangle^{\frac{1}{2}} = 2\langle I^2 \rangle^{\frac{1}{2}} = 0.005 = 1.07h$. The non-equal mass distribution also reduces the instability time of the autonomous protoplanet system. This is ascribed to the energy equi-partition by which the velocity dispersion of the small-mass bodies goes up, and enhanced eccentricities increase the probability of close encounters (CWB).

As the evolution of protoplanet system goes on, the velocity dispersion and mass distribution would be enhanced. These two facts accelerate the instability of the protoplanet system and the evolution into the present planetary system. However, collisional evolution of the protoplanet system means that the total number of the bodies decreases and the averaged mass of the bodies increases. Decrease of the total number of protoplanets reduces the probability of encounters, which will lead to the deceleration of the instability. Also, according to the numerical results of CWB, increase of average mass causes the increase of the instability time because it seems that an appropriate unit of distance in the multi-body case varies as $m^{\frac{1}{4}}$ instead of $m^{\frac{1}{3}} \propto R_H$. An extreme example of the numerical results in the case of high velocity dispersion ($\langle e^2 \rangle^{\frac{1}{2}} = 2\langle I^2 \rangle^{\frac{1}{2}} = 0.015$) and large mass distribution ($2.0 \times 10^{-7} M_\odot < m < 8.0 \times 10^{-7} M_\odot$ with the average mass $\langle m \rangle = 5.0 \times 10^{-7} M_\odot$) is shown in Fig. 3(b). In this case, the instability times can be extrapolated to nearly 10^7 years at $\Delta \sim 17$, and will be longer toward the present value of $\Delta > 25$. In addition, too large velocity dispersion can prevent the planets produced by the accumulation of protoplanets from having nearly circular and planar orbits since the velocity dispersion must increase through collision and scattering among protoplanets. The present eccentricity of the Earth is as small as 0.0167 which is equivalent to $1.67h$, and that of Venus is $0.0068 = 0.73h$. Though the enhanced eccentricities and inclinations must be calmed down by some kind of dissipative mechanism such as gas drag by the solar nebula, $\langle e^2 \rangle^{\frac{1}{2}} = 2\langle I^2 \rangle^{\frac{1}{2}} = 0.015 = 3.26h$ may be an extreme estimation. Actual timescale of instability would lie between the midpoint of the two extrema of low and high velocity dispersion cases.

As for the autonomous planetary systems, present jovian planetary system is actually a typical example. It is not under any perturbation by more massive perturbers. Their separations are similar to those of the terrestrial protoplanet system, $8 < \Delta < 14$ (Table I). The velocity dispersion is small, e.g. the eccentricity of Jupiter is $0.0485 = 0.7h$. They have large mass variation such as Saturn/Uranus ~ 6.54. Results of the long-term numerical integration (Kinoshita and Nakai 1996) and the high-order theory of secular perturbation (Laskar 1996) show that the orbits of jovian planets are stable for over 10^{10} years, about 10^9 revolutions of Jupiter. This

may be another indirect testimony which indicates the stability of the autonomous protoplanet systems with small velocity dispersion.

Thus the autonomous protoplanet system is too slow to evolve into the present form of planets. We have to take into account some kind of acceleration mechanism for instability in the growth process of terrestrial protoplanet system. In the following sections we perform the numerical experiments for measuring the instability time of protoplanet systems perturbed by jovian planets, mainly in the case of small velocity dispersion.

3.4 Perturbed protoplanet systems

3.4.1 Restricted cases

We performed some numerical experiments to examine the stability of the perturbed protoplanet systems under the disturbance of Jupiter and Saturn. Initial orbital elements of Jupiter and Saturn are taken from DE245 of JPL/NASA (cf. Standish 1990). We do not consider the effect of dynamical growth (increasing mass) or the migration (secular change of the semimajor axes) of jovian planets. Masses of jovian planets are fixed in our calculation.

On the orbital evolution of small particles under the perturbation by more massive bodies, we first think of the purely restricted problems which handle the motion of massless particles like artificial satellites, asteroids, or comets. The mass ratio of Jupiter to protoplanets is more than 10^3 to 10^4, so it would seem reasonable to consider them as the restricted problems, which is soon proved to be incorrect. But it is still meaningful to know the behavior of the restricted cases to understand the similarity and difference from the non-restricted cases. So at first we briefly explain some characters of the restricted cases.

In the case of the restricted problem under the perturbation by Jupiter and Saturn, secular resonance is one of the most important causes of the enhancement of eccentricities of the perturbed bodies. In particular, the synchronized oscillation of the longitudes of perihelion ϖ of the perturbed body and Jupiter with the period of about 300000 years is important. It is called the secular resonance ν_5 where the secular frequency of the massless particle becomes equivalent to one of the planetary basic frequencies, g_5 (Williams 1969). g_5 is close to the frequency of the circulatory motion of Jupiter's longitude of perihelion, ϖ_J. Mean motion resonances with Jupiter or Saturn do exist, but the regions are mainly in the midst of asteroidal belt, away from the orbit of Mars.

In general, when there are n perturbers in the planetary system, the semimajor axis a of the perturbed body at which secular resonance occurs can be determined by solving the following equation derived from the linear theory of secular perturbation (Brouwer and Clemence 1961, Gomes 1997)

$$g_i = \frac{1}{4}\sqrt{\frac{Ga}{M_\odot}}\sum_j^n \frac{m_j}{a_j^2} b_{3/2}^{(1)}(\alpha_j) \equiv g(a) \quad (i = 1, \cdots, n), \tag{2}$$

where G is the gravitational constant, m_j and a_j are the mass and the semimajor axis of the j-th perturber, $b_{3/2}^{(1)}$ is the Laplace coefficient, and $\alpha_j = a/a_j$. $g_i (i = 1, \cdots, n)$ are the basic planetary frequencies that are functions of m_j and a_j. To get the zone of secular resonance ν_5, we put $g_i = g_5$ in the left-hand side of Eq. (2), and solve for a. Then we get $a = 0.72$AU as the

semimajor axis of secular resonance ν_5 in the case that the four jovian planets are perturbers. A solid line named "JSUN" in Fig. 4 represents the secular frequency $g(a)$ as a function of semimajor axis a under the perturbation from four jovian planets. Intersection of the solid line and the dotted line named "g_5" indicates the semimajor axis of the secular resonance ν_5. FIG. 4

The value of g_5 is little modified even when we remove two outer jovian planets (Uranus and Neptune) from the system because of their smaller mass than the two inner planets. Hence in most of our numerical calculation, we have neglected Uranus and Neptune to reduce the amount of calculation. It is not unreasonable because the formation timescale of the outer part of jovian planets is considered to be fairly long. Existence of Uranus and Neptune would become effective only in the very latest stage of the planet formation for the terrestrial protoplanet system. Note that the value of g_5 is somewhat different depending on whether we consider or not the term derived from the 5:2 mean motion commensurability between Jupiter and Saturn called "the great inequality" into the original disturbing function in the procedure of getting the basic planetary frequencies $g_i (i = 1, \cdots, n)$ (Hill 1897, Brouwer and van Woerkom 1950). If we omit the effect of the great inequality, the value of g_5 becomes smaller by several percent, and the location of ν_5 shifts inward. The fact, though not of much qualitative significance, is clearer in Section 4 where comparison between the numerical integration and the secular perturbation theory is performed.

One of the results of the numerical integration is Fig. 5, showing the time evolution of eccentricities of several massless particles (a = 0.40AU, 0.68AU, 0.72AU, 0.76AU, 1.22AU) under the effect of Jupiter and Saturn. The largest eccentricity which exceeds 0.5 is that of a particle close to the zone of the secular resonance ν_5 (a = 0.72AU). Eccentricities are large near around ν_5 zone (a = 0.68AU and a = 0.76AU), but rapidly decrease as the particles leave the resonance area (a = 0.40AU and a = 1.22AU). Thus the width of the secular resonance ν_5 is not so wide. The relationship between eccentricity and difference of longitude of perihelion $(e, \varpi - \varpi_J)$ clearly shows the feature of secular resonance (Fig. 6(a)). $\varpi - \varpi_J$ librates around 180°, and the eccentricity of the perturbed body is pumped up to 0.5 toward the libration center. FIG. 5 FIG. 6

Enhancement of the eccentricity in the secular resonance area is well reproduced by the semi-analytical equi-Hamiltonian map as in Fig. 6(b). Based on the averaging theory by Lie transformation (e.g. Hori 1966, Deprit 1969), the Hamiltonian can be averaged in terms of the fast moving variables, and degrees of freedom can be reduced to one if we assume that only Jupiter affects the protoplanets and its orbit precesses uniformly keeping the ellipse fixed in the invariable plane; the system can become integrable up to the first order approximation (Nakai and Kinoshita 1985). Then we can track the motion of a massless particle under the secular perturbation by Jupiter along the contours of equi-Hamiltonian map. Figure 6(b) shows a good agreement with the result of numerical integration (Fig. 6(a)), and indicates that a particle with initially small eccentricity can have quite a large value by the secular resonance with Jupiter.

However, such a large amplitude of eccentricity of protoplanets is not convenient to make the present terrestrial planets which have nearly circular orbits. Thus the approximation by the superposition of restricted problems seems to be excluded.

3.4.2 Non-restricted cases with small mass variation

The actual behavior of the protoplanets with non-zero mass is different from the one deduced from the superposition of restricted problems. When we take the finite mass of the protoplanet into account, their own existence "blocks" the effect of secular resonance by Jupiter and Saturn: Let us consider a case with Jupiter, Saturn, and several protoplanets as perturbers, not as perturbed bodies. In this case, we can again solve Eq. (2) and get the secular frequency as a function of semimajor axis. The oscillatory line in Fig. 4 named "20 protoplanets + JSUN" illustrates the $(a, g(a))$ diagram of the system with twenty protoplanets with equal masses ($m = 3 \times 10^{-7} M_\odot = 0.1 M_\oplus$) and equal separation $\Delta = 14$, Jupiter, and Saturn. A simple theory of linear perturbation used here is not applicable in the area very close to the position of perturbers; there are singularities around the semimajor axes of perturbers (singularities in calculating the Laplace coefficients $b^{(1)}_{3/2}(\alpha_j)$ at $\alpha_j \to 1$). But it is clear that the zone of the secular resonance ν_5 migrates far inward from Jupiter due to the mutual interaction of protoplanets themselves. The variation amplitude of eccentricity by ν_5 must be much smaller than the case of the restricted problems. This can be seen in the equi-Hamiltonian map (Fig. 6(c)). We placed twenty protoplanets with circular orbits as perturbers in addition to Jupiter, and averaged the Hamiltonian of a massless particle near the zone of ν_5, $a = 0.72$AU. In this case, no libration region is seen in the $(e, \varpi - \varpi_J)$ diagram. It means that the secular resonance ν_5 with Jupiter is suppressed to a large extent. Variation amplitude of eccentricity becomes much smaller. Actually it is not a correct approximation to consider protoplanets as perturbers since their orbits moves under the perturbation from jovian planets. In a word, protoplanets act as perturbers as well as perturbed bodies in the actual system. But the suppression of the secular resonance in the protoplanet system is also realized in the numerical integrations later, which shows some validity of the approximation.

As mentioned in the previous section, too large eccentricities of the protoplanets are not convenient to explain the low eccentricities of the present terrestrial planets, especially Venus and the Earth. Protoplanets with non-zero mass prevent themselves to suffer from too strong secular resonance with jovian planets, and keep their eccentricities moderately low. Secular resonance with Jupiter will be again important and effective when the mutual interaction of protoplanets is weakened due to the creation of mass distribution.

One of the CWB diagrams in the case of perturbed protoplanet systems ($N = 17$) with Jupiter and Saturn having small velocity dispersion ($\langle e^2 \rangle^{\frac{1}{2}} = 2 \langle I^2 \rangle^{\frac{1}{2}} = 0.005$) and small mass variation ($2.5 \times 10^{-7} M_\odot < m < 3.5 \times 10^{-7} M_\odot, \langle m \rangle = 3.0 \times 10^{-7} M_\odot$) is shown in Fig. 7(a). Small variation of spacing is also added between $0.8 \Delta R_H$ and $1.2 \Delta R_H$. Compared with the autonomous case (Fig. 3(a)), the instability time is little shorter in low Δ region. There seems a little reduction in T_I in high $\Delta (> 17)$ area, but the absolute value of the instability time is near 10^7 years. Little reduction in the instability times is probably due to the prevention effect by the mutual interaction among protoplanets from secular resonance with Jupiter mentioned above. Figures 7(b) and 7(c) show the semimajor axis and the serial number of the inner protoplanets of the pair which exhibited the first close encounter, respectively. Inner protoplanets are likely to be unstable earlier than the outer ones, possibly because of their short timescale of revolution. FIG. 7

In the numerical calculation for Fig. 7 we have reduced the number of protoplanets to $N = 17$,

from $N = 20$ in the case of autonomous system (cf. Fig. 3). This is to avoid the confusion of the effects of secular resonance and mean motion resonance (a little more discussion is given in Section 5). To explain this, we performed some numerical experiments which is similar to $N = 17$ case in Fig. 7 but with three additional protoplanets, $N = 20$. One of the resulting CWB diagrams is shown as Fig. 8(a). Figures 8(b) and 8(c) show the semimajor axis and the serial number of the inner protoplanets of the pair which exhibited the first close encounter, respectively. Inner protoplanets are likely to be unstable earlier than the outer ones. But in large Δ area as $\Delta > 18$, furthermost protoplanets become selectively and rapidly unstable. Semimajor axes of the furthermost protoplanets reach around 1.8AU when $\Delta > 17$ in this case, near the 5:1 mean motion resonance with Jupiter (Fig. 8(b)). As well as the famous 2:1 or 3:1 mean motion resonance with Jupiter, 5:1 resonance is also strong enough to enhance the eccentricities of the perturbed bodies which immediately leads to close encounters among neighboring bodies (Yoshikawa 1989). Mean motion resonance itself is quite a significant problem, and must have occurred. It would be the cause of the gaps in the asteroidal belt and of the enhancement of the random velocity of asteroids. But here what we are interested in is the instability time of the terrestrial protoplanet system which may have produced the Earth or Venus. So we concentrate on the secular resonance ν_5 which can be effective within the orbit of Mars, instead of the mean motion resonances with Jupiter mainly effective in the asteroidal belt. FIG. 8

Figure 9 shows some more detailed look at the orbital evolution of protoplanets for the first 500000 years in the system calculated for the CWB diagram of Fig. 7(a) at $\Delta = 13.0$. Resonance with the motion of Jupiter's perihelion is only slightly recognized. Enhancement of eccentricities is small. Dynamical link among protoplanets are strong enough to "block" the effect of the secular resonance ν_5 at the narrow separation of $\Delta = 13.0$. On the other hand at $\Delta = 19.0$, resonant motion of perihelia becomes clearer, and the enhancement of eccentricities are larger with the period of 300000 years (Fig. 10); it is the secular resonance ν_5. As the spacing among protoplanets becomes larger, dynamical interaction among protoplanets becomes less, and the blocking effect of protoplanet system against the secular resonance may thus be weakened. A little reduction of the instability time in high Δ region in the CWB diagram (Fig. 7(a)) compared with the autonomous systems is probably the result of such kind of forced increase of eccentricities by the secular resonance. FIG. 9 FIG. 10

Secular resonance in the case of protoplanet system with finite mass thus described is quite interesting in itself. Unlike the restricted problems, perihelia of many of the protoplanets move together; not only their frequencies are nearly the same, but also their phases are nearly synchronized with Jupiter in spite of the initially random distribution of the perihelia. Their eccentricities also show similar concurrence. They vary almost simultaneously, though their amplitudes are still much smaller than the case of restricted problems. We will mention a little more on the secular resonance in the protoplanet systems in Section 4.

3.4.3 Larger mass variation

Growth of protoplanets into planets does not proceed keeping the state of equal-mass; they would have produced some degree of mass distribution among them. Mass ratio among the present terrestrial planets (Earth/Mars $\sim$ 10, or Earth/Venus $\sim$ 1.2) implies that the proto-

planets themselves may have experienced a kind of runaway accretion processes toward the present planets as well as the planetesimals are considered to. In this case the Earth and Venus would be "runawayed" particles, and Mercury and Mars would correspond to remained particles. Variation of mass causes the enhancement of eccentricities of lighter bodies through the equi-partition of energy (dynamical friction) which leads to the overall reduction of the instability time.

Mass distribution of the protoplanets, not only causes the enhancement of random velocity through the dynamical friction, but also contributes to make the secular perturbation effective in the protoplanet system. Figure 11(a) shows a CWB diagram of perturbed protoplanet systems with large mass variation $2.0 \times 10^{-7} M_\odot < m < 8.0 \times 10^{-7} M_\odot$ with the average mass $\langle m \rangle = 5.0 \times 10^{-7} M_\odot$ under the effect of Jupiter and Saturn. $N = 14$ in this case. In $\Delta > 10$ area, we can recognize that the instability times are bounded under 10^6 years. It is considered to be owing to the effect of secular perturbation by jovian planets. Figures 11(b) and 11(c) show the semimajor axis and the serial number of the inner protoplanets of the pair which exhibited the first close encounter, respectively. Note that the effect of mean motion resonance with Jupiter becomes dominant in $\Delta > 16$ area. Furthermost protoplanets near 5:1 commensurability with Jupiter become selectively and rapidly unstable (Fig. 11(b)). There is another interesting point that the concentration of the location of close encounters near the inner boundary of the protoplanet system is not remarkable compared to the case of small mass variation (cf. Fig. 7(b) and 8(b)). The randomness of the location of close encounters is probably due to the effect of energy equi-partition; eccentricities of small protoplanets are enhanced, which leads to close encounters. FIG. 11

Evolution of the orbital elements of 14 protoplanets at $\Delta = 13.0$ is shown in Fig. 12. Here the character of the secular resonance ν_5 is clearer than the former case of small mass variation at the same Δ (Fig. 9). Synchronization of the longitudes of perihelion is more rigorous, and 300000-year oscillation of eccentricities is apparent. Degree of enhancement of eccentricities is larger than the system with small mass variation, which is probably the direct reason of reduction in the instability time. FIG. 12

Individual plots of each eccentricities and longitudes of perihelion give more information (Fig. 13). Behavior of neighboring protoplanets are similar, but varies little by little from inner to outer. In the motion of eccentricity, the 300000-year oscillation is clearer in the inner part of the protoplanet system. In the outer part of the system the amplitude of the 300000-year oscillation in eccentricities is weak, and the oscillation with shorter periods is dominant. In the motion of perihelion, near 1:1 or 2:1 secular resonance with Jupiter is apparent in all region. As long as the synchronization of perihelion movement is concerned, width of the secular resonance with Jupiter is more than 1AU which is wider than in the restricted cases. FIG. 13

Detailed and analytic explanation of such characters of the secular resonance in the protoplanet systems is not yet done, but now under our investigation. Instead, qualitative behavior of synchronization of perihelia or eccentricities has been reproduced by the first order perturbation theory as described in the next section.

4 Secular perturbation by the jovian planets

4.1 Secular resonance ν_5

As mentioned in the previous sections, secular resonance ν_5 exerting on the protoplanet system is characterized by the concurrent motion of perihelia and eccentricities of protoplanets and Jupiter, although the amplitude is largely suppressed by the mutual interaction among protoplanets compared with the restricted cases. Synchronized motion of protoplanets shown by the numerical integration is qualitatively reproduced by the first-order perturbation theory. Given the initial orbital elements $(a_{i,0}, e_{i,0}, \varpi_{i,0}, I_{i,0}, \Omega_{i,0})$ and mass m_i of the i-th body, the evolution of the orbital elements is expressed up to the first-order ($O(m)$) approximation of the disturbing function and second-order of eccentricity and inclination (Brouwer and van Woerkom 1950) as,

$$e_i \sin \varpi_i = \sum_{j=1}^{N} M_i^j \sin(g_j t + \beta_j), \quad e_i \cos \varpi_i = \sum_{j=1}^{N} M_i^j \cos(g_j t + \beta_j), \tag{3}$$

where N is the total number of the celestial bodies excluding the central star. The characteristic eigenfrequencies (basic planetary frequencies) g_i are functions of masses m_i and semimajor axes a_i, and they are obtained by solving the eigenvalue problem of $N \times N$ matrix derived from the equations of motion. Corresponding eigenvectors M_i^j and β_j are determined by the initial values $(e_{i,0}, \varpi_{i,0}, I_{i,0}, \Omega_{i,0})$. Equations and solutions for I_i and Ω_i can similarly be obtained. One of the resulting motions of perihelia and eccentricities starting from the same initial conditions with those of the numerical integration is shown in Fig. 14. Compare them with the results of numerical integration (Fig. 12). Synchronization of the eccentricities and longitudes of perihelion is well reproduced, but the amplitude of the eccentricity variation is smaller than the numerical integration. Note that the oscillation period of perihelia and eccentricities becomes a little longer (about 360000 years) than the numerical integration (about 300000 years). This is due to the neglect of the great inequality in the linear secular perturbation theory we used here as mentioned in the previous sections. Neglect of the great inequality reduces the value of g_5 a little, so the period of ν_5 oscillation ($2\pi/g_5$) becomes longer. Quantitative difference between the numerical integration and the secular perturbation theory indicates that the mechanism of secular resonance in the protoplanet system is largely affected by higher-order interaction ($O(m^2)$) among protoplanets.

FIG. 14

Concurrent motion of perihelia is also the case for the particles in the elliptic rings of Uranus shepherded by the nearby satellites (Kozai 1992, 1993). In the elliptic rings of Uranus, small particles are considered to be under the secular perturbation by the shepherding satellites, equatorial gravitational oblateness (J_2) of Uranus, and the Sun. Their perihelia are considered to move together with that of the inner and the outer shepherding satellites. The biggest difference is that the synchronization phenomena in the protoplanet system is also caused by the mutual interaction among protoplanets: protoplanets seem to shepherd each other, whereas the particles in the elliptic rings of Uranus seem simply to be shepherded by the perturbing satellites without little interaction among them.

4.2 Perturbation by a single perturber

In the actual solar system, there must be some time-lag after the formation stage of Jupiter till the formation stage of Saturn due to the difference of their distances from the Sun. In the meantime there is only Jupiter as a perturber, orbiting on nearly fixed ellipse. In this case, secular resonance ν_5 cannot occur because the perihelion of Jupiter does not move without the existence of Saturn. However, we show that the existence of a single perturber does affect the motion of protoplanets through an interesting resonance-like mechanism. We integrated a protoplanet system under the effect only of Jupiter. Figure 15 shows the time variation of FIG. 15
eccentricities and perihelia of the protoplanets initially placed on the same orbits as in the two-perturber case, Fig. 12. The perihelion of Jupiter is nearly fixed in the inertial space (actually it moves very slowly due to the interaction with protoplanets). Nevertheless there appears some synchronization again in the motion of perihelia and eccentricities of protoplanets with the period of about 150000 years. As the perihelia of protoplanets oscillate, their eccentricities increase up to 0.03, which is smaller than the two perturber case as in Fig. 12.

Individual plots of eccentricities and longitudes of perihelion again give more information (Fig. 16). Behavior of neighboring protoplanets are similar, but varies little by little from inner FIG. 16
to outer. In the outer protoplanet system, 15000-year oscillation is not remarkable, and the perihelia of protoplanets are likely to librate around the fixed perihelion of Jupiter, instead of circulation as in the inner protoplanet system. Libration of perihelia of the protoplanets is a character which was not seen in the case of the two-perturber cases.

The synchronization phenomenon in the single-perturber system is also well reproduced by the first-order secular perturbation theory (Fig. 17) as well as in the two-perturber system. FIG. 17
Compare them with the results of numerical integration (Fig. 15). Libration of perihelia is also seen in the result of secular perturbation theory, but the amplitude of eccentricities is smaller than the numerical integration. The oscillation period of perihelia and eccentricities becomes a little shorter than the case of numerical integration.

The enhancement of eccentricities should affect the instability time of protoplanet systems. The corresponding CWB diagram confirms our expectation (Fig. 18(a)). Logarithmic average FIG. 18
of the instability times is somewhat lower than what is expected from the linear trend seen in the autonomous systems in large Δ region. It implies that the instability of the terrestrial protoplanet system may be accelerated just after the formation of Jupiter has been finished, not waiting for the formation of Saturn. Figures 18(b) and 18(c) show the semimajor axis and the serial number of the inner protoplanets of the pair which exhibited the first close encounter, respectively. The randomness of the location of close encounters is similarly seen as in the two-perturber case, Fig. 11(b).

Synchronization of perihelia does not occur if the mutual interaction among protoplanets does not exist (i.e. restricted cases) as in Fig. 19. Figure 19 shows the time evolution of longitudes FIG. 19
of perihelion and eccentricities by the secular perturbation theory of 14 massless protoplanets under the effect only of Jupiter. Massless particles which locate on the same initial orbits as in Fig. 17 show no synchronization in the motion of perihelia nor eccentricities. As for the restricted cases, the situation — eccentricity of a perturbed body is enhanced according as the oscillation of perihelion under the effect of Jupiter orbiting on the fixed orbit — is similar to

the so-called "Kozai resonance" (Kozai 1962, Thomas and Morbidelli 1996). But the Kozai resonance is a different kind of phenomena from the synchronization in protoplanet systems. The Kozai resonance occurs in three-dimensional, highly inclined orbit of a test particle, whereas the synchronization of the orbits of the protoplanet system occurs in nearly two-dimensional (planar) cases. Moreover, we have confirmed that the synchronization of perihelion motion and the enhancement of eccentricities do not occur if the orbit of Jupiter is circular (Fig. 20). Figure 20 shows one of the numerical results of the time evolution of longitudes of perihelion and eccentricities of 14 protoplanets when the orbit of Jupiter is circular. Initial orbits of the protoplanets are the same as in Fig. 15. The Kozai resonance occurs even if the orbit of the perturber is circular (Kinoshita and Nakai 1991, Michel and Thomas 1996). We are now searching for the analytical explanation of the synchronization mechanism in the protoplanet system in the single-perturber case. FIG. 20

In relation to the concurrent motion of eccentricities and perihelion longitudes, we may consult the similar case in recent studies: concurrent motion of longitudes of ascending node of jovian planets under the influence of hypothetical solar companion (Innanen *et al.* 1997). In their numerical calculation it is shown that the jovian planets act as if they compose a rigid disk, keeping their mutual inclinations small and their nodes precessing with the same period and the same phase ("dynamical rigidity" they call). After some extensional calculation of theirs, we found that there are various kinds of state in dynamical rigidity, not only the synchronization of the ascending nodes and inclinations, depending on the parameters of perturbers and perturbed planets. This may suggest that the concurrent motion of eccentricities and perihelia in the case of the terrestrial protoplanet system is one of the representations of the dynamical rigidity.

5 Discussion

A working hypothesis on the late stage of planet formation. Numerical calculation of the CWB diagrams with Jupiter and Saturn as perturbers can help us to construct a possible working hypothesis on the final stage of planet formation after the runaway growth of planetesimals into protoplanets.

Terrestrial protoplanets are located having nearly equal separations around $8R_H$ just after they have been formed through the runaway growth of planetesimals. Their velocity dispersion is small, and instability time is long. As the collisional evolution of protoplanets proceeds, their number decreases and the normalized separation increases, which ever prolong the instability time. Scattering and collision among protoplanets increase their velocity dispersion and mass variation, both of which act as decreasing the instability time. But the averaged timescale of instability is still long, nearly 10^7 years (Fig. 3(b)). It means that the autonomous protoplanet systems with the separation $\Delta > 20$ would take quite a long time to evolve into the present configuration of planetary system, possibly longer than the age of the solar system.

In the meantime, jovian planets (Jupiter and Saturn) begin to capture the nebula gas rapidly and get the present mass within the timescale of $10^6 \sim 10^7$ years. At this point, growth of the jovian planets catch up, or even go ahead of, the growth of the terrestrial planets. When the jovian planets become massive, their gravitational effect on the terrestrial region becomes non-

negligible. Before the formation of Saturn has been finished, existence of Jupiter would cause the enhancement of eccentricities of protoplanets by a mechanism similar to the Kozai resonance or the dynamical rigidity. Enhanced eccentricities lead to the reduction in the instability time through the increment of collisional probability. In addition, secular resonance ν_5 becomes effective after the formation of Saturn. Enhancement of eccentricities becomes more remarkable, and the instability time gets shorter. In this stage, mass variation among protoplanets plays an important role in the acceleration of instability. The effect of the secular resonance ν_5 is suppressed largely by the mutual interaction of protoplanets, especially when the masses of protoplanets are nearly equal. As the collision among protoplanets goes on, mass distribution must be created which is considered to weaken the mutual interaction among protoplanets against the perturbation from outside. Thus the effect of secular perturbation becomes more effective in the later stage when the collisional evolution of protoplanets has proceeded to some extent.

Stability of the present planetary system. Now take a look at the present planetary system. Even under the gravitational perturbation from massive jovian planets, the orbital motion of the terrestrial planets seems to be stable for more than 10^8 years (Sussman and Wisdom 1992), and probably 10^9 years (Laskar 1996). Jovian planetary system whose normalized distances are much smaller than in the terrestrial planetary system seems also stable more than 10^{10} years (Kinoshita and Nakai 1996, Laskar 1996). Stability of the jovian planetary system whose normalized separation is not so large ($8 < \Delta < 14$) may be able to be explained: it is almost an autonomous system with small velocity dispersion, $\langle e^2 \rangle^{\frac{1}{2}} < 1h$. Mass variation among the jovian planets is large, but the smaller planets (Uranus and Neptune) locate further away from the larger ones (Jupiter and Saturn) having wide separation of about $14R_H$. It may reduce the effect of equi-partition of energy. Moreover, the instability time should be normalized by some characteristic period of the system when we compare the systems with different spatial scales. If we consider the mean motion as the characteristic frequency of the system, the actual instability time of jovian planetary system is one or two orders of magnitude longer than the autonomous protoplanet system in the terrestrial region having the normalized separation $8 < \Delta < 14$.

As for the stability of the present terrestrial planetary system, it is not so simple to explain it. It is still a perturbed planetary system under the effect of massive jovian planets. But their separation is much larger than the protoplanet systems we have investigated here. Their mutual interaction is not so strong as the protoplanet system. There is no prominent resonant relationship (neither secular nor mean motion) between any pair of terrestrial planets. Under the effective perturbation by Jupiter and Saturn, the instability time of the terrestrial protoplanet system can be shorter than 10^6 years according to the CWB diagram (Fig. 11(a)) if the mass variations of protoplanets is fairly large. During this stage having such a short timescale of instability, terrestrial planets may have been accumulated quickly, and the separation between Venus and the Earth has been enlarged up to $25R_H$. Mercury and Mars can be considered as remnant protoplanets. The origin of the moon may also be explained; one of the remnant protoplanets collided with proto-Earth in the final stage of the Earth formation. Accumulation

of a circumterrestrial disk of debris generated by the giant impact became a source of the Moon within a very short timescale of one year (Ida *et al.* 1997).

In this context, numerical experiments presented by Kimmo Innanen which was introduced by Asker (1997) is quite interesting; the stability of the terrestrial planets may be governed by the existence of the Earth itself. Following their presentation, we have confirmed that if we removed Mercury and the Earth and left Venus and Mars in the terrestrial planets, the orbit of Venus became largely eccentric ($e \sim 0.6$, Fig. 21(a)). Addition of Mercury makes the orbit of Venus calm down, but the orbit of Mercury itself becomes highly eccentric ($e \sim 0.8$, Fig. 21(b)). Only when the Earth is added, all the four planets behave as they are known to (Fig. 21(c)). These phenomena are explained by the migration of secular resonance. When only Venus and Mars are in the terrestrial region, Venus locates just on the zone of secular resonance ν_5 with Jupiter (Fig. 22(a)). See Fig. 4 as the relationship between the semimajor axis a and the secular frequency $g(a)$ of the perturbed body. Semimajor axis of Venus (0.723AU) is just on the zone of the secular resonance ν_5. Although Venus is not a massless particle, in this case its motion is well approximated by that of a massless particle on the secular resonance ν_5 with Jupiter. When Mercury is added, the situation becomes more complex: two or more secular resonances occur simultaneously (perihelion movements of Mercury and Venus (Fig. 22(b)), Mercury and Jupiter (Fig. 22(c))). Longitudes of perihelion of Venus and Jupiter also show a resonance-like motion. The existence of the Earth migrates the secular resonance ν_5 away from $a = 0.72$AU which is nearly equal to the semimajor axis of Venus, and the system becomes stable finally. Thus the stability of the terrestrial planets are kept by their own location which must be determined by the accumulation process of protoplanets into planets.

FIG. 21

FIG. 22

Problems and evidence. Effect of the secular perturbation by jovian planets may solve two problems simultaneously: one is the too long evolutionary timescale of terrestrial protoplanet system due to the isolation of protoplanets, and the other is the difference of normalized separation Δ between the terrestrial planets and jovian planets. Normalized separation in the terrestrial region seems to have been enlarged by the secular perturbation from the massive jovian planets. Due to the secular perturbation, terrestrial protoplanet system with small separation like $\Delta = 15$ cannot exist stably for the age of the solar system according to the CWB diagram of Fig. 11(a). On the other hand, to make the secular resonance ν_5 effective, narrower separation in the present jovian planetary system is necessary. If the normalized separation of the jovian planets are far wider than the present value, amplitude of the secular resonance will be much smaller, and the terrestrial protoplanet system may not evolve into the present stage within the reasonable timescale.

Of course our working scenario has many uncertainties which need future individual investigations in detail. For example, (1) evolution of velocity dispersion and mass distribution of the protoplanets, (2) relationship between the instability time and the actual collision timescale, (3) effect of gas drag and remnant planetesimals, (4) effect of the mean motion resonance with Jupiter outside the orbit of Mars, (5) formation timescale of jovian planets, and (6) detailed structure of the secular resonances by Jupiter and Saturn. On the other hand, There seem to be a few pieces of potential evidence in the dynamical and physical status of the present solar system which partly support our hypothesis.

Velocity dispersion and mass distribution are key parameters of the instability of protoplanet systems. Large velocity dispersion reduces the instability time much, but too large velocity dispersion is not convenient because the orbits of the present terrestrial planets, especially those of Venus and the Earth, are nearly planar and circular. Gas drag in the solar nebula and the dynamical friction by the remnant planetesimals has possibly acted to reduce the velocity dispersion which was enhanced by collisional evolution of protoplanets. However, nebula gas is considered to have been dissipated before the formation of terrestrial planets is completed, because the present atmosphere of the terrestrial planets is the secondary (degassed) atmosphere through the internal activity of the planets afterwards, not the primary atmosphere composed of captured nebula gas as in the jovian planets. The fact that the atmosphere of the terrestrial planets is not the captured one may be evidence of the earlier formation of Jupiter and Saturn which have the primary atmosphere. It is possible that the nebula gas has been dissipated after the formation of Jupiter or Saturn, before the terrestrial protoplanets finished the accumulation. As for the dynamical friction by the remnant planetesimals, it is not expected to be so strong since the number density of planetesimals must be much less due to the runaway accretion of protoplanets.

Relationship between the instability times defined in this paper and the actual collision timescales is not clear. Previous studies of restricted problems show that only a fraction of close encounters (defined by close approach within Hill radius or activity sphere) lead to the actual collision. Detailed two-dimensional calculation of the close encounters of planetesimals (Tanikawa *et al.* 1991) showed that the collisional probability of particles which entered within the Hill surface of the planet is at most 10% . If it can be applicable to the protoplanet systems, evolutionary timescale of protoplanet systems should be considered to be even longer, by several or several tens of times in the case of three-dimensional orbits.

Though we excluded the effect of mean motion resonances with Jupiter to concentrate on the instability caused by the secular resonance in the region of the present terrestrial planet, they should have played a significant role in the origin of the outer region of the terrestrial planetary system, including the asteroidal belts. Since the effective timescale of instability due to the mean motion resonances is shorter than that by the secular resonance (cf. Figure 8(a)), collision and scattering may have started at first in the outermost region of the terrestrial planetary system due to the mean motion resonances. But the random velocities of protoplanets produced by the mean motion resonances can be large, maybe larger than the escape velocities in the region, and they prevent the accumulation of the protoplanets into the planets. Non-existence of large planets outside the Earth may be a result by the large random velocities due to the effect of mean motion resonances with Jupiter. It may also be the case in the asteroidal belts.

Evolution of jovian planets is a difficult problem itself. What we suppose is their rather quick formation (e.g. Pollack *et al.* 1996, Fernández 1997). Large velocity dispersion in the asteroidal belt is one of the consequences which indicates that Jupiter had been formed before the protoplanets in the terrestrial and asteroidal region were able to complete their accretion. It stands on the claim that the planetesimals in those region had been strongly scattered before the growth to the protoplanets. The consequence is now observed as the total mass of the asteroids of only $10^{-3}M_{\oplus}$ which is much less than that expected to have been present in the region of a smoothly varying protoplanetary disk, and the small size of Mars (Lissauer 1987). Velocity

dispersion of the asteroids are much larger than the escape velocities from their surfaces, which may also show evidence of stirring from outside.

Timescales of gas capture of Jupiter and Saturn is also certified from another point of view that the migration of Jupiter and Saturn during their formation caused the migration of the secular resonance ν_6 and ν_{16} which leads to the enhancement of eccentricities in the asteroidal belt (Gomes 1997). Gomes considered the inward drift of Jupiter and outward drift of Saturn which causes the migrating effect of secular resonance in the asteroidal region. He concluded that the accretion time of Jupiter is about 10^6 to 10^7 years, which is consistent with the result of the direct calculation of gas capture. Maximum and minimum of the accretion time are limited by the present population and eccentricities of the asteroidal belt. Lecar and Franklin (1997) also took into account the scanning of secular resonance by the dispersal of the solar nebula advocated by Ward (1976, 1981) and tried to explain the eccentricities and existence of gaps in the asteroidal belt.

To include accurately the effect of accretion of Jupiter and Saturn, we should perform some numerical experiments with varying mass of Jupiter and Saturn. But our calculation assuming the present masses and orbits of jovian planets has partly its validity. Timescale of instability in the autonomous protoplanet systems with the normalized separation $\sim 18R_H$ is as long as 10^7 years (Fig. 3(b)), which may be comparable with the total timescales of the core accumulation by the runaway growth and the rapid accretion of gas envelop of Jupiter; the masses of the jovian perturbers can reach the present value during the accumulation of terrestrial protoplanets is still going on. Thus the effect of secular perturbation from the jovian planets of the present sizes, at least from Jupiter, is significant anyway during a phase somewhere in the late stage of terrestrial planet formation.

On the separation of jovian planetary system, it may be reasonable when we consider the process of rapid gas capture (Ida 1997). Since the growth timescale of the solid cores (protoplanets) is shorter in the inner part of the system, at first the process of gas capture should begin in the zone around Jupiter when the mass of the core reaches the critical core mass, $> 10M_\oplus$. Once the gas capture has started, the mass of gas envelop approaches $300M_\oplus$ within a short timescale ($\sim 10^6$ years), and the Hill radius of Jupiter rapidly increases. Hence the region which was rather far and beyond the effect of Jupiter's gravitation can be under the influence of Jupiter. Planetesimals, and maybe protoplanets on their way to grow in that region are attracted by Jupiter and dissolved into the gas envelop, or scattered. Eccentricities and inclinations of the scattered bodies are decreased by gas drag. Mechanism of the orbit repulsion (Kokubo and Ida 1995) which keeps the separation of the bodies in the protoplanet system also works here, and the scattered bodies would be stored around $8R_H$ outside Jupiter's orbit. It partly explains the present separation of the jovian planetary subsystem, $< 15R_H$. It also has an effect to reduce the formation timescale of the planets beyond Jupiter through the accumulation of scattered particles outside Jupiter. The effect of orbital repulsion on the accumulation of jovian planets during their growth is worthy of further study in detail.

On the viewpoint of traditional celestial mechanics, synchronization of perihelia of protoplanets by the secular perturbation from jovian planets is quite an interesting problem. Unlike the restricted problems whose theoretical analysis is well done, the phenomena are deeply involved with the mutual interaction of protoplanets. Though the first-order secular theory well

reproduces the synchronization qualitatively, more specific expression of the analytical solution of the concurrent orbital motion of protoplanets is desired for both two-perturber case and single-perturber case. Solution of the single-perturber case may also give the explanation to the dynamical rigidity.

Problem of planet formation has been considered as eminently and exclusively suitable for statistical approach or direct numerical N-body simulation by special-purpose computers and vector/parallel supercomputers. However, as we have shown here there is still room for which traditional celestial mechanics can give much suggestion, especially when the number of particles decreases. Though we have to consider many dynamical and physical processes which we have neglected here, it will be still significant to consider the Hamiltonian dynamics and its basic processes which are the fundamental of celestial motion in the solar system. Even in the final stage of planet formation it will be true, because the later the formation phase goes on, the more Hamiltonian dynamics becomes dominant.

Acknowledgments

The authors have greatly benefited from several stimulating discussion and encouragement from Kimmo Innanen, Seppo Mikkola, Makoto Yoshikawa, Eiichiro Kokubo, and Hiroshi Kinoshita. This study was supported by the Decoding Earth Evolution Program (DEEP), intensified study area program of Ministry of Culture and Education (No. 259, 1995–1997), and the scientific simulation projects of ADAC, National Astronomical Observatory (kti31/1997).

Appendix 1. Definition of the Hill radius and the normalized separation

The mutual Hill radius $R_H^{i,j}$ between the i-th and j-th planet in CWB is defined as

$$R_H^{i,j} \equiv \left(\frac{m_i + m_j}{3M_\odot}\right)^{\frac{1}{3}} \left(\frac{d_i + d_j}{2}\right). \tag{4}$$

where (m_i, d_i) and (m_j, d_j) are the mass and heliocentric distance of the i-th and j-th planets, respectively. Usual Hill radius of the i-th planet r_H^i is defined as

$$r_H^i \equiv \left(\frac{m_i}{3M_\odot}\right)^{\frac{1}{3}} d_i. \tag{5}$$

If masses of the i-th and j-th bodies are the same ($m_i = m_j = m$), the averaged Hill radius $\bar{r}_H^{i,j}$ of i-th and j-th body becomes

$$\begin{aligned} \bar{r}_H^{i,j} \equiv \frac{r_H^i + r_H^j}{2} &= \frac{1}{2}\left[\left(\frac{m_i}{3M_\odot}\right)^{\frac{1}{3}} d_i + \left(\frac{m_j}{3M_\odot}\right)^{\frac{1}{3}} d_j\right] \\ &= \left(\frac{m}{3M_\odot}\right)^{\frac{1}{3}} \left(\frac{d_i + d_j}{2}\right). \end{aligned} \tag{6}$$

Similarly, if masses of the i-th and j-th bodies are equal, the mutual Hill radius between i-th and j-th planets becomes

$$\begin{aligned} R_H^{i,j} &= \left(\frac{2m}{3M_\odot}\right)^{\frac{1}{3}} \left(\frac{d_i + d_j}{2}\right) \\ &= 2^{\frac{1}{3}} \bar{r}_H^{i,j}. \end{aligned} \tag{7}$$

The normalized separation of protoplanets of around $10r_H$ in the description of Kokubo and Ida (1998) can be considered to be nearly equal to $10\bar{r}_H$ since the masses of protoplanets are all similar. Hence by (6) and (7),

$$10r_H \sim 10\bar{r}_H^{i,j} = \frac{10}{2^{\frac{1}{3}}} R_H^{i,j} \sim 8R_H. \tag{8}$$

Actually, $j = i + 1$ in the case of neighboring particles. Thus we interpret the normalized separation of $10r_H$ in Kokubo and Ida (1998) as $8R_H$.

Appendix 2. Equi-Hamiltonian maps

Based on the perturbation theory by Lie transformation (e.g. Hori 1967, Deprit 1969), Hamiltonian can be averaged in terms of the fast moving variables, and degrees of freedom can be reduced to one; i.e. the system can become integrable system up to the first order approximation. We express Hamiltonian of the system using modified Delauney canonical variables

$$\begin{array}{ll} L = \sqrt{\mu a}, & l, \\ G - H = \sqrt{\mu a(1-e^2)}(1-\cos I), & g = \omega, \\ H = \sqrt{\mu a(1-e^2)}\cos I, & g + h = \varpi, \end{array} \tag{9}$$

where a is the the semimajor axis, e is the eccentricity, I is the inclination, l is the mean anomaly, ω is the argument of perihelion, and ϖ is the longitude of perihelion. At first we suppose only one perturber such as Jupiter whose orbit is assumed to be the ellipse with a fixed eccentricity, precessing in the invariable plane. The inclination and the nodal motion of perturber are neglected. As for the orbital elements of perturbed body, there are no assumptions. Then the Hamiltonian K becomes

$$K = -\frac{\mu^2}{2L^2} - \frac{\mu'^2}{2L'^2} + R(L, G, H, l, g, h; L', G', H', l', g', h') \tag{10}$$

where primed ($'$) variables denote those of perturbing body and variables without prime are those of perturbed body. We use the symbol K instead of usual H as the Hamiltonian in order to avoid confusion with the Delauney canonical variable. Since the orbit of perturber is supposed to be fixed ellipse precessing in the invariable plane, a', e', I', ω' do not appear in K from the beginning. This leads to the removal of L', G', H', g' from the original Hamiltonian. So the disturbing function R expressed by the orbital elements becomes

$$R = R(a, e, I, l, \omega, \varpi; -, -, -, l', -, \varpi') \tag{11}$$

$$= -Gm'\left(\frac{1}{\Delta} - \frac{r}{r'^2}\cos S\right), \tag{12}$$

$$\Delta = \sqrt{r^2 + r'^2 - 2rr'\cos S}, \tag{13}$$

$$\cos S = \frac{1+\cos I}{2}\cos(f + (\varpi - \varpi') - f') + \frac{1+\cos I}{2}\cos(f - (\varpi - \varpi') + 2\omega - f'), \tag{14}$$

where m' is the mass of perturber, Δ is the mutual distance between the perturber and the perturbed body, r and r' are the heliocentric distances, f and f' are the true anomaly. Sign $-$ in the disturbing function R denotes the consequence of elimination of the variable.

Now we assume that the perihelion of perturber precesses uniformly with time, that is

$$\varpi' = \nu_5 t + \text{constant}, \tag{15}$$

where ν_5 is the precession rate of the orbit of perturber. In addition, we find in (14) that ϖ and ϖ' appear in the form of $\varpi - \varpi'$. So the new variable θ is introduced instead of y_3 as

$$\theta = y_3 - \varpi' (= \varpi - \varpi'). \tag{16}$$

Due to the presence of (15), Hamiltonian K contains the time t explicitly. To eliminate t from Hamiltonian, we perform a canonical transformation from (H, ϖ) to (Θ, θ) using the generating function $W = -(\varpi - \varpi')\Theta$.

$$\theta = -\frac{\partial W}{\partial \Theta} = \varpi - \varpi', \tag{17}$$

$$H = -\frac{\partial W}{\partial \varpi} = \Theta. \tag{18}$$

Then the new Hamiltonian $\tilde{K}$ becomes as

$$\begin{aligned} \tilde{K} &= K - \frac{\partial W}{\partial t} && (19)\\ &= K + \nu_5 \Theta && (20)\\ &= -\frac{\mu^2}{2L^2} + R(a, e, I, l, \omega, \theta; -, -, -, l', -, -) + \nu_5 H. && (21) \end{aligned}$$

Now the Hamiltonian (21) is averaged with respect to the short periodic variables l and l' as

$$\begin{aligned} \tilde{K}^* &= \frac{1}{(2\pi)^2} \int_0^{2\pi} \int_0^{2\pi} \tilde{K} dl dl' && (22)\\ &= \tilde{K}^*(-, e, I, -, \omega, \theta; -, -, -, -, -, -). && (23) \end{aligned}$$

Since the variable l does not exist in the new Hamiltonian $\tilde{K}^*$, its conjugate L becomes constant. This means that the semimajor axis $a = L^2/\mu$ is constant, and omitted from $\tilde{K}^*$. We carry out the quadrature (23) numerically from $l = [0 : 2\pi], l' = [0 : 2\pi]$ neglecting the mean motion commensurability. This is justified because there are no area of strong mean motion resonance with the giant planets in the terrestrial region ($a < 1.5$AU).

Hamiltonian (23) has still three degrees of freedom, so we average $\tilde{K}^*$ by ω, assuming that the argument of perihelion is a fast and uniformly moving variable as

$$K^{**} = \frac{1}{\pi} \int_0^{\pi} K^* d\omega = K^{**}(-, e, I, -, -, \theta; -, -, -, -, -, -). \tag{24}$$

We carry out the quadrature (24) numerically from $\omega = [0 : \pi]$ since ω appears in the form of 2ω in the perturbing function R in (14). Since K^{**} does not contain $\omega (= g)$, its conjugate $G - H = \sqrt{\mu a(1 - e^2)}(1 - \cos I)$ becomes constant. Then we can find a new constant,

$$C \equiv \sqrt{1 - e^2}(1 - \cos I). \tag{25}$$

C is determined by the initial values of e and I. It leads to the elimination of variable e or I using (25). If we remove I from the Hamiltonian, final form of the Hamiltonian becomes

$$K^{**} = K^{**}(-, e, -, -, -, \theta; -, -, -, -, -, -). \tag{26}$$

Since K^{**} has only one degree of freedom because there is an energy integral, equi-Hamiltonian curves can be drawn on the (θ, e) plane, and we can get information on the global dynamics of the system. As for the constant C, we can determine it by initial conditions. Choice of C does not affect the result very much if the initial orbit of perturbed bodies are nearly circular.

In the semi-analytical method explained above, we can not add any perturbers with precessing elliptic orbit any more because it increases the degree of freedom. However, if the orbit of

perturber is circular, the degree of freedom does not increase whatever number of perturbers we add.

In general perturbation theory, the disturbing function can be developed in a series of cosine terms of the form (Brouwer and Clemence, 1961)

$$R = m' \sum c_{j_1,j_2,j_3,j_4,j_5,j_6} \cos(j_1\lambda + j_2\varpi + j_3\Omega + j_4\lambda' + j_5\varpi' + j_6\Omega'), \tag{27}$$

where the coefficients $c_{j_1,j_2,j_3,j_4,j_5,j_6}$ are functions of a, e, I, a', e', I' and $\lambda = l + \varpi$ is the mean longitude. When the orbit of perturber is planar and circular, ϖ and Ω vanishes from the disturbing function. In addition, averaging by the short-periodic angles (λ, λ') reduces R into the form

$$R^* = m' \sum c_{j_2,j_3} \cos(j_2\varpi + j_3\Omega). \tag{28}$$

Since the disturbing function does not change by a rotation of the coordinate system about z-axis, and since the angles appearing in the arguments of the cosines are reckoned from a common origin, it follows that $j_2 + j_3 = 0$ (d'Alembert characteristic), which gives

$$R^* = m' \sum c_{j_2,j_3} \cos j_2(\varpi - \Omega) = m' \sum c_{j_2} \cos j_2\omega, \tag{29}$$

and if we consider ω as a fast and uniformly variable angle and average R^* by ω, the disturbing function becomes a constant with no angles. Hence when we consider the system with two or more perturbers in which one has the orbit of precessing ellipse and others have circular orbits, averaged Hamiltonian becomes

$$K^{**} = \int_0^{2\pi}\int_0^{2\pi}\int_0^{2\pi}\int_0^{\pi} (H_{kepler} + R_e + R_c) d\lambda'' dl' dl d\omega \tag{30}$$

$$= \int_0^{2\pi}\int_0^{2\pi}\int_0^{\pi} H_e dl' dl d\omega + \text{constant}, \tag{31}$$

where H_{kepler} denotes the keplerian part of Hamiltonian, R_e and R_c symbolically denotes the disturbing function due to the elliptic and circular perturber respectively. λ'' denotes the mean longitude of the circular perturber, $\lambda'' = l'' + \varpi''$. In (31), degree of freedom of the averaged Hamiltonian is still one. We can also draw the two-dimensional equi-Hamiltonian map, $K^{**}(e, \theta)$.

More specific formulation of averaging is given as follows in the case of perturbers with circular orbits. We use true longitude $\psi'' \equiv \varpi'' + f''$ and mean longitude $\lambda'' \equiv \varpi'' + l''$ instead of f and l respectively when we handle circular orbits. Double primed ($''$) variables denote those of circular perturbers. Hamiltonian H_c for the case with circular perturber is written as

$$H_c = -\frac{\mu^2}{2L^2} - \frac{\mu''^2}{2L''^2} + R_c. \tag{32}$$

In R_c, ψ'' is used instead of f'', so

$$R_c = -Gm'' \left(\frac{1}{\Delta_c} - \frac{r}{r''^2} \cos S_c \right), \tag{33}$$

$$\Delta_c = \sqrt{r^2 + r''^2 - 2rr'' \cos S_c}. \tag{34}$$

As for the relative angle S_c, f'' is replaced by ψ'' or ϖ''. The first term becomes

$$f + (\varpi - \varpi'') - f'' = f + \varpi - (f'' + \varpi'') = f - (\psi'' - \varpi), \tag{35}$$

and the second term becomes

$$\begin{aligned} f - (\varpi - \varpi'') + 2\omega + f'' &= f - \varpi + 2\omega + (\omega'' + \Omega'' + f'') \\ &= f - \varpi + 2\omega + \psi'' \\ &= f + 2\omega + (\psi'' - \varpi). \end{aligned} \tag{36}$$

Then, $\cos S_c$ becomes

$$\begin{aligned} \cos S_c &= \frac{1}{2}(1 + \cos I)\cos(f - (\psi'' - \varpi)) \\ &\quad + \frac{1}{2}(1 + \cos I)\cos(f + 2\omega + (\psi'' - \varpi)). \end{aligned} \tag{37}$$

Angles which describes the disturbing function R_c are $f, 2\omega$, and $\psi'' - \varpi$ here.

We again perform the averaging operation here on the fast and uniform moving variables as well as the case of elliptic perturbers. There is one point to notice here. Angle variable which should be averaged is the true anomaly f for the perturbed body. But for the circular perturber, $\psi'' - \varpi$ should be averaged since the argument of perihelion ω'' and the longitude of ascending node Ω'' cannot be defined in circular orbit. We are likely to average by ψ for the perturbed body, but it is not correct. ψ includes the longitude of perihelion ϖ, and ϖ indicates the orientation of orbit of the perturbed body, and it should not be averaged. On the other hand, there is no meaning in the definition of ϖ''. Only ψ'' can be defined. Once we average the disturbing function over ψ'', gravitational potential due to the circular perturber becomes axisymmetric around the vertical axis. It means that the averaging over ψ'' and $\psi' - \varpi$ give the same results in (35) or (36). So we perform averaging as

$$H_c^* = \int_0^{2\pi}\int_0^{2\pi}\int_0^{\pi} H_c d\lambda'' dl d\omega. \tag{38}$$

In the actual quadrature, averaging operation by ψ'' is replaced by averaging by λ'', and f is replaced by l.

In the case of n circular perturbers as

$$H = H_e + H_{c,1} + H_{c,2} + \cdots + H_{c,n}, \tag{39}$$

the operation of averaging can be done in the same manner as

$$H^* = \int_0^{2\pi}\int_0^{2\pi}\cdots\int_0^{2\pi}\int_0^{\pi}(H_e + H_{c,1} + H_{c,2} + \cdots + H_{c,n})dl'd\lambda''\cdots d\lambda^{(n+1)\prime}dld\omega \tag{40}$$

$$= \int_0^{2\pi}\int_0^{2\pi}\int_0^{\pi} H_e dl' dl d\omega + \int_0^{2\pi}\int_0^{2\pi}\int_0^{\pi} H_{c,1} d\lambda'' dl d\omega \tag{41}$$

$$+ \int_0^{2\pi}\int_0^{2\pi}\int_0^{\pi} H_{c,2} d\lambda''' dl d\omega + \cdots + \int_0^{2\pi}\int_0^{2\pi}\int_0^{\pi} H_{c,n} d\lambda^{(n+1)\prime} dl d\omega. \tag{42}$$

The degree of freedom of the system is still one.

In the case that the circular perturber locates nearer to the Sun than the perturbed body, potential due to the perturber can be averaged and included into the solar gravitational oblateness (Nacozy and Diehl, 1978).

References

Asker, J.R. 1997, New orbit may suit satellites, *Aviation Week and Space Technology*, **146**, February 3, 62, (Introduction to the paper presented by Kimmo Innanen at the winter meeting of the American Astronomical Society in Tronto, December 1996).

Bodenheimer, P. and Pollack, J.B. 1986, Calculations of the accretion and evolution of giant planets: the effects of solid cores, *Icarus*, **67**, 391–408.

Brouwer, D. and Clemence, G.M. 1961, *Methods of Celestial Mechanics*, Academic Press, New York.

Brouwer, D. and van Woerkom, A.J.J. 1950, The secular variations of the orbital elements of the principal planets, *Astron. Pap. Amer. Ephemeris. Naut. Alm.*, **13**, 2, 81–107.

Chambers, J.E., Wetherill, G.W., and Boss, A.P. 1996, The stability of multi-planet systems, *Icarus*, **119**, 261–268.

Danby, J.M.A. 1992, *Fundamentals of Celestial Mechanics* (second edition, third printing), Willmann-Bell Inc., Richmond, Virginia.

Deprit, A. 1969, Canonical transformations depending on a small parameter, *Celes. Mech.*, **1**, 12–30.

Ebisuzaki, T., Makino, J., Fukushige, T., Taiji, M., Sugimoto, D., Ito, T., and Okumura, S.K. 1993, GRAPE project: an overview, *Publ. Astron. Soc. Japan*, **45**, 269–278.

Fernández, J.A. 1997, The formation of the Oort cloud and the primitive galactic environment, *Icarus*, **129**, 106–119.

Gladman, B. 1993, Dynamics of systems of two close planets, *Icarus*, **106**, 247–263.

Gomes, R.S. 1997, Dynamical effects of planetary migration on the primordial asteroid belt, *Astron. J.*, **114**, 396–401.

Hill, G.W. 1897, On the values of the eccentricities and longitudes of the perihelia of Jupiter and Saturn for distant epochs, *Astron. J.*, **17**, 81–87.

Hori, G. 1966, Theory of general perturbations with unspecified canonical variables, *Publ. Astron. Soc. Japan*, **18**, 287–296.

Hori, G. 1967, Non-linear coupling of two harmonic oscillations, *Publ. Astron. Soc. Japan*, **19**, 229–241.

Ida, S. 1997, Comparative planet formation theory, in Matsui, T., Sumi, A., Taira, A., and Toriumi, M. eds., *Comparative planetology*, No. 12 in The Earth and Planetary Science Series, Iwanami, Tokyo, chapter 3, 131–232, (in Japanese).

Ida, S. and Makino, J. 1992, N-body simulation of gravitational interaction between planetesimals and a protoplanet I. velocity distribution of planetesimals, *Icarus*, **96**, 107–120.

Ida, S. and Makino, J. 1993, Scattering of planetesimals by a protoplanet: slowing down of runaway growth, *Icarus*, **106**, 210–227.

Ida, S., Canup, R.M., and Stewart, G.R. 1997, Lunar accretion from an impact-generated disk, *Nature*, **389**, 353–357.

Innanen, K.A., Zheng, J.Q., Mikkola, S., and Valtonen, M.J. 1997, The Kozai mechanism and the stability of planetary orbits in binary star systems, *Astron. J.*, **113**, 1915–1919.

Kinoshita, H. and Nakai, H. 1991, Secular perturbations of fictitious satellites of Uranus, *Celes. Mech. Dyn. Astron.*, **52**, 293–303.

Kinoshita, H. and Nakai, H. 1996, Long-term behavior of the motion of Pluto over 5.5 billion years, *Earth, Moon, and Planets*, **72**, 165–173.

Kinoshita, H., Yoshida, H., and Nakai, H. 1991, Symplectic integrators and their application to dynamical astronomy, *Celes. Mech. Dyn. Astron.*, **50**, 59–71.

Kokubo, E. and Ida, S. 1995, Orbital evolution of protoplanets embedded in a swarm of planetesimals, *Icarus*, **114**, 247–257.

Kokubo, E. and Ida, S. 1996, On runaway growth of planetesimals, *Icarus*, **123**, 180–191.

Kokubo, E. and Ida, S. 1998, Oligarchic growth of protoplanets, *Icarus*, **131**, 171–178.

Kozai, Y. 1962, Secular perturbations of asteroids with high inclination and eccentricity, *Astron. J.*, **67**, 591–598.

Kozai, Y. 1992, Shepherding satellites and dynamical structure of the rings of Uranus, *Publ. Astron. Soc. Japan*, **44**, 135–139.

Kozai, Y. 1993, Shepherding satellites and dynamical structure of the rings of Uranus. II, *Publ. Astron. Soc. Japan*, **45**, 263–267.

Laskar, J. 1990, The chaotic motion of the solar system: A numerical estimate of the size of the chaotic zones, *Icarus*, **88**, 266–291.

Laskar, J. 1994, Large scale chaos in the solar system, *Astron. Astrophys.*, **287**, L9–L12.

Laskar, J. 1996, Large scale chaos and marginal stability in the solar system, *Celes. Mech. Dyn. Astron.*, **64**, 115–162.

Laskar, J. 1997, Large scale chaos and the spacing of the inner planets, *Astron. Astrophys.*, **317**, L75–L78.

Lecar, M. and Aarseth, S.J. 1986, A numerical simulation of the formation of the terrestrial planets, *Astrophys. J.*, **305**, 564–579.

Lecar, M. and Franklin, F. 1997, The solar nebula, secular resonances, gas drag, and the asteroid belt, *Icarus*, **129**, 134–146.

Lecar, M., Franklin, F., and Murison, M. 1992, On predicting long-term orbital instability: a relation between the Lyapunov time and sudden orbital transitions, *Astron. J.*, **104**, 1230–1236.

Levison, H.F. and Duncan, M.J. 1994, The long-term dynamical behavior of short-period comets, *Icarus*, **108**, 18–36.

Lissauer, J.J. 1987, Timescales for planetary accretion and the structure of the protoplanetary disk, *Icarus*, **69**, 249–265.

Makino, J. 1991, Treecode with a special-purpose processor, *Publ. Astron. Soc. Japan*, **43**, 621–638.

Makino, J. and Aarseth, S.J. 1992, On a Hermite integrator with Ahmad-Cohen scheme for gravitational many-body problems, *Publ. Astron. Soc. Japan*, **44**, 141–151.

Makino, J., Taiji, M., Ebisuzaki, T., and Sugimoto, D. 1997, GRAPE-4: a massively parallel special-purpose computer for collisional N-body simulations, *Astrophys. J.*, **480**, 432–446.

Michel, P. and Thomas, F. 1996, The Kozai resonance for near-Earth asteroids with semimajor axis smaller than 2 AU, *Astron. Astrophys.*, **307**, 310–318.

Mikkola, S. 1997, Practical symplectic methods with time transformation for the few-body problem, *Celes. Mech. Dyn. Astron.*, **67**, 145–165.

Mizuno, H. 1980, Formation of the giant planets, *Prog. Theor. Phys.*, **64**, 544–557.

Mizuno, H., Nakazawa, K., and Hayashi, C. 1978, Instability of gaseous envelope surrounding a planetary core and formation of giant planets, *Prog. Theor. Phys.*, **60**, 669–710.

Morbidelli, A. and Froeschlé, C. 1996, On the relationship between Lyapunov times and macroscopic instability times, *Celes. Mech. Dyn. Astron.*, **63**, 227–239.

Nacozy, P.E. and Diehl, R.E. 1978, A semianalytical theory for the long-term motion of Pluto, *Astron. J.*, **83**, 522–592.

Nakai, H. and Kinoshita, H. 1985, Secular perturbations of asteroids in secular resonance, *Celes. Mech.*, **36**, 391–407.

Pollack, J.B., Hubickyj, O., Bodenheimer, P., Lissauer, J.J., Podolak, M., and Greenzweig, Y. 1996, Formation of the giant planets by concurrent accretion of solid and gas, *Icarus*, **124**, 62–85.

Saha, P. and Tremaine, S. 1992, Symplectic integrators for solar system dynamics, *Astron. J.*, **104**, 1633–1640.

Saha, P. and Tremaine, S. 1994, Long-term planetary integrations with individual time steps, *Astron. J.*, **108**, 1962–1969.

Standish, E.M. 1990, The observational basis for JPL's DE200, the planetary ephemerides of the astronomical almanac, *Astron. Astrophys.*, **233**, 252-271.

Sugimoto, D., Chikada, Y., Makino, J., Ito, T., Ebisuzaki, T., and Umemura, M. 1990, A special-purpose computer for gravitational many-body problem, *Nature*, **345**, 33-35.

Sussman, G.J. and Wisdom, J. 1988, Numerical evidence that the motion of Pluto is chaotic, *Science*, **241**, 433-437.

Sussman, G.J. and Wisdom, J. 1992, Chaotic evolution of the solar system, *Science*, **257**, 56-62.

Tajima, N. 1998, *Evolution and dynamical stability of the proto-giant-planet envelop*, PhD thesis, University of Tokyo, Tokyo.

Tanikawa, K., Kikuchi, N., and Sato, I. 1991, On the origin of the planetary spin by accretion of planetesimals II. collisional orbits at the Hill surface, *Icarus*, **94**, 112-125.

Thomas, F. and Morbidelli, A. 1996, The Kozai resonance in the outer solar system and the dynamics of long-period comets, *Celes. Mech. Dyn. Astron.*, **64**, 209-229.

Ward, W.R. 1981, Solar nebula dispersal and the stability of the planetary system I. scanning secular resonance theory, *Icarus*, **47**, 234-264.

Ward, W.R., Colombo, G., and Franklin, F. 1976, Secular resonance, solar spin down and the orbit of Mercury, *Icarus*, **28**, 441-452.

Wetherill, G.W. and Stewart, G.R. 1989, Accumulation of a swarm of small planetesimals, *Icarus*, **77**, 330-357.

Williams, J.G. 1969, *Secular perturbations in the solar system*, PhD thesis, University of California, Los Angeles.

Wisdom, J. and Holman, M. 1991, Symplectic maps for the N-body problem, *Astron. J.*, **102**, 1528-1538.

Yoshikawa, M. 1989, A survey of the motions of asteroids in the commensurabilities with Jupiter, *Astron. Astrophys.*, **213**, 436-458.

Tables

TABLE I. Distances in the present planetary system measured by the real distance (AU) and the mutual Hill radius (R_H). Data for mass and semimajor axes are taken from DE245 of JPL/NASA.

planet	AU	R_H
Mercury		
|	0.3362	63.40
Venus		
|	0.2767	26.25
Earth		
|	0.5237	39.95
Mars		
|	3.6806	16.02
Jupiter		
|	4.3777	7.95
Saturn		
|	9.6474	13.98
Uranus		
|	10.8743	13.93
Neptune		
|	9.1605	10.24
Pluto		

Figure Captions

FIG. 1. Relationship between the original data of the instability times and their logarithmic average in the CWB diagram of the autonomous protoplanet systems for $4 < \Delta < 10$. "Delta" in the label of x axis denotes Δ. (a) Original data and their logarithmic average in $\langle e^2 \rangle^{\frac{1}{2}} = 2 \langle I^2 \rangle^{\frac{1}{2}} = 0.005$ case. Ten data by different initial conditions are plotted together. (b) Logarithmic averages of ten data in $\langle e^2 \rangle^{\frac{1}{2}} = 2 \langle I^2 \rangle^{\frac{1}{2}} = 0.005$, 0.010, 0.015, and 0.020 cases. In both panels, $N = 17$, $2.5 \times 10^{-7} M_\odot < m < 3.5 \times 10^{-7} M_\odot$ with average mass $\langle m \rangle = 3.0 \times 10^{-7} M_\odot$, $a_1 = 0.25$AU. Small variation of spacing is also added between $0.8 \Delta R_H$ and $1.2 \Delta R_H$. Note that $\langle e^2 \rangle^{\frac{1}{2}}$ is replaced by $\langle e \rangle$ in the labels on the panel.

FIG. 2. Instability times with its logarithmic averages and number of repetition for the random initial orbits. (a) $\langle e^2 \rangle^{\frac{1}{2}} = 2 \langle I^2 \rangle^{\frac{1}{2}} = 0.005$, (b) $\langle e^2 \rangle^{\frac{1}{2}} = 2 \langle I^2 \rangle^{\frac{1}{2}} = 0.010$, (c) $\langle e^2 \rangle^{\frac{1}{2}} = 2 \langle I^2 \rangle^{\frac{1}{2}} = 0.015$, and (d) $\langle e^2 \rangle^{\frac{1}{2}} = 2 \langle I^2 \rangle^{\frac{1}{2}} = 0.020$. $N = 17$, $2.5 \times 10^{-7} M_\odot < m < 3.5 \times 10^{-7} M_\odot$ with average mass $\langle m \rangle = 3.0 \times 10^{-7} M_\odot$, $a_1 = 0.25$AU in all systems. Small variation of spacing is also added between $0.8 \Delta R_H$ and $1.2 \Delta R_H$. Δ is fixed to 9.0. Note that $\langle e^2 \rangle^{\frac{1}{2}}$ is replaced by $\langle e \rangle$ in the labels on the panel.

FIG. 3. Typical CWB diagrams of autonomous protoplanet systems. (a) Low velocity dispersion and small mass variation case ($N = 20$, $\langle e^2 \rangle^{\frac{1}{2}} = 2 \langle I^2 \rangle^{\frac{1}{2}} = 0.005$, $2.5 \times 10^{-7} M_\odot < m < 3.5 \times 10^{-7} M_\odot$ with $\langle m \rangle = 3.0 \times 10^{-7} M_\odot$, $a_1 = 0.25$AU). Points just on the upper boundary line ($T_I = 5.0 \times 10^7$ years) means that the system has been stable at least for 5.0×10^7 years. (b) High velocity dispersion and large mass variation case ($N = 10$, $\langle e^2 \rangle^{\frac{1}{2}} = 2 \langle I^2 \rangle^{\frac{1}{2}} = 0.015$, $2.5 \times 10^{-7} M_\odot < m < 10.0 \times 10^{-7} M_\odot$ with $\langle m \rangle = 6.25 \times 10^{-7} M_\odot$, $a_1 = 0.35$AU). Small variation of spacing is also added between $0.8 \Delta R_H$ and $1.2 \Delta R_H$ in both cases.

FIG. 4. Relationship between the secular frequency $g(a)$ and the semimajor axis a of a massless particle under the secular disturbance of perturbers. A solid line denoted as "JSUN" indicates the case with four jovian planets as perturbers. An oscillatory solid line denoted as "20 protoplanets + JSUN" indicates the case with four jovian planets and twenty protoplanets with finite mass as perturbers. Protoplanets have equal mass of $3.0 \times 10^{-7} M_{\odot}$, and have equal separation of $14 R_H$, starting from $a_1 = 0.35$AU.

FIG. 5. Numerical result of the time evolution of eccentricities of massless particles whose semimajor axes are $a = 0.40$AU, 0.68AU, 0.72AU, 0.76AU, 1.22AU for over 9 million years under the effect of Jupiter and Saturn. All of the particles are initially placed on planar and circular orbits.

FIG. 6. (a) Relationship between the eccentricity of a test particle located just on the secular resonance ν_5 (the particle with $a = 0.72$AU in Fig. 5) and the difference of the longitudes of perihelion from that of Jupiter, $\varpi - \varpi_J$. Note that the symbol of longitude of perihelion ϖ is replaced by "p" or "p_jupiter" in the labels of the panels. (b) An equi-Hamiltonian map of the massless particle just on the secular resonance ν_5 drawn by the semi-analytical method of averaging. (c) Similar to (b), an equi-Hamiltonian map of the massless particle on $a = 0.72$AU, but under the effect of Jupiter and twenty protoplanets having circular orbits described in Fig. 4.

FIG. 7. (a) The CWB diagram of perturbed protoplanet systems by Jupiter and Saturn with small mass variation. $N = 17$, $\langle e^2 \rangle^{\frac{1}{2}} = 2 \langle I^2 \rangle^{\frac{1}{2}} = 0.005$, $2.5 \times 10^{-7} M_{\odot} < m < 3.5 \times 10^{-7} M_{\odot}$ with $\langle m \rangle = 3 \times 10^{-7} M_{\odot}$, $a_1 = 0.25$AU. Small variation of spacing is also added between $0.8 \Delta R_H$ and $1.2 \Delta R_H$. (b) Semimajor axes of the inner protoplanets of the pair which exhibited the close encounter. Two solid lines denote the inner and outer boundary of the averaged initial distribution of protoplanets. (c) The serial number of the inner protoplanets of the pair which exhibited the close encounter. Protoplanets are numbered from 1 to N from the innermost one.

FIG. 8. (a) The CWB diagram of perturbed protoplanet systems by Jupiter and Saturn with small mass variation. $N = 20$, $\langle e^2 \rangle^{\frac{1}{2}} = 2 \langle I^2 \rangle^{\frac{1}{2}} = 0.005$, $2.5 \times 10^{-7} M_\odot < m < 3.5 \times 10^{-7} M_\odot$ with $\langle m \rangle = 3 \times 10^{-7} M_\odot$, $a_1 = 0.25$AU. Small variation of spacing is also added between $0.8 \Delta R_H$ and $1.2 \Delta R_H$. (b) Semimajor axes of the inner protoplanets of the pair which exhibited the close encounter. Two solid lines denote the inner and outer boundary of the averaged initial distribution of protoplanets. (c) The serial number of the inner protoplanets of the pair which exhibited the close encounter.

FIG. 9. Time evolution of longitudes of perihelion (upper) and eccentricities (lower) of a protoplanet system of $N = 17$, $\langle e^2 \rangle^{\frac{1}{2}} = 2 \langle I^2 \rangle^{\frac{1}{2}} = 0.005$, $2.5 \times 10^{-7} M_\odot < m < 3.5 \times 10^{-7} M_\odot$ with $\langle m \rangle = 3.0 \times 10^{-7} M_\odot$, $\Delta = 13.0$, $a_1 = 0.25$AU. Small variation of spacing is also added between $0.8 \Delta R_H$ and $1.2 \Delta R_H$. Thick line in the upper panel denotes the longitude of perihelion of Jupiter. All data of 17 protoplanets are plotted together.

FIG. 10. Time evolution of longitudes of perihelion (upper) and eccentricities (lower) of a protoplanet system of $N = 17$, $\langle e^2 \rangle^{\frac{1}{2}} = 2 \langle I^2 \rangle^{\frac{1}{2}} = 0.005$, $2.5 \times 10^{-7} M_\odot < m < 3.5 \times 10^{-7} M_\odot$ with $\langle m \rangle = 3.0 \times 10^{-7} M_\odot$, $\Delta = 19.0$, $a_1 = 0.25$AU. Small variation of spacing is also added between $0.8 \Delta R_H$ and $1.2 \Delta R_H$. Thick line in the upper panel denotes the longitude of perihelion of Jupiter. All data of 17 protoplanets are plotted together.

FIG. 11. (a) The CWB diagram of perturbed protoplanet systems by Jupiter and Saturn with large mass variation. $N = 14$, $\langle e^2 \rangle^{\frac{1}{2}} = 2 \langle I^2 \rangle^{\frac{1}{2}} = 0.005$, $2.0 \times 10^{-7} M_\odot < m < 8.0 \times 10^{-7} M_\odot$ with $\langle m \rangle = 5 \times 10^{-7} M_\odot$, $a_1 = 0.5$AU. Small variation of spacing is also added between $0.8 \Delta R_H$ and $1.2 \Delta R_H$. (b) Semimajor axes of the inner protoplanets of the pair which exhibited the close encounter. Two solid lines denote the inner and outer boundary of the averaged initial distribution of protoplanets. The existence of some points outside the upper boundary is due to randomness of initial mass distribution. (c) The serial number of the inner protoplanets of the pair which exhibited the close encounter.

FIG. 12. Time evolution of longitudes of perihelion (upper) and eccentricities (lower) of a perturbed protoplanet system by Jupiter and Saturn. $N = 14$, $\langle e^2 \rangle^{\frac{1}{2}} = 2 \langle I^2 \rangle^{\frac{1}{2}} = 0.005$, $2.0 \times 10^{-7} M_\odot < m < 8.0 \times 10^{-7} M_\odot$ with $\langle m \rangle = 5.0 \times 10^{-7} M_\odot$, $a_1 = 0.5$AU, $\Delta = 13.0$. Small variation of spacing is also added between $0.8 \Delta R_H$ and $1.2 \Delta R_H$. Thick line in the upper panel denotes the longitude of perihelion of Jupiter. All data of 14 protoplanets are plotted together.

FIG. 13. Individual plots of the longitudes of perihelion and eccentricities shown in Fig. 12. a is the semimajor axis, m is the mass of each protoplanet, respectively. M_e means the mass of the Earth ($M_\oplus$).

FIG. 14. The same plot as Fig. 12, but the solution is obtained by the linear secular perturbation theory.

FIG. 15. Numerical result of the time evolution of longitudes of perihelion (upper) and eccentricities (lower) of a protoplanet system under the effect only of Jupiter. Initial orbits of the protoplanets are the same as in the two-perturber case, Fig. 12. $N = 14$, $\langle e^2 \rangle^{\frac{1}{2}} = 2 \langle I^2 \rangle^{\frac{1}{2}} = 0.005$, $2.0 \times 10^{-7} M_\odot < m < 8.0 \times 10^{-7} M_\odot$ with $\langle m \rangle = 5.0 \times 10^{-7} M_\odot$, a_1=0.5AU, $\Delta = 13.0$. Small variation of spacing is also added between $0.8\Delta R_H$ and $1.2\Delta R_H$. Thick line in the upper panel denotes the longitude of perihelion of Jupiter. All data of 14 protoplanets are plotted together.

FIG. 16. Individual plots of longitudes of perihelion and eccentricities in Fig. 15. a is the semimajor axis, m is the mass of each protoplanet, respectively. M_e means the mass of the Earth ($M_\oplus$).

FIG. 17. The same plot as Fig. 15, but the solution is obtained by the linear secular perturbation theory.

FIG. 18. (a) The CWB diagram of perturbed protoplanet systems only by Jupiter with large mass variation. $N = 14$, $\langle e^2 \rangle^{\frac{1}{2}} = 2 \langle I^2 \rangle^{\frac{1}{2}} = 0.005$, $2.0 \times 10^{-7} M_\odot < m < 8.0 \times 10^{-7} M_\odot$ with $\langle m \rangle = 5 \times 10^{-7} M_\odot$, a_1=0.5AU. Small variation of spacing is also added between $0.8\Delta R_H$ and $1.2\Delta R_H$. Points just on the upper boundary line ($T_I = 5.0 \times 10^7$ years) means that the system has been stable at least for 5.0×10^7 years. (b) Semimajor axes of the inner protoplanets of the pair which exhibited the close encounter. Two solid lines denote the inner and outer boundary of the averaged initial distribution of protoplanets. The existence of some points outside the upper boundary is due to randomness of initial mass distribution. (c) The serial number of the inner protoplanets of the pair which exhibited the close encounter. Note that in (b) and (c) there are no points corresponding to the points on the upper boundary of (a) since they did not exhibit any close encounters.

FIG. 19. Time evolution of longitudes of perihelion (upper) and eccentricities (lower) of massless protoplanets under the effect only of Jupiter by the first-order secular perturbation theory. $N = 14$, and initial orbits of the particles are the same as Fig. 17. Thick line in the upper panel denotes the longitude of perihelion of Jupiter.

FIG. 20. Numerical result of the time evolution of longitudes of perihelion (upper) and eccentricities (lower) of a protoplanet system when the orbit of Jupiter is circular. $N = 14$, $\langle e^2 \rangle^{\frac{1}{2}} = 2\langle I^2 \rangle^{\frac{1}{2}} = 0.005$, $2.0 \times 10^{-7} M_\odot < m < 8.0 \times 10^{-7} M_\odot$ with $\langle m \rangle = 5.0 \times 10^{-7} M_\odot$, $a_1 = 0.5\mathrm{AU}$, $\Delta = 13.0$. Small variation of spacing is also added between $0.8\Delta R_H$ and $1.2\Delta R_H$. Initial orbits of the protoplanets are the same as Fig. 15. All data of 14 protoplanets are plotted together.

FIG. 21. Variation of eccentricities of hypothetical and actual terrestrial planetary systems. (a) The system without Mercury and the Earth. (b) The system without the Earth. (c) The actual planetary system which consists of eight planets from Mercury to Neptune, neglecting Pluto. Eccentricity of Mars is not plotted in (c).

FIG. 22. $(e, \delta\varpi)$ diagram of the terrestrial planetary subsystems ($\delta\varpi$ means the difference of the longitudes of perihelion). Note that the symbol of longitude of perihelion ϖ is replaced by "p" or "p_jupiter" in the labels of the panels. (a) $(e_{venus}, \varpi_{venus} - \varpi_{jupiter})$ in the case without Mercury and the Earth, corresponding to Fig. 21(a). (b) and (c) are the cases without the Earth, corresponding to Fig. 21(b). (b) $(e_{mercury}, \varpi_{mercury} - \varpi_{venus})$, (c) $(e_{mercury}, \varpi_{mercury} - \varpi_{jupiter})$.

Figures

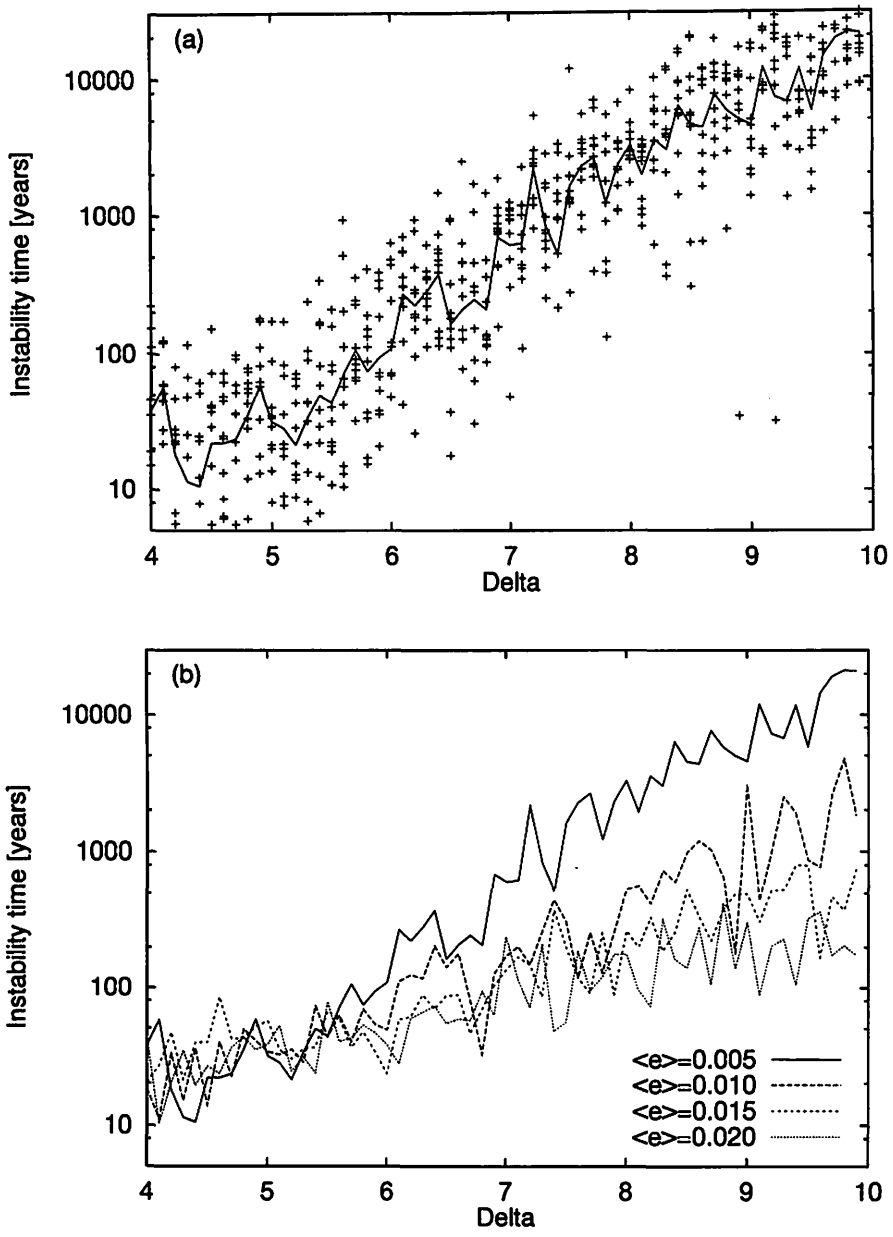

Ito and Tanikawa, Fig. 1

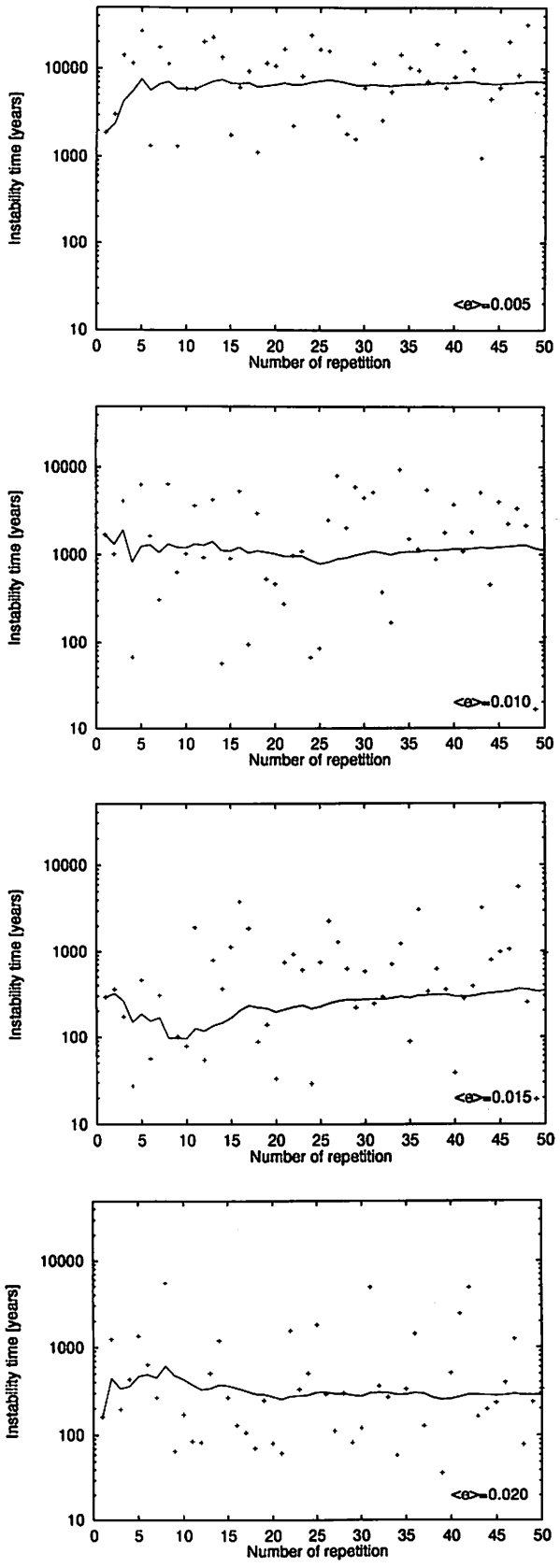

Ito and Tanikawa, Fig. 2

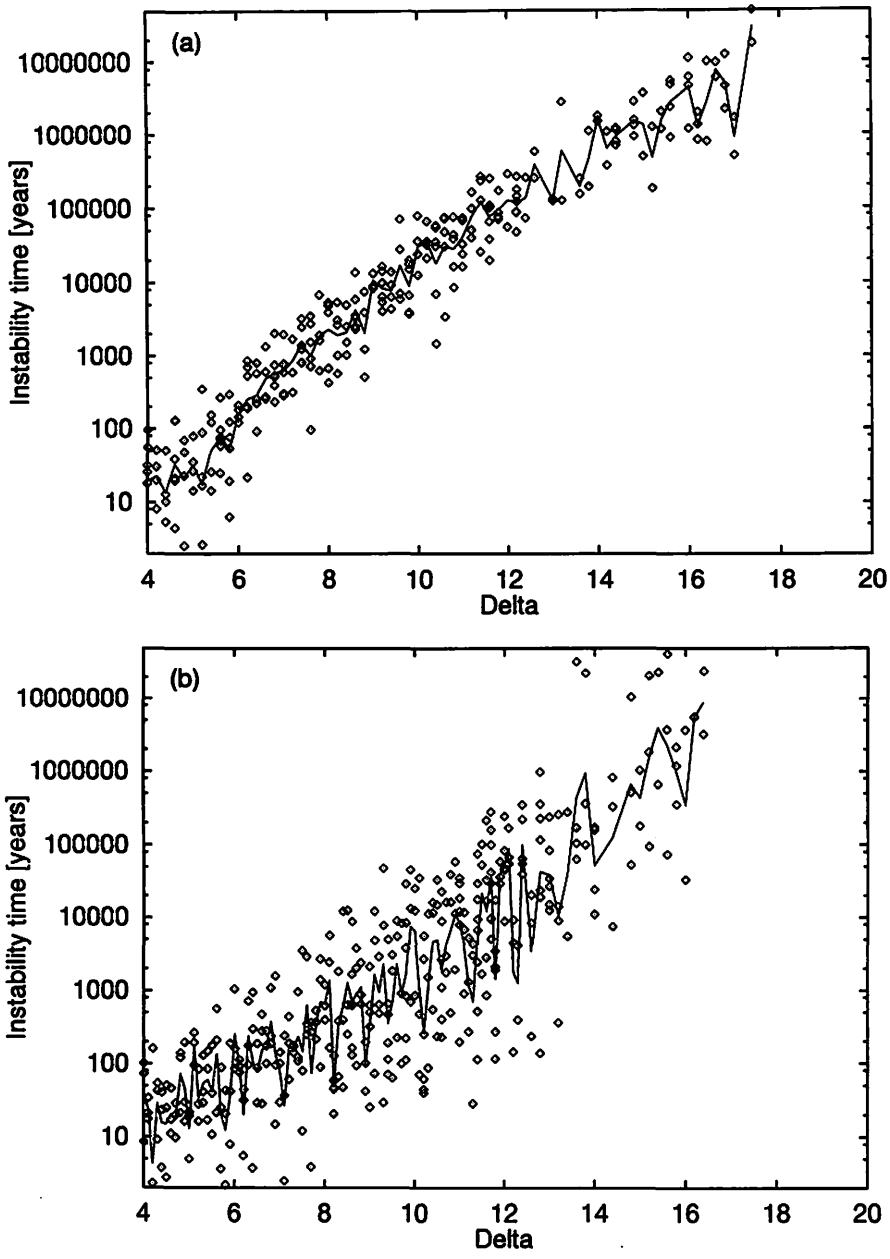

Ito and Tanikawa, Fig. 3

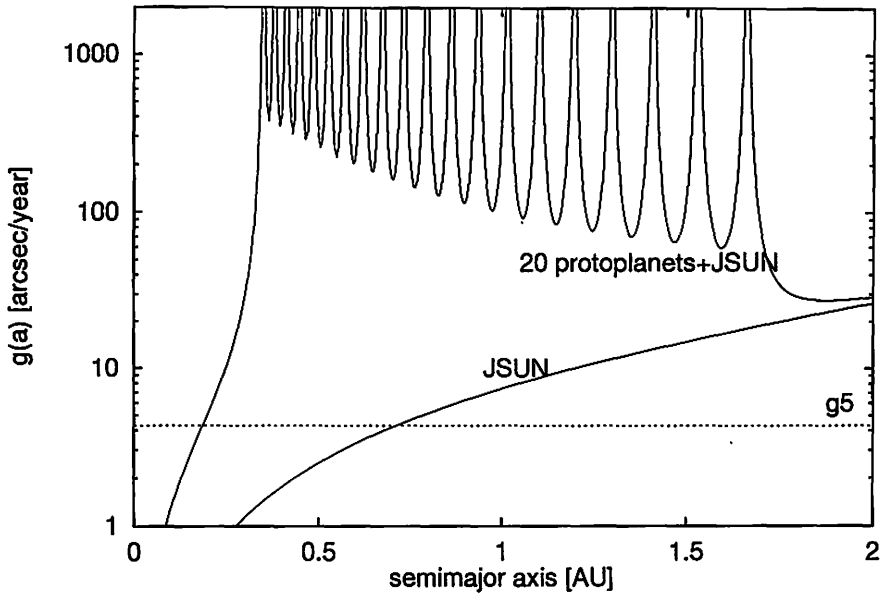

Ito and Tanikawa, Fig. 4

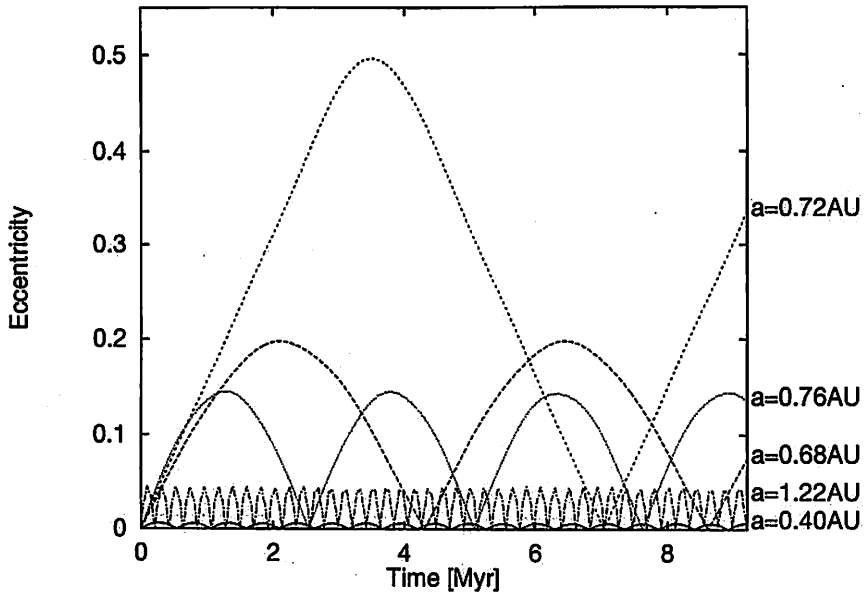

Ito and Tanikawa, Fig. 5

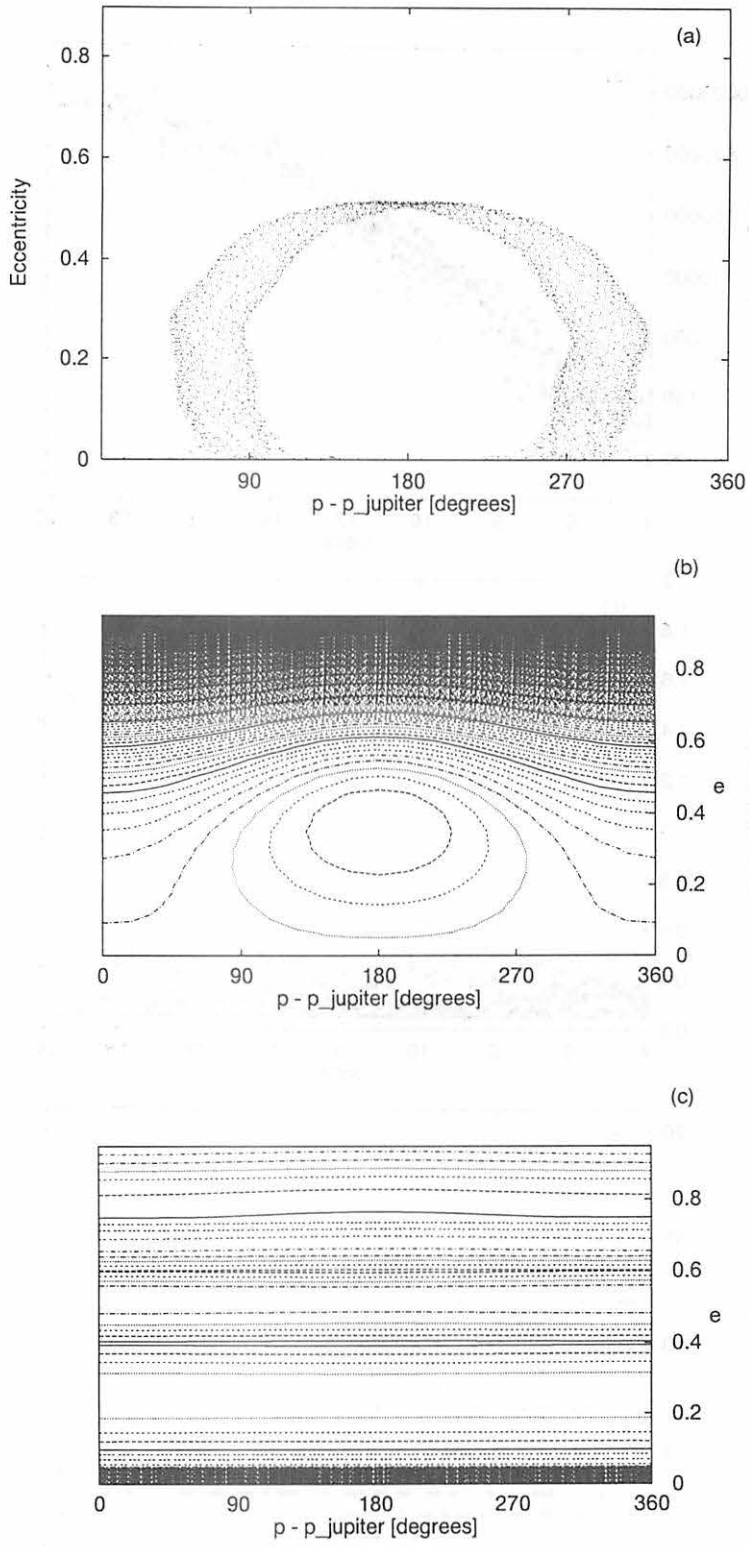

Ito and Tanikawa, Fig. 6

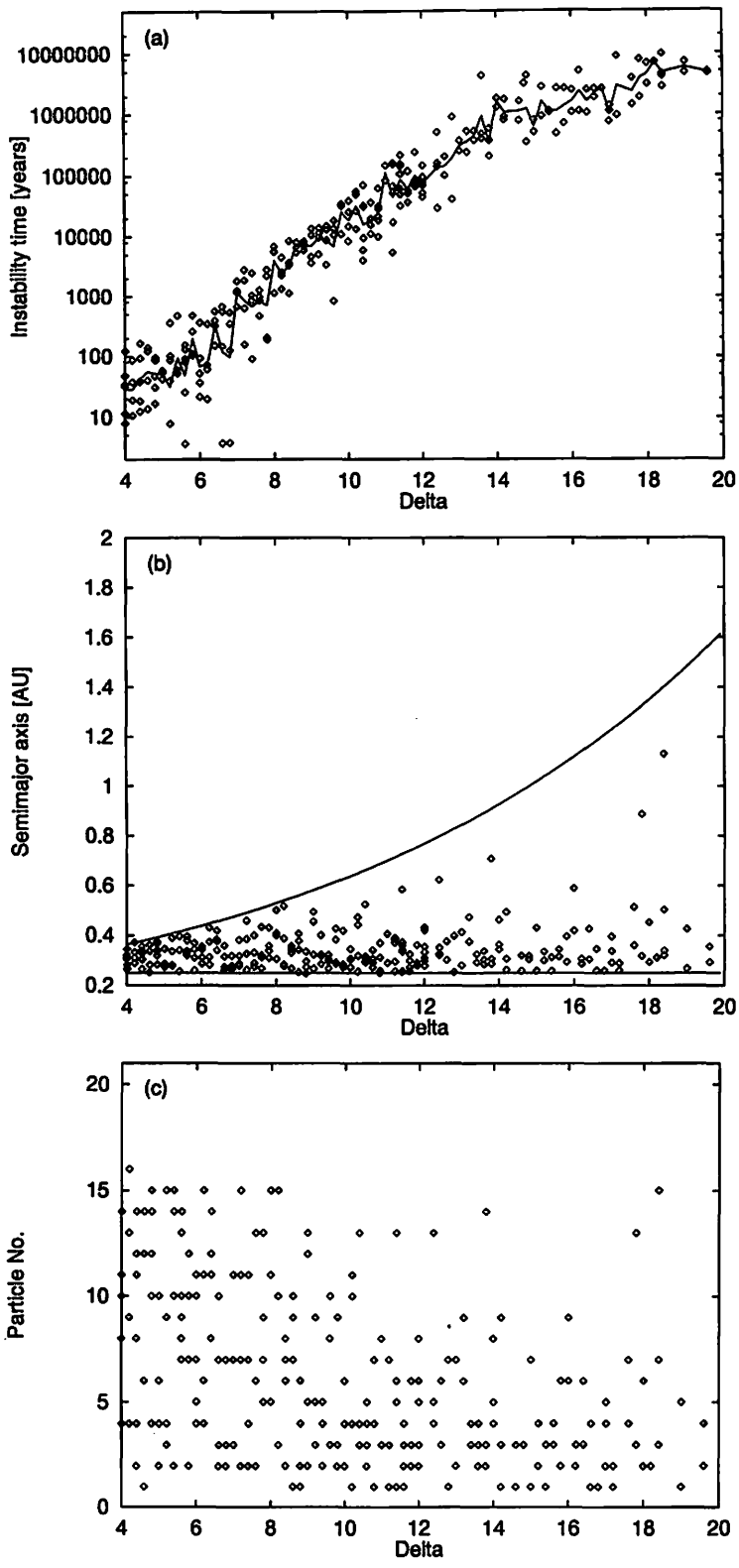

Ito and Tanikawa, Fig. 7

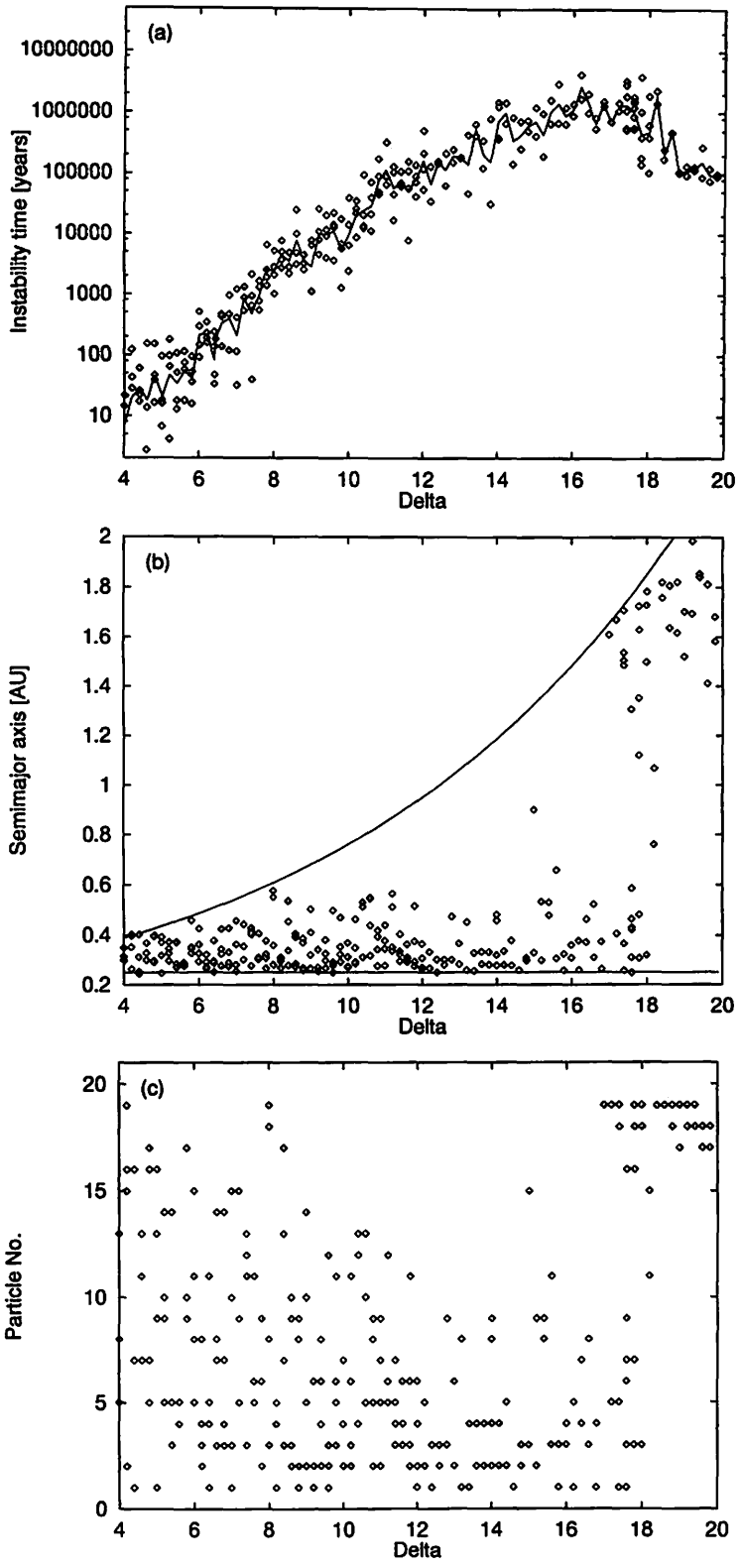

Ito and Tanikawa, Fig. 8

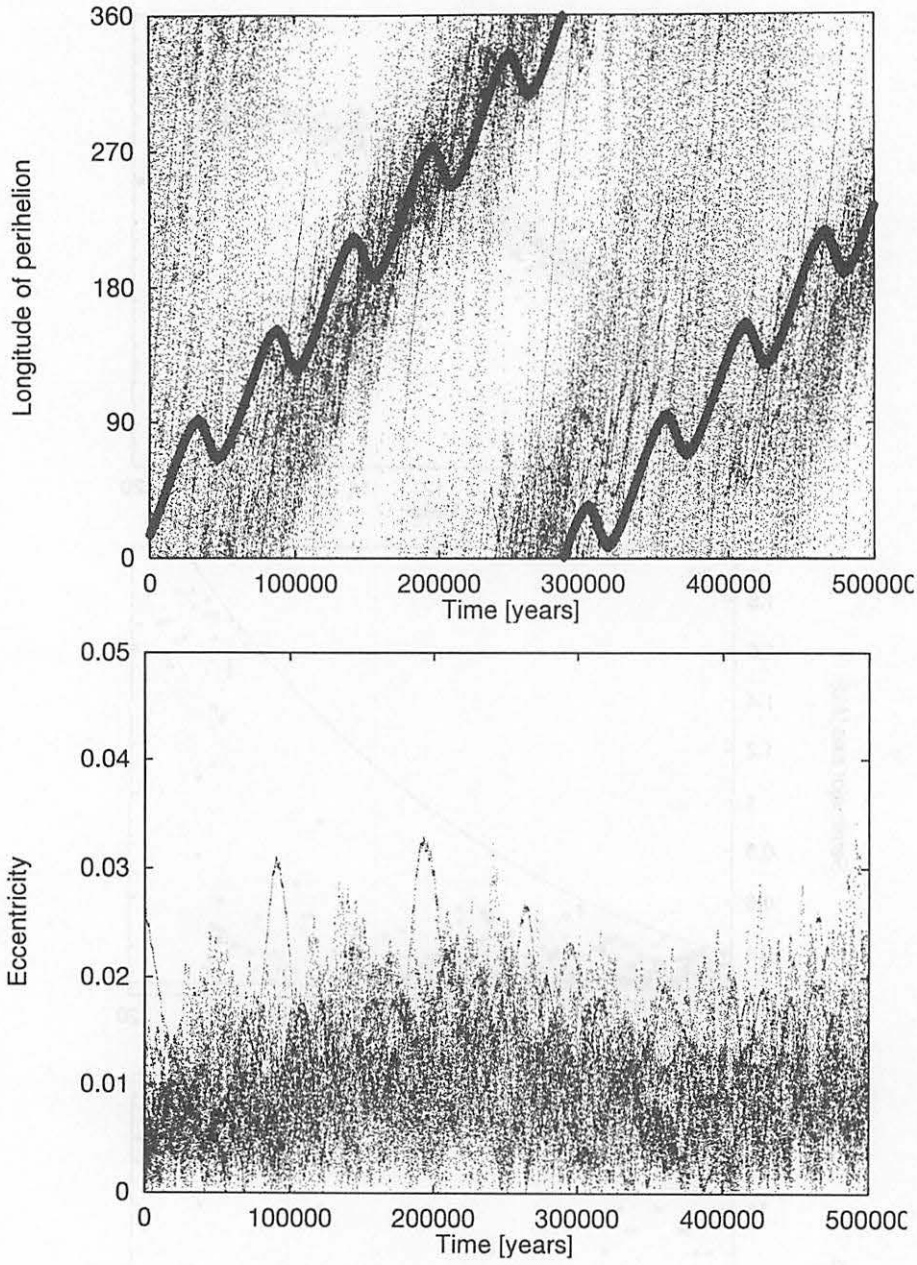

Ito and Tanikawa, Fig. 9

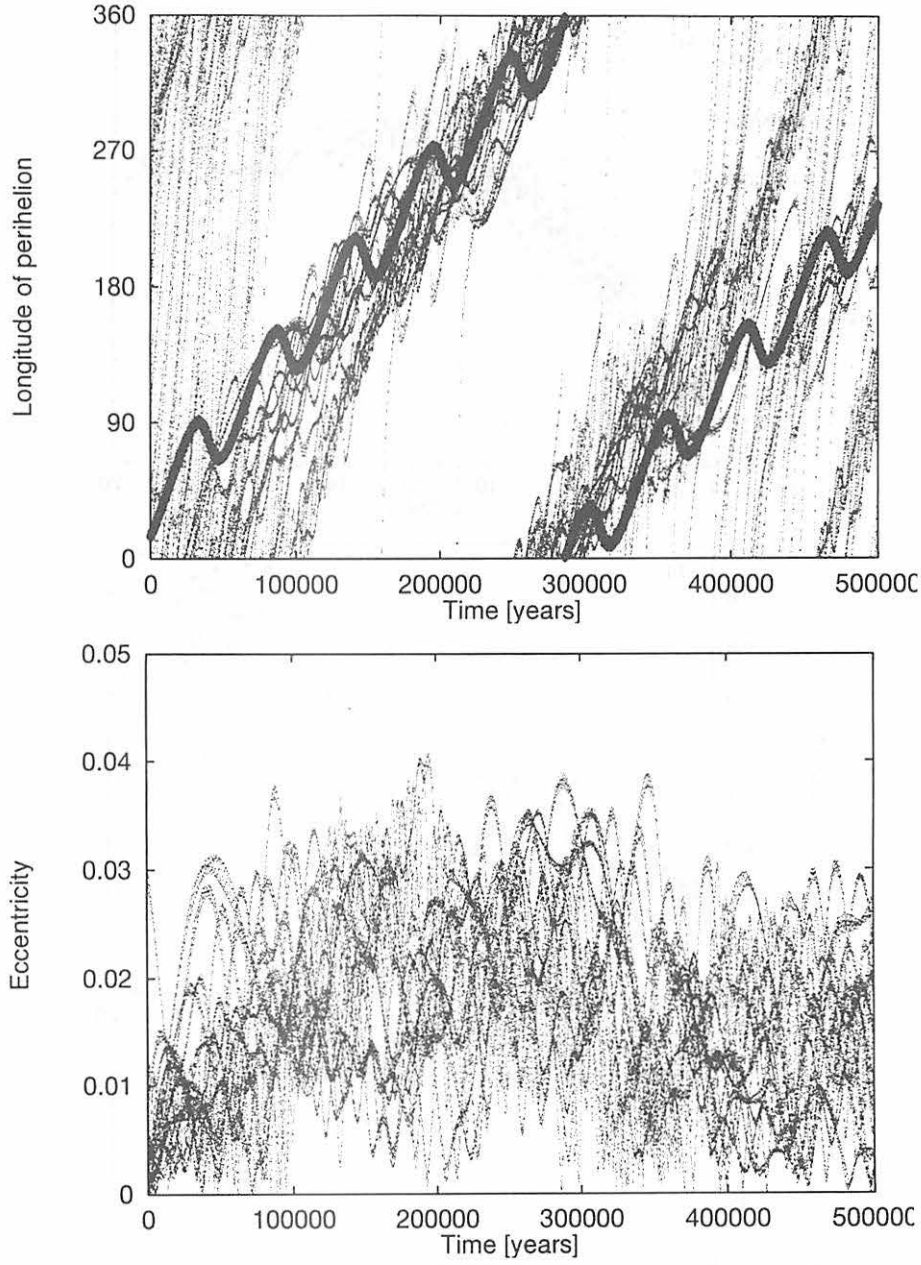

Ito and Tanikawa, Fig. 10

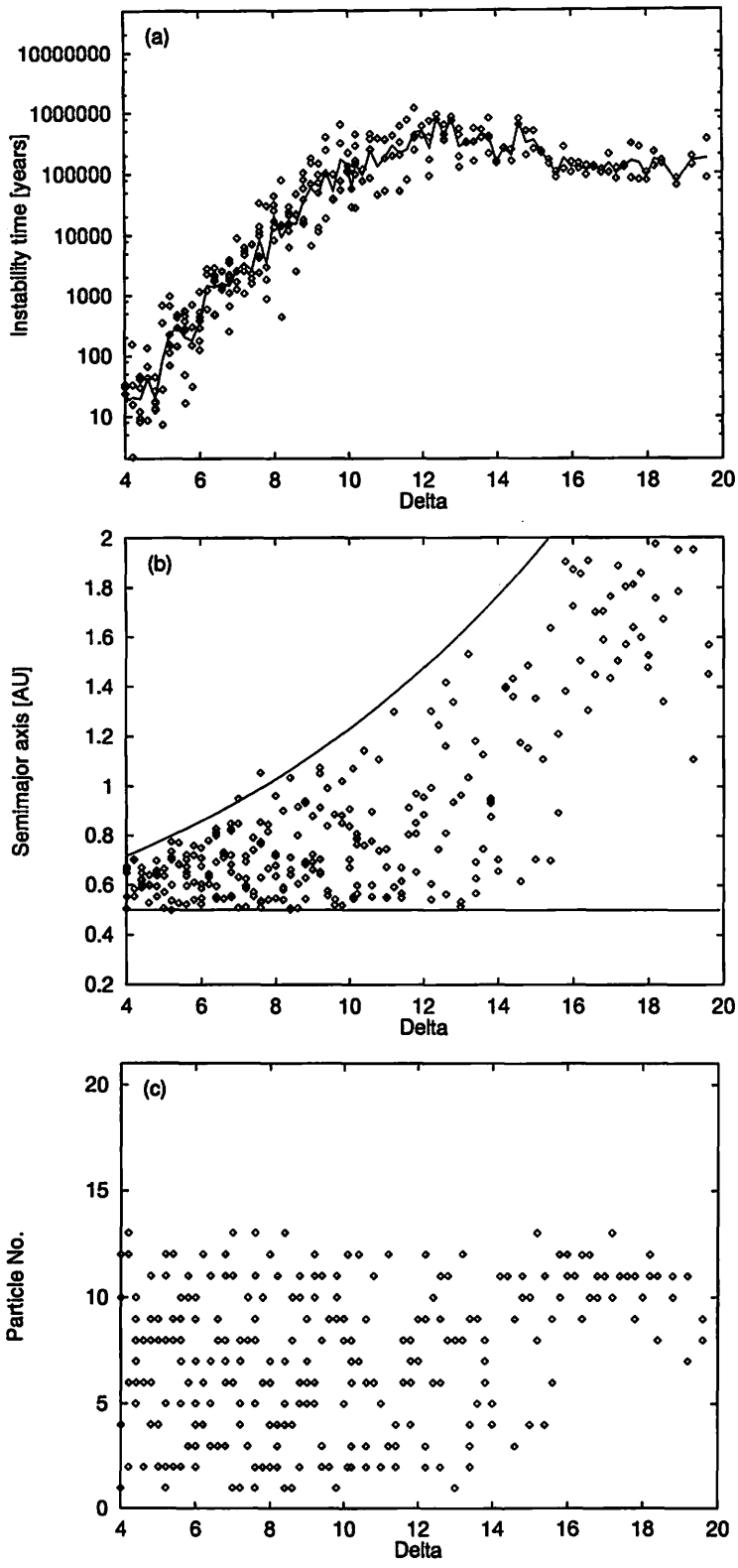

Ito and Tanikawa, Fig. 11

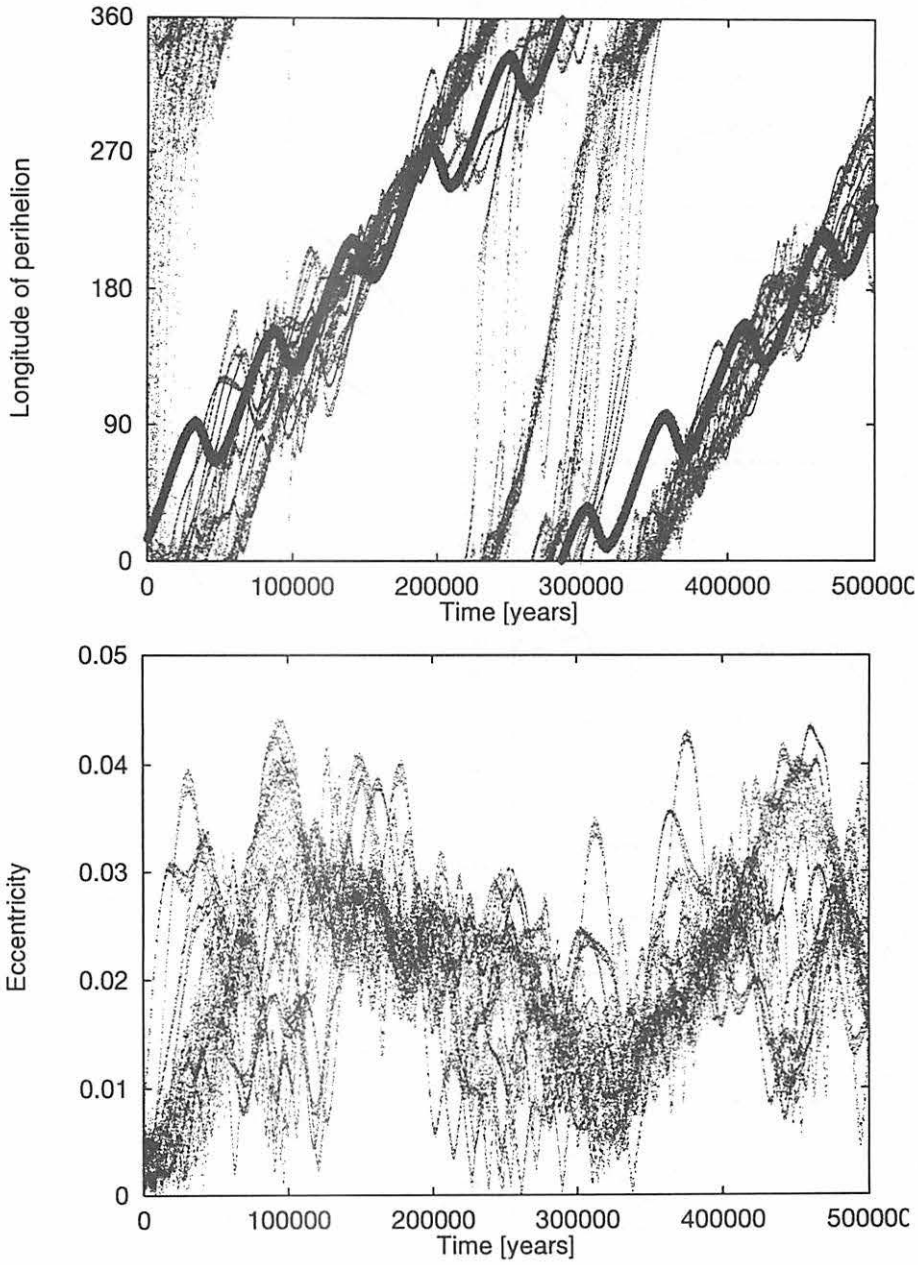

Ito and Tanikawa, Fig. 12

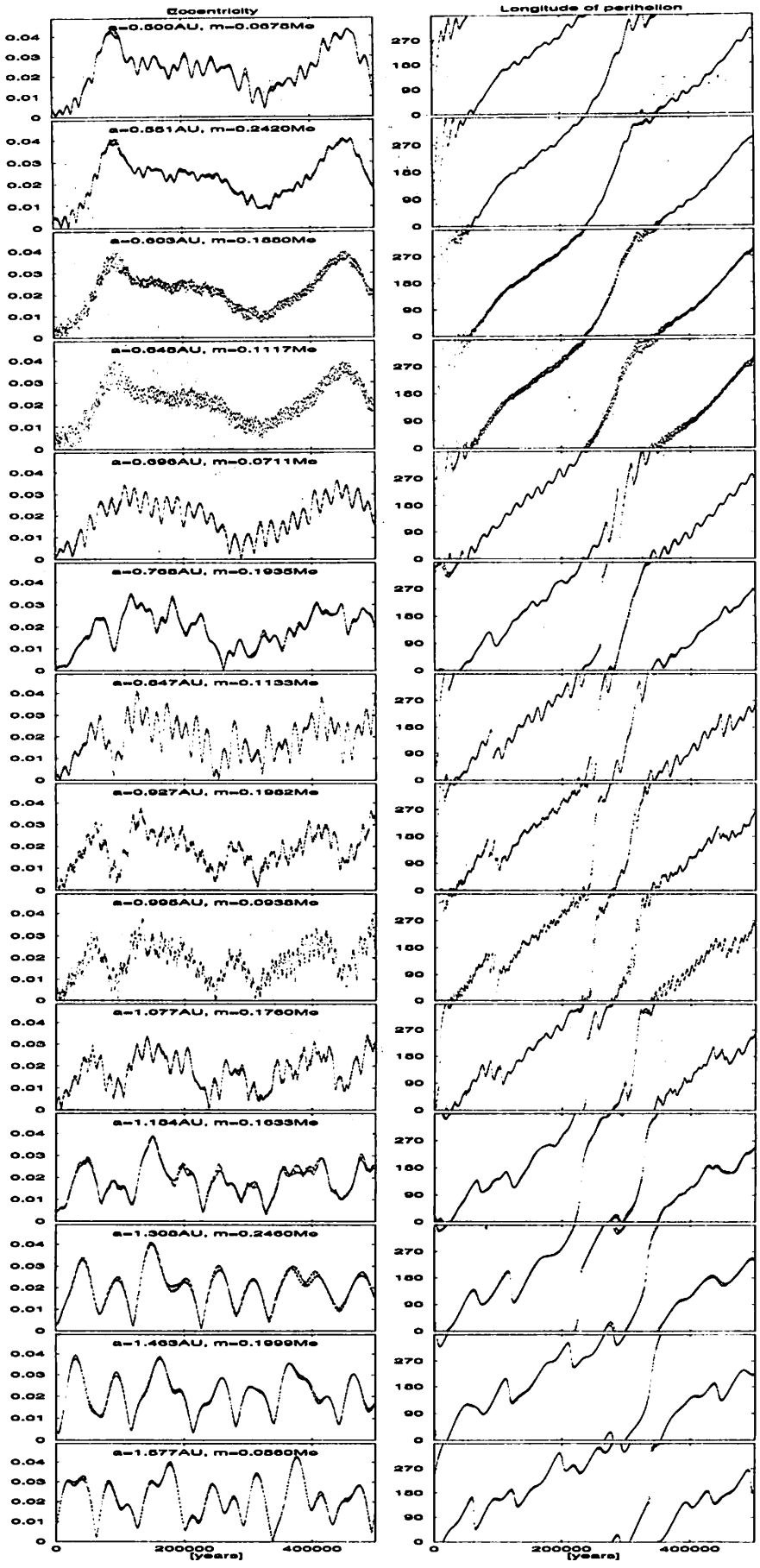

Ito and Tanikawa, Fig. 13

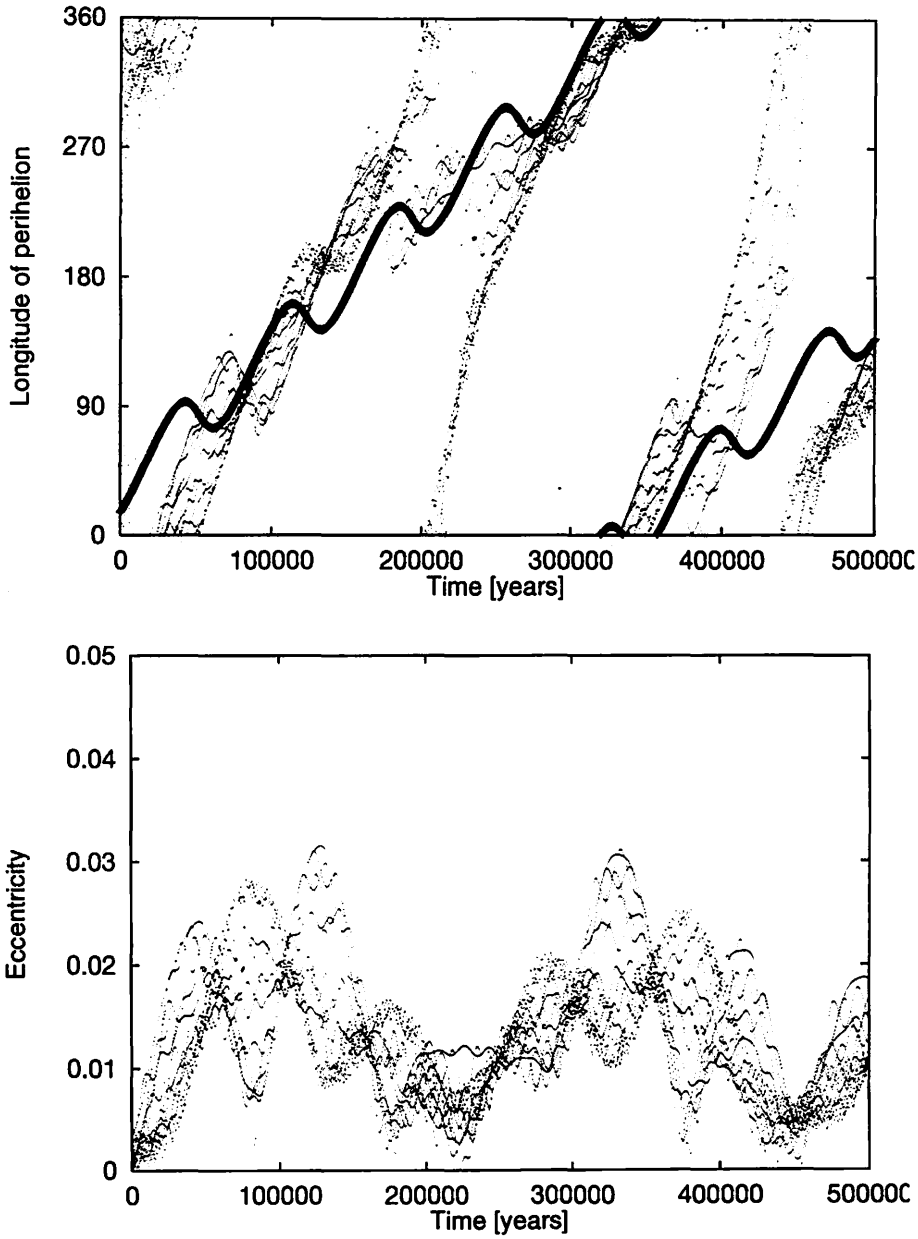

Ito and Tanikawa, Fig. 14

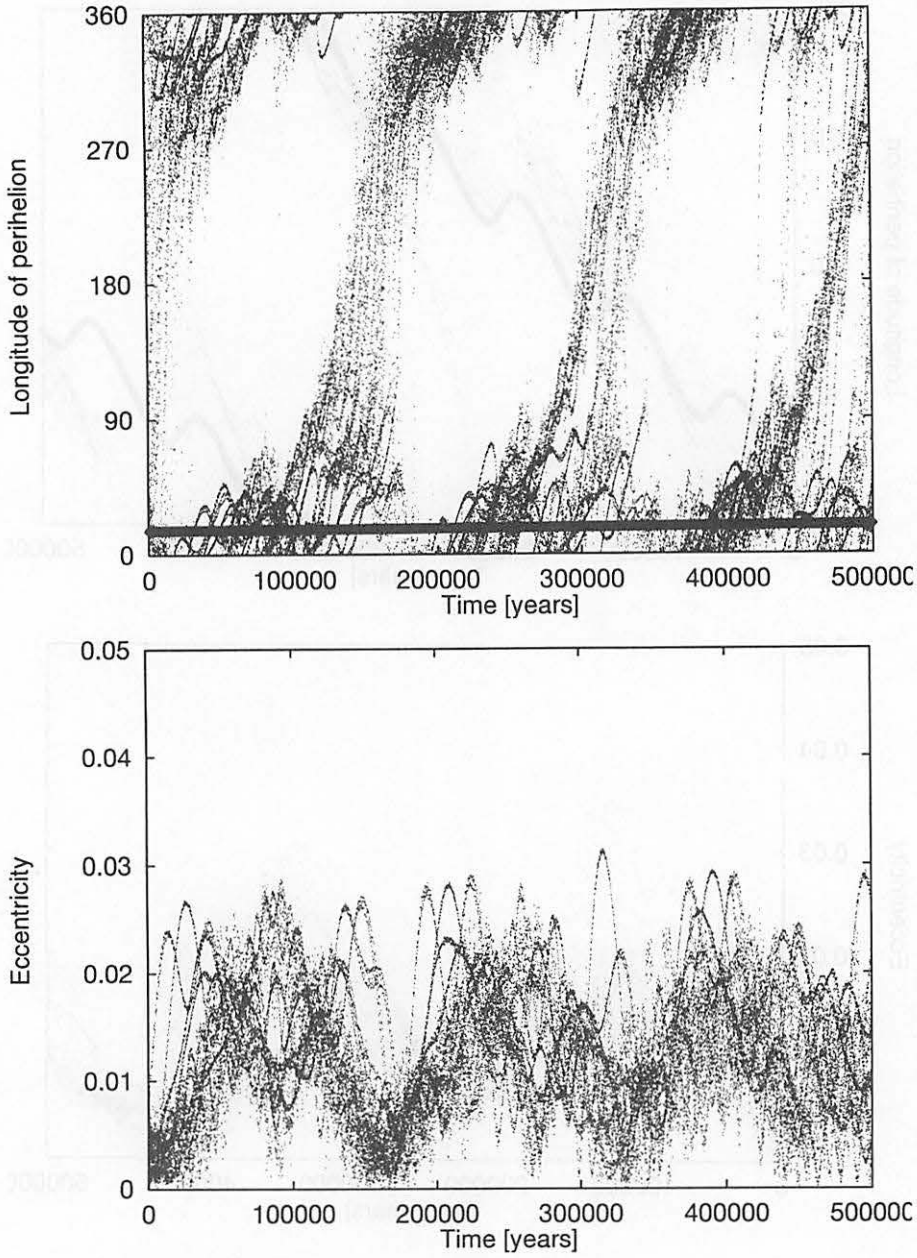

Ito and Tanikawa, Fig. 15

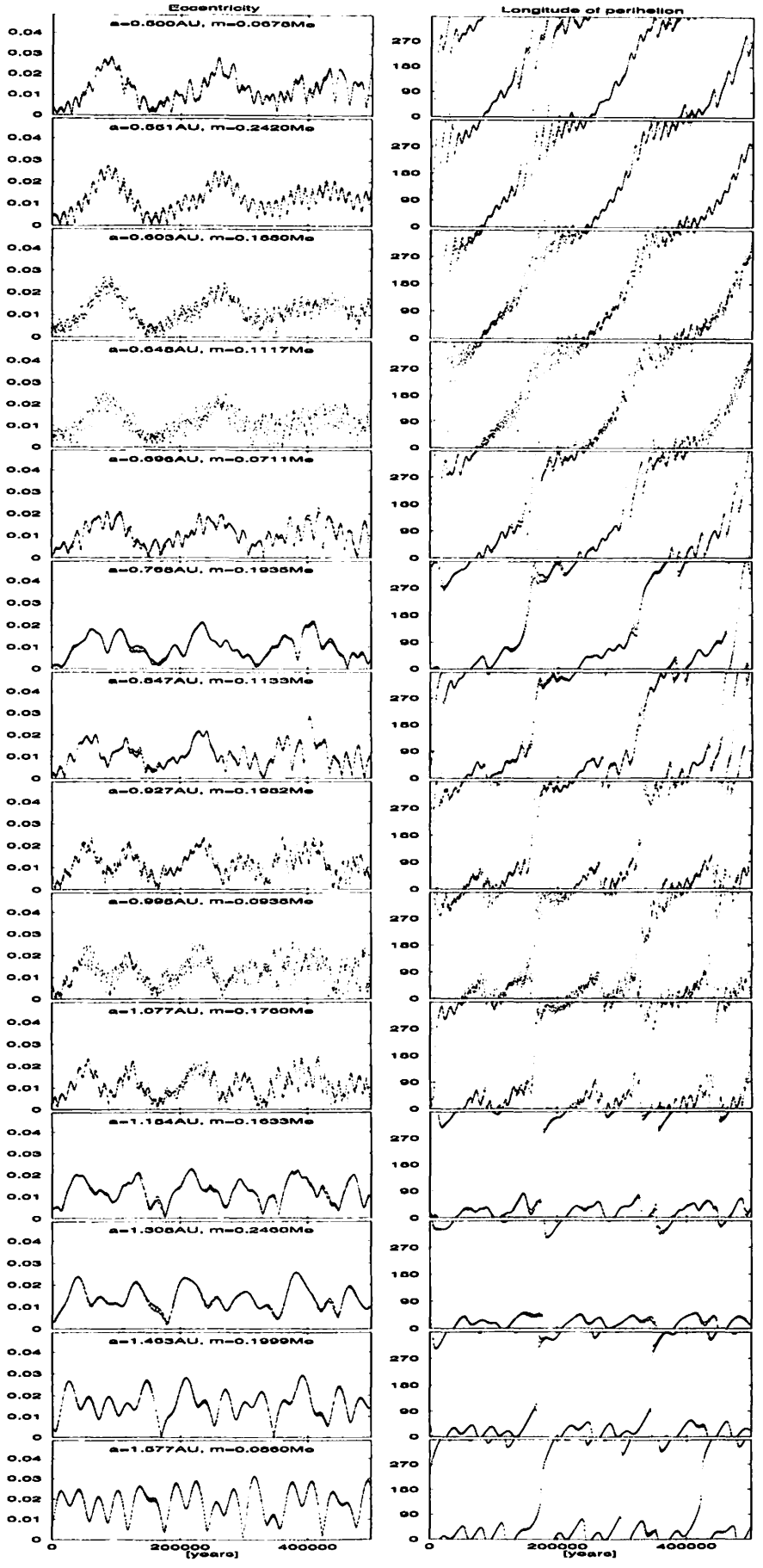

Ito and Tanikawa, Fig. 16

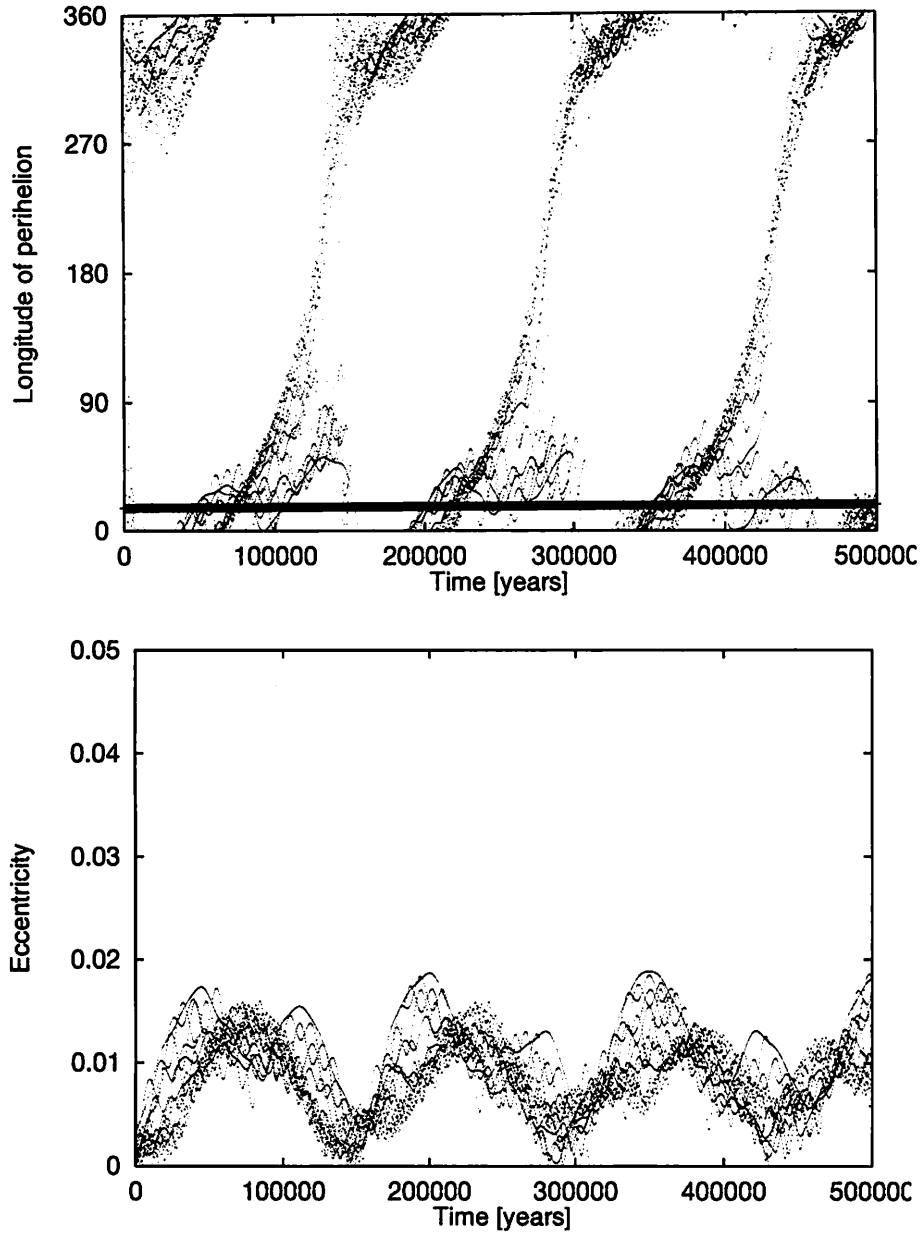

Ito and Tanikawa, Fig. 17

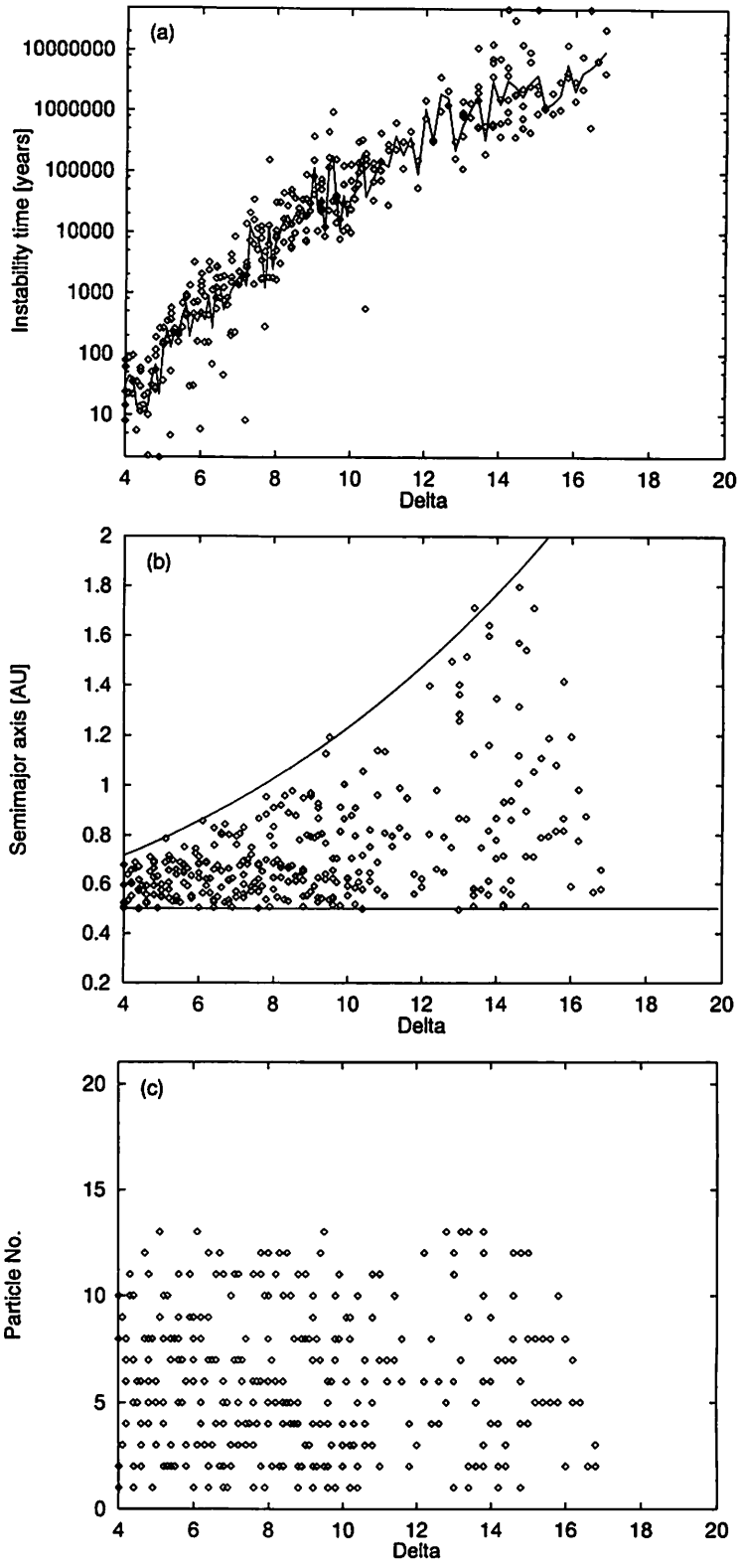

Ito and Tanikawa, Fig. 18

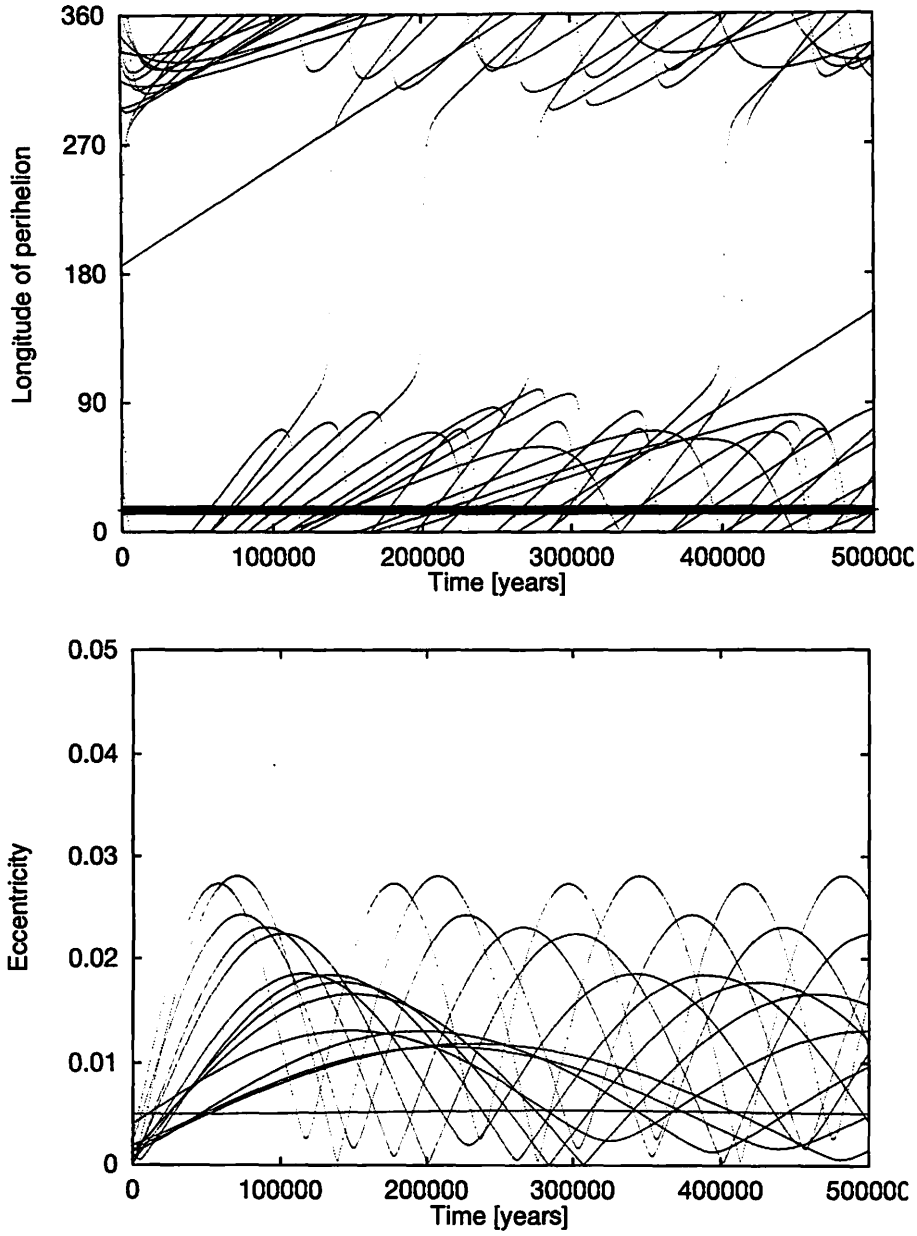

Ito and Tanikawa, Fig. 19

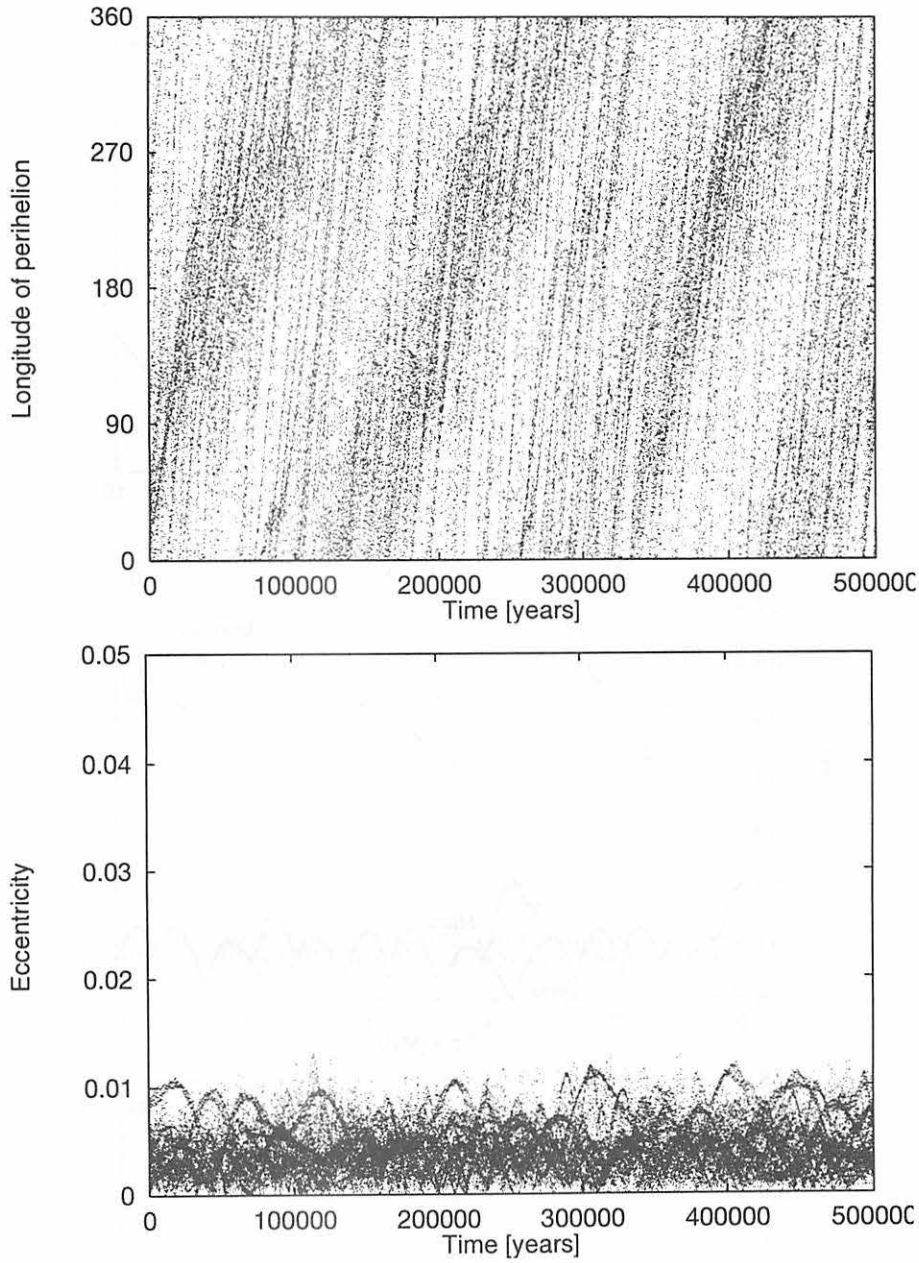

Ito and Tanikawa, Fig. 20

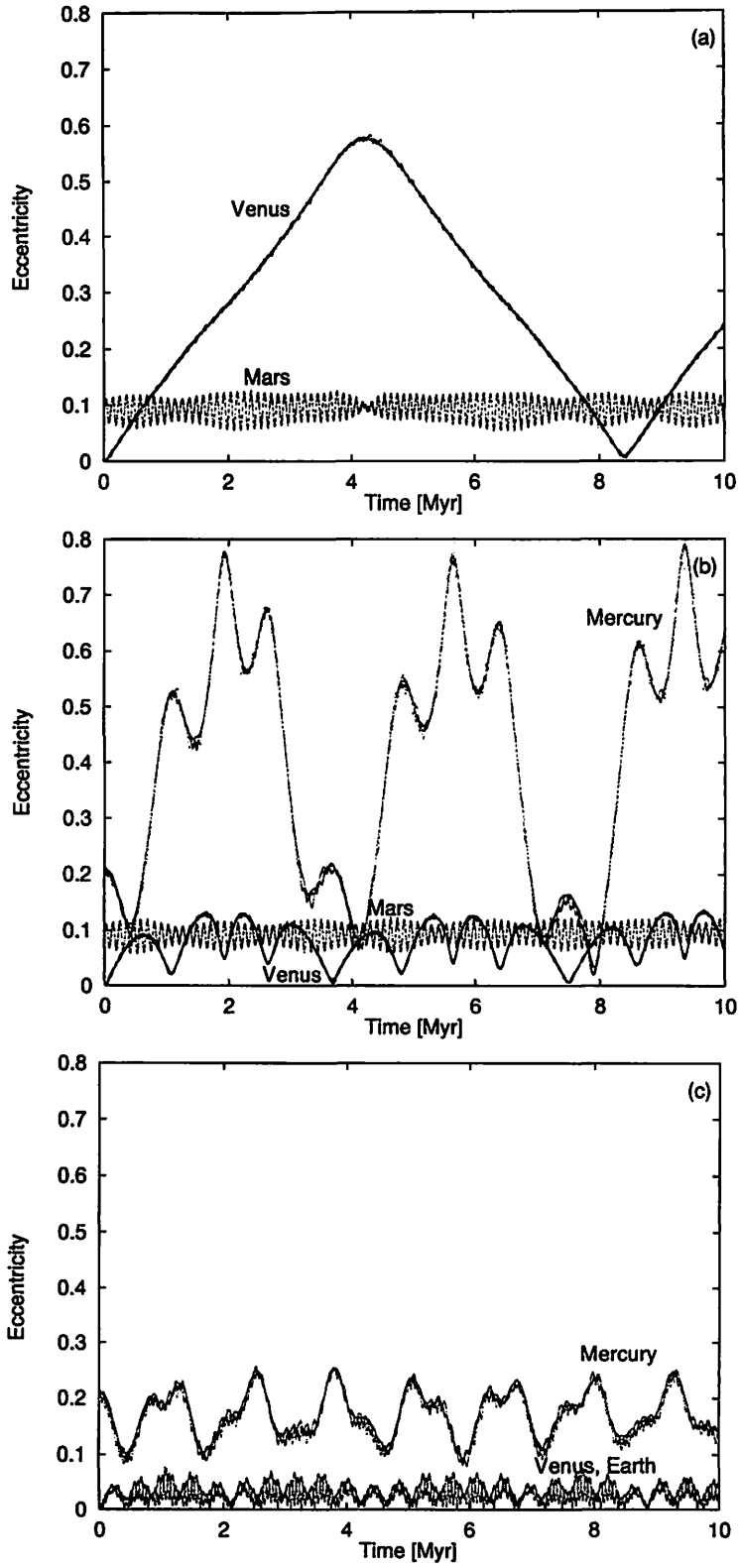

Ito and Tanikawa, Fig. 21

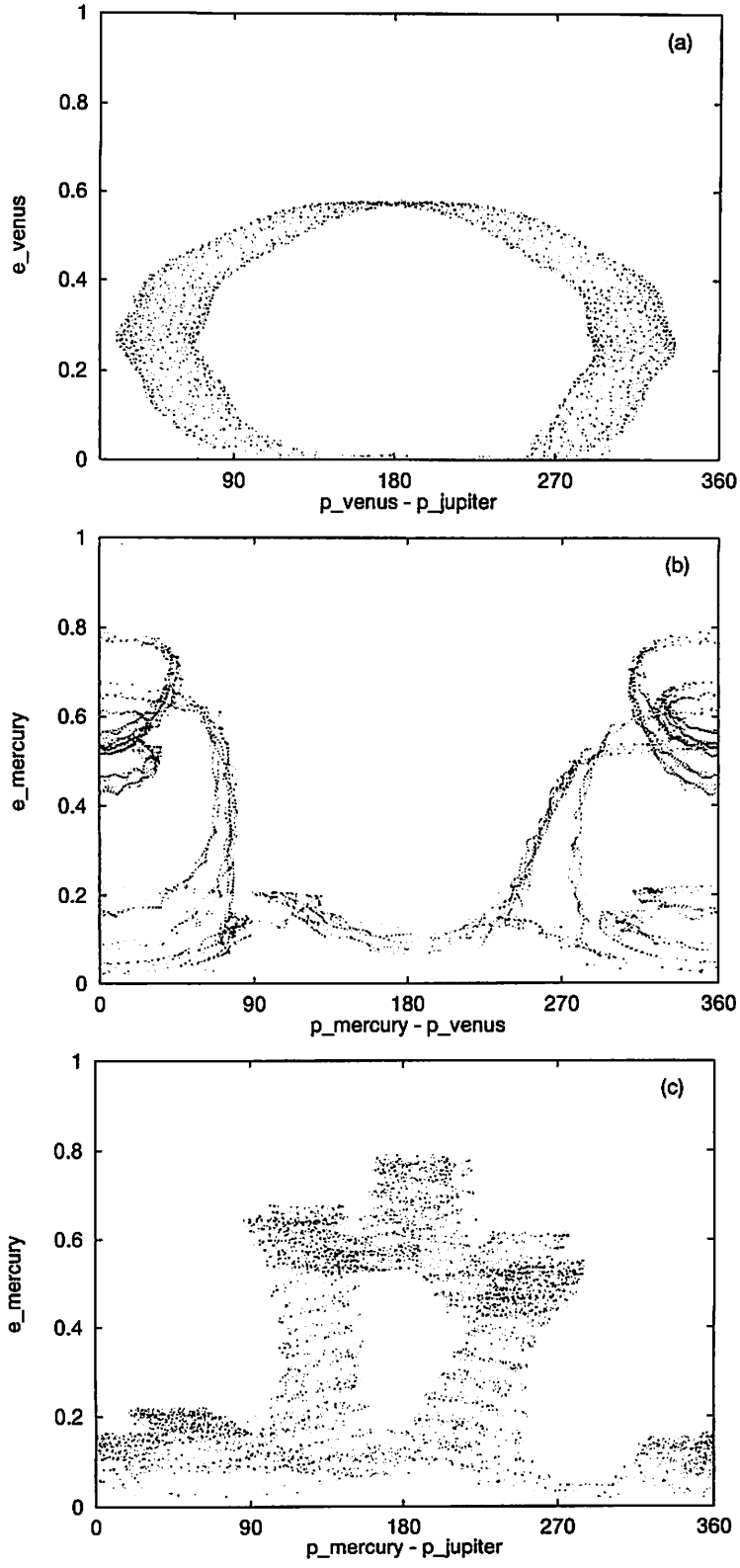

Ito and Tanikawa, Fig. 22

The Stability of Protoplanet Systems

Keiko Yoshinaga, Eiichiro Kokubo, and Junichiro Makino
Department of General Systems Studies, Collage of Arts and Sciences, University of Tokyo,
3-8-1 Komaba, Meguro-ku, Tokyo, 153 Japan
TEL and FAX: 81-3-3465-3925
E-mail: yosinaga@chianti.c.u-tokyo.ac.jp

Abstract

We investigated the stability of 10 protoplanet systems using three-dimensional N-body simulations. We found that the timescale of instability T depends strongly on the initial random velocities v (eccentricities e and inclinations i) and orbital separations Δa. For zero initial random velocities, we confirmed the result of Chambers et al. (1996) that T is proportional to $\exp(\Delta a)$. For finite random velocities, we found that T depends strongly on the initial velocity dispersion. The relation between T and Δa is still expressed as $\log T = c + b\Delta a$. However, both b and c depend on initial random velocities and the slope, b, becomes smaller for larger v. Even for relatively small initial eccentricities such as $e \sim 2r_{\rm H}/a$, where $r_{\rm H}$ is the Hill radius, the timescale can be reduced by a factor of 10, compared with the case of the zero random velocity. So the timescale of the formation of inner planets might be much shorter than what suggested by Chambers et al.

1 Introduction

It is now widely accepted that terrestrial planets and cores of Jovian planets are formed through the accretion of many small bodies known as planetesimals (Safronov 1969, Hayashi et al. 1985). During this accretion process, larger planetesimals grow more rapidly than smaller ones, resulting in the formation of massive "protoplanets". This growth mode of planetesimals is called "runaway growth" (Greenberg et al. 1978, Wetherill and Stewart 1989). Kokubo and Ida (1996) investigated this runaway growth phase of planetary formation by means of direct N-body simulation. They found that the "protoplanet" with roughly equal masses form as the result of the runaway growth (Kokubo and Ida 1997). Their typical orbital separations

are about $10r_{\rm H}$, where $r_{\rm H}$ is the Hill radius, and they grow up to mass of about 10^{25}g in a short timescale. After the formation of protoplanets, the growth slows down because the velocity dispersion of the planetesimals around the protoplanets is increased by the viscous stirring (Ida and Makino 1993). Thus runaway growth is effectively halted well before the terrestrial planets are formed. Note that in the outer region, protoplanets may grow to the critical mass for gravitational instability of the surrounding solar nebula gas, thereby capturing a large amount of gas to become massive giant planets. Thus, Jovian planets would be formed directly through the runaway growth of solid cores (Kokubo and Ida 1997).

There are very few studies on the planetary growth after the runaway stage. When the runaway is halted in the terrestrial planet region, a typical protoplanet has the mass about 1/10 of the present planets. At present, it is not at all understood how these protoplanets evolve into the present terrestrial planets. Chambers et al. (1996) investigated the stability of systems of three or more protoplanets by numerical integration. They found that multi-planet systems are unstable. The time of the first close encounter T is expressed approximately as $\log T = b\Delta a + c$, where b and c are constants, and Δa is the initial separation of the planets in the unit of their Hill radius $r_{\rm H}$. If we extrapolate their result to $\Delta a \sim 10r_{\rm H}$, the instability timescale would be well beyond 10^8 years. In other words, it would have taken very long time for terrestrial planets to be actually formed. However, the result of Chambers et al. (1996) is based on several assumptions, some of which might not be very appropriate. For example, all planets are initially on coplanar, circular orbits and the effect of Jupiter is ignored.

In this paper, we investigated the effect of the initial random velocities of protoplanets on the stability of protoplanet system by performing three-dimensional N-body simulations. We performed many simulations in which orbits of protoplanets have initial eccentricities and inclinations. For coplanar, circular cases, our result agrees well with that of Chambers et al. (1996). For cases with finite eccentricities e and inclinations i, we found that the timescale becomes shorter as initial eccentricity and inclination become larger. Even for relatively small initial eccentricities such as $e \sim 2r_{\rm H}/a$, the timescale can be reduced by a factor of 10. In other words, the timescale of the formation of inner planet might be much shorter than what implied by Chambers et al. (1996). If the gas of protoplanetary nebula is dissipated at early stage of the accretion, it is possible that eccentricities and inclinations of protoplanets become large.

This paper is organized as follows. We describe the numerical method of N-body simulation, initial conditions, and method of analysis in Section 2. In Section 3, we show the results of the systems of 10 protoplanets. Section 4 contains the summary and a discussion on the timescale of the formation of terrestrial planets.

2 Method of Calculation

2.1 P(EC)^n Hermite Integrator

We used the 4th-order P(EC)^n Hermite scheme (Makino and Aarseth 1992, Kokubo et al. 1997) with individual timestep. This scheme is effectively time-symmetric when applied to a nearly circular orbit, and therefore conserves important orbital elements, in particular, the semi-major axis and the eccentricity, up to the round off error. For details, see Kokubo et al. (1997).

Chambers et al. (1996) used the second-order MVS (Wisdom and Holman 1992, Levison and Duncan 1994). We decided not to use MVS, because of the following two reasons. First, there is no known way to change timesteps without loosing the good properties of MVS. Second, the validity of MVS is questionable when the mutual gravity between planets is strong. Since we want to treat the cases where orbits of planets are changed significantly by close encounters between planets, the above limitations of MVS are rather significant. The P(EC)^n Hermite scheme is better than MVS, as far as the above respects are concerned. It can handle close encounters without too much degradation of accuracy, because the basic integrator is 4th-order.

Here we present the results of test calculations for the 2-body problem. The system consists of the sun and one small planet. Initial values of the semi-major axis a and the eccentricity e are 1 and 0.1, respectively. The orbital period is 2π in the system of units we used. The orbit of the planet is integrated with a constant timestep of $\Delta t = 2^{-6}$. Therefore, the number of steps is about 400 per orbit. Figure 1 shows the relative error of total energy for 10^5 orbital periods. There is no secular error for $n \geq 3$. In the case of $n = 2$, we can see that the energy error first goes down and then goes up again. This is simply because we plotted the absolute error. The actual error is an combination of linear term and initial offset. For $n = 2$, we still have a non-zero linear term in the error. Therefore we used $n = 3$ for all calculations in the next section. The eccentricity is also conserved up to similar accuracy and showed no secular error for $n \geq 3$.

The argument of pericenter ω is not conserved by the time-symmetric schemes. Therefore, when we use the time-symmetric Hermite scheme, the timestep must be chosen so that the error in ω is acceptable. Otherwise, the numerical error can override the change of the orbital elements due to the interaction between protoplanets. The error is proportional to Δt^4, since the Hermite scheme is the 4th-order scheme. In our test calculation, we get the result that even for a large eccentricity such as $e \sim 0.1$, the behavior of $\Delta\omega$ is independent of e. In practice, protoplanets have small eccentricities at the final stage of planetary formation. For $\Delta t = 2^{-6}$, $\Delta\omega$ per orbit is 10^{-8} (rad), which is small enough if we stop integration at $\sim 10^6$ orbits.

Finally, we integrated the system of 10 equal-mass protoplanets using the P(EC)^3

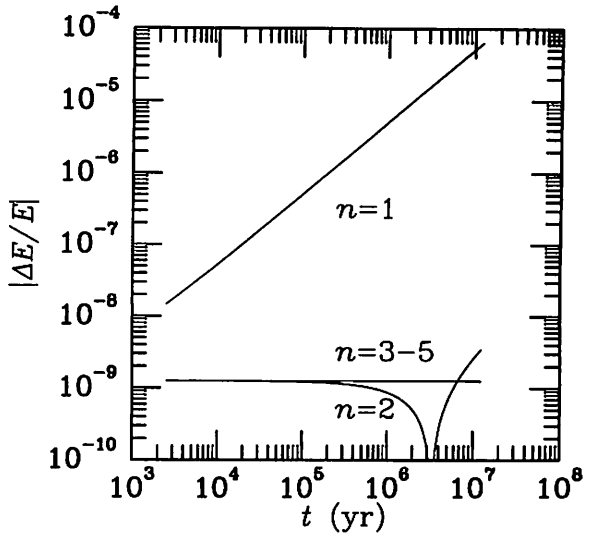

Figure 1: The relative energy error of the 4th-order Hermite scheme for the 2-body problem for 10^5 periods. The results for the P(EC)^n schemes with $n = 1$ through 5 are shown.

Hermite integrator. We set the mass of all protoplanet to $10^{-7}M_\odot$, and the initial orbital separation to $\Delta a = 11 r_{\rm H}$. The semi-major axis of the innermost protoplanet was 1 (AU). We used individual timesteps, with several different maximum timesteps. For all timestep choices, we confirmed that there is no secular error and the error is about 10^{-11}.

2.2 Initial Conditions

We investigate the evolution the system of 10 protoplanets. We set the initial masses of protoplanets all equal ($m = 10^{-7}M_\odot$). This value is about 1/10 of the earth mass. The initial orbital separation $\Delta a_{\rm ini}$, eccentricity $\langle e^2 \rangle_{\rm ini}^{\frac{1}{2}}$ and inclination $\langle i^2 \rangle_{\rm ini}^{\frac{1}{2}}$ are given in Table 1, where $r_{\rm H}$ is the mutual Hill radius,

$$r_{\rm H} = \left(\frac{2m}{3M_\odot} \right)^{\frac{1}{3}} a \tag{1}$$

and h is the reduced Hill radius defined as $h = r_{\rm H}/a$. (When $m = 10^{-7}M_\odot$, $h \simeq 4.055 \times 10^{-3}$.) We define the scaled eccentricity and inclination as $\tilde{e} = e/h$, and $\tilde{i} = i/h$. The Hill radius for the outer pair of protoplanets is larger than that for the inner pair, so the orbital separations are not equal spaced.

We assigned initial eccentricities and inclinations so that they obey the Rayleigh distribution with dispersions $\langle \tilde{e}^2 \rangle_{\rm ini}^{\frac{1}{2}} = 2\langle \tilde{i}^2 \rangle_{\rm ini}^{\frac{1}{2}}$ (Ida and Makino 1992a). Protoplanets are distributed at random phases. We calculated 40 cases with different random numbers for the same set of $\Delta a_{\rm ini}, \langle \tilde{e}^2 \rangle_{\rm ini}^{\frac{1}{2}}, \langle \tilde{i}^2 \rangle_{\rm ini}^{\frac{1}{2}}$.

$\log(\Delta a / r_{\rm H})$	4	4.5	5	5.5	6	6.5	7	7.5	8	9	10
$\langle \tilde{e}^2 \rangle^{\frac{1}{2}} = 2\langle \tilde{i}^2 \rangle^{\frac{1}{2}}$	0	1	2	3	4						

Table 1: Initial Condition Parameters

2.3 Criterion for Instability

Chambers et al. (1996) calculated the multi-planet system until two planets approached to one mutual Hill radius or until a preset time limit of 10^7 years. For coplanar circular orbits, their criterion is appropriate. However, for 3-dimensional orbits, it is possible that the system become unstable before any two planets approach within one mutual Hill radius.

We decided to use a different criterion. Let us define a_j as the semi-major axis of the protoplanet initially at the jth location counted from the innermost protoplanet. Initially, the condition

$$a_j < a_{j+1} \qquad (j = 0, 1, \cdots 8) \tag{2}$$

is satisfied. We regard the system as unstable when orbital crossing occurs, in other words, when the condition

$$a_j > a_{j+1} \tag{3}$$

is satisfied for at least one value of j. We call the time at which this condition is satisfied as $T_{\rm cross}$. In addition, we define $T_{\rm collision}$ as the time when two protoplanets physically collide, in other words, when the distance of protoplanets i and j, r_{ij}, becomes smaller than the sum of the physical radii of two planets, $r_i + r_j$, where r_i, r_j are the radii of protoplanets i and j, respectively. We define the the instability timescale T as,

$$T = \min(T_{\rm cross}, T_{\rm collision}) \tag{4}$$

Note that, our criterion is not just the crossing of orbit. We require two protoplanets to exchange their locations as the result of interactions. In our results, after $T_{\rm cross}$ the system becomes unstable quickly, in the sense that a_i and a_j start

to show complex non-periodic change of large amplitude. We can therefore use the time $T_{\rm cross}$ as a reasonable timescale of the instability.

3 Results

3.1 Time Evolution of Semi-major Axis and Eccentricity

The time evolution of the semi-major axes of all protoplanets are shown in Figure 2 for the cases, $\Delta a_{\rm ini} = 8r_{\rm H}$. Figures 2(a) are the results for $\langle \tilde{e}^2 \rangle_{\rm ini}^{\frac{1}{2}} = 0$ and Figures 2(b) are for $\langle \tilde{e}^2 \rangle_{\rm ini}^{\frac{1}{2}} = 2$. Solid curves shows the average value a for 1000 years. Dashed curves shows the value $a(1 \pm |e|)$. In all plots, the eccentricities increase with time. The system with $\langle \tilde{e}^2 \rangle_{\rm ini}^{\frac{1}{2}} = 0$ is stable for a much longer period, but the system with an finite $\langle \tilde{e}^2 \rangle_{\rm ini}^{\frac{1}{2}}$ became unstable faster than the system with $\langle \tilde{e}^2 \rangle_{\rm ini}^{\frac{1}{2}} = 0$ does.

The maximum value of the eccentricities of 10 protoplanets, $e_{\rm max}$, increase with time. The growth of $e_{\rm max}$ seems to be somewhat faster for larger $\langle \tilde{e}^2 \rangle_{\rm ini}^{\frac{1}{2}}$. However, run-to-run variation of the result for the same initial set of $\Delta a_{\rm ini}$, $\langle \tilde{e}^2 \rangle_{\rm ini}^{\frac{1}{2}}$, $\langle \tilde{i}^2 \rangle_{\rm ini}^{\frac{1}{2}}$ is very large. In some cases, $e_{\rm max}$ grows, but in other cases $e_{\rm max}$ remains small. Run-to-run variation is the largest for the case with $\langle \tilde{e}^2 \rangle_{\rm ini}^{\frac{1}{2}} = 0$.

3.2 Timescale of Instability

Figure 3 shows the instability timescale T defined in section 2.3 against initial orbital separations. The value of T is the median of the results of 40 runs with different random numbers. Figure 3 strongly suggests that T and $\Delta a_{\rm ini}$ satisfy the relation,

$$\log T = b \exp(\Delta a_{\rm ini}) + c \tag{5}$$

We determined the values of the coefficients b and c, by the least square fit. The results are given in Table 2. We use the data for $\Delta a_{\rm ini} = 4 - 7r_{\rm H}$ in the case of the zero random velocity, and that for $\Delta a_{\rm ini} = 4 - 7.5r_{\rm H}$ in the non-zero random velocity cases. In the case of the zero initial random velocity, $\langle \tilde{e}^2 \rangle_{\rm ini}^{\frac{1}{2}} = 0$, our result ($b = 0.82 \pm 0.057, \quad c = -0.78 \pm 0.33$) is in good agreement with that of Chambers et al. (1996) ($b = 0.756 \pm 0.027, \quad c = -0.358 \pm 0.176$). In the cases of the non-zero initial random velocity, T gets smaller as we increase $\langle \tilde{e}^2 \rangle_{\rm ini}^{\frac{1}{2}}$. The reduction is larger for larger $\Delta a_{\rm ini}$. As a result, the slope b is smaller for larger $\langle \tilde{e}^2 \rangle_{\rm ini}^{\frac{1}{2}}$.

To show this relation more clearly, we shows the value of b, the coefficient of $\log T = b \exp(\Delta a_{\rm ini}) + c$ by the least squares fit in Figure 4. It seems to decrease linear with $\langle \tilde{e}^2 \rangle_{\rm ini}^{\frac{1}{2}}$ increasing within the range of $\langle \tilde{e}^2 \rangle_{\rm ini}^{\frac{1}{2}}$.

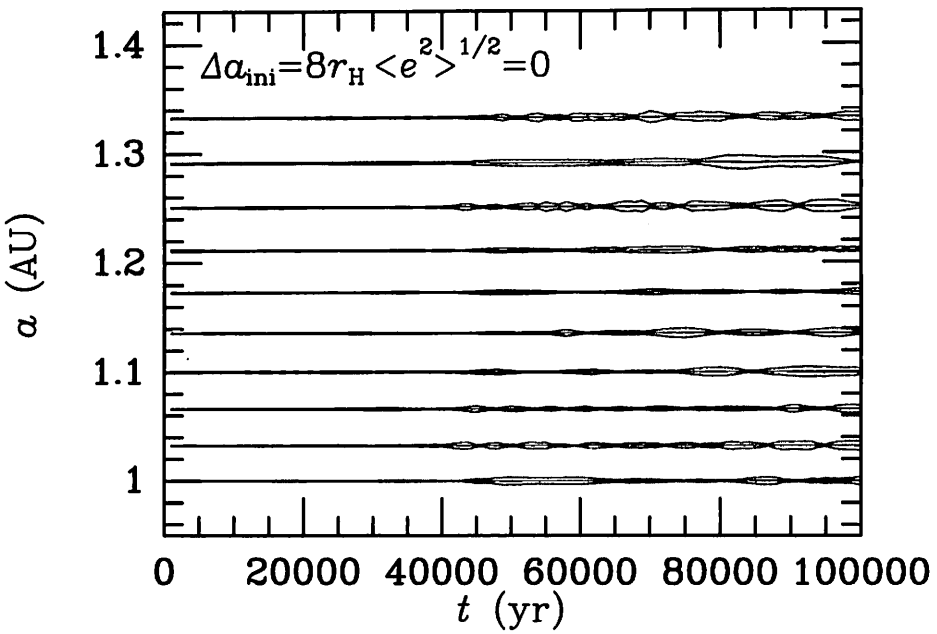

(a)

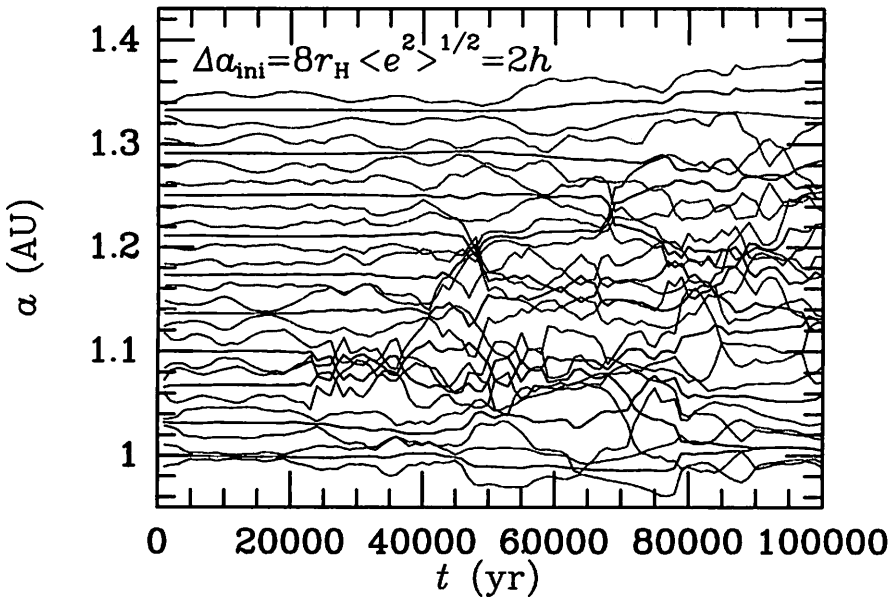

(b)

Figure 2: The time evolution of semi-major axes of 10 protoplanets for the cases $\Delta a_{\rm ini} = 8r_{\rm H}$ with $\langle \tilde{e}^2 \rangle_{\rm ini}^{\frac{1}{2}} = 0$ and 2. Solid curves show the average value a for 1000 years. Dashed curves show the value $a(1 \pm |e|)$.

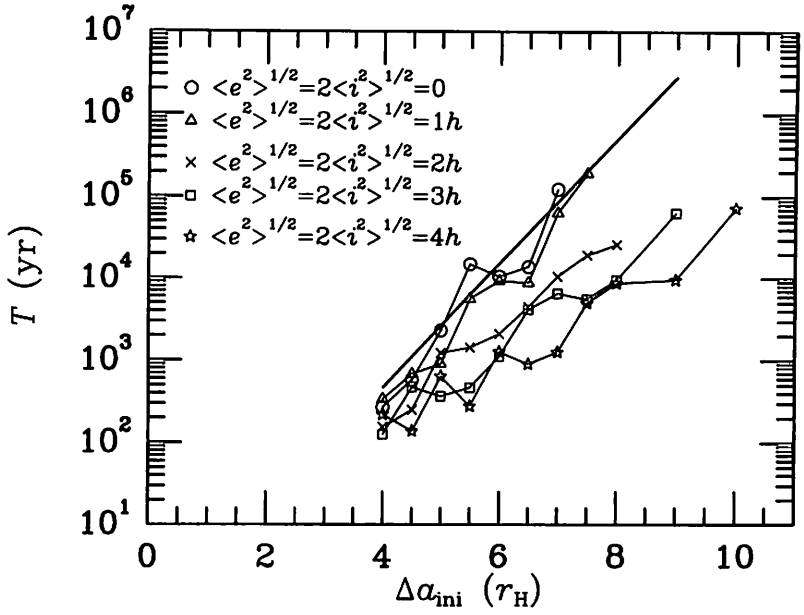

Figure 3: The timescale of instability against plotted $\Delta a_{\rm ini}$ with $\langle \tilde{e}^2 \rangle_{\rm ini}^{\frac{1}{2}} = 0$ through 4. The value plotted is the median of 40 cases with different random numbers for the initial distribution. The thick straight line is the result of Chambers et al.

$\langle \tilde{e}^2 \rangle_{\rm ini}^{\frac{1}{2}}$	b	c
0	0.82 ± 0.057	-0.78 ± 0.33
1	0.75 ± 0.072	-0.64 ± 0.42
2	0.59 ± 0.12	-0.15 ± 0.69
3	0.51 ± 0.15	0.12 ± 0.91
4	0.33 ± 0.15	0.94 ± 0.84

Table 2: Coefficient in $\log T = c + b\Delta a_{\rm ini}$ for results with various $\langle \tilde{e}^2 \rangle_{\rm ini}^{\frac{1}{2}}$

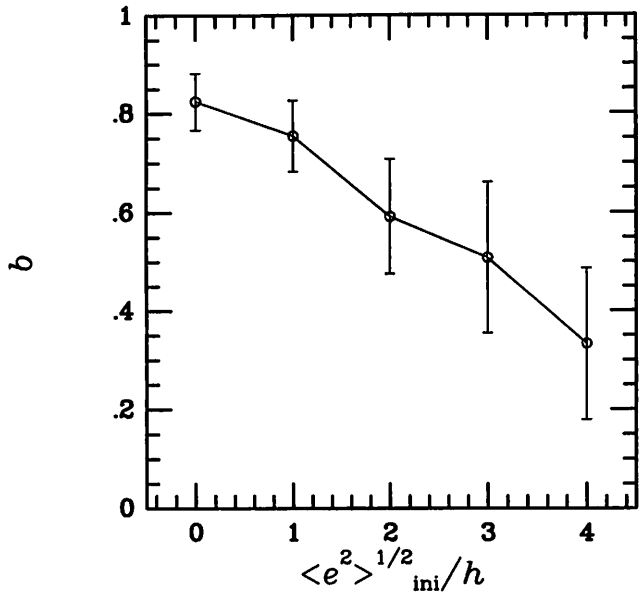

Figure 4: The value of b, the coefficient in this fitting formula $\log T = c + b\Delta a_{\rm ini}$ is plotted as a function of $\langle \tilde{e}^2 \rangle_{\rm ini}^{\frac{1}{2}}$. Error bars are $1-\sigma$ values.

4 Summary

We investigated the stability of protoplanet system. We found that the timescale of the instability depends strongly on the initial random velocities, $\langle \tilde{e}^2 \rangle_{\rm ini}^{\frac{1}{2}}$ and $\langle \tilde{i}^2 \rangle_{\rm ini}^{\frac{1}{2}}$. For the case of zero random velocity, i.e, $\langle \tilde{e}^2 \rangle_{\rm ini}^{\frac{1}{2}} = \langle \tilde{i}^2 \rangle_{\rm ini}^{\frac{1}{2}} = 0$, our result is in good agreement with that of Chambers et al. (1996). The instability timescale is expressed as $\log T = b\Delta a_{\rm ini} + c$. The values obtained for b and c are in good agreement with that of Chambers et al. (1996), even though both the time integration method and the criterion for the instability are different. For the cases of non-zero initial random velocity, we found that for large $\langle \tilde{e}^2 \rangle_{\rm ini}^{\frac{1}{2}}$ T becomes much smaller than that for the zero initial velocity cases. Both b and c are affected by $\langle \tilde{e}^2 \rangle_{\rm ini}^{\frac{1}{2}}$, and for large $\langle \tilde{e}^2 \rangle_{\rm ini}^{\frac{1}{2}}$, b is smaller.

In conclusion, the timescale of the instability depends on the initial random velocities and the orbital separation of protoplanets. Recent works have shown that the typical separation of protoplanets that are formed by runaway growth is $10 r_{\rm H}$. Therefore, if we consider only the case with $\langle e^2 \rangle_{\rm ini}^{\frac{1}{2}} = 0$, it would take very long time to form terrestrial planets. However, if protoplanets have non-zero e or i, the timescale can be grossly reduced. If protoplanets have small eccentricities,

$\langle e^2 \rangle^{\frac{1}{2}} = 4h \sim 0.01$, the timescale of instability is reduced to $10^{-1} \sim 10^{-2}$ times that of $\langle e^2 \rangle^{\frac{1}{2}} = 0$.

References

[1] Chambers,J.E., G.W.Wetherill, and A.P.Boss The stability of multi-planet systems. *Icarus* **119,** 261-268

[2] Greenberg,R., J.Wacker,C.R.Chapman, and W.K.Hartman 1978 Planetesimals to planets: Numerical simulation of collisional evolution. *Icarus* **35,** 1-26

[3] Hayashi,C., K.Nakazawa, and Y.Nakagawa 1985 in Protostars and Planets II ed D.C.Black and M.S.Matthew 1100 (Tucson: Univ. Arizona Press)

[4] Ida,S.,and J.Makino, 1992 a N-body simulation of gravitational interaction between planetesimals and a protoplanet I. Velocity distribution of planetesimals. *Icarus* **96,** 107-120.

[5] Ida,S.,and J.Makino, 1993 Scattering of planetesimals by a protoplanet: Slowing down of runaway growth. *Icarus* **106,** 210-227

[6] Kinoshita,H.,and H.Nakai 1996 Long-team behavior of the motion of Pluto over 5.5 billion years. *Earth, Moon, and Planets* **72,** 165-173.

[7] Kokubo,E.,and S.Ida 1996 On runaway growth of planetesimals. *Icarus* **123,** 180-191

[8] Kokubo,E.,and S.Ida 1998 Oligarchic growth of protoplanets. *Icarus* **131,** 171-178

[9] Kokubo,E., K.Yoshinaga and J.Makino 1997 On a time-symmetric Hermite integrator for planetary N-body simulation. *MNRAS,* in press.

[10] Levison,H.F., and M.J.Duncan The long-term dynamical behavior of short-period comets. 1994 *Icarus* **108,** 18-36

[11] Makino,J., and S.J. Aarseth On a Hermite integrator with Ahmad-Cohen scheme for gravitational many-body problems. 1992 *PASJ* **44,** 141-151

[12] Safronov,V.S. 1969 Evolution of the Protoplanetary Cloud and Formation of the Earth and Planets. Moscow: Nauka

[13] Wetherill,G.,and G.R.Stewart 1989 Accumulation of a swarm of small planetesimals. *Icarus* **77,** 330-367

[14] Wisdom,J., and M.Holman 1992 Symplectic maps for the n-body problem: stability analysis. *AJ* **104,** 2022-2029

Orbital Evolution of Asteroids due to Sweeping Resonances

Makiko NAGASAWA

Department of Earth and Planetary Sciences, Tokyo Institute of Technology, Meguro-ku, Tokyo 152, Japan

E-mail:nagasawa@geo.titech.ac.jp

Abstract

The origin of the high eccentricities in the asteroid belt is studied. Present observations show the asteroids have large mean eccentricities and inclinations that cannot be explained by planetary perturbations only. For this origin, the sweeping of secular resonances had been proposed. Associated with the dissipation of the primitive solar nebula, the locations of secular resonances pass through asteroid belt to pump up the eccentricities of asteroids. As all the previous works on this mechanism were restricted to the two-dimensional models, they cannot address the origin of high inclination. We study three-dimensional orbital evolution of asteroids due to the sweeping secular resonances. To give high eccentricities to asteroids, the dissipation time scale of nebula must be of over 10^4 years, which agrees with the results obtained by two-dimensional nebula model. If the dissipation time scale longer than 2×10^4 years, the nebula removed the asteroids from the region out of the 2:1 resonance (by close encounters with Jupiter), which is also the same as two-dimensional result. Inclinations are not pumped up within the range of dissipation time we adopted in our simulations. We need another mechanism to pump up asteroidal inclinations.

1 Introduction

Present observations show the asteroids have large mean eccentricities and inclinations that cannot be explained by planetary perturbations only. Fig.1a shows the eccentricity distribution. Mean eccentricity of the asteroids is large independently of semi-major axis. As shown in Fig. 1b, the inclination distribution is also essentially independent of semi-major axis but is characterized by secular resonances.

There are some unsolved problems in the asteroid distribution. The first one is that the estimated total mass from the observations (a few $\times 10^{24}$ g) is only 0.1% of that from the mass distribution of the minimum mass solar nebula (Hayashi 1981). Since it may be difficult that the amount of material is originally depleted in the region of the asteroid belt, the material would have been lost in the formation process of the solar system.

The second problem is the depletion between the 3:2 and 2:1 resonances. As shown in Fig.1, asteroids are depleted in the region with larger semi-major axis than the 2:1 resonance.

The third problem is that asteroids have rather large eccentricities and inclinations than those of planets. Mean eccentricity and inclination are 0.17 and 0.19, respectively. The asteroids would have acquired some eccentricities and inclinations by the perturbation of Jupiter and Saturn. The attained eccentricities and inclinations, however, are at most 0.1 except small regions of resonances (Brouwer and Van Woerkan 1950). Planetary perturbations in the present configrations cannot account for such

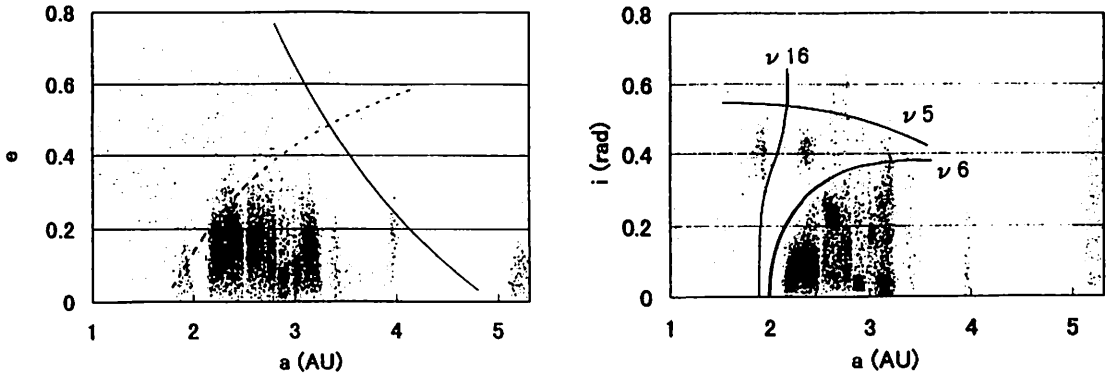

Figure 1: (a) The distribution of eccentricities versus semi-major axes for present asteroids. Over the solid line, asteroid orbit cross Jupiter's orbit, while they cross Mars' orbit over the dotted line. (b) The distribution of inclinations versus semi-major axes of present asteroids. Three lines show the locations of the principal secular resonances in the asteroid belt (after Williams 1969).

large eccentricities as observed now. The origin of the large eccentricities and inclinations is a chief problem in this paper. This problem may also be related to the former two problems.

2 Sweeping of Secular resonances

It is considered that the mass of the nebula gas is as large as 0.01 $M_\odot$, which is one hundred times as much as the mass of solid material in the solar system (e.g., Hayashi 1981), hence the gravity of nebula gas would play an important role in the primitive solar system. In particular, the addition of the nebula potential rotates apse of planets, since the nebula potential is not a point source potential then the planetary orbits are slightly deviated from the Keplerian ones. The secular resonances are related with apsidal and nodal rotations through planetary perturbations. Hence, the nebula gravity affects the secular resonances. As the nebula dissipates, the apsidal rotation rate changes and the location of secular resonances moves. This resonance sweeping may result in the high eccentricities and inclinations of the asteroids.

Ward et al. (1976) first suggested an importance of sweeping secular resonances due to the dissipation of the solar nebula. Heppenheimer (1980) derived a relation between surface density of the nebula and the location of secular resonances by two-dimensional analytical argument (see Fig.2). The upper line shows the position of secular resonance with Jupiter, and under line shows that of with Saturn. These lines suggest that the positions of secular resonances pass through asteroid zone as the nebula dissipates and nebula density decreases. He found that the eccentricities could be pumped up to the magnitude of present ones. Assuming exponential decay of the nebula surface density, he found that the dissipation time scale must be of the order of 10^{4-5} years in order for calculated eccentricities of Mars and asteroids to coincide with their present eccentricities. Ward (1981) gave a more complete two-dimensional linearized model and concluded that in order to avoid the pumping up of terrestrial eccentricities in excess of the observed values, the dissipation time scales must be of the order of 10^{4-5} years. He included effects of nebula gaps around Jupiter by tidal interaction between planets and nebula.

The nebula gas is important not only as the source of gravity but also as drag to the planetary

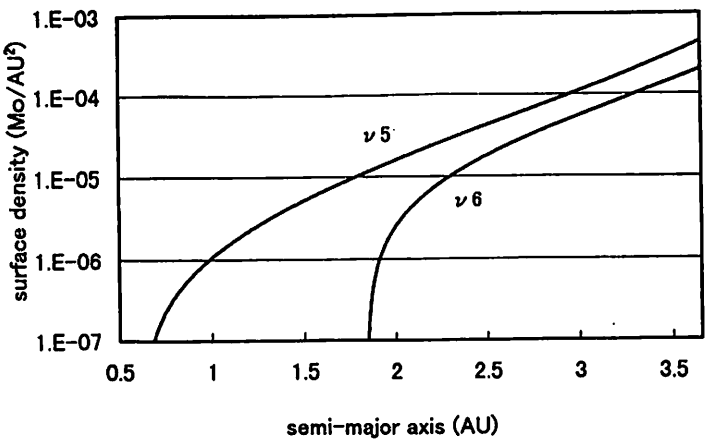

Figure 2: Locations of the ν_5 and ν_6 secular resonances as functions of nebula density. The surface density is 1.9 $\times 10^{-4}$ $M_\odot/AU^2$ in the minimum mass solar nebula model.

motion. Including the effect of gas drag, Lecar and Franklin (1997) numerically calculated the effect of sweeping secular resonances in the nebula gas (by two-dimensional model). If the dissipation is too fast, the resonance sweeping is too fast to have enough time to pump up eccentricities of asteroids. On the other hand, if the dissipation is too slow, the eccentricities pumped up by the secular resonances are completely damped by gas drag, and simultaneously all the asteroids spiral into inner solar system. They suggest that if the dissipation time scale is moderate, around 10^{4-5} years, the nebula cleans up the asteroids (of 10 km size) only in the outer region of the 2:1 resonances and residual asteroids still have large eccentricities which may give an explanation for both the second and the third problems.

Thus all the previous authors concluded that the nebula dissipation time is 10^{4-5} years. Furthermore, as all these previous works were restricted to the two-dimensional models, they cannot follow the evolution of inclinations.

2.1 Methods of Numerical Simulations

In our simulations, we adopt the minimum mass solar nebula model by Hayashi(1981), where distribution of solid material is reproduced by present terrestrial planets and solid cores of present Jovian planets. The distribution of gas density is

$$\rho = 1.4 \times 10^{-9} \left(\frac{a}{1\mathrm{AU}}\right)^{-11/4} \exp\left(-\frac{\Omega_{\mathrm{kep}}^2}{2c_s^2} z^2\right) \quad \mathrm{g/cm^3}. \tag{1}$$

where Ω_{kep} is a Keplerian time and c_s is a isothermal sound velocity. We assume that the nebula extends from zero AU to 36 AU.

We assume that the nebula's surface density (σ) decreases exponentially.

$$\rho(t) = \rho_0 \exp(-t/\tau), \tag{2}$$

where characteristic dissipation time τ dose not depend on heliocentric distance. We start with a system that consists of Jupiter, Saturn, massless asteroids, and nebula gas (which have a gap along Jupiter orbit) with no gas drag.

As we investigate secular resonances, we have to calculate evolution of apse accurately. In ordinary integration schemes, the error of angle variables increases linearly or quadratically with time.

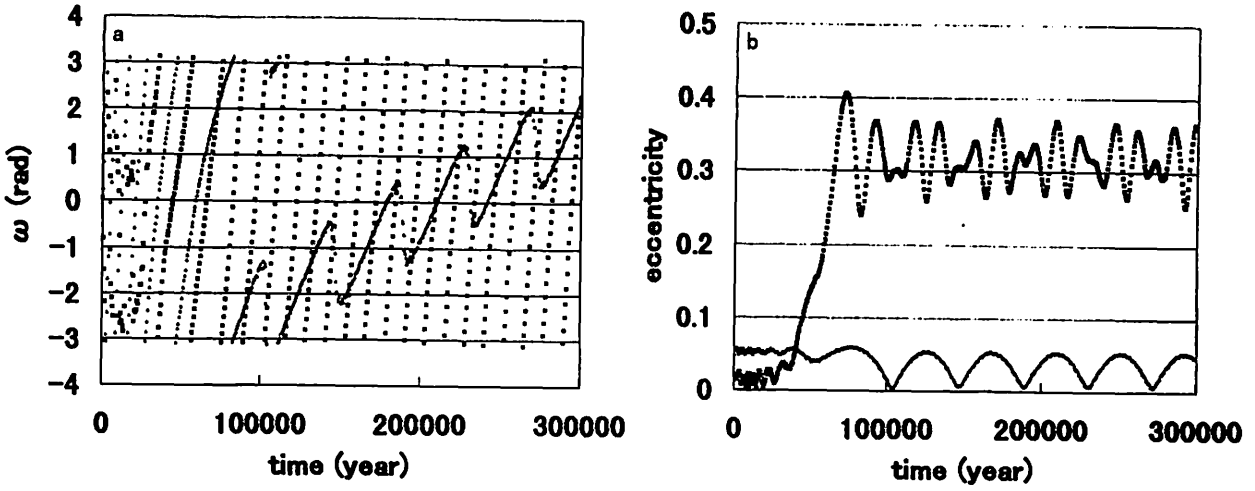

Figure 3: Orbital evolution of an asteroid with initial conditions $a = 3$ AU, $e = 0.02$, $i = 0$ and the nebula dissipation time scale of 2×10^4 years. Present orbital elements are assumed for Jupiter and Saturn at $t = 0$ except for zero inclinations. (a) The evolution of the longitudes of perihelion of asteroid and Jupiter. Filled triangles and crosses express perihelion for Jupiter and the asteroid, respectively. The secular resonances occur around 50000 years. (b) The evolution of eccentricities.

Moreover, the effect of perturbation would be easily covered up by the truncation error of the strong solar gravity. To overcome these difficulties, we use time symmetrical Encke's method to integrate orbital motion.

For the integration of nebula potential, we adopt good lattice point method. This method employs Fibonacci numbers, which make highly uniform nodes and actualize high accuracy. To apply this method, we must transform the integrand to the function whose derivatives (including higher order) converge rapidly into zero at the boundary.

3 Results

We simulated orbital evolutions of asteroids in the case of three-dimensional nebula model with no gas drag. We show examples of the evolutions of an eccentricity and a longitude of perihelion of an asteroid in our simulations. Figs.3a and 3b show the case that dissipation time scale is 24000 years and initial position of the asteroid is 3 AU. Filled triangles and crosses express the orbital evolutions of Jupiter and the asteroid, respectively. For asteroids, perturbation by both Jupiter and Saturn are included. Jupiter's apse rotates due to the effect of nebula potential, and asteroid's apse rotates due to the effect of nebula, Jupiter and Saturn's potential. As nebula dissipates, the progression speed of asteroids and Jupiter's apse slow down. At $t \sim$50000 years, these rotation speeds coincide with each other, and the secular resonance occurs. The eccentricity increases to 0.3.

Fig.4a and b show the final eccentricities and inclinations of the test particle. In the simulations, initial eccentricities of asteroids are 0.02 and initial inclinations of asteroids are zero. The present orbital elements of Jupiter and Saturn are taken as initial conditions. Assuming the exponential decay of nebula density (equation (2)), we examined the cases of $\tau = 4.7 \times 10^3$, 2.4×10^4, and 6×10^4 years, where τ is the dissipation time scale. Fig.4a shows that the secular resonances do not have a chance to increase the eccentricities sufficiently if the dissipation time scale is 5×10^3 years, while they pump

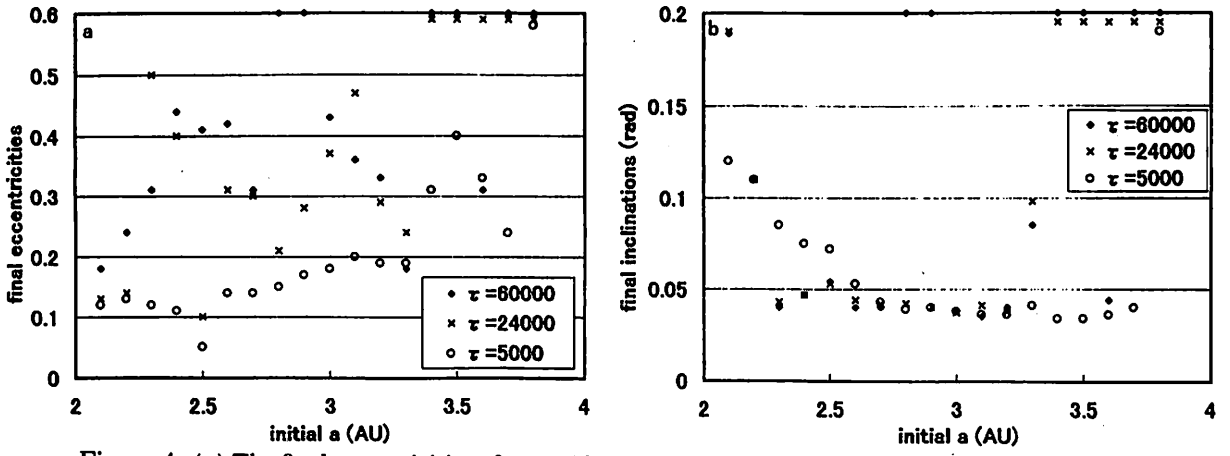

Figure 4: (a) The final eccentricities of asteroids. Present orbital elements are assumed for Jupiter and Saturn at $t = 0$ (inclinations are not zero). The initial e and i of asteroids are 0.02 and 0. (b) Final inclinations of the asteroids.

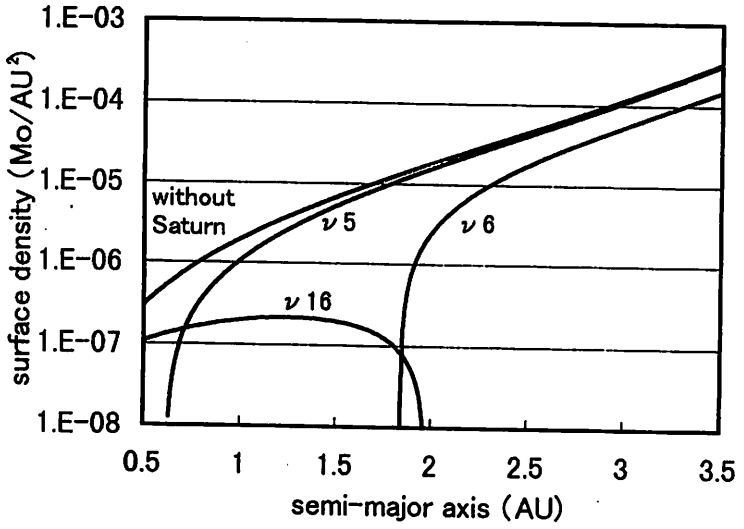

Figure 5: Locations of the ν_{16} secular resonances as functions of nebula density. The line S shows the location of secular resonance without Saturn.

up the eccentricities up to magnitude of observed asteroids if $\tau \geq 2 \times 10^7$ years. The figure also shows that the secular resonances succeed in removing the asteroids in the region out of the 2:1 resonances by the encounter with Jupiter. Inclinations are, however, not sufficiently pumped up. The reason is that the ν_{16} resonance does not pass through the asteroid belt region in the way of nebula dissipation. Fig.5 shows the relation between nebula surface density and the position of secular resonances. The resonances, which sweep asteroid belt, are the ν_5 and the ν_6 resonance, and these resonances are ones that correspond to apsidal motion.

4 Conclusion

We found the eccentricity evolution is similar to that in the two-dimensional model. Sweeping secular resonances pump up eccentricities of asteroids up to the present values, if the time scale of dissipation of the nebula is longer than 2×10^7 years, and that remove the asteroids in the region out of the 2:1

resonances by the encounter with Jupiter.

When we take time scales longer than 10^6 years, most of asteroids are removed from main belt region by close encounter with Jupiter due to the highly pumped up eccentricities, which accounts for the depletion in the asteroid belt. The inclinations of asteroids are not pumped up in our simulations as large as observation. The reason is that the ν_{16} resonance does not pass in the asteroid belt region. We need another mechanism to pump up asteroidal inclinations. The eccentricities are pumped up, then, it is permitted asteroids to close encounter with Jupiter or Mars, and it may be possible to increase asteroidal inclinations. We must carry out detailed simulations with longer dissipation time scale including close encounter with planets.

References

Brouwer, D., and van Woerkam, A. J. J. 1950. The secular variations of the orbital elements of the principal planets.*Astron Papers Amer. Ephem. and Naut. Almanac* **13**, Part 2, 79-107.

Hayasi, C. 1981. Structure of the solar nebula, growth and decay of magnetic fields and effects of magnetic and turbulent viscosities on the nebula. *Prog. Theor. Phys. Suppl.***70**, 35-53.

Heppenheimer, T. A. 1980. Secular resonances and the origin of eccentricities of Mars and the asteroids. *Icarus* **41**, 76-88.

Lecar, M. and Franklin, F. 1997. The solar nebula, secular resonances, gas drag, and the asteroid belt. *Icarus* **129**, 134-146.

Ward, W. R., Colombo, G., and Franklin, F. A. 1976. Secular resonances, solar spin down, and the orbit of Mercury. *Icarus* **28**, 441-452.

Ward, W. R., 1981. Solar nebula dispersal and the stability of the planetary system. *Icarus* **47**, 234-264.

Williams, J. G. 1969. Secular perturbations in the solar system. *Ph.D. Thesis* Univ. of California, Los Angeles.

A dynamical model of CH Cygni and its implication

Kiyotaka Tanikawa[1] and Seppo Mikkola[1,2]
[1]National Astronomical Observatory, Mitaka, Tokyo, Japan
[2]Turku Univeristy Observatory, Finland

Basic characteristics of CH Cygni related to its dynamics are listed. Previously published models of CH Cygni are briefly criticized. The meaning of the new model which we proposed(Mikkola & Tanikawa, 1998) is explained and some possible mechanism of activity is suggested.

1. Characteristics of the activity of CH Cygni

Symbiotic variable CH Cygni has been observed and investigated for more than one hundred years(Mikolajewski et al., 1990). Although immense amount of data have been accumulated until now, its basic geometrical or dynamical picture is yet to be clarified. What can be done in this kind of tangled situation? As dynamists, we are not going into the details of astrophysical observational data because these are out of our reach. Instead, we are interested in fixing the dynamical configuration of the system based on the belief that the underlying mechasnism of its activity is simple.

In order to do this, we should select basic evidence which we think most important for the dynamics of CH Cygni. We consider that the following three are the most important characteristcs.

(a) No activity during 1885 $\sim$ 1963(Mikolajewski et al., 1990).

Until 1920's, CH Cygni was a standard M7III star. After that it was classified as a semi-regular M6III star and it suddenly started symbiotic activity in 1963.

(b) 15 years and 2 years variations of radial velocities (Hinkle et al., 1993).

It is generally accepted that the 15 years variation comes from the orbital motion of components(Yamashita and Maehara, 1979), that is, CH Cygni is considered at least as a binary system.

(c) 15 years radial velocity variation of the active component (Mikolajewski et al., 1987; Mikkola and Tanikawa, 1998).

This may be most contraversial in selecting models.

Let us introduce typical models of CH Cygni thus far proposed and criticize them in relation to the above characteristics.

(1) Binary model(Munari et al., 1996)

A binary of 15 years period has an accretion disk. 2 years periodicity comes from the pulsation of the main component, the red giant.

Characteristics (a) cannot be explained by this model. Doubt has been cast to this model with respect to the possibility of the formation of an accretion disk in such a wide binary.

(2) Triple star model(Hinkle et al., 1993; Skopal, 1997)

A third body revolves round a close binary of 2 years period. The close binary has an accretion disk. Activity of the system occurs around this disk.

This model ignores Characteristics (c). These authors do not propose any mechanism which explains Characteristcs (a).

2. Our model

We consider that Characteristics (a) is the most essential one among the three for the dynamics of CH Cygni. Is the absence of activity for more than 80 years due to an age effect or the expression of non-activity phase of a longer period? Then it is natural to ask: **Can a system like CH Cygni have a period more than 80 years in addition to 2 years and 15 years periods?**

Our idea is that this is possible if we take into account a resonance in a triple system. There are a few candidates of resonance.

Mean motion resonance: This resonance is attractive since the ratio of two periods of CH Cygni, 15 years and 2 years, is close to 7 : 1. However, the effect may be weak because the ratio is large.

Secular resonance: In this case, the periastron of the perturbing third body should move in order that the resonance become effective. Non-linear interactions between the perturber and perturbed body might force the periastron to move.

Kozai resoance: This mechanism is effective for a rather wide range of parameter values. This is most attractive.

If resonance is effective in CH Cygni, its activity can be desribed as follows.

1. A third body revolves round a binary of 2 years period in 15 years and gives a dynamical effect on the binary.
2. The eccentricity of the orbit of the binary changes in a long period more than 80 years.
3. Mass outflow occurs when the companion approaches the primary at their periastron if the eccentricity is large.
4. Mass outflow does not occur if the eccentricity is small and the binary components do not approach each other so much. This implies long absence of activity during the small eccentricity phase.

Kozai mechanism (Kozai, 1962; Kinoshita and Nakai, 1991; Innanen et al., 1997) represents the angular momentum preservation. Suppose that a third body is revolving round a close binary. We look at the motion of the companion of the binary. The gravitational attraction from the third body is considered as a perturbation to the main attraction from the primary. Suppose further that initially the orbital planes of the third body and of the companion do not coincide. Then due to the perturbation from the third body, the orbital plane of the companion oscillates with oscillation center at the orbital plane (x, y) of the third body. In addition, the z component of the angular momentum of the companion preserves. This is the so-called Kozai mechanism. As a consequence, the eccentricity of the orbit of the companion

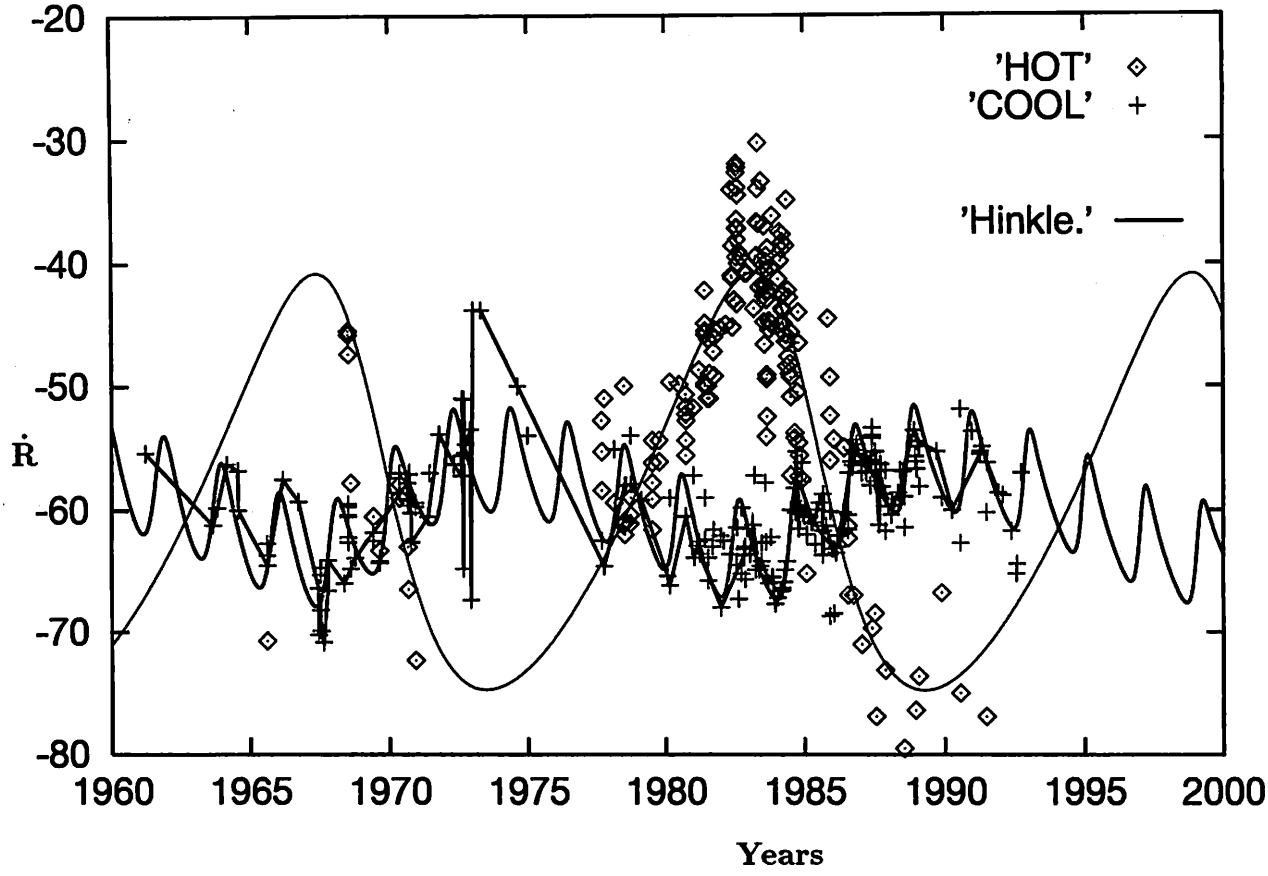

Figure 1: Comparison of the triple model radial velocities with observations. Note that the model agrees well with the infrared data of Hinkle *et al.*(1993). (Mikkola & Tanikawa, 1998)

oscillates with the inclination. The larger the initial inclination, the larger is the amplitude of eccentricity oscillation.

Mikkola & Tanikawa(1998) searched for a best fit orbit starting from the mass and orbital parameters of Hinkle *et al.*(1993). In this case, the data to be fitted are the radial velocities taken from various sources. Their result is shown in Fig.1 (Mikkola & Tanikawa, 1998). In this parameter values, the period of eccentricity oscillation is longer than 400 years(Fig.2), and is compatible with observations.

3. Implication of the model

Our model explains Characteristics (a) and (b). In particular, the secular increase of activity of CH Cygni starting at 1920's is well interpreted in our model as due to the secular increase of the eccentricity since then. However, to explain resonably Characteristics (c) we need some mechanism. It is rather a serious problem: the active component is the third body. Of course, this has been obvious from the start as long as Characteristics (c) is true. And this seems to be the very point where some authors hesitate to adopt a triple model.

Hinkle *et al.*(1993) did not adopt Characteristics (c). Characteristics (c) may not be so firmly established as (a) or (b). It should be observationally checked more fully.

Here we go to the opposite direction, i.e., try to find a mechanism of the third body's activity. In our model, mass overflows from the main component of the binary. Moreover, the companion may dive into the atmosphere of the main component. In such a situation, is it possible that the activity does not occur around the companion?

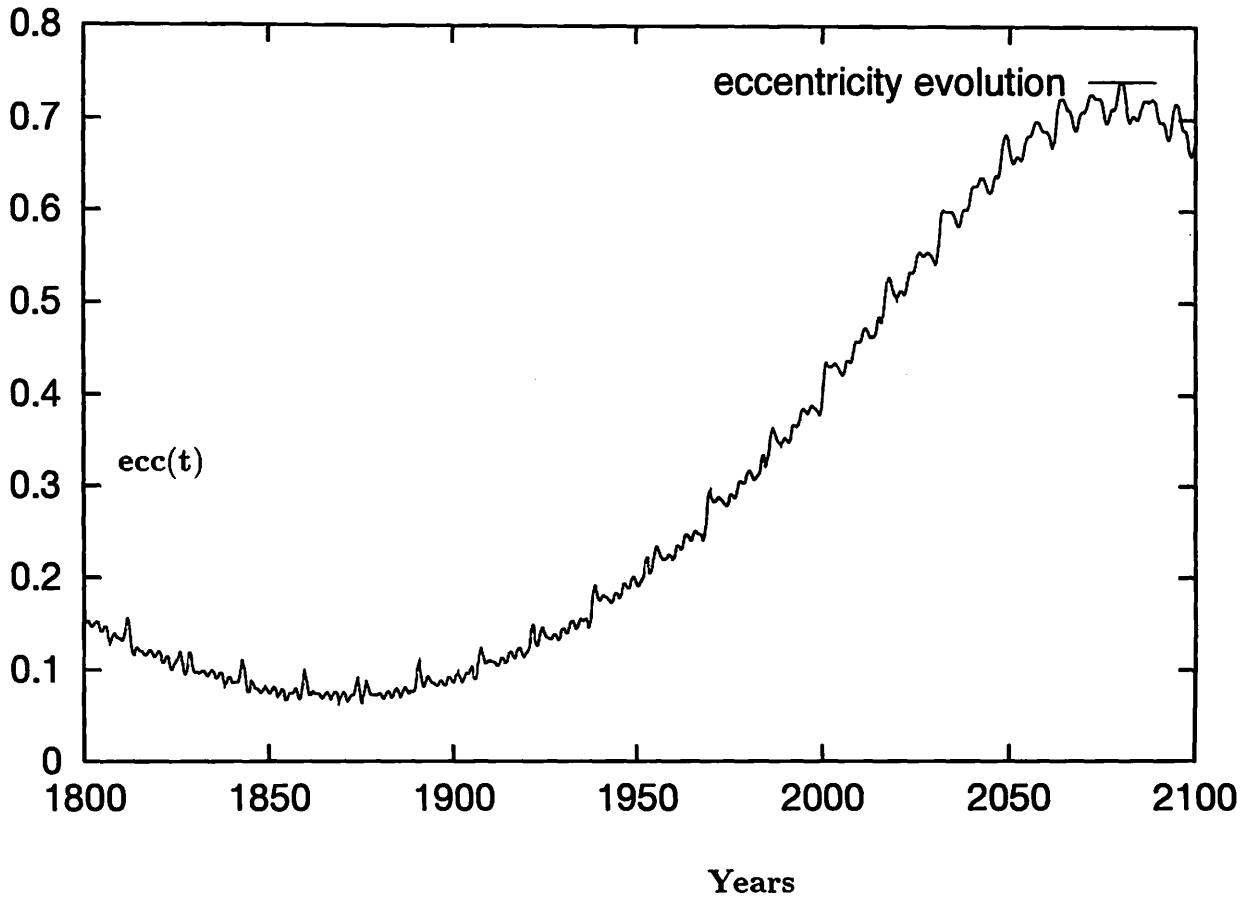

Figure 2: Evolution of eccentricity of the inner binary. The long period of low eccentricity explains the non-activity of CH Cygni prior to 1963. This behavior of eccentricity is due to the Kozai resonance and depends critically on inclination and longitude of perihelion. (Mikkola & Tanikawa, 1998)

We suggest a possible mechanism of the third body's activity.

Let us consider a mechanism of jets, or more precisely the acceleration mechanism of matter in a multiple system. There is a gravitational mechanism called 'slingshot' (Anosova & Tanikawa, 1996; Umehara & Tanikawa, 1998). This mechanism works both in two-dimensional and three-dimensional settings. If a particle passes through a point on the arc connecting the components of the binary, or cross the syzygy when they are receding each other, then it is accelerated gravitationally. If the direction of motion of the particle at syzygy crossing is out of the plane of the binary, the direction of motion after the acceleration is more or less three-dimensional. If the setting is two-dimensional, the particle is accelerated in the plane of the binary. Efficiency of the mechanism, i.e., the energy increase of the particle, dependes on various parameters. Roughly speaking, it depends on the receding speed of the binary

components, and the position and direction of motion of the particle at syzygy crossing. For example, if the position of the particle at syzygy crossing is close to either of the components, efficiency is low.

Mass overflow occurs at a position on the arc connecting the centers of two components of the binary. If the velocity of the outflowing matter has transverse component to this arc and the binary is receding, then slingshot may be effective. However, it is generally believed that the initial velocity is small, so the acceleration by slingshot is small. The next chance of syzygy crossing comes when the overflowed mass revolves round the companinon once. In this occasion, the transverse velocity will be large. But the distance from the companion is very small at this syzygy crossing if the initial velocity is small. This is because the small initial velocity means that matter free-falls to the companion in a rotating system.

It seems that slingshot is not effective if there is a stationary accretion disk into which the overflowed matter quickly falls and settles down. However, if there is not a stationary accretion disk as suggested in Mikkola & Tanikawa(1998), the matter flowing out of the primary can be accelerated by slingshot because there are two syzygy crossings during its one revolution round the companion and there can be a timing in which conditions for the effective slingshot are satisfied.

Now, the matter accelerated by slingshot escapes from the binary. If the acceleration is not large enough, the matter will come back to the system and may eventually hit the third body.

References

[1] Anosova, J. and Tanikawa,K., 1995, *Ap & SS* **234**, 191-205.

[2] Hinkle, K. H, Fekel, F.C., Johnson, D.S, and Scharlach, W.W.G. 1993, *AJ* **105**, 1074.

[3] Innanen, K.A., Zheng, J.Q., Mikkola, S. and Valtonen, M.J., 1997, *AJ* **113**, 1915.

[4] Kinoshita, H. and Nakai, H., 1991, *Cel. Mech. Dyn. Astr.* **52**, 293.

[5] Kozai, Y., 1962, *AJ* **67**, 591.

[6] Mikkola, S. and Tanikawa, K, 1998, *Astronomical Journal* (in press).

[7] Mikołajewski, M., Mikołajewska, J., and Khudyakova, T.N., 1990, *A&A* **235**, 219.

[8] Mikołajewski, M., Tomov, T., and Mikołajewska J., 1987, *Ap&SS* **131**, 733.

[9] Munari, U., Yudin, B.F., Kolotilov, E.A. and Tomov, T.V., 1996, *A&A* **311**, 484.

[10] Skopal, A., 1997, p.99 in: J. Mikolajewska (ed.), "Physical processes in symbiotic binaries and related systems", proceedings of the conference, Koninki 1996.

[11] Umehara, H. and Tanikawa, K, 1998, *Cel. Mech. Dyn. Astron* (submitted).

[12] Yamashita, Y. and Maehara H., 1979, *PASJ* **31**, 307.

Analytical Expression of the Kozai Resonance

Hiroshi Kinoshita and Hiroshi Nakai
National Astronomical Observatory
2-21-1 Osawa, Mitaka, Tokyo, Japan
e-mail: Kinoshita@nao.ac.jp

Abstract

When Kozai(1962) studied the secular resonance of asteroids, he found the so-called Kozai resonance and expressed the analytical solution with use of Weierstrass $\wp$. Here we give the analytical solution with use of the Jacobi elliptic functions, which are more familiar than the Weierstrass $\wp$.

1 Introduction

When Kozai(1962) investigated the secular resonance of asteroids with high inclination and eccentricity, he found the argument of the perihelion of an asteroid does librate and even if the initial eccentricity is very small, the eccentricity does become very large. This phenomenon is recently called the Kozai mechanism or the Kozai resonance, since the mean motion of the perihelion longitude is equal to that of the longitude of node. The Kozai mechanism appears in the similar dynamical systems as the asteroidal case (see Table 1). The disturbing body in the system of Table 1 is located outside the disturbed body. Thomas and Morbidelli discussed the Kozai mechanism, where the disturbing body is inside of the disturbed body.

Kozai(1962) obtained the analytical solution of the Kozai resonance by an elliptic function of Weierstrass $\wp$. Since Weierstrass $\wp$ is not familiar, Kinoshita(1991) expressed the solution with use of Jacobi elliptic functions. This analytical expression, however, turned out to be only applicable to the case where the argument of the perihelion circulates. So here we give the analytical solution for the case where the argument of perihelion librates.

Table 1: Application of the Kozai Mechanism

	Central Body	Small Body	Disturbing Body
1)Kozai(1962)	Sun	Asteroid	Jupiter
2)Kinoshita(1991)	Uranus	Satellites	Sun
3)Innanen(1997)	Sun	Planets	Companion Star
4)Holman(1997)	16 Cyg B	Planet	16 Cyg A
5)Wiegert(1997)	α Cen A	Planets	α Cen B

2 Equations of Motion

Kozai(1962) discussed a massless asteroid disturbed by the outer giant planets. The Hamiltonian for this system in terms of Delaunay elements is

$$F = F(L, G, H, l, g, h, \lambda'), \tag{1}$$

where λ' is the longitude of the disturbing planet. The explicit expression is given in Kozai(1962). After the elimination of short periodic terms the new Hamiltonian F^* does not include l and λ' and also h since the disturbing potential becomes axial symmetric. Since the new L and H (the z-component angular momentum) are constant, we have the following relation between the eccentricity and the inclination

$$\sqrt{1-e^2}\cos I = \text{constant} = \Theta. \tag{2}$$

Now we give the explicit expression the new Hamiltonian(Kozai 1962):

$$\begin{aligned} F^* &= \gamma\Big((2+3e^2)(3\cos^2 I - 1) + 15e^2 \sin^2 I \cos 2g\Big) \\ &\quad + O((a/a_d)^2), \end{aligned} \tag{3}$$

$$\gamma = \frac{1}{16}\frac{m_d}{m_d + m_c}\frac{n_d^2}{(1-e_d^2)^{3/2}}a^2 \tag{4}$$

where m_d, n_d, a_d, and e_d are the mass, the mean motion, the semi-major axis, and the eccentricity of a disturbing body and m_c is the mass of the central body. For the asteroidal case the central body is the Sun and the disturbing bodies are the outer planets.

From this Hamiltonian the equations of motion take the form

$$\frac{d\eta}{dt^*} = -\frac{15}{8}e^2 \sin^2 I \sin 2g \tag{5}$$

$$\frac{dg}{dt^*} = -\frac{3}{8\eta}\Big(\eta^2 - 5\cos^2 I + 5(\cos^2 I - \eta^2)\cos 2g\Big) \tag{6}$$

with the constraint $\eta \cos I = \text{constant} = \Theta$, where

$$\eta = \sqrt{1-e^2}, \tag{7}$$

$$t^* = \beta^* t, \beta^* = \frac{m_d}{m_d + m_c}(1-e_d^2)^{-3/2}\frac{n_d^2}{n}. \tag{8}$$

Even though these equations do not seem to be integrable, the solution can be obtained with use of an elliptic function. Kozai(1962) expressed the solution by an elliptic function of Weierstrass $\wp$. Kinoshita and Nakai(1991) gave the analytical expression with use of Jacobian elliptic functions, which are more familiar and easier in handling than Weierstrassian elliptic functions. This analytical expression, however, turned out to be only applicable to the case where the argument of the perihelion circulates. So here we give the analytical solution for the case where the argument of perihelion librates in the next section in addition to the analytical solution for the circulation case.

3 Analytical Solution

At first we give the solution of (5) and (6) for the case where the argument of the pericenter circulates. The initial values for the equations (5) and (6) are $e = e_0, I = I_0$ and $g = 0$ at $t = 0$. We define $x_0, x_1, x_2 (x_2 > x_1)$ as

$$x_0 = 1 - e_0^2, \tag{9}$$

$$x_1 + x_2 = \frac{1}{3}(5 + 5\Theta^2 - 2x_0), \tag{10}$$

$$x_1 x_2 = \frac{5}{3}\Theta^2, \tag{11}$$

where

$$\Theta = \sqrt{1 - e_0^2}\cos I_0. \tag{12}$$

With use of the Jacobian elliptic functions the solution of (5) and (6) takes the form (Kinoshita and Nakai 1991)

$$e^2 = e_0^2 + (1 - e_0^2 - x_1)cn^2(\beta t + K), \tag{13}$$

where

$$\beta = \frac{3\sqrt{6}}{4}\sqrt{x_2 - x_1}\frac{m_d}{m_d + m_c}(1 - e_d^2)^{-3/2}\frac{n_d^2}{n}. \tag{14}$$

The parameter K in the argument cn is the complete elliptic Integral of the first kind with the modulus k^2

$$k^2 = (x_0 - x_1)/(x_2 - x_1). \tag{15}$$

Now we give the solution for the case where the argument of the pericenter librates around $\pi/2$. We define the initial values such that $e = e_0, I = I_0$, and $g = \pi/2$ at $t = 0$. The expressions (13), (14), and (15) for the circulation case are also applied to the libration case, except for the expressions of the parameters x_1 and x_2:

$$x_1 = \frac{5}{3}\cos^2 I_0, \tag{16}$$

$$x_2 = 1 + \frac{1}{2}e_0^2(3 - 5\cos^2 I_0) \tag{17}$$

The period of the variation of the eccentricity for both the circular and librational case is given by

$$P_e = 2K/\beta \tag{18}$$

and the period of the argument of pericenter is

$$P_g = 2P_e. \tag{19}$$

The maximum eccentricity is obtained from (13) as

$$e_{max} = \sqrt{1 - x_1} \tag{20}$$

The figures 1 (the libration case) and 2(the circulation case) shows the maximum eccentricity as a function of the initial eccentricity, where the initial eccentricity is a parameter. The maximum eccentricity for the librational case does not depend on the initial eccentricity (see (16) and (20)). The figure 3 shows the period P_e normalized by the factor

$\beta^*(8)$ as a function of the initial eccentricity, where the initial eccentricity is a parameter.

References

Kozai,Y:1962, "Secular Perturbations of Asteroids with High Inclination and Eccentricity, *Astron. J.*, **67**, 591-598.

Kinoshita, H. and Nalkai, H.:1991, Secular Perturbations of Fictitious Satellites of Uranus, *Celest. Mech.*, **52**, 293-303.

Innanen, K.A.,Zheng, J.Q., Mikkola, S., and Valtonen, M.J.:1997, *Astron. J.*, The Kozai Mechanism and the Stability of Planetary Orbits in Binary Star Systems, **113**, 1915-1919.

Holman, M., Touma, J., and Tremaine, S.:1997, Chaotic Variations in the Eccentricity of the Planet Orbiting 16 Cygni B, *Nature*, **386**, 254-256.

Wiegert, P.A. and Holman, M.:1997, The Stability of Planets in the Alpha Centauri System, *Astron. J.*, **113**, 1445-1450.

Thomas, F. and Morbidelli,A.: 1996, The Kozai Resonance in the Outer Solar System and the Dynamics of Long-Period Comets, *Celest. Mech.*, **64**, 209-229.

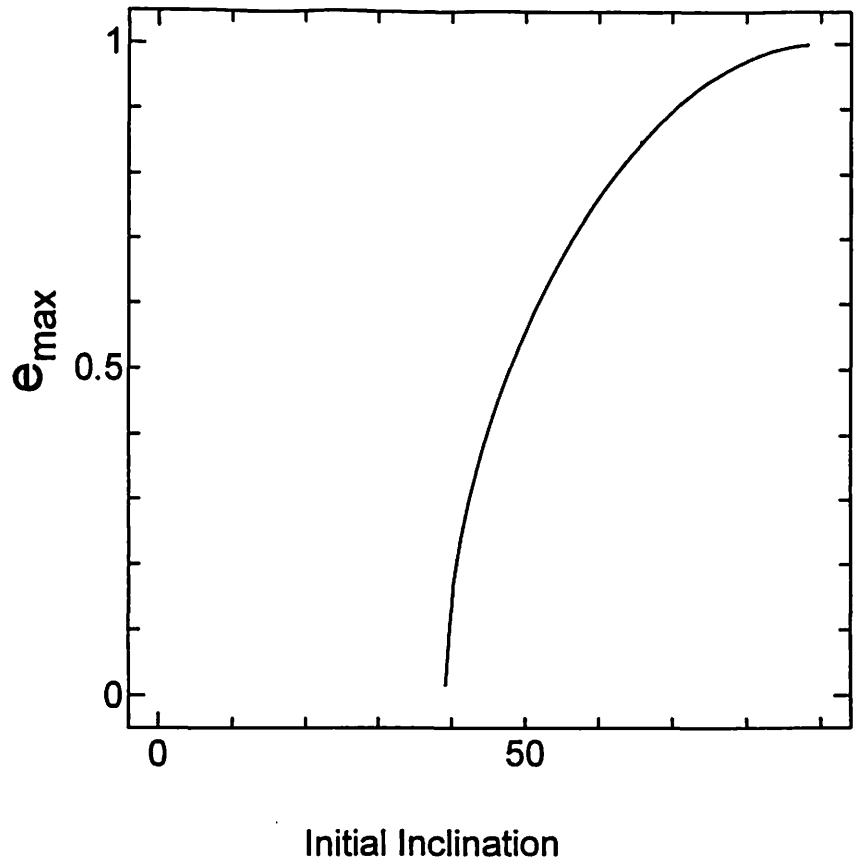

Figure 1: the maximum eccentricity for the libration case

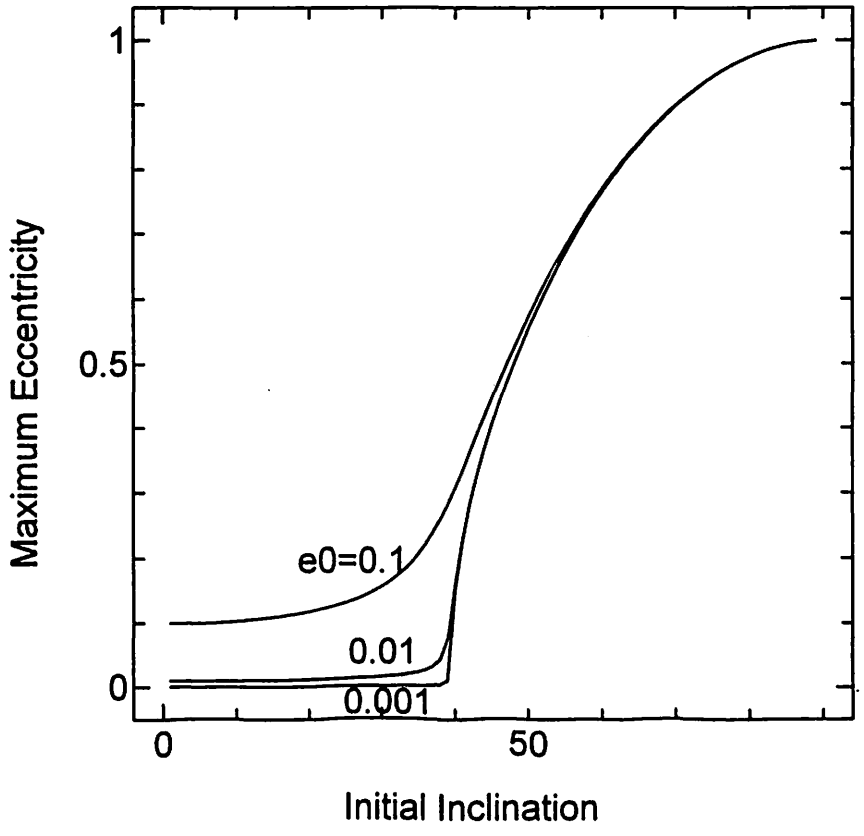

Figure 2: the maximum eccentricity for the circulation case

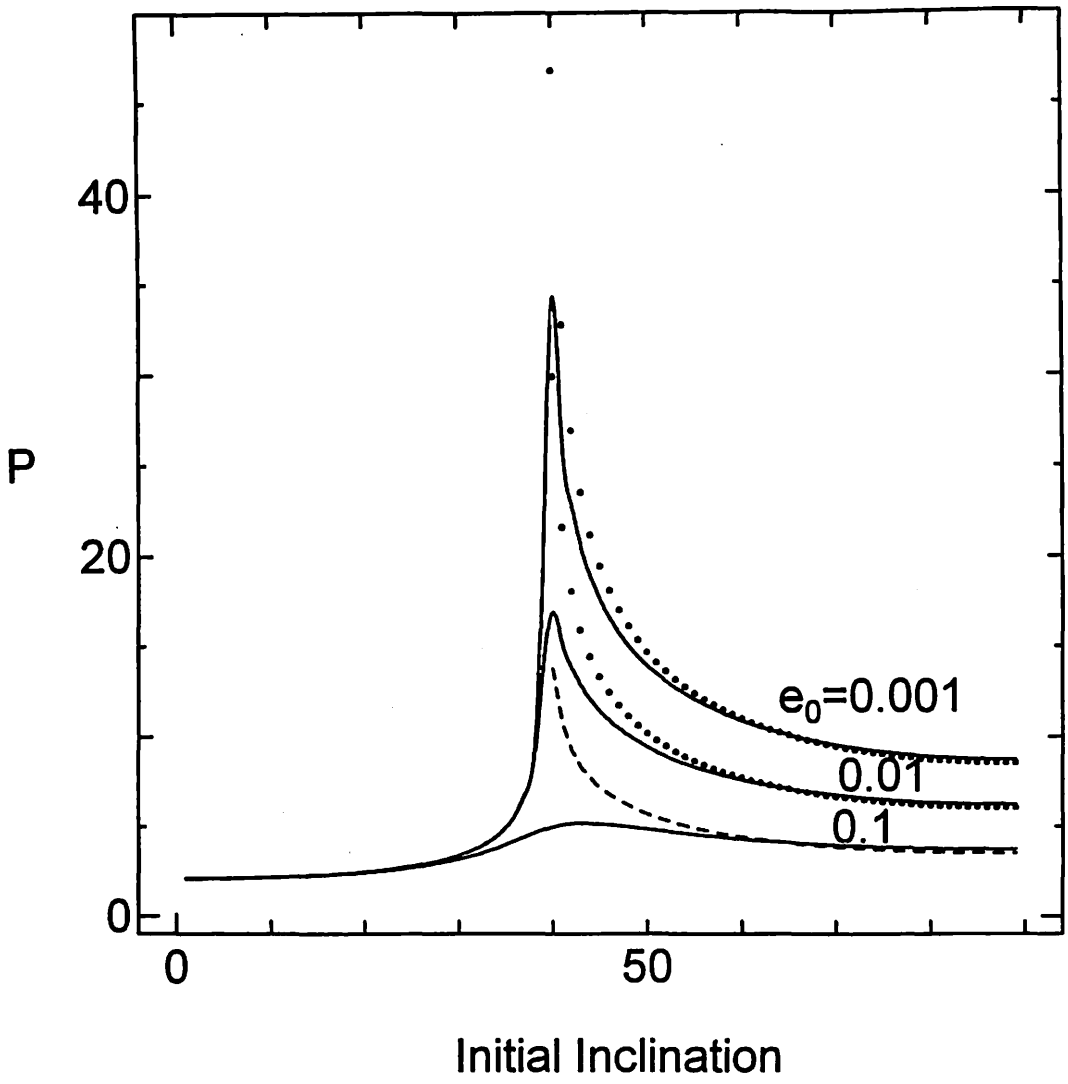

Figure 3: The normalized period $P = P_e \times \beta^*$
The dotted lines for the libration case
The solid lines for the circular case

小惑星ネレウスの運動
－そのカオス的性質と軌道運動予測－

Motion of asteroid Nereus
- Chaotic nature and orbital evolution -

吉川　真（通信総合研究所）
クリスチャン・フロッシュレ，パトリック・ミッシェル（ニース天文台）

Makoto Yoshikawa (CRL)
Christiane Froeschlé、Patrick Michel (Observatoire de Nice)

概要

小惑星ネレウスは、地球などの惑星に頻繁に接近するため、その運動は非常にカオス的である。そのような天体について、どのくらい軌道進化というものが推定可能なのかを調べてみた。方法は、オリジナルの軌道のまわりに観測誤差程度ずれた多くの「クローン・ネレウス」を考え、それらの軌道計算をして軌道要素などの分布の様子を調べたのである。その結果、ネレウスの軌道進化を確定的に言えるのは高々200年間ほどであるが、約5000年間にわたっては確率的に最も可能性の高そうな軌道というものを求めることができそうであることが分かった。また、太陽系空間での分布という観点から見ると、ネレウスの存在領域がかなり限定されることも分かった。

Abstract

Asteroid Nereus approaches the earth frequently, so its orbital motion is very chaotic. In this paper, we have studied how long we can estimate the orbital evolution of such strongly chaotic object. We calculated orbital evolution of many 'clones' of Nereus, and we analyzed how the clones are distributed as time passes. From our calculation, we found that the orbital evolution of Nereus can be determined only for 200 years precisely, but we found that it is possible to estimate the most probable orbital evolution of Nereus for 5000 years. We also found that the region where Nereus existed about 5000 years ago can be confined in a narrow region in the solar system.

１．ネレウスのカオス的な運動

小惑星ネレウス（Nereus：確定番号4660番）は、その軌道がほぼ地球軌道に接するようなものになっている（図１）。このため、ネレウスは探査の候補ともなった小惑星であるが、その軌道運動は非常にカオス的なものとなっている。このカオスの原因は、ネレウスが地球や火星に頻繁に接近することによる。そのためにネレウスの軌道進化を計算で求めることは非常に難しい。例えば、Michel et al. (1996)では、ネレウスの軌道要素の初期値を少しだけ変化させただけで、軌道進化予測が全く異なることが示されている。さらにこの論文では、全く同一の条件で計算したとしても、用いた計算機の機

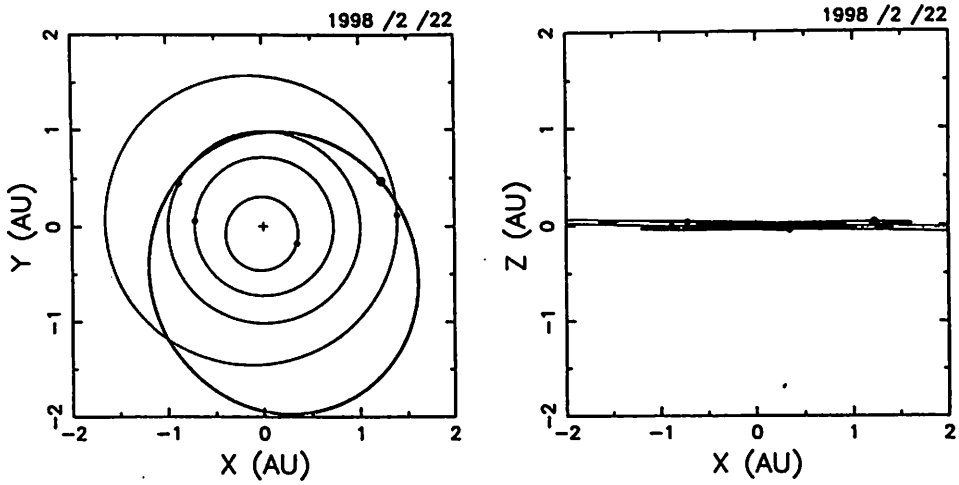

図1　小惑星ネレウスの軌道。左が黄道面に投影した図で右が黄道面に垂直な平面に投影したもの。細い線で描かれた軌道は惑星（内側から、水星、金星、地球、火星）。

Fig.1 The orbit of Nereus.　Face on view (left) and edge on view (right).

種が異なるだけでも計算結果が異なることも示されている。

ここでは、このようにカオス的な性質が強いネレウスの軌道進化について、どのくらい軌道運動の予測が可能であるのかを調べることを目的に解析を行ってみた。

2．解析の方法

解析方法は、現時点でのネレウスに対して、少しだけ初期条件をずらした「クローン・ネレウス」を多数作って、その軌道進化を調べるというやり方で行った。このクローン・ネレウスは、軌道6要素のそれぞれについてその有効数字の最小桁を1（軌道長半径[AU]と離心率で10^{-8}、他の角度要素[度]で10^{-6}）だけ増減させることで生成した。実際に用いた軌道要素の初期値は次のようになる。

a =1.48967216	±0	±0.00000001
e =0.36044461	±0	±0.00000001
i = 1.424857	±0	±0.000001
ω=157.881625	±0	±0.000001
Ω=314.784653	±0	±0.000001
M=164.701958	±0	±0.000001

つまり、ネレウス本体を含めて計算した天体の総数は729個（3^6個）である。また、計算した期間は、現在より過去に5千年間、未来に千年間である。摂動としては、9惑星および月を考慮したが、それらの位置データはDE404から取った。数値積分法は外挿法を用いた。

3．計算の結果

まず、現在の軌道要素から計算したネレウスの軌道進化を図２に示す。この軌道変化のようすから一目瞭然なように、ネレウスの軌道要素は非常にランダム的に変化していることがわかる。その理由は、前述したようにネレウスが地球や火星と頻繁にクローズ・エンカウンターを起こすためである。地球とのニアミスについて図にしたものが図３である。ここでは、地球との距離が 0.2AU 以下になるような接近について拾い出してあるが、そのようなニアミスは計算した 6 千年間に 320 回余り起こっている。そのニアミス時の地球との相対速度は 5km/s から 13km/s 程度である。また、ネレウスは火星にもよく接近するが、現時点では接近の距離は地球の場合ほど小さくない。火星は地球に比べてその質量は 10 分の 1 程度であるから、火星からの影響は地球よりもずっと小さい。

では、計算したクローン・ネレウスについて、その軌道進化はどうなっているのであろうか。図４には、計算した 729 個のクローンのうち 13 個について軌道要素の変化を重ねて示してみた。この 13 個は、オリジナルのネレウスと１つの軌

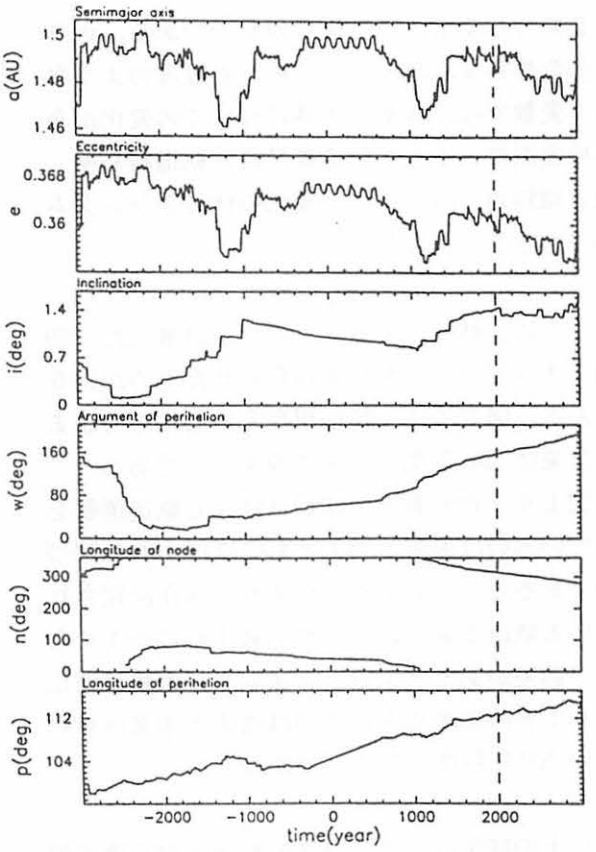

図２　ネレウスの軌道要素の変化

Fig.2　Orbital change of Nereus
(a : semimajor axis, e : eccentricity, i : inclination, w : argument of perihelion, n : longitude of node, p : longitude of perihelion)

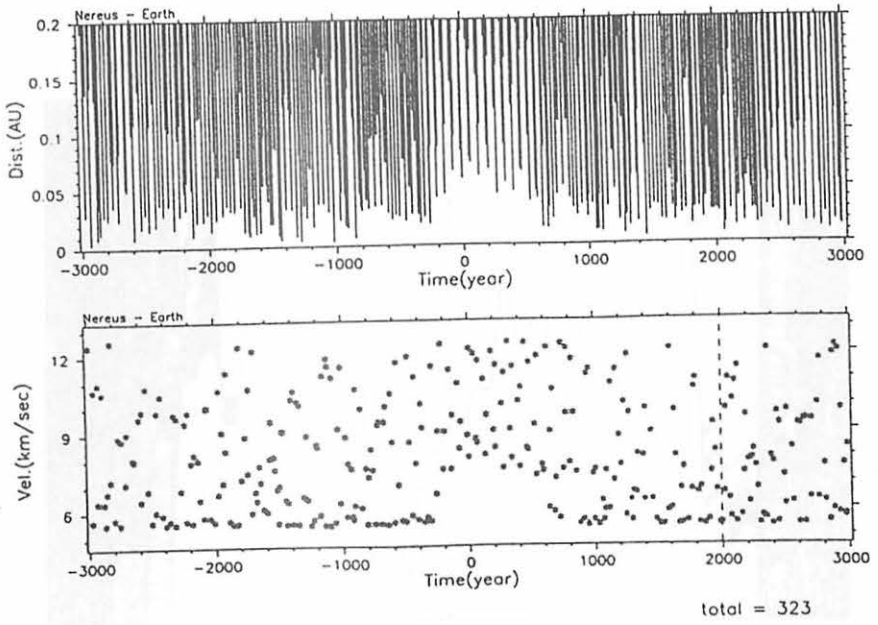

図３　ネレウスと地球とのニアミス。接近距離（上）と相対速度（下）。

Fig.3　Near-miss between Nereus and the earth.

道要素のみ変化させた場合のものである。近日点引数や昇交点経度そして近日点経度のような角度変数では、13 個の天体についての変化がある程度似ているが、軌道長半径、軌道離心率、軌道傾斜角については、変化の仕方がランダム的であることが分かる。

さらに、軌道長半径について、計算した 729 個のすべてのデータを重ね合わせたものが図５である。図５では、特に現在を中心にして過去と未来に 300 年間の部分のみを示してある。この図より、729 個の天体がほぼ同じ軌道運動をしているのは未来と過去ともにほぼ 150 年間づつであることが分かる。つまり、現在決定されている軌道要素においてその最小桁に±１くらいの誤差があるとすると、ネレウスの軌道進化として正確に求められるのは過去と未来へせいぜい 200 年程度であることになる。

以上の結果は、ネレウスの軌道進化を確定的に求めることができるのは高々200 年間くらいであるということを意味しているわけであるが、それでは、計算したクローン・ネレウスについてその軌道要素の分布の時間変化はどのようになっているのであろうか。図６には、軌道長半

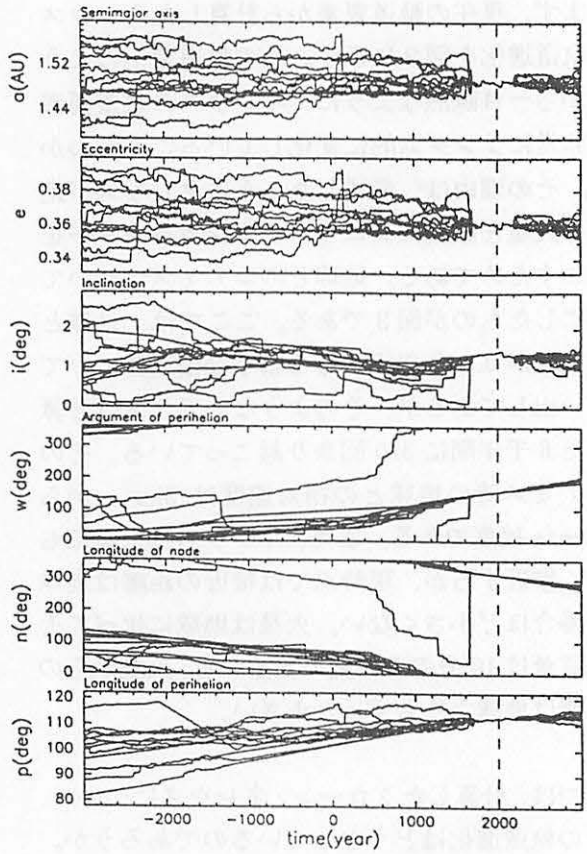

図４　13 個のクローンの軌道進化を重ね合わせたもの

Fig.4　Orbital evolution of 13 clones of Nereus

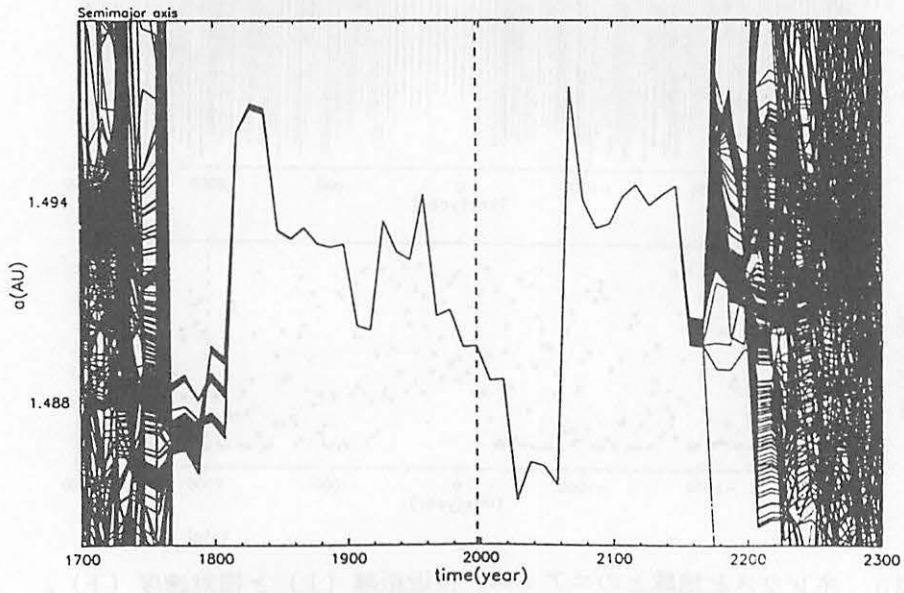

図５　729 個のクローン・ネレウスの軌道長半径の変化。

Fig.5　Variation of semimajor axis of 729 clones of Nereus.

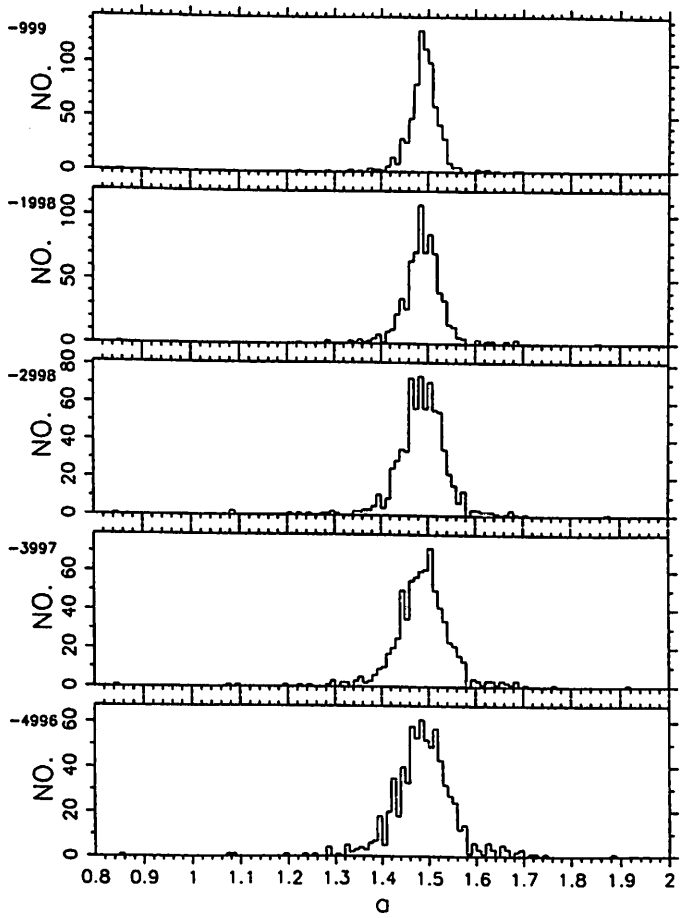

図６　729 個のクローン・ネレウスについての軌道長半径の値の分布。
　　各図の左上の数字が計算を初めてから何年前かを示す。上から順にほぼ千年おきになっている。

Fig.6 Distribution of samimajor axis of 729 clones of Nereus. The numbers upper left show the time from the starting point.

径について、計算した 729 個のクローンの分布がほぼ 1000 年おきに示されている。この図より、時間が経つにつれて分布がだんだん分散していくことがわかる。しかし、５千年遡っても軌道長半径の分布にはある傾向が見られる。この分布のピークにあたる値が、確率的に言うと、５千年前のネレウスの軌道長半径として最も可能性が高いものとなろう。ここでは軌道長半径についてのみ結果を示したが、他の軌道要素についても同様の傾向が見られる、従って、例えば５千年前のネレウスの軌道を確定的に言うことはできないが、確率的に最もありそうな軌道というものは推定することができるのである。

さらに、計算した 729 個について５千年前の軌道を重ね合わせて描いてみると、図７のようになる。この図を見ると、明らかに軌道が集中した帯が見られる。つまり、５千年前のネレウスがどこにいたのかは分からないが、図７で軌道が集中した帯の中にいたということだけは、かなり確実であろう。

最後に、全く別の話題であるが、大塚（東京流星ネットワーク）らによって、ネレウス起源ではないかという流星が報告されている。そこに示されている流星の軌道を描いてみると、図８のようになる。これを図７と比べてみると、かなり似ていることがわかる。つまり、ここでの解析からネレウス起源の流星についても何か手がかりが得られるかも知れない。これは、今後の課題である。

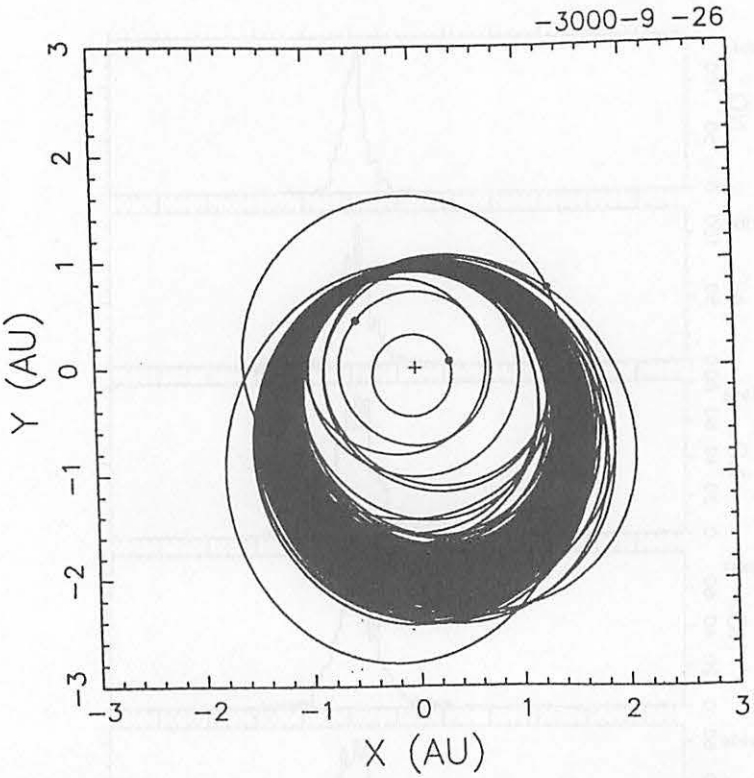

図7　5000年前における729個のクローンの軌道。水星から火星までの惑星軌道も描かれている。
Fig.7　The orbits of 729 clones at 5000 years ago.　The orbits of planets are also shown.

4．まとめ

ここでの計算で、やはりネレウスのようなカオスの強い天体の軌道運動予測は難しく、現在の観測誤差を考慮すると、せいぜい200年くらいしか精度を保って計算できないことが分かった。しかし、軌道の初期値のまわりにたくさんのクローン・ネレウスを配置してそれら全体の軌道進化の様子を見ることを行えば、最も可能性が高そうな軌道進化というものを推定することはできそうであることも分かった。また、確かに軌道要素の変化のし方を見ると、ランダム的になっており予測ができなさそうであるが、太陽系空間の中で存在した可能性が高い領域という観点からみると、比較的狭い領域に限定できる。今後の課題は、同様な解析方法をより長期にわたって行うことである。

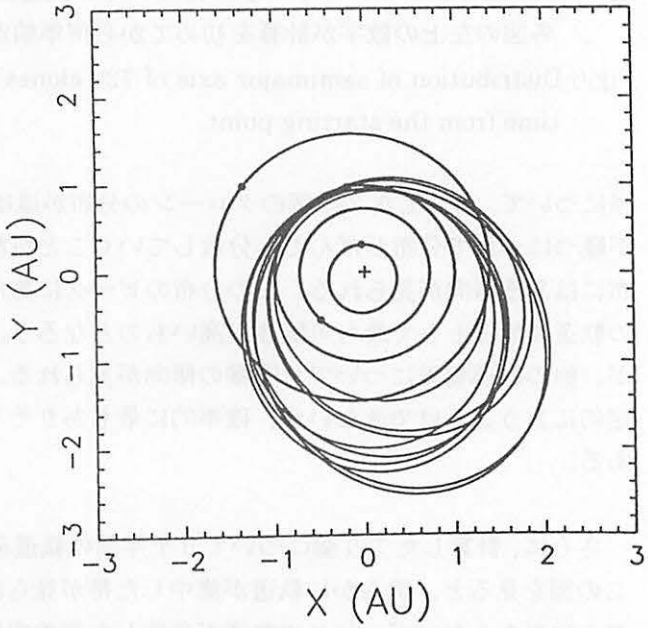

図8　ネレウス起源であると思われている流星の軌道
Fig.8 The orbits of meteors which are supposed to come from Nereus.

参考文献

Michel,P., Froeschlé,Ch., Farinella,P., 1996, Dynamical evolution of two near-Earth asteroids to be explored by spacecraft: (433) Eros and (4660) Nereus, Astron.Astrophys. 313, 993-1007

小惑星探査のための超多数回フライバイ軌道

Super multiple flyby orbits for exploration of asteroids

吉川　真（通総研）、安部　正真（宇宙研）

Makoto Yoshikawa (CRL),　Masanao Abe (ISAS)

概要

小惑星を探査するために、多数の小惑星のそばをフライバイできるような探査機の軌道を求めるプログラムを作成した。対象とする小惑星を軌道が求められている34000個ほどにし、接近距離を0.03AU以内とすると、10年間の探査期間で100個くらいの小惑星に接近できる軌道を多数見つけることができた。ただし、ここでの解析では、探査機の軌道はケプラー運動としてあり、惑星による摂動や人為的な制御は考慮していない。実際の探査では、各小惑星により接近するように軌道制御をする必要があるが、ここでは多数の小惑星探査を計画するときの軌道としてその候補を探すことが目的である。探査機の制御も考慮したより現実的なミッションを提案することが、今後の課題である。

Abstract

We have developed an program that can search such orbits of spacecraft that can approach many asteroids. If we pick up about 34000 asteroids for the targets of exploration, we can find many orbits that can approach about 100 asteroids in the distance of less than 0.03 AU during 10 year mission periods. In this study, we assume that the motion of spacecraft is Kepler motion, that is, the perturbations of planets are not taken into account. This is because we can control spacecraft in real missions, and we must control it so that it approach much closer to asteroids. The orbits that we obtained in this study can be helps for planning real missions. Our next study is to make much more realistic plans for exploration of asteroids.

１．小惑星の素顔を知るために

現在、確定番号が付けられた小惑星（軌道が正確に求められたもの）が約８千個あり、さらにまだ軌道がそれほど正確ではないものも含めると、３万７千個もの小惑星の軌道が公開されている（図１）。このように、小惑星は非常に多数存在するのであるが、その「素顔」を直接撮影できた小惑星は、わずか３つ（ガスプラ、イダ、マティールド）にすぎない。

小惑星の形状やその表面の状況は、小惑星の起源や進化を知る上で基礎的な情報でありかつ重要な手がかりとなる。つまり、小惑星のそばからその写真を撮影するだけでも、かなり有益な情報を得ることができる。ただし、小惑星は非常にたくさん存在するものであるため、小惑星の本質に迫るためには、数多くの小惑星について写真を撮る必要があろう。ここでは、１機の探査機でなるべく多くの小惑星に接近することができる探査機の軌道について検討してみることにした。そのような軌道があれば、将来の小惑星探査にとって有効なものになる可能性がある。

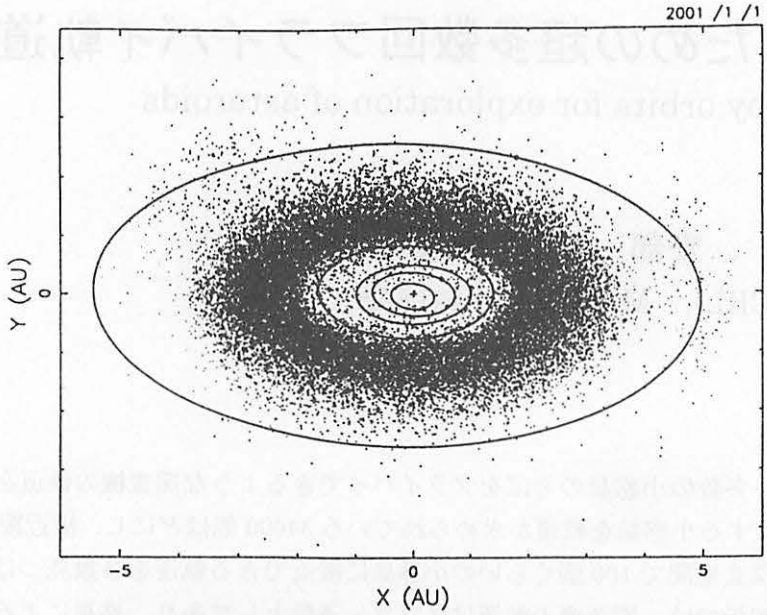

図１　小惑星の分布の様子。ここでは約 37000 個の小惑星が描いてある。

Fig.1　Distribution of asteroids.　About 37000 asteroids are plotted here.

２．多数回フライバイ軌道の求め方

探査機の軌道を決めるということは、軌道６要素を決定すればよい。最初から６要素すべてをフリーパラメータとして求めるのは計算量が多くなるので、まず、探査機の軌道として、ある時刻における地球の位置を近日点とするような軌道についてのみ考えることにした。つまり、地球から打ち上げられるときが探査機の軌道の近日点であるという仮定をおいたのである。この場合は、打ち上げにおいて、エネルギー的には最も都合がよい。

このように仮定すると、決定すべきフリーパラメータとしての軌道要素は、事実上、遠日点距離と軌道傾斜角の２つとなる。正確に言えば、昇交点経度は一意には決まらないのであるが、１つの軌道傾斜角について２通りの昇交点経度が考えられるに過ぎない。また、この昇交点経度と連動して、近日点引数の値が変わることになる。

探査機の出発地点がその軌道の近日点になるという仮定は、かなり軌道を制限するものである。ここでの解析ではこの条件を付けているが、将来的にはこの条件をはずして解析をするつもりにしている。なお、先ほどから地球を出発する時が近日点になると言っているが、実はここでの解析では出発地点が遠日点になる場合も含んで計算している。もちろん、多数の小惑星にフライバイするような軌道は、小惑星帯を横切るようなものになるから、出発地点が近日点となるのが普通である。

また、探査機は惑星の摂動を受けずに、単に初期に設定されたケプラー軌道上を動くと仮定している。その理由は、実際にミッションでは、探査機は制御されることになるためである。つまり、ここでは、実際のミッションとして候補となりそうな軌道を探すということが目的であり、本当に実現可能かどうかは、次のステップで検討するということにした。

一方、小惑星については、軌道が出されているすべての小惑星（ここでは 34931 個）について、惑星の摂動を考慮して位置を計算した。そして、探査期間（ここでは 10 年を仮定）になるべく多くの小惑星と遭遇するような探査機の軌道を探すということを行った。なお、ここでは小惑星に 0.03 天文単

位以内に近づく場合を「接近」として取り上げてある。この接近距離は、小惑星の写真を撮影したりするには遠すぎるものであり、実際のミッションではより接近するように探査機の軌道が制御されることになる。

小惑星を多数回フライバイするような軌道の求め方について簡単に示すと次のようになる。

（1）探査機を打ち上げる時刻（t）における地球の位置（R_t）を求める。
　　＜DE404等を用いる＞
（2）考慮する小惑星について、探査を行う期間中の1日ごとにその位置を求める。それぞれの小惑星（i）の各時刻（t'）における位置を$r^i_{t'}$とする。
　　＜数値積分による＞
（3）時刻tにR_tを出発して時刻t'に$r^i_{t'}$に着くようなケプラー軌道があるかどうかを調べる。そのような軌道があるときには、その軌道要素とともに小惑星と最接近する時刻やそのときの小惑星の位置・速度を出力しておく。　　→ **[フライバイ基本データ]**
（4）「フライバイ基本データ」を用いて、特定の小惑星をフライバイする軌道が他の小惑星についても接近するかどうかを調べる。　　→ **[多数回フライバイ軌道データ]**
（5）「多数回フライバイ軌道データ」から、より多くの小惑星に接近する軌道を取り出し、詳細な情報を出力する。　　→ **[超多数回フライバイ軌道]**

各データの内容について：

フライバイ基本データ

・ミッション期間中について、考慮している各小惑星に到達できる探査機の軌道や関連する情報を収めてあるデータ。
・探査機の打ち上げ時刻ごとに作成する。
・各小惑星については、探査期間中の1日ごとに探査機が到達できるかどうかを確認する。
・ここでは、探査機が小惑星に0.03AU以内に近づくことができれば「到達できる」とする。
※このデータ作成には、少し長いCPU時間が必要。

多数回フライバイ軌道データ

・「フライバイ基本データ」より、特定の小惑星をフライバイする軌道を抜き出したデータ。
・このときに、他の小惑星にも接近する可能性があるかもチェックし、0.03AU以内の接近があれば、そのデータも出力する。
※このデータ作成には、CPU時間は短い。

超多数回フライバイ軌道

・「多数回フライバイ軌道データ」より、より多くの小惑星に接近するものや興味深い小惑星に接近するものを選んで、詳細なデータを出力したデータ。
※このデータ作成には、ほとんどCPU時間はかからない。

3．計算結果

まず、34931 個の小惑星について、探査機を 2001 年 1 月 1 日から 3 日までのそれぞれの日に打ち出したとして、超多数回フライバイ軌道を求めてみた。この場合、1 日分のフライバイ基本データを作成するのに、ワークステーション（DEC Alpha server）で 4 日ほどかかった。また、このデータの大きさは、約 55MB になった。

次に、確定番号が付いた 7000 個の小惑星についてのみ同様な計算を行ってみた。こちらについては、探査機の打ち上げる日として、2001 年 1 月 1 日から 2 月 19 日までの 50 日間について計算してみた。この場合の計算時間は 1 日分のデータを作成するのに約半日くらいかかった。またデータの大きさは、1 日あたり約 11MB となった。検討する小惑星の数に比例して計算時間が長くなるし、データは大きくなることになる。

［注：出発地点が軌道の近日点であるという条件を使うと計算時間はより短くできるが、ここでは、この条件をはずした場合を念頭に入れた計算をしているので、余分に計算時間がかかっている。］

計算結果の 1 例として、Ceres を含めた 84 個の小惑星にフライバイするものを表 1 に示す。このように、80 個程度の小惑星に 0.03AU 以内に接近するような軌道はかなり沢山求めることができる。これだけ多くの数の小惑星に接近できるのは、もとのデータの数が 34000 個あまりと多いからで、7000 個の確定番号の付いた小惑星に限ればフライバイの数は多いもので 20 個程度となる。その例として、表 2 に Vesta を含めた 18 個の確定番号のついた小惑星にフライバイする例を示す。

なお、多数の小惑星にフライバイするような軌道は、やはり小惑星帯の中にあるような軌道であり、仮にトロヤ群の小惑星である Achilles にフライバイするという条件で多数回フライバイ軌道を求めると、小惑星の数として 34000 個余りを入れてもフライバイできる小惑星の数は 10 個程度となってしまう（表 3）。

4．今後の課題

ここでの解析により、接近距離が 0.03AU 以下とすると、10 年間のミッションで 100 回ほど小惑星に接近するような軌道もあることが分かった。これを、確定番号が付いている 7 千個の小惑星に限定すると、約 20 回の接近があることになる。もちろん、0.03AU の接近というのは探査するには遠すぎるので、探査機を制御することで個々の小惑星により近づきながら多数の小惑星に接近できるかどうかのチェックが必要となる。さらに、単に接近回数が多いだけでなく、なるべく興味深い小惑星に多く接近するような軌道を探すことも重要である。実現可能でサイエンスとしてもより意義の深いミッションを提案することが今後の課題である。

（表１）Ceres を含めた 84 個をフライバイ

打ち上げ　　：2001 年 1 月 2 日
ミッション期間　　：１０年間
フライバイする小惑星数：８４個
条件　　：小惑星(1)Ceres をフライバイする

探査機の軌道要素　：

time of dep.	a	e	i	ω	Ω	M
2001/ 1/ 2.0	1.98066	0.50355	0.932	179.998	281.650	0.000

注意：Ceres に接近するのはミッションの最後なので、Ceres をターゲットとしたミッションとしてはあまり適さない。

	時刻	距離 (AU)	相対速度 (km/s)	NO	小惑星のデータ a	e	i	name
1	2001/ 2/10.1	0.02496	12.310	28613	2.49	0.573	3.0	1997 GH3
2	2001/ 7/15.7	0.01983	13.310	29098	2.58	0.213	4.0	1997 HK9
3	2001/ 7/19.5	0.02823	13.996	20916	2.45	0.198	1.4	1994 PM5
4	2001/ 8/13.6	0.01293	12.595	960	2.25	0.165	3.0	Birgit
5	2001/ 8/28.0	0.01359	9.869	21100	2.52	0.072	2.2	1994 PT16
6	2001/ 9/10.5	0.02021	12.400	33396	2.35	0.199	2.1	4564 T-2
7	2001/ 9/23.1	0.00686	13.167	17881	2.47	0.261	5.4	1993 FA32
8	2001/ 9/23.9	0.02856	10.468	21075	2.51	0.112	1.5	1994 PJ15
9	2001/ 9/24.0	0.02717	10.926	29465	2.79	0.148	4.7	1997 NZ2
10	2001/12/ 7.9	0.01971	9.175	1686	3.15	0.168	0.6	De Sitter
11	2002/ 3/13.9	0.01536	6.860	8769	2.63	0.160	14.8	1979 EL
12	2002/ 4/21.8	0.02662	5.291	10728	2.58	0.230	3.7	1982 VN3
13	2002/11/ 9.3	0.01872	9.080	25294	3.16	0.167	1.6	1996 HS19
14	2002/11/28.9	0.02486	9.271	25314	3.17	0.167	1.2	1996 HR21
15	2002/11/30.8	0.02690	7.861	12591	2.79	0.044	5.3	1989 SP2
16	2002/12/ 1.2	0.00750	7.844	24619	2.79	0.040	3.4	1996 BJ3
17	2002/12/ 3.8	0.02887	11.812	27919	2.70	0.285	2.6	1997 CL5
18	2003/ 1/11.3	0.01133	7.865	16090	2.15	0.171	1.0	1992 EC16
19	2003/ 1/25.0	0.01834	9.731	18258	2.61	0.075	0.9	1993 FP48
20	2003/ 2/ 4.9	0.01500	11.411	9644	2.57	0.141	3.1	1981 ES16
21	2003/ 2/ 5.0	0.02431	8.929	4881	2.31	0.047	8.1	1975 XJ
22	2003/ 2/ 8.0	0.00866	8.262	23643	2.50	0.067	0.5	1995 UW13
23	2003/ 2/20.9	0.02825	10.124	29445	3.06	0.238	1.7	1997 NA1
24	2003/ 3/ 9.1	0.01514	8.936	9922	2.27	0.054	4.2	1981 EF31
25	2003/ 3/20.6	0.01383	14.106	8785	2.23	0.212	6.1	1979 MF
26	2003/ 3/22.7	0.02598	8.834	31894	2.25	0.097	6.1	2243 T-1
27	2003/ 3/26.5	0.01606	10.096	16528	3.03	0.301	9.4	1992 PR6
28	2003/ 4/11.5	0.01368	7.837	27954	2.41	0.224	6.7	1997 CF9
29	2003/ 4/27.0	0.01919	9.985	28094	2.43	0.199	1.6	1997 CW27
30	2004/ 4/19.6	0.01938	13.853	29097	2.29	0.171	1.6	1997 HL9
31	2004/ 5/23.1	0.01542	11.234	24700	2.34	0.084	1.0	1996 CS1
32	2004/ 5/31.9	0.02268	11.567	30525	2.28	0.114	2.3	4604 P-L
33	2004/ 6/20.2	0.00442	15.072	13946	2.37	0.344	2.7	1990 UA3
34	2004/ 7/18.6	0.02386	8.966	1967	2.23	0.139	3.9	Menzel
35	2004/ 7/23.2	0.02828	8.309	24018	2.28	0.112	5.8	1995 WE5
36	2004/ 7/23.4	0.02580	6.250	5946	2.34	0.125	2.6	1984 UC1
37	2004/ 9/ 3.0	0.02766	6.957	8661	2.27	0.180	5.9	1978 VH7
38	2004/10/14.5	0.00767	7.547	14753	2.79	0.083	0.9	1991 PT12
39	2004/11/19.3	0.01485	5.101	31031	2.43	0.190	0.4	6281 P-L
40	2004/12/16.2	0.02212	6.184	26644	2.92	0.065	1.2	1996 VM3
41	2005/ 1/10.4	0.00979	6.536	1189	2.93	0.111	9.9	Terentia
42	2005/ 4/22.0	0.00839	5.556	23744	3.11	0.052	0.6	1995 UU44
43	2005/ 6/16.0	0.02441	6.313	27394	3.07	0.142	11.9	1997 AP1
44	2005/ 8/11.9	0.02325	5.801	32546	2.79	0.082	1.3	1326 T-2
45	2005/ 9/14.9	0.02665	5.389	22005	2.51	0.146	4.3	1994 WL3
46	2005/ 9/24.9	0.01377	5.049	31482	2.58	0.185	4.0	7611 P-L
47	2005/10/ 8.0	0.01998	8.788	21681	2.48	0.083	2.2	1994 TL10
48	2005/10/31.4	0.00809	6.082	822	2.26	0.156	0.7	Lalage
49	2005/11/26.3	0.02460	10.872	22917	2.99	0.208	1.2	1995 OY3
50	2005/12/21.8	0.01729	10.848	3798	2.17	0.078	2.4	de Jager
51	2006/ 1/19.2	0.02702	12.810	5763	2.46	0.168	0.3	1982 NA
52	2006/ 2/ 8.0	0.01644	8.997	32308	2.19	0.146	1.6	1038 T-2
53	2006/ 2/ 9.7	0.02094	13.848	7395	2.27	0.175	5.7	1985 RP1
54	2006/ 2/12.4	0.01269	10.716	6646	1.93	0.100	17.6	1991 CA3
55	2006/ 3/ 8.4	0.02952	10.166	19355	2.15	0.185	2.1	1993 TQ1
56	2007/ 3/ 9.1	0.02364	10.404	813	2.22	0.026	6.3	Baumeia
57	2007/ 3/28.8	0.00258	12.455	30075	2.50	0.172	5.6	3067 P-L
58	2007/ 4/10.3	0.00887	12.825	34384	2.44	0.223	2.5	3501 T-3
59	2007/ 4/22.9	0.01443	11.094	25080	2.30	0.177	6.7	1996 GS4
60	2007/ 4/25.1	0.02237	10.899	19911	2.40	0.151	5.3	1993 UD3
61	2007/ 5/17.8	0.01906	7.192	11008	3.05	0.185	0.6	1985 CD2
62	2007/ 6/17.0	0.02150	9.592	33283	2.46	0.203	3.4	4169 T-2
63	2007/ 7/30.7	0.02834	7.731	16926	2.53	0.180	3.8	1992 UZ6
64	2007/12/26.0	0.01473	4.705	17315	2.73	0.130	2.9	1993 FD7
65	2008/ 4/30.8	0.01124	6.806	18782	2.89	0.031	3.0	1993 OK9
66	2008/ 5/21.4	0.02450	7.013	30237	2.41	0.184	2.3	4101 P-L
67	2008/ 6/ 7.3	0.01001	6.100	6209	2.41	0.136	1.4	Schwaben
68	2008/ 6/27.4	0.01949	5.042	19392	2.47	0.155	2.0	1993 TL6
69	2008/ 8/18.9	0.02604	8.759	6779	2.26	0.108	1.9	1990 DM1
70	2008/ 9/ 9.0	0.02113	13.037	23323	2.69	0.221	3.8	1995 SZ30
71	2008/10/17.0	0.02897	11.991	17117	2.71	0.194	4.6	1993 BH4
72	2009/ 5/ 8.1	0.02145	30.158	24288	1.70	0.827	3.6	1995 YR1
73	2009/12/ 2.3	0.01605	13.698	15013	2.16	0.181	3.1	1991 RB16
74	2010/ 1/18.8	0.01985	8.708	24404	2.17	0.103	1.0	1995 YH23
75	2010/ 3/ 2.0	0.00592	10.884	21108	3.10	0.213	2.1	1994 PG17
76	2010/ 3/14.1	0.02776	7.542	22028	2.24	0.174	1.4	1994 WB5
77	2010/ 3/14.7	0.01453	4.629	19859	2.37	0.215	4.7	1993 TU39
78	2010/ 5/27.1	0.02408	6.065	1	2.77	0.077	10.6	Ceres
79	2010/ 6/ 6.7	0.01758	7.677	23960	2.54	0.233	3.8	1995 WQ1
80	2010/ 6/27.8	0.01828	5.430	18399	2.54	0.145	3.7	1993 FO62
81	2010/ 7/ 3.2	0.02120	3.996	28843	2.56	0.158	1.7	1997 GX18
82	2010/ 9/14.2	0.02207	4.873	1955	2.85	0.061	1.0	McMath
83	2010/12/ 9.8	0.02825	6.582	7347	3.08	0.124	0.5	1993 EW
84	2010/12/16.7	0.01654	5.430	338	2.91	0.017	6.0	Budrosa

（表２）Vesta を含めた 18 個（確定番号の小惑星）をフライバイ

打ち上げ　　：2001 年 1 月 1 日
ミッション期間　　：１０年間
フライバイする小惑星数：18 個（確定番号のみ）
条件　　：小惑星(4)Vesta をフライバイする

探査機の軌道要素　：

time of dep.	a	e	i	ω	Ω	M
2001/ 1/ 1.0	1.87475	0.47550	5.952	0.000	100.629	0.000

	時刻	距離 (AU)	相対速度 (km/s)	NO	小惑星のデータ a	e	i	name
1	2001/ 7/19.6	0.02195	14.161	6790	2.34	0.207	11.1	1991 SF1
2	2001/ 7/29.7	0.02307	10.966	5930	2.25	0.090	4.8	Zhiganov
3	2002/ 2/ 2.3	0.01602	6.444	2671	2.61	0.121	1.5	Abkhazia
4	2002/ 7/23.9	0.00647	5.569	5298	2.99	0.218	2.2	1966 PK
5	2002/ 8/11.1	0.01013	7.954	1391	2.55	0.169	7.6	Carelia
6	2002/11/ 8.4	0.00922	7.639	2756	2.55	0.115	5.8	Dzhangar
7	2002/12/ 4.6	0.02002	6.453	1089	2.21	0.127	3.7	Tama
8	2004/ 1/27.6	0.02450	12.387	2887	2.26	0.150	4.4	Krinov
9	2004/ 7/25.6	0.02826	7.113	19	2.44	0.158	1.6	Fortuna
10	2004/ 8/24.5	0.02168	6.456	6395	2.41	0.202	1.5	Hilliard
11	2004/ 9/21.2	0.02451	6.191	1809	2.93	0.097	3.3	Prometheus
12	2005/ 6/ 1.9	0.02825	8.985	2841	2.25	0.084	4.9	Puijo
13	2006/11/20.7	0.02741	10.005	1084	2.69	0.129	3.9	Tamariwa
14	2007/ 5/15.9	0.00452	5.116	4619	2.69	0.031	1.8	Polyakhova
15	2007/ 8/29.8	0.02946	5.800	3670	2.74	0.016	6.4	Northcott
16	2008/ 1/17.0	0.02847	10.047	4	2.36	0.090	7.1	Vesta
17	2009/ 8/12.6	0.02008	4.919	5562	2.48	0.116	7.6	1991 VS
18	2009/ 9/26.0	0.01546	7.761	1247	3.15	0.159	1.8	Memoria

（表 3）Achilles を含めた 10 個をフライバイ

打ち上げ　　：2001 年 1 月 1 日
ミッション期間　　：１０年間
フライバイする小惑星数：１０個
条件　　：小惑星(588)Achilles をフライバイする

探査機の軌道要素　：

time of dep.	a	e	i	ω	Ω	M
2001/ 1/ 1.0	3.98731	0.75339	6.800	0.000	100.629	0.000

注意：Achilles はトロヤ群の小惑星であるため、探査機の軌道長半径が大きくなっている。またフライバイできる小惑星数も少ない。

	時刻	距離 (AU)	相対速度 (km/s)	NO	小惑星のデータ a	e	i	name
1	2001/ 5/25.4	0.00960	21.086	20218	2.18	0.213	6.9	1994 AN10
2	2001/ 6/19.9	0.02347	20.558	29060	2.65	0.239	10.1	1997 HK2
3	2001/ 6/21.0	0.02730	19.779	16966	2.25	0.203	7.4	1992 WR1
4	2001/ 7/19.7	0.02375	16.623	24914	2.78	0.066	7.4	1996 EB9
5	2001/ 8/ 7.0	0.01666	18.007	197	2.74	0.164	8.8	Arete
6	2001/ 8/14.9	0.02876	14.324	24566	2.67	0.084	5.4	1996 BC
7	2001/ 9/11.2	0.01783	15.388	21559	2.65	0.180	8.6	1994 SK9
8	2006/11/30.1	0.02522	7.481	588	5.18	0.148	10.3	Achilles
9	2007/ 3/29.6	0.02677	9.356	25885	5.21	0.029	3.6	1996 RE11
10	2008/ 6/29.1	0.02046	20.438	31782	2.94	0.201	30.2	2026 T-1

木曽シュミット望遠鏡による木星外衛星の位置観測精度
Astrometric Accuracy of the Jovian Outer Satellites Observed by the Kiso Schmidt Telescope

中村士、佐々木五郎、木下宙（国立天文台）、R.A. ジェーコブソン（JPL, NASA）
Tsuko Nakamura, Goro Sasaki, Hiroshi Kinoshita (NAO), and R.A. Jacobson (JPL, NASA)

アブストラクト

木星の外部領域には、2群の特異な衛星が存在する。各群のメンバーはそれぞれ4個である。内側のグループは順行軌道で周期は約1年、外側のものは逆行軌道で2年の周期を持つ。逆行軌道であることと群をなすことから、捕獲と衝突の過程がそれらの起源に拘っていると想像されるが詳細は不明である。これら衛星の力学的起源の手がかりを得るためには精密な軌道決定がまず必要である。しかし近年は木星外衛星は余り観測がない。そこで、まず高精度な軌道改良を目指して1986年から、木曽観測所の1mシュミット望遠鏡を用いて乾板による位置観測を始めた。観測は乾板が利用できなくなった1992年まで継続した。

従来の望遠鏡に比べて木曽シュミットでより精度の高い観測ができると期待した理由は、木曽の乾板では全ての木星外衛星（J13は暗すぎて写せない）が1枚の乾板に写るからである。そうすると全部の衛星の位置は共通な乾板定数を用いて求められるので、衛星間の相対位置を軌道改良に使用すれば、位置の計算に用いた星表に含まれる系統誤差が打ち消せることになる。軌道改良には昔の位置観測データを多数集める必要があるが、これが予想外に難しいことが観測を始めて数年すると分ったので、軌道改良は見送っていた。

最近、我々の観測データも含めた軌道改良がフランス（Bureau des Longitudes）と米国（JPL）とで行なわれ、軌道改良後の残差も入手出来るようになったので、木曽データの良否を検討した。それによると、絶対座標では我々の観測は同じ時期のマクドナルド天文台での観測より10-20%残差が小さく、また相対座標による軌道改良では絶対座標によるものより更に数10%小さい残差を与えることが分った。つまり、木曽データは最も精度の高い観測であることが示され、木星外衛星観測における広視野シュミット望遠鏡の優秀性が証明されたことになる。一方、フランスでの軌道改良は、本来逆行衛星よりも位置精度が良い筈の順行衛星に対して原因不明の大きな残差を与えており、彼等の軌道改良にはほぼ確実に何かの誤りがあると想像される。

なお、次頁以降の英文は、Astronomical Journalの1998年4月号に掲載予定のものである。

Astrometric Observations of the Jovian Outer Satellites for 1990-1992

Tsuko Nakamura and Goro Sasaki

National Astronomical Observatory, Osawa, Mitaka, Tokyo 181, Japan

Received _____; accepted _____

ABSTRACT

We observed precise astrometric positions of the faint outer satellites of Jupiter J6–J12 with the Kiso 105cm Schmidt telescope. The observational period is from November 1990 through March 1992. We discuss the post-fit residuals after orbital improvement for our 1986–1990 observations, kindly provided by R.A. Jacobson (JPL) prior to publication, and thereby emphasize the superiority of the inter-satellite measures available only from wide-field Schmidt observations which can cover all the satellites in a single plate.

1. Introduction

In 1986 we started photographic astrometric observations of the jovian outer satellites in an attempt to give their improved positions making good use of wide-field coverage by Schmidt telescopes. Precise astrometric positions 1986–1990 for the seven satellites except J13 were reported (Nakamura et al. 1991). This is the second report covering 1990–1992. In Section 2 we tabulate all the measured positions and in Section 3 discuss the post-fit residuals after orbital improvement for our 1986–1990 observations, which were kindly supplied by R.A. Jacobson (JPL) prior to publication.

2. Observations and Results

We made photographic observations of the jovian outer satellites with the Kiso 105cm Schmidt telescope of University of Tokyo. The plates used cover the field of view of 6.3 deg. by 6.3 deg., so that images of all the outer satellites can be taken in a single plate with Jupiter located near the plate center. For details on the telescopic specifications and observations, see Nakamura et al. (1991). The standard exposure time was 25 minutes for Kodak IIa-O emulsion without hypersensitization. Automatic guiding was made using the center of the jovian disk as a guiding target.

We measured the orthogonal coordinates for both the reference stars and satellites with a XY measuring machine developed at the Kiso Observatory (1μmm resolution). In case of the automatic bi-section mode where the machine calculates by hardware the center of plate density for stellar images above the sky-background level, repeated measurements are unnecessary and this mode was always used for bright satellites. We made the manual bi-section several times for each faint satellite near detection level. We used Astrographic Catalog Reference Stars (ACRS: U.S. Naval Observatory) as our reference star catalog

(Corbin and Urban 1990). Several tens of stars fainter than magnitude 10 from the ACRS were generally adopted as the reference stars, uniformly distributed over the plate.

Use of this large number of reference stars is because the outer satellites appear almost everywhere in the plate and in such cases simulations show that the positional error for satellites is sometimes a few times larger than the standard deviation of the residuals for the reference stars, especially for reference star numbers of less than about 50 (Nakamura and Sekiguchi 1993). Adopted plate model is the third-order polynomials for each of x and y standard coordinates (Smart 1949). We used an astrometric plate reduction software PDSP, developed at the Kiso Observatory (Nakamura et al. 1991).

The reduced positions of the satellites J6–J12 are presented in Table 1 as the topocentric right ascension and declination. Site coordinates of the Kiso Observatory are given in Nakamura et al. (1991). The meaning of each column is as follows:

Column 1. Plate number given at the Kiso Observatory.

Column 2. Midtime of exposure (in year, month and day fraction) in Universal Time (UTC).

Column 3 and 4. Right ascension (in hours, minutes and seconds of time) and declination (in degrees, minutes and seconds of arc) in B1950.0. These positions are the ones obtained *directly* from the plate reduction software PDSP, so that they are astrometric positions affected by the E-terms of abberation.

Column 5 and 6. Right ascension and declination in J2000.0. These positions are astrographic positions free from the E-terms of abberation, which were converted from B1950.0 to J2000.0 using the procedure recommended by the Commission 20 Ad Hoc System Transition Committee of IAU (1990). The conversion formulae are basically the same as those seen in Explanatory Supplement to the Astronomical Almanac (1992).

This conversion from B1950.0 to J2000.0 may be made by those who attempt orbital improvement of the satellites.

Column 7: Number of the reference stars used in plate solution.

Column 8 and 9: The formal standard deviations of the residuals in the plate solution for right ascension ($S1$ for $\Delta\alpha\cos\delta$) and declination ($S2$ for $\Delta\delta$) in units of arcseconds.

3. Discussion

Our observations with the Kiso Schmidt telescope are characterized by plate constants that are common to all the satellites. This fact is significant in that use of Schmidt plates allows us to adopt the inter-satellite positions (coordinates of other satellites referred to those for a specified satellite) for orbital improvement and then is likely to give a better orbital fitting because errors due to the reference catalog can effectively be cancelled in inter-satellite positions. This was just the initial reason why we started the Kiso Schmidt telescope observations, though we could not have confirmed the superiority because we had no chance to make orbital improvement of the satellites by ourselves.

Recently two orbital improvements for the jovian outer satellites have been done by French and US astronomers. The first is due to Rocher and Chapront (1996) and the second due to Jacobson (1997). First let us talk about Jacobson's results. Jacobson (1997) made orbital improvements for the J6–J12 satellites with the observations up to 1994 including ours (Nakamura et al. 1991). Jacobson (1997) included dynamical effects by the Galilean satellites and Jupiter's J_2 oblateness, in addition to the Saturnian and the solar perturbations. Table 2 shows the standard deviations of the post-fit residuals after orbital improvement for our 1986–1990 observations, which were kindly provided by Jacobson prior to publication. "Absolute" in the first column stands for the ordinary right

ascension and declination, whereas "Relative" means the inter-satellite positions, namely positions of satellites measured relative to a specified satellite. P and R refer to prograde and retrograde satellites. Note that the standard deviations for P and those for R in Table 2 are respectively the combined ones for J6, J7 and J10 and for J8, J9, J11, and J12. N represents the total number of our positional data used in orbital improvement. The standard deviations $\sigma(\Delta\alpha\cos\delta)$ and $\sigma(\Delta\delta)$ are given in the fourth and fifth columns in arcsec. According to Jacobson (1997), our σ's in absolute positions are nearly 10-20% smaller than modern positions available from other observations.

Considering that the averaged errors ($S1$ and $S2$) for reference stars in Nakamura et al. (1991) and Table 1 are around 0.″3–0.″35, values of the standard deviations of absolute positions for P-satellites in Table 2 indicate that the orbital fitting error is comparable to the plate reduction error; this seems quite reasonable. About 40% larger σ's in absolute positions for R-satellites than those for P-satellites also make sense, since the retrograde satellites are generally fainter than the prograde satellites and hence we were forced to make repeated measurements of the former in manual bi-section mode. We can also see that, for both P- and R-satellites, the σ's for relative positions are improved by a few tens of a percent compared with the σ's for absolute positions except $\sigma(\Delta\delta)$. As the $\sigma(\Delta\delta)$ in absolute positions for P-satellites is minimum among others, it may be natural that the σ was not improved appreciably in relative position analysis. Therefore, it is concluded that the relative positions are better than the absolute ones in performing orbital improvement. Taylor and Shen (1988) had already shown in their orbital improvements of Saturnian satellites that the inter-satellite positions gave the smallest residuals among other measures. However, our observations here seem to be the first case in which a direct comparison has been made between the inter-satellite positions and the absolute ones using the *same* set of data.

Rocher and Chapront (1996) have made independently orbital improvements for the

two prograde satellites J6 and J7, and the two retrograde ones J8 and J9. They used observed positions till 1993 including ours (1991) and their dynamical model takes account of all the planetary perturbations and the J_2 oblateness effects of Jupiter; seemingly they did not include perturbations by the Galilean satellites. The post-fit residuals after orbital improvement provided via anonymous ftp reveal that, for our Kiso observations, the averaged σ's for $\Delta\alpha\cos(\delta)$ are respectively 1.″4, 1.″9, 0.″5, and 0.″5 for J6,J7, J8, and J9. The σ's for $\Delta\delta$ are also found to be 1.″1, 0.″5, 0.″5, and 0.″5; similar trends are seen in the residuals for observations at other observatories. Although the σ's for J8 and J9 are roughly comparable to the ones by Jacobson (1997), those for J6 and J7 are obviously inconsistent with both the errors in our plate reduction and Jacobson's residuals. Time history of the residuals for J6 and J7 also seems to show some short-term variations. As far as our observations are concerned, we do not see any reasons that our astrometric positions for J6 and J7 are worse than those for J8 and J9, because our images of J6 and J7 were bright and well-defined and the plate constants were common to all the four satellites. Inferring that the large σ's for the inner prograde satellites J6 and J7 may be caused by the inner perturbing sources such as the Galilean satellites, we tried to make order-estimates of the short-period analytic perturbations using the formulae given by Tisserand (1896). However, their magnitude was no more than the order of 0.″1. Therefore, possible causes of the large σ's for J6 and J7 by Rocher and Chapront (1996) are unknown yet to us.

We are heartily grateful to R.A. Jacobson who kindly supplied us with the residuals of the jovian outer satellites after their orbital improvements prior to publication. We thank the staff of the Kiso Observatory whose support in observations was helpful. Discussion with H. Kinoshita on perturbations by the Galilean satellites was also useful.

REFERENCES

Corbin, T.E., and Urban, S.E. 1990, in IAU Symposium 141: Inertial Coordinate System on the Sky, eds. by J. Lieske and V.K. Abalakin, (Kluwer, Dordrecht), p433

Jacobson, R.A. 1997, personal communication

Nakamura, T., H. Kinoshita, and Kosai, H. 1991, AJ, 101, 290

Nakamura, T., and Sekiguchi, M. 1993, Publ. Astron. Soc. Japan, 45, 119

Rocher, P., and Chapront, J. 1996, A&A, 311, 710

Smart, W.M. 1949, Textbook on Spherical Astronomy, (Cambridge Univ. Press, Cambridge), Chap. 17

Taylor, D.B., and Shen, K.X. 1988, A&A, 200, 269

Tisserand, F. 1896, in Traité de Mécanique Céleste, Tome IV, Gauthier-Villars et fils (Paris)

Table 1: Observed topocentric positions of the jovian satellites J6–J12

Provided as "camera-ready" form.

Table 2: Standard deviations (arcsec) of the post-fit residuals for the Kiso 1986–1990 observations

Measures	P/R	N	$\sigma(\Delta\alpha\cos\delta)$	$\sigma(\Delta\delta)$
Absolute	P	90	0.51	0.43
Absolute	R	70	0.62	0.65
Relative	P	43	0.35	0.44
Relative	R	28	0.57	0.43

This manuscript was prepared with the AAS LaTeX macros v4.0.

スバル望遠鏡による惑星の外部衛星探査計画
Survey-Observation Plan of Outer Faint Satellites of Planets with the SUBARU 8m-Telescope

中村士（国立天文台）
Tsuko Nakamura (National Astronomical Observatory, Tokyo)

Abstract:
Recently, two faint outer satellites of Uranus have been discovered by the US astronomers. These outer satellites, including eight Jovian outer ones and the Saturnian satellite Phoebe, are supposed to be members dynamically captured from the outside. Considering the size spectrum of small bodies in the solar system, fainter satellites not yet detected are likely to exist in the outskirts of the sphere of influence of each planet. Gigantic telescopes like SUBARU now under construction in Hawaii are most suitable for observations of such objects. This short report is a feasibility study on survey observations using SUBARU of possible faint satellites around each planet, in terms of limiting magnitude, detectable size, survey sky area, observing conditions, and so on. It is shown that SUBARU CCDs can cover the necessary sky areas for search with two sets of exposures, each of which consists of a few hours, and can detect bodies roughly one order of magnitude smaller than the smallest known satellites.

1. はじめに

1997年10月に、天王星に新たな2個の衛星の発見報告がなされた（IAUC 6764, 6765, 6780）。従来、天王星の衛星はいずれも横倒しの赤道面内で天王星のごく近傍にしか存在しなかったので、天王星衛星の起源は他の惑星衛星に比べて特異であると見なされていた。今回発見された2個の衛星は、両方とも逆行軌道であり、離心率も大きいらしく（現在、値が仮定されている）、軌道半長径は天王星半径の250–300倍であるので（まだ衛星であることは100%確実ではないらしいが）、天王星と共に生まれたのではなく、後から捕獲された可能性が高い。

このような外部衛星は木星に8個、土星に1個が知られている。木星の外衛星は軌道がよく似た2つのグループを成している。それぞれのグループは4個のメンバーを持ち、内側のグループ衛星は順行で周期は約1年、外側衛星は逆行で周期は約2年である。外部衛星であることと逆行軌道であることは捕獲されたものであることを示唆し、軌道が似たグループを成すことは衝突現象が関係していることを暗示する。実際、Colombo and Franklin (1971) は2つのグループ衛星は外部からやって来た天体が衝突して出来たと主張し、Pollack et al.(1978) は木星が始源惑星の時に周囲に残していた厚い原始大気に外部天体が衝突して分裂した破片がグループ衛星を形成したとしている。捕獲だけでは、軌道が良く似た4個ものグループを偶然で作るのは困難であるから、何らかの意味での衝突過程が寄与していると考えるのが自然であろう。

衝突起源でしばしば問題にされるのは、サイズ分布である。衝突起源なら小さい物の数が大きな物に比べてずっと多い筈である。木星外衛星のサイズ（半径）の度数分布と、衝突現象では典型的なサイズの(-3)乗分布とを、**Table 1.** に比較した。衝突から予想される数に対して、木星外衛星では小さいメンバーの数が明らかに不足してい

るのが分る。土星衛星のPhoebeの場合も半径が110kmで、数10kmの物があれば充分見つかっていても良い筈なのに、1個しか発見されていない。この原因が、これら微小衛星は現在の望遠鏡の観測限界近くで発見されたための見かけの効果なのか、それとも本当に小さいメンバー数が少ないのかは現状では判断できない。木星では、1975年にC. Kowalが21等の新衛星らしき天体を発見して、2週間ほど追跡されたがその後見失われた。よって、木星外部には少なくとも1個の未発見の衛星は存在するらしい。なお、木星に衝突した彗星Shoemaker-Levy 9の母天体を探す組織的な乾板サーベイの仕事（Fuse et al., 1997）によって、J13番衛星（非常に暗い）を除く7個の外衛星と同程度の明るさの新木星衛星がまだ存在する見込みはほとんど残っていない。

Table 1. Radius distributions for Jovian outer satellites (N_{obs}) and for the (-3) power-law (N_{cal})

Range(km)	N_{obs}	N_{cal}
80–40	1	1
40–20	4	1
20–10	16	5
10–5	64	1

本報告では、1999年の終りから稼働が予定されている口径8mのスバル望遠鏡（主焦点）を用いて、上に述べた未知の微小衛星がどの程度探査できるかを簡単に検討したものである。

2. 外部微小衛星探査の意義

未知の外部衛星が複数個発見された場合の意義はいくつか挙げられる。外部衛星が捕獲産物とすると、発見された軌道の大きさからまず惑星の実質的な影響圏（Sphere of influence）の大きさがよりはっきりすることである。**Table 2.** に各惑星に対する影響圏、ヒル圏、実際に発見されている最外部衛星の軌道の大きさを比較した。

Table 2. Search regions for possible new satellites (near opposition)

Planet	Sph. of Inf.	Hill's Sph.	Outermost Sat.	CCD Frames
Jupiter	48.3×10^6km	51.9×10^6km	23.6×10^6km	
	(4.4 deg)	(4.7 deg)	(2.1 deg)	88
Saturn	54.5	64.1	13.0	
	(2.4 deg)	(2.8 deg)	(0.6 deg)	7
Uranus	51.7	69.5	9.3(S/1997U2)	
	(1.1 deg)	(1.5 deg)	(0.47 deg)	4–5
Neptune	86.8	115.2	5.6	
	(1.0 deg)	(1.3 deg)	(0.1 deg)	a few
Mars	0.56	1.08	small	
	(0.41 deg)	(0.79 deg)	($\sim$ 0 deg)	a few
Pluto	3.21		small	
	(0.041 deg)			a few

この表から、大惑星に関しては最外部衛星の軌道領域は影響圏の大きさの数分の1以下の大きさであることが分る。新しい微小衛星が惑星からどの位の距離に見つかるかで、

衛星としての力学的安定性に、影響圏より更に強い安定領域の目安と与えることができるかも知れない（Hamilton and Burns 1991）。

衛星がもっと外側に存在する可能性も勿論否定はできないが、探すとすれば既存の衛星が居るあたりをまず探すのが筋道であろう。適当な数の新しい外衛星が発見されれば、その惑星に対する捕獲の効率を推定することができるであろう。木星と土星の場合、微小メンバーの数が衝突現象から予測されるサイズ分布にどれだけ近いかが興味の焦点である。小さい破片の数が不足している原因が、小さいものは惑星原始大気にガス抵抗で取り込まれたためとすると、不足している程度を調べることで衝突捕獲されてから原始大気が散逸するまでの時間スケールに関する手がかりも得られるかも知れない。

たとえまったく新しい衛星が発見されなくとも、スバルほどの大型望遠鏡によるサーベイの結果であれば、これは惑星の捕獲効率の上限値に関する情報を担っており、相当数が発見される場合同様に重要な結論となる。

3. 捜索範囲と限界等級

スバルの第1焦点に付くモザイクCCDカメラ（Supreme-CAM）は30'x24'の視野をカバーする。カメラ仕様書によれば、V-バンドのフィルターに対して5分露出でS/N=5の場合の限界等級は$m_V = 25$等であるので、この条件で以下は計算した（露光中に移動して限界等級が低下する分は考慮されている）。この条件は、微小ベルト小惑星のサーベイ観測計画として昨年、天体力学研究会で紹介したものと同じである（Nakamura 1997）。

現在発見されている最外部衛星の軌道半径をサーベイの範囲として考えることにすれば、**Table 2.** で、最外部衛星の欄のカッコ内に示した角度範囲（半径）が捜索範囲となる。この範囲を上記のCCDカメラで撮影するには何枚のフレームが必要かを最後の欄に示した。木星の場合は1晩中撮影を続けて2夜掛かるが、他の惑星では1-2時間以内の観測で済むことが分る。実際には、移動を確認するために続いた2夜の撮影と、衛星であることを確かめるために、約1ケ月の間隔をおいた観測が要求される。

次に、どの位のサイズの衛星まで撮影可能かを、各惑星に対して**Table. 3**に比較した。第2欄は発見されている外部衛星で最小のもののサイズ、第3欄は上記の撮影条件で達成可能なサイズである。最後の欄は両者のサイズの比である。火星では直径僅か50mまで探すことができる。土星の場合の比が大きいのは唯一発見されている衛星Phoebeがたまたま大きいためであろう。よって、おおざっぱにはスバルでは既知の最小衛星より約1桁小さいものまで見えることになる。現実には、露出時間を20分程度まで伸ばすのは容易だし、望遠鏡の追尾を惑星の移動速度に合わせることで更に限界等級を下げることが出来るので、**Table. 3**の半分程度のサイズまで探査するのは困難ではない。

4. 観測条件

ハワイの緯度は+20度であり、黄道付近にある惑星の地上高度は少なくとも南中付近では問題ない。移動天体がどの程度暗いものまで検出できるかは、背後に写る星の密度でほぼ決まる。天の川の中では新衛星の捜索はほとんど不可能であるから、各惑星が天の川から離れているというのが条件となる。2004年までで調べると、冥王星以外はみな数回の衝における観測が可能であることが分った。

References

Colombo, G., and Franklin, F.A. (1971): Icarus **15**, 186-189.
Fuse, T., Nakamura, T. and Kinoshita, H. (1997): Planet. Space Sci. **45**, 1351-1357.
Hamilton, D.P., and Burns, J.A. (1991): Icarus **92**, 118-131.
Nakamura, T. (1997): Proc. of the 29th Sympo. on Cel. Mech., Jan. 28-29 (Tokyo), 274-278 (in Japanese).
Pollack, J.B., Burns, J.A., and Tauber, M.E. (1979): Icarus **37**, 587-611.

Table 3. Limiting satellite sizes for SUBARU survey

Planet	Min. size(dia.)	Attainable size	Ratio
Mars	14km (Deimos)	0.05km	280
Jupiter	10 (Leda)	1.5	7
Saturn	220 (Phoebe)	4	55
Uranus	80 (1997U1)	20	4
Neptune	340 (Nereid)	50	7
Pluto	1170 (Cahron)	70	17

Astrometric Observations Made with the 65cm Refractor

Yoshizumi Hatanaka
National Astronomical Observatory

Abstract

This is a total list of the photographic plates obtained with the 65cm refractor at the National Astronomical Observatory of Japan. Observations consist of astrometric photographs of Saturnian satellites, Uranian satellites, Comet Halley, μDra (double stars), several open clusters and other objects.

The former report gave a collection of Saturnian satellite observations which had been made by the author until the 1996 opposition (Hatanaka,1997). The present list of Saturnian satellites includes the last observation made during the 1997 opposition. These observations have been carried out with the 65cm refractor (plate scale: 20.180 arcsec/mm) at the National Astronomical Observatory of Japan, Mitaka, since the 1966 opposition of Saturn. This program will be stopped because the author is going to retire this year. The plates obtained during the 1970 and 1971 oppositions were measured and reduced by a new method, but the other are not analyzed (Hatanaka,1995).

Photographic plates of Saturnian satellites are collected in the Table 1 which gives Saturn's opposition date (UT), number of observational nights, observation period, serial number of the plate and plate size.

Table 1: Photographic Plates of Saturnian Satellites.

Opposition Date (UT)	Number of Night	Observation Period (UT)	Plate Number	Plate Size (cm)
1966. 9.19	20	1967. 1.13 - 1967. 1.31	1 - 28	8.2x10.7
1967.10. 2	37	1967. 7.20 - 1967.12.30	29 - 176	16.4x21.4
1968.10.15	34	1968. 8.17 - 1969. 1.17	209 - 305	"
1969.10.29	28	1969. 8.23 - 1970. 2. 3	307 - 382	"
1970.11.11	38	1970. 9. 1 - 1971. 2.10	383 - 458	16 x 16
1971.11.25	31	1971. 9.17 - 1972. 2.15	474 - 508	"
1972.12. 9	36	1972.10.13 - 1973. 2.26	509 - 560	"
1973.12.23	43	1973.10.23 - 1974. 2.28	562 - 610	"
1975. 1. 6	40	1974.11.15 - 1975. 3.25	612 - 676	"
1976. 1.20	10	1976. 2. 2 - 1976. 4. 5	677 - 686	"
1977. 2. 2	30	1976.11.24 - 1977. 3.15	687 - 760	"
1978. 2.16	28	1977.12. 6 - 1978. 3. 2	774 - 823	"
1979. 3. 1	26	1978.12.12 - 1979. 4.14	824 - 894	"
1980. 3.14	36	1979.12.17 - 1980. 5.24	906 - 999	"
1981. 3.27	29	1981. 2. 7 - 1981. 5.26	1001 - 1077	"
1982. 4. 9	14	1982. 1.24 - 1982. 5.28	1082 - 1121	"
1983. 4.22	7	1983. 3.14 - 1983. 5. 8	1128 - 1149	"
1984. 5. 3	5	1984. 4. 8 - 1984. 7. 3	1150 - 1171	"
1985. 5.15	8	1985. 5.16 - 1985. 7.26	1174 - 1203	"
1986. 5.27	12	1986. 4. 7 - 1986. 8.11	1363 - 1411	"
1987. 6. 9	10	1987. 5.20 - 1987. 8.21	1438 - 1474	"
1988. 6.20	8	1988. 6. 4 - 1988. 9.13	1478 - 1500	"
1989. 7. 2	18	1989. 4.29 - 1989. 9.13	1501 - 1554	"
1990. 7.14	31	1990. 5.26 - 1990.11.16	1555 - 1631	"
1991. 7.27	11	1991. 8.15 - 1991.10. 3	1633 - 1661	"
1992. 8. 7	22	1992. 7.30 - 1992.11.23	1662 - 1693	"
1993. 8.19	27	1993. 8.24 - 1993.12.25	1694 - 1730	"
1994. 9. 1	14	1994. 9.30 - 1994.12. 4	1734 - 1751	"
1995. 9.14	2	1995.12.11 - 1995.12.14	1756 - 1757	"
1996. 9.26	10	1996.12. 2 - 1997. 1.13	1758 - 1766	"
1997.10.10	24	1997.10.10 - 1997.12.31	1767 - 1790	"

Table 2: Photographic Plates of μDraconis.

Observation Period (UT)	Nights	Plate Number (plate size: 16 x 16 cm)
1979. 5. 2 - 7. 6	4	895 - 905
1980. 5.18 - 7.13	3	992,997,1000
1981. 7. 7 - 7. 8	2	1078 - 1080
1982. 5.24 - 5.25	2	1110,1113,1116
1984. 7. 1 - 7. 3	2	1164 - 1173
1985. 6. 4 - 7.26	4	1182,1191,1192,1200,1204
1986. 6. 9 - 6.12	3	1388,1392,1396
1987. 7.23 - 8.10	3	1461,1462,1469
1988. 8. 8 - 8.13	2	1488 - 1489
1989. 6. 1 - 6.12	4	1510,1513,1517,1521
1990. 8.15 - 8.30	5	1577,1578,1581,1584,1587,1591
1991. 8.15 - 9. 7	5	1632,1635,1641,1648,1655
1992. 8.14 - 8.16	3	1665 - 1667
1994. 9. 9 - 9.10	2	1732 - 1733

Table 3: Photographic Plates of Miscellaneous Objects.

Observation Period (UT)	Nights	Plate Number (plate size: 16 x 16 cm)
Uranian satellites		
1977. 5.11 - 5.27	3	764,766 - 771
Comet Halley		
1985.11. 8 - 1986. 3.7	46	1205 - 1362
M 67		
1976.12.22	1	719
1994.12. 4	1	1752
1995. 1. 2	1	1755
NGC 1647		
1980. 1. 8	1	913,914
1995. 1. 2	1	1753

Double stars μ Draconis have been observed photographically for fifteen years. Table 2 shows observation period, number of observational nights and serial number of the plate.

Table 3 gives photographic plates of miscellaneous objects with observation period and serial number of the plate. In the plates of open clusters, M 67 and NGC 1647 were observed at two epochs. No open cluster without the second epoch are listed in the table.

References

Hatanaka,Y.: Publ.Natl.Astron.Japan vol.4,23-65 (1995).

Hatanaka,Y.: Proceedings of the Twenty-ninth Symposium on "Celestial Mechanics" Held in Tokyo, pp 306-307, 1997.

「水星中間軌道」の有効性

Usefulness of " the Intermediary Orbit" for cleaning up the problem of the excess advance in the longitude of the perihelion of Mercury

井上　猛　(京都産業大学)
T. Inoue
Kyoto Sangyo University

Abstract. With the aid of the idea of an intermediary orbit, we were well able to reveal the true reason for the appearance of the excess secular advance in the longitude of the perihelion of Mercury (Inoue, 1992). In traditional treatments, one includes a portion of planetary perturbations in the elliptic orbit. This technic modifies a fixed elliptic orbit to a moving one. If one takes this circumstances into accout for the theory of motion of Mercury due to Le Verrier, one does not need to add 43″/century for the longitude of the perihelion. This means that his theory was one of perfectly established ones (Inoue, 1994).

1．「水星近日点黄経に於ける余剰の前進運動 $\delta\varpi_{(s)}$」の存在が Le Verrier の研究に端を発して居ると云う事に異を唱える者は居ないであろう。彼が建設した水星の運動理論及び彼が用いた観測データの両方が今日でも通用するものである事は既に立証済みである（井上、1991）。しかしその直後に彼の運動理論の建設過程に『余剰運動 $\delta\varpi_{(s)}$ 発生の秘密が潜んで居る』のが判明したのであった（Inoue, 1992）。

Le Verrier の運動理論は、次の平均要素で与えられる楕円軌道から出発する（1859）。ここで、t は 1850年 1月 1日の正午を起点に年単位で計ったものを表わす。頁を表わす以下の数字は、Ｐａｒｉｓ天文台報第Ｖ巻（１８５９年）のものである。

$$a = 0.387\ 0987 \qquad \text{(p. 23)}$$
$$e = 0.205\ 6105 + 0.'041\ 95t - 0.'000\ 0009t^2 \qquad \text{(p. 21)}$$
$$i = 7°\ 0'\ 8.''16 + 0.''063\ 14t - 0.''000\ 0056t^2 \qquad \text{(p. 20)}$$

$$\Omega = 46°\ 33'\ 3.''25 + 42.''643\ 0\ t + 0.''000\ 0835\ t^2 \qquad \text{(p. 20)}$$
$$\varpi = 75°\ 7'\ 1.''03 + 55.''530\ 8\ t + 0.''000\ 1111\ t^2 \qquad \text{(p. 21)}$$
$$\ell = 327°\ 15'19.''89 + 538\ 1066.''441\ 00t + 0.''000\ 11289t^2 \qquad \text{(p. 21)}$$

これに金星から海王星迄の諸惑星に依る摂動を考慮して、先ずは申し分の無い運動理論が完成する。ところが、水星の場合には極めて高い精度の太陽面通過現象の観測が使える。これを用いて要素改良を試みた結果は、上記の値の殆どが改変されなければならない事になったのであった。 Le Verrier に依る改変量は以下の如し（p. 96）。

$$\delta a = 0$$
$$\delta e = -1.''18$$
$$\delta i = -0.''45$$

$$\delta\Omega = +5.''5$$
$$\delta\varpi = +12.''90 + 0.''383\ t$$
$$\delta\ell = +0.''54 + 0.''103\ 9t$$

以上の諸補正を施す事に依り漸くにして、Le Verrierは水星の運動理論の完成を見る事が出来たのであった（p.107, p.108）。

$$
\begin{aligned}
a &= 0.387\ 0987 \\
e &= 0.205\ 60478 + 0.''041\ 95t - 0.''000\ 0009t^2 \\
i &= 7^\circ\ 0'\ 7.''71 + 0.''063\ 14t - 0.''000\ 0056t^2 \\
\\
\Omega &= 46^\circ\ 33'\ 8.''75 + \quad 42.''643\ 0\ t + 0.''000\ 0835\ t^2 \\
\varpi &= 75^\circ\ \ 7'13.''93 + \quad 55.''913\ 8\ t + 0.''000\ 1111\ t^2 \\
\ell &= 327^\circ\ 15'20.''43 + 538\ 1066.''544\ 9\ t + 0.''000\ 11289t^2
\end{aligned}
$$

しかし、上記 $\delta\varpi$ 中の時間 tに比例する項 $\delta\varpi_{(s)} \equiv 0.''383$/年 の出現は、惑星運動理論に新たな難題を提出する事になった。即ち“Ｎｅｗｔｏｎ力学で説明不可能な余剰の前進量 ： 43 秒角/世紀 ”として広く知られる様になったのは周知の通りである。

２．先ずは、「文字表記約束」の目的で、二体問題の解表式を次の形に書き出して置く。

$$M = u - e \sin u = \ell - \varpi \quad , \tag{1}$$

$$\tan(f/2) = \sqrt{\{(1+e)/(1-e)\}} \cdot \tan(u/2) \ ; \tag{2}$$

$$r = a\,(1 - e \cos u) \quad , \tag{3}$$

$$\phi = \varpi + f \ . \tag{4}$$

ここで、量ａ、ｅ及びϖは、長半径、離心率および近日点黄経を、またM、uおよびｆは平均近点離角、離心近点離角および真近点離角を表わすものとする。ℓは平均黄経を、ｒ及びϕは夫々、動径および真黄経を表わすものとする。

Le Verrierの場合、これらの式群を其の儘に計算するのでは無くして、伝統的な手法に則って平均近点離角 M の正弦・余弦に依る展開表式に訴えるのである（p.22, p.23）。

$$\text{中心差：}\quad f - M = (84\ 376.''212 + 0.''082\ 59t)\sin M + \cdots\cdots \tag{5}$$

$$\text{動　径：}\quad r = 0.395\ 281\ 13 + 0.000\ 000\ 016\ 2t + -(0.078\ 333\ 47 - 0.000\ 000\ 075\ 0t)\cos M + \cdots\cdots \tag{6}$$

中心差の方は、先の離心率の値 0.205 6105 + 0.''041 95tの採用で、上記 sin M の係数 84 376.''211 9 + 0.''082 589t を直ちに導く事が出来るので問題は無い。しかし、動径の方は cos M の係数が 0.078 333 461 - 0.000 000 075 0t となって、末位で１ほど合わない。我々は、これを‘単なるミスとして看過する事はせずして其れなりの理由が必ずや何処かに潜んで居るに違いない’と考えて、其の原因究明に努めて来た。

我々の Le Verrier の研究追試の動機は、どちらかと言えば‘不純なもの’であった。卓抜した洞察力と抜群の計算力が“あの海王星発見の快挙を成し遂げさせた”と云うのは万人の認める処である。これは、言ってみれば太陽系の最遠側に‘惑星を創った’と云う事である。そうした時に、大いなる野心家が次に考える事は‘太陽系の最近側に惑星を創る事’である。水星の運動に不等性を残存させ、それが未知の惑星に起因するものであるとして‘発見’を促せば、その野望が満たされる様な事が起らないとも限らないではないか？「余りにも穿ち過ぎ」等と言う勿れ。此の人物、自分が発見に導いた‘あの海王星を一度も望遠鏡で覗こうとはしなかった’と云うではないか（Flammarion, 1880）！‘益々以て怪しい’と思ったとしても、強ち見当外れでは無いであろう。しかし、この様な‘偏見’も、虚心にＰａｒｉｓ天文台報を見て行くうちに、‘手の内の総てを見せる’と云うオープンな研究態度に気付くに及び、彼に対する見方も大きく変って行ったのであった。

水星の真黄経 ϕ 及び動径 r に対する他の惑星に依る多種多様な摂動の中には、先の展開表式 (5)、(6) に於けるのと同じ sin M、cos M に比例する項が存在して居る。Le Verrierは、金星、地球および木星に依るものが特に大であるとして、以下の様に掲げて居る (p.13, p.14, p.15) 。

惑　星	真黄経に於ける摂動　$\delta\phi$		動径に於ける摂動　δ r	
	sin ℓ の係数	cos ℓ の係数	sin ℓ の係数	cos ℓ の係数
金　星	+0.″017	−0.″063	−0.″011	−0.″003
地　球	+0.″005	−0.″017	* * *	* * *
木　星	+0.″008	−0.″031	* * *	* * *

ここで $\ell = \varpi + M$ であるから、$\varpi = 75°\ 7'1.''03$ を考慮する時は、上記の表を次の形に書き換える事が出来る。

惑　星	真黄経に於ける摂動　$\delta\phi$		動径に於ける摂動　δ r	
	sin M の係数	cos M の係数	sin M の係数	cos M の係数
金　星	+0.′065 2528	+0.′000 2483	+0.′000 0740	-0.′011 4015
地　球	+0.′017 7139	+0.′000 4658	* * *	* * *
木　星	+0.′032 0147	-0.′000 2306	* * *	* * *
総　和	+0.′114 9815	+0.′000 4835	+0.′000 0740	-0.′011 4015

Newcomb は、此の種の摂動は二体問題の解の展開表式と分離困難であるとして、上記の量を、初発の軌道要素の中に吸収させる事を考えた。真黄経に於ける、金星、地球および木星に依るものの総和 +0.′114 9815 を sin M の主要係数 2e の修正分 2 Δe に等しいと置いて、$\Delta e = 0.'058$ を初発の離心率に加え、同じく総和 +0.′000 4835 を cos M の係数に於ける修正分 $-2e\Delta\varpi$ と等置して $\Delta\varpi = 0.'0$ として居る (Clemence, 1943) 。

同じ様な事は、既に、Le Verrierに依っても為されて居るのである。彼は、金星に依るものだけを水星の軌道要素の中に吸収させようとし、地球および木星に依る摂動はその儘の形で残して置いたのである。この時、金星に依るものの取り込み方に問題があったのである。金星の場合には、真黄経のみならず動径の方にも摂動がある。これを、次の等式を要求する事に依って、相殺させる様にしたのである (p.16) 。

(7)　　$+ 2\,\Delta e_M + 0.'065\ 2528 = 0$　　($\delta\phi$に於ける sin M の係数から)

(8)　　$-a\,\Delta e_r - 0.'011\ 4015 = 0$　　(δ r に於ける cos M の係数から)

単一で有るべき離心率に対する修正が、二様に為されなければならない事になって来た。

(9)　　$\Delta e_M = -\ 0.'032\ 6264$

(10)　　$\Delta e_r = -\ 0.'029\ 4537$

両者の差は僅少であるが 0.′003 の大きさは、 Le Verrier の理論構築の精度からすれば無視するのは許されない事である (p.12) 。

3．Le Verrierの研究結果を追試し批判して行く過程で『二個の離心率を持った軌道』のアイディアに到達したのであった。そうした時に、次の二つの表式に出逢ったのであった（Brumberg, 1991）。表記の一部は、我々流に書き換える。

$$\delta\varpi_{(s)} = 2\pi m\,(2\gamma + 2 - \beta)\,/\{a(1-e^2)\} \qquad (3.1.66)$$

$$u - \{e + (-2\gamma - 2 + \alpha)\,(m/a)\,e\}\sin u = M \qquad (3.1.68)$$

ここで、量α、β、γは定数であるが、一般相対論では、何れもが１に等しい値を取る。従って、$\delta\varpi_{(s)}$は、一公転当り $2\pi\times 3m/\{a(1-e^2)\}$ の前進量を有する事になる。この時に、‘Ｋｅｐｌｅｒ方程式’の方は、$(1-3m/a)e$ なる離心率を有する事になって居るのである。此の相互関連が、我々に、その後の大きな進展を齎らす事になったのである。

我々は（9)、(10）の両式が示唆する処から、上の形の‘Ｋｅｐｌｅｒ方程式’の存在に気付いては居た。しかし、“金星に依る純粋な周期摂動が、斯かる永年摂動を生み出すとは、とても考えられない”として、其処で頓挫して居たのであった。上の二つの表式はそうした皮相な見方を払拭して呉れた。そうして、勢いを得た後は迷う事なく、次の形の『中間軌道』の導入を図ったのであった（Inoue, 1992）。

(11) $$M^* = u^* - e_M \sin u^* = \ell - \varpi^* \ ,$$

(12) $$\tan(f^*/2) = \sqrt{\{(1+e_M)/(1-e_M)\}}\cdot\tan(u^*/2)\ ;$$

(13) $$r = a^*(1 - e_r\cos u^*)\ ,$$

(14) $$\phi = \varpi^* + f^*\ ;$$

(15) $$e_r \equiv e_M + \Delta e\ ,$$

(16) $$\Delta e \equiv \Delta e_r - \Delta e_M = +1.53\ 8156\times 10^{-8}\ .$$

ここで、量a^*、e_M及び ϖ^*は、長半径、離心率及び近日点黄経に類似の量を、また M^* u^*、f^*は平均近点離角、離心近点離角、真近点離角に類似の量を表わすものとする。この時、ℓが平均黄経を、r及びϕが夫々、動径および真黄経を表わす事には変りはない。

此の『中間軌道』に依って、先の表式（5)、（6）の再現が可能か否かを試みてみる。中心差の方は、離心率 $e=0.205\ 6105 + 0.000\ 000\ 203\ 379t$ で捉える事が出来て居るので、e_M は 0.205 6105 の値を取るものとして、展開表式に代入してみる。

(17) $$\begin{aligned} f^*-M^* = &\{(2e_M - e_M^3/4 + 5e_M^5/96 + 107e_M^7/4608 + \cdots) + \\ &+ (2 - 3e_M^2/4 + 25e_M^4/96 + \\ &+ 749e_M^6/4608 + \cdots)\times 0.''041\ 95t\}\sin M^* + \cdots = \\ &= (84\ 376.''211\ 9 + 0.''082\ 589t)\sin M^* + \cdots \end{aligned}$$

(18) $$\begin{aligned} r = &\ a^*\{(1 + e_r e_M/2) + e_M\times 0.000\ 000\ 203\ 379t\} + \\ &+ a^*\{-e_r(1 - 3e_M^2/8 + 5e_M^4/192 + 7e_M^6/9216 + \cdots) + \\ &- (1 - 9e_M^2/8 + 25e_M^4/192 + \\ &- 49e_M^6/9216 + \cdots)\times 0.000\ 000\ 203\ 379t\}\cos M^* + \cdots = \\ = &\ 0.395\ 281\ 130 + 0.000\ 000\ 016\ 18t + \\ &-(0.078\ 333\ 467 - 0.000\ 000\ 075\ 00t)\cos M^* + \cdots \end{aligned}$$

結果は、我々の把捉の適切なる事を如実に物語るものとなって居る。

4．只今の『中間軌道』が、‘固定した’楕円軌道と如何なる関係に在るかは明らかにされるべき事である。此の系は、次の形のエネルギー積分を有する（Inoue, 1994)。

(19) $$-\mu/(2a^*) = \{\dot{r}^2 + (r\dot{\phi})^2\}/2 - \{\mu/r + \epsilon R\} ,$$

(20) $$\epsilon R \equiv (\mu/p_M)(\Delta e/e_M)\{-\eta_M^4 + 3\eta_M^2\xi_M - \xi_M^2 - \xi_M^3\}/\eta_M^2 ;$$

(21) $$(\mu \equiv G(m_{太陽}+m_{水星}),\ \eta_M \equiv \sqrt{(1-e_M^2)},\ p_M \equiv a^*\eta_M^2,\ \xi_M \equiv p_M/r) .$$

我々の『中間軌道』は、どの様な運動方程式系の解となって居るのであろう？　これを知る目的で、次の形の Lagrange 函数を導入し Lagrange の運動方程式を書いてみる。

(22) $$L^* = \{\dot{r}^{*2} + (r^*\dot{\phi}^*)^2\}/2 + \mu/r^* + \epsilon R^{*s} ,$$

(23) $$\epsilon R^{*s} \equiv \epsilon R^{*s}(r^*, \phi^*; \dot{r}^*, \dot{\phi}^*) =$$

$$= (\mu\Delta e/e_M)\{-1/a^* + 3/r^* - a^*/r^{*2} - (a^* p_M)/r^{*3}\} .$$

(24) $$d(\partial L^*/\partial \dot{r}^*)/dt - \partial L^*/\partial r^* = 0 ,$$

(25) $$d(\partial L^*/\partial \dot{\phi}^*)/dt - \partial L^*/\partial \phi^* = 0 .$$

この系に変数変換を施して、新しい変数（$r^*, \phi^*; p_r^*, p_\phi^*$)から成る Hamilton 系に移る事を考える。

(26) $$p_r^* \equiv \partial L^*/\partial \dot{r}^* = \dot{r}^* + \partial \epsilon R^{*s}/\partial \dot{r}^* ,$$

(27) $$p_\phi^* \equiv \partial L^*/\partial \dot{\phi}^* = r^{*2}\dot{\phi}^* + \partial \epsilon R^{*s}/\partial \dot{\phi}^* ;$$

(28) $$H^* = \{p_r^{*2} + (p_\phi^*/r^*)^2\}/2 - \{\mu/r^* + \epsilon R^*\} + O(\epsilon^2) ,$$

(29) $$\epsilon R^* = \epsilon R^*(r^*, \phi^*; p_r^*, p_\phi^*) =$$

$$= \epsilon R^{*s}(r^*, \phi^*; \dot{r}^*, \dot{\phi}^*) .$$

ここで、只今の系を、我々の『水星中間軌道』の系に結び付ける事を考える。

(30) $$r^* = r,\ \phi^* = \phi\ ;\ p_r^* = \dot{r}\ ,\ p_\phi^* = r^2\dot{\phi}\ ;$$

これらに依って、上の Hamilton 函数 (28) 式を書いてみる。

(31) $$H^* = \{\dot{r}^2 + (r\dot{\phi})^2\}/2 - \{\mu/r + \epsilon R^*\} + O(\epsilon^2) ,$$

(32) $$\epsilon R^* = \epsilon R^*(r, \phi; \dot{r}, r^2\dot{\phi}) =$$

$$= (\mu\Delta e/e_M)\{-1/a^* + 3/r - a^*/r^2 - (a^* p_M)/r^3\} .$$

これは、我々の『水星中間軌道』のエネルギー積分 (19)、(20) 式に外ならない。以上に依って『水星中間軌道』の系と Hamilton の系との差が、$(\Delta e)^2 \fallingdotseq 2.3\times10^{-16}$ の大きさでしか無いのが判明した。それ故に Hamilton 系に立脚して議論を進めて行きさえすればそれで、『中間軌道』に関する情報が得られる様になっている訳である。

方針が明らかになったので、先ず Hamilton 函数に関する運動方程式を書く。この時に差の$O(\epsilon^2)$の項を無視するのは勿論の事である。

(33) $$H^* = \{p_r^{*2} + (p_\phi^*/r^*)^2\}/2 - \{\mu/r^* + \epsilon R^*\}\ ;$$

(34) $$dr^*/dt=\partial H^*/\partial p_r^*= \quad p_r^* \quad -\partial \epsilon R^*/\partial p_r^* \quad ,$$

(35) $$d\phi^*/dt=\partial H^*/\partial p_\phi^*=p_\phi^*/r^{*2}-\partial \epsilon R^*/\partial p_\phi^* \quad ;$$

(36) $$dp_r^*/dt=-\partial H^*/\partial r^*=p_\phi^{*2}/r^{*3}-\mu/r^{*2}+$$
$$-\partial \epsilon R^*/\partial r^* \quad ,$$

(37) $$dp_\phi^*/dt=-\partial H^*/\partial \phi^*= 0 \quad + \partial \epsilon R^*/\partial \phi^* \quad .$$

此の系を、所謂“定数変化の方法”で解く事を考える。この事に付いては、既に詳細に亘って議論して来た処である（井上、1995）。其処で、『人工系』と呼んだ補助的な微分方程式系を構成する必要がある。‘新しい変数’と‘変換式’とを見い出す為にである。我々は、次の文字表記で与えられる系を考える。これは「二体問題の系」に外ならない。

(38) $$dr^*/dt= \quad p_r^* \quad ,$$

(39) $$d\phi^*/dt=p_\phi^*/r^{*2} \quad ;$$

(40) $$dp_r^*/dt=p_\phi^{*2}/r^{*3}-\mu/r^{*2} \quad ,$$

(41) $$dp_\phi^*/dt= 0 \quad .$$

此の系を満たす積分定数を、a、e、ϖ及びℓ_0とすれば、標準的な「二体問題の系の解表現」が得られる事になる。これらの積分定数を一纏めにして‘c’と表記して、次の形に解表式を表わす事にする。

(42) $$r^* = \Phi_r(c\ ;\ t) \quad ,$$

(43) $$\phi^* = \Phi_\phi(c\ ;\ t) \quad ;$$

(44) $$p_r^* = \Psi_r(c\ ;\ t) \quad ,$$

(45) $$p_\phi^* = \Psi_\phi(c\ ;\ t) \quad .$$

ここで、定数（要素）‘c’を、新変数‘ζ’であるとして、これら‘ζ’に関する微分方程式を書いたならば、それが外ならぬ「楕円要素」に対する『要素変化の式』となる訳である。具体的に書いてみれば以下の如し。ここでは、脚符の‘$_M$’は省略する事にした。

(46) $$d\zeta_k/dt=\sum_{j=1}^{4}\{\zeta_j,\zeta_k\}\partial \epsilon R/\partial \zeta_j \quad , \quad (k=1,2,3,4) \quad ;$$

(47) $$\epsilon R=\epsilon R(\zeta\ ;\ t)=\epsilon R^*(r^*,\phi^*;p_r^*,p_\phi^*)=$$
$$=(\mu\Delta e/e)\{-1/a+3/r-a/r^2-(ap)/r^3\} \quad .$$

ここで、記号$\{\zeta_j,\zeta_k\}$，$(j,k=1,2,3,4)$は、Ｐｏｉｓｓｏｎの括弧を表わす。特に興味があるのは、近日点黄経 ϖ に於ける永年変化である。そこで、上の摂動函数 ϵR の永年部 $\epsilon R_{(s)}=(\mu\Delta e/e)(2/a)(1-1/\eta)$ で考える事にする。量 n は平均運動を表わすものとする。 $(n\equiv\sqrt{(\mu/a^3)})$。

(48) $$d\varpi_{(s)}/dt=\{\eta/(n\,a^2e)\}\partial \epsilon R_{(s)}/\partial e=$$
$$=-(\Delta e/e)\{2/(1+\eta)\}\{1/\eta+(e/\eta)^2\}n \quad .$$

数値を代入すれば、既に求めた事のある次の量が得られる（Inoue, 1992）。

(49)　　$\delta\varpi_{(s)} = -43.374\ 896$ 秒角/世紀　.

これに依り、『水星中間軌道』が固定した「楕円軌道」に対して、１世紀当り４３秒角の割合で“後退”して居るのが再確認された訳である。此の事実に気付く事なしに、水星の太陽面通過現象の予報を行なったのであるから“４３秒角足りない”となった訳である。此の事は、上の $\delta\varpi_{(s)}$ を初めとする Δe に依る影響を、Le Verrier が彼の運動理論の中に正しく取り込んで居さえすれば、太陽面通過の現象も余す処なく完璧に予報する事が出来たに違いない事を意味して居る。つまり、水星の運動に、問題とすべきものは何一つ存在などしては居なかったと云う訳である。

５．以上で、我々の関心事の「水星近日点黄経に於ける余剰の前進運動の問題」に対する調べは、総て終った事になる。これ迄に報告して来たものの中に‘甘い認識’に基づいた議論が少なからず散見するので、これを機会に、それらを糺して置きたいと思う。

第２５回天体力学研究会集録（1992）p.208

(23)　　$\tan(f/2) = \sqrt{\{(1+e_r)/(1-e_r)\}} \cdot \tan(u/2)$

☆これは、e_r では無くして、e_M でなければならないのであった。

第２６回天体力学研究会集録（1994）p.166, p.167

☆ Lagrange 函数を見付ける為に以下の式群を考えなければならないとして、近似の解表式を求めたりして居る。今回の扱いに依って知れる様に、これらが無意味であったとは言わない迄も、無駄な事ではあった。

(32)　　$L \equiv \{\dot r^2 + (r\dot\phi)^2\}/2 + \mu/r + \epsilon V(r,\phi;\dot r,\dot\phi;t)$;
(33)　　$H = \{\dot r^2 + (r\dot\phi)^2\}/2 - \{\mu/r + \epsilon R\}$,
(35)　　$\epsilon R = \epsilon V - (\partial\epsilon V/\partial\dot r)\cdot\dot r - (\partial\epsilon V/\partial\dot\phi)\cdot\dot\phi\}$.

第２８回天体力学研究会集録（1996）p.108, p.109

(17)　　$d\dot r/dt - r\dot\phi^2 = -\mu/r^2 + \mathcal{R}_0$,
(18)　　$d(r^2\dot\phi)/(r\,dt) = \mathcal{T}_0$;
(19)　　$\mathcal{R}_0 \equiv (\Delta e/e)(\mu/r^2)\{-3 + 2a/r + a^2\eta^2/r^2\}$,
(20)　　$\mathcal{T}_0 \equiv (\Delta e/e)(\mu/r^2)\{2a/r\}\ e\ \sin f$.

☆《$\mathcal{R}_0$ と $\mathcal{T}_0$ の双方を零に等しいと置けば、微分方程式系は二体問題のそれに帰着し要素 ϖ に対する変化を通常の要素変化の式を適用して計算出来る》等として、次の変化の表式を与えて居る。

(23)　　$\delta\varpi = (\Delta e/e)(1/e^2\eta^2)\{3\eta^2 - 2\xi - \xi^2\}\ e\ \sin f$.

☆上に出て来て居る $r, \phi; \dot r, \dot\phi$ は、総てが『中間軌道』を記述する量なのである。従って、文字記号は (11)～(16) 式のものでなければならず、ϖ^* と ϖ とは別物で上の (23) 式も、次の様に表記されるべき処であった。それ故に $\delta\varpi_{(s)}$ が (48)式で与えられるものである時に、$\delta\varpi^*_{(s)}$ が０であっても、一向に構わないのである。

$$\delta\varpi^* = (\Delta e/e_M)(1/e_M^2\eta_M^2)\{3\eta_M^2 - 2\xi_M - \xi_M^2\}\ e_M\ \sin f^* .$$

第２９回天体力学研究会集録（1997） p.12, p.14

$$(f-M)^{*}\equiv\{\ 2\ \Delta e_{M}+(\ 2e-e^{3}/4+5e^{5}/96+\cdots\cdots)\}\ \sin\ M\ +\cdots\cdots \quad (34)$$

$$r^{*}\ \equiv\ a(1+e^{2}/2)\ +\ +a\{-\Delta e_{r}+(-e+3e^{3}/8+\cdots\cdots)\}\ \cos\ M\ +\cdots\cdots \quad (35)$$

☆上記の形で《金星に依る周期摂動項の影響を取り込むべきである》と述べて居るがこれは適切な謂ではなかった。これらの表式では、 Le Verrier が与えた（ 5）及び（ 6）式に依る数値表現は得られない。此の事からも、『中間軌道』の有用性が出て来る事になる。
☆此処でも《εＲを０と置けば、二体問題の系のに相当するエネルギー積分が得られる》等と言って居る。これが不適切なるは、今更、繰り返す迄も無い事である。

参考文献

1. Brumberg, V.A. : 1991, *Essential Relativistic Celestial Mechanics*, 85.
2. Clemence, G.M. : 1943, *Astronomical Papers of the American Ephemeris*, 38.
3. Flammarion, C. : 1880, *Astronomie Populaire*, 584.
4. 井上 猛 : 1991, 第２４回天体力学研究会集録 148.
5. Inoue, T. : 1992, *Proceedings of the Twenty-Fifth Symposium on Celestial Mechanics*, 205.
6. Inoue, T. : 1994, *Proceedings of the Twenty-Sixth Symposium on Celestial Mechanics*, 164.
7. 井上 猛 : 1995, 第２７回天体力学研究会集録 155.
8. 井上 猛 : 1996, 第２８回天体力学研究会集録 107.
9. Inoue, T. : 1997, *Proceedings of the Twenty-Ninth Symposium on Celestial Mechanics*, 6.
10. Le Verrier, U.J. : 1859, *Annales de l'Observatoire Impérial de Paris*, V.

(98329D)

潮汐力による地殻の水平変動について

On the Horizontal Movement of the Earth's Crusts due to Tidal Generating Forces.

河合雅司（富山商船高等専門学校）
Masashi KAWAI(Toyama National College of Maritime Technology)

Abstract

It was tried to verify horizontal movement of the earth's crusts by orbital analysis of Communication Satellite-3b(CS-3b) which is geosynchronous satellite. CS-3b data ovserved at Kimitsu Satellite Control Center on June and July 1993 and on June 1994 was used in the orbital analysis. The results of the orbital analysis are as follows.

(1) It was confirmed that periodic fluctuations of 12-hour period appears in post-fit range residuals not only when tidal generating forces are large but also when tidal generating forces are small.

(2) The phase lag of the periodic fluctuations in post-fit range residuals to the phase of tidal generating forces is about 30° to 45°.

(3) It is estimated that the amplitude of the periodic earth's crusts movement is about 1 to 2 meters.

It is considered that there are currents in the inside of the earth corresponding to ocean currents and tidal currents in ocean, and the earth's crusts move horizontally with these currents which are generated due to tidal generating forces.

1．緒言

潮汐力による地殻の水平変動について，1993年 6月， 7月及び1994年 6月に君津衛星管制センターで観測された通信衛星（CS-3b）の48時間アークの測距，測角データを解析することにより調べた。

その結果，大潮（地球，月，太陽がほぼ一直線上に存在する場合）の場合のみならず，小潮の場合も含めて全てのデータについて，48時間アークのデータによる軌道決定後の観測距離と計算距離の残差に12時間周期の変動を確認することが出来た。

それらの結果について以下に報告する。

2．衛星力学モデル[1]

(1)地球万有引力による加速度

地心引力定数 （$GM=3986004.4\times10^{8}$ [m^3/s^2]）

(2)地球重力乱れポテンシャルによる加速度

重力モデルGEM-10B[2]（次数は４次）を用いた。又，重力ポテンシャル係数C_{21}，S_{21}は真の地球固定座標系における地球形状軸の位置を表す係数であり，本研究では真の地球固定座標系としてITRF(IERS Terrestrial Reference Frame)を用いているので正規化されたC_{21}，S_{21}の係数はIERS Standards[3]に基づいて，次の値を用いた。

$$\bar{C}_{21}=-0.17\times10^{-9} \qquad \bar{S}_{21}=1.19\times10^{-9}$$

(3) 月，太陽，惑星の引力による加速度

月，太陽，水星，金星，火星，木星，土星の引力を考慮
天体暦：DE200/LE200 JPL エフェメリス[4]

(4)太陽輻射圧による加速度
地球・月による食モデルを考慮した。

(5)地球潮汐による加速度
ラブモデル[5]を使用（ラブ定数は0.25，月，太陽にかんするLag Angleは2.5°）

(6)一般相対性理論による加速度

(7)未知の力による加速度
衛星がスピンすることにより生じる慣性座標系における衛星速度ベクトル方向の加速度（速度ベクトルの方向が正，その逆方向が負）

3．補正
3．1　電波伝搬補正
(1)距離データの補正
電離層における補正（土屋モデル）[6]
対流圏における補正モデル（GSFC NONAME 式）[7]

(2)角度データの補正
補正は全く行わなかった。

3．2　地球潮汐による観測局位置の変動
地球潮汐による観測局位置の変動については、IERS Standards(1992)に紹介されているWahrの理論によるモデル（2次の潮汐まで考慮）を用いて補正を行った。

4．解析データ
君津衛星管制センターで1993年 6月， 7月及び1994年 7月に観測された通信衛星(CS-3b)のデータを用いた。それらのデータをTable 1.に示す。距離データの精度約0.4m，角度データの精度は約 2/1000°（距離換算で約1000m）である。

Table 1.　CS-3b Data Observed at Kimitsu

Data	Data-Span (JST)
Cb1	1993.06.05.08^{H}～1993.06.07.07^{H}
Cb2	1993.06.12.08^{H}～1993.06.14.07^{H}
Cb3	1993.06.19.08^{H}～1993.06.21.07^{H}
Cb4	1993.06.26.08^{H}～1993.06.28.07^{H}
Cb5	1993.07.03.08^{H}～1993.07.05.07^{H}
Cb6	1993.07.10.08^{H}～1993.07.12.07^{H}
Cb7	1993.07.17.08^{H}～1993.07.19.07^{H}
Cb8	1994.06.04.08^{H}～1994.06.06.07^{H}
Cb9	1994.06.11.08^{H}～1994.06.13.07^{H}
Cb10	1994.06.18.08^{H}～1994.06.20.07^{H}
Cb11	1994.06.25.08^{H}～1994.06.27.07^{H}

[One Data(One Arc) : 48hours]

以上11個の48時間データを用いて通信衛星（CS-3b）の軌道解析を行い，軌道決定後の観測距離と計算距離の残差を求めた。これらの各48時間データの中間時刻における月と太陽の赤経，赤緯及び地球における月と太陽のなす角θをTable 2.に示し，観測局（君津衛星管制センター）に月が正中する時刻（日本標準時）をTable 3.に示す。又，Table 4.は通信衛星(CS-3b)の測距データと測角データを観測したアンテナの位置である。

Table 2. Right ascensions and declinations of the sun and the moon.
λ is right ascensions [DEG] and d is declinations [DEG].
θ is the angle between the sun and the moon at the earth.

Data	Date(JST)	λ_{MOON} , d_{MOON}	λ_{SUN} , d_{SUN}	θ
Cb1	1993. 6. 6. 8^H	273.4°,-21.5°	74.1°, 22.6°	162°
Cb2	1993. 6.13. 8^H	358.0°, 4.6°	81.4°, 23.2°	82°
Cb3	1993. 6.20. 8^H	87.0°, 22.1°	88.6°, 23.4°	2°
Cb4	1993. 6.27. 8^H	183.2°, -6.6°	95.9°, 23.3°	90°
Cb5	1993. 7. 4. 8^H	282.5°,-20.4°	103.1°, 22.9°	177°
Cb6	1993. 7.11. 8^H	5.4°, 7.4°	110.3°, 22.1°	101°
Cb7	1993. 7.18. 8^H	96.1°, 21.2°	117.4°, 21.1°	20°
Cb8	1994. 6. 5. 8^H	23.2°, 12.4°	72.8°, 22.5°	48°
Cb9	1994. 6.12. 8^H	111.7°, 17.5°	80.1°, 23.1°	30°
Cb10	1994. 6.19. 8^H	202.9°,-12.2°	87.3°, 23.4°	118°
Cb11	1994. 6.26. 8^H	308.0°,-13.8°	94.6°, 23.4°	147°

Table 3. The time of transit of the moon across the Kimitsu meridian.

Data	Meridian transit of the moon (JST)
Cb1	1993. 6. 6. 1^H , 1993. 6. 7. 2^H
Cb2	1993. 6.13. 6^H , 1993. 6.14. 7^H
Cb3	1993. 6.19.11^H , 1993. 6.20.12^H
Cb4	1993. 6.26.17^H , 1993. 6.27.18^H
Cb5	1993. 7. 3.23^H , 1993. 7. 5. 0^H
Cb6	1993. 7.11. 5^H , 1993. 7.12. 5^H
Cb7	1993. 7.17.10^H , 1993. 7.18.11^H
Cb8	1994. 6. 4. 8^H , 1994. 6. 5. 8^H
Cb9	1994. 6.11.13^H , 1994. 6.12.14^H
Cb10	1994. 6.18.19^H , 1994. 6.19.20^H
Cb11	1994. 6.26. 2^H , 1994. 6.27. 3^H

Table 4. The locations of tracking stations.
TSCJ-C2 is station for observing range of CS-3b at Kimitu.
TSCJ-ANG is station for observing angle of CS-3b at Kimitu.

Station	Coordinate	Latitude	Longitude	Height
TSCJ-C2	GEM-10B	35°11'35.795"N	140°04'29.486"E	189.742m
TSCJ-ANG	GEM-10B	35°11'36.822"N	140°04'31.221"E	200.836m

Table 5.は観測局の位置の水平変動が各衛星の測距データに与える影響を表にしたものであり，$\cos\beta$は観測局が方位135°の方向に 1m移動した場合の測距データの変化量をしめしている。例えばCS-3bの場合$\cos\beta$=0.4であるから観測局が135°方向に1m移動すると測距データが約0.4m減少することが分かる。

Table 5. Effect of horizontal movement of station to satellite range data.
ELE : Elevation of satellite AZI : Azimuth of satellite
β : Angle of intersection between vector from station to satellite and vector directed to 135°.

Satellite	Station	Longitude	ELE	AZI	β	$\cos\beta$
CS-3a	TSCJ-C1	132°E	48.255°	193.840°	69.848°	0.345
CS-3b	TSCJ-C2	136°E	48.925°	187.052°	66.168°	0.404
BS-3a	TSCJ-K1	110°E	38.198°	225.163°	90.128°	-0.002
ETS-V	KTDS	150°E	47.849°	163.472°	53.848°	0.590
ETS-V	MTDS	150°E	48.824°	145.892°	49.721°	0.647
ETS-V	OTDS	150°E	50.514°	137.674°	50.565°	0.635

距離データの重みを1，角度データを距離に換算した量の重みを0.0001として重み付き最小自乗法によりパラメタを推定した。同時に推定されたパラメータは次の通りである。

(1) 衛星6軌道要素(X, Y, Z, V_X, V_Y, V_Z)
(2) 太陽輻射圧における反射係数
(3) 慣性座標系における衛星速度ベクトル方向の加速度
（速度ベクトルの方向が正，その逆方向が負）
(4) 定誤差
角度データ（高度，方位角）の定誤差

5．解析結果

Table 6. RMS of post-fit range residuals

Data	Cb1	Cb2	Cb3	Cb4	Cb5	Cb6	Cb7	Cb8	Cb9	Cb10	Cb11
RMS[m]	0.9	0.7	0.9	0.9	0.9	0.5	0.8	0.9	0.9	0.8	1.4

データCb1～Cb11の軌道決定後の O-Cの 1時間毎の平均値を図1～図11に示す。図中の縦線は観測局（君津衛星管制センター）に月が正中した時刻を示している。図1～図4は月，地球，太陽がほぼ一直線上にあり潮汐力が大（大潮）の時のものであり，図5～図8は潮汐力が中の時のものであり，図9～図11は潮汐力が小（小潮）の時のものである。図9及び図10には一見12時間周期の変動が存在しない様に思われるがよく見ると大きな変動の上に12時間周期の変動が重なっているのが確認できる。

潮汐力による日本周辺の地殻の水平変動の方向は北西～南東方向と仮定した場合，これらの図から潮汐力に対する O-Cの周期変動の位相遅れは，大潮及び小潮の場合ともに 2時間～ 3時間（30°～45°）程度であることが分かる。振幅については，12時間周期の地殻の水平変動をモデル化して推定する必要があるが，ここではモデル化による推定は行わず O-Cの周期変動の振幅を 0.4で割ることによりおおざっぱな推定を行ったところ大潮の場合で2m程度，小潮の場合で1m程度であることが確認出来た。

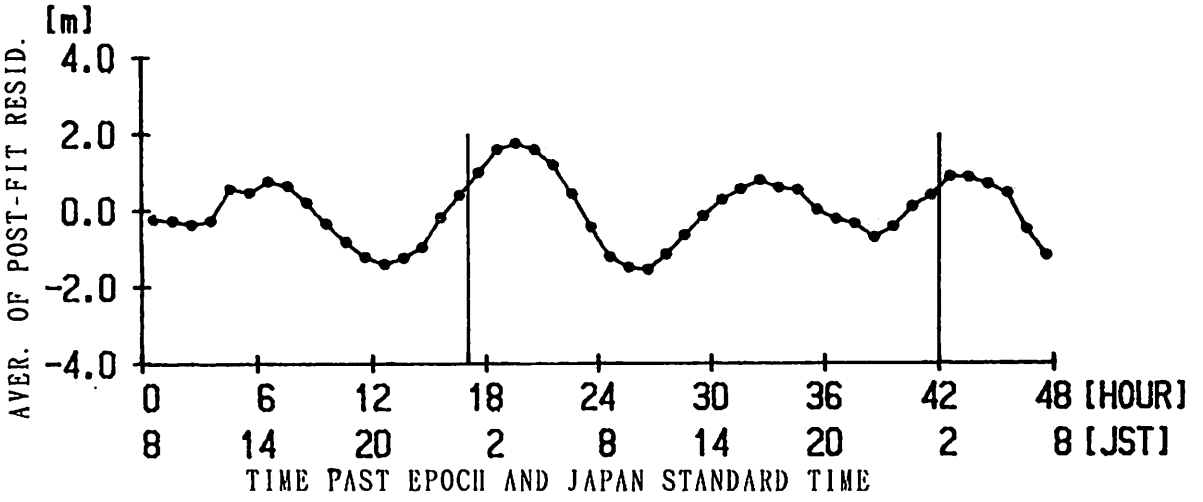

Fig. 1 The averages of post-fit residuals of range data Cb1 for every hour. Vertical line shows time of transit of the moon across the station meridian. (RMS=0.9m, θ =162°)

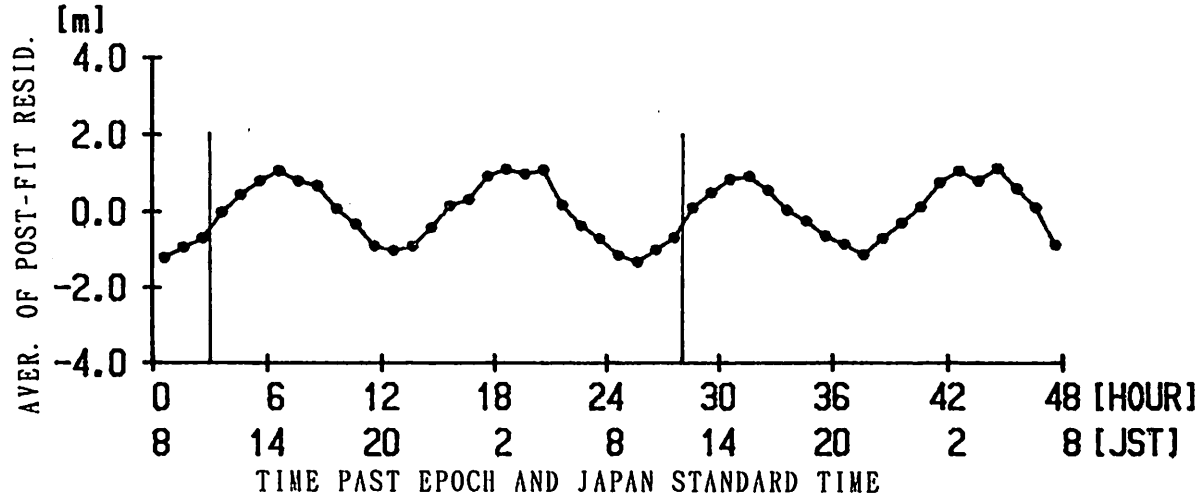

Fig. 2 The averages of post-fit residuals of range data Cb3 for every hour. Vertical line shows time of transit of the moon across the station meridian. (RMS=0.9m, θ = 2°)

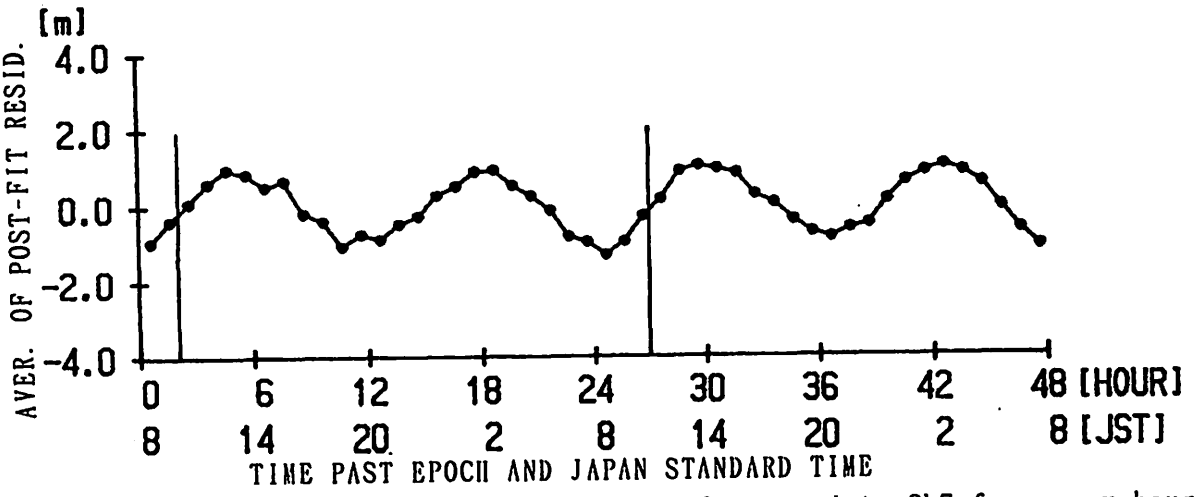

Fig. 3 The averages of post-fit residuals of range data Cb7 for every hour. Vertical line shows time of transit of the moon across the station meridian. (RMS=0.8m, θ = 20°)

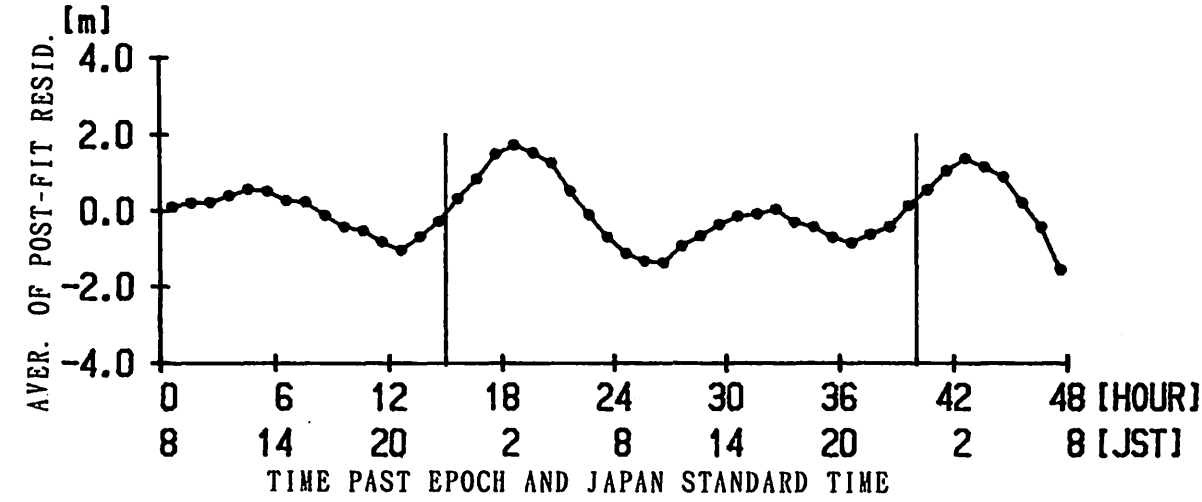

Fig. 4 The averages of post-fit residuals of range data Cb5 for every hour. Vertical line shows time of transit of the moon across the station meridian. (RMS=0.9m, θ =177°)

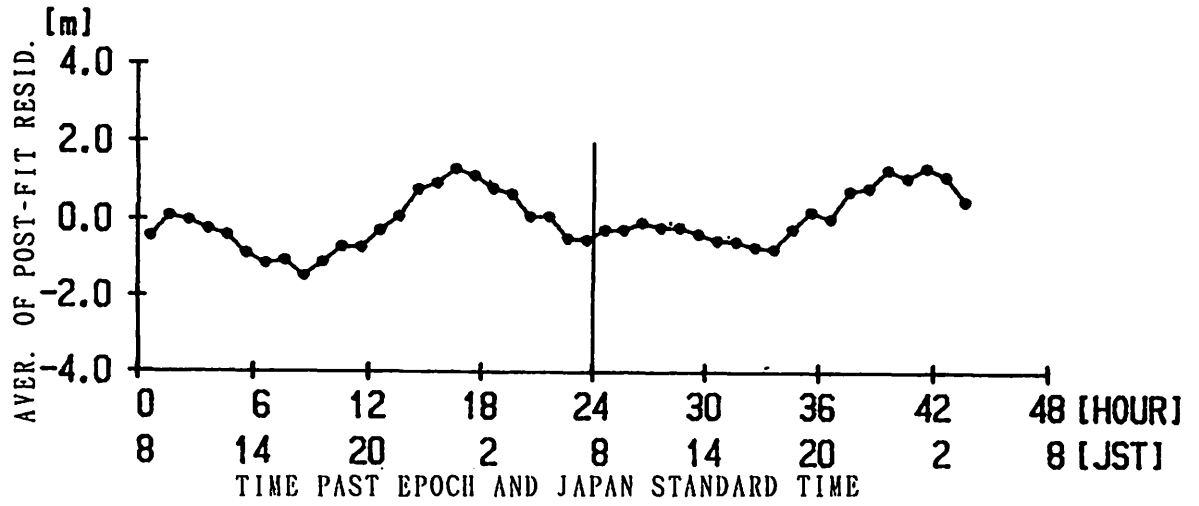

Fig. 5 The averages of post-fit residuals of range data Cb8 for every hour. Vertical line shows time of transit of the moon across the station meridian. (RMS=0.9m, θ = 48°)

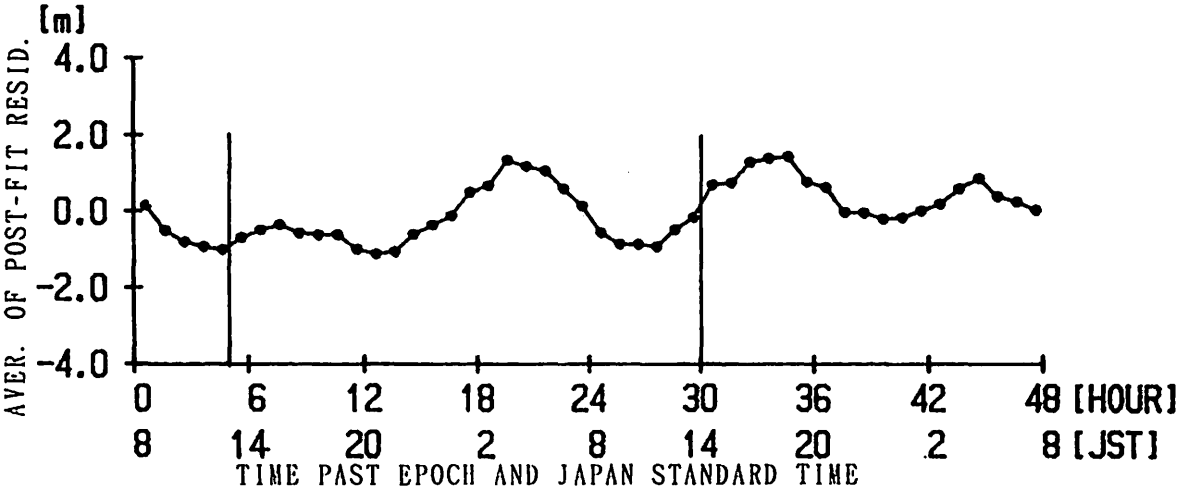

Fig. 6 The averages of post-fit residuals of range data Cb9 for every hour. Vertical line shows time of transit of the moon across the station meridian. (RMS=0.9m, θ = 30°)

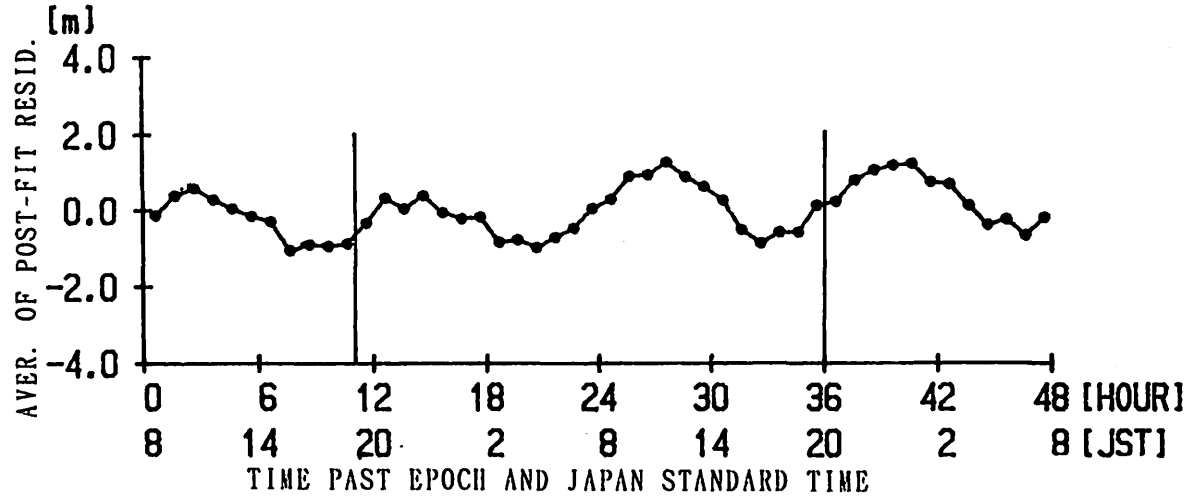

Fig. 7 The averages of post-fit residuals of range data Cb10 for every hour. Vertical line shows time of transit of the moon across the station meridian. (RMS=0.8m, θ =118°)

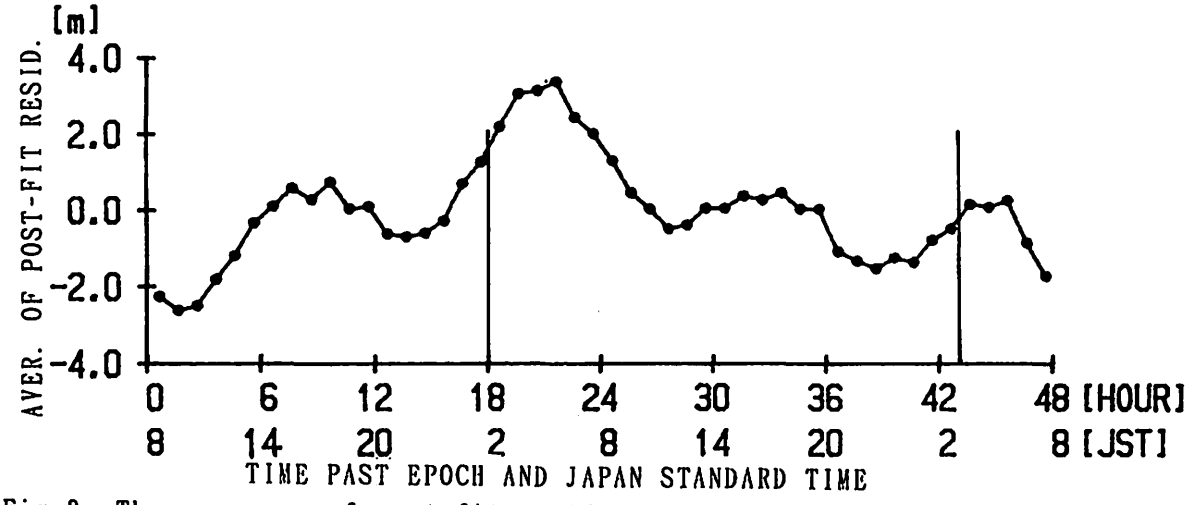

Fig. 8 The averages of post-fit residuals of range data Cb11 for every hour. Vertical line shows time of transit of the moon across the station meridian. (RMS=1.4m, θ =147°)

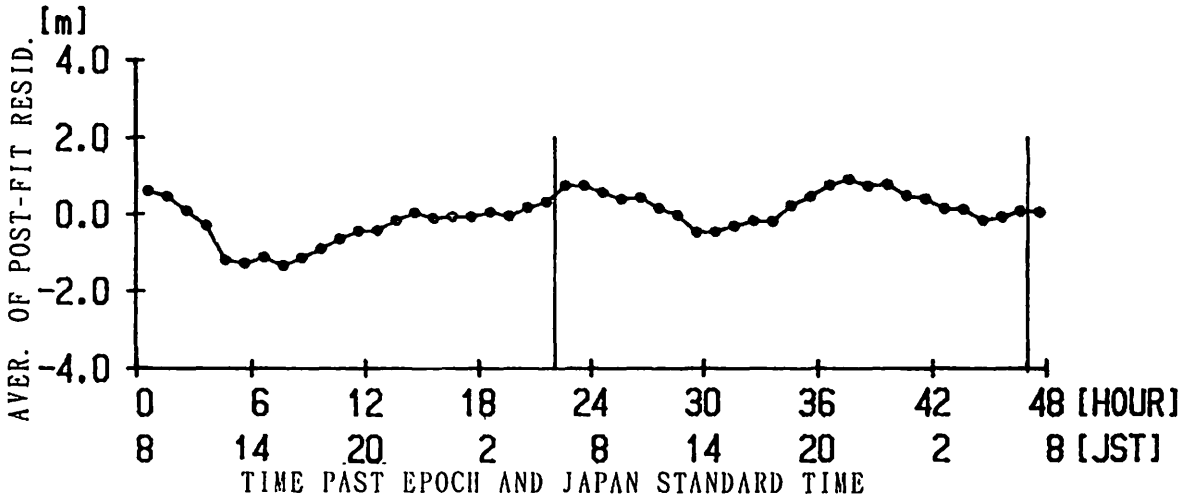

Fig. 9 The averages of post-fit residuals of range data Cb2 for every hour. Vertical line shows time of transit of the moon across the station meridian. (RMS=0.7m, θ = 82°)

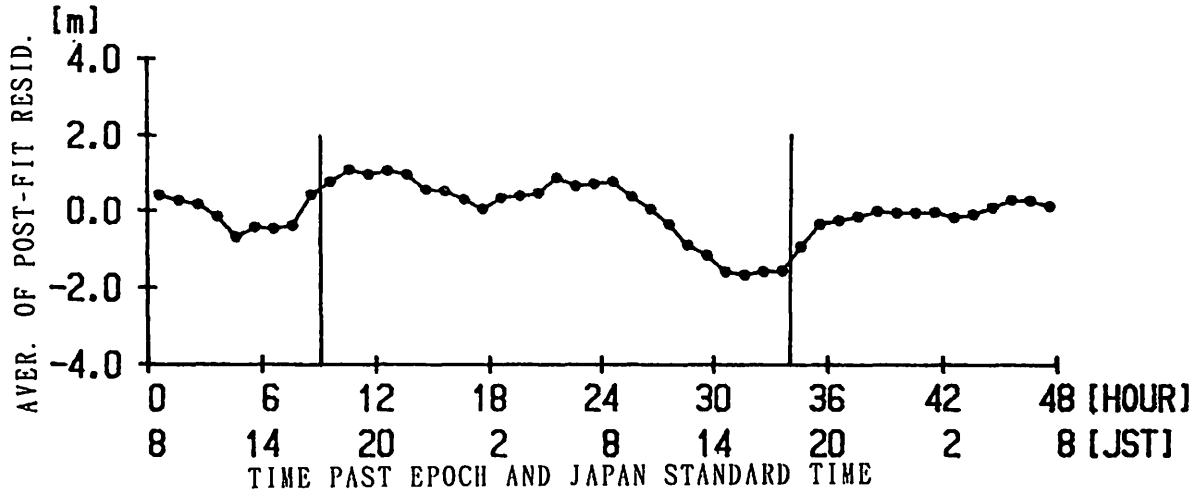

Fig. 10 The averages of post-fit residuals of range data Cb4 for every hour. Vertical line shows time of transit of the moon across the station meridian. (RMS=0.9m, θ = 90°)

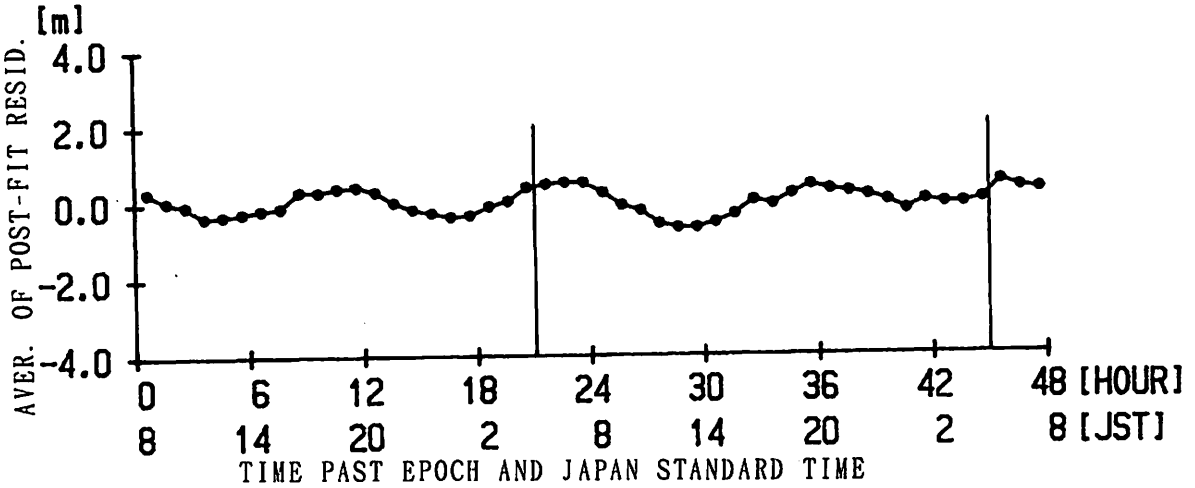

Fig. 11 The averages of post-fit residuals of range data Cb6 for every hour. Vertical line shows time of transit of the moon across the station meridian. (RMS=0.5m, θ=101°)

6．結言

(1) 全てのデータについて軌道決定後の O-Cに12時間周期の変動を確認することが出来た。

(2) 全てのデータについて O-Cの周期変動の位相は潮汐力に対して 2～ 3時間程度遅れていることが確認出来た。

この様な潮汐力による地殻の水平変動については，海洋に存在する潮流や海流の様な水平方向の流れが地球内部にも存在し，この様な地球内部の流れとともに地殻が変動しているものと考えることができる。

以下については今後の課題である。

(1) 海洋潮汐による地殻変動の様子を詳しく調べる。

(2) 未知の力の原因について調べる。

最後に通信衛星（CS-3a,CS-3b）の貴重な観測データを提供して頂いた通信・放送機構に心から感謝の意を表する。

参考文献

(1)Minoru Sasaki:STUDY OF THE EARTH'S DYNAMICS BY MEANS OF SATELLITE LASER RANGING TECHNIQUES, Report of Hydrographic Researches, No. 26, pp. 99-187, 1990.

(2)Francis J. Lerch, Barbara H. Putney, Carl A. Wagner and Steven M. Klosko:Goddard Earth Models for Oceanographic Applications(GEM10B and 10C), Marine Geodesy, Vol. 5, No. 2, pp. 145-187, 1981.

(3)Dennis D. McCarthy:IERS STANDARDS 1992, International Earth Rotation Service, 1992.

(4)E. M. Standish, Jr. :Orientation of the JPL Ephemerides, DE200/LE200, to the Dynamical Equinox of J2000, Astronomy and Astrophysics, 114, pp. 297-302, 1982.

(5)古在由秀:人工衛星による地球・海洋潮汐の検出，月刊海洋科学，地球と海洋潮汐，106号，pp. 640-643, 1978.

(6)宇宙開発事業団:レンジとレンジレートの補正，宇宙開発事業団データベース，ABS No. 2612. C.

(7)J. H. Berbert and H. C. Parker:GEOS Satellite Corrections for Refraction in the Troposphere, International Symposium on Electromagnetic Distance Measurement and Atmospheric Refraction, Boulder Colorado, 1969.

SELENEによる月重力場推定に関する考察

On Lunar Gravitational Potential Recovery from SELENE satellites

仙石　新
海上保安庁水路部
Arata Sengoku
Hydrographic Department of Japan, Maritime Safety Agency
asengoku@cue.jhd.go.jp

Abstract

SELENE is the first lunar mission to directly observe the lunar gravitational field of the far side. The orbiter of SELENE has high sensitivity to higher order lunar gravitational field, while the relay satellite tracking data will reveal lower order terms. Higher order terms have to be recovered from the short periodic perturbations of the orbiter, since the orbit will be changed every eight hours. To improve the quality of the lunar gravitational field from SELENE satellites, it is highly important 1) to model surface forces acting on the satellites such as radiation pressure, 2) to track the satellites continuously from ground stations with excellent precision, and 3) to obtain good observation models.

1．SELENE計画の概要

SELENEは2003年に打ち上げが予定されている日本の月ミッションで、月の近傍を周回し各種センサーにより月面の観測を行う周回衛星と、周回衛星が月の裏側にある時に周回衛星のデータをリレーするリレー衛星とで構成されている。周回衛星には、地形カメラの他分光計や高度計など様々なセンサーが搭載され、月の起源と進化を明らかにする貴重なデータが得られる予定である。

月の重力場を測る、ということがSELENEの重要なテーマの一つになっている。SELENEは14のミッションからなるが、そのうち3つが重力場に関係している。それは、

1）VRAD：月面（表側）に電波源を着陸させ、リレー衛星の電波源との間の角距離を地上からVLBIにより測定する。ミッション期間（14ヶ月）の最後の2ヶ月間のみ行われる。

2）RSAT：地上から周回衛星、リレー衛星までのDoppler観測（追跡局－衛星－追跡局と往復させて測定するので2 way Dopplerという、2 way Dopplerは衛星に搭載されている周波数標準の誤差がキャンセルできる）を行う。また、リレー衛

星を介して周回衛星までのDoppler観測（追跡局－リレー衛星－周回衛星－リレー衛星－追跡局という測定なので、4 way Doppler観測である）を行う。これらは、ミッション期間中をとおして行われる。但し、最後の2ヶ月間は、周回衛星の一部を月に着陸させるため、4 way Doppler観測は行われない。

3）LALT：レーザーアルチメータにより、衛星から月面までの高さを測定する。ただし、LALTについては月の表面形状（topography）は明らかになるが、ただちに重力場に結びつかない。LALTによって同一地点で2回の測定がされれば（cross-over point）軌道に関する情報が得られるが、footprintが小さいためそのようなことはまれであろう。

これまでにも、アポロのサブ衛星、Lunar Orbiter、Clementineなどが月を周回し、その間地上から衛星までの2 way Doppler観測が行われている。現在、Lunar Prospectorが月を周回しているが、これでも同様の観測が行われている。SELENEで月重力場を解明しようとする試みのこれまでにない新しいポイントは、2 way Dopplerでは観測できない月の裏側の衛星の軌道を4 way Dopplerにより直接捕らえようとするところにある。これまでの観測からも、月の裏側の重力場についてある程度の知見が得られているが、地上から軌道が追跡可能な月の表側の軌道を元に間接的に決められてものである。SELENEに対する期待を一言で言い表すならば、裏側の軌道を直接観測してはっきりと知りたい、ということに尽きるだろう。

2．リレー衛星と周回衛星

リレー衛星と周回衛星の軌道に関する諸元をTable 1に示す。但し、これらの値は将来変わり得ることに注意する。

Table 1. Orbital parameters of SELENE satellites

	orbiter	relay satellite
a	1840km	3200km
e	0	0.4255
i	90 or 95 deg	90 or 95 deg
n	8.87×10^{-4}rad/sec	3.87×10^{-4}rad/sec
	12.2 rev/day	5.3 rev/day
$\dot{\Omega}$	0, 2.1×10^{-8}rad/sec	0, 4.5×10^{-9}rad/sec
	0, 0.10 deg/day	0, 0.022 deg/day
$\dot{\omega}$	1.2×10^{-7}rad/sec	2.6×10^{-8}rad/sec
	0.60 deg/day	0.13 deg/day
v	1.6 km/sec	1.2 km/sec

リレー衛星は、かなり離心率が高く、月のまわりをほぼ4時間半で一周する。近

月点高度が100kmで、周回衛星の飛行高度と一致する。リレー衛星の軌道半径はもう少し小さくなるかもしれない。周回衛星は円軌道で、飛行高度が100km、公転周期は約2時間である。軌道傾斜角は、両衛星とも90度ないしは95度であるため、J_2による昇交点経度の永年摂動は小さく、昇交点経度はミッション期間中ほとんど変化しない。

リレー衛星は、ミッション期間中衛星の軌道と姿勢を制御しないが、周回衛星は両者とも制御し、軌道については8時間ごとに燃料を噴射するなどして変更する（マヌーバ）。Clementineなどでも軌道の制御はかなり頻繁に行われ、数日おきに軌道が不連続になったが、SELENEはさらに数時間で軌道が不連続となる。マヌーバの前後の軌道は、軌道解析のプロセスでは連続して扱えないため、別々のアークとして個別に解析しなくてはならないことに注意しなくてはならない。

3．SELENE衛星に加わる摂動

月の重力場を球面調和展開したときの各次数のパワーをFigure 1に示す。地球の場合と比べて、2次の係数は小さいが、それ以上の高次の項については月の重力場の係数は1桁ないしは1桁半大きいことが読みとれる。

SELENE衛星に加わる摂動をTable 2に示す。表の値は加速度である。主要項以外については、主要項の絶対値で正規化されている。

表から明らかなように、周回衛星への摂動は高次項までかなり大きい。Doppler観測の精度が0.3mm/60secとすると、衛星の公転速度の3×10^{-9}程度であり、周回衛星については、短周期摂動であっても十分に高次項まで観測にかかるはずである。但し、これは伝搬補正、アンテナの動きによる運動学的補正など観測モデルの精度が十分保証されなくてはならない。

逆に、リレー衛星への月重力場の高次の摂動は小さい。短周期摂動については、リニアスケールで、6次で数m程度、18次で1mm以下の振幅しかない。このため、リレー衛星から高次の項を検出するためには長周期ないしは永年摂動を見るしかないが、2ヶ月ではたかだか1000倍程度しか振幅が増幅せず、高次項を見ることは難しい。また、共鳴項も100次以上の高次にならないと存在しない。

太陽光の輻射圧については、10^{-8}から10^{-9}のオーダーである。しかし、複雑な形をした衛星の輻射圧のモデル化は一般的に難しいため、モデル誤差により、リレー衛星の軌道解析に対しては長周期摂動により大きな影響がある。例えば、非等方な輻射圧が10％あった場合、衛星が月の影に入ると1日あたりalong-trackに2m、1ヶ月で2kmの位置の誤差を生じる。周回衛星については、軌道が8時間ごとに不連続となるため、輻射圧のモデル誤差は問題にならない。

月の照り返しによる輻射圧は、リレー衛星に対してはモデル化が必要かも知れない。地球の照り返しによる輻射圧は月の1/250程度であり、ほとんど問題にならない。

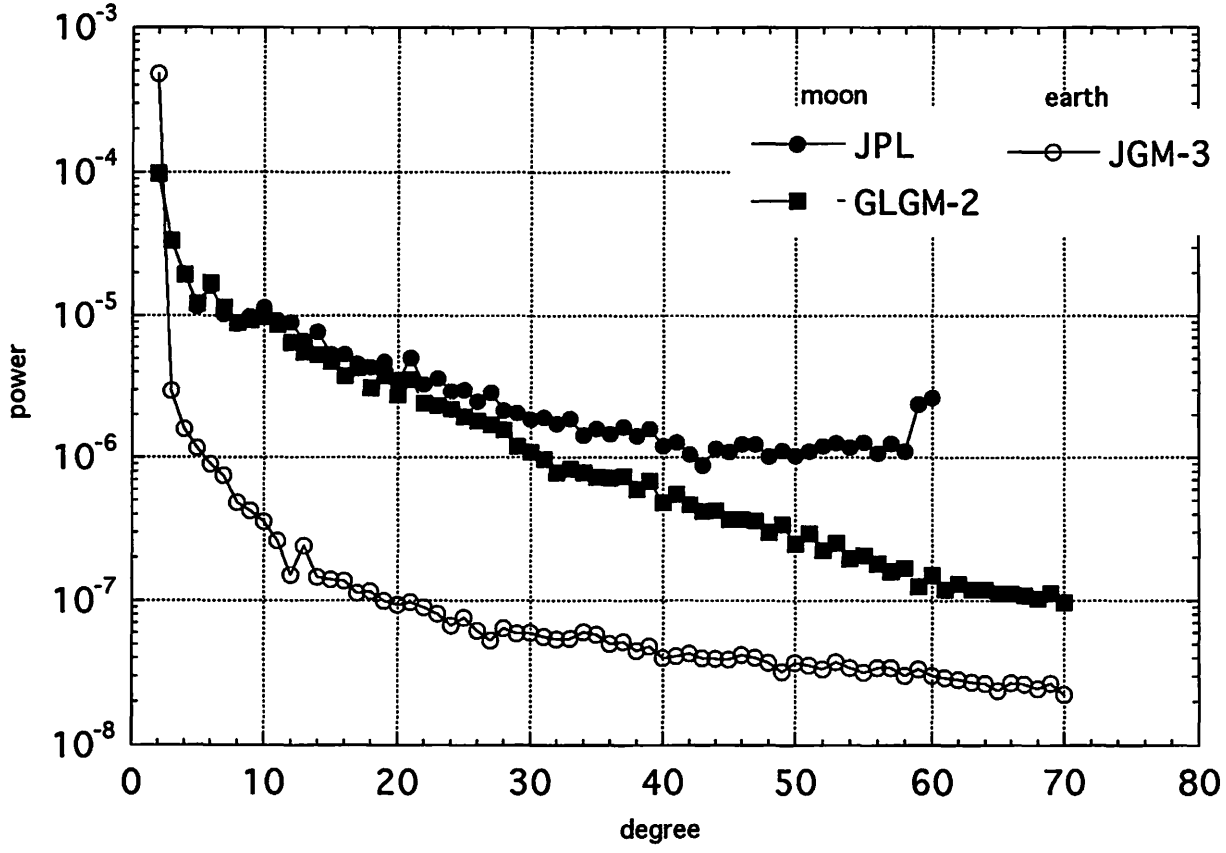

Figure 1. The power spectrum of the present lunar and earth gravitational field models.

Table 2. Summary of perturbations acting on SELENE satellites scaled by the main term of the lunar gravitational field

	orbiter	relay satellite
Lunar gravitational field		
-main term		
$\alpha_0 = \frac{GM_M}{r^2}$	1 (1.45m/s/s)	1 (0.48m/s/s)
-J2($\bar{J}_2 = 9.07 \times 10^{-5}$)		
$\alpha_{J_2} / \alpha_0 = 3(\frac{R_M}{r})^2 \bar{J}_2$	2.4×10^{-4}	8.1×10^{-5}
-low order harmonics		
$\alpha_{C_{2,2}} / \alpha_0 = 3(\frac{R_M}{r})^2 \overline{C}_{2,2}$	9.1×10^{-5}	3.0×10^{-5}
$\alpha_{C_{6,6}} / \alpha_0 = 7(\frac{R_M}{r})^6 \overline{C}_{6,6}$	2.6×10^{-5}	9.4×10^{-7}
-high order harmonics		
$\alpha_{C_{18,18}} / \alpha_0 = 19(\frac{R_M}{r})^{18} \overline{C}_{18,18}$	1.9×10^{-6}	9×10^{-11}
$\alpha_{C_{50,50}} / \alpha_0 = 51(\frac{R_M}{r})^{50} \overline{C}_{50,50}$	1.1×10^{-7}	$1. \times 10^{-19}$
Third body attraction		
-Earth		
$\alpha_E / \alpha_0 = 2\frac{M_E}{M_M}(\frac{r}{r_E})^3$	1.5×10^{-5}	9.7×10^{-5}
-Sun		
	8.4×10^{-8}	5.2×10^{-7}
Air drag		
	0	0
Radiation pressure		
-solar radiation		
$\alpha_R / \alpha_0 = \frac{A}{M}\frac{\Phi}{c} / (\frac{GM_M}{r^2})$	6×10^{-9}	5×10^{-8}
-lunar albedo radiation		
$\alpha_A / \alpha_0 = \frac{A}{M}\frac{\Phi}{c} A_{lbedo}(\frac{R_M}{r}) / (\frac{GM_M}{r^2})$		
	4×10^{-10}	1×10^{-9}

輻射圧などの表面力は、事前にモデル化されていないと、軌道解析において観測値（例えばDopplerデータ）の残差が小さくならず、重力場のシグナルが見えてこないため、あらかじめ十分な検討がされなくてはならない（久保岡、1998）。

4．考察

Clementineは、月全体を初めてグローバルかつ均質に観測したという意義あるミッションであったが、月面上の細かい重力異常のプロファイルなどの短波長成分は、それ以前のLunar Orbiterなどのデータが主として貢献している（Lemoine et al., 1997）。リレー衛星はClementineとほとんど同程度の軌道半径を持つため、リレー衛星のトラッキングデータだけでは、重力場の短波長成分は見えてこない。このため、周回衛星のデータから短波長成分を、リレー衛星から長波長成分をそれぞれ決定する戦略が必要である。また、いうまでもなく、SELENEのみでなく、Clementine、Lunar Prospector、Lunar Orbiterなど、過去あるいは今後得られるデータを網羅して、重力場決定を目指すべきである。

また、周回衛星は8時間ごとに軌道を制御する計画であるから、振幅が大きくなる長周期摂動を観測することができない。このため、周回衛星の追跡観測は、1）観測精度（Doppler観測そのものの精度）が良く、2）地上からの追跡が途絶えず（追跡局が相当数必要）、3）観測モデルが十分の精度を持つことなどが是非必要である。3）を満たすためには、例えば衛星の姿勢、衛星に設置されたアンテナの位置情報の精度などを十分保証する必要がある。衛星にアンテナが複数ある場合は、どちらのアンテナで受信されたか明確でなければならない。電離層や水蒸気による伝搬補正についても、あらかじめ十分な考察が必要である。

最後に、SELENE衛星による重力場推定のシミュレーションを行い、より良い推定のためにミッションへの提案をするとともに、従来の衛星データの解析に着手し、重力場推定のノウハウを蓄積することが肝要である。日本国内では、これまで数値的な軌道推定による重力推定は行われたことがないため、海外の研究者との交流も必要となるだろう。

これまでできなかった月の裏側の重力場の直接観測が、SELENE計画ではじめて行われる。どのような事実が明らかになるのか、大いに期待したい。

参考文献

久保岡（1998）：SELENE計画のリレー衛星と月周回衛星に作用する非重力効果，本集録.

Lemoine, F. G. R., D. E. Smith, M. T. Zuber, G. A. Neumann, D. D. Rowlands (1997): A 70th degree lunar gravity model (GLGM-2) from Clementine and other tracking data, *Journal of Geophys. Res.*, 102, E7, 16339.

SELENE計画のリレー衛星と月周回衛星に作用する非重力効果

Non-Gravitational Effect on the Relay Satellite and the Lunar Orbiter of SELENE

久保岡 俊宏（海上保安庁・水路部）

Toshihiro Kubo-oka

Hydrographic Department, Maritime Safety Agency

Abstract

In order to calculate the lunar gravitational coefficients from the orbits of lunar orbiters, it is very important to assess the non-gravitational effects on their orbits. In the cases of the relay satellite and the lunar orbiter of SELENE, a Japanese lunar mission which will starts in 2003, solar radiation pressure is the largest non-gravitational force. In this paper, we present a new model describing the solar radiation pressure on the relay satellite of SELENE. We included the model into GEODYN-II, an orbit analysis software developed at NASA Goddard Space Flight Center and investigated the variation of osculating orbital elements of the relay satellite. We compared three cases: (1) "octagonal model" developed in this paper, (2) default model prepared in GEODYN-II, and (3) without solar radiation pressure. We found that the difference between octagonal model and default model is about a half as large as the effect of the solar radiation.

1 Introduction

日本が2003年に実施を予定している月探査計画「SELENE」では、月面の精密マッピング、月周辺の磁場計測等、数多くの科学的目標を掲げている。その中の一つが、「月の重力場、特にこれまで殆ど測られていない月の裏側の重力場を、高精度で決定すること」である。SELENE計画では、月周回衛星⇔リレー衛星、リレー衛星⇔地上局という二重のドップラー観測、およびΔ-VLBI観測から、衛星の軌道の揺らぎを求め、それを解析して月の重力場を測定することを目指している（仙石、1998）。ただし、この目的のためには、重力以外の力が、衛星の軌道に及ぼす影響について調べておく必要がある。リレー衛星と月周回衛星の場合、非重力効果の内、最大のものは太陽からの輻射圧である。

今回は、主にリレー衛星に作用する太陽輻射圧に注目し、輻射圧の大きさを計算するための「モデル」を造った。その結果を軌道解析ソフトウェアGEODYN-IIに組み込み、実際にリレー衛星の軌道計算を行ってみた。GEODYN-IIは、NASA Goddard Space Flight Center (GSFC)で開発された汎用の軌道解析ソフトウェアで、測地解析、軌道予報等数多くの機能を有している（Eddy et al, 1990）。SELENE計画では、月の重力場係数を計算するソフトウェアとして、GEODYN-IIを改造したものを用いる方針となっている。そのソースコードには、海洋観測衛星TOPEX/Poseidon、GPS衛星、Mars Observerといった、個々の衛星に特化したルーチンが含まれている。また、独自の「モデル」を追加することも可能である。水路部でも、測地衛星「あじさい」の非等方輻射圧モデルを追加し（Sengoku et al, 1995）、グローバル観測局と日本列島の位置の結合、プレート運動の解析等に利用している（藤田、仙石, 1997）。

本稿では、まずリレー衛星の「八角柱太陽輻射圧モデル」について説明する。次に、(1) 輻射圧を無視した場合、(2) GEODYN-IIにデフォルトで用意されている輻射圧モデル、(3) 今回造った「八角柱モデル」、の3つの場合について、軌道計算の結果の違いについて述べる。最後に、月周回衛星に関してどのようなモデルを作るべきかについても簡単に触れる。

2 リレー衛星の輻射圧モデル（八角柱モデル）

リレー衛星の形状をFig. 1に示す。大雑把に言うと、幅99[cm]、高さ77[cm]の正八角柱に通信用のアンテナが突き出た形になっている。衛星は、月周回衛星から切り離され、毎分10回というペースで自転しながら、近月点高度100[km]、遠月点高度2500[km]という比較的長細い楕円軌道上を周回し、周回衛星と地上局との通信の中継局の役割を担う。

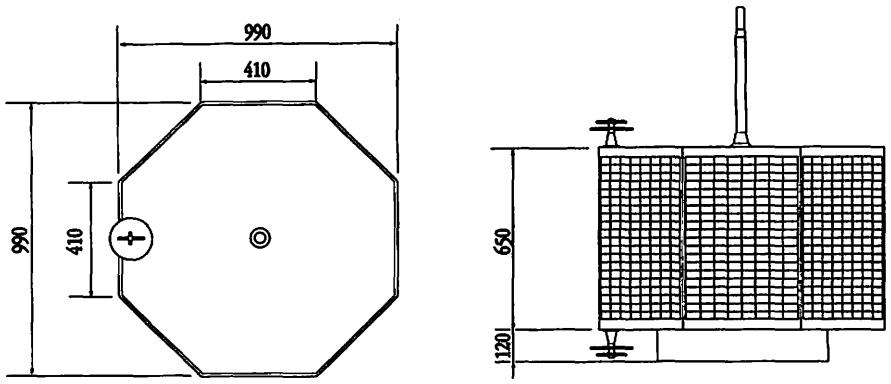

Fig. 1　Shape of the relay satellite.

リレー衛星のモデルを作る際に、以下の様な仮定をおく。

1　衛星のスピン軸は、Epochにおける月の北極方向に平行
2　衛星のスピンの周期は、公転周期に比べて十分短い。
3　衛星は高さ77[cm]、質量30[kg]の八角柱。突き出ているアンテナは無視。
4　月からの照り返しの影響は無視。
5　側面は、太陽電池、天板と底板は、金箔張り。

これらの仮定のうち、1、3、4に関しては注意が必要である。計画では、実際のリレー衛星はスピン軸が白道面に垂直になるように投入される予定になっている。また、太陽輻射圧等のトルクによって、スピン軸が変動することが予想される。しかし、現状では、主としてプログラミング上の問題で、これらの影響を無視している。3に関しても、本来は、八角柱＋円柱（取り付け部）とすべきだが、現段階では単純に八角柱とみなしている。これも今後の課題である。また4に関しては、GEODYN-IIには中心天体からの照り返しの効果を計算するルーチンが用意されている。特に、地球周回衛星に関してはalbedoの緯度依存性を考慮した特別なルーチンが用意されている。これらのルーチンは、入力ファイルに「ALBEDO」という1行を入れるだけで適用される。ただし、今回は、月のalbedoの値がどの変数に格納されているのか不明であることもあって、月からの照り返しの効果は無視した。

まず、一般にn角柱の場合を考える。ここで、座標系をFig. 2の様にとる。太陽方向の単位ベクトルを$\mathbf{s}$とすると、側面を構成する一つのパネル（面積A_S、法線ベクトル$\mathbf{n}$）
に作用する太陽輻射圧による加速度は、

$$d\mathbf{a} = -\frac{A_S \Phi}{m_S c}\left[(1-\rho_S)\,\mathbf{s} + 2\left(\frac{\delta_S}{3}+\rho_S\cos\beta\right)\mathbf{n}\right]|\cos\beta| \qquad (1)$$

で表される（Milani et al, 1987）。ここで、Φ、m_s、c、ρ_s、δ_sは、それぞれ、太陽定数、衛星の質量、光速度、specular reflectivity、diffuse reflectivityである。また、βは、面の法線ベクトル$\mathbf{n}$と、太陽方向の単位ベクトル$\mathbf{s}$のなす角である。次に太陽光の当たっている面について、(1)式の加速度を加え合わせる。さらに自転周期が公転周期に比べて短いという仮定から、自転周期に渡っ

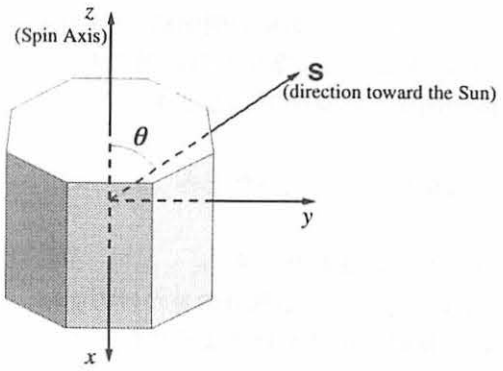

Fig. 2　Satellite body-fixed coordinate system.
Unit vector toward the Sun **s** is in x-y plane.

て時間平均をとる。すると、x 成分（スピン軸及び太陽方向に垂直な方向）の成分は、消えてしまう。結局残る z 成分（スピン軸方向の成分）と、y 成分（スピン軸と太陽方向の張る面内にあり、かつスピン軸に垂直な成分）は、それぞれ

$$\left(\mathbf{a}_z\right)_{\text{Side}} = -n\,\frac{A_S\Phi}{\pi m_S c}\left(1-\rho_S\right)\sin\theta\,\cos\theta \tag{2}$$

$$\left(\mathbf{a}_y\right)_{\text{Side}} = -n\,\frac{A_S\Phi}{3m_S c}\,\sin\theta\left\{\frac{3+\rho_S}{\pi}\,\sin\theta + \frac{\delta_S}{2}\right\} \tag{3}$$

となる。一見すると、(2) と (3) 式は $n\to\infty$ の極限で発散するように見えるが、現実にはそうはならない。なぜなら、角柱の半径を a, 高さを h とすると、側面パネル 1 枚の面積は、

$$A_S = 2ah\sin\left(\frac{\pi}{n}\right) \tag{4}$$

で表される。従って $n\to\infty$の極限で、$n\,A_S\to 2\pi ah$ となる。これは円柱の場合に対応している。リレー衛星の場合は、$n=8$ とすればよい。

天板、及び底板にかかる輻射圧による加速度は、(1)式をそのまま使って、

$$\left(\mathbf{a}_z\right)_{\text{Top}} = -\,\frac{A_T\Phi}{m_S c}\,\cos\theta\left\{\left(1+\rho_T\right)\cos\theta + \frac{2}{3}\delta_T\right\} \tag{5}$$

$$\left(\mathbf{a}_y\right)_{\text{Top}} = -\,\frac{A_T\Phi}{m_S c}\left(1-\rho_T\right)\,\sin\theta\,\cos\theta \tag{6}$$

となる。ここで、ρ_T、δ_T はそれぞれ、天板及び底板の specular reflectivity と diffuse reflectivity である。

GEODYN-II には、デフォルトの輻射圧モデルとして、"canonball" モデルと呼ばれるものが用意されている。このモデルでは、輻射圧を、

$$\mathbf{a}_S = -\left(1+\rho_S\right)\frac{A_S}{m_S}\frac{\Phi}{c}\mathbf{r}_S \tag{7}$$

の式で与えている。つまり、輻射圧による加速度の向きは、常に太陽と反対の方向であり、なおかつ、加速度の大きさは衛星の姿勢と太陽の位置関係に依存しない。また、(7) 式から分かるように、デフォルトのモデルでは、衛星の「有効」断面積 A_S と、specular reflectivity ρ_S の 2 つの量をパラメータとして与えることになる。今回、canonball モデルを用いて軌道計算する場合には、

有効断面積は 77 [cm] × 99 [cm] （衛星の側面積）、反射率は太陽電池パネルの値を用いた。

なお、GEODYN-II の内部では、衛星が月の影に入っているかどうかに対応して、

○太陽全体が衛星から見えているとき、

$\nu = 1$

○完全に太陽が月の影に入ったとき

$\nu = 0$

○太陽が部分的に隠されたとき

ν = （太陽の見えている部分の見かけの面積）／（太陽の見かけの面積）

で定義される係数 ν を輻射圧項にかけるようになっている。影に入ったかどうかの判断は、以下の様にして行う。まず、

$$D = \mathbf{r}_{Sat} \cdot \mathbf{r}_{Sun} \tag{8}$$

を計算する。D が正の場合 の場合は、常に「日向」にいるものとする。次に $D<0$ かつ、

$$\left(\mathbf{r}_{Sat} - D\mathbf{r}_{Sun}\right)\cdot\left(\mathbf{r}_{Sat} - D\mathbf{r}_{Sun}\right) < R_M^2 \tag{9}$$

が成り立つとき、月の影の中にいるものと判断する。ここで、R_M は月の半径である。それ以外の場合は、やはり「日向」にいるものとみなす。

Table 1 に、表面の材質の違いによる反射率の違いを示す（Antreasian and Rosborough, 1992）。ここで、specular reflectivity と diffuse reflectivity の比は 1 : 4 を仮定した。

Surface Coating	α	ρ	δ
Front of solar array	0.79	0.042	0.168
Back of solar array	0.18	0.164	0.656
Silver Teflon	0.07	0.186	0.744
White paint	0.18	0.164	0.656
Black paint	0.98	0.004	0.016
Gold plate	0.08	0.184	0.736

Table. 1　Optical properties of the surface (from Antreasian and Rosborough, 1992).

八角柱モデルと、canonball モデルから計算される加速度の θ 依存性を Fig. 3 に示す。当然、canonball モデルの方は、z 成分については cos、y 成分に関しては sin で変化する。y 成分に θ=90 [deg] 付近で大きな差が見られるのは、天板と底板に作用する輻射圧が効いているためである。

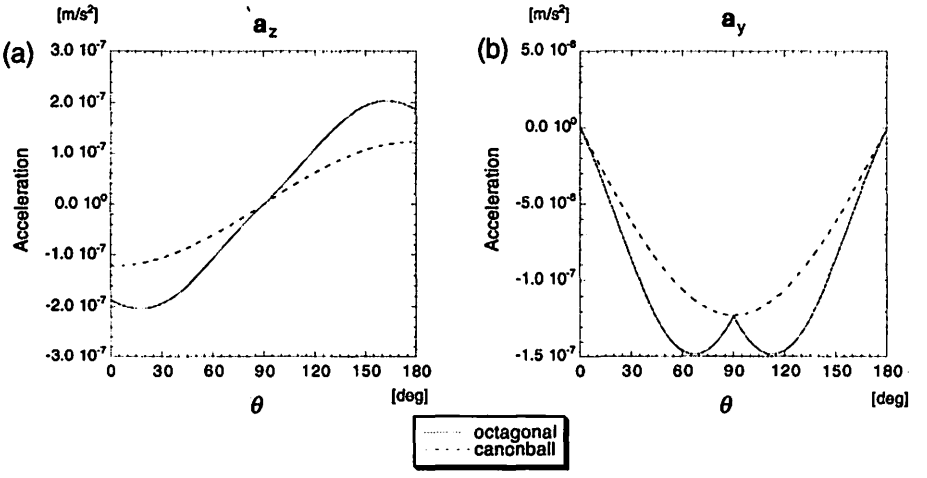

Fig. 3　Acceleration due to the solar radiation presusre: (a) component parallel to spin axis, (b) component normal to spin axis. Solid lines represents the "octagonal" model and dashed lines represents the "canonball" (GEODYN-II default) model.

3 リレー衛星の軌道計算

今回作った八角柱モデルをGEODYN-IIに組み込み、実際にリレー衛星の軌道計算を行ってみた。Epochは2003年8月1日0時0分で、計算する期間はEpochより360日間である。リレー衛星の初期軌道要素をTable 2に示す。これらは、現実のリレー衛星とおおよそ同じ条件である（軌道に投入される時の値はまだ確定していない）。月の重力場データは、ジェット推進研究所（JPL）のKonopliv らがLunar OribterとApollo計画のSubsatelliteの軌道から計算した60×60のモデルを用いた（Konopliv et al, 1993）。地球及びその他の惑星の重力の影響は、冥王星まで全て考慮している。また一般相対論的効果に関しては、GEODYN-IIに用意されているルーチンをそのまま利用した。なお、リレー衛星は約3ヶ月おきに月の影に入る期間と入らない期間を繰り返す。今回の計算条件では、2003年11月7日から2004年2月4日まで、2004年5月5日から計算終了までが月の影に入る期間に当たる。

semi-major axis	a	3000 [km]
eccentricity	e	0.38
inclination	i	95°
longitude of ascending node	Ω	270°
argument of perigee	ω	133°
mean anomaly	M	0°

Table. 2　Initial orbital elements of the relay satellite.

八角柱モデルを用いた場合の、360日間のリレー衛星の接触軌道要素の時間変化をFig. 4に示す。Fig. 4において、横軸はEpochからの日数を表わしている。リレー衛星が1周回の間に月の影に入る期間は、98日目～187日目までと、277日目～360日目に対応している。軌道長半径と軌道面傾斜角のグラフに顕著に見られる変動の周期は約14日で、これは地球の重力の効果によるものと考えられる。また、接触軌道要素の時間変化の「全体的な」傾向は太陽輻射圧のモデルには依存しないことが分かった。

次に、

(1) 輻射圧を考慮しない場合

(2) Canonballモデル（GEODYN-IIのデフォルト）

(3) 八角柱モデル

について、各時刻の接触軌道要素の差を計算した結果をFig. 5 ～ 9に示す。canonballモデルと八角柱モデルによる違い（Fig. 5 ～ 9の(c)）は、輻射圧を考慮するかどうかによる違い（Fig. 5 ～ 9の(a)と(b)）の1/2程度となっており、決して無視できる程小さくないことが分かる。これは、Fig. 3に示されているように、太陽方向と衛星のスピン軸のなす角によっては輻射圧による加速度に大きな差が生じることが影響しているものと推測される。また、モデルによる差は、衛星が月の影に入るようになってから増大する傾向がある。なお、輻射圧を考慮するかどうかで、i及びΩに長周期の変動が出ているのは、eの1次のオーダーから輻射圧による長周期摂動がでてくるためと考えられる（Milani et al, 1987）。なお、座標値に関しては、具体的にグラフには示さないが、Epochから3ヶ月後には、輻射圧を考慮するか否かでkmのオーダー、輻射圧のモデルの違いによって100mのオーダーで差が生じることが分かった。ただし、このような太陽輻射圧モデルの違いが月の重力場係数の推定結果にどの程度影響を及ぼしているのかについては、仮想的な観測データを用いて実際に重力場係数を計算するというシミュレーションを行って確かめる必要がある。

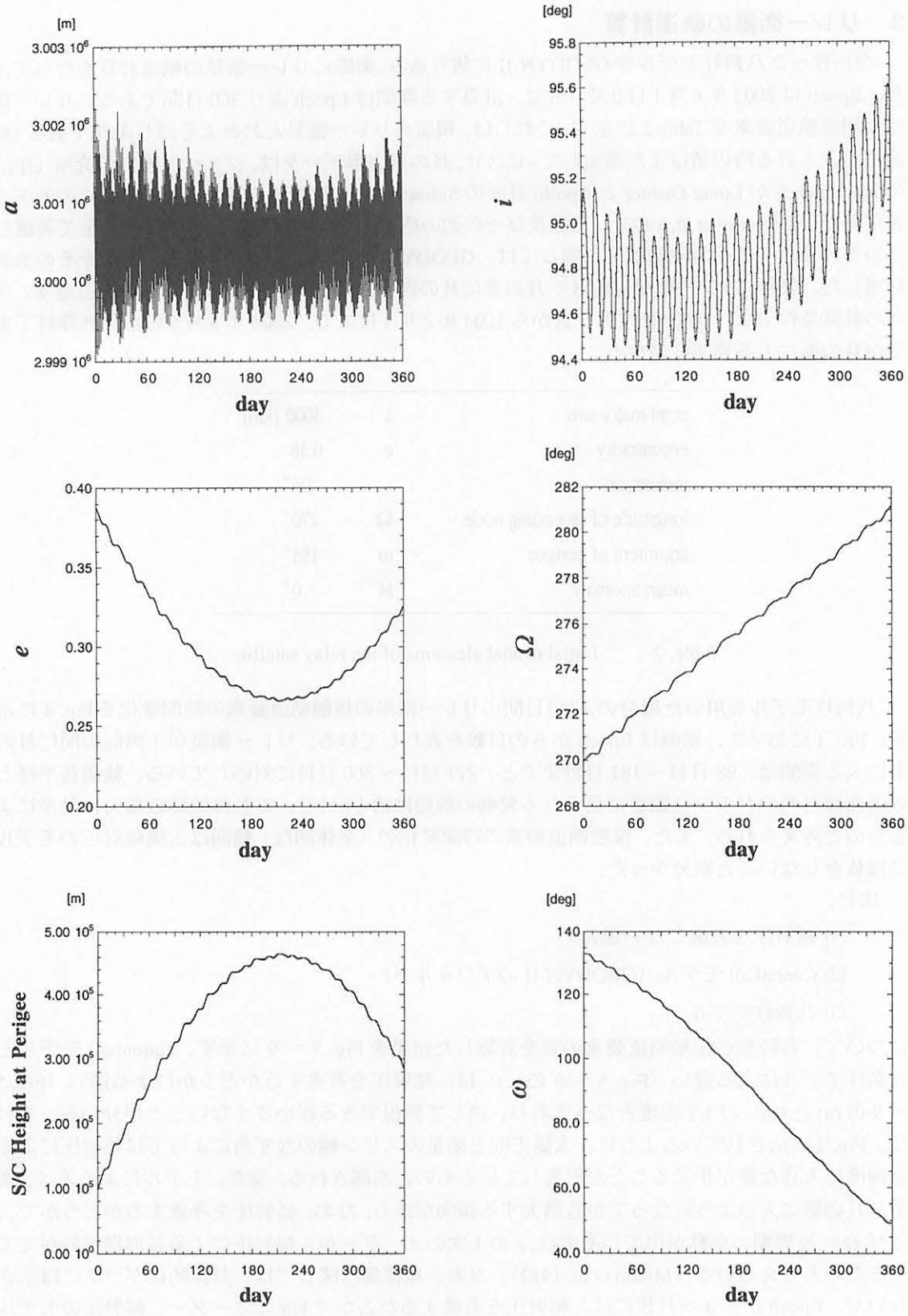

Fig. 4 Variation of the osculating orbital elements of the relay satellite. The orbit was integrated by use of "octagonal" radiation pressure model.

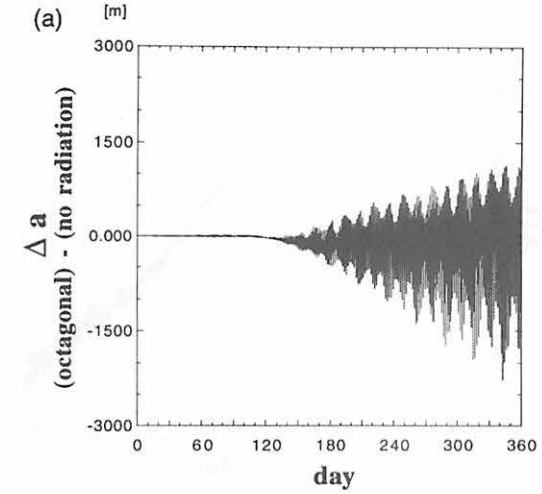

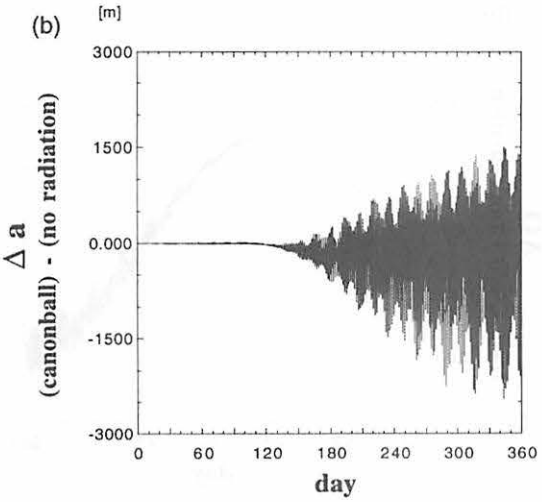

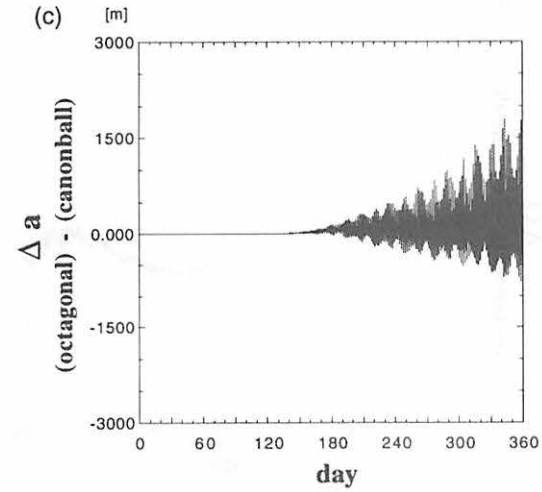

Fig. 5 Deferences in semimajor axis between radiation pressure models:
(a) octagonal model - w/o radiation pressure,
(b) canonball model - w/o radiation pressure,
(c) octagonal model - canonball model.

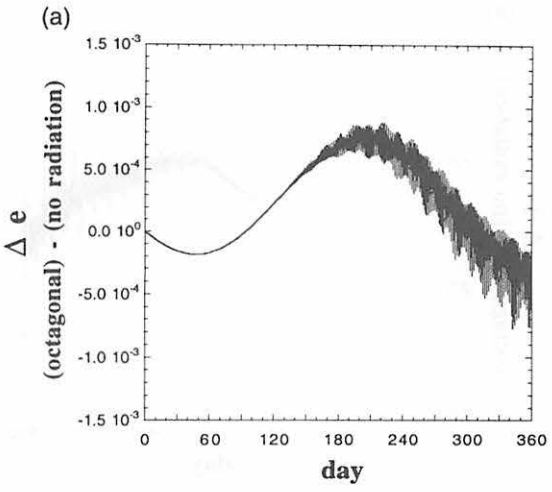

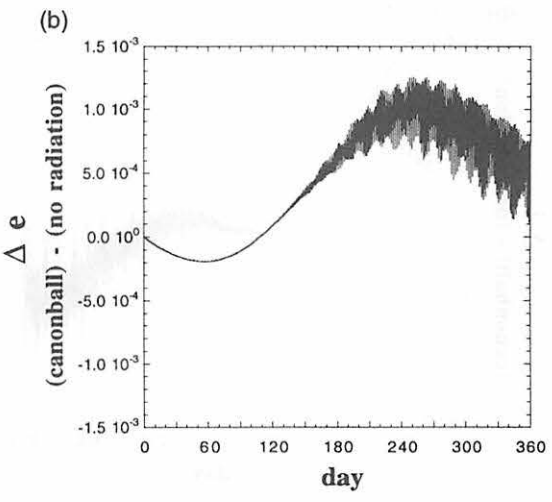

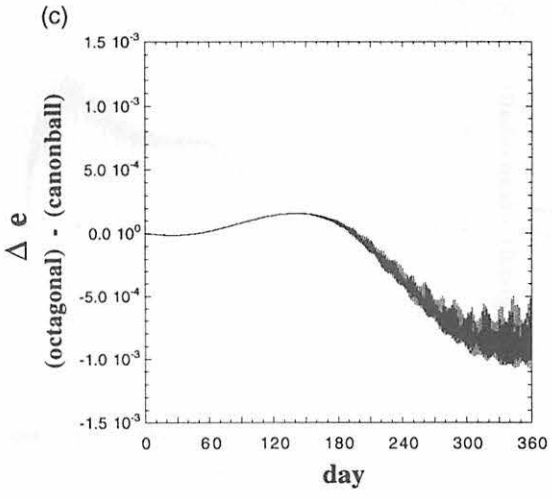

Fig. 6 Deferences in eccentricity between radiation pressure models:
(a) octagonal model - w/o radiation pressure,
(b) canonball model - w/o radiation pressure,
(c) octagonal model - canonball model.

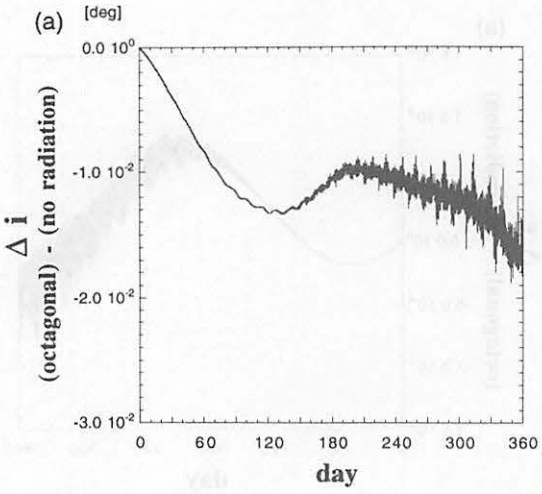

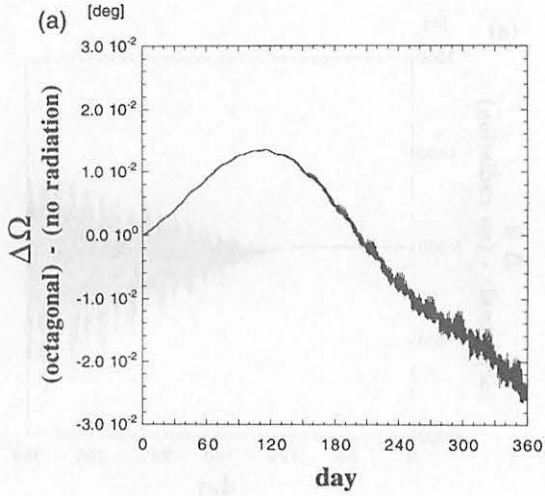

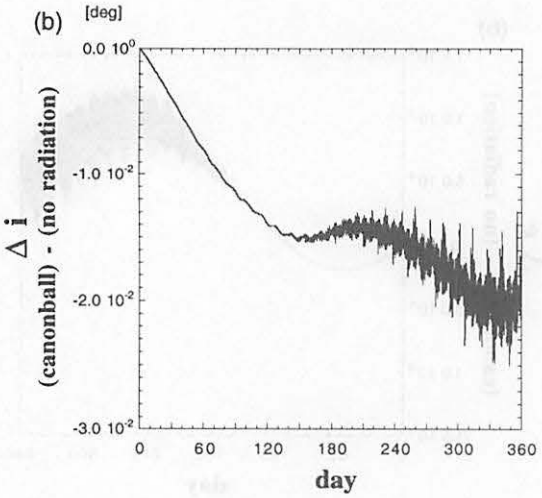

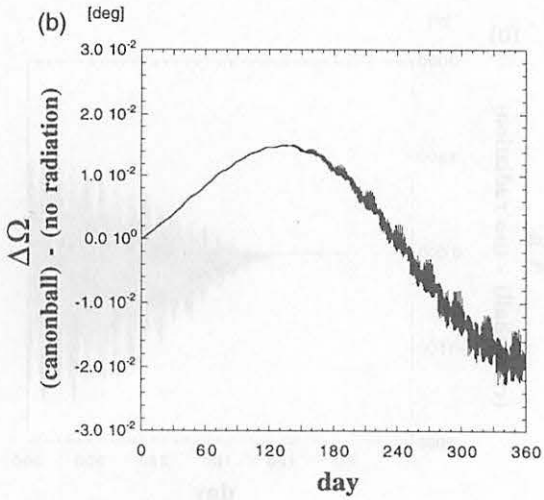

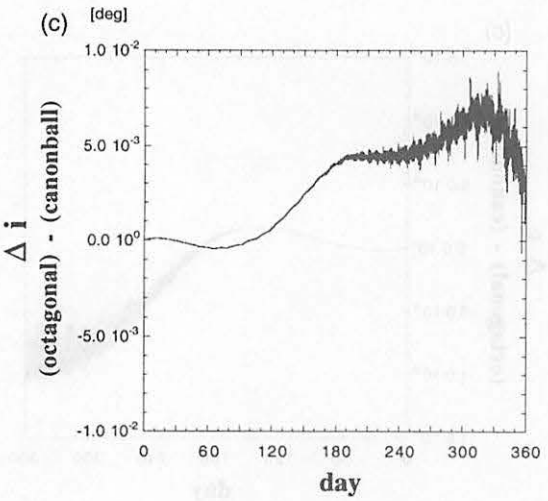

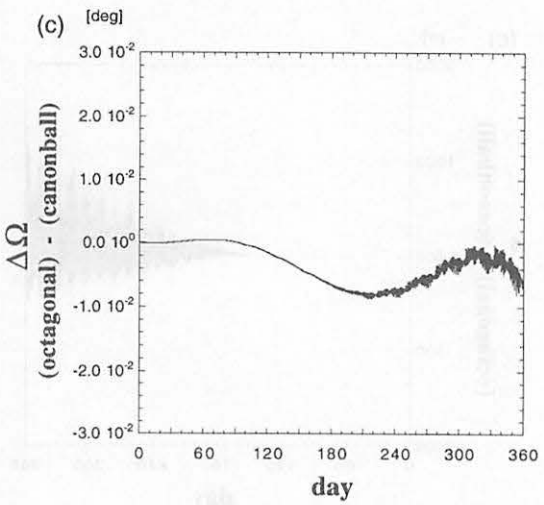

Fig. 7 Deferences in inclination between radiation pressure models:
(a) octagonal model - w/o radiation pressure,
(b) canonball model - w/o radiation pressure,
(c) octagonal model - canonball model.

Fig. 8 Deferences in longitude of ascending node between radiation pressure models:
(a) octagonal model - w/o radiation pressure,
(b) canonball model - w/o radiation pressure,
(c) octagonal model - canonball model.

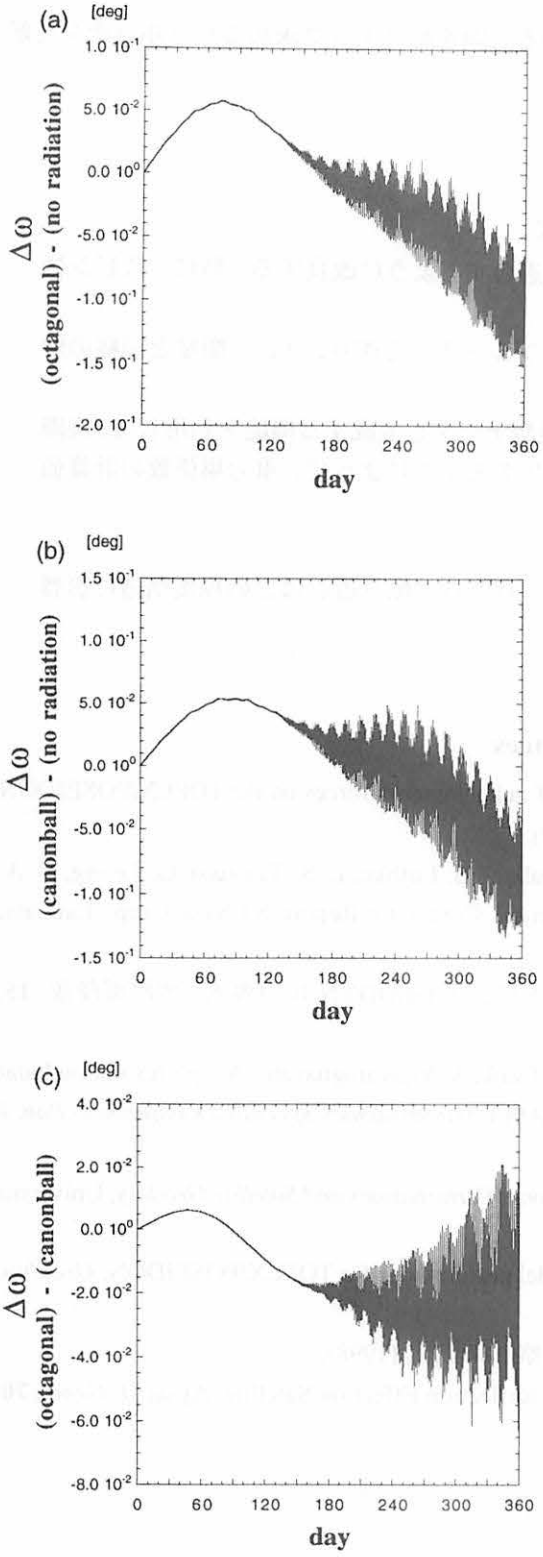

Fig. 9 Deferences in argument of perigee between radiation pressure models:
(a) octagonal model - w/o radiation pressure,
(b) canonball model - w/o radiation pressure,
(c) octagonal model - canonball model.

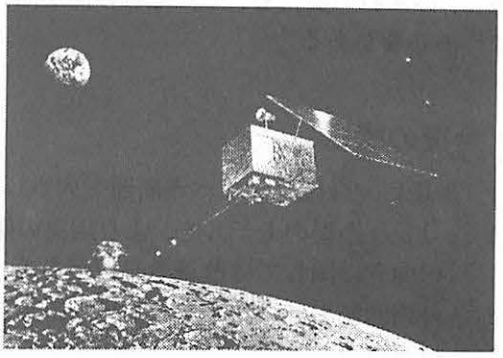

Fig. 10 Lunar orbiter of SELENE.

4 月周回衛星に関する補足

月周回衛星に関して、どのような「モデル」を作る必要があるのかについて簡単に述べる。月周回衛星の概念図を Fig. 10 に示す。大雑把に言うと月周回衛星は「箱」状の本体と太陽電池パネルから構成されるものとみなせる。このような比較的複雑な形状を持つ衛星に作用する輻射圧を GEODYN-II の中で計算するための手順について、海洋観測衛星 TOPEX/Poseidon を例にとって説明する。

まず、衛星をあらかじめ 300 以上の細かい素片に分割して、あらゆる方向から太陽光が当たる場合の輻射圧を厳密に計算しておく。ただし、この "Micro Model" と呼ばれるモデルは、実際に GEODYN-II に組み込んで計算するには複雑すぎる。そこで、衛星を箱（Box）＋パネル（Wing）とみなし、"Micro Model" の結果を近似できるように、Box 6 + Wing 2、計 8 つの面の面積、反射率といったパラメータを最小自乗法によって決定する（Marshall and Luthcke, 1994）。GEODYN-II の内部では，これら8つの面に作用する力をそれぞれ計算して加えあわせることにより，衛星に作用する摂動力を求めている。

月周回衛星についても、同様の作業を行う必要があるか否かについては、今後検討する必要がある。ただし、第 1 段階としては、衛星の本体と太陽電池パネルのおおよそのサイズと、表面材質に対応した反射率のデータを入力すればよいものと思われる。

しかし、いずれの場合も、それぞれの面が向いている方向を毎ステップ求めるサブルーチンを新たに作る必要がある。

5 今後の課題

最後に、今後検討すべき問題を列挙しておく。

1 リレー衛星のモデルを、より現実の衛星に適合するように改良する。特に、スピン軸の向きに関しては改善の必要がある。

2 月周回衛星に作用する輻射圧を計算するサブルーチンを作り、リレー衛星と同様の解析を行う。

3 GEODYN-II に用意されている、仮想的な観測データを生成する機能を利用して、実際に重力場解析のシミュレートを行い、輻射圧のモデルによって、重力場係数の計算値にどれくらいの差が生じるのかを調べる。

4 その他の非重力効果の影響は？
例えば、リレー衛星の天板からの熱放出や、月からの照り返しはどの程度軌道に影響を及ぼしているのかを調べる必要がある。

References

Antreasian, P. G., and G. W. Rosborough : Prediction of radiant energy forces on the TOPEX/POSEIDON spacecraft, *J. Spacecr. Rockets*, **29**, 81-92, (1992).

Eddy, W. F., J. J. McCarthy, D. E. Pavlis, J. A. Marshall, S. B. Luthke, L. S. Tsaoussi, G. Leung, D. A. Williams : *GEODYN-II System Operations Manual*, Contractor Report, ST Syst. Corp., Lanham, Md., (1990).

藤田雅之, 仙石新 : NASA の衛星データ解析ソフトウェア GEODYN-II の導入, *水路部技報*, **15**, 5-10, (1997).

Konopliv, A. S., W. L. Sjogren, R. N. Wimberly, R. A. Cook, A. Vijayaraghavan : A high resolution lunar gravity field and predicted orbit behavior, *AAS/AIAA Astrodynamics Specialist Conference, Pap. #* **AAS 93-622**, Victoria, B.C., August, (1993).

Milani, A., A. M. Nobili, and P. Farinella : *Non-gravitational Perturbations and Satellite Geodesy*, Universita di Pisa, Italy, (1987).

Marshall, J. A. and S. B. Luthcke : Radiative force model performance for TOPEX/POSEIDON, *Geophys. Res. Lett.*, **21**, 2171-2174, (1994).

仙石新 : SELENE による月重力場推定に関する考察, *本収録*, (1998).

Sengoku, A., M. K. Cheng, B. E. Schutz : Anisotropic Reflection Effect on Satellite, Ajisai, *J. Geod.*, **70**, 140-145, (1995).

New Regions of Escape in the Free-Fall Three-Body Problem with masses 3, 4 and 5

Takeshi Nakamura
Okayama Shoka University, 2-10-1 Kyomachi Tushima Okayama, 700-8601, Japan

Abstract. We consider the free-fall three-body problem with masses 3, 4 and 5. We obtain numerically new regions of escape near the equilateral triangular position among already known three kinds of regions of escape. All orbits in our new regions of escape have only one minimum of moment of inertia.

1. Introduction

We consider the free-fall three-body problem with masses m_1=4, m_2=5 and m_3=3. In 1995, Broucke gave numerically the regions of escape in this three-body problem [3]. In Figure 1, we sketch Broucke's regions of escape I , II and III near the equilateral triangular position L_4 , and the masses indicate the escape bodies. The same kinds of regions were obtained for the equal masses by Umehara and Tanikawa [6] and Zare and Szebehely [9]. In this case, between two of these three regions of escape there exists a small region of escape near the equilateral triangular position [6] (see Figure 2). The orbits in the large regions are called *simple pass through orbits* by Anosova [2] (see Figure 3 (a)). On the other hand, the orbits in the small regions are called *pass through orbits with a turn* [2] (see Figure 3 (b)). We simply call these orbits *quick return orbits* according to [9]. Our aim of this article is to examine the three narrow regions among Broucke's three kinds of regions of escape I , II and III near the equilateral triangular position L_4 to obtain new small regions of escape. The escape orbits in our regions have only one minimum of moment of inertia.

We find that there exists clearly a small region of escape with the quick return orbits in every narrow regions. Furthermore, we also have two more regions of escape between I and III. The same regions are obtained between II and III. While, between I and II there exists only one region of escape, which has the quick return orbits. Moreover we can see not only the simple pass through orbits but also the *exchange orbits* in I . The exchange orbits were defined also by [2] and an example is illustrated in Figure 3(c). For the equal masses, these orbits do not appear near L_4. The orbits between I and III are more complicated. For example, there exist new escape orbits called *pass through orbits with a rotation*. These orbits are shown in Section 4.

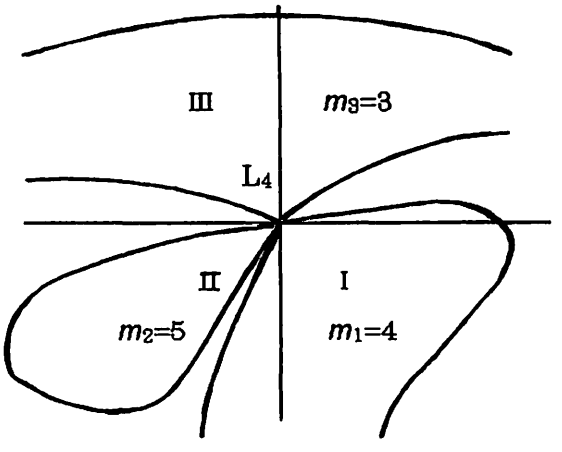

Fig. 1. Broucke's regions of escape near the equilateral triangular position L_4.

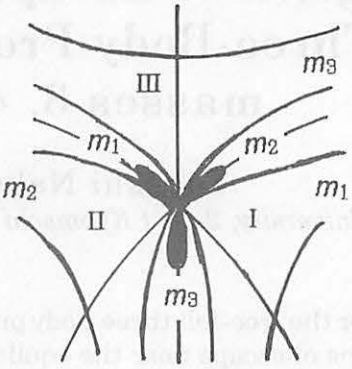

Fig. 2. Umehara and Tanikawa's region of escape for the equal masses near the equilateral triangular position L_4.

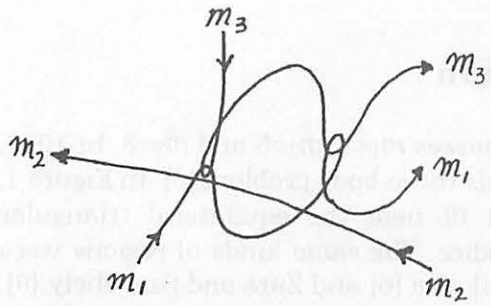

Fig. 3(a). A simple pass through orbit.

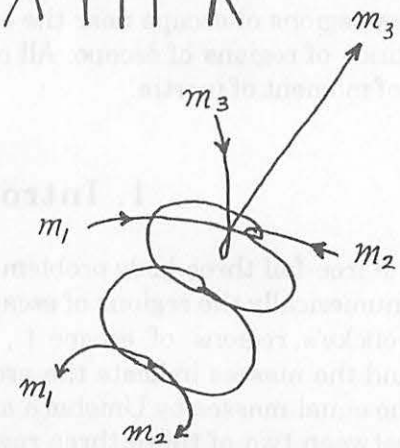

Fig. 3(b). A quick return orbit.

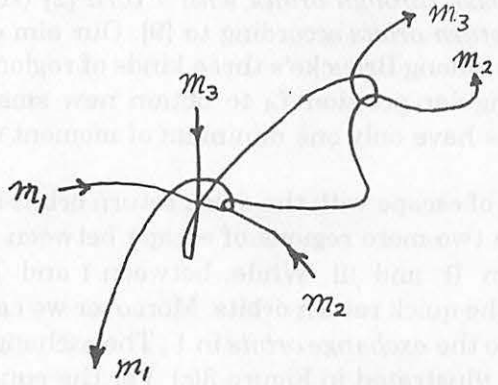

Fig. 3(c). An exchange orbit.

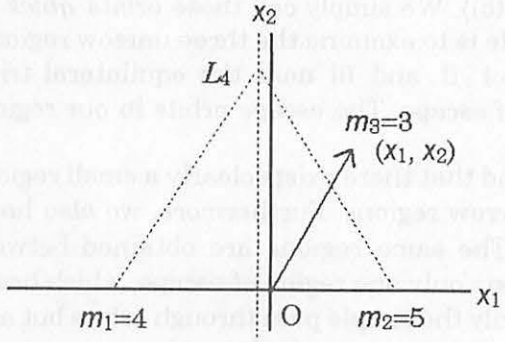

Fig. 4. The initial positions of masses.

2. Configuration of Masses

We show the configuration of masses $m_1=4$, $m_2=5$ and $m_3=3$ in Figure 4. Let m_1 and m_2 be set at $(-m_2/(m_1+m_2), 0)=(-5/9, 0)$ and $(m_1/(m_1+m_2), 0)=(4/9, 0)$, respectively. The distance between m_1 and m_2 is 1. The mass m_3 has coordinates (x_1, x_2). Let $L_4=(-1/18, \sqrt{3}/2)$ be the equilateral triangular position.

We consider a circle at center L_4 with radius 0.01(see Figure 7). We restrict $m_3=3$ on this circle, and examine the regions of escape on it using an angle variable θ $(0° \leqq \theta < 360°)$, where

$$x_1=0.01\cos\theta - 1/18, \quad x_2=0.01\sin\theta + \sqrt{3}/2.$$

3. Conditions for the moment of inertia and escape

3.1. A condition for the moment of inertia

This section is due to Yoshida [7], and see Agekian and Martynova [1] and Zare [8]. Let I be the half of the moment of inertia

$$I=(1/2\mathrm{M})\sum_{1\le i<j\le 3} m_i m_j r_{ij}^2 . \tag{1}$$

where r_{ij} be the mutural distances, and $\mathrm{M}=m_1+m_2+m_3$. The Lagrange-Jacobi identity is

$$\ddot{I}=2h+U, \tag{2}$$

where $h=\mathrm{T}-\mathrm{U}$ is the integral of energy and $U=G\sum_{1\le i<j\le 3} m_i m_j/r_{ij}$. Let $\mathrm{M}^*=\sum_{1\le i<j\le 3} m_i m_j$. Then,

$$(2I)^{1/2}\,U \ge G(\mathrm{M}^{*3}/\mathrm{M})^{1/2} . \tag{3}$$

Therefore, from the Lagrange-Jacobi identity we have

$$\ddot{I} \ge 2h+G(\mathrm{M}^{*3}/\mathrm{M})^{1/2}(2I)^{-1/2}. \tag{4}$$

Let

$$I_c=G^2\mathrm{M}^{*3}/(8h^2\mathrm{M}). \tag{5}$$

If $I<I_c$, then $\ddot{I}>0$, and $I=I(t)$ has only one minimum. The system in which $U>-2h$ (i. e., $\ddot{I}>0$) is called *triple close approach* by Agekian and Martynova [1]. In our case, G=1 and when $h=-13.2883$, we have $I_c=6.1246$. Although the energy value h changes according to θ, the bounds of h are $-13.288<h<-13.289$ for all orbits, and so $6.1240<I_c<6.1249$.

The initial value of I is I_0= 24.5 and all our orbits enter the region $I<I_c$. After that, the orbits escape. Therefore, our orbits have only one minimum of moment of inertia and in other wards, have only one triple close approach before escape (see Figure 5).

3.2. Escape conditions

We used the escape conditions due to Lasker and Marchal [4], one of which is rewritten by I [5]. Let m3 escape and $m_1\le m_2$. Let $(\mathbf{r},\rho)$ be the Jacobi coordinates, where $\mathbf{r}$ is a vector from m_1 to m_2 and ρ from the center of mass of m_1 and m_2 to m_3, and $r=|\mathbf{r}|$, $\rho=|\rho|$. Then, the escape conditions are

$$\text{(i)}\quad \rho \ge kr, \qquad \text{(ii)}\quad \dot{I} \ge a+b\,I^{1/4}, \tag{6}$$

where

$$\left.\begin{aligned} a &= m_1 m_2\{2G\mathrm{M}^*/(-h(m_1+m_2))\}^{1/2},\\ b &= \{2m_3(m_1+m_2)/\mathrm{M}\}^{3/4}K(k)^{1/2},\\ K(k) &= G\mathrm{M}\{\alpha_1/(1-\alpha_2/k)^2+\alpha_2/(1+\alpha_1/k)^2\},\\ \alpha_1 &= m_1/(m_1+m_2), \qquad \alpha_2=1-\alpha_1, \end{aligned}\right\} \tag{7}$$

and k is lager than the ratio ρ/r corresponding to the collinear central configuration L_1

with an arrangement (m_2, m_1, m_3). In our case L_1 = 1.4411, 1.5645 and 1.6357 according to the arrangements (m_2, m_1, m_3), (m_2, m_3, m_1) and (m_1, m_3, m_2), respectively. Therefore, we take k = 1.7. Figure 5(a-2) shows the three curves of escape condition (ii) according to the escape bodies m_1, m_2 and m_3.

Note that if (i) and (ii) of (6) are satisfied at $t=t_1$, then (i) is forever satisfied after t_1. While (ii) is not necessary satisfied after t_1. The original escape conditions of Lasker and Marchal are both satisfied forever after t_1. On the other hand, the condition (ii) of (6) is not. It is a sufficient condition of Laskar and Marchal's escape condition. Figure 5 shows the examples of the escape orbits. Figure 5(a-1) is a quick return orbit and Figure 5(b-1) is a more complicated escape orbit (see Figure 10). Figure 6 shows an example of the orbit which does not escape after the first minimum of the moment of inertia I.

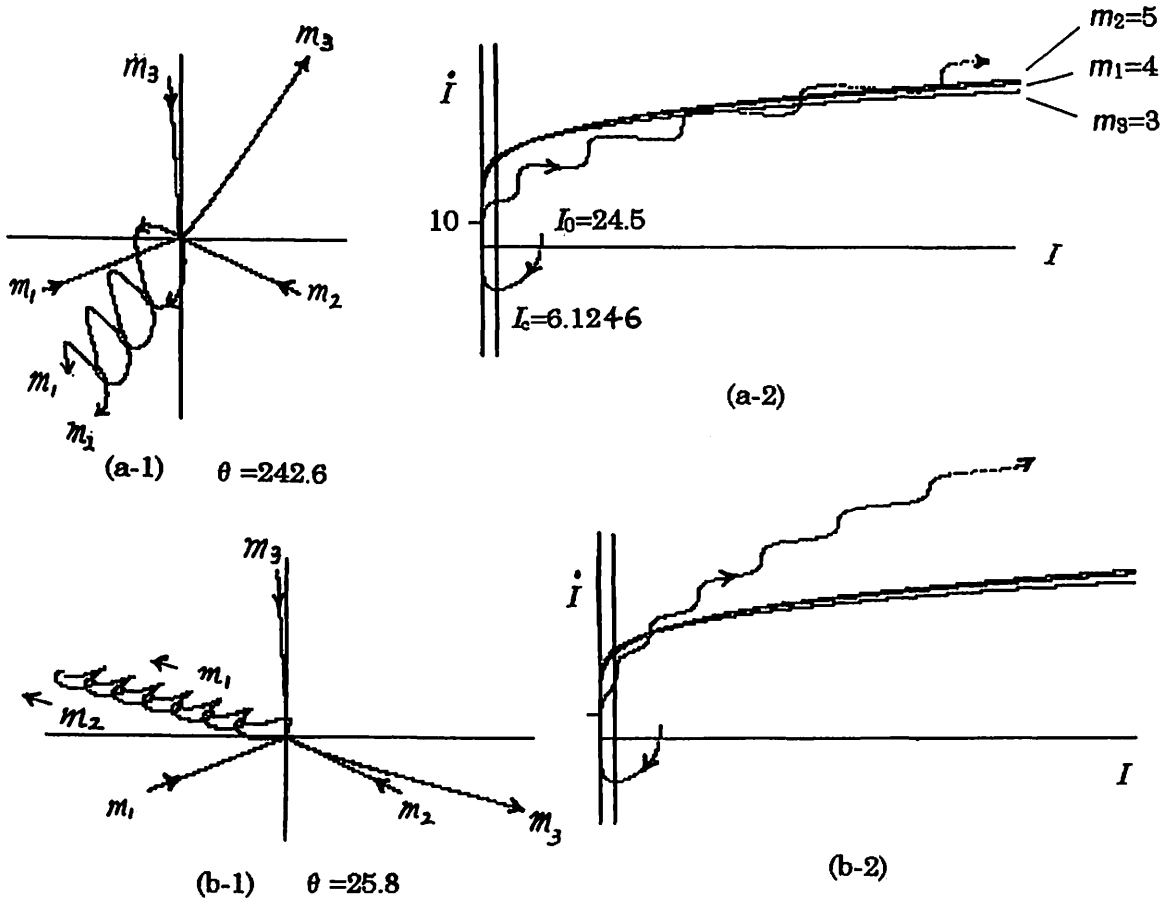

Fig. 5. The examples of the escape orbits.

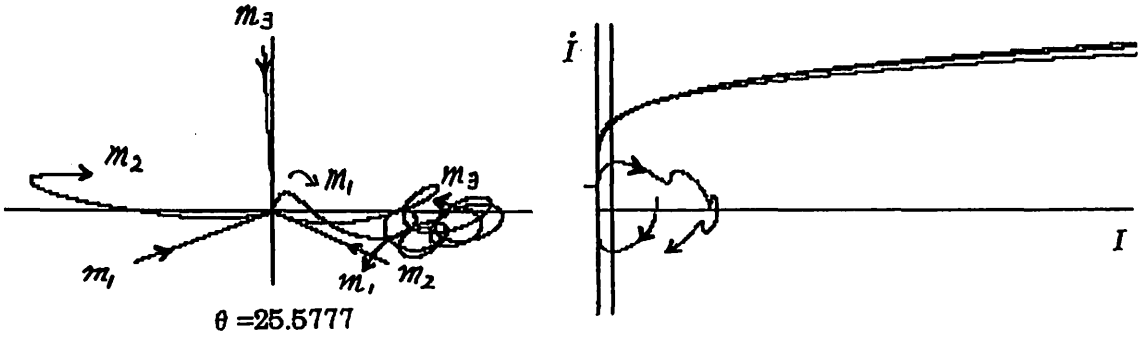

Fig. 6. An example of the nonescape orbit after the first minimum of I.

4. Results of Numerical Integrations

Our results are sketched in Figure 7. The large regions I , II and III are Broucke's regions of escape, and the masses indicate the escape bodies. There is only one region of escape between I and II, where m_3=3 escapes. On the other hand, there exist three kinds of regions of escape between I and III, where m_2=5 and m_3=3 escape. The same three regions also exist between II and III, where m_1=4 and m_3=3 escape. The detailed values of θ and (x_1, x_2) are summarized in Table 1 for regions I , II and III, and in Table 2 for small regions named (a), (b), (c), (d), (e), (f) and (g).

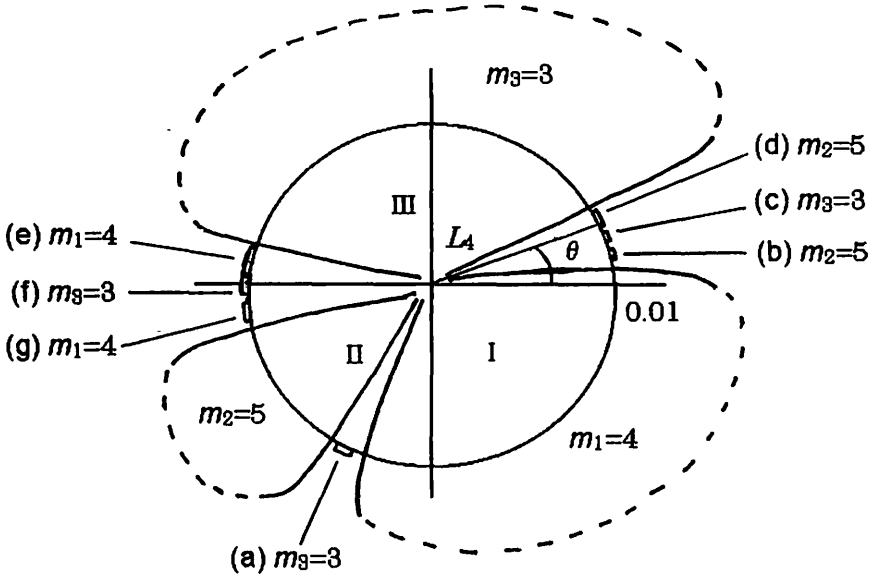

Fig. 7. The new regions of escape on the circle at center L_4 with radius 0.01 after the first minimum of the moment of inertia.

$\frac{\sqrt{3}}{2}=0.866025$

Escape region (Escape body)	θ (degree) ($0° \leqq \theta < 360°$)	(x_1, x_2)
I (m_1=4)	0	(−0.045555, 0.866025)
	6.5	(−0.045619, 0.867157)
	248.0	(−0.059301, 0.856753)
	360	(−0.045555, 0.866025)
II (m_2=5)	192.8	(−0.065307, 0.863809)
	238.0	(−0.060854, 0.857544)
III (m_3=3)	25.7	(−0.046544, 0.870361)
	169.47	(−0.065387, 0.867852)

Table 1. Intervals of Brouck's regions of escape on the circle at center L_4 with radius 0.01.

Escape region		Escape body	θ (degree) ($0° \leqq \theta < 360°$)	(x_1, x_2)
between I and II	(a)	m_3=3	241.3 244.3	(−0.060357, 0.857253) (−0.059892, 0.857014)
between I and III	(b)	m_2=5	9.0 11.0	(−0.045678, 0.867589) (−0.045739, 0.867933)
	(c)	m_3=3	12.8 17.635	(−0.045804, 0.868240) (−0.046025, 0.869054)
	(d)	m_2=5	17.655 25.45	(−0.046026, 0.869058) (−0.046525, 0.870322)
between II and III	(e)	m_1=4	169.53 179.29	(−0.065389, 0.867842) (−0.065554, 0.866149)
	(f)	m_3=3	179.32 186.3	(−0.065554, 0.866144) (−0.065495, 0.864928)
	(g)	m_1=4	187.5 191.5	(−0.065470, 0.864720) (−0.065354, 0.864031)

Table 2. Intervals of escape of new regions of escape on the circle at center L_4 with radius 0.01.

Let us see the typical orbits in these regions.

Orbits between I and II

Figure 8 shows the change of the orbits from II, (a) to I. The orbits θ=217 and θ=230 are the simple pass through orbits with escape body m_2=5 in II. In θ=239.3 and θ=240, m_1=4 change the mass component of a temporary binary system from m_3=3 to m_2=5. And in θ=242 and θ=244, m_3=3 escapes. These orbits are the quick return orbits in the small region of escape (a). Then, after the change of the mass components, we have the exchange orbits θ=249.5 and θ=255.5 in I. In these orbits, m_1 and m_2 interact closely at first, then m_2 and m_3 form a binary system with escape body m_1=4. Finally, θ=282 is a simple pass through orbit in I.

Orbits between I and III

Figure 9 and 10 show the change of the orbits from I, (b), (c), (d) to III. The orbit θ=3 is a simple pass through orbit with escape body m_1=4 in I. After the change of the mass components, we have a new type of the pass through orbits θ=9 and θ=11 in (b), where m_2=5 escapes. These orbits are called *pass through orbits with a rotation*, because m_2=5 has a small rotation before escape. Then, after having the change of the mass components, we enter the region (c), where the orbits are the exchange orbits with the escape body m_3=3, since at first m_1 and m_3 interact closely, then m_1 and m_2 form a binary system.

Between θ=17.7 and θ=25.2, we have the orbits in the region (d), where m_2=5 escapes. Between θ=17.7 and θ=20 we have the quick return orbits. We note that after the quick

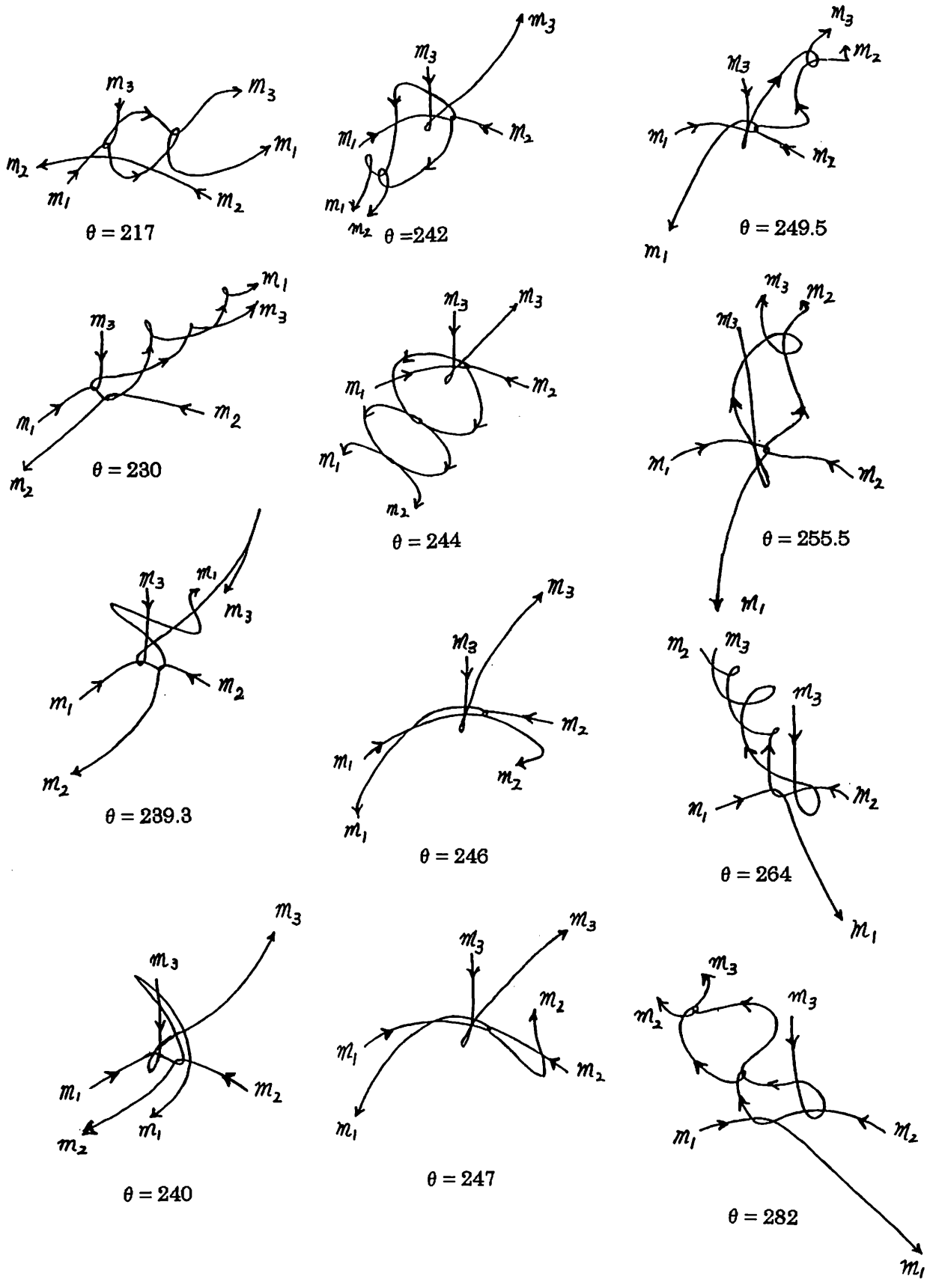

Fig. 8. The change of the orbits from II, (a) to I.

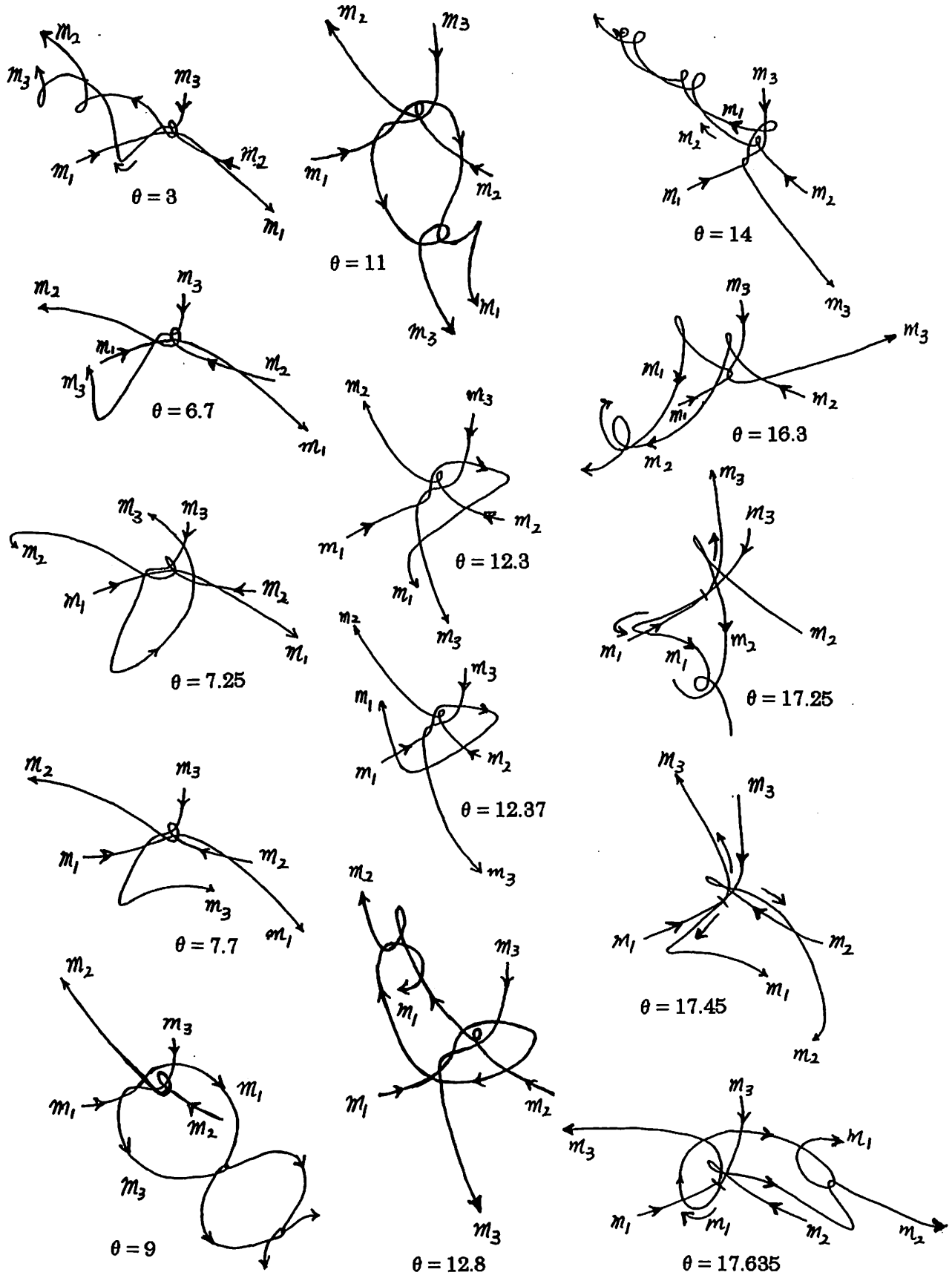

Fig. 9. The change of the orbits from I , (b), (c), (d) to III.
(from θ =3 to θ =17.635)

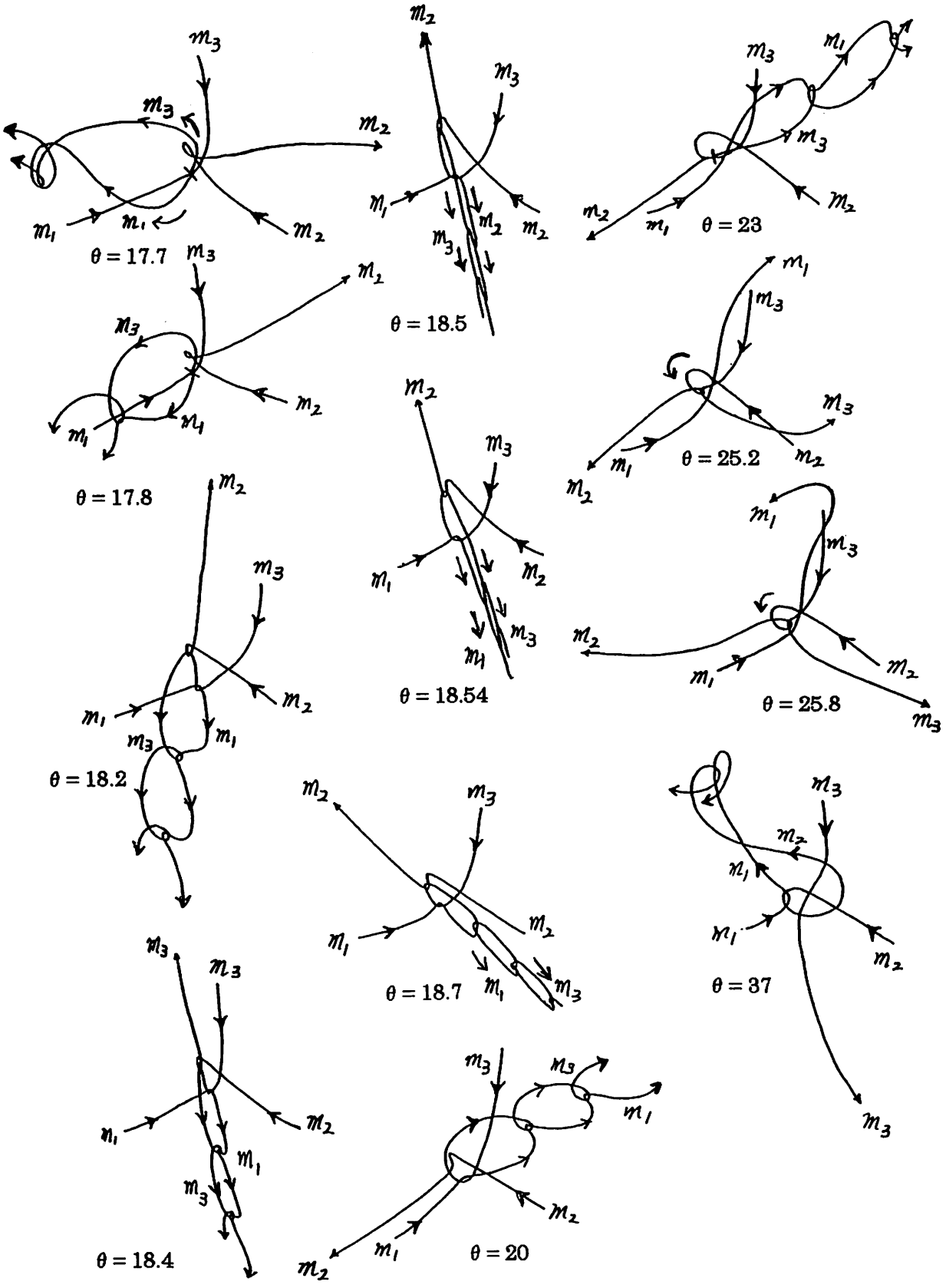

Fig. 10. The change of the orbits from I , (b), (c), (d) to III.
(from θ =17.7 to θ =37)

return of m_2=5 the direction of escape of it changes almost 180°. The surprising fact is that the orbits θ =18.5 and θ =18.54 are very close to the collinear motion. In θ =23, a binary collision of m_2 and m_3 occurs. In θ =25.2 and θ =25.8, m_1 changes the component of mass of the binary system from m_3 to m_2. In θ =25.2, m_2 escapes, while in θ =25.8, m_3 escapes. The orbits in θ =23,..., θ =25.8 are very complicated. They experience the binary approach three times with different mass components before escape, near the minimum of the moment of inertia I (see Figure 11). This was mentioned in Section 3.2.

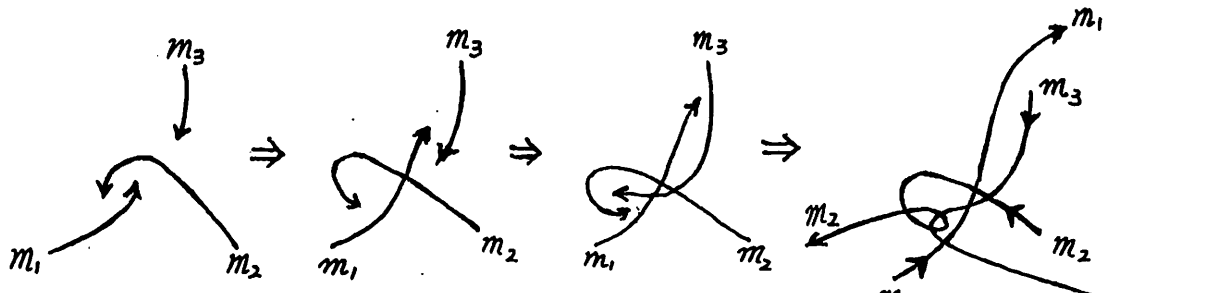

(1) The interplay of m_1 and m_2.

(2) The interplay of m_1 and m_3.

(3) The interplay of m_2 and m_3.

Fig. 11. θ =25.8 .

Acknowledgement

We would like to thank Dr. K. Tanikawa, Dr. H. Umehara and Prof. J. Yoshida for giving us many printed materials. We also appreciate Dr. T. Hukushima for his valuable comments.

References

[1] Agekian, T. A. and A. I. Martynova: 1973, *Messeng. Leningrad Univ.*, **28**, 85.

[2] Anosova, Zh. P.: 1989, States of strong gravitational interaction in the general three-body problem, *Sov. Astron*, **33(1)**, 79.

[3] Broucke, R. A.: 1995, On the role of the moment of inertia in three-body scattering, in *From Newton to chaos*, A. E. Roy and B. A. Steeves ed., Plenum Press, New York, 327.

[4] Laskar, J. and C. Marchal: 1984, Triple close approach in the three-body problem: A limmit for the bounded orbits, *Celest. Mech.*, **32**, 15.

[5] Nakamura, T.: 1993, Condition of the hyperbolic-elliptic escape, in *Proceedings of the 26th symposium on celestial mechanics*, H. Kinoshita and H. Nakai ed., 109.

[6] Umehara, H. and K. Tanikawa: 1995, Escape probability at the first collapse in the free-fall three-body problem, in *Proceedings of the 27th symposium on celestial mechanics*, H. Kinoshita and H. Nakai ed., 219.

[7] Yoshida, J.: 1990, Triple close approach, not printed.

[8] Zare, K.: 1981, Propoerties of the moment of inertia in the problem of three bodies, *Celest. Mech.*, 24, 345.

[9] Zare, K. and V. Szebehely: 1995, Order out of chaos in the three-body problem: Regions of escape, in *From Newton to chaos*, A. E. Roy and B. A. Steeves ed., Plenum Press, New York, 299.

Structure of KAM Curves in the Standard Mapping

Yoshihiro YAMAGUCHI
Teikyo Heisei University,Ichihara,Chiba 290-0193,Japan.

Kiyotaka TANIKAWA
National Astronomical Observatory,Mitaka,Tokyo 181-8588,Japan.

Abstract

The structure of KAM curves in the standard mapping on the surface of cylinder is investigated. We report the results on the symmetry structure of KAM curve, and the mechanism of disappearence of KAM curve.

1 Introduction

Birkhoff[1] proved that homotopically non-trivial KAM curves of twist maps of the annulus are Lipschitz continuous. This implies that these KAM curves of twist maps are at least once differentaible almost everywhere on the KAM curve in the sense of Lebesgue measure(Herman[2]). When we consider a one-parameter($0 < a < \infty$) family of smooth twist maps starting from an integrable map, we can generally expect that the smoothness of the KAM curves decreases as the maps become more and more apart from the integrable one(Moser[3]).

In the present paper, based on the above expectation, we consider a typical example of analytical family of twist maps, the standard mapping, and first develop a numerical method for the determination of the critical values of the destruction of KAM curves and then examine how the twice differentiability of KAM curves are deteriorated until the critical value of their destruction.

In doing this we assume that KAM curves are once differentiable at some particular points(see §7). Though this assumption is not assured, our results seem to justify it.

We introduce the standard mapping in §2, and the involution form in §3. In §4, we derive the functional equation for KAM curves and intoduce the circle map. The properties of KAM curve in the phase space are obained in §5 and the properties of the circle map are obtained in §6. In §7, we calculate the critical value a_c, and discuss the structure change of distribution of mapped points. In §8, we shall give the discussion.

2 The standard mapping $T(x, y)$ on the cylinder

The standard mapping $T(x, y)$ $[-\infty<y<\infty, 0 \leq x<2\pi]$ on the surface of cylinder is expressed as[4].

$$y_{n+1} = y_n - a \sin x_n, \tag{1}$$
$$x_{n+1} = x_n + y_{n+1} (\mathrm{Mod}\ 2\pi) \tag{2}$$

where $a>0$ is assumed. In the following, we let $f(x_n) = -a \sin x_n$.

The standard mapping has the measure preserving and order preserving properties, and is a typical twist mapping. The standard mapping has two fixed points(p and q). One of the fixed point $q = (0, 0)$ is an elliptic point when $0<a<4$, and is a saddle with reflection when $a>4$. The other fixed point $p = (\pm\pi, 0)$ is always a saddle for $a > 0$. We can easily observe three types of motion in the phase space(See Fig.1): (1) the periodic motion, (2) the quasi-periodic motion, and (3) the chaotic motion. In this paper, we study the structure of KAM curves constructed by the quasi-periodic motion encircling the cylinder.

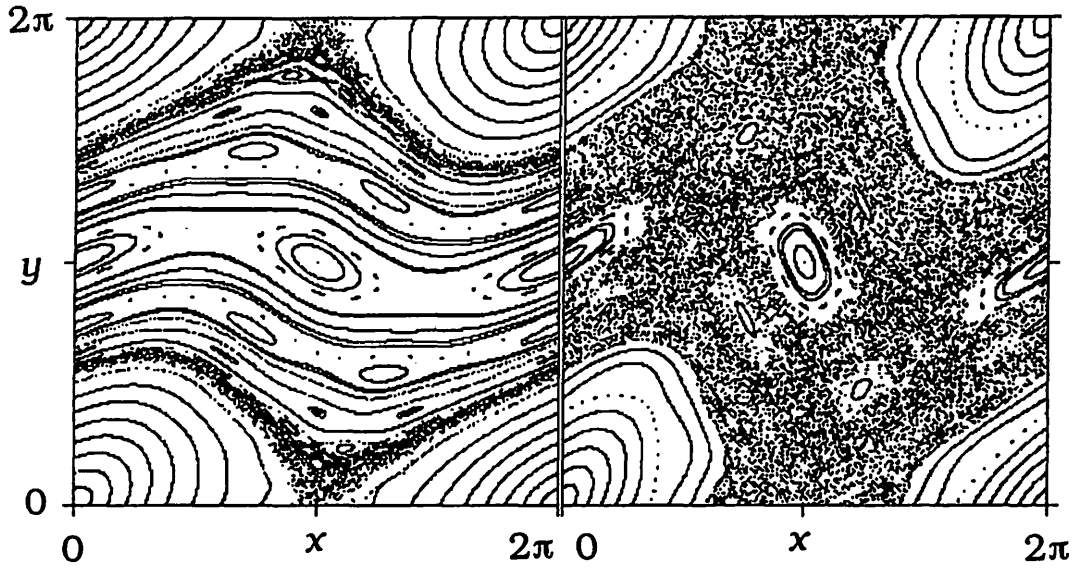

Fig.1 Several motions in the phase space($a = 0.8$(left), $\frac{4}{3}$(right)).

3 Involutionary forms of the standard mapping

The standard mapping T has the factorisation into two involutions h and g.

$$T = h \circ g. \tag{3}$$

Two involutions h and g satisfy the follwoing properties.

$$h \circ h = g \circ g = id., \tag{4}$$
$$\det Dh = \det Dg = -1. \tag{5}$$

It is noted that the inverse map of T is given by $T^{-1} = g \circ h$.

If the mapping functions have the factorisation into invlutions, the system has the reversiblity[4]. As the standard mapping has double reversibility[5], there are two types of involution forms.

[1] The first form

$$h : y_{n+1} = y_n,\ x_{n+1} = -x_n + y_n. \tag{6}$$
$$g : y_{n+1} = y_n + f(x_n),\ x_{n+1} = -x_n. \tag{7}$$

The set of fixed points of h and g give the symmetry lines illustrated in Fig.2.

$$h : y = 2x,\ y = 2(x \pm \pi), \tag{8}$$

$$g : x = 0,\ \pm\pi. \tag{9}$$

These symmetry lines of the first form show the left and right symmetry of KAM curve. We use this property in the following discussions.

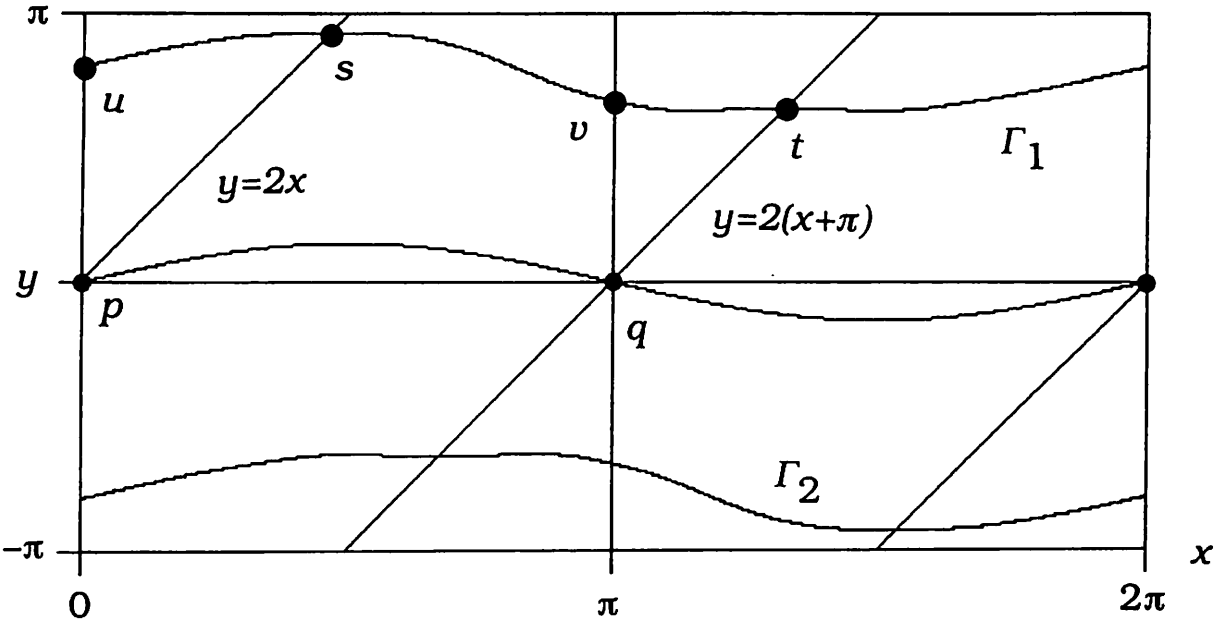

Fig.2 Symmetry lines in the phase space. Two KAM curves $\Gamma_{1,2}$ exist symmetrically above and below the x-aixs. The explanations of the points $u, v, \ldots$ are in §5.2.

[2] The second form

$$h' : y_{n+1} = -y_n,\ x_{n+1} = x_n - y_n, \tag{10}$$

$$g' : y_{n+1} = -y_n - f(x_n),\ x_{n+1} = x_n. \tag{11}$$

The symmetry lines are also obtained (see Fig.2).

$$h' : y = 0, \tag{12}$$

$$g' : y = \frac{a}{2}\sin x. \tag{13}$$

These symmetry lines show the symmetrical structure of two KAM curves existing above and below the x-axis. If one KAM curve(Γ_+) exists above the x-axis, another KAM curve(Γ_-) must exist at the symmetrical position corresponding to Γ_+ below the x-axis. Such a situation is illustrated in Fig.2. This symmetry does not give information to determine the structure of KAM curve($\Gamma_{+,-}$) itself. Then we do not use this symmetry.

4 The functional equation for KAM curves

A KAM curve is assumed to be expressed by $y_n = F(x_n)$ in the phase space. Here we introduce the circle map: $x_{n+1} = G(x_n)$ which defines the relation between x_n and x_{n+1}

on KAM curve. Using the mapping equations, we can derive the functional equations for $F(x)$ and $G(x)$, and give the relation between $F(x)$ and $G(x)$.

$$F(x+F(x)+f(x)) = F(x)+f(x), \tag{14}$$
$$G(x)+G^{-1}(x) = 2x+f(x), \tag{15}$$
$$G(x) = x+F(x)+f(x) \tag{16}$$

where the suffix n is omitted.

Hereafter we use the abbreviated notations:

$$\xi_n = \frac{dF(x_n)}{dx_n}, \qquad \zeta_n = \frac{dG(x_n)}{dx_n}, \qquad \epsilon_n = \frac{df(x_n)}{dx_n}.$$

Here ξ_n means the slope of KAM curve at x_n and ζ_n implies the gradient of $G(x_n)$ at x_n.

Differentiating Eqs.(14) and (15) with respect to x_n, we also have the functional equations for ξ_n and ζ_n.

$$\xi_{n+1} = \frac{\xi_n+\epsilon_n}{1+\xi_n+\epsilon_n}, \tag{17}$$
$$\zeta_{n+1} = -\frac{1}{\zeta_n}+2+\epsilon_{n+1}. \tag{18}$$

These equations are rewritten in the following forms.

$$\xi_{n-1} = \frac{\xi_n}{1-\xi_n}-\epsilon_{n-1}, \tag{19}$$
$$\zeta_{n-1} = \frac{1}{2+\epsilon_n-\zeta_n}. \tag{20}$$

These equations connect the derivative of mapping function to its past. In §5-7, we use Eq.(17) for ξ_n and Eq.(20) for ζ_n.

5 Properties of KAM curves in the phase space

5.1 Symmetrical structure of KAM curves

First, we shall give a property of motion of mapped points restricted on the KAM curve encircling the cylinder.

Proposition 5-1: Any KAM curve encircling the cylinder is invariant under g, and hence invariant under h.

Proof: If we prove any KAM curve is invariant under g, its invariance under h follows from $T = h \circ g$. Since KAM curve intersects the symmetry lines of g, let us take a point a of intersection. Let $O(a) = \{a_i | a_i = T^i a, i \in \mathbf{Z}\}$ be its orbit. By reversibility,

$g(a_n) = g \circ T^n a = T^{-n} \circ g(a) = T^{-n} a = a_{-n}$. This means that the orbit of a is invariant under g.

The orbit $O(a)$ are dense in the KAM curve. Let b be an arbitrary point of the curve. Then there exists a sub-sequence a_{n_i} ($n_i \to \infty$ as $i \to \infty$) which converges at b. By continuity of the reversibility, $g(b)$ is on the KAM curve and consequently its orbit is invariant under g. □

According to Proposition 5-1, let us take two positions $l = (x_l, y_l)$ and $r = (x_r, y_r)$ satisfying the relation $r = h(l)$ or $r = g(l)$ on the specified KAM curve. Using Eqs.(6) and (7), we can derive the relations of slopes at l and r. Here ξ_l and ξ_r mean the slopes at l and r. In the following expressions, we can exchange two suffices l and r.

[1] Relations with respect to the symmetry lines($y = 2x, y = 2(x \pm \pi)$) of h.

$$\xi_r = \frac{\xi_l}{\xi_l - 1}. \tag{21}$$

[2] Relations with respect to the symmetry lines($x = 0, x = \pm\pi$) of g.

$$\xi_r = -\xi_l - f'(x_l). \tag{22}$$

Eqs.(21) and (22) give imformation on the slope of KAM curves at their intersection points with the symmetry lines. Using the relation $\xi_l = \xi_r$ at the intersection points, we have the following results.

(1) At the intersection points of KAM curves and the symmetry lines of h.

$$\xi = 0. \tag{23}$$

(2) At the intersection points of KAM curves and the symmetry lines of g.

$$\xi(0) = -\frac{1}{2} f'(0) = \frac{a}{2}, \tag{24}$$

$$\xi(\pi) = -\frac{1}{2} f'(\pi) = -\frac{a}{2}. \tag{25}$$

Take a point $A = (x, y)$ on the KAM curve. The point $B = (x', y') = g(A)$ also locates on the same KAM curve due to Proposition 5-1. Using the relations $x' = -x, y' = y + f(x), y = F(x)$ and $y' = F(x')$, Eq.(14) can be rewritten in the form

$$F(x) - F(-x) = -f(x). \tag{26}$$

Here we separate the function $F(x)$ into the even and odd functions.

$$F(x) = F_{even}(x) + F_{odd}(x), \tag{27}$$

and then we have

$$F_{odd}(x) = -\frac{1}{2} f(x). \tag{28}$$

We need to determine the even part $F_{even}(x)$ to get the full expression of KAM curve. This problem will be discussed later.

Here we have an important result on the slope of KAM curves.

Proposition 5-2: The relation $\xi(x)<1$ holds for all KAM curves.

Proof: Suppose that there exists a point A with $\xi > 1$ on the KAM curve. But by Eq. (21), the slope at $B = h(A)$ is positive. Let take a small arc AA' on the KAM curve in the vicinity of A where the x-coordinate of A' is larger than that of A. Note that the y-coordinate of A' is larger than that of A since the slope at A is positive. The involution h maps this arc to an arc BB' where both x and y-coordinates of B' are larger than those of B since the slope of the KAM curve at B is positive. As three points A',the intersection point(C) of the KAM curve and the symmmetry line of h, and B' locate in order on the KAM curve. Then the arc CB' of the KAM curve must includes the point(D) where the slope diverges. If the slope at A is equal to 1, the value of slope at B diverges. Then the KAM curve does not satisfy the Lipschitz condition. This contradicts the result obtained by Birkhoff[1]. □

5.2 Summary of properties of KAM curve

In Table I, we list up the properties of KAM curve(see Fig.2) in the phase space in terms of the results obtained in §5.1.

Name	Position in phase space	Slope
u	$\stackrel{\text{def}}{=}(0,\alpha)$	$\frac{a}{2}$
Tu	(α,α)	$-\frac{a}{2-a}$
$T^{-1}u$	$(-\alpha(+2\pi),\alpha-a\sin\alpha)$	$a\cos\alpha+\frac{a}{2-a}$
v	$\stackrel{\text{def}}{=}(\pi,\beta)$	$-\frac{a}{2}$
Tv	$(\pi+\beta,\beta)$	$\frac{a}{2+a}$
$T^{-1}v$	$(\pi-\beta,\beta+a\sin\beta)$	$-a\cos\beta-\frac{a}{2+a}$
s	$\stackrel{\text{def}}{=}(\gamma,2\gamma)$	0
Ts	$(3\gamma-a\sin\gamma,2\gamma-a\sin\gamma)$	$\frac{a\cos\gamma}{a\cos\gamma-1}$
$T^{-1}s$	$(-\gamma(+2\pi),2\gamma-a\sin\gamma)$	$a\cos\gamma$
t	$\stackrel{\text{def}}{=}(\delta+\pi,2\delta)$	0
Tt	$(3\delta+a\sin\delta+\pi,2\delta+a\sin\delta)$	$\frac{a\cos\delta}{a\cos\delta+1}$
$T^{-1}t$	$(\pi-\delta,2\delta+a\sin\delta)$	$-a\cos\delta$

Table I: u is the intersection point of KAM curve and $y-$axis, v is the intersection point of KAM curve and $x = \pi-$axis, s is the intersection point of KAM curve and the line $y = 2x$, and t is the intersection point of KAM curve and the line $y = 2(x - \pi)$.

Proposition 5-2 gives information on the positions of u, v, s and t.

Property 5-3: The positions u, v, s and t satisfy the relations

$$(1)\ a\cos\alpha < \frac{2(1-a)}{2-a},\ (2)\ a\cos\beta > -1 - \frac{a}{2+a},\ (3)\ a\cos\gamma < 1,\ (4)\ -a\cos\delta < 1.$$

6 Property of the circle map $G(x)$

6.1 Symmetry of $G(x)$

Proposition 6-1 : The graph of $G(x)$ is symmetrial with respect to the lines $y = -x(\pm\pi)$. Then the relation $G(x) = -G^{-1}(-x)$ holds.

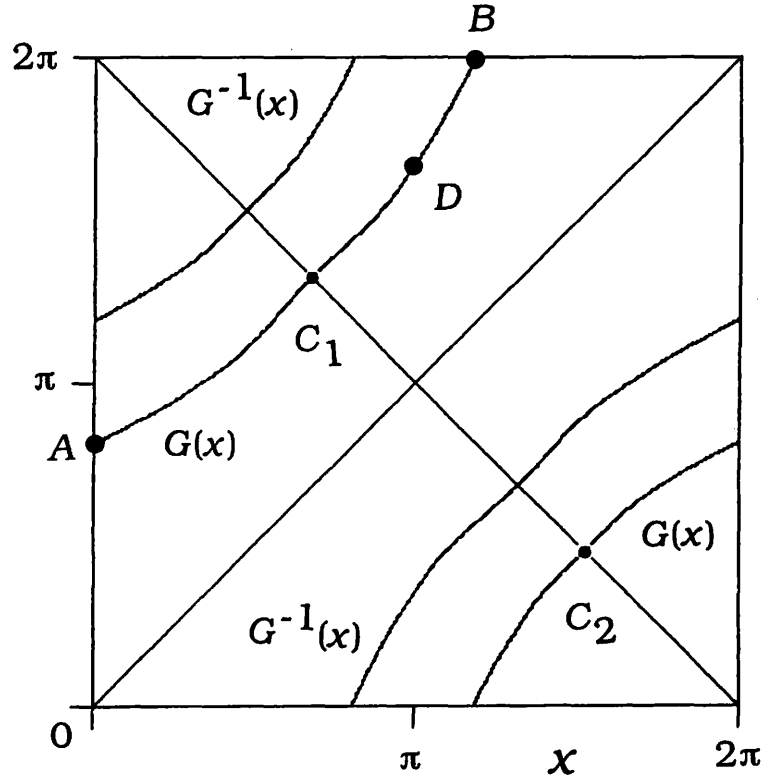

Fig.3 The circle map $G(x)$ and its symmetry structure

Proof: Inserting the relation $x_n = G^{-1}(x_{n+1})$ into Eq.(2), we have

$$G^{-1}(x_{n+1}) = x_{n+1} - y_{n+1}.$$

Omitting the suffices and inserting the relation $y = F(x)$ into the above equation, we have the relation

$$G^{-1}(x) = x - F(x). \qquad (*)$$

Eq.(*) is rewritten in the form

$$-G^{-1}(-x) = x + F(-x). \qquad (**)$$

Combining Eq.(16) and Eq.(**) we have

$$G(x) - (-G^{-1}(-x)) = F(x) - F(-x) + f(x). \qquad (***)$$

Inserting Eq.(27) into the r.h.s of Eq.(***), we have

$$(\text{r.h.s. of Eq.}(***)) = 2F_{odd}(x) + f(x).$$

Using Eq.(28), we can show that the r.h.s. of the above equation is equal to zero. Then Proposition is proved. □

Proof: Here we shall give another proof in terms of the relation between the phase space and the circle map. We shall list several correspondence of the phase space and the circle map.

Operation in Phase Space	$\Leftrightarrow$	Operation in Circle Map
g	$\Leftrightarrow$	$x \mapsto -x$
h	$\Leftrightarrow$	$G(-x)$
T	$\Leftrightarrow$	$G(x)$

Then $-G^{-1}(-x)$ is considered as the composition of succesive three operations

$$(1)\ x \mapsto -x,\ \ (2)\ G^{-1},\ \ (3)\ x \mapsto -x.$$

These operations are transformed into the operations in the phase space

$$(1)\ \text{Operate } g,\ \ (2)\ \text{Operate } T^{-1},\ \ (3)\ \text{Operate } g.$$

As a result, we have

$$g \circ T^{-1} \circ g = g \circ g \circ h \circ g = h \circ g = T.$$

This final operation T is transformed into the operation $G(x)$ of circle map. Then Proposition 6-1 is proved. □

Here it is important to note that the reversibility($T \circ g = g \circ T^{-1}$) determines the expression of $F_{odd}(x)$(see Eq.(28)), and gives the symmetry of $G(x)$ stated in Proposition 6-1.

Using this Propositin, we shall give several properties of circle map in §6.2.

6.2 Properties of G_{odd} and the functional equation for G_{even}

We shall give the explicit expressions of G_{odd} and G_{odd}^{-1} and derive the functional equaiton for G_{even}.

Property 6-2: $G_{odd}(x) = G_{odd}^{-1}(x) = x + \frac{1}{2}f(x)$.

Proof: Combining the relation of Proposition 6-1 and Eq.(15), we have

$$G(x) - G(-x) = 2x + f(x). \tag{29}$$

Here we divide $G(x)$ into the even and odd functions

$$G(x) = G_{even}(x) + G_{odd}(x). \tag{30}$$

As a result, Eq.(29) defines the odd function G_{odd}.

$$G_{odd}(x) = x + \frac{1}{2}f(x). \tag{31}$$

Using the same method, we have

$$G^{-1}_{odd}(x) = x + \frac{1}{2}f(x). \tag{32}$$

Then we have Property 6-2. □

Using Eqs.(15) and Property 6-2, the relation of $G_{even}(x)$ and $G^{-1}_{even}(x)$ is derived.

$$G_{even}(x) + G^{-1}_{even}(x) = 0. \tag{33}$$

Combining the relation $G^{-1}(G(x)) = x$, Eqs.(29), (33), and Property 6-2, the functional equation for $G_{even}(x)$ is obtained.

$$G_{even}(G(x)) = G_{even}(x) + \frac{1}{2}f(x) + \frac{1}{2}f(G(x)). \tag{34}$$

The initial condition $(G(0))$ to solve Eq.(34) are obtained as follows. Since $G(0) = G_{even}(0) + G_{odd}(0) = G_{even}(0) \equiv m \times 2\pi$ and $F(0) = G(0) = G_{even}(0)$, the value of m is determined by the initial condition $(0, m \times 2\pi)$ in the phase space.

Applying the same procedure mentioned above to the circle map $G(x+\pi)$, we also have the same results for $G_{even}(x)$. Then we have Property 6-3:

Property 6-3 The even part function $G_{even}(x)$ has two symmetry lines $x = 0$ and $x = \pi$.

We can derive the functional equations for $G'_{even}(x)$.

$$G'_{even}(G(x)) = \frac{1}{2}f'(G(x)) + \frac{G'_{even}(x) + \frac{1}{2}f'(x)}{G'_{even}(x) + \frac{1}{2}f'(x) + 1}. \tag{35}$$

The property of even function and Property 6-3 give the initial coditions to solve Eq.(35).

$$G'_{even}(0) = G'_{even}(\pm\pi) = 0.$$

6.3 Structure of the golden mean KAM curve

Here we study the structure of KAM curve characterized by the golden mean rotation number. To do so, we have to solve the functional equations for G_{even} and G'_{even} numerically. The KAM curve with the golden mean $\frac{\sqrt{5}-1}{2}$ is identically equal to that with the rotation number $1-\frac{\sqrt{5}-1}{2}$. Hereafter we calculate the KAM curve with the rotation number $1-\frac{\sqrt{5}-1}{2}$.

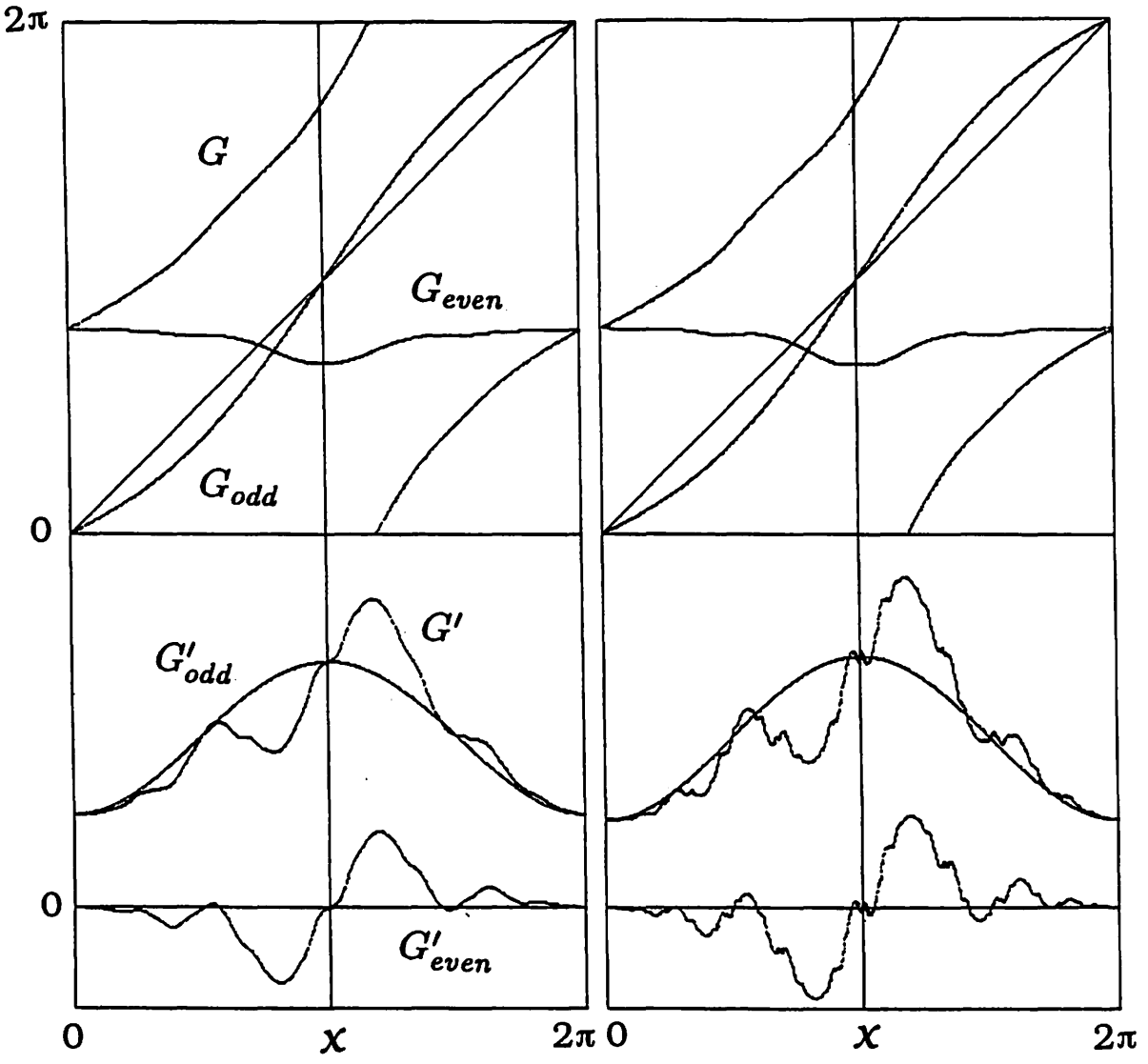

Fig.4 The upper figures show G_{even}, G_{odd}, and G, and the lower figures show G'_{even}, G'_{odd} and G'(a=0.9(left), 0.97(right)).

We show the procedure to solve the functional equations.

Procedure

[Step 1] Calculate the time series starting from the intersection point ($m \times 2\pi$) of y-axis and KAM curve and specify the rotation number. Using this imformation, determine the value m to give the golden mean KAM curve.

[Step 2] Calculate the mapping T, G_{even}, and $G'_{even}(x)$ with the initial conditions.
(1)the position of phase space $(0, m \times 2\pi)$.
(2)the initial value of $G_{even}(x)$:$G_{even}(0) = m \times 2\pi$.
(3)the initial value of $G'_{even}(x)$: $G'_{even}(0) = 0$.

The numerical results are shown in Fig.4. The symmetry of G and the several relations menstioned §6.2 are confirmed. For the structure of $G'_{even}(x)$, we observe the transition from the smooth curve to the notched curve when the parameter a is increased toward the critical value $a_c = 0.971635\ldots$(see §7.2)[6]. This is caused by the amplification of non-anylitic property of G_{even} in the vicinity of the critical value. This transition is also found in KAM curves with other irrational rotation number.

6.4 Estimation of maximum and minimun values of $G'(x)$

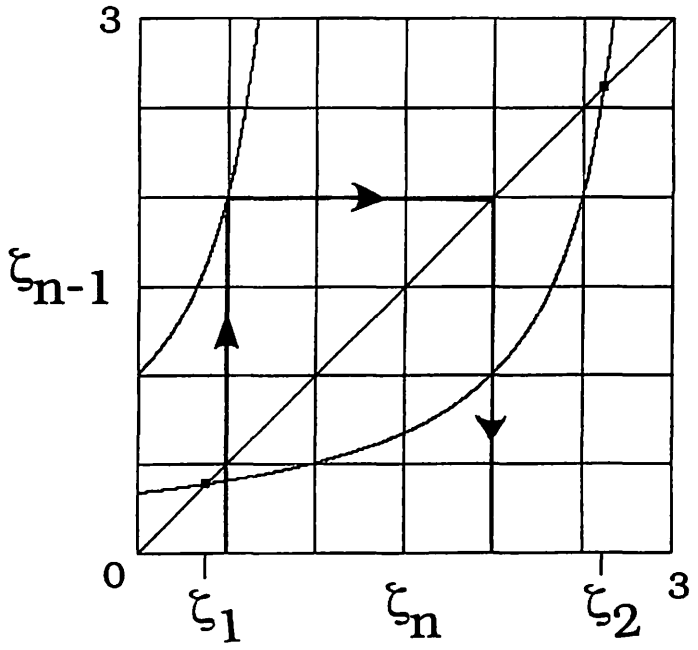

Fig.5 Mapping function of $\zeta_n \mapsto \zeta_{n-1}(a = 1)$.

If the maximum value of $\zeta(x)(= G'(x))$ is M, then the minimum value ζ_{min} is $\zeta_{min} = \frac{1}{M}$ due to the symmetry of $G(x)$(Proposition 6-1). The position with the maximum value M exists at the symmetrycal position of that with the minimum value $\frac{1}{M}$ where the symmetry lines are $y = -x(\pm\pi)$. Hereafter we estimate M. Eq.(20) with $a = 1$ is illustrated in Fig.5. The lower(upper) curve shows the mapping function with $\epsilon_n = 1(-1)$. All mapping functions exist in the region sandwiched by these two curves. Then if there exists the integer n satisfying $\zeta_n > \zeta_2$, the series $\{\zeta_i\}(i \geq n+1)$ diverges. If there exists the integer n satisfying

$0 < \zeta_n < \zeta_1 = \frac{1}{\zeta_2}$, there exists the integer $m \neq n$ satisfying $\zeta_m = \frac{1}{\zeta_n}$ due to the symmetry and then the series $\{\zeta_i\}(i \geq m+1)$ diverges. As a result, we have the maximum value M of ζ_n.

$$M = \frac{2 + a + \sqrt{a^2 + 4a}}{2}. \tag{36}$$

The following inequality relation for any integer n holds.

$$\frac{1}{M} \leq \zeta_n \leq M. \tag{37}$$

This result is equal to that obtained by Herman [2]. Herman estimated the minimum value ζ_{min}.

$$\frac{2 + a - \sqrt{a^2 + 4a}}{2} \leq \zeta_{min} \leq 1 - \frac{a}{2}. \tag{38}$$

According to the numerical results shown in Fig.6, we have

$$\text{Minimum value} \approx 1 - \frac{a}{2}, \quad \text{Maximum value} \approx \frac{1}{1 - \frac{a}{2}}.$$

Can we have better esimation for the maximum and minimum values compared with Eq.(37)?

The abovementioned property of the slope of G corresponds to Theorem by Denjoy[7].

Theorem: If $G : S^1(\text{circle}) \to S^1$ is a C^1 diffeomorphism and its derivative is a function of bounded variation then G does not have a wandering interval.

Then the property of bounded variation of $G'(x)$ limitted by Eq.(37) guarantees the existence of KAM curve. This fact requires that $G(x)$ is a C^2–deffeomorphism. If the C^2–property of $G(x)$ for KAM curve with certain irrationa rotation number does not hold for certain value of a, it is possible to appear a wanderring interval in KAM curve. As a result, the infinitely many holes appear in KAM curve, and then KAM curve dissappears and the Cantor set(so called Aubry-Mather set[8]) appears. The Cantor set does not play the role of barrier.

6.5 Summary of the properties of $G(x)$

[1] Here A shows the position of $G(0)$ in Fig.3.

$$\zeta(A) = 1 - \frac{a}{2}, \tag{39}$$

$$\zeta(B) = \frac{1}{1 - \frac{a}{2}} \tag{40}$$

where $A = G(B)$. The first relation gives Eq.(24) in the phase space.

[2] At the intersection points C_1 and C_2 of $G(x)$ and $y = -x(\pm\pi)$ is 1 due to Proposition 6-1.

[3] Using the same method in [1], We have the slope at D in Fig.3.

$$\zeta(\pi) \;=\; 1+\frac{a}{2}. \tag{41}$$

This relation gives Eq.(25) in the phase space.

7 Disappearance of KAM curves

7.1 Relation of the slopes of $F(x)$ and of $G(x)$

Differntiating the functional equation

$$F(G(x)) = F(x) + f(x), \tag{42}$$

we have the relation of ζ and ξ.

$$\xi(G(x))\zeta(x) \;=\; \xi(x)+\epsilon(x) = \zeta(x) - 1, \tag{43}$$

$$\zeta(x) \;=\; \frac{1}{1-\xi(G(x))}. \tag{44}$$

The invertibility of the circle map $G(x)$ gives the necessary condition $\zeta(x) > 0$ to exist KAM curve. Using Eq.(44),the relation $\xi(x)<1$(Proposition 5-2) is derived. We shall give the upper and lower bounds of ξ which are equivalent to Eq.(37).

$$1 - M \le \xi(x) \le 1 - \frac{1}{M}. \tag{45}$$

We already know that the slope of KAM curve at the intersection point u of KAM curve and $y-$axis is $\frac{a}{2}$. Combining this fact and Proposition 5-2, we have

Proposition 7-1 : There is no KAM curves at $a \ge 2$.

Using Proposition 5-3(1), we also have

Proposition 7-2 : There is no KAM curves at $a \ge \sqrt{2}$.

7.2 Estimation of the critical value a_c at which all KAM curves disappear

We shall give more improved estimation of the critical value in terms of the criterion (37) which is identically equal to Eq.(45). Here we consider the series of mapping point $\{T^{-n}u\}$ in the phase space, and investigate the slope of G at $T^{-n}u$. The mapping function (20) gives ζ_{-1}(slope of G) at $G^{-1}(0)$($T^{-1}u$ in the phase space)

$$\zeta_{-1} = \frac{1}{2-a-(1-\frac{a}{2})}. \tag{46}$$

ζ_{-1} must satisfy the relation

$$\frac{1}{M} \leq \frac{1}{1-\frac{a}{2}} \leq M. \tag{47}$$

The right inequality gives the condition to exist KAM curve. $a \leq \frac{4}{3}$. The left inequality does not give the condition. Then we have Proposition 7-3.

Proposition 7-3 : There is no KAM curves at $a > \frac{4}{3}$.

Using the following procedure and the infomation on ζ_{-n}, we can estimate the critical value a_c, numerically.

Procedure

[Step 1] Input $n(\geq 2)$.

[Step 2] Input a.

[Step 3] Input the initial position $(0, m\times 2\pi)$ in the phase space. According to the symmetry, we trace the region $0 \leq m \leq \frac{1}{2}$,only. Caluculate $\zeta_{-1}, \ldots, \zeta_{-n}$ in order. If $\zeta_{-i}(1 \leq i \leq n)$ does not satisfy the relation (37), we delete the initial position in the interval $(0, \pi)$ of initial conditions. If all $\zeta_{-i}(1 \leq i \leq n)$ satisfy the relation (37), we do not delete such a initial condition.

[Step 4] Go back Step [3] and change the initial condition. If the remainder interval exist, go back Step [2] and increase the value of a.

[Step 5] Repeating Steps[2-4], if we find the values of a at which the remainder interval does not exist, we put a_n =Minimum of a.

[Step 6] Go back to Step [1] and increase the value of n.

In Table II, our numerical results are obtained.

Table II: The critical value

n	a_n	n	a_n
3	1.198	89	0.97908
5	1.116	144	0.97619
8	1.0579	233	0.97429
13	1.0250	377	0.97335
21	1.0039	610	0.97269
34	0.9914	987	0.97219
55	0.9837	1597	0.97196

Proposition 7-4:There is no KAM curves at $a \geq \frac{243}{250}$.

Our estimation gives the upper bound of the ctirical value. The lower bound is estimated as $a_c = 0.971635\ldots$ by Greene[9].

Our result is very close to the lower bound, and is improved compared with Mather's estimation($\frac{4}{3}$), and with Mackay-Percival's estimation($\frac{63}{64} = 0.98439\ldots$). Then we can conclude that the true ctirical value a_c exists in the region $(0.971635\ldots, 0.97196\ldots)$.

7.3 Other critical values

Using the mapping function (20) and the criterion (37), we can estimate the ctirical value for KAM curve with any irrational rotation number ν. We show the procedure to calculate it. Let $\nu(y)$ be the calculated rotation number for the orbit with the initial condition $(0, y)$.

Procedure

[Step 1] Input the rotation number ν that we want to know the critical value.

[Step 2] Input a.

[Step 3] Calculate T with initial condition $(0, y)$, and the rotation number $\nu(y)$. Find two initial positions y_{max} and y_{min} satisfying $\nu(y_{max}) > \nu$ and $\nu(y_{min}) < \nu$ with condition $\Delta y = y_{max} - y_{min} < \epsilon$(for example,$10^{-7}$).

[Step 4] Check the criterion (37) for the orbit starting from the initial condition $(0, y_i)(y_i = y_{min} + \Delta y \times i/10 : i = 0, \ldots, 10)$. If all orbits do not satisfy Eq.(37), decrease the value of a and go back [Step 3]. If not so, increase a and go back [Step 3]. Stop Procedure if the desired precision for a is obtained.

Using the program to calculate Procedure, we show several critical values in Tables III.

ν	a_c	ν	a_c
$\sqrt{2}-1 = [2^\infty]$	0.9577	$(\sqrt{13}-3)/2 = [3^\infty]$	0.8911
$\sqrt{3}-1$	0.8765	$\sqrt{5}-2 = [4^\infty]$	0.8053
$\sqrt{6}-2$	0.8738	$\sqrt{7}-2$	0.8815
$\sqrt{8}-2$	0.6841	$\sqrt{10}-3$	0.6474

ν	a_c	ν	a_c	ν	a_c
$[2,1^\infty]$	0.9717	$[3,1^\infty]$	0.9047	$[4,1^\infty]$	0.8200
$[2^2,1^\infty]$	0.9601	$[3^2,1^\infty]$	0.8950	$[4^2,1^\infty]$	0.8090
$[2^3,1^\infty]$	0.9593	$[3^3,1^\infty]$	0.8922	$[4^3,1^\infty]$	0.8059
$[2^4,1^\infty]$	0.9580	$[3^4,1^\infty]$	0.8913	$[4^4,1^\infty]$	0.8050
$[2^5,1^\infty]$	0.9580	$[3^5,1^\infty]$	0.8911	$[4^5,1^\infty]$	0.8052
$[2^6,1^\infty]$	0.9577	$[3^6,1^\infty]$	0.8911	$[4^6,1^\infty]$	0.8053

Table III: The critical values for several KAM curves. Notation of the continued fraction expansion of irrational number:$[2^\infty] \stackrel{\text{def}}{=} [2,2,\ldots]$, and $[2^k,1^\infty] \stackrel{\text{def}}{=} [\underbrace{2,\ldots,2}_{k \text{ times}},1,\ldots]$. Note that KAM curve with the rotation number $\sqrt{2}-1$(for example) do not exist at $a = 0.9577$.

7.4 Distribution of mapping points on KAM curves

Here we study the structure change of distribution of mapping points on KAM curve with the golden mean rotation number(see Fig.6). Increasing the value of a, we approach toward the critial value a_c. Note that the following results on the structure change hold for KAM curve charaterized by the silver mean($\sqrt{2}-1$), and by copper mean($\frac{\sqrt{13}-3}{2}$). Then our results are the universal properties holding for any KAM curves in the vicinity of the ctirical value.

(1) The distribution decreases toward zero at the intersection point u of KAM curve and the symmetry line $x=0$. A steep-walled valley appears at the points $T^n u(n=0,\pm 1,\ldots)$.

(2) The distribution increases at the intersection point v of KAM curve and the symmetry line $x=\pi$. The peak appears at the points $T^n v(n=0,\pm 1,\ldots)$.

(3) The distribution increases at the intersection point s and t of KAM curve and the symmetry lines $y=2x$ and $y=2(x\pm\pi)$. The peak appears at the points $T^n s, T^n t(n=0,\pm 1,\ldots)$.

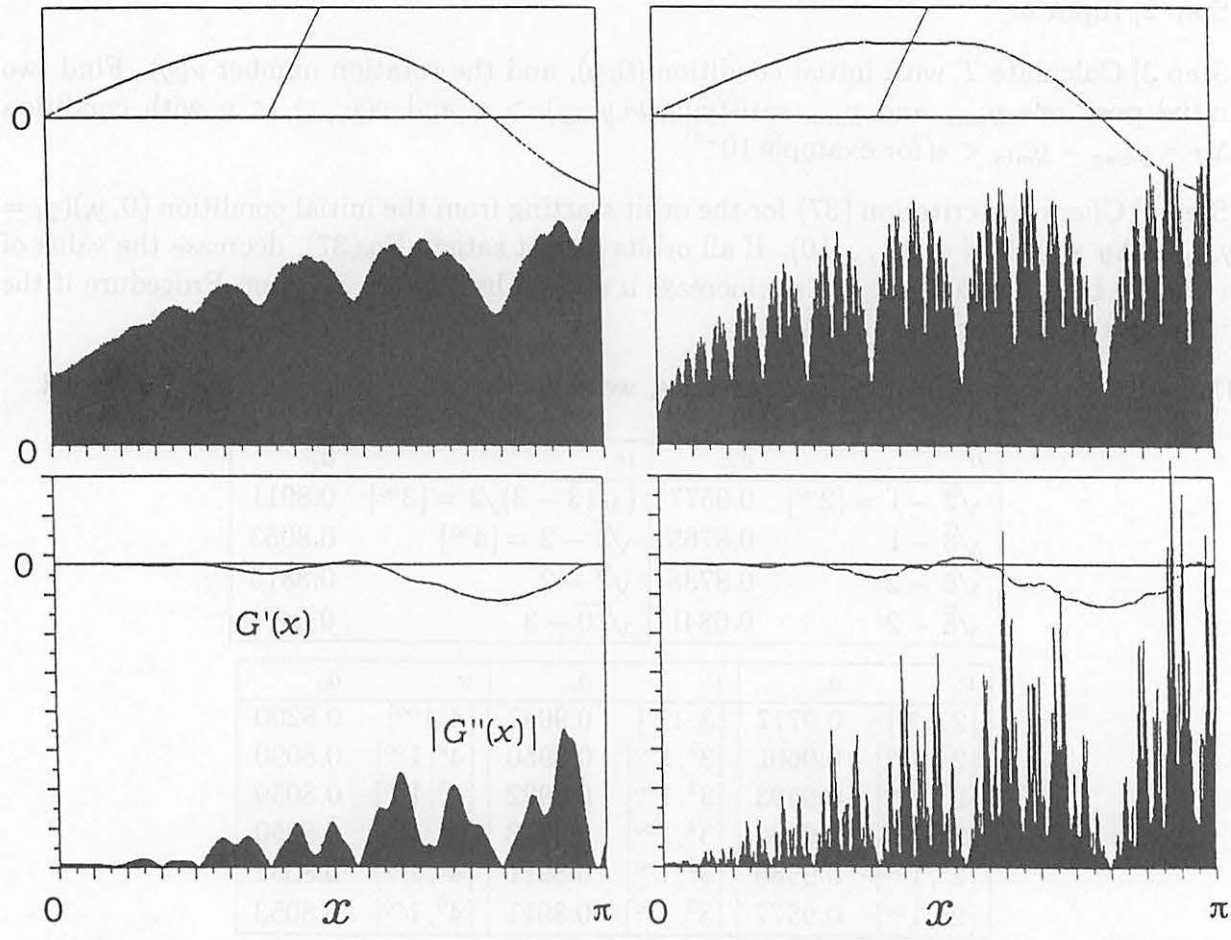

Fig.6 $a=0.92$(left) and 0.97(right).[Upper Fig.] Distribution(lower) of the mapping points on KAM curve(upper) with golden mean rotation number. [Lower Fig.] Shapes of $G'_{even}(x)$ and $|G''_{even}(x)|$. In order to compare the disribution and $|G''_{even}(x)|$, $|G''_{even}(x)|$ is drawn by the bar-graph. The diagonal line shows $y=2x$.

7.5 Structure of the second-derivative $G''_{even}(x)$

Aparting from the integrable state, the smoothness of KAM curve may be destroyed step by step. We believe that the destruction of smoothness gives rise to the structure change of distribution function as shown in Fig.6. Here we calculate the second derivative G''_{even} to study the structure change which is not detected by the infomation on the slope of G_{even}. If the second derivative exists, the follwoing functional equation for $G''_{even}(x)$ holds.

$$G''_{even}(G(x)) = \frac{1}{2}f''(G(x)) + \frac{G''_{even}(x) + \frac{1}{2}f''(x)}{(G'_{even}(x) + \frac{1}{2}f'(x) + 1)^3}. \tag{48}$$

But we have the difficulty to solve Eq.(48) for $G''_{even}(x)$. We have no information on the initial condition, for example, $G''_{even}(0)$. In order to avoid this difficulty, we use the spline interpolation to the data obtained for $G'_{even}(x)$ and calculate the second derivative. As a result, we have the following results(see Fig.6).

[1]The distribution decreases in the vicinity of the point with $G''_{even}(x) \approx 0$, and increases in the vicinity of the point with large $|G''_{even}(x)|$.

[2]he space pattern of $G''_{even}(x)$ is very similar to that of distribution at which the paramter a is very close to a_c.

In both figures of the distribution and the second derivative, the fractal structure with the peak and steep-walled valley is observed when the parameter a is close to the critical value. The relation of the distribution and the structure of $G''_{even}(x)$ and the reason of appearance of fractal structure is not understood,clearly. These are the impotant problems to be studied.

8 Discussion

The higher order derivatives of $G_{even}(x)$ give the impotant informations on the structure change of KAM curve. Differentiating Eq.(34) in sequence, the functional equations for the n-oder derivative $G^{(n)}(x)(n \geq 1)$ are obtained. The functional equation for $G^{(n)}(x)$ includes all lower order derivatives $G'(x), \ldots,$ and $G^{(n-1)}(x)$. This fact implies that the property of bounded variation of all higher oder derivetives does not hold if the bounded variation of $G'(x)$ does not hold. Even if the bounded variation of the higher oder derivetive does not hold,the bounded variation of $G'(x)$ is not necessarily destroyed. If the bounded variation of $G^{(n)}(x)$ does not hold, the smoothness of KAM curve is destoryed due to Theorem by Herman[2]. Before stating Theorem, we define the Herman index $H_r(f)$ to be

$$H_r(f) = \sup(|Df^n| + \ldots + |D^r f^n|)(n \in \mathbf{Z}).$$

Theorem: If $G : S^1(\text{circle}) \to S^1$ is a $C^r(r \geq 1)-$diffeomorphism with irrational rotation number is C^r-conjugate to a rotation if and only if $H_r(f) < \infty$.

This theorem plays an impotant role when we consider the process of breakdown of KAM curve. In order to study it, we have to check the abnormality of the higher oder derivatives of $G(x)$.

References

[1] G.B.Birkhoff, *Acta Math.* **43**,44(1920).

[2] M.R.Herman, *Publ.Math.I.H.E.S.* No.49,5-233(1979).

[3] R.S.Mackay, *Renormalisation in area-preserving maps.* World Scientific(1993).

[4] R.DeVogelaere, in *Contribution to the theory of nonlinear oscillation*, Vol.IV ed.by S.Lefschetz. pp.53-84(1958).

[5] K.Tanikawa and Y.Yamaguchi, *J.Math.Phys.* **28**,921(1987).
K.Tanikawa and Y.Yamaguchi, *J.Math.Phys.* **30**,608(1989).

[6] S.J.Shenker and L.P.Kadanoff, *J.Stat.Phys.* **27**,631(1982).

[7] A.Denjoy, *J.Math.Pures Appl.*(9) **11**,333-375(1932).
W.de.Melo and S.van Strien, *One-dimensional dynamics*(Springer,1993).
See also [2].

[8] S.Aubry, *Physica*,**7D**,240(1983).
J.N.Mather, *Publ.Math.I.H.E.S.*,**63**,153(1986).

[9] J.Greene, *J.Math.Phys.* **20**,1183(1979).

[10] J.N.Mather, *Erg.Th.Dyn.Sys.* **4**,301(1984).

[11] R.S.Mackay and I.C.Percival, *Commun.Math.Phys.* **98**, 469(1985).

ノンツイスト写像のカオスへの遷移機構

Transition to Global Chaos in Nontwist Maps

篠原 晋*、 相澤 洋二
早稲田大学 理工学研究科
Susumu SHINOHARA * and Yoji AIZAWA
Department of Applied Physics, Waseda University

Abstract

We study the transition to global chaos in a nontwist map. We succeeded in obtaining the breakup boundary in the entire parameter space, where the transition to global chaos occurs. Because of the violation of the twist condition, the transition routes to chaos in the nontwist map are quite different from those in monotonic twist maps. The relation between the structure of the breakup boundary and the reconnection phenomena is discussed.

§1. Introduction

次のような二次元保測写像 quadratic twist map を考える。

$$T:\begin{cases} I_{n+1} = I_n - K\sin(\theta_n) \\ \theta_{n+1} = \theta_n + f(I_{n+1}) \end{cases} \qquad (\mathrm{mod}\ 2\pi) \tag{1}$$

$$f(I) = 2\pi\mu - I^2$$

$$(I,\theta) \in \mathbf{R}\times\mathbf{S}$$

ここで、K は摂動パラメータ、μ はツイスト関数 $f(I)$ の極大値を調節するパラメータである。この写像のようにツイスト関数 $f(I)$ が非単調関数である写像は、ツイスト条件

$$\frac{df}{dI} \neq 0 \quad \text{for}\ {}^{\forall}I \tag{2}$$

を満たさないため、ノンツイスト写像と呼ばれる。ツイスト条件はハミルトン系の非退化条件に相当するものである。ハミルトン系では、摂動の強さを増していった時の相空間構造の変化のシナリオは、Poincaré-Birkhoff の定理や、KAM の定理などによって与えられるが、これらの定理はツイスト条件を仮定しているため、ノンツイスト系には直接適用出来ない [1]。これまでの研究により、ノンツイスト系では、リコネクションと呼ばれる独特な相空間構造の変化が見られることや、大域的なカオスへの遷移の臨界パラメータ値が摂動の増し方のわずかな違いによって大きく変化してしまうことなど、興味深い性質が分かってきた [2-7]。

ノンツイスト写像の特殊な点は、shearless 曲線と呼ばれる不変曲線が相空間に存在することである。ツイスト条件はこの shearless 曲線上で破れている。Fig.1 に摂動を強くしたときの典型的な相空間の図を示した。Shearless 曲線は摂動に対して非常に頑丈である。Quadratic twist map の場合は、写像の可逆性 (reversibility) と対称性を用いて、shearless 曲線が唯一本存在する場合は、次の四つの座標を通ることを示すことが出来る [6,7]。

*E-mail address: susumu@aizawa.phys.waseda.ac.jp

$$x_1^{\pm} = \begin{bmatrix} I_1^{\pm} \\ \theta_1^{\pm} \end{bmatrix} = \begin{bmatrix} \pm K/2 \\ \pm\pi/2 \end{bmatrix} \qquad (3)$$

$$x_2^{\pm} = \begin{bmatrix} I_2^{\pm} \\ \theta_2^{\pm} \end{bmatrix} = \begin{bmatrix} 0 \\ \pi(\mu \pm 1/2) \end{bmatrix} \qquad (4)$$

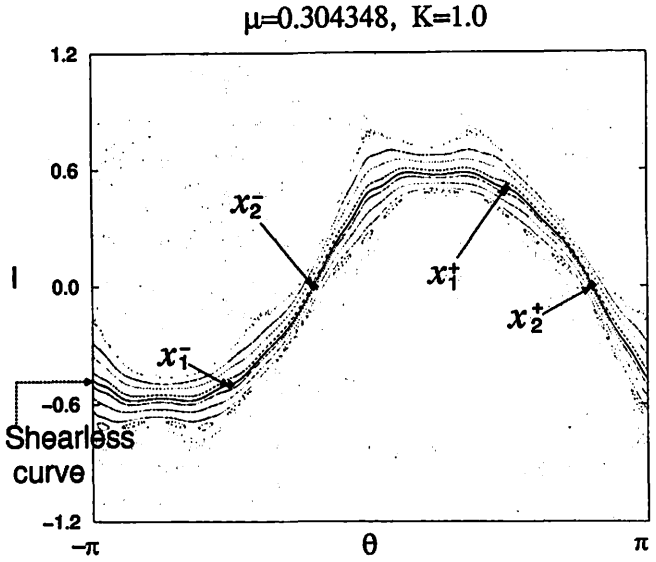

Fig. 1 The shearless curve and robust KAM curves.

§2. Transition to global chaos in the quadratic twist map

Fig.1 のように、頑丈な KAM 曲線は shearless 曲線周辺に存在するため、$x_1^{\pm}$、$x_2^{\pm}$ を初期点とする軌道 (i.e., $T^n x_j^{\pm}$ $(n \in \mathbf{Z}; j = 1,2)$) の振舞を調べることにより、相空間を二分するような KAM 曲線が全く存在しない大域的なカオスへと遷移する臨界パラメータ値を求めることが出来る [6]。すなわち、もし $T^n x_j^{\pm}$ が $n \to \infty$ の極限で、有界領域に留まっているならば、shearless 曲線が存在するか、あるいは、shearless 曲線は崩壊したものの周りの頑丈な KAM 曲線が軌道を有界領域に閉じ込めていることを表す。いずれの場合も、相空間を二分するような KAM 曲線の存在を保証する。一方、$T^n x_j^{\pm}$ の運動が非有界の場合は、もはや相空間には KAM 曲線が存在しないことを表す。よって、$T^n x_j^{\pm}$ の運動が有界から非有界へ遷移する時の臨界パラメータ値は、大域的なカオスへ遷移する臨界パラメータ値に等しい。

数値計算の結果を Fig.2 に示した。Fig.2 の灰色の領域のパラメータ値では、軌道 $T^n x_j^{\pm}$ は有界領域に留まっており、灰色領域と白色領域の境界が、大域的なカオスへと遷移する臨界パラメータ値 (breakup boundary) を表す。数値計算では、各パラメータ値について、x_1^+, x_2^+ を初期点とする軌道 $T^n x_1^+$, $T^n x_2^+$ を $n = 10^5$ まで計算し、それらの I 成分の絶対値が 2 よりも小さいときは有界運動と判断した。

Fig.2 より、臨界パラメータ値は、摂動パラメータ K の増し方に鋭敏に依存することが分かる。Fig.3 は、Fig.2 の一部分の拡大図であるが、微細な構造がさらに見られる。Breakup boundary の無数の微細な構造は、次に述べるリコネクション閾値と一対一に対応している。

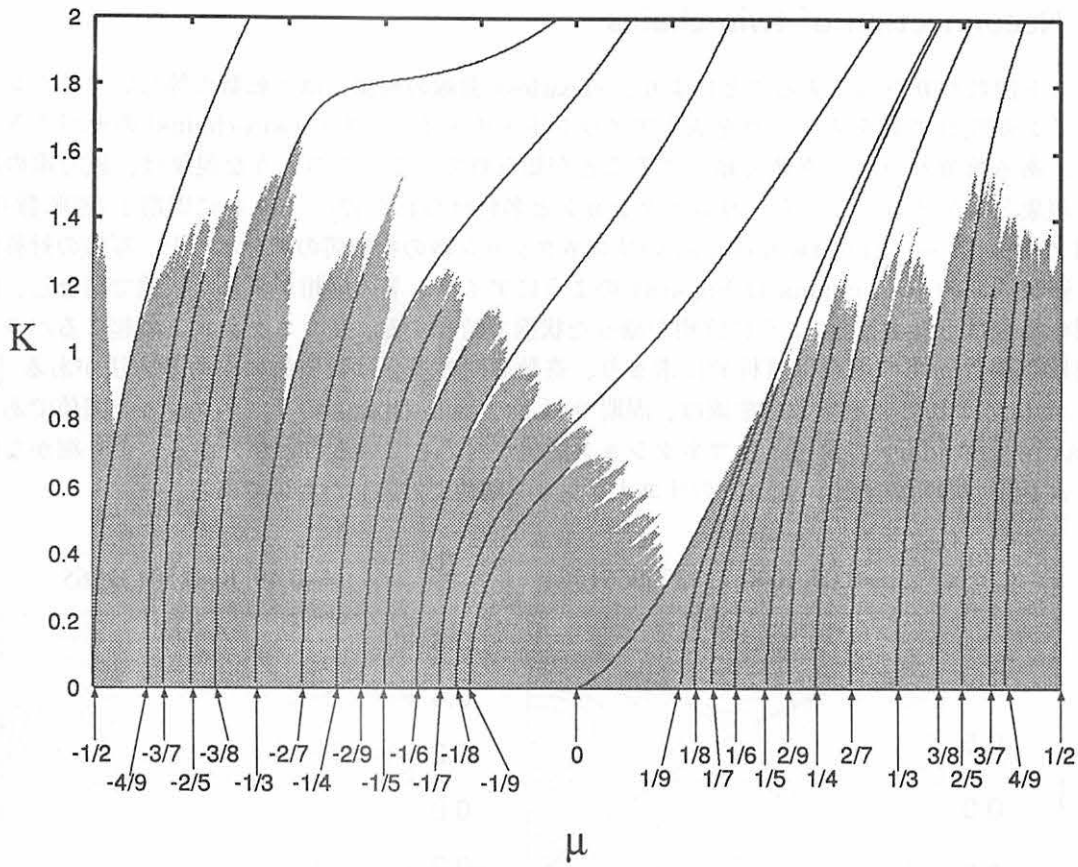

Fig. 2 The breakup boundary and the reconnection thresholds. For the μ-K parameter values in the gray region, the iterates of $x_j^{\pm}$ $(j = 1, 2)$ are confined in bounded regions in the phase space. The boundary between the gray and the white regions corresponds to the breakup boundary, where the transition to global chaos occurs. The solid lines represent the reconnection thresholds of the twin-chains with the rotation number P/Q.

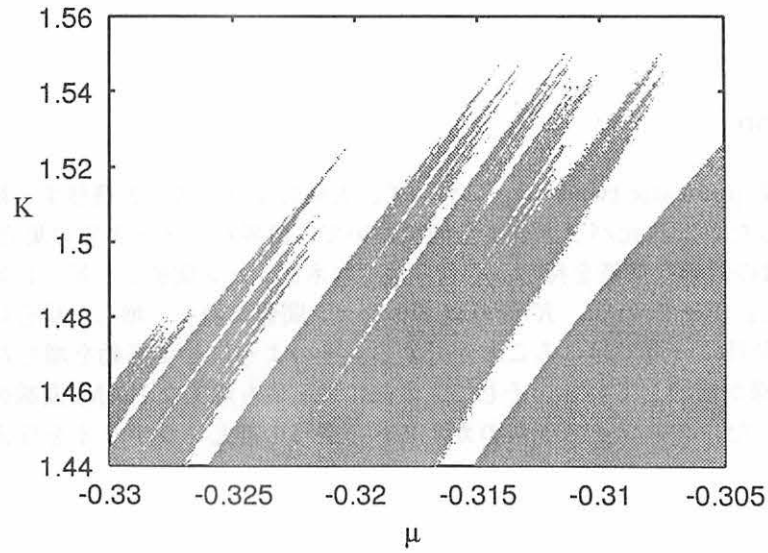

Fig. 3 Magnification of a small region in Fig.2

§3. Reconnection of twin-chains

ツイスト関数が非単調であることにより、shearless 曲線の両側には回転数の等しいアイランド・チェインが現れて対を成す。対を成すアイランド・チェイン (以下 twin-chains) のセパラトリクスは、ある臨界パラメータ値で結合することが知られている。このような現象は、磁力線の結合する現象とのアナロジーから、リコネクションと名付けられた [2]。Fig.4 に周期 1 (回転数 0) と周期 2 (回転数 $-1/2$) の twin-chains のリコネクション時の相空間の図を示した。写像の対称性から、奇数周期の twin-chains は Fig.4(a) のようにアイランドの位相がずれた状態で結合し、偶数周期の場合は Fig.4(b) のように位相が揃った状態で結合する。リコネクションの起こるパラメータ値は、偶数周期の場合は解析的に求まり、奇数周期の場合は数値的に求める方法がある [7]。Fig. 4 に描かれている多数の曲線は、周期 9 以下の twin-chains のリコネクション閾値である。Breakup boundary の構造とリコネクション閾値が対応していることが分かる。より細かな構造は、より長い周期の twin-chains のリコネクション閾値に対応したものである。

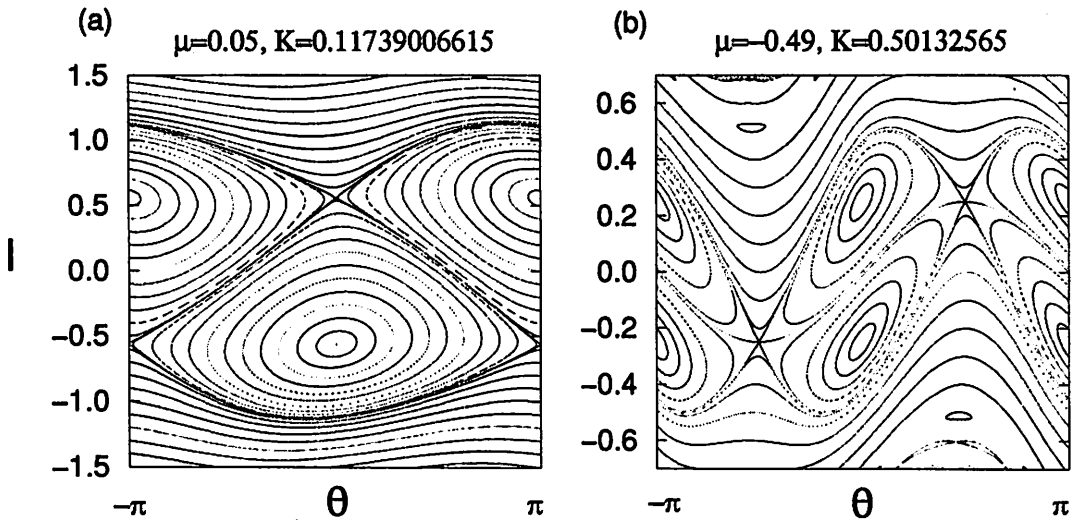

Fig. 4 Phase space portraits of twin-chains at reconnection thresholds.
(a) period-one twin-chains and (b) period-two twin-chains.

§4. Conclusion

ノンツイスト写像 quadratic twist map において、大域的なカオスへと遷移する臨界パラメータ値を数値的に決定した。二次元パラメータ空間において、臨界パラメータ値の集合が描く breakup boundary は無数の微細な構造を持ち、それらはリコネクション閾値と一対一に対応していることが明らかとなった。Fig.2 から、K をリコネクション閾値に沿って増した場合は、カオスへの遷移がパラメータ空間の一点で起こることが分かる。そのようにして摂動を増した場合、どの様な順序で KAM 曲線が崩壊していき、そして、最後に残る最も頑丈な KAM 曲線の回転数はいくつになるのかといった、ノンツイスト系のカオスへの遷移の詳しいシナリオを与えることは、今後の課題である。

References

[1] A.J.Lichtenberg and M.A.Lieberman, *Regular and Chaotic Dynamics*, 2nd Ed. (Springer, New York, 1992).

[2] J.E. Howard and S.M. Hohs, Phys. Rev. **A29** (1984), 418.

[3] J.E. Howard and J. Humpherys, Physica **D80** (1995), 256.

[4] D. del-Castillo-Negrete, J.M. Greene and P.J. Morrison, Physica **D91** (1996), 1.

[5] D. del-Castillo-Negrete, J.M. Greene and P.J. Morrison, Physica **D100**(1997), 311.

[6] S. Shinohara and Y. Aizawa, Prog.Theor.Phys. **97** (1997), 379.

[7] S. Shinohara and Y. Aizawa, *in preparation.*

自由度3ハミルトン系カオスの諸概念と技法—-: トーラスの不安定化

黒崎 暁 早大理工

March 30, 1998

De-stabilization of Invariant Tori in Three Degrees of Freedom Hamiltonian Systems

Satoru Kurosaki Department of Applied Physics, Waseda University, Tokyo 169

abstract De-stabilization near various invariant tori in four dimensional symplectic maps is studied. The breakup of KAM tori is numerically studied. The succession to the breakup depends on the perturbations which determine the dominant type of small divisors in the conjugation function. The persistence of invariant tori and diffusion of nearly integrable systems are studied in the frequency space. Elliptic normal modes are robust than KAM tori under strong perturbation.

保存系の軌道の安定性を考える上で最も重要な力学構造は不変トーラスである。ここでは自由度3保存系の写像で、KAMトーラスの崩壊の順序についての最近の著者らの仕事のスケッチと、不変トーラスの残存／崩壊と近可積分系の拡散を大域的に調べた結果、について報告する。

1 高次元KAMの崩壊

トーラス崩壊の仕組みを明らかにすることはハミルトン系の力学の基本問題の一つである。それは予測可能な運動からカオスへの転移を示す。自由度2の場合には、Greeneの先駆的な研究のあと、位相空間の自己相似な構造や普遍的なスケーリング則が発見され、もっとも摂動に強いトーラスの崩壊を扱うくりこみの技法が開発されていった。[3][4] 今ではスケーリングの理論は、しきい以下でのくりこみの厳密化も含めて、確立されている。[5][6] しかし高次元の場合(自由度が

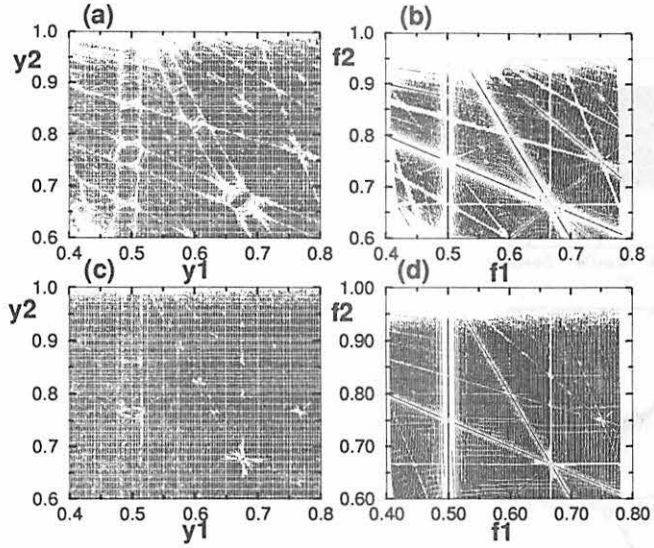

Figure 1: (a)(c)The set of stable initial points (y_1, y_2). $x_1 = x_2 = 0$. (a) parameters are (a)$c_1 = c_2 = 0.2, c_3 = 0.06$,(c) $c_1 = c_2 = 0.2, c_3 = 0.006$. (b),(d) rotation vectors of each initial points of (a),(c), respectably.

2をこえるとき) ではそのようなスケーリング則は見られない。[7] 複雑なくりこみ群の流れが報告されているが、そのような振舞いの詳細はよく理解されていない。[8]

文献 [4] ではある自由度2にあたる写像の数値計算の結果からトーラスの小さいスケールの力学は非線形摂動の詳細によらず、回転数のみで決まるのではないか、と主張されている。[5] 自由度2の写像のコンジュゲイション関数に出てくる小さい分母が1次元の有理近似のもので尽きることも、これを支持すると考えられる。

最近我々は自由度3の保存系 flow のポアンカレ断面にあたる, 次の4次元シンプレクティック写像 $R^2 \times T^2 \to R^2 \times T^2((\boldsymbol{y}, \boldsymbol{x}) \mapsto (\boldsymbol{y}', \boldsymbol{x}'))$ でKAMトーラスの崩壊する順番と非線形摂動の性質の関係を調べた。[1]

$$
\begin{aligned}
y_1' &= y_1 + \frac{c_1}{2\pi}\sin(2\pi x_1) + \frac{c_3}{2\pi}\sin(2\pi(x_1 + x_2)) \\
x_1' &= x_1 + y_1' \\
y_2' &= y_2 + \frac{c_2}{2\pi}\sin(2\pi x_2) + \frac{c_3}{2\pi}\sin(2\pi(x_1 + x_2)) \\
x_2' &= x_2 + y_2'.
\end{aligned} \tag{1}
$$

ここで、$\boldsymbol{x} = (x_1, x_2)$ は作用角変数、$\boldsymbol{y} = (y_1, y_2)$ は作用変数で、c_i(i=1,2,3) はパラメタである。自由度3では加える非線形摂動によってコンジュゲイション関数の小さい分母に1次元と2次元の有理近似のもの両方が出てくるため、写像の詳細（パラメタの変化）でより強いトーラスは変わってしまうことを次のような数値例で確かめた。1次元の有理近似のものを導くパラメタ c_1, c_2 が大きいと quadratic number、2次元の有理近似のものを導くパラメタ c_3が大きいと cubic number のトーラスがより摂動に対して強くなる。後者は2次元有理近似の理論から、自由度3で典型的であると推測されていた状況にあたる。[9] 前者は Bollt, Meiss らの発見に対応する。[10] これは自由度3のトーラスの崩壊では自由度2におけるような先に述べたような単純な"universality" は期待できないことを意味する。技術的詳細は文献に譲る。[1]

コンジュゲイション関数に現れる小さい分母を考えると、文献 [7][8] で観察されたされたような高次元の"universality" の消失は、非線形摂動に2次元有理近似のもののみ現れる形を選ぶことで回復することが期待される。またコンジュゲイション関数によるトーラスの直接構成で、トーラスを近似する周期点列の是非がチェックできる。(局所的な意味で) 高次元 last KAM 近傍の多様体の微細構造の探求への道が開けたといえる。保存系で見られる 1/f タイプのスペクト

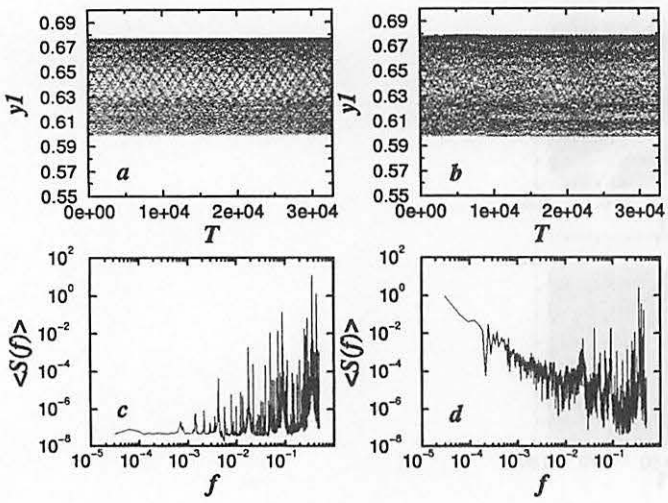

Figure 2: Typical time series of y_1 (a) just before the break up of nearby KAM tori, (b) just after the breakup. (c) PSD of time series (a),(d) PSD of time series (b).

ルの起源と絡めて、これも今後の課題である。

2 大域的な情報

有限の摂動について高次元の不変集合と拡散を絡めて扱う端初を開いたのが Laskar の frequency analysis である。[11] 自由度 3 に対応する写像に適用すると作用変数の力学が非常に明解になり、アーノルド拡散に関係付けられる共鳴帯に沿った拡散、共鳴帯を横断する拡散（以降 Laskar の速い拡散と呼ぶ）が視覚で捉えられる。ここでは Laskar の用いた方法より簡便な方法で大域的に位相空間の構造を調べる。

2.1 不変集合

まず初期値空間から不変集合を拾い出す手法について述べる。その結果写像（1）の力学を反映したアーノルド・ウェブに対応する構造が回転数空間（この写像では平均化した作用変数空間）で見られる。摂動の強さが増すと KAM トーラスは速やかに崩壊するのに対し、elliptic normal modes（後述）は摂動に強いことが観察される。

図 (1)(a) は $c_1 = c_2 = 0.2, c_3 = 0.06$ で、(y_1, y_2) 初期値平面の一部に 200X200 のメッシュをきって近傍に KAM または elliptic normal modes のトーラスが残存している初期点をプロットしている。KAM トーラス上でトーラスコンジュゲイションの等位相線を考慮すると、$x_1 = x_2 = 0$ に初期値を固定することで KAM トーラスは全て捕捉できることが分かる。（文献 [1] の式（8）で $\theta_1 = \theta_2 = 0$ とおく。）トーラスの残存の判定は各初期値からの軌道の作用変数の時系列が secular な成分を持つか否かを、フーリエ変換の低周波成分を計算することでチェックした。この図では計算を軽くするために手順を思い切って簡素化した。時系列は $2^{15} \times 2$ で揃え、計算するのはもっとも低周波の成分のみにし、閾値 10^{-5} より小さいものをプロットする。図 (1) のスケール（オーダー 1）ではこれで十分である。

典型的な例として回転数ベクトル (τ^{-2}, τ^{-1}) $(\tau = 2\cos(2\pi/7))$ の KAM トーラスの周り、周期 1 4 2 9 の近似周期点の初期点からの軌道の安定性を図 (2) に示す。KAM トーラスの崩壊直前・直後の作用変数 $y_1 (= x_1' - x_1)$ の長さ 2^{15} の時系列、そのパワースペクトルである。パワースペクトルは長さ 2^{15} のデータの FFT で図には連続した 8 本のデータからの平均を示した。

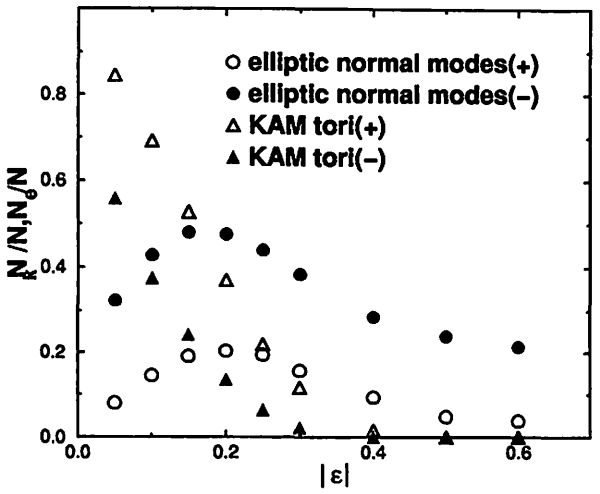

Figure 3: $N_e/N, N_K/N$ under various perturbation. $c_1 = c_2 = \epsilon, c_3 = 0.3\epsilon$.

(近傍の KAM トーラスの崩壊直前) (a) が y_1 の時系列を示す。トーラス上の流れを反映して準周期性が図の模様となって現れている。(c) は y_1 のパワースペクトル $< S(f) >$ を示す。低周波の成分はない。$\epsilon = c_1 = c_2 = 0.358, c_3 = 0.3\epsilon$ の初期値.

(近傍の KAM トーラスの崩壊直後) (b) が y_1 の時系列を示す。準周期性はすでに見えない。このスケールでは一見定常に見えるが (a) に比べて外形に 10^{-3} 程度のゆがみがあり、軌道はいずれ不安定になる。(d) パワースペクトルは $f \sim 0$ に小さいピークを持つ。$\epsilon = c_1 = c_2 = 0.372, c_3 = 0.3\epsilon$.

摂動が非常に小さい場合の有理回転数でその周期が長い周期点の近傍のトーラスでは、まれに非常に長い周期の構造が現れる。このような初期値では時系列がこの周期を含むだけ長くないと、対応するピークは最も低周波の成分より左側に現れる。本来トーラスが残っているのにこのピークのすそを引っかけてしまうので、上述の方法では正しく判定されない。ここではそのような初期値が効果を及ぼす計算 (例、共鳴帯の近傍の拡大) はやっていない。

図 (1) (b) は (a) で残った初期値について回転数ベクトルを $f_i = (x_i(2^{15}) - x_i(1))/(2^{15} - 1)$(mod はとらない)(i=1,2) で便宜的に計算したものである。厳密には不変集合の上でなければ回転数ベクトルは定義できない。(b) で白抜きになっているところは回転数空間でみた不安定帯である。これは $\epsilon = 0$ の極限でアーノルド・ウェブに対応する。両者の違いの重要な点は (b) が写像 (1) の力学を反映していることと、不安定帯には中央に線が入っているものと入っていないものがあることである。

写像 (1) では摂動のない場合 y_i は回転数ベクトルの i 成分と一致する。(i=1,2) いま摂動は小さいのでこの対応はかなりよく残っている。(a) (b) の各点の対応は次のようになっている。(a) の $(y_1, y_2) = (0.5, 0.75)$ の付近の丸い一団の初期値が (b) の $(f_1, f_2) = (0.5, 0.75)$ の一点に潰れている。これらの初期値の集団のほとんどは回転数 $(0.5, 0.75)$ の楕円型不動点の周りに共鳴で出来上がった 2-torus であり、このトーラスがもつ $(0.5, 0.75)$ の不動点に対する相対的な回転数は (b) には現れないためである。(a) のほうで丸い一団の初期値から別の丸い一団の初期値へと伸びている四角い初期値の集合 (例、$(y_1, y_2) = (0.5, 0.75)$ のまわりから $(y_1, y_2) = (2/3, 2/3)$ のまわりの集団へ) のほとんどは不動点とトーラスの直積から先と同じように高次共鳴で出来た 2-torus である。これらは (b) では共鳴帯の中の直線となって現れる (先の例なら $(f_1, f_2) = (0.5, 0.75)$ から $(f_1, f_2) = (2/3, 2/3)$ の直線)。これらのトーラスは elliptic normal modes と呼ばれ、中間次元も許す。elliptic normal modes の周辺の軌道の安定性について KAM トーラスと同様な議論がされている。 [2]

図 (1)(c)(d) はパラメタ $c_1 = c_2 = 0.2, c_3 = 0.006$ の結果である。図 (1)(a)(b) と (c)(d) では高次元効果の結合パラメタ c_3が異なる。f_1, f_2 が互いに独立な共鳴 (例、$f_1 = 0.5$) ではこの c_3

の変化はほとんど影響がない。このことと f_1, f_2 が互いに線形に依存する共鳴、これは $c_3 \neq 0$ でのみ生じる高次元特有の共鳴である、とを比べると、ごく小さい c_3 で高次元特有の共鳴が発達することが分かる。

写像（1）の初期値面 $x_1 = x_2 = 0$ での残存している elliptic normal modes あるいは KAM トーラスの測度を考える。(y_1, y_2) 平面上の $[0,1) \times [0,1)$ 区間を N=200X200 の等間隔で切った格子上の初期値の集合を用意する。図 (1)(a) の計算で安定と判定された各初期値で次の量 h を評価する。

$$h = f_1 m + f_2 n \quad (mod 1) \quad (h \leq 0.5) \tag{2}$$

$$= f_1 m + f_2 n - 0.5 \quad (mod 1) \quad (h > 0.5), \tag{3}$$

ここで m,n の組は 5 以下の整数で左辺を最小にするものを選ぶ。$h \leq 10^{-5}$ を共鳴、$h > 10^{-5}$を非共鳴とし、それぞれ elliptic normal modes の近傍、KAM トーラスの近傍の軌道とみなして、それぞれの数 N_e, N_K を数える。図 (3) に正負の両方の摂動の関数として $N_e/N, N_K/N$ を示す。粗い評価であるが、摂動の大きい領域での elliptic normal modes の重要性は明かである。パラメタは $\epsilon = c_1 = c_2, 0.3\epsilon = c_3$.

最後に図 (1)（b）は不変集合の大域的な理解の本質は回転数ベクトルの数論的な性質につきることを示すことを強調する。

2.2 近可積分系の拡散

近可積分系の拡散を扱う。自由度 3 以上では KAM トーラスがその内部と外部とに位相空間を孤立させることが出来ないのでトーラスの存在は軌道の永久の安定性を保証しない。軌道の拡散をみる場合は摂動による変形の寄与を落してやらなければならないので作用変数をある時間で平均化したものを考える。

各軌道の作用変数の時系列 $\{X_{(i)}\}$ から時系列 $\{\bar{X}_{(i)}\}$ を作る。ここで$\bar{X}_{(i)} = \frac{\sum_{j=i}^{i+m} X_{(j)}}{m}$. m の値は考察する位相空間のスケールで適当な値をとる。以降初期値は $x_1 = x_2 = 0$ で固定する。

この写像では作用変数の空間で長時間平均の極限をとると回転数空間になる。図 (4) に、$\{(\bar{y_1}, \bar{y_2})\}$ の回転数空間での時間発展の一例として Laskar の速い拡散を、図 (1) と同様の計算をしたものに重ねて示す。中央に (1/3,1/3) の共鳴がある。その右上、左下には安定な領域があり、もちろん数値計算による傍証に過ぎないが、ここでは KAM トーラスの多くが残存している。右下の白く抜けている不安定な領域の (1/3,1/3) 共鳴を中心とする円に沿う曲線は一本の軌道を表す。KAM トーラスの多くが残存している領域には、この曲線は侵入しない。$\{(\bar{y_1}, \bar{y_2})\}$ の時系列で、512 回毎に十字を打った。図 (5) は図 (4) の一部を拡大したもので、elliptic normal modes の周りに巻き付いてはまた離れて、といった様子が回転数空間への射影の形で見える。このような拡散は多くの共鳴帯が一点に集中する低次の共鳴の周りによく見られる。

共鳴帯の中の構造を考える。平均化した作用変数の空間で初期値からの到達距離の時間 $T = 2^{15}$ での最大値 $\Delta = \max_{1 \leq i \leq T}\{\delta_i\}$, ここで $\delta_i = ((\bar{y_1}(1) - \bar{y_1}(i))^2 + (\bar{y_2}(1) - \bar{y_2}(i))^2)^{1/2}$の (y_1, y_2) の初期値平面 $(x_1 = x_2 = 0)$ での値を図 (6) に示す。

低次の共鳴帯のまわりではこのような構造が一般的に見られる。共鳴帯内の運動は中央の共鳴からの距離でほぼ振舞いがきまることが分かる。

References

[1] S. Kurosaki and Y. Aizawa, Prog. Theor. Phys.**98** (1997), 783.

[2] M. B. Sevryuk, preprint mp-arc 97-615.

[3] J. M. Greene, J. Math. Phys. **20** (1979), 1183.

[4] S. J. Shenker and L. P. Kadanoff, J. Stat. Phys. **27** (1982), 631.

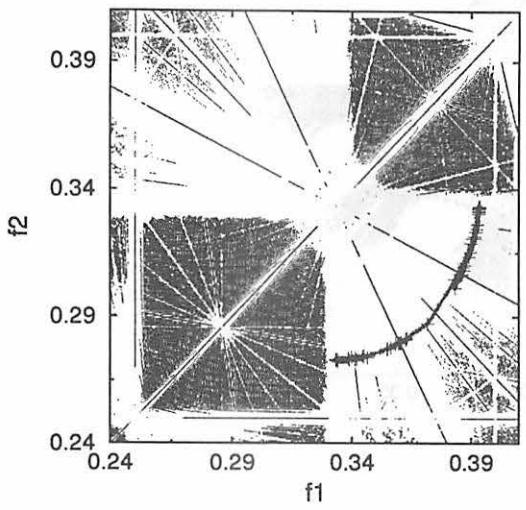

Figure 4: The diffusion around (1/3,1/3) resonance. Invariant tori are represented as same as figure 1(b) in background. Parameters are $c_1 = c_2 = 0.4, c_3 = 0.04, m = 2000$.

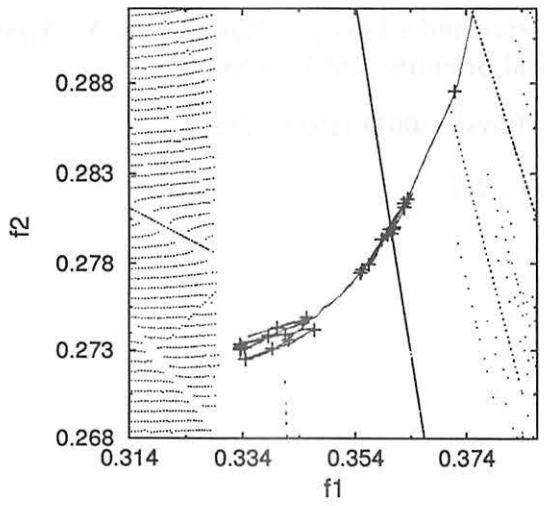

Figure 5: Magnification of figure 4. Each cross is plotted every 512 steps.

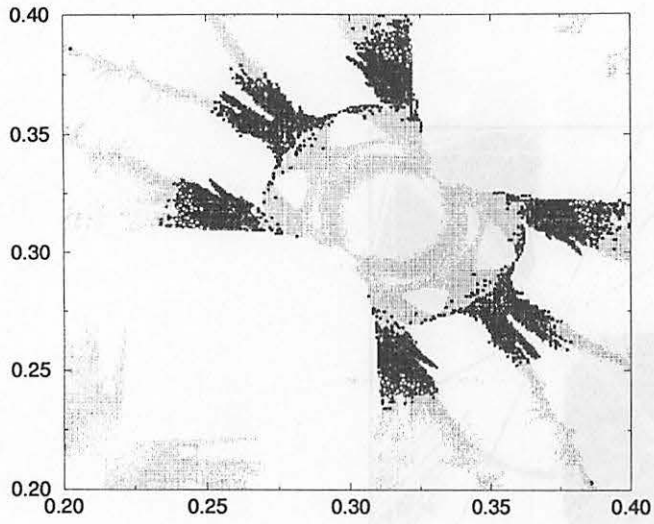

Figure 6: Δ on the (y_1, y_2) initial points plane ($x_1 = x_2 = 0$). Parameters are $c_1 = c_2 = 0.4, c_3 = 0.04, m = 1024$. Gray points indicate $\Delta \geq 0.005$, Black squares indicate $\Delta \geq 0.04$, White circles indicate $\Delta \geq 0.08$. Figures (4) and (5) correspond to $\{(\bar{y_1}, \bar{y_2})\}$ calculated from the orbit of one initial point of white circles.

[5] R. S. MacKay: Physica **7D** (1983) 283.

[6] YA. G. Sinai and K. M. Khanin, Int. J. Mod. Phys. **B2** (1988), 147.

[7] J. Mao and R. H. G. Helleman, Nuovo Cimento, **104B** rm (1989), 177.

[8] R. Artuso, G. Casati and D. L. Shepelyansky, Europhys. Lett. **15** (1991), 381.

[9] J. D. Meiss, *Dynamical Systems and Chaos 2: Physics*, eds. Y. Aizawa, S. Saito and K. Shiraiwa, (World Scientific, 1995), p.385.

[10] E. M. Bollt and J. D. Meiss, Physica **66D** (1993), 282.

[11] J. Laskar, Physica **67D** (1993), 257.

Blow-up Analysis of Solutions Close to Triple Collision in the Free-Fall Three-Body Problem

Hiroaki UMEHARA[1] and Kiyotaka TANIKAWA[1,2]

[1] Department of Astronomical Science, School of Mathematical and Physical Science
The Graduate University for Advanced Studies
Mitaka, Tokyo, 181, Japan *
e-mail address: umehara@milano.mtk.nao.ac.jp

[2] National Astronomical Observatory
Mitaka, Tokyo, 181, Japan

Abstract. It is proved that the homothetic equilateral orbit is isolated from other triple collision orbits as far as the collision at the first triple encounter concerns in the three-body problem with zero initial velocities and equal masses. In order show this, variational equations around the homothetic equilateral solution are formulated in the regularizing coordinate system, and solved qualitatively. The present paper is the complement to the preceding paper (Umehara and Tanikawa, 1997a, Proceedings of the 29th symposium on Celestial Mechanics in Tokyo, pp.188–199) where the existence of escape and non-escape orbits arbitrarily close to the homothetic equilateral triple collision orbit is considered analytically.

1 Introduction

It is well-known that triple encounter and triple collision are crucial to the instability of the gravitational three-body systems. Here, the instability means an escape phenomenon where one particle recedes from the others when the total energy is negative. Let $I(t)$ denote the time dependent moment of inertia. Birkhoff (1927) proved the following: if the angular momentum is not equal to zero, there is a positive and sufficiently small number I_c such that $I(t) \to \infty$ as $t \to \infty$ after I satisfies $I(t) < I_c$ at some time.

On the other hand, in the case with zero angular momentum, triple collision may occur. McGehee (1974) analyzed triple collision orbits and near-collision orbits, and found one possible mechanism for escape in the collinear three-body problem: one particle may get an arbitrarily large velocity as three particles approach each other. Devaney (1980) established that the same statement is true in the planar isosceles problem where the system maintains a symmetric configuration. In the collinear and planar isosceles systems, the close triple encounter seems to be the only factor effective for escape phenomenon.

In the above theoretical works, however, it is still unknown whether bounded orbits distribute close to a triple collision orbit or not in the planar problem. It is also unknown how escape orbits distribute around a triple collision orbit in the planar problem. In fact, there are many numerical results in the planar problem with $c = 0$. However, previous works could not fix any critical I leading to escape (Agekian and Anosova, 1968, Aarseth et al., 1994). Therefore, it

*Current address: Communications Research Laboratory, 893-1 Hirai, Kashima, Ibaraki 314-0012, Japan

is naturally expected that there is another factor than close triple encounter effective for escape phenomenon.

In the present paper, we will analyze the distribution of escape orbits close to the triple collision orbit by the "blow-up method". In almost all cases, triple collisions show non-regularizable features, and so the continuity of the solutions does not hold at the configuration point representing triple collision. Therefore, the solution close to triple collision is complicated and difficult to analyze. However, the research of the motion close to triple collision has begun with the aid of a device due to Waldvogel (1973) and McGehee (1974) which blows up the singular point in the configuration space to a high-dimensional manifold. This manifold is referred to as the triple-collision manifold.

McGehee (1974) developed blow-up variables in the collinear three-body problem. Although the flow on the triple-collision manifold is entirely fictitious since orbits on it do not correspond to any orbit in the original phase space, the flow in the blow-up coordinates extends smoothly over the fictitious flow on the triple-collision manifold. We can describe the solutions close to the triple collision if the fictitious flow is described. By investigation of flows in the triple-collision manifold, we can understand behavior close to triple collision. The set of orbits ending in triple collision in the original phase space is interpreted so as to form the stable manifold of the equilibrium point on the triple-collision manifold. The orbit close to triple collision corresponds to the flow starting to recede in the direction of the unstable manifold of the equilibrium point after approaching the equilibrium point along the stable manifold.

Umehara and Tanikawa (1997a, b) analyzed the free-fall three-body problem with equal masses. The free-fall problem means the case with zero initial velocities. This problem is a special case of the planar three-body system with the zero-angular-momentum case.

Furthermore, the initial-value space is a low-dimensional subspace in a high-dimensional phase space. The phase space with constant energy in the planar system is a five-dimensional manifold. So, in general, a systematical survey by numerical integrations is difficult in the planar system. In the free-fall problem, however, the initial-value space is reduced to a two-dimensional surface which we will explain below. The dimension is low, and so the systematical survey is possible.

2 Preliminaries

Let us introduce the definition of the free-fall three-body problem (Agekian and Anosova, 1967; Tanikawa et al, 1995; Broucke, 1995). See also Umehara and Tanikawa (1997a, b). We consider the three-body problem in $\mathbf{R}^2$ of particles with positive masses $m_j > 0$, $j = 1, 2, 3$ which interact according to the mutual gravitational attraction. Let $q_j \in \mathbf{R}^2$, $j = 1, 2, 3$ be the positions of the particles of mass m_j. Their dynamical evolution is described by the Newtonian equations of motion as

$$\ddot{q}_j = \sum_{k \neq j}^{3} \frac{m_k}{r_{jk}^3}(q_k - q_j) \qquad \text{where} \quad r_{jk} = |q_k - q_j|. \tag{1}$$

Following Broucke (1995), we consider the rectangular (x, y)-coordinates in the plane. The half-plane $\{(x, y)|y \geq 0\}$ is denoted by $\grave{D}$. Let three mass points m_1, m_2 and m_3 stand still at $P(x, y) \in \{(x, y)|y \geq 0\}$, $A(-0.5, 0)$ and $B(0.5, 0)$, respectively. If m_1 changes its position on $\grave{D}$, then triangles with given masses located at the respective vertices are exhausted. Conversely, any weighted triangle is similar to one of the triangles formed by m_1, m_2 and m_3 under rotation in $\mathbf{R}^2$ and reflection. Motions starting from similar weighted triangles transform into one another with appropriate changes of scales of length and time, so we identify these motions. Then the positions of m_1 specify all possible initial conditions, i.e., $\grave{D}$ is the initial-value space of the free-fall three-body problem with given masses.

The present paper explores the case where all particles have equal masses, i.e., $m_i = 1$, $i = 1, 2, 3$. In this case, the initial-value set of isosceles configurations with the base of the same pair forms one-dimensional curve. We will call this an *isosceles curve*. Orbits starting from this curve maintain isosceles configurations. Let I_j denote an isosceles curve corresponding to the isosceles configuration with base $m_k m_l$ where each j, k, l belongs to a cyclic permutation of $1, 2, 3$. The equations of I_j, $j = 1, 2, 3$ can be represented by x and y:

$$I_1 : x = 0, \quad I_2 : (x + 0.5)^2 + y^2 = 1, \quad I_3 : (x - 0.5)^2 + y^2 = 1. \tag{2}$$

Here, let us introduce the definition of triple encounter. Junzo Yoshida (1998) defined a time interval of the triple encounter as follows:

Definition of triple encounter *The system with negative energy is called to be in triple encounter if* $I < I_{\text{enc}}$, *where*

$$I_{\text{enc}} = \frac{M_*^3}{4Mh^2}, \tag{3}$$

and $M = m_1 + m_2 + m_3$ *and* $M_* = m_1 m_2 + m_2 m_3 + m_3 m_1$.

Agekian and Martynova (1973) define the triple encounter as the state satisfying $\ddot{I}(t) > 0$. However, $I(t)$ becomes concave even during the close approach between two particles. Therefore, Junzo Yoshida (1998) searched a suitable critical value of I for saying that the system is in triple encounter, and proved that $\ddot{I}(t) > 0$ during the system satisfies $I(t) < I_{\text{enc}}$. In other words, $I(t)$ has a minimal value only once during such a time interval if the system does not end in triple collision. Even if $I(t)$ becomes minimal and sufficiently small, $I(t)$ increases monotonically at least until $I(t) = I_{\text{enc}}$. Nakamura (1998) uses this definition of the triple encounter. Umehara (1997) modified the definition since it is not available for so-called non-close triple encounter where the minimal value of $I(t)$ is larger than I_{enc}. In the present paper, we study orbits near triple collision. All of such orbits is considered to experience the close triple encounter, i.e., $I(t)$ becomes sufficiently small. Thus we use the criterion by Junzo Yoshida (1998).

We will introduce several terms. An initial point of an orbit ending in triple collision will be called a *triple collision point.* An initial point leading to hyperbolic-elliptic escape or parabolic-elliptic escape after the first triple encounter will be called a *hyperbolic-elliptic point*

or a *parabolic-elliptic point*, respectively. Here a hyperbolic-elliptic (or parabolic-elliptic) escape means that one particle escapes to infinity with positive (or zero) limiting velocity. From the continuous dependence of solutions, hyperbolic-elliptic points form an open set in the two-dimensional initial-value space. Thus an open region formed with the hyperbolic-elliptic points will be called a *hyperbolic-elliptic region.* Similarly, an initial point of a non-escape orbit after the first triple encounter will be called a *non-escape point*, and a region with non-escape points will be called a *non-escape region.*

We will concentrate our attention to the initial-value dependence of solutions in a neighborhood of the initial value $(0, \sqrt{3}/2)$ corresponding to the equilateral configuration. Hereafter this homothetic equilateral triple collision point $(0, \sqrt{3}/2)$ will be called a *homothetic equilateral point* and denoted by T_1.

Umehara and Tanikawa (1997a) proved the following theorem with an assumption:

Theorem. *In an arbitrarily close to $T_1(0, \sqrt{3}/2)$, at least six hyperbolic-elliptic regions exist and the six hyperbolic-elliptic regions are located around the respective isosceles curves on the initial-value space $\grave{D}$ of the free-fall three-body problem with equal masses. Non-escape points after the triple encounter also exist in an arbitrarily close to T_1.*

For proofs, the follwoing two lemmas is necessary to be proved.

Lemma A *There is no initial point ending in triple collision during the first triple encounter in a sufficiently small neighborhood of T_1 on the initial-value space $\grave{D}$ except T_1.*

Lemma B *On the planar isosceles curves, all initial points in a sufficiently small neighborhood of T_1 except T_1 are hyperbolic-elliption points.*

Lemma A remains unproved in the work by Umehara and Tanikawa (1997a), and so we prove it in the present paper. Note that Umehara and Tanikawa (1997b) have combined the present work with the one by Umehara and Tanikawa (1997a).

3 Proofs

3.1 Outline of the proof

In the present section, we will prove Lemma A using the blow-up variables developed by Waldvogel (1982). There are equilibrium points corresponding to triple collision in the blow-up phase space, and a set of triple collision orbits is transformed into a stable manifold of an equilibrium point. Thus an intersection of the stable manifold and the initial-value space with zero-initial velocities is a set of initial values leading to triple collision in the free-fall three-body problem.

The phase space of the planar three-body problem with a given energy is a five-dimensional

manifold. The equilibrium point corresponding to triple collision of the equilateral-triangle type has a three-dimensional stable manifold. The initial-value space with zero-initial velocities is a two-dimensional manifold. Therefore, the intersection is a zero-dimensional manifold, i.e., points, if the stable manifold and the initial-value space are transversal. However, it is difficult to prove the transversality. It is also hard to distinguish whether initial values leading to triple collision are isolated points or not. The results of Tanikawa and Umehara (1997) investigating the initial-value instability until the third triple encounter suggest a fractal distribution of initial values leading to triple collision in the initial-value space.

Nevertheless, if we restrict ourselves to the behavior of orbits up to and including the first triple encounter, we can prove the isolation of the initial values leading to triple collision. In order to avoid the difficulty of proving transversality, we will consider the position of a phase point released with zero-initial velocities with respect to the stable manifold of the equilibrium point when the phase point approaches the equilibrium point. Further, we only consider the case of the homothetic equilateral solution.

First, we introduce blow-up variables, and derive tools necessary for the proof: a tangent space of an equilibrium point corresponding to triple collision, the homothetic equilateral solution, and the variation of the homothetic equilateral solution. After that, a necessary condition for a solution approaching the equilibrium point to be included in the local stable manifold of the equilibrium point is established in Lemma 1.

Second, we will set up two lemmas. In Lemma 2, we will prove that any solution curve starting sufficiently close to the initial point of the homothetic equilateral solution on the initial-value space is not included in the local stable manifold of the equilibrium point when the solution curve passes close to the equilibrium point for the first time. In Lemma 3, we will show that if such a near-homothetic-equilateral solution is included in a global stable manifold of a certain equilibrium point, it ends in triple collision after surviving the first triple encounter. From this result, it is easy to prove Lemma A.

3.2 blow-up variables by Waldvogel

Let us introduce blow-up variables in the planar three-body problem. In the present paper, we consider only the case of zero angular momentum. Let $q_j \in \mathbf{C}$, $j = 1,2,3$ be the complex Cartesian coordinate of the mass m_j in the center-of-mass system. The canonically conjugate momenta are $p_j = m_j \cdot dq_j/dt \in \mathbf{C}$ where t is the time. Let $a_j \in [0,\infty)$ and $\phi_j \in [0,2\pi]$, $j = 1,2,3$ be defined as follows:

$$q_l - q_k = a_j e^{i\phi_j}, \tag{4}$$

where (j,k,l) is $(1,2,3)$ or its cyclic permutation. Let $b_j \in \mathbf{R}$, $j = 1,2,3$ be defined as

$$p_j = b_k e^{i\phi_k} - b_l e^{i\phi_l}. \tag{5}$$

Note that a_j is the mutual distance between particles m_k and m_l. We consider the equal-mass case: $m_j = 1$, $j = 1,2,3$. According to van Kampen and Wintner (1937), the Hamiltonian of the system with zero angular momentum is written by a_j and b_j as

$$\mathcal{H} = \frac{1}{2}\sum_{jkl}\left(b_k^2 + b_l^2 + b_k b_l \frac{a_k^2 + a_l^2 - a_j^2}{a_k a_l}\right) - \sum_{j=1}^{3}\frac{1}{a_j}. \tag{6}$$

The equations of motion are

$$\frac{da_j}{dt} = \frac{\partial \mathcal{H}}{\partial b_j}, \quad \frac{db_j}{dt} = -\frac{\partial \mathcal{H}}{\partial a_j}, \qquad j = 1, 2, 3. \tag{7}$$

The system is of three degrees of freedom and admits the energy integral

$$\mathcal{H} = h = \text{const.} \tag{8}$$

There are two kinds of singularities in the phase space: $a_j = 0$ for each of $j = 1, 2, 3$ corresponding to binary collisions, and $a_1 = a_2 = a_3 = 0$ corresponding to triple collision.

Let us introduce blow-up variables $\tilde{\alpha}_j$ which also regularize the binary collision singularity. These are related to the mutual distances a_j as follows:

$$\tilde{a}_j = \tilde{\alpha}_k^2 + \tilde{\alpha}_l^2, \tag{9}$$

with

$$a_j = r\tilde{a}_j, \tag{10}$$

where r is defined by the square root of the moment of inertia:

$$r = \sqrt{\frac{1}{3}\sum_{j=1}^{3} a_j^2}. \tag{11}$$

The variables $\tilde{\beta}_j$ are introduced by

$$\tilde{\beta}_j = 2r^{\frac{1}{2}}\tilde{\alpha}_j(b_k + b_l). \tag{12}$$

Scaling the time by

$$\frac{dt}{d\tau} = r^{\frac{3}{2}}\tilde{a}_1\tilde{a}_2\tilde{a}_3, \tag{13}$$

we get the following seven equations from eqs.(7):

$$\begin{aligned}
\frac{dr}{d\tau} &= \frac{r}{2}\tilde{a}_1\tilde{a}_2\tilde{a}_3\tilde{v}, \\
\frac{d\tilde{\alpha}_j}{d\tau} &= \frac{1}{4}\{2(\tilde{a}_j^2 + \tilde{a}_j\tilde{\alpha}_j^2 - \tilde{\alpha}_k^2\tilde{\alpha}_l^2)\tilde{\beta}_j - \tilde{a}_l\tilde{\alpha}_j\tilde{\alpha}_k\tilde{\beta}_k - \tilde{a}_k\tilde{\alpha}_j\tilde{\alpha}_l\tilde{\beta}_l - \tilde{a}_1\tilde{a}_2\tilde{a}_3\tilde{v}\tilde{\alpha}_j\}. \\
\frac{d\tilde{\beta}_j}{d\tau} &= -\frac{1}{2}\{\tilde{a}_j\tilde{\alpha}_j\tilde{\beta}_j^2 + \tilde{\alpha}_j(2\tilde{\alpha}_j^2 + \tilde{a}_j)(\tilde{\beta}_k^2 + \tilde{\beta}_l^2)\} + \frac{\tilde{\beta}_j}{4}\{(2\tilde{\alpha}_j^2 + \tilde{a}_l)\tilde{\alpha}_k\tilde{\beta}_k + (2\tilde{\alpha}_j^2 + \tilde{a}_k)\tilde{\alpha}_l\tilde{\beta}_l\} \\
&\quad + 2\tilde{\alpha}_j(2\tilde{a}_j + \tilde{a}_k + \tilde{a}_l) + 2hr\tilde{\alpha}_j\tilde{a}_j(\tilde{a}_k + \tilde{a}_l),
\end{aligned} \tag{14}$$

for $j = 1, 2, 3$, where

$$\tilde{v} = \sum_{j}^{3} \tilde{\alpha}_j\tilde{\beta}_j. \tag{15}$$

They admit the following invariant relations:

$$\frac{1}{8}\sum_{jkl}\tilde{a}_j[(\tilde{\alpha}_1^2 + \tilde{\alpha}_2^2 + \tilde{\alpha}_3^2)\tilde{\beta}_j^2 + (\tilde{\alpha}_k\tilde{\beta}_l - \tilde{\alpha}_l\tilde{\beta}_k)^2] - \sum_{jkl}\tilde{a}_k\tilde{a}_l \quad - \quad hr\tilde{a}_1\tilde{a}_2\tilde{a}_3 = 0, \tag{16}$$

and

$$\sum_{j}^{3} \tilde{a}_j^2 = 3. \tag{17}$$

These invariant relations correspond to the energy conservation and scale normalization, respectively.

Let $\tilde{M}(h)$ and $\tilde{M}_0$ denote a blow-up phase space with a given energy h and its subset satisfying $r = 0$, respectively. Both subsets constitute invariant submanifolds for the vectorfield (14). These have dimensions five and four, respectively. The orbits in $\tilde{M}_0$ have no direct physical meaning. Their behavior, however, reflects the behavior of orbits in $\tilde{M}(h) \setminus \tilde{M}_0$ while these are close to triple collision.

The initial-value space in the blow-up coordinate system will be considered instead of the initial-value space $\grave{D}$ defined in the preceding section. In the free-fall problem, initial values of b_j are equal to zero for $j = 1, 2, 3$, and so $\tilde{\beta}_j(0) = 0$. The initial-value space with zero-initial velocities in $\tilde{M}(h)$ can be defined as $(\tilde{\alpha}_1, \tilde{\alpha}_2, \tilde{\alpha}_3)$ where eq.(17) holds. Therefore, any of the two-dimensional surfaces $(\tilde{\alpha}_i, \tilde{\alpha}_j)$, $1 \leq i < j \leq 3$ can be used as an initial value space. Let us denote them by S_{ij}.

Let H_0 be the initial point on S_{12} corresponding to $T_1(0, \sqrt{3}/2)$ on $\grave{D}$. Surfaces S_{12} around H_0 and $\grave{D}$ around T_1 are topologically equivalent. Indeed the Jacobian determinant of the transformation $(x, y) \mapsto (\tilde{\alpha}_1, \tilde{\alpha}_2)$ is $-y\tilde{a}_1(\tilde{a}_1 + \tilde{a}_2)/(24r^4\tilde{\alpha}_1\tilde{\alpha}_2\tilde{a}_2\tilde{a}_3)$ and the variables $y, \tilde{a}_j, \tilde{\alpha}_1$ and $\tilde{\alpha}_2$ are positive around H_0, and so the Jacobian determinant keeps negative. This property holds in the other S_{ij}.

3.3 The homothetic equilateral solution

Let us describe the homothetic equilateral solution which starts at the initial point H_0 with zero-initial velocities. The configuration of this solution maintains equilateral triangle, and so the equalities $\tilde{\alpha}_1(\tau) = \tilde{\alpha}_2(\tau) = \tilde{\alpha}_3(\tau) = \tilde{\alpha}(\tau)$ and $\tilde{\beta}_1(\tau) = \tilde{\beta}_2(\tau) = \tilde{\beta}_3(\tau) = \tilde{\beta}(\tau)$ always hold with appropriate functions $\tilde{\alpha}(\tau)$ and $\tilde{\beta}(\tau)$. Thus the solution has the form

$$\psi_{\text{homo}}(\tau) = (r(\tau), \tilde{\alpha}(\tau)\mathbf{e}, \tilde{\beta}(\tau)\mathbf{e})^T, \tag{18}$$

where $\mathbf{e} = (1, 1, 1)$, and $\tilde{\alpha}(\tau)$, $\tilde{\beta}(\tau)$ and $r(\tau)$ are described explicitly as

$$\tilde{\alpha}(\tau) = \frac{1}{\sqrt{2}},$$

$$\tilde{\beta}(\tau) = \frac{4}{\sqrt{3}} \cdot \frac{1 - \exp(\sqrt{6}\tau)}{1 + \exp(\sqrt{6}\tau)}, \tag{19}$$

$$r(\tau) = 1 - \frac{3}{16}\tilde{\beta}^2(\tau) = \frac{4\exp(\sqrt{6}\tau)}{\{1 + \exp(\sqrt{6}\tau)\}^2}.$$

The fact that $\tilde{\alpha}(\tau)$ is constant is obtained from the invariance (17). The variable $\tilde{\beta}(\tau)$ is obtained from the following differential equation:

$$\frac{d\tilde{\beta}}{d\tau} = -\frac{3}{4}\sqrt{2}\left(\tilde{\beta}^2 - \frac{16}{3}\right) + 2\sqrt{2}rh = \frac{3}{8}\sqrt{2}\left(\tilde{\beta}^2 - \frac{16}{3}\right). \tag{20}$$

This equation is derived using the third equation of the system (14). The latter equality is derived from the energy integral (16). Note that $h = -3$ in this case.

Next let us derive the variational equations along ψ_{homo}. We introduce a variation $\delta\psi_{\text{homo}}$ in the tangent space to $\mathbf{R}^7$. Let a 3×3 matrix $J[x, y]$ be

$$\begin{bmatrix} x & y & y \\ y & x & y \\ y & y & x \end{bmatrix}. \tag{21}$$

Then

$$\frac{d}{d\tau}\begin{bmatrix} \delta r(\tau) \\ \delta\tilde{\boldsymbol{\alpha}}(\tau) \\ \delta\tilde{\boldsymbol{\beta}}(\tau) \end{bmatrix} = \begin{bmatrix} \frac{3}{2\sqrt{2}}\tilde{\beta}(\tau) & \frac{7}{2}\left(1 - \frac{3}{16}\tilde{\beta}^2(\tau)\right)\mathbf{e} & \frac{1}{2\sqrt{2}}\left(1 - \frac{3}{16}\tilde{\beta}^2(\tau)\right)\mathbf{e} \\ \mathbf{o}^T & J_{\tilde{\alpha},\tilde{\alpha}} & J_{\tilde{\alpha},\tilde{\beta}} \\ -6\sqrt{2}\mathbf{e}^T & J_{\tilde{\beta},\tilde{\alpha}} & J_{\tilde{\beta},\tilde{\beta}} \end{bmatrix}\begin{bmatrix} \delta r(\tau) \\ \delta\tilde{\boldsymbol{\alpha}}(\tau) \\ \delta\tilde{\boldsymbol{\beta}}(\tau) \end{bmatrix}, \tag{22}$$

where $\mathbf{o} = (0, 0, 0)$,

$$\tilde{\boldsymbol{\alpha}} = (\tilde{\alpha}_1, \tilde{\alpha}_2, \tilde{\alpha}_3)^T, \qquad \tilde{\boldsymbol{\beta}} = (\tilde{\beta}_1, \tilde{\beta}_2, \tilde{\beta}_3)^T, \tag{23}$$

and

$$\begin{aligned} J_{\tilde{\alpha},\tilde{\alpha}} &= J\left[-\tfrac{5}{2\sqrt{2}}\tilde{\beta}(\tau),\ -\tfrac{1}{4\sqrt{2}}\tilde{\beta}(\tau)\right], & J_{\tilde{\alpha},\tilde{\beta}} &= J\left[\tfrac{1}{2},\ -\tfrac{1}{4}\right], \\ J_{\tilde{\beta},\tilde{\alpha}} &= J\left[\tfrac{3}{2}\tilde{\beta}^2(\tau) - 12,\ \tfrac{21}{8}\tilde{\beta}^2(\tau) - 12\right], & J_{\tilde{\beta},\tilde{\beta}} &= J\left[0,\ -\tfrac{3}{2\sqrt{2}}\tilde{\beta}(\tau)\right]. \end{aligned} \tag{24}$$

The conditions so that the variations belong to $\tilde{M}(h)$ are

$$\sum_j^3 \delta\tilde{\alpha}_j(\tau) = 0, \qquad \delta r(\tau) = -\frac{1}{8}\tilde{\beta}(\tau)\sum_j^3 \delta\tilde{\beta}_j(\tau). \tag{25}$$

3.4 Local stable manifold of Lagrangian equilibrium point

In the blow-up phase space, a solution ending in triple collision approaches asymptotically an equilibrium point. We will derive a position of the equilibrium point and vectors spanning the stable manifold of the equilibrium point. Let E_h be the equilibrium point which $\psi_{\text{homo}}(\tau)$ tends to approach as $\tau \to \infty$. The local stable manifold of E_h in an ε-neighborhood of E_h is denoted by $W^s_{\text{loc}}(E_h)$ where ε is a small positive number. Similarly, $W^u_{\text{loc}}(E_h)$ denotes the local unstable manifold of E_h. The tangent space to a manifold M at a point P is denoted by $T_P M$.

The position of E_h in the phase space is

$$(r^{\text{eq}}, \tilde{\boldsymbol{\alpha}}^{\text{eq}}, \tilde{\boldsymbol{\beta}}^{\text{eq}})^T = \{(r, \tilde{\alpha}\mathbf{e}, \tilde{\beta}\mathbf{e})^T | r = 0, \tilde{\alpha} = \frac{1}{\sqrt{2}}, \tilde{\beta} = -\frac{4}{\sqrt{3}}\}, \tag{26}$$

since r and $\tilde{\beta}$ tend 0 and $-4/\sqrt{3}$, respectively, as $\tau \to \infty$. Therefore, variational equations at E_h are obtained by substituting $\tilde{\beta} = -4/\sqrt{3}$ in eq.(22).

We obtain $T_{E_h}W^s_{\rm loc}(E_h)$ as the following three-dimensional subspace:

$$\begin{bmatrix} \delta\tau^{\rm eq} \\ \delta\tilde{\alpha}_1^{\rm eq} \\ \delta\tilde{\alpha}_2^{\rm eq} \\ \delta\tilde{\alpha}_3^{\rm eq} \\ \delta\tilde{\beta}_1^{\rm eq} \\ \delta\tilde{\beta}_2^{\rm eq} \\ \delta\tilde{\beta}_3^{\rm eq} \end{bmatrix} = \zeta_1 \begin{bmatrix} 1 \\ 0 \\ 0 \\ 0 \\ \frac{2}{\sqrt{3}} \\ \frac{2}{\sqrt{3}} \\ \frac{2}{\sqrt{3}} \end{bmatrix} + \zeta_2 \begin{bmatrix} 0 \\ 1 \\ 0 \\ -1 \\ \kappa_- \\ 0 \\ -\kappa_- \end{bmatrix} + \zeta_3 \begin{bmatrix} 0 \\ 0 \\ 1 \\ -1 \\ 0 \\ \kappa_- \\ -\kappa_- \end{bmatrix}, \tag{27}$$

for any real numbers ζ_1, ζ_2 and ζ_3, where

$$\kappa_- = -\frac{\sqrt{6}(5+\sqrt{13})}{3}. \tag{28}$$

From the above expression, we can derive the following lemma.

Lemma 1. *If a variation at E_h is included in $T_{E_h}W^s_{\rm loc}(E_h)$, then*

$$\delta\tilde{\beta}_i^{\rm eq} - \delta\tilde{\beta}_j^{\rm eq} = \kappa_- \left(\delta\tilde{\alpha}_i^{\rm eq} - \delta\tilde{\alpha}_j^{\rm eq}\right), \tag{29}$$

where $(i,j) = (1,2),(2,3)$ and $(3,1)$.

3.5 Variation with zero initial velocities

In order to prove Lemma 2 that follows, we transform the variational equations (22) and examine the behavior of solutions. Although this system is five dimensional, we can independently solve the two-dimensional subsystem $(q(\tau), p(\tau))$ definded by

$$q(\tau) = \delta\tilde{\alpha}_1(\tau) - \delta\tilde{\alpha}_2(\tau), \quad p(\tau) = \delta\tilde{\beta}_1(\tau) - \delta\tilde{\beta}_2(\tau). \tag{30}$$

From eq.(22) we obtain

$$\begin{aligned} q'(\tau) &= -\tfrac{9}{4\sqrt{2}}\tilde{\beta}(\tau)q(\tau) + \tfrac{3}{4}p(\tau) \\ p'(\tau) &= -\tfrac{9}{8}\tilde{\beta}^2(\tau)q(\tau) + \tfrac{3}{2\sqrt{2}}\tilde{\beta}(\tau)p(\tau), \end{aligned} \tag{31}$$

and so

$$\begin{aligned} z' &= -\tfrac{3}{4}z^2 + \tfrac{15}{4\sqrt{2}}\tilde{\beta}(\tau)z - \tfrac{9}{8}\tilde{\beta}^2(\tau) \\ \rho' &= \left\{\tfrac{3\sqrt{2}}{4}\tilde{\beta}(\tau)z^2 + \left(\tfrac{3}{4} - \tfrac{9}{8}\tilde{\beta}^2(\tau)\right)z - \tfrac{9}{4\sqrt{2}}\tilde{\beta}(\tau)\right\}\rho\cos^2(\arctan z), \end{aligned} \tag{32}$$

where a prime ($'$) means differentiation with respect to τ, and

$$\rho = \sqrt{q^2+p^2}, \tag{33}$$

$$z = \frac{p}{q} \quad (\text{if } \rho \neq 0). \tag{34}$$

Let $\varphi(\tau)$ be a solution $z(\tau)$ with the initial value $z(0) = 0$ corresponding to zero velocities in the first equation of the system (32). We assume $\rho(0) > 0$. The origin is the fixed point showing

isosceles motion including the homothetic equilateral solution. Thus $\rho(\tau) \neq 0$ for $\tau > 0$, and so $\varphi(\tau)$ is well-defined.

We will investigate the behavior of $\varphi(\tau)$. On the (τ, z)-plane, there are two boundaries satisfying $z'(\tau) = 0$ represented as

$$z = \left\{ \zeta_{\pm}(\tau) \middle| \ \zeta_{\pm} = \frac{5 \pm \sqrt{13}}{2\sqrt{2}} \tilde{\beta}(\tau) \right\}. \tag{35}$$

Note that $\zeta_+(\tau) \leq \zeta_-(\tau) \leq 0$. The equality holds if and only if $\tau = 0$. We have $z' > 0$ if $\zeta_+(\tau) < z(\tau) < \zeta_-(\tau)$, and $z' < 0$ if $z(\tau) < \zeta_+(\tau)$ or $z(\tau) > \zeta_-(\tau)$. The solution $\varphi(\tau)$ stays in the region $\{z | z \geq \zeta_-\}$. Indeed $\varphi(\Delta) > \zeta_-(\Delta)$ for a sufficiently small $\Delta > 0$, and if there is a $\tau > \Delta$ such that $\varphi(\tau)$ reaches the boundary $z = \zeta_-(\tau)$, then $\varphi'(\tau)$ becomes 0. Since the boundary $z = \zeta_-(\tau)$ is monotone decreasing with respect to τ, $\varphi(\tau)$ returns to the region $\{z(\tau) | z > \zeta_-(\tau)\}$. As a result, the relations $\varphi(\tau) \geq \zeta_-(\tau)$ and $\varphi'(\tau) \leq 0$ hold for $\tau \geq 0$. Hence, for $\tau_0 \in [0, \infty)$

$$\varphi(\tau_0) > \lim_{\tau \to \infty} \varphi(\tau) = \kappa_- + \frac{2\sqrt{78}}{3}. \tag{36}$$

With respect to τ, $\rho(\tau)$ along $\varphi(\tau)$ is monotone increasing. For, the second equation of (32) shows that on the (τ, z)-plane there are two boundaries satisfying $\rho'(\tau) = 0$ represented as

$$z = \left\{ \varpi_{\pm}(\tau) \middle| \ \varpi_{\pm} = \frac{3\tilde{\beta}^2(\tau) - 2 \pm \sqrt{9\tilde{\beta}^4(\tau) + 36\tilde{\beta}^2(\tau) + 4}}{4\sqrt{2}\tilde{\beta}(\tau)} \right\}. \tag{37}$$

We have $\rho' > 0$ for any $\tau > 0$ since $\varpi_+(\tau) < \varphi(\tau) < \varpi_-(\tau)$.

In the above, we assumed $\rho(0) > 0$. If $\rho(0) = 0$, we will define $q = \delta\tilde{\alpha}_2 - \delta\tilde{\alpha}_3$ and $p = \delta\tilde{\beta}_2 - \delta\tilde{\beta}_3$ instead of the above. Then we again obtain the relation (36) for $\rho(0) \neq 0$, $\delta\tilde{\alpha}_1(0) \neq 0$. It is not necessary to consider the case $\delta\tilde{\alpha}_1(0) = \delta\tilde{\alpha}_2(0) = 0$ since this solution is ψ_{homo} itself.

Finally, let us estimate the direction of $W^s_{\text{loc}}(E_h)$ on the (q, p)-plane at $H(\tau_0)$. From eq.(27), $W^s_{\text{loc}}(E_h)$ has dimension three in $\tilde{M}(h)$. According to Devaney (1980) an intersection between $W^s_{\text{loc}}(E_h)$ and the isosceles subspace has dimension two. Isosceles orbits are degenerated at the origin on the (q, p)-plane. Therefore, $T_{H(\tau_0)}W^s_{\text{loc}}(E_h)$ has at most one-dimensional direction σ on the (q, p)-plane. From Lemma 1, a direction of $T_{H(\tau_0)}W^s_{\text{loc}}(E_h)$ formally tends $z \to \kappa_-$ as $\tau_0 \to \infty$. Since $W^s_{\text{loc}}(E_h)$ is a real analytic manifold, for an any $\chi > 0$ there is a sufficiently small $\varepsilon > 0$ (i.e., a sufficiently large τ_0) such that the direction of $T_{H(\tau_0)}W^s_{\text{loc}}(E_h)$ is limited to

$$\kappa_- - \chi < \sigma < \kappa_- + \chi. \tag{38}$$

Now we can establish the following lemma. Let $N_d(P)$ denote a d-neighborhood of a point P. Let $\psi(\tau, \psi_0)$ be a solution starting at the initial value $\psi_0 \in \tilde{M}(h)$ in the system (22). τ_0 is the time τ when $\psi_{\text{homo}}(\tau)$ enters $N_\varepsilon(E_h)$ for the first time.

Lemma 2. *No solution ψ starting in a sufficiently small neighborhood of H_0 on the initial-value space S_{12} except H_0 itself belongs to $W^s_{\text{loc}}(E_h)$ when ψ enters an ε-neighborhood of E_h for the first time.*

Proof. Suppose the contrary. Then, there is an infinite sequence of points $P_n \in S_{12}$ converging to H_0 such that the direction of $\{\psi(\tau_0, P_n) - \psi_{\rm homo}(\tau_0)\}$ on the (q,p)-plane tends to σ of eq.(38) as $n \to \infty$. However, it contradicts eq.(36). Hence, there is a $d > 0$ such that $\psi(\tau_0, \{N_d(H_0) \cap S_{12} \setminus H_0\}) \not\subset W^s_{\rm loc}(E_h)$. □

In this stage, the following transversality is shown simply:

Corollary. *The stable manifold of E_h intersect the initial-value space transversally at T_1.*

In fact, any solution curve crossing the initial-value space is perpendicular to the initial-value space. Lemma 2 says that all solutions starting sufficiently close to T_1 except T_1 are not included in the local stable manifold of E_h. The stable manifold and the initial-value space are three- and two-dimensional manifolds, respectively, in the five-dimensional phase space.

3.6 Behavior of near-collision solutions after bypassing the equilibrium point

Once $\psi(\tau, \{N_d(H_0) \cap S_{12} \setminus H_0\})$ leaves the equilibrium point E_h, variational equations are invalid. Let E_x be any equilibrium point corresponding to triple collision including E_h. It is possible that the solution enters the stable manifold of E_x eventually. If it happens, there is an initial point leading to triple collision in a sufficiently small neighborhood of the point H_0. In this case, however, we can prove that such a solution survives the first triple encounter.

In order to prove it, it is sufficient to show that the system experience a minimal value of the moment of inertia $I(t)$ at least once even if the system starting near T_1 ends in triple collision. If $I(t)$ becomes minimal, $I(t)$ continues to be concave during $I(t) < I_{\rm enc}$, where $I_{\rm enc}$ is introduced in eq.(3). In this time interval, $I(t)$ does not have any other minimal value. From the definition of triple encounter, it implies that the system survives the first triple encounter.

The global stable and unstable manifolds of E_h are defined by

$$W^s(E_h) = \bigcup_{\tau \le 0} \psi(\tau, W^s_{\rm loc}(E_h)), \tag{39}$$

$$W^u(E_h) = \bigcup_{\tau \ge 0} \psi(\tau, W^u_{\rm loc}(E_h)), \tag{40}$$

respectively. From Lemma 2, $\psi(\tau, \{N_d(H_0) \cap S_{12} \setminus H_0\})$ flows away from E_h along $W^u(E_h)$ since the equilibrium point E_h is of a hyperbolic type.

Lemma 3. *If a solution starting in any small neighborhood of H_0 on S_{12} except H_0 itself is included in $W^s(E_x)$, then the system survives the first triple encounter.*

Proof. It will be shown that for any small $d > 0$, $\psi(\tau, \{N_d(H_0) \cap S_{12} \setminus H_0\})$ experiences the minimal value of the moment of inertia. It means that the system survives the first triple encounter by the definition of triple encounter.

From the equations of motion (14), we have $r' < 0$ if $\tilde{v} < 0$, and $r' > 0$ if $\tilde{v} > 0$. Recall that $r^2(\tau)$ is the moment of inertia of the system. According to Waldvogel (1982), motions in $\tilde{M}_0$ are

gradient-like with respect to $\tilde{v}$. Since $W^u(E_h)$ lies in $\tilde{M}_0$, $\tilde{v}$ increases along any non-stationary solution curves in $W^u(E_h)$.

First consider a solution curve which lies in $W^u(E_h)$. There is a $\tau_1 > 0$ such that $\tilde{v}(\tau_1) = 0$ and $\tilde{v}(\tau) > 0$ during $\tau \in (\tau_1, \infty)$ along every $\psi(\tau, W^u_{\rm loc}(E_h))$ since there is no equilibrium point between E_h and a section $\tilde{v} = 0$ in $\tilde{M}_0$. Any equilibrium point E_x corresponding to triple collision satisfies $\tilde{v} < 0$. All the equilibrium configurations are classified in only two types: the collinear central configuration and the equilateral triangle one. Let $\tilde{v}^{\rm C}$ and $\tilde{v}^{\rm T}$ be values of $\tilde{v}$ at the equilibrium points of the collinear type and the equilateral-triangle type, respectively. Then $\tilde{v}^{\rm C} < \tilde{v}^{\rm T} < 0$. Thus, $W^u(E_h)$ is not connected to any E_x.

Next consider a solution curve $\psi(\tau, \{N_d(H_0) \cap S_{12} \setminus H_0\})$. Since $\psi \not\subset W^s_{\rm loc}(E_h)$ when ψ passes close to E_h from Lemma 2, ψ follows $W^u(E_h)$. Thus ψ passes through the section $\tilde{v} = 0$ around τ_1. The non-decreasing value $\tilde{v}(\tau)$ of ψ changes sign from negative to positive for the first time. The moment of inertia of ψ begins to increase. It survives the first triple encounter by the definition. □

From the above lemma, the system survives the first triple encounter if there is an initial point leading to triple collision in a sufficiently small neighborhood of the point H_0 on S_{12}. The initial-value space S_{12} is topologically equivalent to the initial-value space $\grave{D}$. Therefore, Lemma A follows at once.

Acknowledgement

The authors would like to thanks to Drs. J.Yoshida, H.Kinoshita, H.Yoshida and Tekeshi Nakamura for discussions.

References

Agekian, T.A. and Anosova, J.P., 1967, A study of the dynamics of triple systems by means of statistical sampling, *Astron. Zh.*, **44**, 1261-1273; translated into English in *Soviet Astronomy*, **11**, 1006-1014 (1968).

Agekian, T.A. and Anosova, J.P., 1968, Investigation of the dynamics of triple systems by the method of statistical tests. II, *Astrofizika*, **4**, 31-40; translated into English in *Astrophysics*, **4**, 11-16 (1968).

Aarseth,S.J., Anosova,J.P, Orlov,V.V. and Szebehely,V.G., 1994, Close triple approaches and escape in the three-body problem, *Celestial Mechanics and Dynamical Astronomy*, **60**, 131-137.

Birkhoff, G.D., 1927, Dynamical Systems, *Am. Math. Soc. Publ., Provedence RI.*

Broucke, R. A., 1995; On the role of the moment of inertia in three-body scattering, *From Newton to Chaos* (eds. Roy, A. and Steves, B.), Plenum Press, New York, pp.327-341.

Devaney, R.L., 1980, Triple collision in the planar isosceles three-body problem, *Inven. Math.*, **60**, 249-267.

McGehee, R., 1974; Triple collision in the collinear three-body problem, *Inven. Math.*,

27, 191-227.

Nakamura, T., 1998; in the present proceedings.

Tanikawa, K., Umehara, H. and Abe, H., 1995, A search for collision orbits in the free-fall three-body problem. I. numerical procedure, *Celestial Mechanics and Dynamical Astronomy*, **62**, 335-362.

Umehara, H. 1997, The free-fall three-body problem: escape and collision,*Thesis.*

Umehara, H. and Tanikawa, K., 1997a, Orbital structure near the homothetic equilateral triple collision in the free-fall three-body problem, *Proceedings of the 29th symposium on Celestial Mechanics in Tokyo*, pp.188-199.

Umehara, H. and Tanikawa, K., 1997b, Orbital distribution arbitrarily close to the homothetic equilateral triple collision in the free-fall three-body problem, *Celestial Mechanics and Dynamical Astronomy*, Submitted.

van Kampen, E.R. and Wintner, A., 1937; On a symmetrical canonical reduction of the problem of three bodies, *Am. J. Math.*, **59**, 153-166.

Waldvogel, J., 1973, Collision singularities in gravitational problems, *Recent Advances in Dynamical Astronomy* (eds., Tapley, B.D. and Szebehely, V.), D.Reidel Publishing Company: Dordrecht-Holland, pp.21-33.

Waldvogel, J., 1982, Symmetric and regularized coordinates on the plane triple collision manifold, *Celestial Mechanics*, **28**, 69-82.

Yoshida, J., 1998, private communication.

The isolated saddle-node bifurcation inside a nontrivial invariant set

SHIN KIRIKI Tokyo Denki Univ.

Dept. of Mathematical Sciences

This study starts from the change which the following Figure 1 shows. A diffeomorphism with a horseshoe has a configuration of invariant manifolds of a saddle fixed point as shown by the left panel of Figure 1. By some perturbation, the saddle-node bifurcation occurs in its nontrivial invariant set, that is, a couple of new hyperbolic fixed points is born, and then a new configuration as shown by the right panel of Figure 1 is obtained. In [2], we clarify a relation between such a saddle-node bifurcation inside the maximal invariant set and a hyperbolicity of its system.

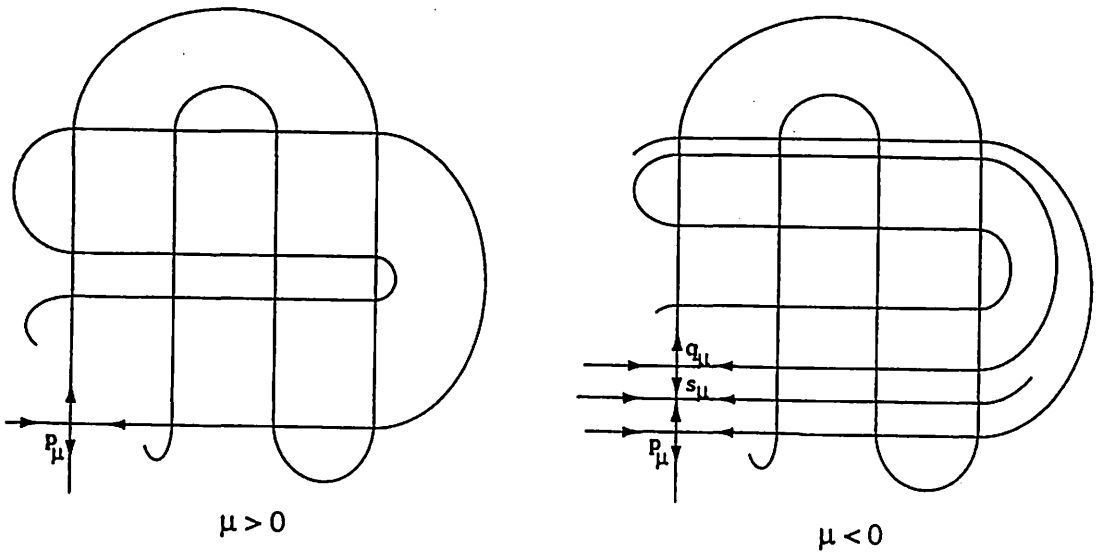

Figure 1

The *first bifurcation* of a parameterized diffeomorphism is an important concept which expresses the first instability of its system. It is significant to detect the first bifurcation for given dynamical systems; besides, it is important to study what happens after the first bifurcation occurring. Then, we here intro-

duce the following somewhat special concept. We say that an arc $\{\varphi_\mu\}$ has an *isolated bifurcation* at $\mu = \mu_0$ if there is a neighborhood of μ_0 such that φ_μ is structurally stable for every μ in this neighborhood except μ_0. When the second author studied about arcs of two-dimensional diffeomorphisms having the first homoclinic tangency inside a horseshoe which is a first bifurcation [1], Prof. Takens suggested that the above saddle-node arc is an important example of the first bifurcation which is different from the first homoclinic tangency [3]. It is clear that such a first homoclinic tangency inside the horseshoe is not an isolated bifurcation. The aim of this paper is to answer the question: *is such a saddle-node bifurcation inside a nontrivial invariant set a first bifurcation, besides, is it isolated?* The same question was brought up by Prof. Díaz and the first author, when they discussed about the bifurcations and hyperbolicity in both quadratic and non-quadratic critical saddle-node cycle of two-parameterized diffeomorphisms. The main result of [2] is

Main Theorem. *There exists a C^2-open sets of smooth arcs of two-dimensional diffeomorphisms such that each of arcs has a generic and attracting saddle-node bifurcation inside the nontrivial invariant set, which is an isolated bifurcation.*

References

[1] S. Kiriki, Hyperbolicity of the special one-parameter family with a first homoclinic tangency, *Dynamics and Stability of Systems*, **11**, **1**, (1996) 3-18

[2] Y. Cao and S. Kiriki, The isolated saddle-node bifurcation occurring inside the horseshoe, *submitted*

[3] F. Takens, *Personal communications.*

Research announcements of a multi-dimensional Hénon family

Shin Kiriki
Department of Mathematical Sciences, Tokyo Denki University, Hatoyama, Hiki, Saitama, 350-03, Japan

Masaki Nakajima
Hitachi Software Engineering Co., Ltd., 6-81, Ogami-cho, Naka-ku, Yokohama, Kanagawa, 231, Japan

1 Introduction

Hénon map $f_{a,b}(x,\ y) = (a - by - x^2, x)$ is one of the most important objects in the chaotic dynamical systems. Through its study, many mathematicians have confirmed the some essential concepts in the dynamical systems presented by Smale [6], and encountered various phenomena and interesting new problems which contain many difficulties originating from its nonlinearity. Computer simulations are also indispensable for the progress of this study. There have been many works on this map. However, we here state briefly some essential works which motivated our study of dynamics with the high-dimensional Hénon-like diffeomorphisms. This planar map was first presented by Hénon with its non-trivial phenomenon called a strange attractor which was discovered by computational experiment [2]. Nitecki and Devany showed in [1] that, when a and b satisfy some conditions, it has the same structure as a horseshoe map, that is, it has a hyperbolic structure and its dynamics is coded perfectly by a topological conjugacy with the 2-shift. Yang moreover showed that this structure is preserved until the first homoclinic tangency occurs when a decreases and b takes very small positive value [8].

Benedicks and Carleson proved that the occurrence of the non-trivial attractors is a persistent phenomenon in the measure-theoretical sense. Mora and Viana extended their result to the more generic one-parameter family of surface diffeomorphisms. In [7], Viana moreover extended their result to higher dimensions, that is, it assures the existence of codimension-1 Hénon-like non-hyperbolic attractors near the homoclinic tangency on the high-dimensional manifold.

In the our paper [5], on a somewhat different ground from that of Viana, we extend the Hénon map to a high-dimensional space. One of the merits of our method is that we can actually have a formula for this extended map which has some properties similar to the 2-dimensional Hénon map. Therefore, one can observe globally its dynamics and its progress of bifurcations by numerical computations. Actually, in the 3-dimensional Euclidean space, we define a family of diffeomorphisms of Hénon type as

$$F_{a,b}(x,\ y,\ z) = (a + bz - x^2,\ x,\ y).$$

As in 2-dimensional case, some non-trivial attractors are observed easily in $\mathbb{R}^3$ by numerical experiments, for example $(a,\ b)$ close to $(1.7,\ -0.1)$, $(0.2,\ 0.8)$, as in Figure 1. However, it is not yet clear whether these attractors are non-hyperbolic and persistently strange. We

showed in [3] that the structure of this 3-dimensional family is globally stable for some combinations of the parameter values. This is the extension of the result in [1] to the high-dimensional family. Moreover, by numerical experiments, we observed the relation between its first homoclinic tangency and its first bifurcation in [3].

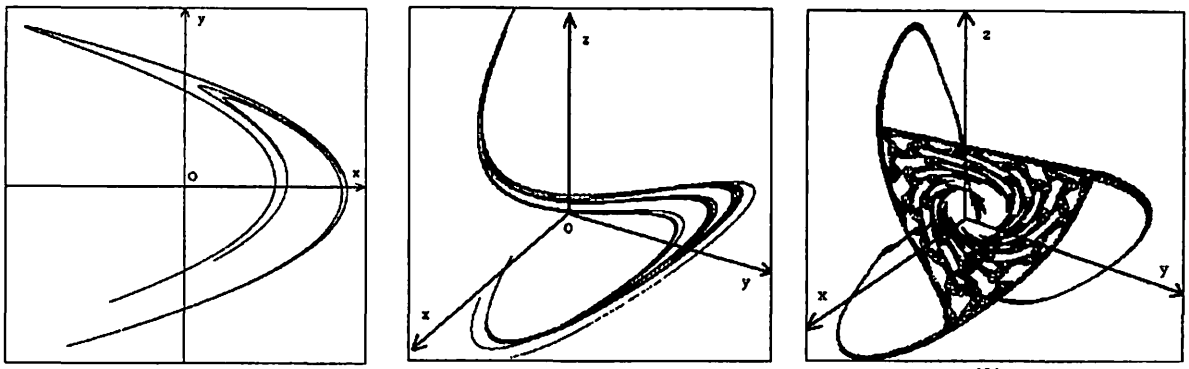

(1) (2) (3)

Figure 1: (1) A 2-dimensional Heńon attractor, for $a = 1.4$ and $b = 0.3$. (2) and (3) The 3-dimensional Heńon attractors for (1.7, −0.1) and (0.2, 0.8), respectively.

As the results of the paper [5], we present a two-parameter family $F_{a,b}$ of diffeomorphisms of Hénon type on the Euclidean space of an arbitrary dimension m, and show that there is an open set $\mathcal{H}_m$ in the product space of parameters such that, for every $(a,\ b) \in \mathcal{H}_m$, $F_{a,b}$ has a hyperbolic structure. In this research announcement, we introduce the our paper [5].

2 Definition of a high-dimensional Hénon family and the main result

Let $m \geq 3$ be an integer, and $\mathbb{R}^m$ be a m-dimensional Euclidean space. We define a two-parameter family $F_{a,b}$ of diffeomorphisms on $\mathbb{R}^m$ treated in our study as

$$F_{a,b}(x_1,\ x_2,\ \ldots,\ x_m) = (a + bx_m - x_1^2,\ x_1,\ x_2,\ \ldots,\ x_{m-1}),$$

where a and b are real parameters. One shall understand the reason why we call this family a *m-dimensional special Hénon family* by the following fundamental properties which are similar to the 2-dimensional Hénon map. When $b \neq 0$, it's inverse is

$$F_{a,b}^{-1}(x_1,\ x_2,\ \ldots,\ x_m) = (x_2,\ x_3,\ \ldots,\ x_m,\ b^{-1}(-a + x_1 + x_2^2)),$$

and it is a bijection. Moreover, $F_{a,b}$ is a diffeomorphism on $\mathbb{R}^m$. When $b = 0$, $F_{a,0}(x_1,\ x_2,\ \ldots,\ x_m) = (a - x_1^2,\ x_1,\ \ldots,\ x_{m-1})$ which maps all points of $\mathbb{R}^m$ to the parabolic surface. The Jacobian of $F_{a,b}$ is equal to the value of the parameter b for every $\mathbf{x} \in \mathbb{R}^m$, that is,

$$\det(DF_{a,b})_{\mathbf{x}} = \det \begin{pmatrix} -2x & 0 & \cdots & 0 & b \\ 1 & 0 & \cdots & 0 & 0 \\ 0 & 1 & \cdots & 0 & 0 \\ \vdots & & \ddots & & \vdots \\ 0 & 0 & \ldots & 1 & 0 \end{pmatrix} = b.$$

$F_{a,b}$ is obtained by the composed mapping of ϕ, ϕ_b and ϕ_a, that is, $F_{a,b} = \phi_a \circ \phi_b \circ \phi$, where

$$\phi(x_1, x_2, \cdots, x_m) = (x_m, x_1, \cdots, x_{m-1});$$

$$\phi_b(x_1, x_2, \cdots, x_m) = (bx_1, x_2, \cdots, x_m);$$

$$\phi_a(x_1, x_2, \cdots, x_m) = (a + x_1 - x_2^2, x_2, \cdots, x_m).$$

These above constructions of this family are similar to those of 2-dimensional Hénon family. Moreover, in the following main theorem, we get an essential property of this family, which is correspond with that of the 2-dimensional Hénon family.

Main Theorem. *Let $F_{a,b}$ be a m-dimensional special Hénon family. Let $\mathcal{H}_m$ be an open set in the product set of parameter spaces such that*

$$\mathcal{H}_m = \left\{(a, b) \in \mathbb{R} \times \mathbb{R} \ : \ a > \frac{(1+|b|)^2}{4}\left(m + 4 + 2\sqrt{m+4}\right), \ |b| > 0\right\}.$$

For any $(a, b) \in \mathcal{H}_m$, the nonwandering set of $F_{a,b}$ is a horseshoe, that is, it is structurally stable.

We can prove the main theorem using the following two theorems. See Figure 2. The open set $\mathcal{H}_m$ occupies a large area in the product space of parameters meaning that the structural stability is easily acquired by this high-dimensional family. However, numerical experiments showed characteristic division of the area outside of $\mathcal{H}_m$ by some typical bifurcations. Moreover, the combinations of parameters causing the non-trivial attractors are located outside $\mathcal{H}_m$. It may be very important to make a systematic investigation of all the types of bifurcations which are present in this family, see [4].

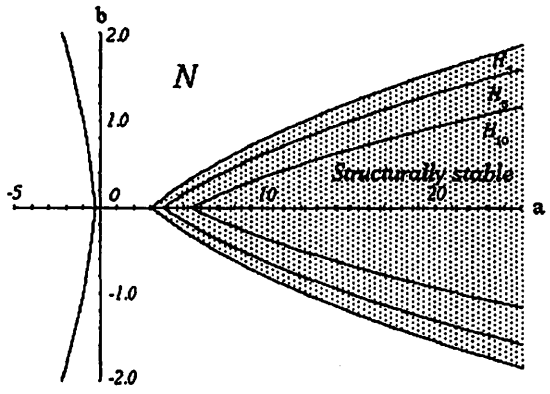

Figure 2: The open set $\mathcal{H}_m$ for m=3, 5, 10.

3 Nonwandering set of the m-dimensional diffeomorphism of Hénon type

Let $F_{a,b}$ be the m-dimensional special Hénon family. We assume $b \neq 0$. We denote the nonwandering set of $F_{a,b}$ by $\Omega_{a,b}$. In this section, we detect the location of $\Omega_{a,b}$. Let

$$r = \frac{1 + |b| + \sqrt{(1+|b|)^2 + 4a}}{2},$$

which satisfies the quadratic polynomial $r^2 - (1+|b|)r - a = 0$. We assume that $(1+|b|)^2 + 4a \geq 0$. Using this r, partition $\mathbb{R}^m$ into $m+1$ areas as follows: for each $i = 2, 3, \cdots, m$,

$$\begin{aligned}
\mathcal{D} &= \{(x_1, x_2, \cdots, x_m) \in \mathbb{R}^m : |x_j| \leq r,\ j = 1, 2, \cdots, m\} \\
\mathcal{T}_1 &= \{(x_1, x_2, \cdots, x_m) \in \mathbb{R}^m : |x_1| > r,\ |x_1| > |x_j|,\ j = 2, 3, \cdots, m\} \\
\mathcal{T}_i &= \{(x_1, x_2, \cdots, x_m) \in \mathbb{R}^m : |x_i| > r,\ |x_i| \geq |x_j|,\ j = 1, 2, \cdots, m,\ j \neq i\}.
\end{aligned}$$

When $m = 3$, these partitions are shown as in Figure 3.

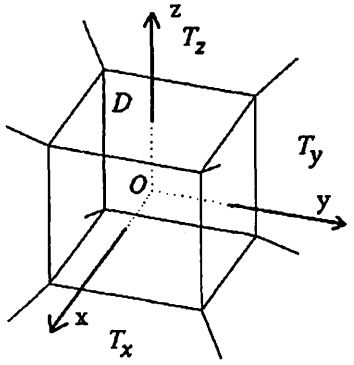

Figure 3: The partitions of $\mathbb{R}^3$.

Theorem 1 *Let $\mathcal{N}$ be a subset of the direct product set of parameter spaces such that*

$$\mathcal{N} = \left\{(a,\ b) \in \mathbb{R} \times \mathbb{R} \ :\ a \geq -(1+|b|)^2/4,\ |b| > 0\right\}.$$

For any $(a,\ b) \in \mathcal{N}$, the nonwandering set $\Omega_{a,b}$ for $F_{a,b}$ is contained in $\mathcal{D}$.

From the following Lemma 3.1 and 3.2, we get directly the proof of this theorem. For any $\mathbf{x} = (x_1, x_2, \cdots, x_m) \in \mathbb{R}^m$, we write

$$\|\mathbf{x}\| = \max\{|x_1|, |x_2|, \cdots |x_m|\}.$$

Lemma 3.1 *For $(a,\ b) \in \mathcal{N}$,*

(1) $F_{a,b}(\mathcal{T}_1) \subset \mathcal{T}_1$;

(2) For every $\mathbf{x} \in \mathcal{T}_1$, $\|F_{a,b}^n(\mathbf{x})\| \to \infty$ as $n \to \infty$;

(3) $F_{a,b}(\mathcal{D}) \subset \mathcal{D} \cup \mathcal{T}_1$.

Lemma 3.2 *For any* $(a,\ b) \in \mathcal{N}$,

(1) $F_{a,b}^{-1}(\mathcal{T}_2) \subset \mathcal{T}_m$;

(2) $F_{a,b}^{-1}(\mathcal{T}_i) \subset \mathcal{T}_{i-1} \cup \mathcal{T}_m$ *for each* $i = 3,\ 4,\ \cdots,\ m$

(3) For every $\mathbf{x} \in \bigcup_{i=2}^{m} \mathcal{T}_i$, $\|F_{a,b}^{-n}(\mathbf{x})\| \to \infty$ *as* $n \to \infty$.

4 Hyperbolicity

From the previous section, we understand that the nonwandering set of $F_{a,b}$ is contained in $\mathcal{D}$. Therefore, in this section, we concentrate on the maximal invariant set of $\mathcal{D}$. Let $\Lambda_{a,b}$ be the maximal invariant set of $\mathcal{D}$ under $F_{a,b}$, i.e. $\Lambda_{a,b} = \bigcap_{i\in\mathbf{Z}} F_{a,b}^{i}(\mathcal{D})$. Our purpose in this section is to prove the next theorem.

Theorem 2 *Let* $F_{a,b}$ *be the m-dimensional special Hénon family. Let* λ *be a real number such that* $\sqrt{m-1} \geq \lambda > 1$, *and let*

$$a_1(b,\ m) = \frac{(1+|b|)^2}{4}\left(m+4+2\sqrt{m+4}\right).$$

For any $|b| > 0$, *if* $a > a_1(b,\ m)$, *then the maximal invariant set* $\Lambda_{a,b}$ *is a hyperbolic set.*

For $m \geq 3$, let us define

$$\mathcal{H}_m = \left\{(a,\ b) \in \mathbf{R}\times\mathbf{R} \ :\ a > \frac{(|b|+1)^2}{4}\left(m+4+2\sqrt{m+4}\right),\ |b| > 0\right\}.$$

For any point $\mathbf{x} \in \Lambda$, we define the unstable cone by

$$C^u(\mathbf{x}) = \left\{(\xi_1,\ \xi_2,\ \cdots,\ \xi_m) \in T_{\mathbf{x}}\mathbf{R}^m \ :\ \lambda\sqrt{\xi_2^2+\xi_3^2+\cdots+\xi_m^2} \leq |\xi_1|\right\},$$

and take a stable cone in the complement of $C^u(\mathbf{x})$ in $T_{\mathbf{x}}\mathbf{R}^m$:

$$C^s(\mathbf{x}) = \left\{(\xi_1,\ \xi_2,\ \cdots,\ \xi_m) \in T_{\mathbf{x}}\mathbf{R}^m \ :\ \sqrt{\xi_2^2+\xi_3^2+\cdots+\xi_m^2} \geq \lambda|\xi_1|\right\},$$

where $\lambda > 1$ is a real number. In the next lemma, we show that these cones are invariant and expanded exponentially by $(DF_{a,b})_{\mathbf{x}}$ and $(DF_{a,b}^{-1})_{\mathbf{x}}$, respectively. Theorem 2 is given directly from this lemma.

Lemma 4.1 *Let* $F_{a,b}$ *be the m-dimensional special Hénon family such that the parameters a and b belong to* $\mathcal{H}_m$. *For each* $\mathbf{x} \in \Lambda_{a,b}$, *there exist the unstable and stable cones in* $T_{\mathbf{x}}\mathbf{R}^m$ *satisfy the following conditions:*

(i) $(DF_{a,b})_{\mathbf{x}}C^u(\mathbf{x}) \subset C^u(F_{a,b}(\mathbf{x}))$ *and* $\|(DF_{a,b})_{\mathbf{x}}\mathbf{v}\| \geq \lambda\|\mathbf{v}\|$ *for all* $\mathbf{v} \in C^u(\mathbf{x})$;

(ii) $(DF_{a,b}^{-1})_{\mathbf{x}}C^s(\mathbf{x}) \subset C^s(F_{a,b}^{-1}(\mathbf{x}))$ *and* $\|(DF_{a,b}^{-m+1})_{\mathbf{x}}\mathbf{v}\| \geq \lambda\|\mathbf{v}\|$ *for all* $\mathbf{v} \in C^s(\mathbf{x})$,

where $\|\mathbf{v}\| = \max\{|\xi_1|,\ |\xi_2|,\ \cdots,\ |\xi_m|\}$ *for* $\mathbf{v} = (\xi_1,\ \xi_2,\ \cdots,\ \xi_m)$.

References

[1] Devany, R., Nitecki, Z.: Shift Automorphisms in the Hénon Mapping. Commun. Math. Phys., **67**, 137-146 (1979)

[2] Hénon, M.: A two-dimensional mapping with a strange attractor. Commun. Math. Phys., **50**, 69-77 (1976)

[3] Kiriki, S., Nakajima, M.: A 3-dimensional diffeomorphism of Hénon type: its hyperbolicity and the first tangency. to appear.

[4] Kiriki, S., Nakajima, M.: An extension of the Hénon family to the higher-dimensional spaces. to appear.

[5] Kiriki, S., Nakajima, M.: Hyperbolicity of a multi-dimensional diffeomorphism of Hénon type. to appear.

[6] Smale, S.: Differentiable dynamical systems. Bull. Amer. Math. Soc. **73** (1967) 747-817.

[7] Viana, M.: Strange attractors in higher dimensions. Bol. Soc. Bras. Mat.**24** No. 1, 13-62 (1993)

[8] Yang, Z.: Hénon-like maps before or at the first tangency. *preprint of PhD theises* (1996)

Reproduction of Hénon-Heiles' Dynamical System

Manabu Yuasa
Research Institute for Science & Technology,
Kinki University, Higashi-Osaka 577,Japan
Shigeko Magono
Department of Information Science, Faculty of Science,
Nara Women's University, Nara 630, Japan

Abstract

Ordinary differential equations for Hénon-Heiles' dynamical system (Hénon, Heiles 1964) are reproduced by using the principal component analysis (PCA) in twice.The adopted method (Unno 1995) is concretely proved to be capable for the empirical construction of dynamical systems from observed data sets. In this paper the data sets are arranged by the numerical integration of Hénon-Heiles' original differential equations. The three figures accuracy is obtained for the reproduced coefficients in the resulting differential equation, which seems to result from the time interval adopted for the data.

Key Words: Dynamical system, Principal component analysis, Hénon-Heiles' system

1 Introduction

The construction of the dynamical system from the observed data sets is an important procedure for developing empirical sciences. If the differential equations for describing the given data sets are determined, we can find the driving agencies in the dynamical system and our understandings for the system will be much advanced.

The new method for this procedure was proposed by Unno (1995), in which the principal component analysis(PCA) is employed repeatedly. Since then this method has been applied to the data sets in mathematical economics (Unno et al. 1996;Yuasa,Unno 1996;Yuasa et al. 1997) and in bio-science (Unno et al. 1997). In this paper we intend to reproduce Hénon-Heiles' system by using this method, in order to check. Then our procedure can be summarized as follows:

1. Arrangements of data sets: we perform the numerical integration of Hénon-Heiles' original differential equations to obtain the sufficient number of

variables values constructed from the variables of Hénon-Heiles' dynamical system, q_1, p_1, q_2, p_2 .

2. Preliminary PCA: we embed the arranged data sets in m-dimensional space, and extract m principal components from this space.

3. Extended PCA: The m principal components which are calculated by prelimenary PCA and the difference of one focused variable (say p_1) of which time dependence should be searched for, are embedded in m+1-dimensional space. Then we extract $m+1$ principal components from this extended space.

4. Reproduction of differential equations: If the arranged data sets can sufficiently represent the whole dynamical system accurately, the average value of the minimum principal component of the extended PCA nearly equals to zero. Then if we put the value to zero,we can obtain the differential equation concerning the focused variable.

With the above mentioned procedure, we have been able to obtain the differential equation system which coincides with the original Hénon-Heiles' equation up to three figures.

2 Arrangements of data sets

The differential equation of Hénon-Heiles' system are writen as follows;

$$\frac{dq_1}{dt} = \frac{\partial H}{\partial p_1} = p_1, \tag{1}$$

$$\frac{dp_1}{dt} = -\frac{\partial H}{\partial q_1} = -q_1 - 2q_1q_2, \tag{2}$$

$$\frac{dq_2}{dt} = \frac{\partial H}{\partial p_2} = p_2, \tag{3}$$

$$\frac{dp_2}{dt} = -\frac{\partial H}{\partial q_2} = -q_2 - q_1^2 + q_2^2, \tag{4}$$

where Hamiltonian H is given by

$$H = \frac{1}{2}(p_1^2 + p_2^2) + \frac{1}{2}(q_1^2 + q_2^2 + 2q_1^2q_2 - \frac{2}{3}q_2^3). \tag{5}$$

We have performed the numerical integration of this system by Runge-Kutta method, adopting the initial condition $q_1(0) = 0.1$, $p_1(0) = -0.3$, $q_2(0) = 0.3$, $p_2(0) = 0.1$ and the step width 0.01 .

Fig.1 shows the orbit between t=0 and t=40 in the $q_1 - q_2$ plane. The horizontal axis is q_1 and the vertial axis is q_2. The orbit is limited within the

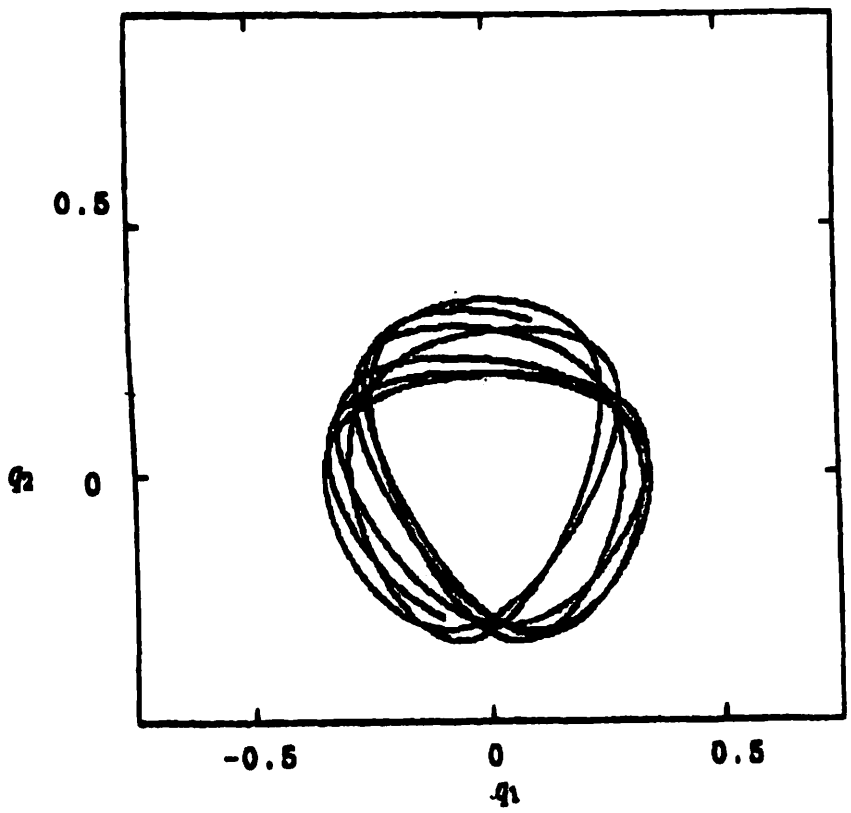

Figure 1: The orbit of Hénon-Heiles' system between $t = 0$ and $t = 40$ in $q_1 - q_2$ plane. The initial conditions are $q_1(0) = 0.1$, $p_1(0) = -0.3$, $q_2(0) = 0.3$ and $p_2(0) = 0.1$. The step width of the numerical integration is 0.01.

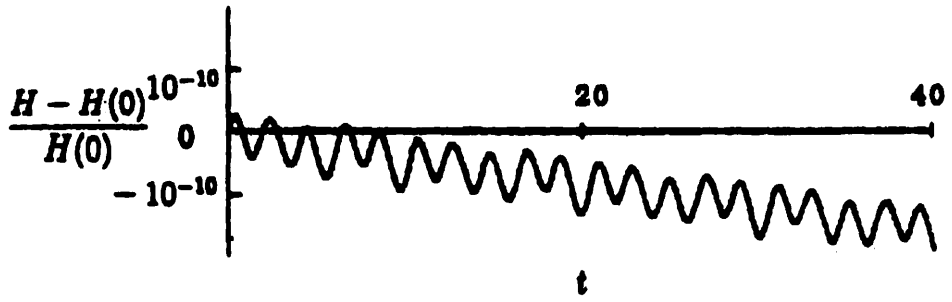

Figure 2: The error of the numerical integration. The initial conditions are the same as the case of Figure 1. The horizontal axis is time and the vertical axis is the relative error of Hamiltonian in the unit of 10^{-10}.

triangular region $-\frac{1}{2} \leq q_2 \leq \pm\sqrt{3}q_1 + 1$, because our initial condition gives $H = 0.0940 < \frac{1}{6}$.

Fig.2 shows the error of the numerical integration. The horizontal axis is time and the vertical axis is the relative error of Hamiltonian in the unit of 10^{-10}.

If the dimension of the dynamical system is d and the each data set has address number n, then the dimension m of the embedding space should satisfy the following inequality:

$$2d + 1 \leq m \leq \log_2 n. \tag{6}$$

Hénon-Heiles' system has two degrees of freedom consisting of second order differential equations, then the system can be written by four simultaneous first order differential equations. On the other side the system has an integral $H = const.$ Therefore, as the dynamical system dimension of Henon-Heiles' equations must be $d = 3$. By the substitution of $d = 3$ to the condition (6), we have adopted $m = 7$ and $n = 1332$. In the 7-dimensional space we have embedded the value of the seven quantities $q_1, p_1, q_2, p_2, q_1^2, q_2^2, q_1q_2$ at every $t = 0.03$ between t=0 and t=40.

3 Preliminary PCA

Before proceeding to the PCA, we have standardized the each data set so as to have mean value 0 and standard deviation 1.

Namely, the standardized variables X_i are given as follows:

$$X_i = (x_i - \overline{x_i})/\delta_{x_i} \quad (i = 1, 2, \cdots, 7), \tag{7}$$

$$where \quad x_1 = q_1, x_2 = p_1, x_3 = q_2, x_4 = p_2, x_5 = q_1^2, x_6 = q_2^2, x_7 = q_1q_2 \tag{8}$$

and $\overline{x_i}, \delta_{x_i}$ represent the mean values and standard deviations of x_i respectively concerning 1332 addresses.

The results of preliminary PCA in the embedded space $(q_1, p_1, q_2, p_2, q_1^2, q_2^2, q_1q_2)$ are as follows:

eigen value	*eigen vector*
1.980	$\vec{a_1}$ = (0.093, 0.591, −0.647, 0.045, −0.322, 0.342, 0.025)
1.926	$\vec{a_2}$ = (0.701, −0.086, 0.046, 0.699, 0.055, −0.015, 0.088)
1.705	$\vec{a_3}$ = (0.010, 0.389, −0.279, −0.013, 0.624, −0.616, 0.043)
1.013	$\vec{a_4}$ = (0.024, −0.032, 0.020, −0.147, −0.096, −0.055, 0.982)
0.236	$\vec{a_5}$ = (−0.047, 0.007, 0.029, −0.007, 0.698, 0.706, 0.107)
0.072	$\vec{a_6}$ = (0.384, 0.589, 0.620, −0.337, −0.051, 0.050, −0.056)
0.068	$\vec{a_7}$ = (−0.591, 0.379, 0.342, 0.612, −0.068, 0.000, 0.105)

With a_{ij} , the $j-th$ component of the $i-th$ eigen-vector $\vec{a_i}$ belonging to the $i-th$ eigen-value λ_i , the value of the $i-th$ principal component y_i is given

by the following equations ($i = 1$ corresponds to the first (maximum) principal component) at every address.

$$y_i = \sum_{j=1}^{7} a_{ij} X_j \quad (i = 1, 2, \cdots, 7). \tag{9}$$

Each X_j and therefore each y_i have 1332 addresses respectively. If the suffix i increases, the standard deviation of the principal components decreases. The square of the standard deviation of each principal component y_i is the corresponding eigen value ($\lambda_i = \overline{y_i^2}$).

4 Extended PCA

In the extexded PCA, we embed the seven principal components y_i $(i = 1, 2, \cdots, 7)$ in the preliminary PCA and the one additional quantity y_8 in the extended eight dimensional space. Then we standardize the variables in the same manner as the preliminary PCA.

$$Y_i = (y_i - \overline{y_i})/\delta_{y_i} \quad (i = 1, 2, \cdots, 8), \tag{10}$$

where $\overline{y_i}$ and δ_{y_i} represent the mean values and standard deviations of y_i respectively concerning 1332 addresses. $\overline{y_i}$ $(i = 1, 2, \cdots,)$ except $\overline{y_8}$ which is generally non-zero are zero because they are the principal components of the preliminary PCA.

Since we want to reproduce the equations (1),(2),(3) and (4), we adopt y_8 as the additional variable in the extended PCA and $y_8 = \Delta q_1$ $y_8 = \Delta p_1$ $y_8 = \Delta q_2$ $y_8 = \Delta p_2$ in case 1, case 2, case 3, and in case 4, respectively. The difference Δq_1 , etc. of the address k is created by the subtraction of the value of the adopted variable at the address $k-1$ from that of the address k $(k = 1, 2, \cdots, 1332)$. At the first address, the difference is approximated by the same value as the second address. The results are given by the following four cases.

case1 :	y_8 *is the difference of* q_1
eigen value	*eigen vector*
2.000	$\vec{b_1}$ = (0.590, −0.074, 0.359, −0.019, 0.002, 0.113, 0.068, 0.707)
1.000	$\vec{b_2}$ = (0.202, −0.096, −0.061, −0.008, 0.516, −0.591, −0.575, 0.000)
1.000	$\vec{b_3}$ = (0.204, 0.738, −0.285, 0.190, 0.428, 0.336, 0.015, −0.000)
1.000	$\vec{b_4}$ = (−0.074, 0.533, 0.380, 0.111, −0.542, −0.153, −0.486, −0.000)
1.000	$\vec{b_5}$ = (0.173, −0.270, −0.284, 0.868, −0.219, 0.042, −0.115, −0.000)
1.000	$\vec{b_6}$ = (0.254, −0.156, −0.499, −0.420, −0.291, 0.396, −0.495, −0.000)
1.000	$\vec{b_7}$ = (0.350, 0.232, −0.428, −0.145, −0.351, −0.575, 0.407, −0.000)
0.000	$\vec{b_8}$ = (−0.590, 0.074, −0.359, 0.019, −0.002, −0.113, −0.068, 0.707)

case2 : y_8 *is the difference of* p_1

eigen value	*eigen vector*
2.000	$\vec{b_1} = (\ 0.086, 0.659, 0.009, 0.214, -0.004, 0.061, -0.096, -0.707\ )$
1.000	$\vec{b_2} = (\ 0.330, -0.008, 0.348, -0.026, -0.314, 0.567, 0.591, -0.000\ )$
1.000	$\vec{b_3} = (\ 0.359, -0.146, -0.210, 0.346, 0.787, 0.200, 0.162, -0.000\ )$
1.000	$\vec{b_4} = (\ 0.124, -0.192, 0.634, 0.606, -0.073, -0.413, -0.061, -0.000\ )$
1.000	$\vec{b_5} = (\ 0.107, 0.141, 0.616, -0.589, 0.444, -0.000, -0.211, 0.000\ )$
1.000	$\vec{b_6} = (\ 0.820, 0.002, -0.232, -0.236, -0.217, -0.409, -0.056, 0.000\ )$
1.000	$\vec{b_7} = (\ -0.217, 0.232, -0.019, -0.134, 0.180, -0.542, 0.745, 0.000\ )$
0.000	$\vec{b_8} = (\ 0.086, 0.659, 0.009, 0.214, -0.004, 0.061, -0.096, 0.707\ )$

case3 : y_8 *is the difference of* q_2

eigen value	*eigen vector*
2.000	$\vec{b_1} = (\ 0.034, 0.686, -0.013, -0.104, -0.002, -0.062, 0.113, 0.707\ )$
1.000	$\vec{b_2} = (\ -0.783, 0.067, -0.029, -0.103, 0.152, -0.361, -0.466, -0.000\ )$
1.000	$\vec{b_3} = (\ 0.336, 0.028, -0.115, 0.240, 0.864, -0.208, -0.163, -0.000\ )$
1.000	$\vec{b_4} = (\ 0.012, 0.068, 0.666, 0.624, -0.173, -0.362, 0.032, 0.000\ )$
1.000	$\vec{b_5} = (\ 0.203, -0.108, 0.628, -0.707, 0.154, -0.155, -0.069, 0.000\ )$
1.000	$\vec{b_6} = (\ -0.340, 0.106, 0.382, 0.126, 0.339, 0.771, 0.048, -0.000\ )$
1.000	$\vec{b_7} = (\ -0.339, -0.158, -0.031, -0.071, 0.249, -0.264, 0.850, 0.000\ )$
0.000	$\vec{b_8} = (\ 0.034, 0.686, -0.013, -0.104, -0.002, -0.062, 0.113, -0.707\ )$

case4 : y_8 *is the difference of* p_2

eigen value	*eigen vector*
2.000	$\vec{b_1} = (\ 0.693, -0.037, 0.058, -0.015, -0.010, -0.107, -0.053, 0.707\ )$
1.000	$\vec{b_2} = (\ -0.104, -0.034, 0.327, 0.003, -0.376, 0.591, 0.625, -0.000\ )$
1.000	$\vec{b_3} = (\ 0.141, 0.492, -0.291, 0.278, 0.617, 0.425, 0.124, -0.000\ )$
1.000	$\vec{b_4} = (\ -0.001, 0.827, 0.082, -0.051, -0.499, -0.077, -0.226, 0.000\ )$
1.000	$\vec{b_5} = (\ -0.081, 0.054, 0.818, 0.468, 0.260, -0.117, -0.147, -0.000\ )$
1.000	$\vec{b_6} = (\ 0.019, -0.109, -0.353, 0.827, -0.356, -0.186, 0.134, 0.000\ )$
1.000	$\vec{b_7} = (\ -0.033, 0.235, 0.034, -0.129, 0.184, -0.627, 0.706, 0.000\ )$
0.000	$\vec{b_8} = (\ 0.693, -0.037, 0.058, -0.015, -0.010, -0.107, -0.053, -0.707\ )$

In the similar manner as the preliminary PCA, the principal components z_i

of the extended PCA can be given by the following equations.

$$z_i = \sum_{j=1}^{8} b_{ij} Y_j \quad (i = 1, 2, \cdots, 8), \tag{11}$$

where b_{ij} indicates the $j-th$ component of the $i-th$ eigen vector $\vec{b_i}$ coresponding to the $i-th$ eigen value of the extended PCA. We have not seven but eight principal components becuase we have embedded the quatities in 8-dimenional space in the extended PCA.

5 Reproduction of Differential Equations

The eighth (minimum) eigen values of the extended PCA are nearly zero ($< 10^{-5}$) in each case. Then the eighth principal components in each case can be put equal to zero. These relations give the following equation in each case.

$$z_8 = \sum_{j=1}^{8} b_{8j} Y j = 0 \tag{12}$$

We have calculated the value of eighth eigen vector $\vec{b_8}$ of extended PCA in section 4. On the other hand the standardized variables Y_j $(j = 1, \cdots, 7)$ of extended PCA can be transformed to the original variables x_j and Y_8 can be transformed to the difference Δx of the focused variables x. In $case1 \sim case4$ Δx represents $\Delta q_1, \Delta p_1, \Delta q_2$ and Δp_2 respectively. With the help of the equation (7),(8),(9),(10), we can solve the equation (12) with respect to the difference of the focused variable as follows:

$$\Delta x = c_0 + \sum_{j=1}^{7} c_j x_j \tag{13}$$

The difference Δx has been created by the subtraction of successive x values. The interval of time Δt of successive values of x is 0.03 in our arranged data, so we have to devide both sides of the equation (13) by Δt to get the differential equations concerning q_1, p_1, q_2 and p_2.

The results are as follows:

$$\begin{aligned} case1 \quad \frac{dq_1}{dt} &= 1.000 p_1 \\ &\quad +0.015 q_1 - 0.000 q_2 - 0.000 p_2 - 0.000 q_1^2 \\ &\quad -0.000 q_2^2 + 0.030 q_1 q_2 - 0.000 \end{aligned} \tag{14}$$

$$\begin{aligned} case2 \quad \frac{dp_1}{dt} &= -1.000 q_1 - 1.999 q_1 q_2 \\ &\quad +0.021 p_1 + 0.005 q_2 - 0.000 p_2 + 0.024 q_1^2 \\ &\quad -0.024 q_2^2 - 0.000 \end{aligned} \tag{15}$$

$$case3 \quad \frac{dq_2}{dt} = \begin{aligned} & 1.000p_2 \\ & +0.000q_1 - 0.000p_1 + 0.015q_2 + 0.015q_1^2 \\ & -0.015q_2^2 + 0.000q_1q_2 + 0.000 \end{aligned} \tag{16}$$

$$case4 \quad \frac{dp_2}{dt} = \begin{aligned} & 1.000q_2 - 1.000q_1^2 + 0.999q_2^2 - 0.048q_1q_2 \\ & -0.005q_1 + 0.000p_1 + 0.021p_2 \\ & -0.000 \end{aligned} \tag{17}$$

6 Discussion

The final results (14),(15),(16),(17) in section 5 show that the coefficients coincide with those of the original equations (1),(2),(3),(4) almost up to the three figures. The accuracy results mainly from the time interval of the arranged data sets.

In the preceeding sections, the dimension m of the embedded space has been chosen as 7. If we choose $m = 10$ and the number of arranged data as 1332 at every $t = 0.03$ between $t = 0$ and $t = 40$, we can obtain the differential equations similar to the equations (14),(15),(16),(17).

In the case of $m = 10$, the variables of embedded space are chosen as $x_1 = q_1$, $x_2 = p_1$, $x_3 = q_2$, $x_4 = p_2$, $x_5 = q_1^2$, $x_6 = q_2^2$, $x_7 = q_1q_2$, $x_8 = p_1^2$, $x_9 = p_2^2$, $x_{10} = p_1p_2$.

The final results are as follows:

$$\frac{dq_1}{dt} = \begin{aligned} & 1.000p_1 \\ & +0.015q_1 - 0.000q_2 - 0.000p_2 - 0.000q_1^2 - 0.000q_2^2 \\ & +0.030q_1q_2 - 0.000p_1^2 - 0.000p_2^2 + 0.000p_1p_2 + 0.000 \end{aligned} \tag{18}$$

$$\frac{dp_1}{dt} = \begin{aligned} & -1.000q_1 - 2.000q_1q_2 \\ & +0.015p_1 + 0.001q_2 + 0.000p_2 + 0.017q_1^2 - 0.014q_2^2 \\ & -0.012p_1^2 + 0.015p_2^2 - 0.002p_1p_2 - 0.000 \end{aligned} \tag{19}$$

$$\frac{dq_2}{dt} = \begin{aligned} & 1.000p_2 \\ & +0.000q_1 + 0.000p_1 + 0.015q_2 + 0.015q_1^2 - 0.016q_2^2 \\ & +0.000q_1q_2 - 0.000p_1^2 - 0.001p_2^2 + 0.000p_1p_2 + 0.000 \end{aligned} \tag{20}$$

$$\frac{dp_2}{dt} = \begin{aligned} & -1.000q_2 - 0.999q_1^2 + 1.000q_2^2 \\ & -0.001q_1 - 0.032q_1q_2 - 0.000p_1 + 0.015p_2 \\ & +0.001p_1^2 + 0.002p_2^2 + 0.028p_1p_2 - 0.000 \end{aligned} \tag{21}$$

The method which we have adopted is proved concretely capable for the empirical construction of dynamical systems from observational data sets. This method is applicable to many research fields and we expect the method will be a strong tool for analyzing the complicated data sets.

References

(1) Hénon,M.,Heiles,C. 1964, A.J 69,73
(2) Unno,W. 1995,Science & Technology, Kinki Univ. 7,1
(3) Unno,W.,Yuasa,M.,Onishi,T. 1996,Science & Technology, Kinki Univ. 8,61
(4) Yuasa,M.,Unno,W. 1996,Science & Technology, Kinki Univ.8,67
(5) Yuasa,M.,Unno,W., Onishi,T. 1997,Science & Technology, Kinki Univ. 9,19
(6) Unno W., Onishi,T., Yuasa M., 1997, Viva Origno 25,139

A Fast Procedure Solving Gauss' Form of Kepler's Equation

TOSHIO FUKUSHIMA
National Astronomical Observatory, 2-21-1, Ohsawa, Mitaka, Tokyo 181, Japan
(Internet) toshio@nao.ac.jp

Abstract. We developed a procedure solving Gauss' form of Kepler's equation, which is suitable for determining position in the nearly parabolic orbits. The procedure is based on the combination of asymptotic solutions, the method of bisection, and the Newton method of succesive correction. It runs 3-4 times as fast as the original Gauss' method.

Key words: Gauss' Method, Kepler's Equation, Nearly Parabolic Orbit

1. Introduction

Recently we developed methods to solve the standard form of Kepler's equation for the elliptic case (Fukushima 1997b), hereafter cited as Paper I, and for the hyperbolic case (Fukushima 1998), hereafter cited as Paper II. As for the extended forms, refer Fukushima (1996b) for the elliptic case, and Fukushima (1997a) for the hyperbolic case, respectively. These are to speed-up the transformation between the osculating orbital elements and the 3-dimensional position and velocity. The transformation is the key procedure in the numerical methods to integrate perturbed orbits by using orbital elements, such as the mixed variable symplectic integrator (Kinoshita, Yoshida, & Nakai 1991); (Wisdom & Holman 1991) or the generalized Encke's method (Fukushima 1996a). Fast procedures to solve Kepler's equation will lead to an acceleration of such computation.

Now, let us return to Kepler's equation. A comprehensive list of methods to solve it is given in Colwell (1993), although its emphasis is on the elliptic orbits. The essence of our methods is the combination of two types of approaches; a slow but robust one and a fast but unstable one. The former is to localize the solution into an interval small enough that the latter rapidly converges. In designing the procedures quoted in the above, we avoided the evaluation of transcendental functions as much as possible since they are time-consuming. Numerical experiments showed that our methods are 2.5-3.7 times as fast as the existing methods.

Both of our methods in Papers I and II obtain succesfully the solution of standard Kepler's equations in the limit of parabolic orbit. However, this is not complete. Consider the nearly parabolic orbits, namely the orbits whose eccentricity e is close to 1. Typical examples are shown in Table I. In such cases, these standard equations become impractical. More specifically speaking, in that case, (1) the practical range of mean anomaly shrinks to a tiny region around zero, whose length is in proportion to $\sqrt{|1-e|}^3$, (2) so does the corresponding region of eccentric anomaly E (or F), whose length is in proportion to $\sqrt{|1-e|}$, and therefore (3) a severe loss of precision occurs in computing $E - e\sin E$ (or $e\sinh F - F$) and its derivative $1 - e\cos E$ (or $e\cosh F - 1$), which are necessary in the Newton method and some other iterative procedures. This is the reason why the nearly parabolic case has been treated separately.

Among the methods proposed for nearly parabolic orbits, Gauss' one has been regarded as the best (Battin 1987); (Colwell 1993). However, it does not run so fast. In fact, the actual CPU time of Gauss' method ranges 45-75 μs in the case of Intel Pentium 120 MHz chip. See Figs 1 and 2. This is quite slow when compared with the typical CPU time in Papers I and II, 5-7μs. Therefore, in this paper, we will present a new procedure solving Gauss' quasicubic form of Kepler's equation. As is seen in the figures, our method runs 3-4 times as fast as Gauss' one.

2. Gauss' Form of Kepler's Equation

Let us give a brief introduction of Gauss' method to solve Kepler's equation for nearly parabolic orbits ((Battin 1987), Sects 5.5 and 5.6; (Colwell 1993), Chapt.5). Here we will follow Herget's notaion ((Benima et al. 1969)).

Gauss rewrote Kepler's equation into a quasicubic form;

$$f(w) \equiv w + \frac{w^3}{3} - W(w) = 0. \tag{1}$$

Here w is a new variable defined as

$$w \equiv \mathrm{sgn}(t)\sqrt{\frac{A(E)}{b(e)}} \tag{2}$$

TABLE I
Examples of Nearly Parabolic Orbits

Object	Name (Code)	e
Comet	Bowell (C/1980 E1)	1.0573
	Sandage (C/1972 L1)	1.0063
	Bradfield (C/1975 V2)	1.000001
	Great January Comet (C/1910 A1)	0.999995
	Wells (C/1882 F1)	0.999994
	Shoemaker-Levy (C/1991 T2)	0.999862
Periodic Comet	Halley (1P)	0.967
	Encke (2P)	0.850
Asteroid	Phaethon (3200)	0.890
	Damocles (5335)	0.866
	Hephaitos (2212)	0.833
	Taros (5786)	0.827
	Icarus (1566)	0.827
Satellite	Nereid	0.75

Shown are some celestial objects with large e. The eccentricities of comets are of osculating nature. Data are taken from Marsden and Williams (1996) for comets, from *Ephemerides of Minor Planets for 1997* (ITA 1996) for asteroids, and from Rohde with Sinclair (1992) for the satellite.

by means of a function of eccentricity

$$b(e) = \frac{5(1-e)}{1+9e} \tag{3}$$

and a function of (elliptic) eccentric anomaly

$$A(E) \equiv \frac{15(E-\sin E)}{9E+\sin E}, \tag{4}$$

and t is the time measured from the pericenter passage. Note that the definition is universal in the sense it remains well-defined in the parabolic and hyperbolic case. In fact, w becomes a function of true anomaly v as

$$w = \tan\frac{v}{2} \tag{5}$$

in the parabolic case. In the hyperbolic case, A is interpreted as a function of hyperbolic eccentric anomaly F as

$$A = \frac{15(F-\sinh F)}{9F+\sinh F}. \tag{6}$$

On the other hand, W is defined as

$$W = B(A)T, \qquad T \equiv t\sqrt{\frac{(1+9e)\mu}{20q^3}} \tag{7}$$

where μ is the gravitational constant of the two body problem, and q is the pericenter distance. Another auxiliary function B is defined as

$$B(A) \equiv \frac{20\sqrt{A}}{9E+\sin E} = \frac{20\sqrt{-A}}{9F+\sinh F} = \sum_{n=0}^{\infty}\beta_n A^n = 1 - \frac{3}{175}A^2 - \cdots, \tag{8}$$

where β_n are the numerical coefficients listed in Table II. See Fig.3 for the relation between A and B. Since A is a function of w as

$$A = bw^2, \tag{9}$$

W is also a function of w. After Eq.(1) is solved with respect to w, the radius vector and position in the orbital plane are obtained as

$$r = \rho\left(1+\tau^2\right), \qquad x = \rho\left(1-\tau^2\right), \qquad y = 2\rho\tau, \tag{10}$$

where

$$\rho = \frac{q}{1+AC^2}, \qquad \tau \equiv \tan\frac{v}{2} = cwC, \qquad c = \sqrt{\frac{5(1+e)}{1+9e}} \tag{11}$$

and C is yet another auxiliary function defined as

$$C(A) \equiv \frac{1}{\sqrt{A}}\tan\frac{E}{2} = \frac{1}{\sqrt{-A}}\tanh\frac{F}{2} = \sum_{n=0}^{\infty}\gamma_n A^n = 1 + \frac{2}{5}A + \frac{38}{175}A^2 + \cdots, \tag{12}$$

where γ_n are another group of numerical coefficients, which have been listed in Table II. Gauss introduced numerical factors in the above such as 9 or 15 in order to make B as insensitive with w as possible; to set $\beta_1 = 0$.

Now, Gauss considered the solution of Eq.(1) as follows. In the case of parabolic orbit, $e = 1, b = A = 0$, and therefore $B = 1$. Thus W remains a constant for any value of w. Then the equation reduces to a cubic equation named Barker's equation ((Colwell 1993), Eq.(5.2)). It is exactly solved by means of Cardano's formula. In the case of nearly parabolic case, W must be weakly dependent on w. Assume that an approximate solution w^* is given. If we regard $W(w^*)$ as a constant, then the equation reduces to Barker's equation again. Denote the procedure to solve it as a function of W as

$$w = S(W). \tag{13}$$

It may be Cardano's formula, the Newton method, or others. Anyway, $S(W(w^*))$ is hopefully a better solution than w^*. Thus, Gauss solved Eq.(1) by repeating the iteration

$$w \leftarrow S(W(w)) \tag{14}$$

with a starter $w = 0$. This is Gauss' method.

Of course, Gauss' method has many attractive features.

1. It is universal in the sense it can solve the elliptic, parabolic, and hyperbolic cases by a single procedure.
2. The closer to 1 the eccentricity is, the faster it runs. This is eminent in the region $0.95 < e < 1.05$. See Fig.2.
3. Only a few iterations are needed for low-precision purposes such as the determination of cometary orbits.

However, there are some drawbacks in Gauss' method.

1. The method does not cover all the orbit. In fact, the method does diverge for large values of $|A|$, say larger than 2. On the other hand, the method rapidly converges only when $|A|$ is sufficiently small, say less than 0.1 or so.
2. The series expansions of B and C converge slowly when $|A|$ is large. For example, 15 and 18 terms are required to compute B and C in 15 digits accuracy for $|A| < A_{\mathrm{MAX}}$, respectively. This makes the speed down considerably. Here
$$A_{\mathrm{MAX}} \equiv \frac{5}{16} = 0.3125 \tag{15}$$
is a bound of applicable region of Gauss' method.
3. The method is of linear convergence. The relative error of the initial guess is roughly $|B-1|$. It is of the order of 0.001, as will be seen in the next section. Thus, 4-6 iterations in average are required to obtain 15 digits of the solution.
4. The method must solve a cubic equation at each iteration. The standard recipe to solve a cubic equation, Cardano's formula, is relatively slow. This is because it calls two external functions `sqrt` and `cbrt`, and because the latter further calls another two, `log` and `exp`, in most computers. On the other hand, the Newton method and other iterative methods requires a good initial guess of the solution to converge. This is a difficult question. Unfortunately no suitable formula has been found.

The first two characteristics are inherent to Gauss' form of Kepler's equation. In this paper, we try to speed-up the procedure solving it by improving the last two points of the original Gauss' method.

TABLE II
Coefficients of Gauss' Method

n	β_n	γ_n
0	1.	1.
1	0	0.4
2	−0.01714285714285714	0.2171428571428571
3	−0.003809523809523809	0.1249523809523809
4	−0.001104267161410019	0.07339814471243044
5	−0.0003673583559297845	0.04351610294467437
6	−0.0001316749463688239	0.02592289191081028
7	−0.00004957686826978545	0.01548367519987016
8	−0.00001932818959065063	0.009262986761370400
9	$-7.734454141163412 \times 10^{-6}$	0.005546934532808591
10	$-3.158438366314071 \times 10^{-6}$	0.003323739342183720
11	$-1.310873532730006 \times 10^{-6}$	0.001992413105115635
12	$-5.513380397300617 \times 10^{-7}$	0.001194679665622428
13	$-2.344697160320328 \times 10^{-7}$	0.0007164817429433940
14	$-1.006539594926664 \times 10^{-7}$	0.0004297493194399960
15	$-4.355835497286856 \times 10^{-8}$	0.0002577892193644137
16	$-1.898214247448393 \times 10^{-8}$	0.0001546472593771683
17	$-8.322913593721420 \times 10^{-9}$	0.00009277685104769930
18	$-3.669031347121318 \times 10^{-9}$	0.00005566104491749808

Listed are the coefficients β_n and γ_n used in Gauss' form of Kepler's equation. They are derived by the following *Mathematica* (Wolfram 1991) program;

```
a[x_]=15(Sqrt[x]-Sin[Sqrt[x]])/(9Sqrt[x]+Sin[Sqrt[x]]);
b[x_]=(20Sqrt[a[x]])/(9Sqrt[x]+Sin[Sqrt[x]]);
c[x_]=Tan[Sqrt[x]/2]/Sqrt[a[x]];
n=20; sx[x_]=InverseSeries[Series[a[x], {x,0,n}],x];
bx[x_]=Normal[b[sx[A]]] /. A -> x;
cx[x_]=Normal[c[sx[A]]] /. A -> x;
bp=Part[Series[bx[x],{x,0,n-2}],3];
cp=Part[Series[cx[x],{x,0,n-2}],3];
Do[Print[i-1," ",N[bp[[i]],16]," ",N[cp[[i]],16]],{i,1,n-1}]
```

3. Method

In a word, our method is the Newton method with a starter obtained by solving Barker's equation. First, the outline of the method will be stated in Section 3.1. We adopted a new procedure in solving Barker's equation. Its summary will be given in Section 3.2 and the details will be explained in Appendix A. The part of Newton method will be described in Section 3.3.

3.1. Strategy

Assume that Gauss' form is applicable. Namely, $|A| < A_{\mathrm{MAX}}$. Our strategy to solve Eq.(1) is something similar as Gauss' approach; (1) to obtain an approximate solution by solving the associated Barker's equation precisely, and (2) to improve it by the Newton method.

In obtaining a rough solution, we notice that B differs from 1 by only a small amount; 0.0018 or so when $|A| < A_{\mathrm{MAX}}$. If the error tolerance is 0.002 or larger, then we can assume that $B = 1$. In that case, we only have to solve Barker's equation

$$f_B(w;T) \equiv w + \frac{w^3}{3} - T = 0 \qquad (0 < T < \infty). \tag{16}$$

The eccentricity dependence disappears here. Remark that this fact greatly owes to Gauss' choice of the variable. As a result, the construction of approximate solutions becomes simple as will be described in Section 3.2 and Appendix A.

Now, assume that such an approximate solution is obtained. If the solution w is so small that the associated A satisfies the condition

$$|A| < A_{\mathrm{TINY}} \equiv \sqrt{\frac{175\epsilon}{3}} \approx 8.048 \times 10^{-8}, \tag{17}$$

where $\epsilon \approx 1.110 \times 10^{-16}$ is the machine epsilon, then the resulting value of B remains 1 practically, and therefore, we may stop here. Otherwise, we move to the part of improvement. Anyway, the error is small enough that almost any unstable correction formula converges. In order to select the best formula in the sense to minimize CPU time, we made extensive experiments to solve Gauss' form by using various correctors as we did in Papers I and II. The result supports the classic Newton method, whose detail will be explained later. This is due to the fact that the evaluation of higher derivatives of the auxiliary function B with respect to the variable w is time-consuming. Note that the Newton method is of quadratic convergence. Since the initial error is less than 0.002, two or three applications of the Newton iteration provides 15 digits accuracy.

3.2. Fast Solution of Barker's Equation

Let us seek a fast procdure to solve Barker's equation, Eq.(16). Of course, its closed form solution is known (Battin 1987, Eq.(4.17)) as

$$w = \frac{2su}{1+s+s^2} \tag{18}$$

where

$$s = \left(\sqrt[3]{u+\sqrt{1+u^2}}\right)^2, \qquad u = \frac{3T}{2}. \tag{19}$$

This Stumpff's rewriting of Cardano's formula (Battin 1987) requires one evaluation of `sqrt` and `cbrt`. Usually the latter is evaluated by the combination of `exp` and `log`. These are somewhat time-consuming. Thus, we look for a different approach.

The parameter domain, $0 < T < \infty$, is of infinite length. Therefore, we face a similar difficulty as in the hyperbolic case of Kepler's equation. In Paper II, we avoided it by transforming the variable from F to $X \equiv \exp F$. Such remedy is not suitable this time since the evaluation of `cbrt`, the inverse function of the main term w^3, is time-consuming. Thus, we separate the solution interval $0 < w < \infty$ into some subintervals and apply different approaches, respectively. See Appendix A for the details.

3.3. Newton Method

The Newton method is to repeat the following operation until convergence:

$$w \leftarrow w^*(w) \equiv w - \frac{f(w)}{f'(w)}. \tag{20}$$

Here

$$f'(w) = 1 + w^2 - \frac{\mathrm{d}B}{\mathrm{d}w}T, \qquad \frac{\mathrm{d}B}{\mathrm{d}w} = 2bwB'(A) \tag{21}$$

and

$$B'(A) = \sum_{n=1}^{\infty} n\beta_n A^{n-1} = -\frac{6}{175}A - \cdots. \tag{22}$$

Note that the Newton corrector is rewritten in a form with a smaller precision loss as

$$w^*(w) = \frac{(2/3)w^3 + B(A)T}{1 + w^2 - 2bwB'(A)T}. \tag{23}$$

The iteration is terminated if

$$\frac{|w^*(w) - w|}{1+|w|} < \delta \tag{24}$$

where δ is the error tolerance, say 10^{-15}.

4. Numerical Comparison

See Figs 1 and 2 again. These show the comparison of CPU time of Gauss' and our methods to solve Eq.(1) and to obtain the position in the orbital plane. The CPU times were obtained by averaging the measurements for 10^6 equally-spaced grid points in an interval of the elliptic mean anomaly $(0, M_{\rm MAX})$ for the case $e < 1$, or of the hyperbolic mean anomaly $(0, M_{H\rm MAX})$ for the case $e > 1$. Here the upper bounds were chosen as

$$M_{\rm MAX} = E_{\rm MAX} - e\sin E_{\rm MAX}, \qquad M_{H\rm MAX} = e\sinh F_{\rm MAX} - F_{\rm MAX}, \tag{25}$$

where $E_{\rm MAX} \approx 1.1434$ and $F_{\rm MAX} \approx 1.0965$ were derived from a bound of Gauss' auxiliary quantity, $A_{\rm MAX} = 0.3125$ by means of the relations Eq.(4) and (6). These figures show clearly the superiority of the new method, which runs 3-4 times as fas as Gauss' method does.

5. Conclusion

We developed a procedure solving Gauss' form of Kepler's equation. It is the Newton method with the solution of the associated Barker's equation as the starter. The associated Barker's equation, is solved by three subprocedures; (1) to compute the inversion series expanded around the zero solution when the solution is small, (2) to evaluate a cubic root when the solution is large, and (3) to reduce the solution interval by shifting bits, which are determined by the bisection method, then to apply the Newton method with the starter given by the minimum of Newton correctors for a discrete set of trial values.

As is shown in Figs 1 and 2, the new procedure runs 3-4 times as fast as Gauss' method. However, the new method is still a little slower than our methods in Papers I and II. Thus, we do not recommend the usage of Gauss' form unless e is sufficiently close to 1, say for the region $0.95 < e < 1.05$. This is the region where Gauss' method is effective and really corresponds to typical orbits of comets as is illustrated in Table I.

References

Battin, R.H., 1987, An Introduction to the Mathematics and Methods of Astrodynamics, AIAA, New York, NY.
Benima B., Cherniack J.R., Marsden B.G., and Porter J.G., 1969, PASP, 81, 121.
Colwell, P., 1993, Solving Kepler's Equation Over Three Centuries, Willmann-Bell, Richmond, VA.
Danby, J.M.A., 1988, Fundamentals of Celestial Mechanics, 2-nd Ed., Willmann-Bell, Richmond, VA.
Fukushima, T., 1996a, Astron. J., 112, 1263.
Fukushima, T., 1996b, Astron. J., 112, 2858.
Fukushima, T., 1997a, Astron. J., 113, 1920.
Fukushima, T., 1997b, Celest. Mech. and Dyn. Astron., 66, 309.
Fukushima, T., 1998, Celest. Mech. and Dyn. Astron., in printing.
Kinoshita, H., Yoshida, H., and Nakai, H., 1991, Celest. Mech. and Dyn. Astron., 50, 59.
Marsden B.W., and Williams G.T., 1996, Catalogue of Cometary Orbits 1996 (11th ed.), IAU Minor Planet Center, Cambridge, MA.
Rohde J.R., with Sinclair A., 1992, Explanatory Supplement to the Astronomical Almanac (P.K. Seidelmann ed.), Univ. Science Books, Mill Valley, CA., Chapt.6.
Wisdom, J., and Holman, M., 1991, Astron. J., 102, 1528.
Wolfram S., 1991, Mathematica (2nd ed.), Addison-Wesley Publ. Co., Inc., Redwood City, CA.

Appendix

A. Fast Solution of Barker's Equation

Let us cosider solving Barker's equation, Eq.(16), which we cite again as

$$f_B(w;T) \equiv w + \frac{w^3}{3} - T = 0 \qquad (0 < T < \infty). \tag{26}$$

From a practical viewpoint, the Newton method and other iterative procedures give the solution faster than Cardano's formula if appropriate starting values are provided. Here we will consider the case of the Newton method.

The parameter domain, $0 < T < \infty$, is of infinite length. Namely, we face a similar difficulty as in the hyperbolic case. Thus, by following the way we adopted in Paper II, we separate the solution interval $0 < w < \infty$ into four subintervals: (1) $0 < w < w_{\rm SMALL}$, (2) $w_{\rm SMALL} \le w < 1$, (3) $1 \le w \le w_{\rm LARGE}$, and (4) $w_{\rm LARGE} < w < \infty$. As will be explained in the followings, the separation is done by comparing T with some values computed beforehand.

A.1. Tiny Solutions

First, consider the case when T is sufficiently small, say less than $T_{\mathrm{SMALL}} \approx 0.017$. In this case, w is expected to be small, too. And therefore, we can invert Eq.(16) as

$$w = T - \frac{1}{3}T^3 + \frac{1}{3}T^5 - \frac{4}{9}T^7 + \frac{55}{81}T^9 - \cdots \tag{27}$$

Assume the usage of double precision computation of standard computers, i.e. the computation with 53 bits mantissa. Then the machine epsilon is

$$\epsilon = 2^{-53} \approx 1.11 \times 10^{-16}. \tag{28}$$

In Eq.(27), the second term is ignorable if

$$\epsilon \geq \frac{T^3}{3}. \tag{29}$$

By solving this condition with respect to w, we obtain the critical value of T as

$$T_A = \sqrt[3]{3\epsilon} \approx 6.932 \times 10^{-6}. \tag{30}$$

Similarly, a series of critical values are given as

$$T_B = \sqrt[5]{3\epsilon} \approx 8.026 \times 10^{-4}, \tag{31}$$

$$T_C = \sqrt[7]{\frac{9\epsilon}{4}} \approx 5.903 \times 10^{-3}, \tag{32}$$

$$T_{\mathrm{SMALL}} = \sqrt[9]{\frac{81\epsilon}{55}} \approx 0.01762, \tag{33}$$

Although we may go further, we stop here. The corresponding series of solutions are:

1. If $T < T_A$, then
$$w = T. \tag{34}$$
2. Else if $T < T_B$, then
$$w = T\left(1 - \frac{1}{3}T^2\right). \tag{35}$$
3. Else if $T < T_C$, then
$$w = T\left\{1 - T^2\left(\frac{1}{3} - \frac{1}{3}T^2\right)\right\}. \tag{36}$$
4. Else
$$w = T\left[1 - T^2\left\{\frac{1}{3} - T^2\left(\frac{1}{3} - \frac{4}{9}T^2\right)\right\}\right]. \tag{37}$$

A.2. Small Solutions

Assume that T is larger than T_{SMALL} but still small, say less than

$$T_1 \equiv \frac{4}{3}, \tag{38}$$

which corresponds to the solution $w = 1$. Then, the solution interval is bound as $w_{\mathrm{SMALL}} < w < 1$ where $w_{\mathrm{SMALL}} \approx 0.01762$ is the solution corresponding to T_{SMALL}. In this case, we obtain the solution by the Newton method. The Newton corrector for Barker's equation is

$$w^*(w) \equiv w - \frac{f_B(w;T)}{f_B'(w;T)} = \frac{T + (2/3)w^3}{1 + w^2}. \tag{39}$$

As the starting formula, we follow the same approach as we took in Paper II; taking the minimum of Newton correctors while restricting the variable space to its discrete subset. Namely, the starter is of the type of

$$\min_{w_k \in \mathcal{K}} w^*(w_k) \tag{40}$$

where $\mathcal{K}$ is a discrete subset of the solution interval. Actually, we adopted the following starter;

$$\min\left(T,\ \frac{4}{5}T+\frac{1}{15},\ \frac{1}{2}T+\frac{1}{3}\right), \tag{41}$$

which corresponds to the discrete variable space;

$$\mathcal{K}=\left(0,\frac{1}{2},1\right). \tag{42}$$

Although 0 is a little outside the solution interval, we included it since the form of associated starter is simple. Note that the selection of starting value is expressed in a simpler manner as

1. If $T < T_D$, then
$$w^* = T. \tag{43}$$
2. Else if $T < T_E$, then
$$w^* = \frac{4}{5}T+\frac{1}{15}. \tag{44}$$
3. Else if $T < T_{\mathrm{SMALL}}$, then
$$w^* = \frac{1}{2}T+\frac{1}{3}. \tag{45}$$

Here the separating values are

$$T_D=\frac{1}{3}, \qquad T_E=\frac{8}{9} \tag{46}$$

which are obtained by solving the condition two neighbouring starters become the same value.

A.3. Huge Solution

Next, consider another limiting case: the case when T is sufficiently large. There w is expected to be large. In Eq.(16), the first term is negligible when compared with the second if

$$w \le \epsilon\frac{w^3}{3}. \tag{47}$$

By solving this condition with respect to w, we obtain its critical value as

$$w_{\mathrm{LARGE}}=\sqrt{\frac{3}{\epsilon}} \approx 1.644\times 10^8. \tag{48}$$

The corresponding value of T becomes

$$T_{\mathrm{LARGE}} \equiv \frac{w_{\mathrm{LARGE}}^3}{3} \approx 1.481\times 10^{24}. \tag{49}$$

Thus, when $T_{\mathrm{LARGE}} < T$, the solution is expressed as

$$w=\sqrt[3]{3T}. \tag{50}$$

Since it is very rare to face this case, we allow us to call transcendental functions.

A.4. Large Solution

When $T_1 < T < T_{\mathrm{LARGE}}$, and therefore $1 < w < w_{\mathrm{LARGE}}$, we reduce the solution interval by shifting bits by using the method of bisection (Fukushima, 1996b). Consider a modification of Eq.(16) as

$$f_P(y;\alpha,P) \equiv \alpha y+\frac{y^3}{3}-P=0. \tag{51}$$

The case $\alpha = 1$ corresponds to the original Barker's equation if $P = T$. The modified equation is invariant with the transformation

$$y^*=2^{-k}y, \qquad \alpha^*=2^{-2k}\alpha, \qquad P^*=2^{-3k}P. \tag{52}$$

In other words, solving $f_P(y;\alpha,P)=0$ is equivalent with solving $f_P(y^*;\alpha^*,P^*)=0$. Based on this fact, we adopt the following procedure:

1. Find a suitable index k such that the solution interval is reduced as
$$\frac{1}{2} < y^* \leq 1. \tag{53}$$
This is done by comparing T with
$$T_k \equiv 2^k + \frac{2^{3k}}{3} = \left(\frac{14}{3}, \frac{76}{3}, \frac{536}{3}, \cdots\right). \tag{54}$$
Since $2^{27} < w_{\text{LARGE}} < 2^{28}$, the range of k to be tested is $(1, 2, \cdots, 27)$. The test is efficiently performed by the bisection method (Fukushima 1996b) of level five. Choose the trial sequence of k_j as
$$\{k_j\} = \{14; 6, 22; 2, 10, 18, 26; 0, 4, 8, 12, 16, 20, 24, 28; \cdots\}. \tag{55}$$
Then k is determined by the algorithm described in Fukushima (1996b, Sect. 2).
2. Compute α and P as
$$\alpha = d_{2k}, \qquad P = d_{3k}T. \tag{56}$$
where
$$d_k \equiv 2^{-k} \tag{57}$$
are the coefficients evaluated beforehand.
3. Solve Eq.(51) with respect to y by the procedure which will be explained in the next subsection.
4. Transform the obtained solution y back to the original variable as
$$w = d_{-k}y. \tag{58}$$

A.5. Solving Modified Barker's Equation

Here we describe how to solve the modified Barker's equation, Eq.(51). Now that the solution interval is bound as $1/2 < y \leq 1$, we adopt the Newton method as we did in the case of small solutions. This time, the Newton corrector becomes

$$y^*(y) \equiv y - \frac{f_P(y; \alpha, P)}{f'_P(y; \alpha, P)} = \frac{P + (2/3)y^3}{\alpha + y^2}. \tag{59}$$

The starter we adopted this time is

$$\min\left(\frac{P + (1/12)}{\alpha + (1/4)}, \frac{P + (2/3)}{\alpha + 1}\right), \tag{60}$$

which corresponds to the discrete subset of variable space;

$$\mathcal{K} = \left(\frac{1}{2}, 1\right). \tag{61}$$

A.6. Numerical Comparison

Fig.5 shows the comparison of CPU time of the new and standard methods to solve Barker's equation as a function of T. The standard method is described in Section 3.2, namely Stumpff's rewriting of Cardano's formula. There we realized `cbrt` by the combination of `exp` and `log`. It is clear that the new method runs roughly as twice as the standard one.

FIG. 1

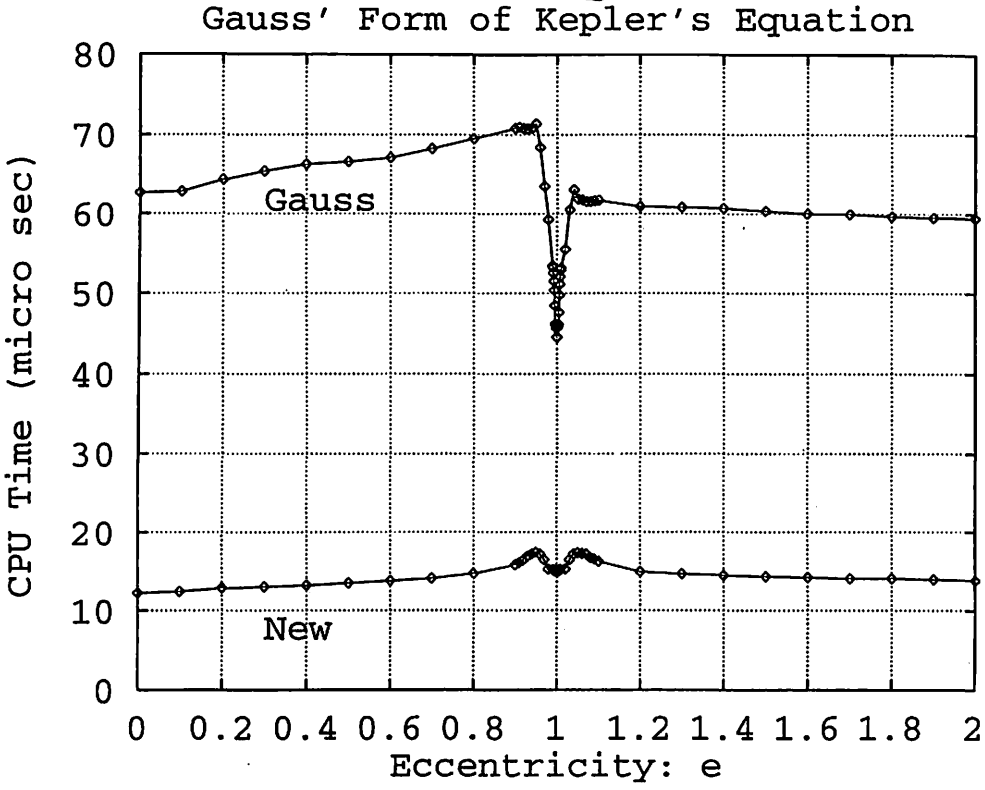
Gauss' Form of Kepler's Equation
CPU Time (micro sec)
80
70
60
50
40
30
20
10
0
Gauss
New
0 0.2 0.4 0.6 0.8 1 1.2 1.4 1.6 1.8 2
Eccentricity: e

FIG. 2

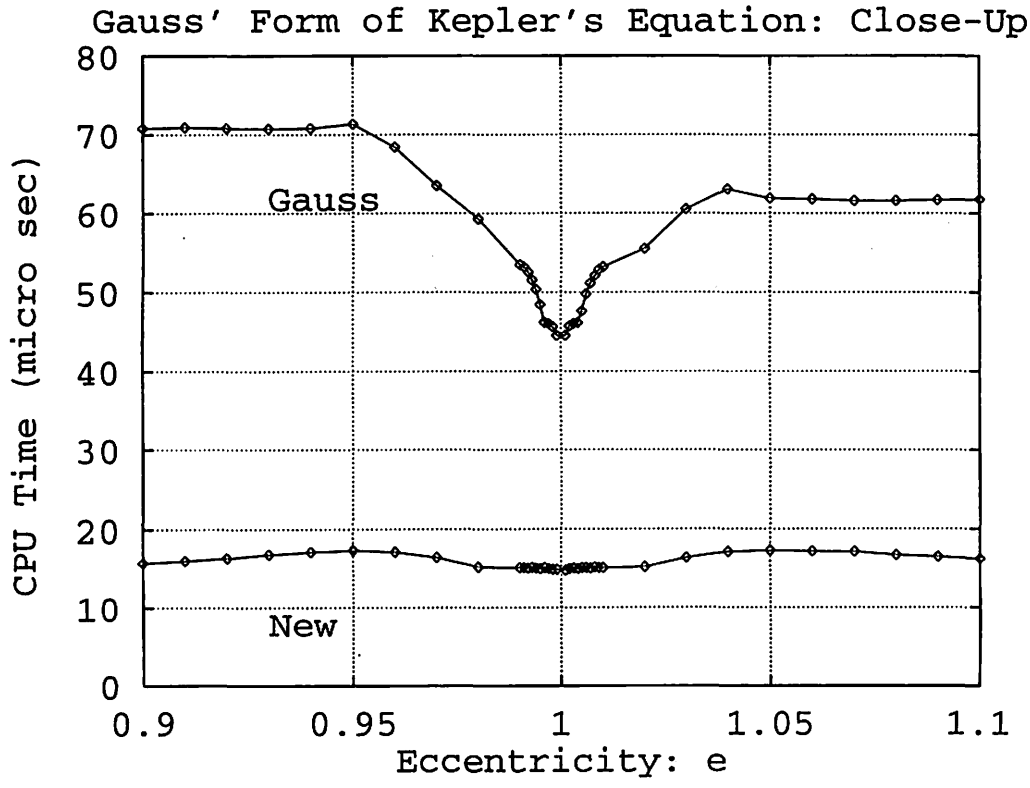
Gauss' Form of Kepler's Equation: Close-Up
CPU Time (micro sec)
80
70
60
50
40
30
20
10
0
Gauss
New
0.9 0.95 1 1.05 1.1
Eccentricity: e

FIG.3

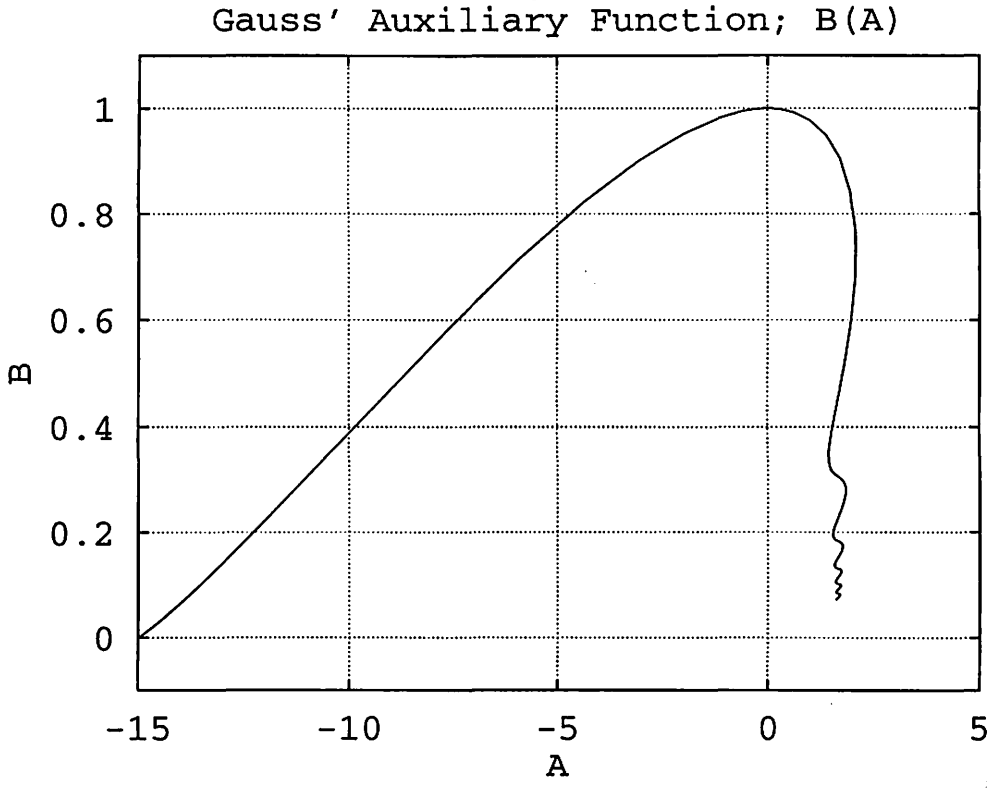
Gauss' Auxiliary Function; B(A)
B
1
0.8
0.6
0.4
0.2
0
-15
-10
-5
0
5
A

FIG.4

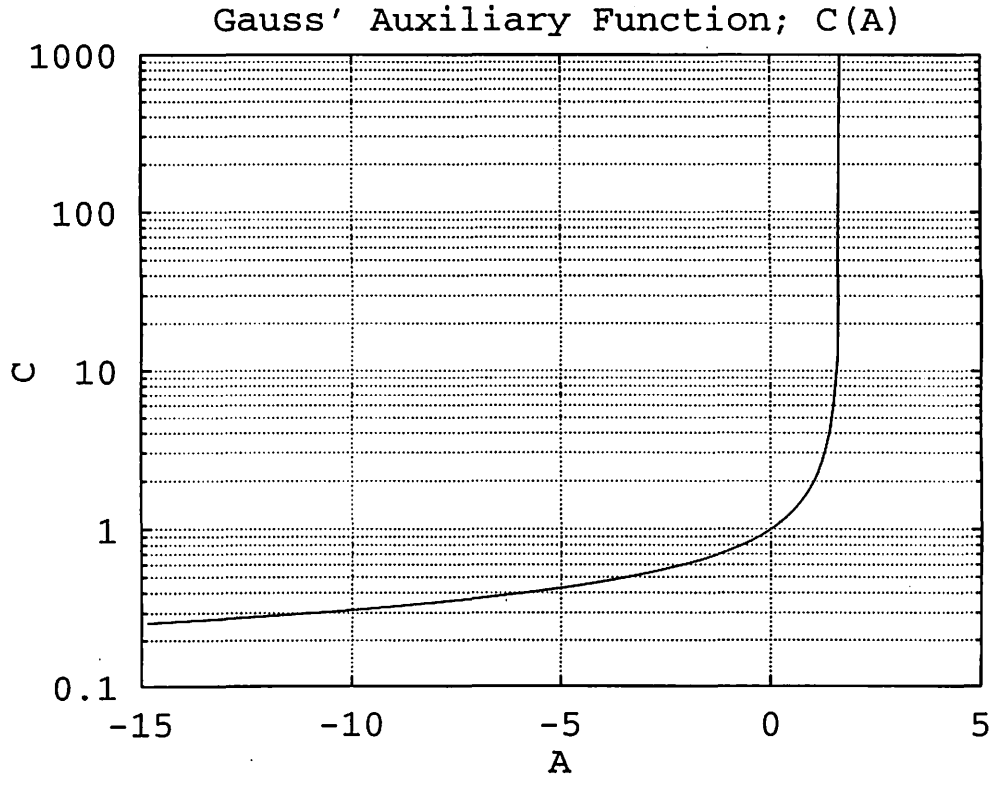
Gauss' Auxiliary Function; C(A)
C
1000
100
10
1
0.1
-15
-10
-5
0
5
A

FIG. 5

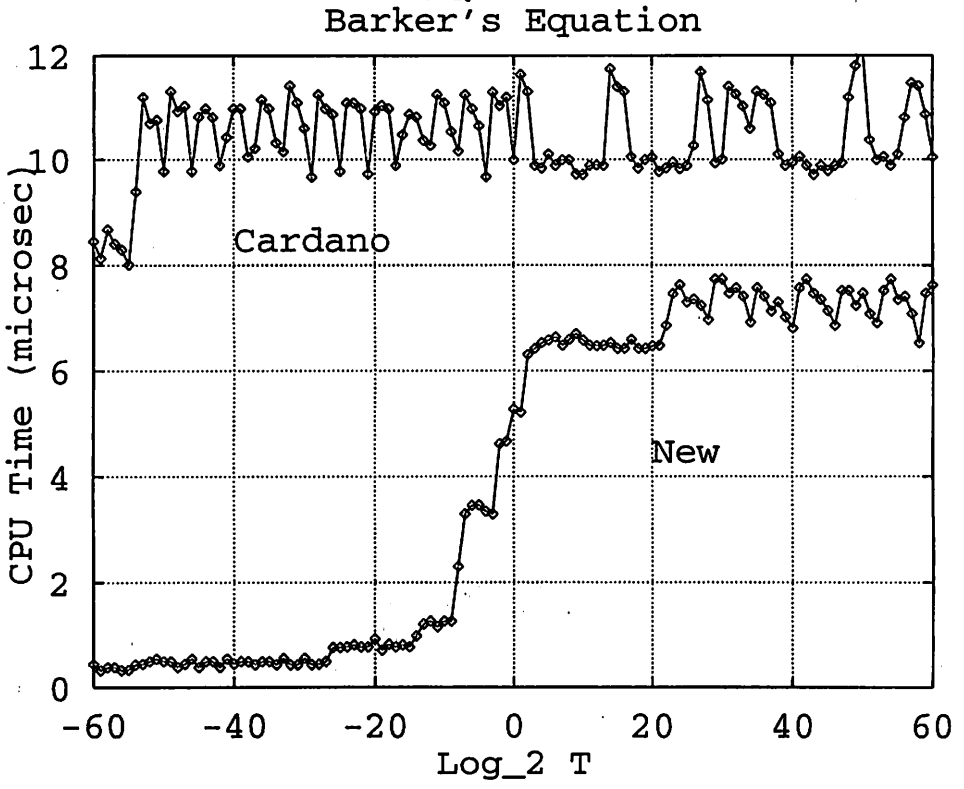
Barker's Equation
CPU Time (microsec)
Log_2 T
Cardano
New
0
2
4
6
8
10
12
-60
-40
-20
0
20
40
60

Symmetric Multistep Methods Revisited

TOSHIO FUKUSHIMA
National Astronomical Observatory, 2-21-1, Ohsawa, Mitaka, Tokyo 181, Japan
(Internet) toshio@nao.ac.jp

Abstract. We discovered a necessary and sufficient condition for irreducible convergent symmetric multistep methods integrating special second order ordinary equations to have a nonvanishing interval of periodicity. By using this, we obtained the explicit and implicit formulas of order 6 to 16 which have the nearly largest interval of periodicity. They are superior to those given in the literature at the point of having longer stability region of stepsize. While they keep the good property of symmetric methods, namely leading linear longitude error in orbital integration. They will be useful for very long integration of oscillatory problems such as the orbital motions of planets and satellites.

1. Introduction

It is well known that the orbital integration by the Störmer-Cowell multistep methods lead to a longitude error which grows quadratically in time. This has been a barrier in conducting long integration in celestial mechanics and dynamical astronomy such as listed in Table 1 of Milani and Nobili (1988). Two methods are known to concur this issue; symmetric multistep integrators (Lambert & Watson 1976) and symplectic integrators. Both of them lead to a longitude error which grows linearly in time. The former is more suitable for high-precision integration since the formulas of high orders such as up to the 14th-order have been constructed (Quinlan & Tremaine 1990).

So far, explicit formulas only were presented for the symmetric methods of 8th- and higher orders. In order to explore the performance of high-order implicit formulas, we started to reexamine the theory on symmetric multistep methods. First, we found a necessary and sufficient condition for a convergent symmetric method to have a nonvanishing interval of periodicity. Remark that the length of *interval of periodicity* is a scale measuring the stable region of multistep methods for oscillatory problems. In other words, having a nonvanishing interval of periodicity means for a multistep method to be numerically stable in integrating orbital motion if the stepsize is sufficiently small. Based on the above condition, we developed a new approach to determine systematically the coefficients of the symmetric method which has the largest interval of periodicity. It will be explained in Section 2. The readers who are not interested in mathematical details may skip it. By using this procedure while posing some restrictions on the coefficients, we obtained explicit and implicit formulas of orders up to 16 which have the nearly largest interval of periodicity. These are illustrated in Section 3.

2. Theory

First, we will summary the theory on general linear multistep methods to integrate numerically a special second order ordinary differential equation. Second, we will do the same for the symmetric multistep methods. Third, we will give a necessary and sufficient condition for a convergent symmetric multistep method to have a nonvanishing interval of periodicity. Then, we will introduce a new set of parameters to characterize the convergent symmetric multistep methods. Finally, we will describe the existing formulas by these tools.

2.1. Multistep Methods

Consider solving the initial value problem of a special second-order ordinary differential equation

$$\frac{\mathrm{d}^2x}{\mathrm{d}t^2} = f(t,x), \tag{1}$$

by a general k-step linear multistep method

$$\sum_{j=0}^{k} \alpha_j x_{n+j} = h^2 \sum_{j=0}^{k} \beta_j f_{n+j} \tag{2}$$

where h is the stepsize. Refer a standard textbook for the details (Hairer *et al.* 1993). Here we assume that $|\alpha_0| + |\beta_0| \neq 0$. If not, we may reduce k until realizing the assumption. Also we assume $\alpha_k = 1$, which loses no generality. The method is characterized by two polynomials $\rho(z)$ and $\sigma(z)$, the generating polynomials of the coefficients α and β,

$$\rho(z) \equiv \sum_{j=0}^{k} \alpha_j z^j, \qquad \sigma(z) \equiv \sum_{j=0}^{k} \beta_j z^j. \tag{3}$$

The local truncation error of the method is expressed as

$$\sum_{j=0}^{k} \alpha_j x(t_n + jh) - h^2 \sum_{j=0}^{k} \beta_j f(t_n + jh, x(t_n + jh)) = \sum_{q=0}^{\infty} C_q h^{q-1} x^{(q)}(t_n) \tag{4}$$

where

$$C_q = \frac{1}{q!} \sum_{j=0}^{k} j^{q-2} \left(j^2 \alpha_j - q(q-1)\beta_j \right) \tag{5}$$

is the q-th order local error constant. On the other hand, the global truncation error of the method is expressed as

$$\Delta x(t_n) \equiv x_n - x(t_n) = \kappa(t_n) h^p + \cdots \tag{6}$$

where $\kappa(t)$ satisfies the following variational equation

$$\frac{\mathrm{d}^2 \kappa}{\mathrm{d}t^2} = \frac{\partial f}{\partial x}(t, x(t))\kappa(t) - C x^{(p+2)}(t). \tag{7}$$

Here $C \equiv C_{p+2}/\sigma(1)$ is the global error constant of the method, which is more important than C_{p+2} itself. In the case of a harmonic oscillator, $f(t,x) = -\omega^2 x$, the leading part of the error function κ is a mixed secular term, i.e. $t\sin\omega t$ or $t\cos\omega t$. Its magnitude relative to that of the solution, namely $|\kappa/x|$, is expressed as $(C\omega^{p+1}/2)t$.

Finally we summarize some technical terms on the multistep methods;

1. The method is said to be *explicit* if $\beta_k = 0$ and *implicit* otherwise.
2. The method is said to be *irreducible* if ρ and σ have no common factor.
3. The method is said to be of *p-th order* if $C_0 = C_1 = \cdots = C_{p+1} = 0$.
4. The method is said to be *consistent* if it is of the order one at least.
5. The method is said to be *(zero-)stable* if (1) all the roots of $\rho(z)$ lie on or within the unit circle, and (2) the multiplicity of the roots on the unit circle is two at most.
6. The method is said to be *convergent* if it is consistent and zero-stable.

Remark that the conditions to be consistent, $C_0 = C_1 = C_2 = 0$, are rewritten in a more straightforward form as $\rho(1) = \rho'(1) = 0$ and $\rho''(1) = 2\sigma(1)$.

2.2. Symmetric Multistep Methods

Refer Lambert and Watson (1976) for the details of the symmetric multistep methods. The multistep method is said to be *symmetric* if the coefficients further satisfy the conditions

$$\alpha_j = \alpha_{k-j}, \qquad \beta_j = \beta_{k-j}, \qquad (j = 0, 1, \cdots, [k/2]). \tag{8}$$

This symmetry makes all the local error constants of odd order zero. It is proved that, for convergent irreducible symmetric multistep methods, (1) the stepnumber k must be even, and (2) all the roots of $\rho(z)$ are on the unit circle. The symmetric methods are important since the stable multistep methods of maximul order for even stepnumbers are known to be symmetric. See Theorem 10.5 (Hairer *et al.* 1993).

The stability of symmetric methods for oscillatory problems such as the case $f(x,t) = -\omega^2 x$ is discussed in term of the *interval of periodicity*; $(0, H_0^2)$. The quantity H_0 is the maximum of $H \equiv h\omega$ where all the roots of

$$\Omega(z, H^2) \equiv \rho(z) + H^2 \sigma(z) \tag{9}$$

remain on the unit circle. If $H_0^2 = \infty$, then the method is called to be P-stable. Unfortunately, the maximul order of P-stable methods is only two. Remark that being irreducible, symmetric, and convergent is not a sufficient but a necessary condition for multistep methods to have a nonvanishing interval of periodicity. A counter example is the 4th-order explicit method

$$x_{n+4} - 2x_{n+2} + x_n = \frac{4h^2}{3}\left(f_{n+3} + f_{n+2} + f_{n+1}\right). \tag{10}$$

The method is irreducible, symmetric, and convergent. However, it has zero interval of periodicity. See later discussion.

The symmetric methods with a nonvanishing interval of periodicity are important in orbit integration. This is because, if h is sufficiently small, the methods can avoid a linear energy error, and therefore a quadratic longitude error, too. As for the detailed explanation, refer the literature (Quinlan & Tremaine 1990). We stress that the most important point is that, the larger the interval of periodicity is, the larger the stepsize can be taken. On the other hand, even if an order is specified, the coefficients of symmetric methods of the order are not uniquely determined. Even if we restrict ourselves to seek only for the zero-stable methods of maximul order, there still remain $m \equiv k/2 - 1$ freedum. Thus, by using this freedum, Quinlan and Tremaine (1990) tried to find the symmetric integrators with the largest interval of periodicity.

However, the existence of symmetric methods with the largest interval of periodicity is not always assured. In fact, H_0^2 of the explicit symmetric method of the order 4 has only an upper bound, 4, which is equal to that of the order 2. See Method IV (Lambert & Watson 1976). Namely, if the coefficients of the 4th-order explicit method are chosen to maximize H_0^2, the order of the method reduces from 4 to 2. At the same time, the error constant becomes infinite. In other words, ρ and σ have a common factor in that case. The same is true for the implicit case of the order 6. Later, we will show that the interval of periodicity has not a maximum but an upper bound for the symmetric methods of the order $4n$ in the explicit case and of the order $4n + 2$ in the implicit case.

2.3. Interval of Periodicity

Consider how to search H_0 effectively. It is cumbersome to obtain all roots of the polynomial $\Omega(z, H^2)$ on a complex plane while changing H. Instead, we introduce a new function

$$g(\theta) \equiv \frac{-\rho\left(e^{i\theta}\right)}{\sigma\left(e^{i\theta}\right)} = \frac{-\left(\alpha_m + 2\sum_{j=1}^{m}\alpha_{m-j}\cos j\theta\right)}{\beta_m + 2\sum_{j=1}^{m}\beta_{m-j}\cos j\theta}, \qquad (-\pi < \theta \leq \pi), \tag{11}$$

which is well defined for irreducible methods since ρ and σ have no common factors. It is tedious but straightforward to show that

$$C_0 = C_1 = \cdots = C_p = 0 \Leftrightarrow g''(0) = 2,\ g^{(j)}(0) = 0,\ (j = 0, 1, 3, 4, \cdots, p) \tag{12}$$

Namely, the Taylor expansion of $g(\theta)$ around 0 becomes

$$g(\theta) = \theta^2 + O\left(\theta^{p+2}\right) \tag{13}$$

for the method of the order $p \geq 2$. Remark that the following two statements are equivalent; (1) the polynomial $\Omega(z, H^2)$ has k complex roots on the unit circle, and (2) the equation $g(\theta) = H^2$ has k real solutions in the interval $(-\pi, \pi]$. Actually, the latter can be rewritten as (2') the equation $g(\theta) = H^2$ has $k/2$ real solutions in the interval $(0, \pi]$. This is because $g(\theta)$ is an even function of θ and $\theta = 0$ cannot be a solution of $g(\theta) = H^2$ for positive H^2 since $g(0) = 0$ for the methods of order one at least. Thus, the problem to find the roots of $\Omega(z, H^2)$ is reduced to the problem to find the solutions of $g(\theta) = H^2$.

Now, consider the condition for irreducible convergent symmetric methods to have a nonvanishing interval of periodicity. If a symmetric method is convergent, it is zero-stable. Thus, all the roots of the polynomial ρ lie on the unit circle with the multipilicity two at most. Therefore, $g(\theta)$ has k roots in the interval $(-\pi, \pi]$ with the multipilicity two at most. The solutions of $g(\theta) = H^2$ for sufficiently small H are regarded as perturbations of the roots of $g(\theta)$. Consider the Taylor expansion of $g(\theta)$ around θ_0, a root of $g(\theta)$;

$$g(\theta) = g'(\theta_0)(\theta - \theta_0) + \frac{g''(\theta_0)}{2}(\theta - \theta_0)^2 + O\left((\theta - \theta_0)^3\right) = H^2 \tag{14}$$

where we note $g(\theta_0) = 0$. The expansion is always possible since (1) $g(\theta)$ is differentiable everywhere except its poles, and (2) the poles of $g(\theta)$, which are the zeros of $\sigma(\exp(i\theta))$, are sufficiently far from the roots of $g(\theta)$, which are the zeros of $\rho(\exp(i\theta))$, because $\rho(z)$ and $\sigma(z)$ have no common factors. In the case of a single root, $g'(\theta_0) \neq 0$. Thus, a real solution always exists near θ_0 such as

$$\theta = \theta_0 + \frac{1}{g'(\theta_0)} H^2 - \frac{g''(\theta_0)}{\{g'(\theta_0)\}^3} H^4 + O\left(H^6\right) \tag{15}$$

for sufficiently small H. While, in the case of a double root, the equation reduces to the following quadratic form approximately since $g'(\theta_0) = 0$ and $g''(\theta_0) \neq 0$;

$$\frac{g''(\theta_0)}{2}(\theta - \theta_0)^2 + \frac{g'''(\theta_0)}{6}(\theta - \theta_0)^3 + O\left((\theta - \theta_0)^4\right) = H^2 \tag{16}$$

Since $H^2 > 0$, the equation has two distinct real solutions near θ_0 for sufficiently small H if and only if $g''(\theta_0) > 0$. In fact, the solutions are expressed as

$$\theta = \theta_0 \pm H\sqrt{\frac{2}{g''(\theta_0)}} - \frac{g'''(\theta_0)}{3\{g''(\theta_0)\}^2} H^2 + O\left(H^3\right) \tag{17}$$

for sufficiently small H. In both cases, the perturbed solutions θ are all distinct, and their correspondence with the unperturbed ones θ_0 is one to one if the multiplicity is taken into account. Therefore the perturbed equation $g(\theta) = H^2$ has k distinct real solutions for sufficiently small H if and only if $g'' > 0$ at all the double roots of $g(\theta)$. The rewritten order conditions, Eq.(12), show that the condition $g'' > 0$ for the principal double root $\theta = 0$ is always satisfied for the methods of order one at least. As a result, we proved the following theorem.

Theorem. *Consider an irreducible convergent symmetric multistep method (ρ, σ). Define a function $g(\theta)$ as $g(\theta) \equiv -\rho(\exp(i\theta))/\sigma(\exp(i\theta))$ Then the method has a nonvanishing interval of periodicity if and only if (1) $g(\theta)$ has no nonzero double roots in the interval $[0, \pi]$, or (2) $g''(\theta)$ is positive on all the nonzero double roots of $g(\theta)$ in the interval $[0, \pi]$.*

We name g the periodicity function and the curve $y = g(x)$ the periodicity curve. Remark that the computation of g'' at the double roots of g is simplified as

$$g''(\theta)|_{g=g'=0} = \frac{2\sum_{j=1}^{m} j^2 \alpha_{m-j} \cos j\theta}{\beta_m + 2\sum_{j=1}^{m} \beta_{m-j} \cos j\theta}. \tag{18}$$

As an application of the above theorem, let us explain the difference between two similar symmetric methods in Lambert and Watson (1976). They presented the methods as a pair of counter examples to prove that neither their Theorems 2 nor 3 gives necessary and sufficient conditions to have nonvanishing interval of periodicity. The examples are

$$\rho(z) = (z-1)^2\left(z^2 - z + 1\right)^2, \ \sigma_1(z) = \frac{1}{2}\left(z^4 + z^2\right), \ \sigma_2(z) = \frac{1}{2}\left(z^5 + z\right). \tag{19}$$

Note that ρ has three double roots expressed in term of θ as $(0, \pm\pi/3)$. In the case of the pair (ρ, σ_1), the periodicity function becomes $g(\theta) = 2(5 - 8\cos\theta + 4\cos 2\theta - \cos 3\theta)/\cos 2\theta$. The numerical values of $g''(\theta)$ at the nonzero double roots are all positive as $g''(\pm\pi/3) = 12$. On the other hand, in the case of the pair (ρ, σ_2), a similar computation shows that the second derivatives are all negative as $g''(\pm\pi/3) = -12$. Thus the former method has a nonvanishing interval of periodicity while the latter does not. This is also clear from their periodicity curves, Figs 1 and 2. Another example is the 4th-order method, Eq.(10), which we cited as a counter example to show that not all convergent symmetric methods have a nonvanishing interval of periodicity. In this case, g has a nonzero double root, π. Since $g''(\pi) = -6 < 0$, the method has zero interval of periodicity.

Now, return to the issue to determine H_0^2 effectively. Assume that we deal only with the symmetric multistep methods with a nonvanishing interval of periodicity. In that case, it is assured that the equation $g(\theta) = H^2$ has $k/2$ solutions in the interval $(0, \pi)$ for sufficiently small H. Remark again that $g(\theta)$ is differentiable everywhere except its poles. Thus, while H is increasing, the number of solutions decreases by two when H^2 passes a local maximum of $g(\theta)$ and increases by two when does a local minimum. Anyway, the number of solutions remain unchanged until H^2 exceeds the least positive extremum of $g(\theta)$. Remark that this least positive extremum is actually a local maximum. If not, the number of solutions becomes $k + 2$ when passing this extremum. However, it contradicts with the fact that the k-th order polynomial Ω has k roots. As a result, we proved a following lemma.

Lemma. *Assume that a symmetric multistep method has a nonvanishing interval of periodicity* $(0, H_0^2)$. *Then,* H_0^2 *is given as the least positive local maximum of the function* $g(\theta)$ *in the interval* $[0, \pi]$.

Once ρ and σ are fixed, it is easy to find H_0^2 by means of this lemma. A quick way is to plot the periodicity curve like Figs 1 and 2 and look for the the least positive local maximum by eye. A more precise and automatic way is described in Appendix.

2.4. New Parameters

In the search for the formulas of the largest interval of periodicity, we must change the forms of ρ and σ while keeping the combination to have a nonvanishing interval of periodicity and assuring the variations to cover all possible cases. To do this clearly, we adopt new parameters in place of α which Quinlan and Tremaine (1990) did.

Let's begin by $\rho(z)$. From the zero-stability conditions, the assumption $\alpha_k = 1$, and the fact that the coefficients α are all real, ρ must be expressed as

$$\rho(z) = (z-1)^2 \prod_{i=1}^{m} \left(z^2 - 2c_i z + 1\right), \tag{20}$$

where

$$c_i = \cos\theta_i, \qquad (i = 1, \cdots, m).$$

Here θ_i denotes the phase of the i-th spurious root on the upper half of the unit circle in a complex plane. The principal double root $z = 1$ corresponds to the case $\theta_0 = 0$, i.e. $c_0 = 1$. From a computational point of view, we adopt the set not of θ_i but of c_i as the free parameters to be moved in the search of the largest interval of periodicity. Then the parameters are ordered as

$$-1 \le c_m \le \cdots \le c_2 \le c_1 < 1. \tag{21}$$

although the restriction on the multiplicity of roots prohibits more-than-two consecutive equality of c_j such as $c_1 = c_2 = c_3$. Also the case like $c_{m-1} = c_m = -1$ is prohibited since $c_m = -1$ means a double spurious root at $z = -1$ by itself. Anyway, the range of the parameters is clearly bound as $|c_i| \le 1$, which makes sure the search to cover all possible cases.

The coefficients α are expressed as polynomials of c_i. Remark that ρ must be unchanged with any permutation of index i. Thus α must be expressed as linear combinations of symmetric forms of the paramaters c_i. Here the ℓ-th order symmetric form of $(c_1, \cdots, c_m)$ is defined as

$$S_\ell^{(m)} = \sum \prod_{a=1}^{\ell} c_{i_a}, \qquad (\ell = 0, 1, \cdots, m) \tag{22}$$

where the summation is taken over all different permutation of indices i_a. Examples of such symmetric forms for $m = 3$ are

$$S_0^{(3)} = 1,\ S_1^{(3)} = c_1 + c_2 + c_3,\ S_2^{(3)} = c_1c_2 + c_2c_3 + c_3c_1,\ S_3^{(3)} = c_1c_2c_3.$$

Remark that the symmetric forms are effectively computed by a following recursive formula;

$$S_0^{(m)} = 1, \qquad (0 \le m), \qquad S_1^{(1)} = c_1, \qquad S_m^{(m)} = c_m S_{m-1}^{(m-1)} \qquad (2 \le m),$$

$$S_\ell^{(m)} = S_\ell^{(m-1)} + c_m S_{\ell-1}^{(m-1)} \qquad (2 \le m; 1 \le \ell < m), \tag{23}$$

By means of them, the expressions of α are given as

$$\alpha_j = \sum_{\ell=0}^{m} (-1)^m \alpha_{j,\ell}^{(m)} S_\ell^{(m)}, \qquad (1 \le j \le m+1, \qquad m = 1, 2, \cdots) \tag{24}$$

where the numerical coefficients $\alpha_{j,\ell}^{(m)}$, which are all positive, are obtained by the following recursive procedure;

$$\alpha_{0,0}^{(m)} = 1, \qquad \alpha_{1,0}^{(m)} = \alpha_{1,1}^{(m)} = 2, \qquad (m = 1, 2, \cdots)$$

$$\alpha_{j,0}^{(m)} = \alpha_{j-2,0}^{(m-1)} + \alpha_{j,0}^{(m-1)}, \qquad (j = 2, 3, \cdots, m; m = 2, 3, \cdots)$$

$$\alpha_{m+1,0}^{(m)} = 2\alpha_{m-1,0}^{(m-1)}, \qquad (m = 2, 3, \cdots)$$

$$\alpha_{j,\ell}^{(m)} = 2\alpha_{j-1,\ell-1}^{(m-1)}, \qquad (\ell = 1, 2, \cdots, j; j = 2, 3, \cdots, m; m = 2, 3, \cdots)$$

$$\alpha_{j,\ell}^{(m)} = 0, \qquad (\ell = j+1, j+2, \cdots, m; j = 2, 3, \cdots, m; m = 2, 3, \cdots)$$

Some of them are listed in Table I. Remark that the zeroth order condition, $C_0 = 0$, which must be satisfied by α by themselves, is actually satisfied by α coefficients determined in the above.

Next, consider σ. Once α are given, β are uniquely determined by solving a set of linear equations $C_q = 0$ for $q = 2, 4, \cdots, p$. Here $p = 2m$ if explicit and $p = 2m + 2$ if implicit. By using the symmetry of coefficients, we rewrite the local error constants of even order as

$$C_0 = \alpha_{m+1} + 2\sum_{j=0}^{m} \alpha_j, \qquad C_2 = -\beta_{m+1} + \sum_{j=0}^{m} \left[(m-j)^2 \alpha_j - 2\beta_j\right],$$

$$C_{2r} = \frac{2}{(2r)!} \sum_{j=0}^{m} (m-j)^{2r-2} \left[(m-j)^2 \alpha_j - 2r(2r-1)\beta_j\right], \qquad (r > 1). \tag{25}$$

The linear equations are solved in a straightforward manner. Thanks to *Mathematica*, we explicitly obtained some of them in Tables II and III. By a similar way, we evaluated the parameter representations of the local error constant C_{p+2} as

$$\text{(explicit)} \qquad C_{p+2} = \sum_{\ell=0}^{m} C_\ell^{(m)} S_\ell^{(m)}. \tag{26}$$

for the explicit case where $p = 2m$, and

$$\text{(implicit)} \qquad C_{p+2} = \frac{-1}{2} \sum_{\ell=0}^{m} C_{\ell+1}^{(m+1)} S_\ell^{(m)} \tag{27}$$

for the implicit case where $p = 2m + 2$. Some of the common coefficients, $C_\ell^{(m)}$ are listed in Table IV. Remark that, in the explicit cases, the coefficients of constant term $C_0^{(m)}$ is positive and much larger than the others. The situation is unchanged in the implicit cases. Thus the local error constants of most explicit methods become positive while those of most implicit methods do negative. On the other hand, the representation of the global error constant $C \equiv C_{p+2}/\sigma(1)$ is straightforward since the expression of the denominator is easily evaluated as

$$\sigma(1) = \frac{\rho''(1)}{2} = \lim_{z \to 1} \frac{\rho(z)}{(z-1)^2} = 2^m \prod_{j=1}^{m} (1 - c_j) \tag{28}$$

for the methods of order one at least. Remark that the local error constants C_{p+2} remain bounded for any combination of c_j while the absolute value of global one $|C|$ goes to infinity when any of spurious roots come close to the principal one. Remark that the signature of the global error constant is the same as that of the local one since the multiplicant of the denominator $1 - c_j$ is always nonnegative.

Thus, we have obtained the expressions of α, β, C_{p+2}, and C as functions of parameters c_i.

2.5. Existing Formulas

Let us express the existing formulas by the newly introduced parameters.

The parameters corresponding to the formulas given in Lambert and Watson (1976) are;

$$(k = 4) \qquad c_1 = \frac{a}{2} \tag{29}$$

for Methods IV (explicit, 4th-order) and V (implicit, 6th-order) where a is the free parameter they introduced, and

$$(k=6) \qquad (c_1, c_2) = \left(\frac{1}{2}, \frac{-1}{2}\right) \tag{30}$$

for Methods VI (explicit, 6th-order) and VII (implicit, 8th-order). Remark that their Methods I (= 2nd-order Störmer method) and III (= Numerov method) are uniqely determined, and therefore with no freedum. The freedum ϕ of their Method II is the pole of $g(\theta)$, which makes H_0^2 the infinity, and therefore makes the method P-stable.

While, the phases for the explicit formulas given in Quinlan and Tremaine (1990) are;

$$(k=8) \qquad (\theta_1, \theta_2, \theta_3) = \left(\frac{\pi}{3}, \frac{2\pi}{5}, \frac{4\pi}{5}\right) \tag{31}$$

for the 8th order,

$$(k=10) \qquad (\theta_1, \theta_2, \theta_3, \theta_4) = \left(\frac{\pi}{3}, \frac{2\pi}{5}, \frac{2\pi}{3}, \frac{4\pi}{5}\right) \tag{32}$$

for the 10th order,

$$(k=12) \qquad (\theta_1, \theta_2, \theta_3, \theta_4, \theta_5) = \left(\frac{2\pi}{9}, \frac{\pi}{3}, \frac{4\pi}{9}, \frac{2\pi}{3}, \frac{8\pi}{9}\right) \tag{33}$$

for the 12th order, and

$$(k=14) \qquad (\theta_1, \theta_2, \theta_3, \theta_4, \theta_5, \theta_6) = \left(\frac{2\pi}{11}, \frac{\pi}{3}, \frac{4\pi}{11}, \frac{6\pi}{11}, \frac{8\pi}{11}, \frac{10\pi}{11}\right) \tag{34}$$

for the 14th order.

Now consider how to maximize H_0^2 of the symmetric method of the order given. Remark that H_0^2 is the least positive local maximum of $g(\theta)$. Since H_0^2 is a sort of minimum, the problem reduces to the so-called *maxmini* problem, which is equivalent with the minimax problem. From the viewpoint of minimax approximation theory, all the local maxima must be the same for the best approximation. Therefore, in order to check whether the interval of periodicity of a specific symmetric method is the largest or sufficiently close to the largest, it is a good way to draw the periodicity curve and to examine the equality of the local maxima. Figs 3 through 8 are the periodicity curves for the existing methods. Here we omitted those for Methods I through V of Lambert and Watson (1976) since they are expressed in general forms and the analytical expressions of H_0^2 are known for these. These figures indicate that H_0^2 of the methods seem far from the largest except the case $k = 8$. Therefore, we decided to seek for the methods of the largest interval of periodicity for the stepnumbers $k \geq 6$ in both the explicit and implicit cases.

3. Search

Now that we have the tools to search the methods with the largest interval of periodicity, we will explain here our strategy to do that.

The straightforward rewriting of Eq.(2) is

$$x_{n+k} = -\sum_{j=0}^{k-1} \alpha_j x_{n+j} + h^2 \sum_{j=0}^{k} \beta_j f_{n+j}. \tag{35}$$

If we ignore the round-off errors in evaluating its right hand side, any real value is possible to be assigned as the coefficients α and β. However, it would be wise to pose some conditions in selecting the coefficients in order to reduce possible round-off errors. Quinlan and Tremaine (1990) did this by limiting the numerical form of α to be integer, or more precisely speaking, to be 0 or powers of 2 such as $(0, \pm 1, \pm 2, \pm 4, \pm 8, \pm 16)$. Unfortunately, not all possible combination of them satisfy the zero-stability condition. Also the condition posed seems too restrictive to lead to the nearly largest interval of periodicity. Instead, we decided to search among c_i in the form of fractions rounded in binaries, namely in the form of $M/2^N$ where M and N are integers and $|M| \leq 2^N$. We adopted not θ_i but c_i in order to make the binary expressions of α rounded as much as possible.

TABLE I
Parameter Representation of α Coefficients

m	j	$S_0=1$	S_1	S_2	S_3	S_4	S_5	S_6	S_7
1	2	2	4						
2	2	3	4	4					
	3	4	4	8					
3	2	4	4	4					
	3	6	6	8	8				
	4	6	8	8	16				
4	2	5	4	4					
	3	8	8	8	8				
	4	10	12	12	16	16			
	5	12	12	16	16	32			
5	2	6	4	4					
	3	10	10	8	8				
	4	15	16	16	16	16			
	5	20	20	24	24	32	32		
	6	20	24	24	32	32	64		
6	2	7	4	4					
	3	12	12	8	8				
	4	21	20	20	16	16			
	5	30	30	32	32	32	32		
	6	35	40	40	48	48	64	64	
	7	40	40	48	48	64	64	128	
7	2	8	4	4					
	3	14	14	8	8				
	4	28	24	24	16	16			
	5	42	42	40	40	32	32		
	6	56	60	60	64	64	64	64	
	7	70	70	80	80	96	96	128	128
	8	70	80	80	96	96	128	128	256

Listed are the numerical coefficients of linear form of α_j with respect to $(-1)^m S_\ell^{(m)}$. Here $S_\ell^{(m)}$ is the ℓth-order m-dimensional symmetric forms of $c_j = \cos\theta_j$ where θ_j denotes the phase of j-th spurious root of the characteristic polynomial $\rho(z)$. The rows for $j=0$ and $j=1$ are omitted since they are the same for all m; $(1,0,0,\cdots)$ and $(-2,-2,0,0,\cdots)$, respectively. Example: the coefficients for the case $m=3$ and $j=4$ are $(6,8,8,16)$, which means $\alpha_4 = -6 - 8S_1^{(3)} - 8S_2^{(3)} - 16S_3^{(3)} = -6 - 8(c_1+c_2+c_3) - 8(c_1c_2+c_2c_3+c_3c_1) - 16c_1c_2c_3$.

First, we performed an experimental search both in explicit and implicit cases for several values of m while increasing N one by one up to 5. The experiments revealed the following tendencies, where we use the word *optimal* in the sense of having the largest interval of periodicity;

(1) The number of double roots is maximal for the optimal method. This is true both for explicit and implicit cases. In other words, the optimal periodicity function has, other than the principal double root, $m/2$ double roots if m is even and $(m-1)/2$ double roots plus one single root if m is odd.
(2) When m is odd, the single root of the optimal periodicity function is the closest to the principal double root. In that case, the optimal periodicity function has a single pole which is a little closer to the principal double root than this single root.
(3) The inclusion of a double root $\theta=\pi$ (i.e. $c=-1$) leads to zero or small interval of periodicity.
(4) The double roots of the optimal periodicity function for odd m are almost the same as those for $m-1$.
(5) All the roots of the optimal periodicity function for even m are well separated with each other.
(6) The roots of the optimal periodicity function for the implicit case are significantly different from those for the explicit case of the same number of roots.
(7) The largest value of H_0^2 of an implicit method is larger than that of the explicit method of the same number of roots. The ratio is roughly 1.5-2.
(8) The largest value of H_0^2 decreases when the number of roots increases. However, the largest value of H_0^2 for odd m is only a little smaller than that for $m-1$.

TABLE II
Parameter Representation of β Coefficients: Explicit Case

m	j	denominator	numerator				
			$S_0 = 1$	S_1	S_2	S_3	S_4
0	1	1	1				
1	1	6	7	−1			
	2	3	−1	−5			
2	1	60	79	−9	−1		
	2	15	−14	−26	6		
	3	30	97	−7	97		
3	1	7560	10993	−1039	−95	−31	
	2	1260	−2215	−2279	473	73	
	3	2520	16661	−491	8261	−2171	
	4	1890	−8723	−7027	1357	−12067	
4	1	226800	358751	−28961	−2209	−641	−289
	2	56700	−157597	−106973	20003	2707	1043
	3	56700	660047	−3377	189647	−47057	−8593
	4	56700	−766819	−344291	53021	−362771	101741
	5	4536	100525	1325	30637	−7411	57517

Same as Table I but for β coefficients of the explicit case. Example: The common denominator and the numerators for the case $m = 3$ and $j = 4$ are 1890 and $(-8723, -7027, 1357, -12067)$, respectively, which means

$$\beta_4 = (-8723 - 7027S_1^{(3)} + 1357S_2^{(3)} - 12067S_3^{(3)})/1890.$$

(9) The magnitude of local error constants C_{p+2} is not sensitive with the distribution of roots, while that of the global one C is. A large interval of periodicity frequently leads to a large error constant.

These are just observations, and we could not prove these. Based on the first three phenomenon, we made the following assumption on the form of roots as

$$0 < \theta_1 < \theta_2 = \theta_3 < \theta_4 = \theta_5 < \cdots < \theta_{m-1} = \theta_m < \pi \tag{36}$$

when m is odd and as

$$0 < \theta_1 = \theta_2 < \theta_3 = \theta_4 < \cdots < \theta_{m-1} = \theta_m < \pi \tag{37}$$

when m is even. In Tables V and VI, we present the best methods we obtained. There we added the existing formulas, too. The periodicity curves of some of them are shown in Figs 9 and after. Clearly these curves show minimax-like feature.

4. Conclusion

We discovered a necessary and sufficient condition for irreducible convergent symmetric multistep methods to have a nonvanishing interval of periodicity. The condition found explains well the difference of two similar symmetric multistep methods, which were cited as a counter example for the condition known so far (Lambert & Watson 1976). By using this new condition and expressing the formulas by a new set of parameters, we established a systematic approach to derive the symmetric multistep methods with large stability regions. As its application, we obtained the explicit and implicit formulas of order 6 to 16 which have the nearly largest interval of periodicity. They are superior to those given in the literature (Quinlan & Tremaine 1990) at the point of having longer stability region of stepsize.

The next target is to check whether these methods, especially the predictor-corrector usage of the implicit methods, will lead the linear longitude error.

References

Hairer, E., Nørsett, S.P., and Wanner, G., 1993, *Solving Ordinary Differential Equations I (2nd ed.)*, Springer-Verlag, Berlin.

Henrici, P., 1962, *Discrete Variable Methods in Ordinary Differential Equations*, Wiley, New York.

TABLE III
Parameter Representation of β Coefficients: Implicit Case

m	j	denominator	numerator				
			$S_0 = 1$	S_1	S_2	S_3	S_4
0	0	12	1				
	1	6	5				
1	0	120	9	1			
	1	15	13	−3			
	2	60	7	−97			
2	0	15120	1039	95	31		
	1	2520	2279	−473	−73		
	2	5040	491	−8261	2171		
	3	3780	7027	−1357	12067		
3	0	453600	28961	2209	641	289	
	1	113400	106973	−20003	−2707	−1043	
	2	113400	3377	−189647	47057	8593	
	3	113400	344291	−53021	362771	−101741	
	4	9072	−1325	−30637	7411	−57517	
4	0	9979200	598507	38635	9963	4139	2219
	1	4989600	4899987	−830317	−98413	−34797	−17453
	2	9979200	−804257	−17088673	3968863	662687	283423
	3	1247400	5543429	−653819	4022789	−1097339	−222331
	4	4989600	−4636837	−26240933	5711963	−31489253	9186203
	5	2494800	17582809	−1705255	16222681	−4336807	31494553

Same as Table II but for the implicit case.

TABLE IV
Parameter Representation of Local Error Constants C_{p+2}

m	$p+2$	denominator	numerator				
			$S_0 = 1$	S_1	S_2	S_3	S_4
0	4	12	1				
1	6	120	9	1			
2	8	15120	1039	95	31		
3	10	453600	28961	2209	641	289	
4	12	9979200	598507	38635	9963	4139	2219

Same as Table II but for the local error constant, C_{p+2}, where p denotes the order. Listed are the coefficients for the explicit case. Those for an implicit case are easily obtained from those for the explicit one of the same order as described in the text.

Lambert, J.D., and Watson, I.A., 1976, J. Inst. Maths Applics, 18, 189-202.
Milani, A., and Nobili, A.M., 1988, Celstial Mechanics, 43, 1.
Quinlan, G.D., and Tremaine, S., 1990, Astron. J., 100, 1694-1700.

Appendix

A. Finding Least Positive Local Maximum of Periodicity Function

Here we will present a procedure to find the the least positive local maximum of the periodicity function in the interval given. Such a procedure may consist of three parts; (1) to provide a set of initial guesses of the interval bracketting it, which assure the next part to reach a group of maxima containing the least positive one, (2) to find local maxima of the function starting from the initial guesses given, and (3) to determine the least positive one from the maxima obtained. In the below, we will describe our method part by part.

TABLE V
Best Symmetric Methods: Explicit

p	H_0^2	$100C$	c_j	Note
2	4.000	8.333		Störmer
4	$(0, 4)$	$(1.667, \infty)$	$(-1, 1)$	LW: Method IV
	2.000	2.36	$\frac{-1}{2}$	recommended
6	0.802	2.27	$\frac{1}{2}, \frac{-1}{2}$	LW: Method VI
	1.369	1.05	$\frac{-1}{4}^*$	recommended
	1.378	1.04	$\frac{-135747}{524288}^*$	largest H_0^2
8	0.516	1.26	$\frac{1}{2}, \cos\frac{2\pi}{5}, \cos\frac{4\pi}{5}$	QT: 8th-order
	1.321	4.17	$\frac{7}{8}, \frac{-1}{4}^*$	recommended
10	0.172	0.384	$\frac{1}{2}, \cos\frac{2\pi}{5}, \frac{-1}{2}, \cos\frac{4\pi}{5}$	QT: 10th-order
	0.693	0.801	$\frac{1}{2}^*, \frac{-3}{8}^*$	recommended
	0.738	0.877	$\frac{542311}{1048576}^*, \frac{-3005769}{33554432}^*$	largest H_0^2
12	0.046	0.623	$\cos\frac{2\pi}{9}, \frac{1}{2}, \cos\frac{4\pi}{9}, \frac{-1}{2}, \cos\frac{8\pi}{9}$	QT: 12次
	0.562	1.581	$\frac{3}{4}, \frac{1}{2}^*, \frac{-3}{8}^*$	reommended
14	0.012	0.487	$\cos\frac{2\pi}{11}, \frac{1}{2}, \cos\frac{4\pi}{11}, \cos\frac{6\pi}{11}, \cos\frac{8\pi}{11}, \cos\frac{10\pi}{11}$	QT: 14次
	0.429	3.120	$\frac{3}{4}^*, \frac{1}{2}^*, \frac{-3}{8}^*$	recommended
	0.469	6.08	$\frac{6144577}{8388608}^*, \frac{8153}{16384}^*, \frac{-3616321}{8388608}^*$	largest H_0^2

Listed are the characteristics of some explicit symmetric methods. Here p is the order, H_0^2 is the upper bound of the interval of periodicity, C is the global error constant, and c_j's are the cosine of the phase of spurious roots where the asterisk means a double root. Remark that C is always positive. Also added are those of the existing formulas; LW for (Lambert & Watson 1976) and QT for (Quinlan & Tremaine 1990). Remark that Method IV contains one freedum indicating the pole of the periodicity function, where the largest H_0^2 leads to the infinite global error constant, unfortunately.

A.1. Bracketting Least Positive Local Maximum

First, consider a set of the subintervals such that one of them is assured to contain only the least positive local maximum as extrema. To do this, we order the zeros of the periodicity function and separate the whole interval into a set of subintervals by them. There exists one and only one subinterval containing the least positive local maximum. Then, the following lemma holds on this specific subinterval.

Lemma A. *Assume that the periodicity function has the least positive local maximum in an open subinterval whose endpoints are a pair of adjacent zeros of the function. Then, in that subinterval, (A1) the function has no pole, (A2) the function is always positive, and (A3) the function has no extremum other than the least positive local maximum. Namely the least positive local maximum is the only extremum in the subinterval and therefore it is the global maximum in the subinterval.*

Proof. (A1) Assume that the periodicity function has poles within the subinterval. Choose the pole nearest to the locus of the least positive local maximum. Consider an open segment of the subinterval whose endpoints are the locus of the local maximum and the pole. Then, the function is continuous on the segment since it is a rational function and no pole exists there. Consider the periodicity curve starting from the local maximum and approaching the pole. Then, there are two possibilities on the behaviour of the functional value near the pole; going to $+\infty$ or to $-\infty$. In the former case, the functional value first decreases (since starting from a local maximum) but must finally increase. Namely the curve must turn over. Since there are no zeros within the segment, the functional value at the turning point must be positive. In other words, the function must have a local positive minimum whose value is less than the local maximum. However, this contradicts with the fact that the local maximum is the least positive extremum as we proved in the main text. In the latter case, the functional value is positive at first but must be finally negative. However, this contradicts with the fact that the function has no zeros and is continuous on the segment. Anyway, the assumption that the function has poles lead to contradictions. Thus the item (A1) is proved.

(A2) Since the item (A1) holds, the periodicity function is continuous in the subinterval. Also the function

TABLE VI
Best Symmetric Methods: Implicit

p	H_0^2	$-10^4 C$	c_j	Note
2	∞	$(1666.7, \infty)$		LW: Method II
4	6.000	41.7		Numerov
6	$(0, 6)$	$(5.29, \infty)$	$(-1, 1)$	LW: Method V
	4.615	8.76	$\frac{-1}{2}$	recommended
8	1.019	7.85	$\frac{1}{2}, \frac{-1}{2}$	LW: Method VII
	2.535	2.01	$\frac{-1}{2}$	recommended
	2.629	1.84	$\frac{-35935}{65536}^*$	largest H_0^2
10	2.427	2.50	$\frac{5}{8}, \frac{-1}{2}^*$	recommended
12	1.374	0.452	$\frac{1}{4}^*, \frac{-1}{2}^*$	recommended
	1.506	0.477	$\frac{363649}{2097152}^*, \frac{-4791869}{8388608}^*$	largest H_0^2
14	1.150	0.502	$\frac{1}{2}, \frac{1}{4}^*, \frac{-5}{8}^*$	recommended
16	0.952	0.465	$\frac{1}{2}^*, \frac{1}{4}^*, \frac{-5}{8}^*$	recommended

Same as Table V but for implicit methods. Remark that C is always negative.

has no zeros within the subinterval. Thus the signature of functional value remains the same within the subinterval. Remark that the function is positive at at least one point in the subinterval because it has a positive local maximum there. Therefore the function remains positive everywhere within the subinterval. Thus the item (A2) is proved.

(A3) Remark that the periodicity function is differentiable in the subinterval since it is a rational function and it has no pole there. Thus its derivative is continuous in the subinterval. Now, assume that the function has extrema other than the least positive local maximum. Choose the extremum whose locus is the nearest to that of the least positive local maximum. Consider a segment of the subinterval whose endpoints are the loci of the least positive local maximum and the nearest extremum. Then, the function has no extremum within the segment. Thus its derivative has no root within the segment. Since the derivative is continuous in the segment, its signature must be the same in the segment. Thus, the functional value continues to decrease on the segment if starting from the local maximum since it first decreases. Therefore, this extremum must be a local minimum. By means of the item (A2), the minimum is positive. Further it is less than the local maximum. However, this contradicts with the fact that the local maximum is the least positive extremum as we proved in the main text. Thus, the item (A3) is proved.

Based on the lemma, we adopt the set of subintervals separated by the zeros of the periodicity function as the initial guesses of the intervals for search of the least positive local maximum. Remark that a subinterval separated by a pair of adjacent zeros of the periodicity functions is not assured to contain only one extremum in it, which is a necessary condition for most methods searching extrema not to fail. However, this is acceptable because the search does not fail to find the least positive local maximum when it is contained in the subinterval to be searched since the above lemma assures that the periodicity function is continuous and has no other extremum in this subinterval. Namely the search based on the above choice of subintervals may not find all local maxima but surely does a group of maxima including the least positive local maximum.

A.2. Finding Positive Local Maxima

Next, consider how to find a local maximum of the periodicity function in the subinterval given.

Before entering into the detail, however, let us introduce a variable transformation. From a computational point of view, it is more suitable to deal with $c \equiv \cos\theta$ in place of θ itself. In that case, the periodicity function becomes a rational function of c as

$$G(c) \equiv g\left(\cos^{-1} c\right) = -R(c)/S(c), \tag{38}$$

where R and S are polynomials defined as

$$R(c) \equiv \rho\left(\exp\left(i\cos^{-1}c\right)\right) = \sum_{j=0}^{m} r_j T_j(c),$$

$$S(c) \equiv \sigma\left(\exp\left(i\cos^{-1}c\right)\right) = \sum_{j=0}^{m} s_j T_j(c), \tag{39}$$

and T_j is the j-th order Chebyshev polynomial of the first kind. The coefficients r and s are just rewritings of α and β as

$$r_0 = \alpha_m,\ r_j = 2\alpha_{m-j},\ s_0 = \alpha_m,\ s_j = 2\beta_{m-j},\ (j = 1, 2, \cdots, m). \tag{40}$$

Remark that finding the least positive local maximum of $g(\theta)$ in the interval $[0, \pi]$ is equivalent with finding that of $G(c)$ in the interval $[-1, 1]$. We adopt the latter approach since $G(c)$ is faster to evaluate numerically.

Now, return to the method of search. Basically speaking, there are two types of approaches; (1) to find an extremum of G directly, and (2) to solve the equation $G'(c) = 0$. We adopt the simplest method in the first category; the golden section search. This is because the evaluation of functional value is so accelerated by the above transformation that the evaluation of derivatives becomes relatively expensive. Further, based on the above lemma, we first set the following conditions to interrupt the search;

(1) when a trial value of the function is negative,
(2) when a local minimum is found, namely when a trial value of the function is less than both of those at the endpoints of the interval bracketting the locus of the trial value, and
(3) when a trial value of the function is sufficiently large, say larger than 6, the maximul value of the implicit method of the order 6. This means that at least one pole of the function is contained in the subinterval.

Experiments showed that the second criterion is fragile against the round-off error. Actually, the procedure was frequently trapped by fake local minima caused by the rounded β coeficients. Thus, we skipped this. Other two conditions greatly accelerate the search. The actual search including these interruption tests goes like this;

1. Initialize the interval:
$$(c_L, c_R) \leftarrow (c_j, c_{j+1}), \qquad (G_L, G_R) \leftarrow (0, 0), \tag{41}$$
where c_j and c_{j+1} are a pair of adjacent roots of G.
2. Prepare the middle value:
$$c_M \leftarrow wc_L + (1-w)c_R, \qquad G_M \leftarrow G(c_M), \tag{42}$$
where $w \equiv (\sqrt{5}-1)/2 = 0.608\cdots$ is the ratio of golden section.
3. Check the middle value. Namely, if $G_M < 0$ or $G_M > 6$, then terminate the search with the convergence flag set as NO.
4. Evaluate a trial value:
$$c_T \leftarrow wc_L + (1-w)c_M, \qquad G_T \leftarrow G(c_T), \tag{43}$$
5. Check the trial value. Namely, if $G_T < 0$ or $G_T > 6$, then terminate the search with the convergence flag set as NO.
6. Reduce the interval. Namely, if $G_T > G_M$, then
$$(c_L, c_M, c_R) \leftarrow (c_L, c_T, c_M), \qquad (G_L, G_M, G_R) \leftarrow (G_L, G_T, G_M) \tag{44}$$
else
$$(c_L, c_M, c_R) \leftarrow (c_R, c_M, c_T), \qquad (G_L, G_M, G_R) \leftarrow (G_R, G_M, G_T) \tag{45}$$
7. Check the convergence. Namely, if $|G_M - (G_L + G_R)/2| < \epsilon_G$, or if $|c_L - c_R| < \epsilon_c$, then terminate the search with the convergence flag set as YES and return G_M as the value of the local maxima found. Here ϵ_G and ϵ_c are certain tolerance of convergence satisfying an approximate condition $\epsilon_G \approx \epsilon_c^2$, say 10^{-12} and 10^{-6} or so.
8. Go to Step 4.

A.3. Determining Least Positive Local Maximum

Finally, consider the process to determine the least positive local maximum. Order the roots of G as

$$-1 \le d_{m'} < \cdots < d_2 < d_1 < 1. \tag{46}$$

Here we ignore the multiplicity of the roots. Unless the least root is exactly equal to -1, there is a possibility that $G(-1)$ is a positive local maximum. This comes from the fact that the original form of the periodicity function $g(\theta)$ is symmetric with respect to the transformation $\theta \to \pi - \theta$. Thus, the procedure of determination becomes as; (1) for the subintervals $(d_{m'}, d_{m'-1}), \cdots, (d_2, d_1)$, find positive local maxima if they exist, (2) evaluate $G(-1)$ and put it into the set of local maxima found if it is positive, and (3) take the minimum of the set of local maxima found.

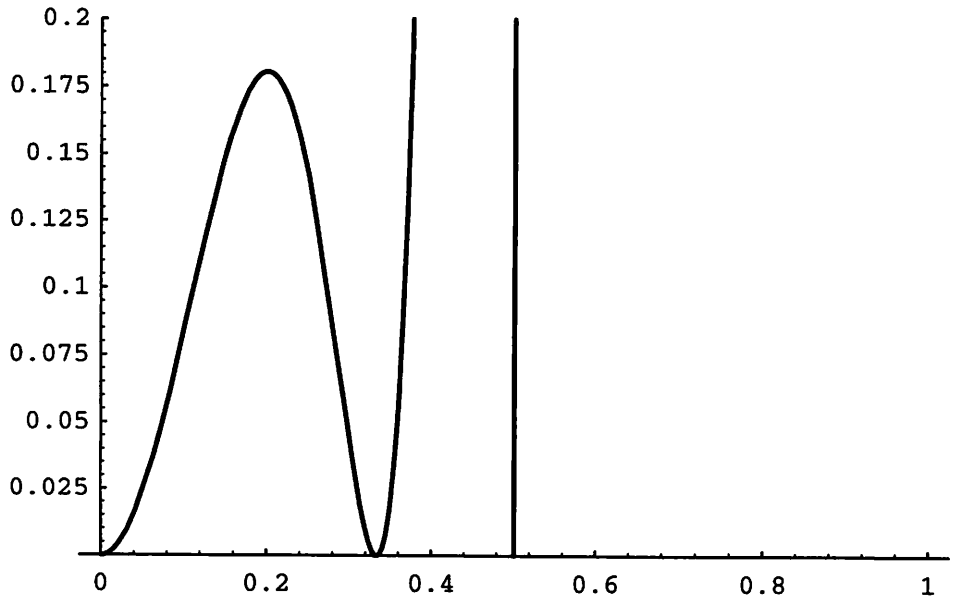

Fig. 1 Periodicity curve of a 4th-order explicit method: stable case

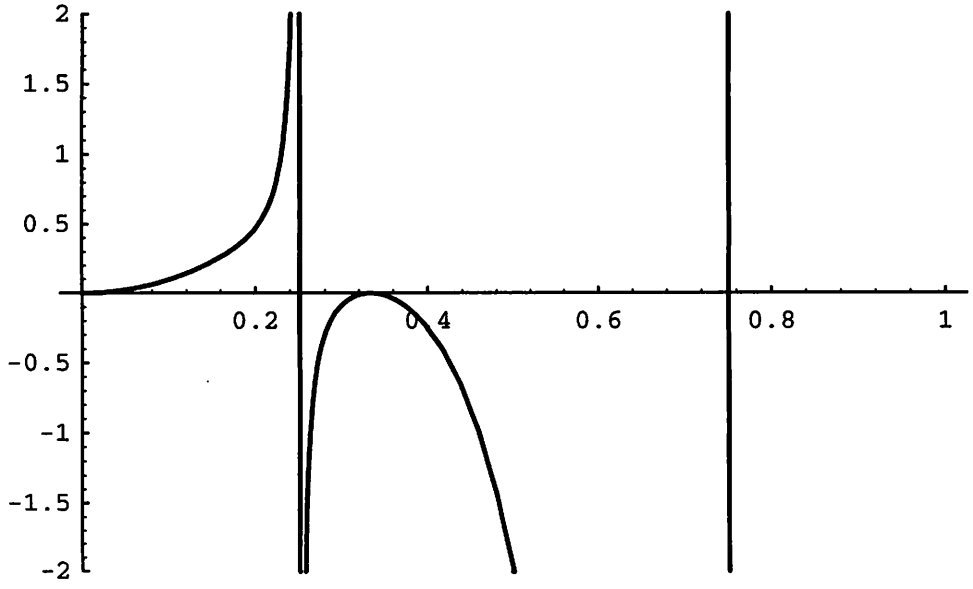

Fig. 2 Periodicity curve of a 4th-order explicit method: unstable case

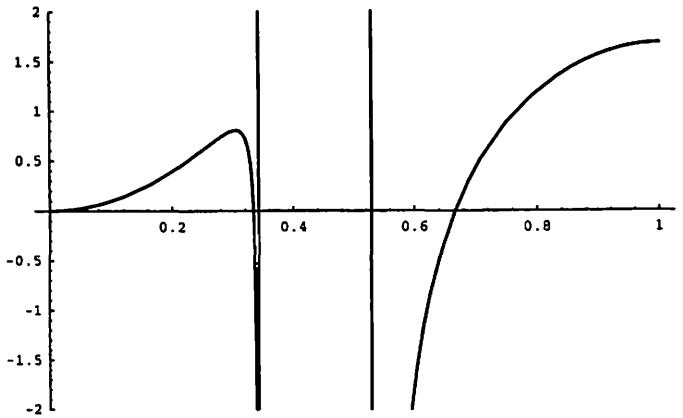

Fig. 3 Periodicity curve of Lambert & Watson's Method VI (6th-order explicit)

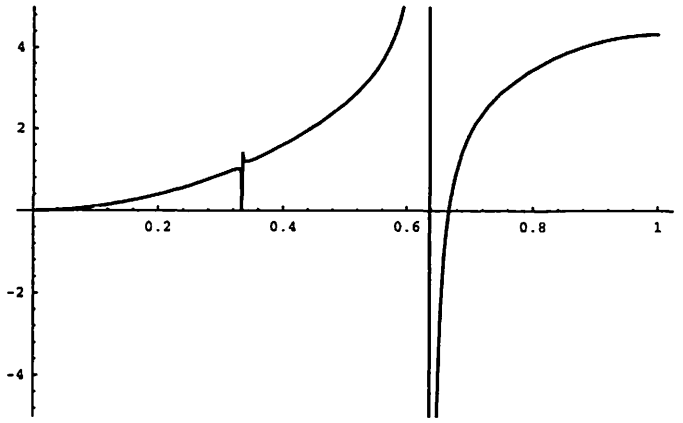

Fig. 4 Periodicity curve of Lambert & Watson's Method VII (8th-order implicit)

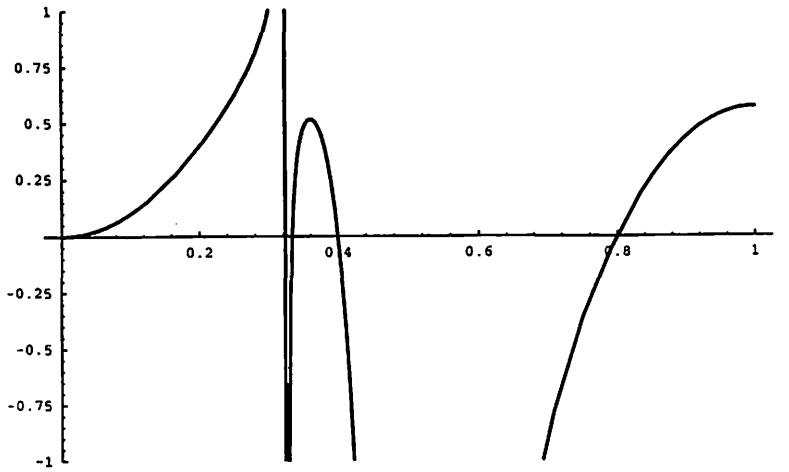

Fig. 5 Periodicity curve of Quinlan & Tremaine's 8th-order explicit method

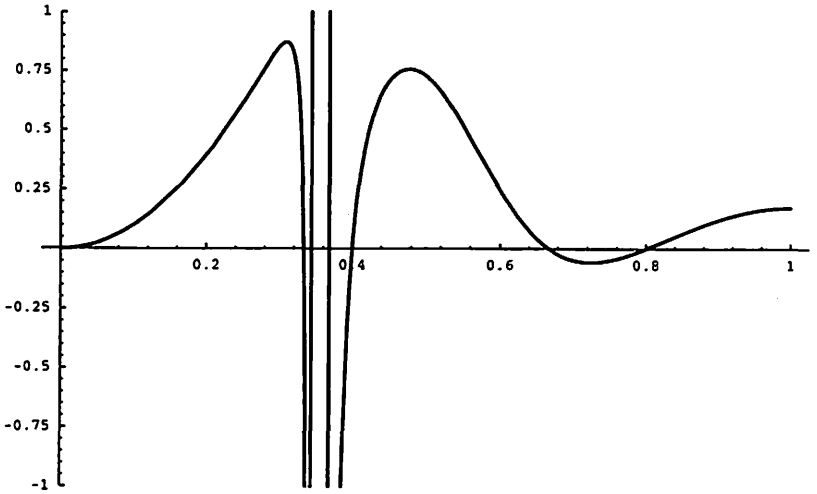

Fig. 6 Periodicity curve of Quinlan & Tremaine's 10th-order explicit method

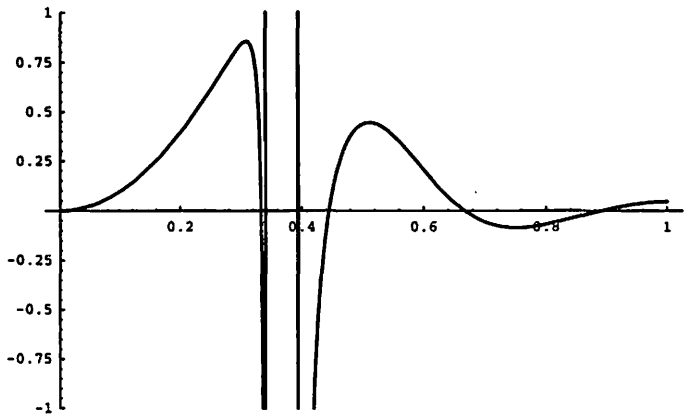

Fig. 7a Periodicity curve of Quinlan & Tremaine's 12th-order explicit method

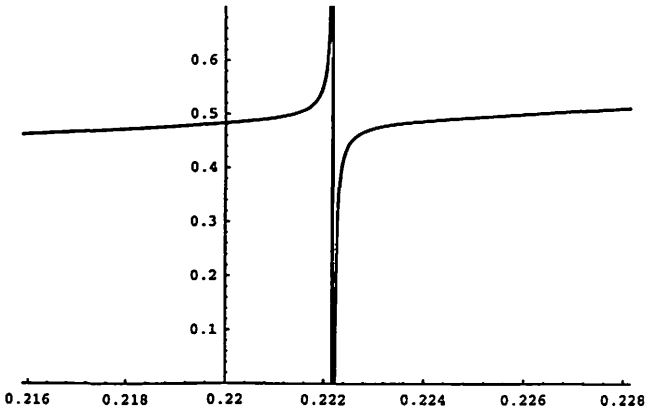

Fig. 7b Periodicity curve of Quinlan & Tremaine's 12th-order explicit method: close

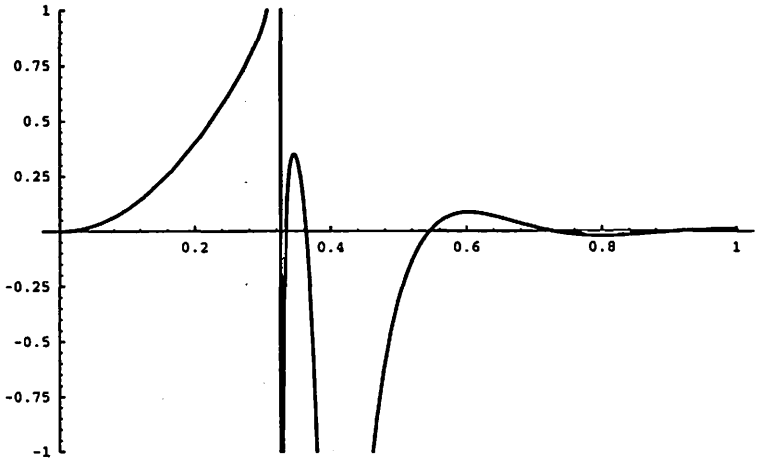

Fig. 8a Periodicity curve of Quinlan & Tremaine's 14th-order explicit method

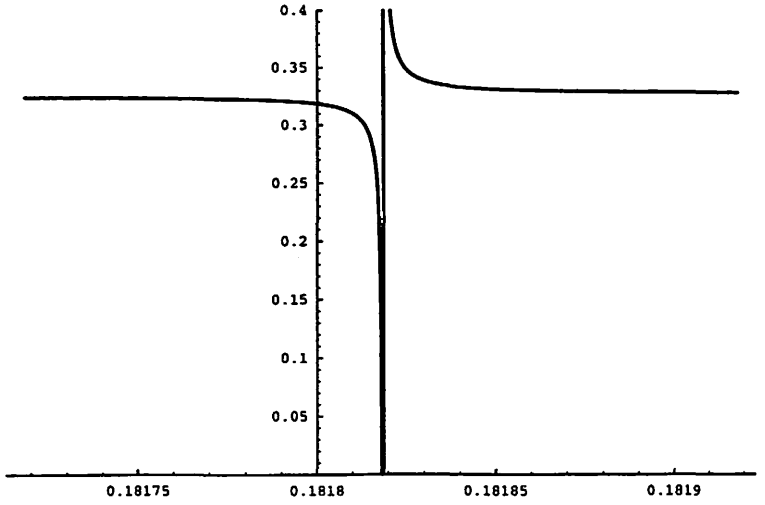

Fig. 8b Periodicity curve of Quinlan & Tremaine's 14th-order explicit method: close

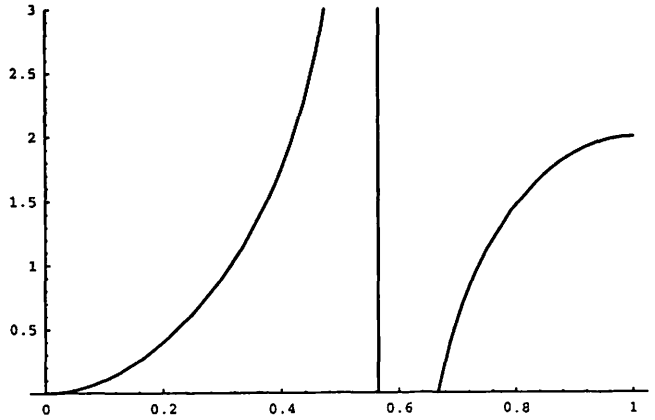

Fig. 9 Periodicity curve of recommended 6th-order explicit method

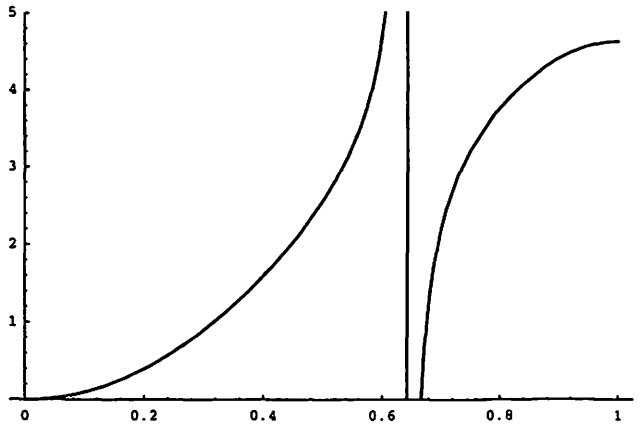

Fig. 10 Periodicity curve of recommended 8th-order implicit method

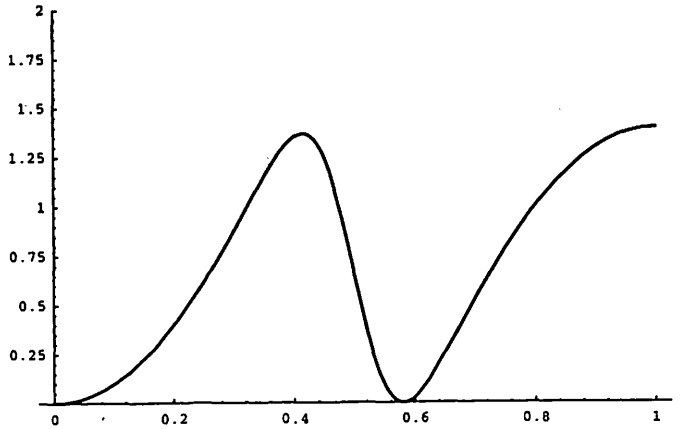

Fig. 11 Periodicity curve of recommended 8th-order explicit method

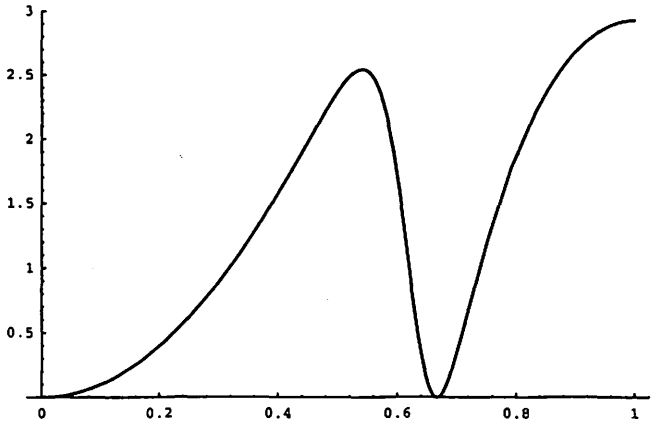

Fig. 12 Periodicity curve of recommended 10th-order implicit method

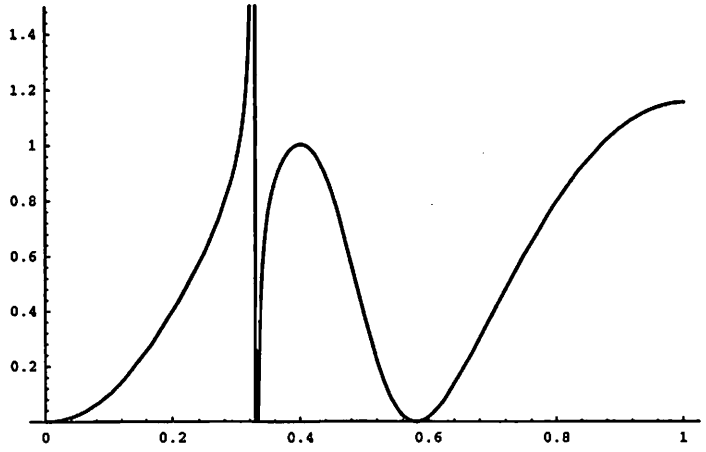

Fig. 13 Periodicity curve of recommended 8th-order explicit method

8

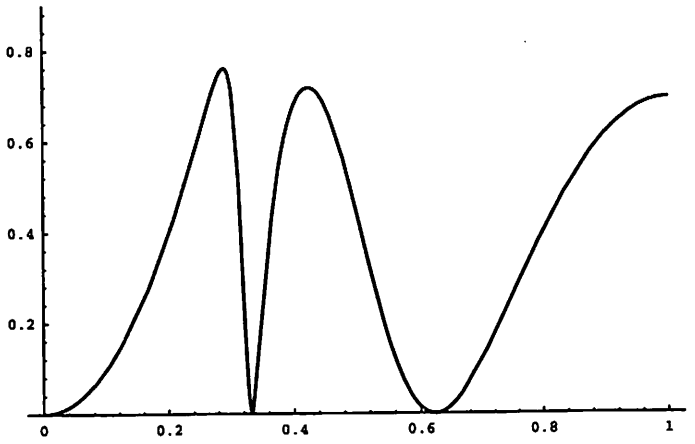

Fig. 15 Periodicity curve of recommended 10th-order explicit method

10

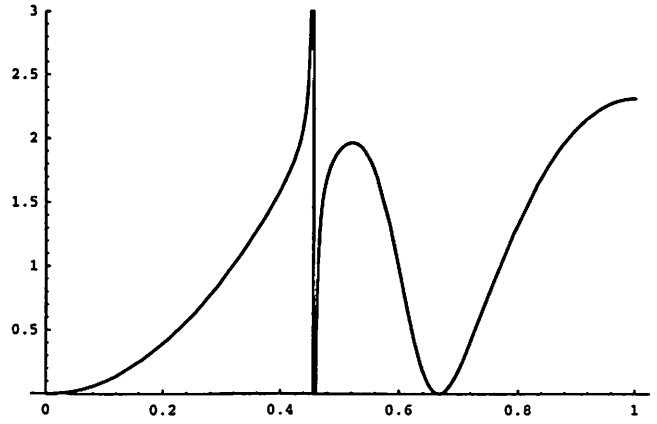

Fig. 14 Periodicity curve of recommended 10th-order implicit method

10

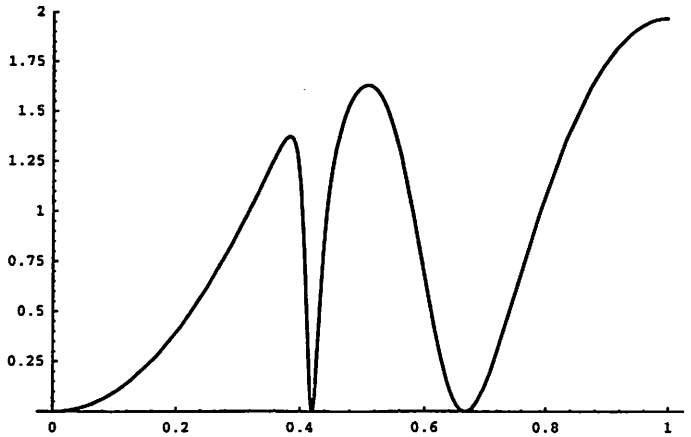

Fig. 16 Periodicity curve of recommended 12th-order implicit method

12

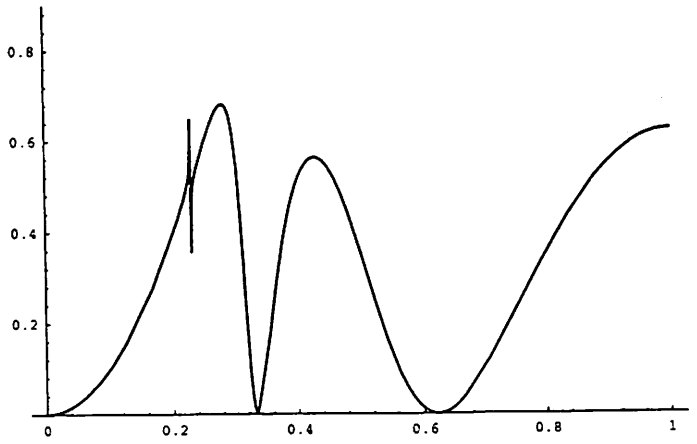

Fig. 17 Periodicity curve of recommended 12th-order explicit method

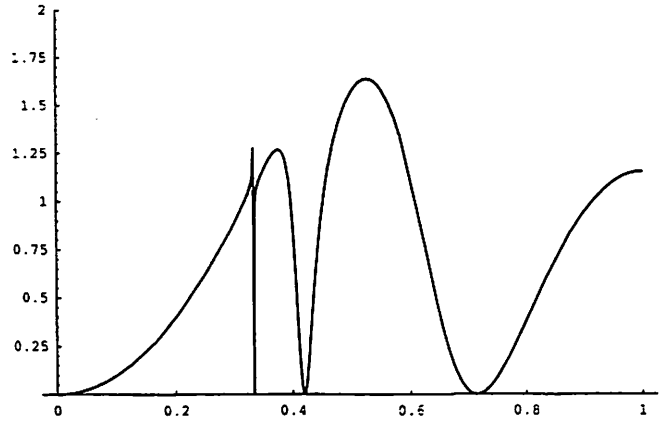

Fig. 18 Periodicity curve of recommended 14th-order implicit method

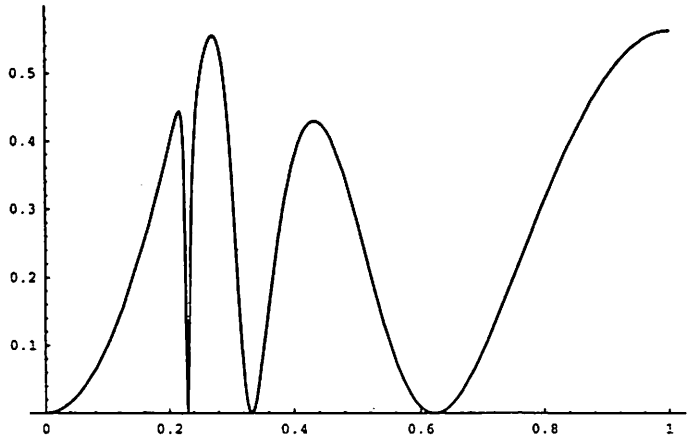

Fig. 19 Periodicity curve of recommended 14th-order explicit method

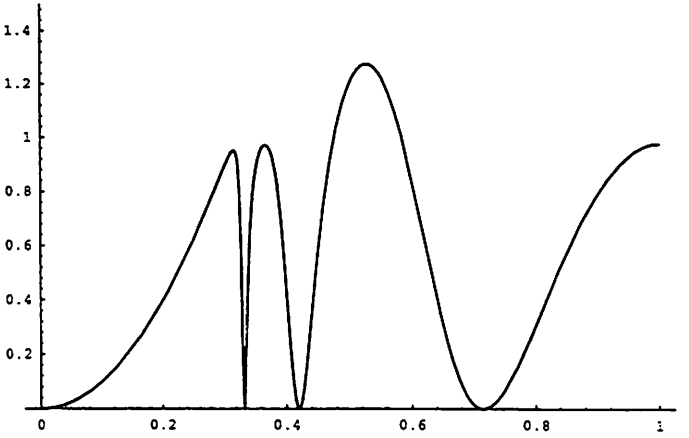

Fig. 20 Periodicity curve of recommended 16th-order implicit method

NEW TIME-SYMMETRIC INTEGRATORS FOR PLANETARY DYNAMICS

Eiichiro Kokubo and Junichiro Makino

Department of Systems Science, Graduate School of Arts and Sciences, University of Tokyo

Abstract

We describe new time-symmetric integrators specialized for long-term integration of planetary orbits. Our new time-symmetric integrators have no secular errors in the semimajor axis and the eccentricity for the integration of two-body Kepler problems as usual time-symmetric and symplectic integrators. Usual time-symmetric or symplectic integrators, however, show a secular drift in the argument of pericenter. Our new family of integrators has one free parameter, which we can adjust to eliminate the leading error in the argument of pericenter without breaking the time-symmetry or changing the order of the integrator.

1 Introduction

Time-symmetric (e.g., Quinlan and Tremaine 1990, Calvo and Sanz-Serna 1994) and symplectic (e.g., Kinoshita, Yoshida, and Nakai 1991, Saha and Tremaine 1992) integrators have recently been used for the study of the long-term stability of planetary orbits. Both integrators have a desirable property that they have no secular errors in the semimajor axis a and the eccentricity e when Keplerian orbit is integrated with a constant timestep, while widely used high-order multi-step integrators, such as the Störmer-Cowell integrator, show secular errors. On the other hand, there are linear errors in the argument of pericenter ω and the time of pericenter passage T for the time-symmetric and the symplectic integrators, while the high-order multi-step integrators show quadratic errors in the time of pericenter passage.

In the field of the structure engineering, numerical integration methods for the dynamic vibration equation (second-order linear differential equation) has been investigated in detail (e.g., Wood 1990). The Newmark method (Newmark 1959) is the most popular integrator for the dynamic vibration equation. It is a family of second-order one-step integrators that has two parameters, which includes the leapfrog (Verlet) scheme and the trapezoidal formula as special cases. It is known that by choosing appropriate parameters, we can remove the error in the phase of the vibration.

In the present paper, we apply this concept of the Newmark method to Kepler problems. Our purpose is to remove or reduce the errors of the angle orbital elements. We focus on the error of the argument of pericenter.

2 α Hermite Integrator

We apply the concept of the Newmark method to the implicit Hermite scheme (Kokubo *et al.* 1998), a fourth-order time-symmetric scheme (for the details of the Newmark method, see e.g., Wood 1990).

The Hermite integrator is based on the Taylor series up to the order of the third time derivative of the acceleration $\boldsymbol{a}_0^{(3)}$, given by

$$\boldsymbol{x}_1 = \boldsymbol{x}_0 + \boldsymbol{v}_0\Delta t + \frac{\boldsymbol{a}_0}{2}\Delta t^2 + \frac{\dot{\boldsymbol{a}}_0}{6}\Delta t^3 + \frac{\boldsymbol{a}_0^{(2)}}{24}\Delta t^4 + \alpha\frac{\boldsymbol{a}_0^{(3)}}{120}\Delta t^5, \tag{1}$$

$$\boldsymbol{v}_1 = \boldsymbol{v}_0 + \boldsymbol{a}_0\Delta t + \frac{\dot{\boldsymbol{a}}_0}{2}\Delta t^2 + \frac{\boldsymbol{a}_0^{(2)}}{6}\Delta t^3 + \frac{\boldsymbol{a}_0^{(3)}}{24}\Delta t^4, \tag{2}$$

where $\boldsymbol{x}$, $\boldsymbol{v}$, $\boldsymbol{a}$, and $\dot{\boldsymbol{a}}$ are the position, the velocity, the acceleration, and the time derivative of the acceleration, respectively. The subscripts 0 and 1 indicate time and Δt is the timestep. The higher derivatives of the acceleration $\boldsymbol{a}_0^{(2)}$ and $\boldsymbol{a}_0^{(3)}$ are obtained by the 3rd-order Hermite interpolation constructed from $\boldsymbol{a}$ and $\dot{\boldsymbol{a}}$ at time t_0 and t_1 as

$$\boldsymbol{a}_0^{(2)} = \frac{-6(\boldsymbol{a}_0 - \boldsymbol{a}_1) - \Delta t(4\dot{\boldsymbol{a}}_0 + 2\dot{\boldsymbol{a}}_1)}{\Delta t^2}, \tag{3}$$

$$\boldsymbol{a}_0^{(3)} = \frac{12(\boldsymbol{a}_0 - \boldsymbol{a}_1) + 6\Delta t(\dot{\boldsymbol{a}}_0 + \dot{\boldsymbol{a}}_1)}{\Delta t^3}. \tag{4}$$

In Eq. (1), we introduced a new parameter α to control integration errors, which corresponds to the Newmark parameter of the Newmark method. The order of the accuracy of the scheme is determined by the $O(\Delta t^5)$ term of the local truncation error of the velocity. We can, therefore, change the weight of the $O(\Delta t^5)$ term of the position without changing the order of the accuracy.

From Eqs. (1) through (4), the Hermite integrator can be rewritten in an implicit form as

$$\boldsymbol{x}_1 = \boldsymbol{x}_0 + \frac{1}{2}(\boldsymbol{v}_1 + \boldsymbol{v}_0)\Delta t - \frac{\alpha}{10}(\boldsymbol{a}_1 - \boldsymbol{a}_0)\Delta t^2 + \frac{6\alpha - 5}{120}(\dot{\boldsymbol{a}}_1 + \dot{\boldsymbol{a}}_0)\Delta t^3, \tag{5}$$

$$\boldsymbol{v}_1 = \boldsymbol{v}_0 + \frac{1}{2}(\boldsymbol{a}_1 + \boldsymbol{a}_0)\Delta t - \frac{1}{12}(\dot{\boldsymbol{a}}_1 - \dot{\boldsymbol{a}}_0)\Delta t^2. \tag{6}$$

It is clear in this formula that the Hermite integrator is time-symmetric, in other words, the physical values with subscripts 0 and 1 are used symmetrically and changing the value of α does not break the time-symmetry of the integrator. Note that the scheme with $\alpha = 1$ corresponds to the Hermite scheme of Makino and Aarseth (1992) and $\alpha = 5/6$ that of Hut *et al.* (1995).

We determine α so that the leading term of the local truncation error of the argument of pericenter vanishes. The leading terms of the local truncation errors of the implicit Hermite scheme are given by

$$\Delta\boldsymbol{x} = \frac{\alpha - 1}{120}\boldsymbol{a}_0^{(3)}\Delta t^5, \tag{7}$$

$$\Delta\boldsymbol{v} = -\frac{1}{720}\boldsymbol{a}_0^{(4)}\Delta t^5. \tag{8}$$

As the eccentricity has no secular error for time-symmetric integrators, it is sufficient to evaluate the error of one component of the eccentricity vector. Here we take the y-component of the eccentricity vector $e_y = e\sin\omega$ which is given by

$$e_y = -v_x(xv_y - yv_x) - \frac{y}{r}, \tag{9}$$

where $r = (x^2 + y^2)^{1/2}$. The leading term of the local truncation error of e_y is given by

$$\Delta e_y = \frac{\partial e_y}{\partial x}\Delta x + \frac{\partial e_y}{\partial y}\Delta y + \frac{\partial e_y}{\partial v_x}\Delta v_x + \frac{\partial e_y}{\partial v_y}\Delta v_y. \tag{10}$$

The symmetry of the Kepler orbit requires that $\Delta\omega$ should cancel out in half an orbital period. Thus, we obtain the following linear equation for α:

$$\int_0^{\frac{T_K}{2}} \Delta e_y dt = \frac{\Delta t^5}{120}\int_0^{\frac{T_K}{2}} \left[(\alpha-1)\left(\frac{\partial e_y}{\partial x}a_x^{(3)} + \frac{\partial e_y}{\partial y}a_y^{(3)}\right) - \frac{1}{6}\left(\frac{\partial e_y}{\partial v_x}a_x^{(4)} + \frac{\partial e_y}{\partial v_y}a_y^{(4)}\right)\right] dt = 0, \tag{11}$$

where T_K is the Kepler period. We see in Eq. (11) that α is independent of Δt. Eq. (11) leads to

$$\alpha = 1 + \frac{1}{6}\frac{\int_0^{\frac{T_K}{2}} \left(\frac{\partial e_y}{\partial v_x}a_x^{(4)} + \frac{\partial e_y}{\partial v_y}a_y^{(4)}\right) dt}{\int_0^{\frac{T_K}{2}} \left(\frac{\partial e_y}{\partial x}a_x^{(3)} + \frac{\partial e_y}{\partial y}a_y^{(3)}\right) dt} = \frac{7}{6}, \tag{12}$$

where we substituted the Kepler solutions.

Figure 1 shows the error in the osculating orbital elements for the two-body Kepler problem solved by the implicit Hermite scheme with $\alpha = 5/6, 1, 7/6$ for 10 orbital periods (20π time units). The initial orbital elements are $a = 1$, $e = 0.1$, $\omega = \pi$, and $T = \pi$. The orbit is integrated with a constant timestep $\Delta t = 2^{-5}$. No schemes have secular errors in a and e. The error in ω is drastically reduced for the scheme with $\alpha = 7/6$. In this scale, the scheme with $\alpha = 7/6$ shows no secular error in ω and T, either. There is, however, a small linear error in ω, which is due to higher order errors of ω that do not cancel out in half an orbit with $\alpha = 7/6$ because α is determined so that the leading error term of ω vanishes. The dependence of $\Delta\omega$ per orbit on Δt is shown in Fig. 2 for $\alpha = 5/6, 1, 7/6$. The initial conditions are the same as those for Fig. 1. It is clear that $|\Delta\omega|$ for $\alpha = 7/6$ is $O(\Delta t^6)$, while $|\Delta\omega|$ for other α is $O(\Delta t^4)$. This means that not only the $O(\Delta t^5)$ term of the local truncation error but also the $O(\Delta t^6)$ term vanishes for $\alpha = 7/6$ (the global error is one order lower than the local truncation error since the number of steps for a period is inversely proportional to Δt). This behavior is quite natural. As discussed by Cano and Sanz-Serna (1997), for any symmetric scheme, the coefficient of the local error is exactly zero for even orders. Thus, if the $O(\Delta t^5)$ term vanishes, the next term is $O(\Delta t^7)$. We also show the same plots for the 4th-order symplectic integrator (e.g., Kinoshita, Yoshida, and Nakai 1990) for comparison. The error $|\Delta\omega|$ for the symplectic integrator is $10^{4\text{-}5}$ times larger than that for the Hermite scheme with $\alpha = 7/6$.

We presented the fourth-order scheme. It is, however, straightforward to apply our method to one-step higher-order time-symmetric integrators.

3 Application to Three-Body Problem

The fact that our scheme with $\alpha = 7/6$ gives very high accuracy for pure Kepler problems does not necessarily guarantee that it gives good results for systems with more than one planet. In order to test our scheme, we integrate a planar Jupiter-Saturn like system for 300,000 years. The masses and the initial orbital elements of the two planets are $M_1 = 2 \times 10^{30}$g, $a_1 = 5$AU, $e_1 = 0.05$ $\omega_1 = \pi/2$, $T_1 = 0$ and $M_2 = 5 \times 10^{29}$g, $a_2 = 10$AU, $e_2 = 0.05$, $\omega_2 = 3\pi/2$, $T_2 = 0$. The evolution of the eccentricity vector $(e\cos\omega, e\sin\omega)$ averaged over 500 years is plotted in Fig. 3. As the reference, the result obtained by the standard $\alpha = 1$ scheme with the timestep $\Delta t = 0.125$ (562 steps per T_K for planet 1) is plotted. The results for the implicit Hermite scheme with $\alpha = 1$ and $7/6$ and the 4th-order symplectic integrator with $\Delta t = 1$ are plotted. Though the timesteps are different by a factor of 8, the reference result and the result for $\alpha = 7/6$ are indistinguishable. Their difference in ω after 300,000 years is about 0.00041. On the other hand, the difference in ω between the reference result and the result for $\alpha = 1$ is about 0.15. The drift in ω is faster than that of the reference result by about 3%, which is due to the integration error. It is shown that the good property of the $\alpha = 7/6$ scheme is retained even when it is used for this kind of three-body problem. The result for the symplectic integrator shows a completely different pattern. In particular, the eccentricity vector rotates in the opposite direction of the results for the implicit Hermite scheme.

4 Summary

We developed new time-symmetric integrators specialized for planetary dynamics. The new time-symmetric integrators have no secular errors in the semimajor axis and the eccentricity. The new time-symmetric schemes have one free parameter, α, which we can adjust to reduce the error of the argument of pericenter drastically without breaking the time-symmetry and changing the order of accuracy. The free parameter α is the coefficient of the highest order term of the position that is one order higher than that of the velocity. The error order of ω becomes two-order higher for a unique value of α. These values of α are independent of orbital elements or the size of timestep.

It is possible to adjust α to reduce the error in the time of pericenter passage. However, in this case, the optimal values depend on the eccentricity. It is also possible to choose α so that the secular error in ω becomes exactly zero for a given timestep and eccentricity. This value is slightly different from the value for which the leading term of the error vanishes and depends on the eccentricity and the size of the timestep.

References

Calvo M. P., Sanz-Serna J. M., 1994, preprint

Cano B., Sanz-Serna J. M., 1997, SIAM J. Num. Anal., 34, 1391

Hut P., Makino J., McMillan S., 1995, ApJL, 443, 93

Kinoshita H., Yoshida H., Nakai H., 1991, Celest. Mech. Dyn. Astron., 50, 59

Kokubo E., Yoshinaga K., Makino J., 1998, MNRAS in press

Makino J., Aarseth S. J., 1992, PASJ, 44, 141

Newmark N. M., 1959, in Proceedings of ASCE, Journal of Engineering Mechanics (EM3), 85, 67

Quinlan G. D., Tremaine S., 1990, AJ, 100, 1694

Saha P., Tremaine S., 1992, AJ, 104, 4

Wood W. L., 1990, Practical Time-stepping Schemes (Clarendon, Oxford)

Figure Captions

Fig. 1 The errors of orbital elements a, e, ω, and T from top to bottom for the the implicit Hermite scheme with $\alpha = 5/6$ (dashed curve), $\alpha = 1$ (dotted curve), and $\alpha = 7/6$ (solid curve) against time for 10 orbital periods. The Kepler period is 2π.

Fig. 2 The error in the argument of pericenter $\Delta\omega$ per orbit is plotted against the timestep for $\alpha = 5/6$ (triangles), $\alpha = 1$ (squares), and $\alpha = 7/6$ (circles). The result for the 4th-order symplectic integrator is also plotted (crosses).

Fig. 3 Time evolution of the eccentricity vector of planet 1 for 300,000 years. The eccentricity vector is averaged over 500 years. A three-body system is integrated by the $\alpha = 1$ (dashed curve) and the $\alpha = 7/6$ (solid curve) schemes with the timestep $\Delta t = 1$. As the reference, the result obtained by the $\alpha = 1$ scheme with $\Delta t = 0.125$ (solid curve) is shown. The result for the 4th-order symplectic integrator with $\Delta t = 1$ is also plotted (dotted curve).

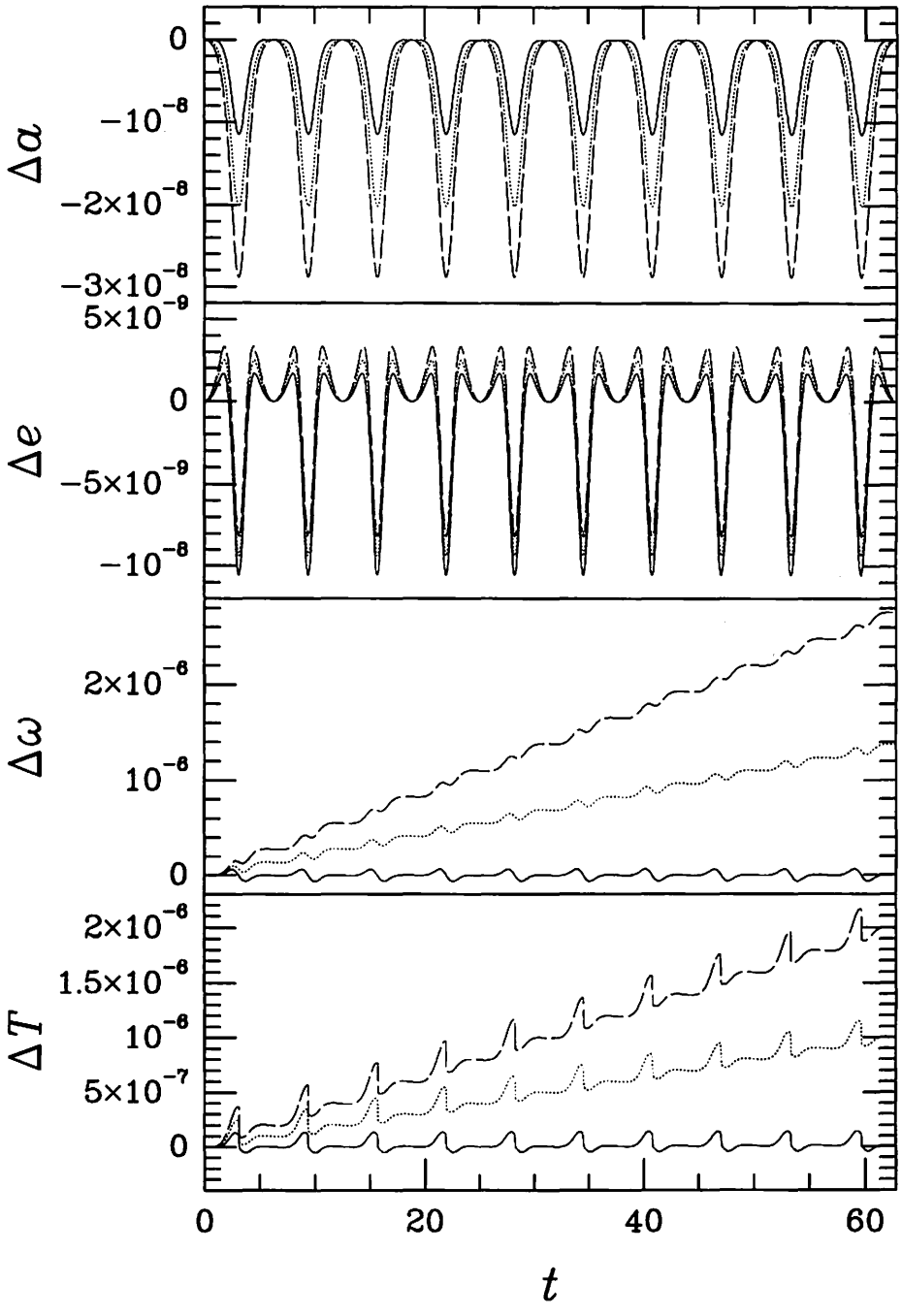
0
-10^{-6}
-2×10^{-6}
-3×10^{-6}
Δa
5×10^{-9}
0
-5×10^{-9}
-10^{-6}
Δe
2×10^{-6}
10^{-6}
0
$\Delta\omega$
2×10^{-6}
1.5×10^{-6}
10^{-6}
5×10^{-7}
0
ΔT
0
20
40
60
t

Fig. 1

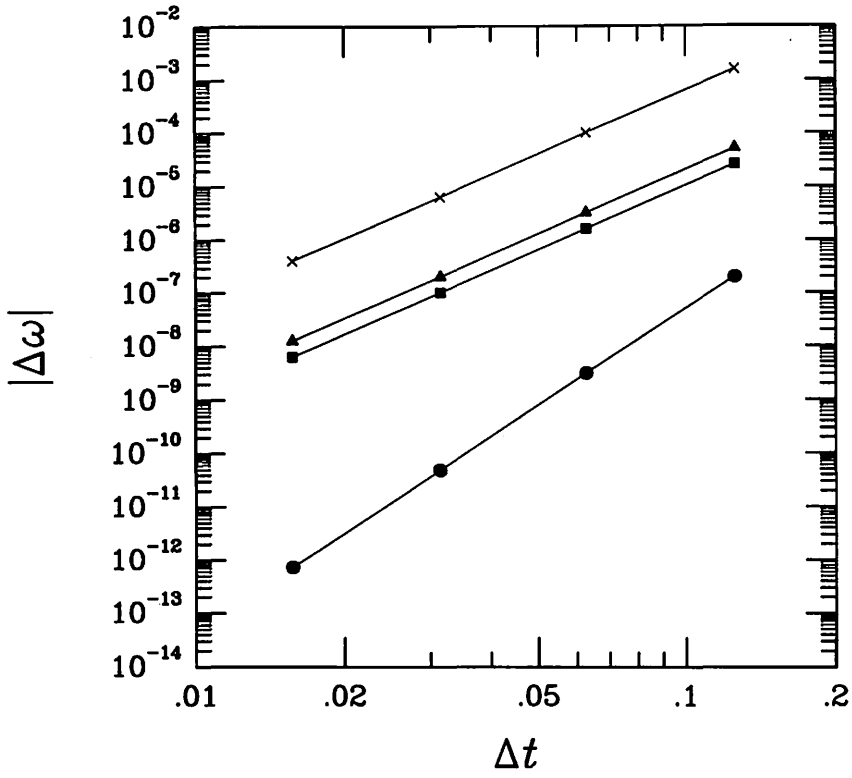
10^{-2}
10^{-3}
10^{-4}
10^{-5}
10^{-6}
10^{-7}
10^{-8}
10^{-9}
10^{-10}
10^{-11}
10^{-12}
10^{-13}
10^{-14}
.01
.02
.05
.1
.2
$|\Delta\omega|$
Δt

Fig. 2

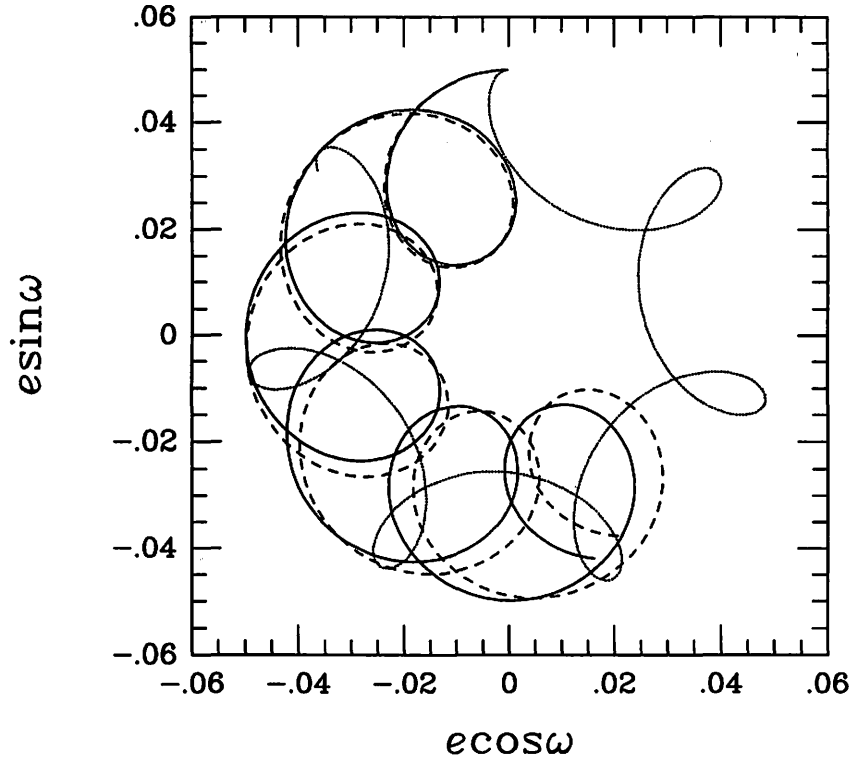
.06
.04
.02
0
−.02
−.04
−.06
−.06
−.04
−.02
0
.02
.04
.06
$e\sin\omega$
$e\cos\omega$

Fig. 3

Improved MVSI and its Application to Dynamics in the Solar System

Tetsuharu Fuse*,
Hiroshi, Kinoshita** and Hiroshi, Nakai**
*Department of Astronomical Science, Graduate University for Advanced Studies, Mitaka, Tokyo 181-8588
** National Astronomical Observatory, Mitaka, Tokyo 181-8588
* E-mail tetsu@pluto.mtk.nao.ac.jp

Abstract

Mixed Variable Symplectic Integrator (MVSI) is one of useful integrator for study of dynamics in the solar system. We adapted the integrator for the dynamics in the outer solar system. In this paper, we report two tests with the new integrator.

1 EKBOs

1992 年夏に発見された 1992 QB1 を筆頭に，太陽系外縁部には現在までにおよそ 60 個の Edgeworth-Kuiper Belt 天体 (EKBOs) が発見されている (布施 他 1998)。これら EKBOs は，惑星になり切れなかった微惑星の生き残りであると考えれている。現在発見されているほとんどの EKBOs は，軌道長半径が 40 - 50 AU，離心率が ~0 程度であり，また海王星と平均運動共鳴にあるものも多いことが特徴である。

これらの力学的な議論は，Nakai & Kinoshita (1997) など現在までに多数あり，いずれの計算も，大規模な数値計算が行なわれている。最近になり，今までの EKBOs とは軌道に関する特徴が異なる '新種の EKBOs (1996TL66[1])' が発見されるなど，太陽系外縁部の力学については話題が豊富である。つまり，今後も長期間の大規模計算を行なう必要性が十分にあることは明らかである。

2 MVSI & MVSI_t

Mixed Variable Symplectic Integrator (MVSI) は，特に太陽系内の天体の長期間の数値積分に適したアルゴリズムである (Ito *et al.* 1996)。MVSI は，2 体問題の間の力と他の惑星による摂動力の比が，十分小さいということから刻み幅が大きく取れ，高速な計算を実現している。

しかし Section 1 で見た EKBOs のような公転周期が惑星に比べて長い天体を数値積分する場合に，全天体に共通の固定刻み幅を用いる MVSI では，計算速度を

[1] a = 84AU, e=0.6, i=23 度

より速くすることはできない。これを克服するために，Duncan & Levison (1994), Duncan *et al.* (1995) では，Regularized MVSI (RMVSI) という改良した MVSI を用いて計算を行っている。この RMVSI は，天体ごとに異なる刻み幅を指定でき，また天体と惑星が接近した場合には，座標原点を変えることで，close approach をも回避している。しかし一方で，惑星による摂動が他の積分法などと比べて，大きく現れているという指摘がある (Tancredi 1996)。

そこで，あらかじめ外惑星 (木星・土星・天王星・海王星) の位置については計算・ファイル化をしておき，小天体 (質量 = 0) の摂動計算をする際に，ファイルから呼び出すという MVSI を開発した (MVSI_t と呼ぶ)。この方法は，惑星よりも公転周期が長い天体については，数値積分の刻み幅を大きく取れることを活用する。具体的には，惑星の計算を適当な小さい刻み幅で行い，小天体を計算するときのより長い刻み幅に合わせて，惑星の位置をファイル出力し，小天体の計算の際にファイルから惑星の位置をもってくる，というものである。つまり，惑星と周期が同程度の天体では効果がない。このアルゴリズムでは，ハミルトニアン F の中に陰に時刻 t が入ってくる。t に共役な運動量を T とすると，2 次の MVSI_t の流れ図は，下の (1) - (5) のようになるが，実際のコードは MVSI と差はほとんどない。

また MVS_t では，ファイルへのアクセス回数を減らし計算を高速化するために，惑星の位置データを一行に複数 step 分格納する機能 (Spooling と呼ぶ) を備えている。しかし次の節に示すテスト計算では，一行に 1 step 分を格納するモードにしている。

$$
\begin{aligned}
F(q,p,t) &= K(p)+U(q,t) \\
\\
\rightarrow H &= F(q,p,t)+T \\
&= K(p)+T+U(q,t) \\
&= K^{*}(p,T)+U(q,t) \\
\\
q_1' &= q_0+\frac{1}{2}\tau\frac{\partial K^{*}}{\partial p}(p_0,T_0)=q_0+\frac{1}{2}\tau\frac{\partial K}{\partial p}(p_0) && (1)\\
t_1 &= t_0+\frac{1}{2}\tau\frac{\partial K^{*}}{\partial T}(p_0,T_0)=t_0+\frac{1}{2}\tau && (2)\\
p_1 &= p_0-\tau\frac{\partial U}{\partial p}(q_1',t_1) \quad \leftarrow \text{時刻 } t_1 \text{ における惑星の位置を呼び出す} && (3)\\
\left(T_1\right. &= \left. T_0-\tau\frac{\partial U}{\partial p}(q_1',t_1)\right) \quad ;\text{計算する必要なし} \\
q_1 &= q_1'+\frac{1}{2}\tau\frac{\partial K}{\partial p}(p_1) && (4)\\
t_2 &= t_1+\frac{1}{2}\tau\ (=t_0+\tau) && (5)
\end{aligned}
$$

3 Application

Section 2 で見たように，MVSI_t の利点を見るためには，惑星よりも長い周期を持つ天体を計算する必要があるが，ここではテストとして，以下の興味深い 2 つの問題を扱う。いずれも惑星と同程度の周期をもつ天体であるため，MVSI_t の正しい評価は得られていない。

3.1 外惑星のラグランジュポイント

Holman & Wisdom (1993) らは，木星・土星・天王星・海王星のそれぞれのラグランジュポイントの周りに，多くのテスト天体 (質量 = 0) をおき，MVSI によりそれらの生き残る期間を計算している。テスト天体の初期値は，

$$
\begin{aligned}
e, i, \Omega, l &= \text{惑星と同じ値} \\
\omega &= 0 - 360 \text{ 度，5 度おき} \\
a &= \text{惑星の軌道長半径} \times \alpha, \ (0.96 \leq \alpha \leq 1.04;\ 0.01 \text{ おき})
\end{aligned}
$$

とした。

土星のラグランジュポイントの周りにおいたテスト天体の中で，最長の計算期間である 2000 万年間生き残った天体の初期値について，横軸に土星から計ったテスト天体の近点の経度，縦軸に上式の α をとる。すると，生き残った天体の初期値は，中の抜けた円の形をしている。他の外惑星については，このようなことはない。

そこで，各惑星のラグランジュポイント付近に，およそ 700 個のテスト天体 (質量 = 0) をおき，MVSI_t による計算を行った。刻み幅は，木星～海王星の惑星の位置を計算するとき，テスト天体の計算をするときのいずれも 300 日とした。惑星のデータファイルは，およそ 1GB である。また，テスト天体の離心率 e が 1 以上になるか，または各惑星の作用圏内に入ったテスト天体は，計算から除いていく。図 1 に 2000 万年間生き延びたテスト天体について，横軸に土星からの経度，縦軸に α のそれぞれ初期値を • で示す (図中の | 印は，全初期値空間を示す)。図 1 より，Holman & Wisdos (1993) と同様な結果が得られた。なぜ土星のみ生き残ったテスト天体の初期値がこのような形になるか，という詳しい議論は Holman & Wisdom (1993) でも行われておらず，今後の課題としたい。

3.2 天王星と海王星の間の小天体

Holman (1997) は，数千個のテスト天体 (質量 = 0) を天王星と海王星の間におき，45 億年間の数値計算を行った。その結果，0.05 % のテスト天体は 45 億年生き延びた。このことから，天王星と海王星の間には，安定な領域があり，そこに小惑星帯と同じような小天体の ' 集団' が存在しているであろうと示唆している。

そこで，MVSI_t により，およそ 1000 個のテスト天体 (質量 = 0) を以下のような初期条件で天王星と海王星の間におき，約 2.4 億年間計算を行った:

$$
a = 24 - 27\text{AU},\ 0.05\text{AU おき}
$$

$$
\begin{aligned}
e &= 0.00 \textit{ or } 0.01 \\
i &= 0.00 \textit{ or } 1.00 \text{ 度} \\
\omega &= \Omega = 0 \text{ 度} \\
l &= 0 - 324 \text{ 度, } 36 \text{ 度おき}
\end{aligned}
$$

刻み幅は，木星～海王星の惑星の位置計算には 300 日，小天体の計算では 1500 日とした。惑星のデータファイルは，およそ 2.4 GB である。図 2 は，横軸は初期値の軌道長半径，縦軸に生き残った期間を示している。図 2 から，およそ 7.6 % の天体が 2.4 億年生き延びた。データファイルの容量の関係から，これ以上の計算は行っていないが，Holman (1997) と同じように，天王星と海王星に安定な領域が存在していることを支持する結果となった。

4 まとめ

MVSI_t のテスト計算を行った。MVSI_t は，惑星の位置をあらかじめ計算しファイル化しておくことで，惑星よりも公転周期の長い天体の計算に向いている。今回行ったテスト計算は，いずれも惑星と同程度の距離にある小天体の計算であるため，MVSI_t の評価を正しくは行っていない。一方，ファイル化によるデータの容量についても，注意が必要である。今回のテスト計算では，数 GB のデータファイルであるが，長期間の計算を行うためには，より多くのデータ容量が必要となる。MVSI_t については，データ容量，計算期間，計算速度 (Spooling) などの面から，検討をしていく必要があるであろう。

References

Holman,M.J. and Wisdom,J., *Astron.J* **105**, 1987, 1993.

Holman,M.J., *Nature* **387**, 785, 1997.

Ito, T., Kinoshita, H., Nakai, H. and Fukushima, T., 第 *28* 回天体力学研究会集録, 123, 1996.

Levison,H.F. and Duncan,M.J., *Icarus* **108**, 18, 1994.

Nakai,H. and Kinoshita,H., 第 *29* 回天体力学研究会集録, 279, 1997.

Tancredi,T., *private communication*, 1997.

布施, 渡部, 関口, 天文月報 **91**, No.5, 1998.

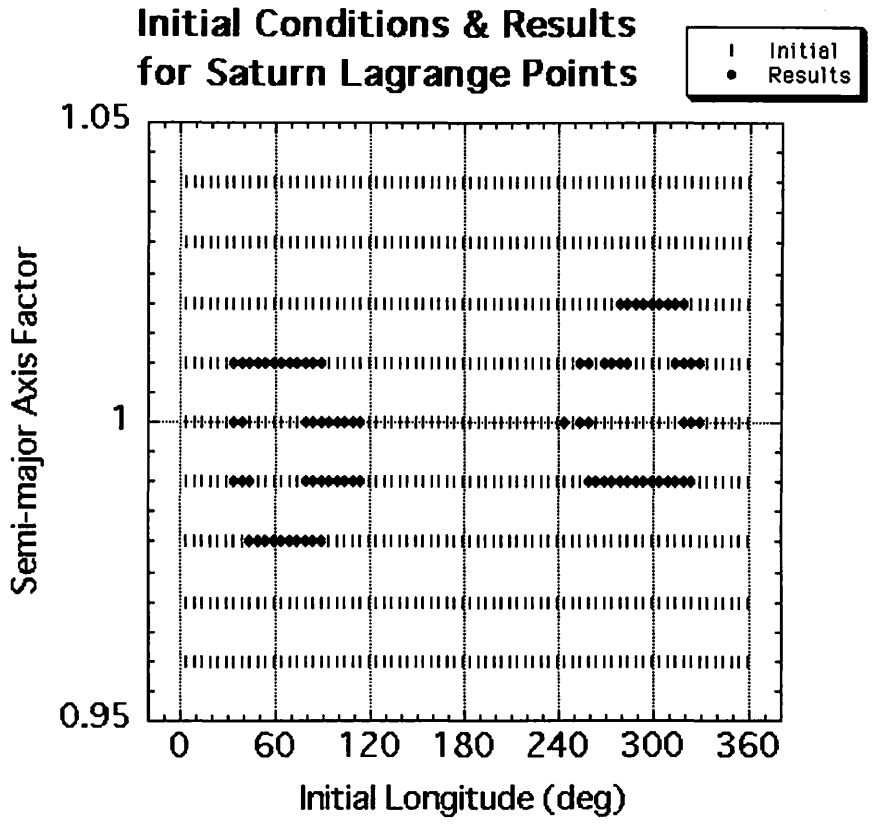

Figure 1: The initial conditions of the test particles survived for 20 Myrs.

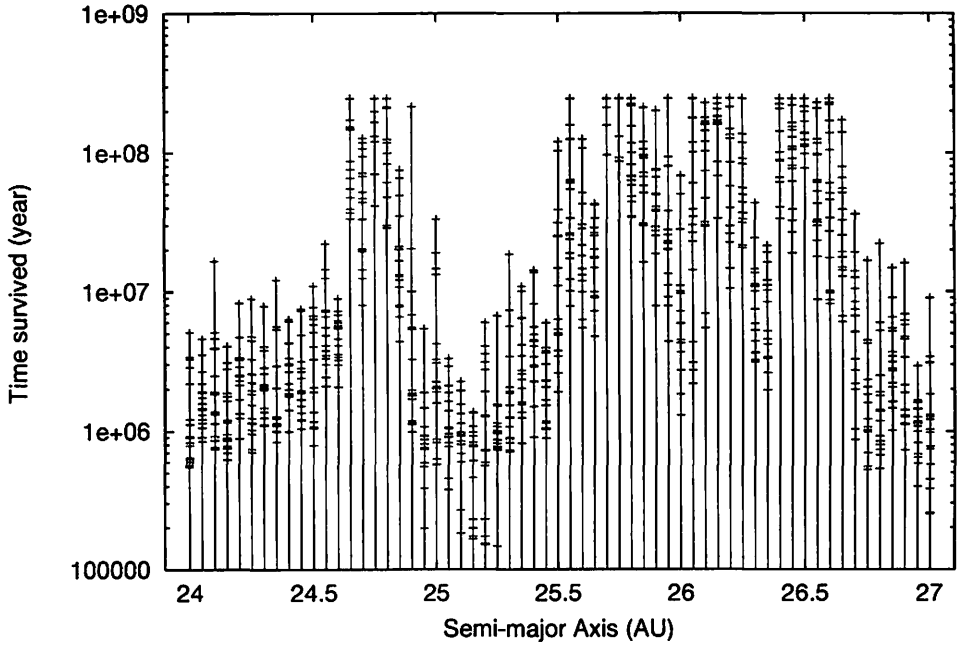

Figure 3: The time survived of the test particles between Uranus and Neptune.

非可積分系のシンプレクティック積分:
ステップサイズ零への極限近傍に見る
複雑なステップサイズ依存性

Symplectic Integrations of Non-integrable Systems:
Complex Step-Size Dependences in the $\Delta t \to 0$ Limit

梅野 健 (理化学研究所)※
Ken Umeno (RIKEN)☆

1998年3月4日

第30回天体力学研究会 (葉山、総研大)

[Abstract]
Various higher-order symplectic integrators are used to track a non-integrable system $H=\frac{1}{2}(p_1^2+p_2^2+q_1^2q_2^2)$. Complex step-size dependences were observed in such a simple two-body dynamics.

[講演要旨]
非可積分系である $H=\frac{1}{2}(p_1^2+p_2^2+q_1^2q_2^2)$ について初期値を $(q_1,q_2,p_1,p_2)=(1000,0.002,0,0)$ に固定してシンプレクティック数値積分した。ここで使ったシンプレクティック法は、3次(Ruthの方法[1]、鈴木の方法[2])と2次のLeap Flog法である。その際時間ステップ幅 Δt に対する時刻 $t=1000$ ($\frac{1000}{\Delta t}$ ステップ)の時の q_2 $(t=1000)$ をプロットしたのが図1~図5である。図1よりかなりの Δt のレンジ ($0.0002 \leq t \leq 0.001$) で Δt に対する q_2 の変動幅が、Δt を小さくするとともに大きくなるという一見予想する様な振る舞いが見られた。この現象はRuth ⟷ Suzuki という同一次数内でのIntegratorの種類にも依存しなかった。(図1,図2参照)。また計算の精度に依存するかどうかを調べるため、倍精度と4倍精度とを比較したが大差はなかった。(図3,図4参照)。図5は2次のLeap Flog法での計算であるが、図2に見られる3次の時の q_2 の収束先と同じ所に近づいているのが見える。この様に、ここで報告した現象はシンプレクティック積分法の種類、次数又計算精度にも依存しないことがわかった。今後多体の系でも同様なことが起きるのか調べてゆきたい。

[参考文献]
1) R.D. Ruth, IEEE Trans. Nucl. Sci NS-30 (1983), 2669.
2) M. Suzuki, J. Phys. Soc. Jpn. 61 (1992) 3015.
3) K. Umeno and M. Suzuki, Phys. Lett. A 181 (1993) 387.
4) K. Umeno, RIKEN Review No.15 (1997) 95.

※ 現在 郵政省通信総合研究所 (1998年4月1日より) E-mail: umeno@crl.go.jp
☆ Present Address: CRL, Ministry of Posts and Communications, Nukui-kitamachi, Koganei, Tokyo 184-8795, Japan
4-2-1

Suzuki's third-order integrator
Ruth's third-order integrator
0.1
0.05
0
-0.05
-0.1
0.0001
0.0002
0.0003
0.0004
0.0005
0.0006
0.0007
0.0008
0.0009
0.001
Δt
δ₂ (Δt; t=1000)

図1

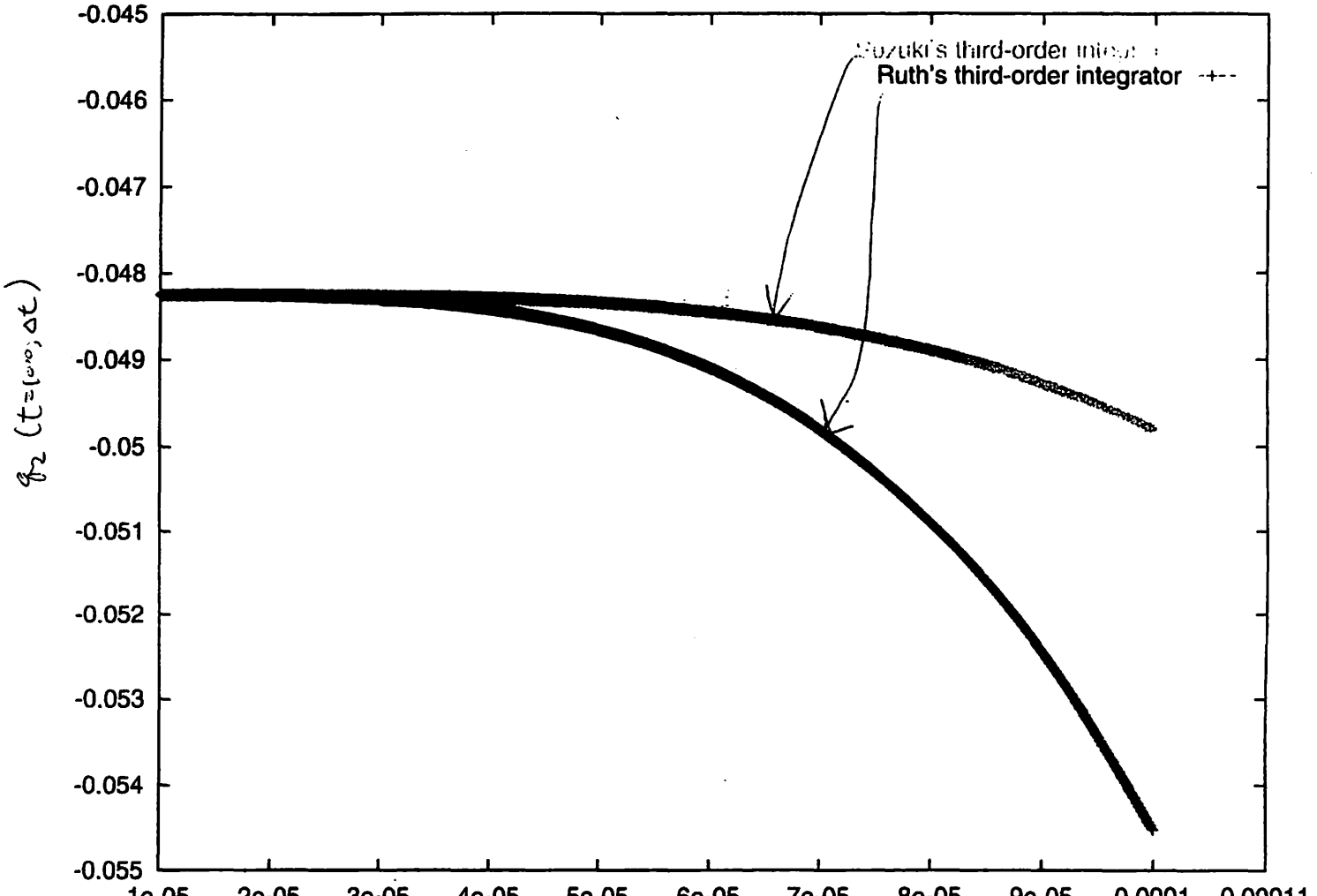
Suzuki's third-order integrator
Ruth's third-order integrator
-0.045
-0.046
-0.047
-0.048
-0.049
-0.05
-0.051
-0.052
-0.053
-0.054
-0.055
1e-05
2e-05
3e-05
4e-05
5e-05
6e-05
7e-05
8e-05
9e-05
0.0001
0.00011
Δt

図2.

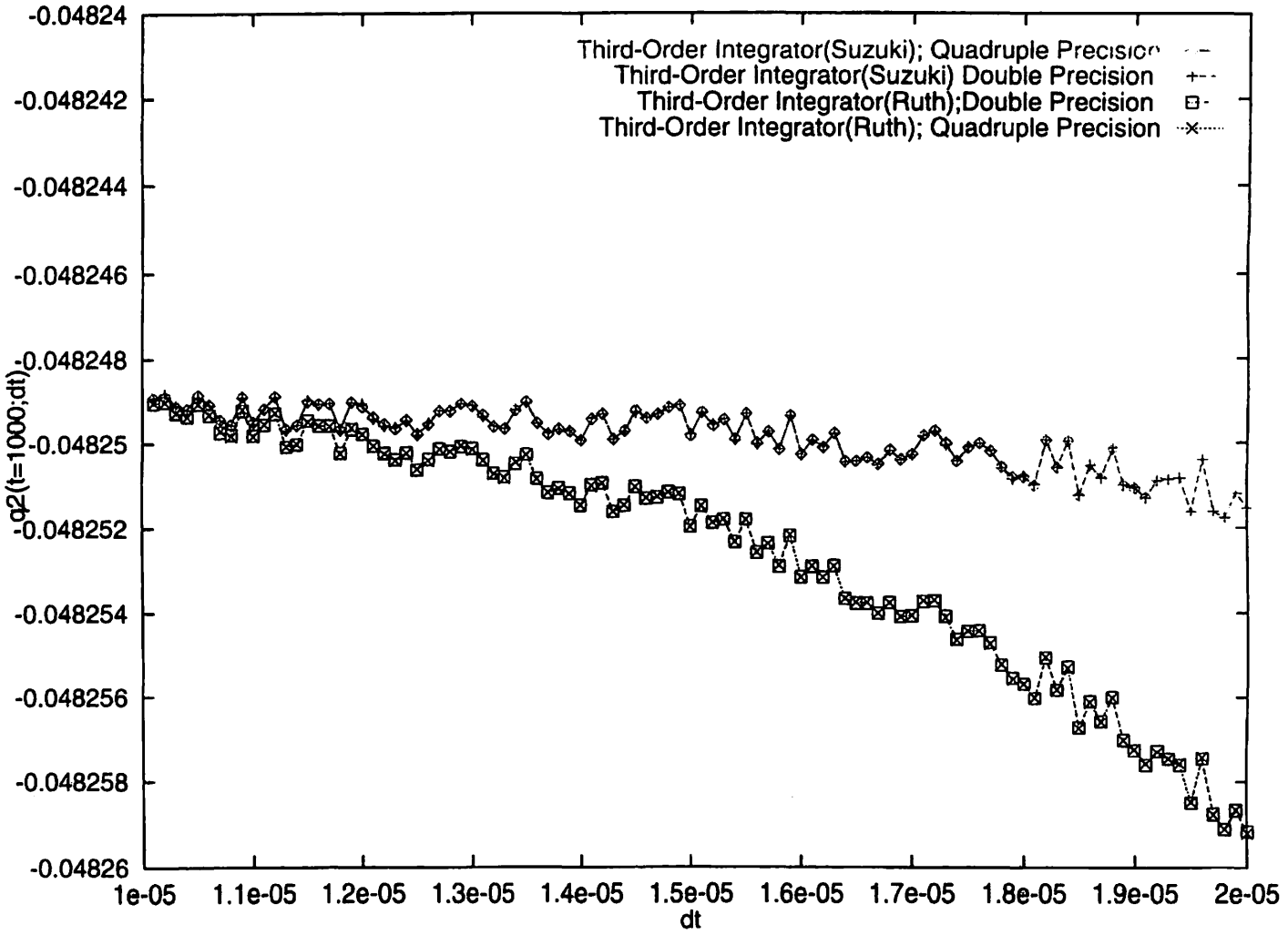
Third-Order Integrator(Suzuki); Quadruple Precision
Third-Order Integrator(Suzuki) Double Precision
Third-Order Integrator(Ruth);Double Precision
Third-Order Integrator(Ruth); Quadruple Precision
-0.04824
-0.048242
-0.048244
-0.048246
-0.048248
-0.04825
-0.048252
-0.048254
-0.048256
-0.048258
-0.04826
-q2(t=1000;dt)
1e-05
1.1e-05
1.2e-05
1.3e-05
1.4e-05
1.5e-05
1.6e-05
1.7e-05
1.8e-05
1.9e-05
2e-05
dt

図3

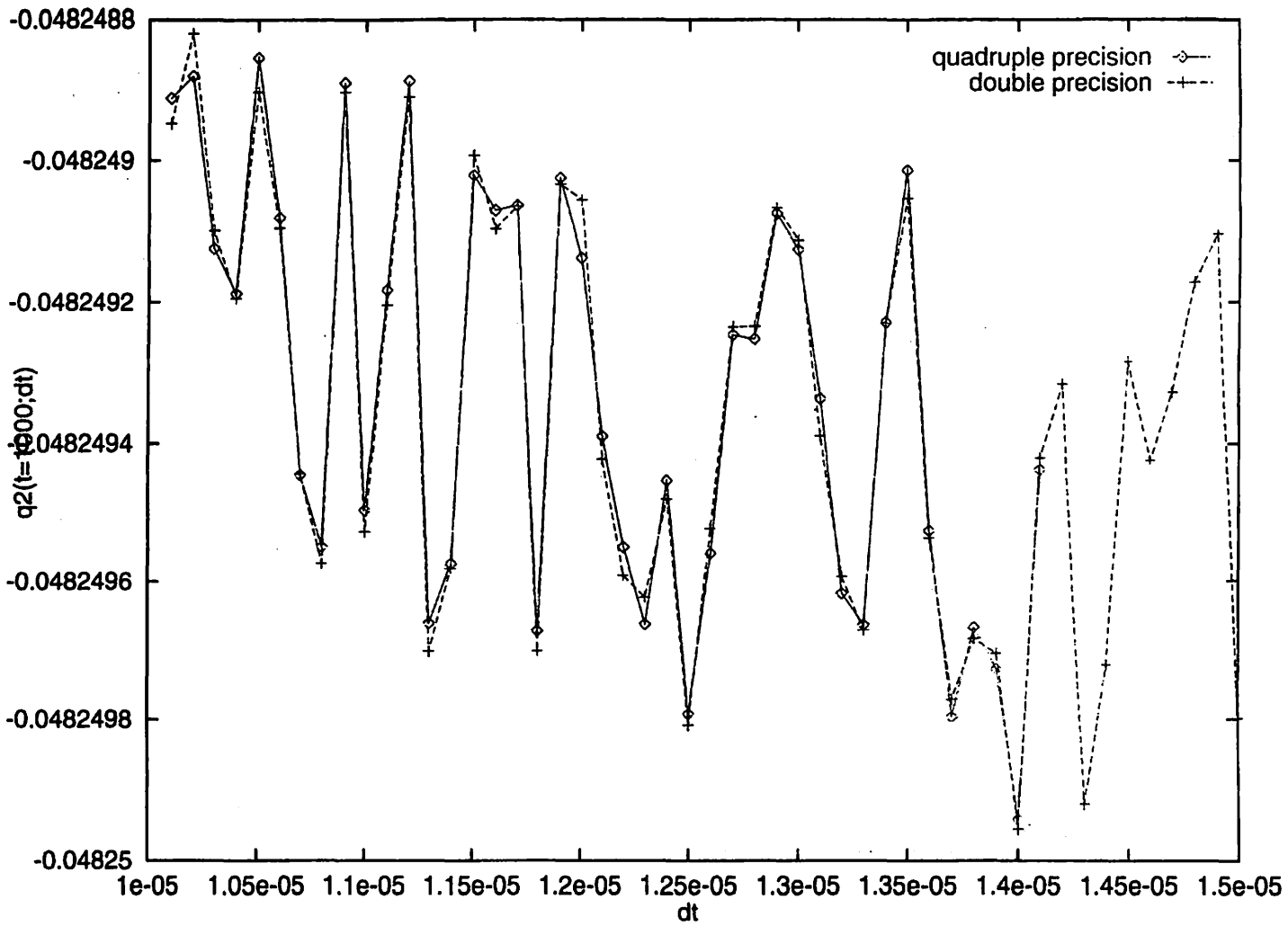
quadruple precision
double precision
-0.0482488
-0.048249
-0.0482492
-0.0482494
-0.0482496
-0.0482498
-0.04825
q2(t=1000;dt)
1e-05
1.05e-05
1.1e-05
1.15e-05
1.2e-05
1.25e-05
1.3e-05
1.35e-05
1.4e-05
1.45e-05
1.5e-05
dt

図.4

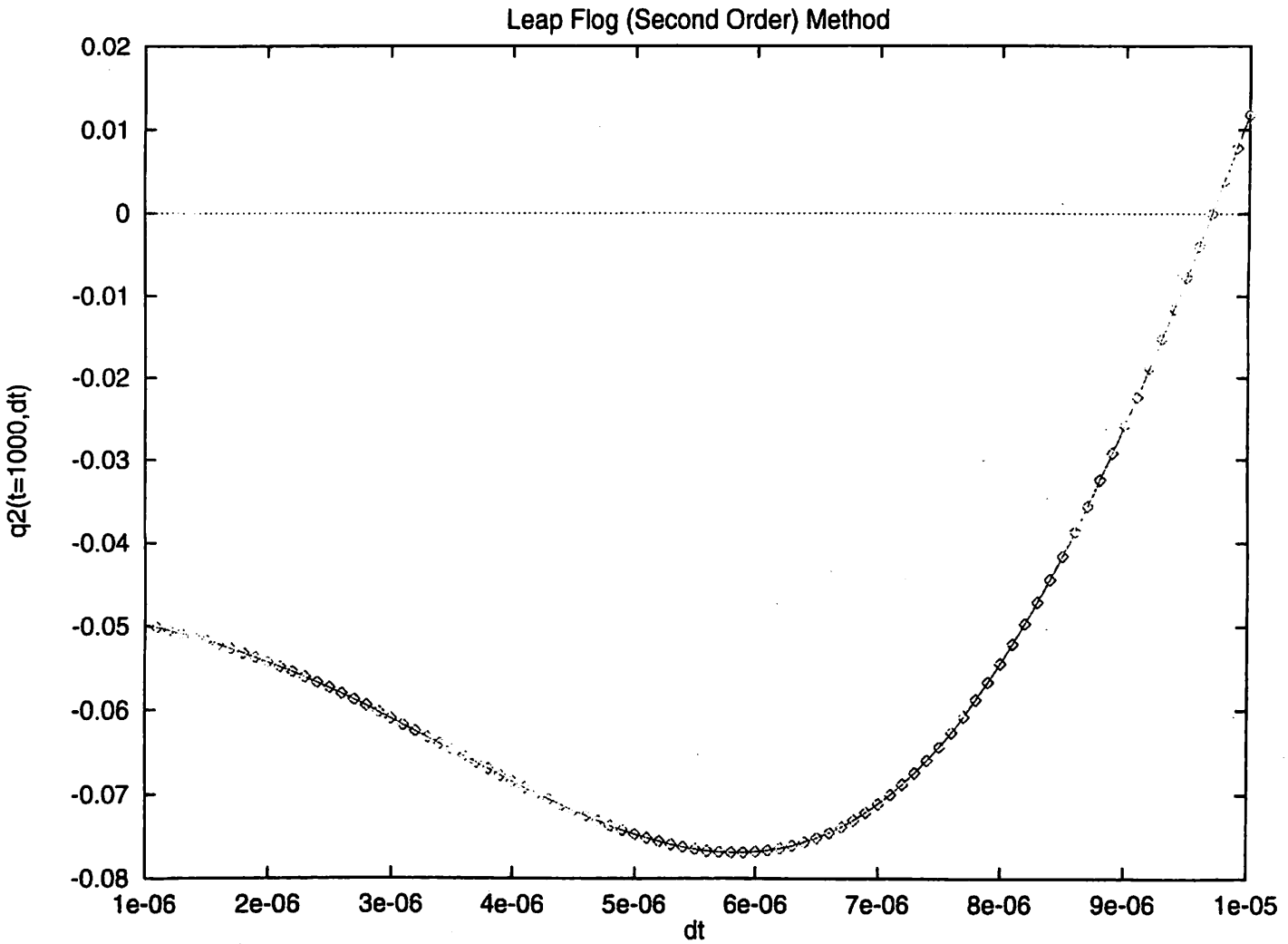
Leap Flog (Second Order) Method
q2(t=1000,dt)
dt
0.02
0.01
0
-0.01
-0.02
-0.03
-0.04
-0.05
-0.06
-0.07
-0.08
1e-06
2e-06
3e-06
4e-06
5e-06
6e-06
7e-06
8e-06
9e-06
1e-05

図5

座標系の違いによる軌道要素の変化
Change of the orbital element by difference of the coordinates system.

中井宏・木下宙（国立天文台）
H. Nakai and H. Kinoshita
National Astronomical Observatory

Abstract

We think the motion with the constant eccentricity at the barycentric coordinate system. But when the motion is expressed in the heliocentric coordinate system, the eccentricity is increased in proportion to the barycentric distance, and the period of eccentricity change is the same as the period of revolution of the heliocentric coordinate referred to the barycentric coordinate system. Besides, in the solar system, Jupiter's longitude of the ascending node circulates referred to the invariable plane, but it vibrates referred to the equator or ecliptic plane. In this paper, we give some examples that the same movement looks like another movement at the different coordinates systems.

1 始めに

ある座標系でみると単純な運動が、別の座標系の軌道要素では非常に複雑な運動にみえることがある。同じように、視点を変えると、今まで気がつかなかった別の現象が見えることがある。この様な例について報告する。

2.1 離心率の見掛けの永年変化

太陽系重心に対して放物線運動や双曲線運動している天体の運動を日心座標で表現した場合の離心率には永年変化が現れる。座標系 x,y（重心座標）の原点の回りをケプラー運動する天体について考える。原点から天体までの距離、天体の位置、速度は

$$
\begin{aligned}
r &= \frac{a\eta^2}{1+e\cos f}, \\
x &= r\cos f, \\
y &= r\sin f, \\
\dot{x} &= -\frac{an\sin f}{\eta}, \\
\dot{y} &= \frac{an(\cos f+e)}{\eta}
\end{aligned}
$$

である。但し、a は軌道長半径、e は離心率、f は真近点離角、η は円の場合1、楕円の場合 $\sqrt{1-e^2}$、放物線の場合$\sqrt{2}$、双曲線の場合$\sqrt{e^2-1}$である。次に原点に対して、半径 a_0、平均運動 n_0 で円運動している別の座標系 X,Y （日心座標）からこの天体の運動を考える。（簡単のために xy と XY は同一平面とする。）XY 座標で表現したケプラー運動している天体の位置、速度は

$$\begin{aligned} X &= r(\cos f - \frac{a_0 \cos n_0 t}{r}), \\ Y &= r(\sin f - \frac{a_0 \sin n_0 t}{r}), \\ \dot{X} &= a_0 n_0 \{-\frac{an}{a_0 n_0 \eta} \sin f + \sin n_0 t\}, \\ \dot{Y} &= a_0 n_0 \{\frac{an}{a_0 n_0 \eta}(\cos f + e) - \cos n_0 t\} \end{aligned}$$

となる。XY 座標で表現した離心率e^*はeとは異なり

$$e^{*2} = 1 + G^2/\mu(\dot{R}^2/\mu - 2/R)$$

となる。但し、$G = X\dot{Y} - Y\dot{X}, \mu = n_0^2 a_0^3, R^2 = X^2 + Y^2, \dot{R}^2 = \dot{X}^2 + \dot{Y}^2$ である。今、$r \gg 1$ とすると

$$e^{*2} \approx 1 + (\frac{r}{a_0})^2 \{1 - \frac{2an}{a_0 n_0 \eta}[\cos(n_0 t - f) + e \cos n_0 t]\} \cos^2(n_0 t - f)$$

となる。XY 座標系で表現した離心率e^*は r/a_0 に比例した振幅で、座標 XY が座標 xy の原点の回りを回転する周期で変動する。図１点線はそれぞれ円($a = 1, e = 0$)、楕円$(a = 1, e = 0.5)$、放物線$(q = 1, e = 1)$、双曲線$(a = 1, e = 2)$運動を、円運動$(a_0 = 0.1$、$n_0 = a^{-3/2})$する座標系で表現した離心率である。実線はr/a_0である。放物線、双曲線では時間と共に r/a_0 が非常に大きくなるので、見かけの離心率も時間と共に増大する。この様に座標系が変われば、同じ運動が見掛け上全く異なった複雑な運動に見えることがある。

2.2 座標系による昇交点経度の動き

昇交点経度と軌道傾斜角を表現する場合、基準面をどう選ぶかにより昇交点経度と軌道傾斜角の動きが異なって見えることがある。図２は１０万年間の木星の昇交点経度の変化を示したもので、上からそれぞれ、不変面（図２a)、赤道面（図２b)、黄道面（図２c）を基準面としたものである。不変面を基準面とすると昇交点経度は逆行し、軌道傾斜角(i_{JI}) は $0.25° \sim 0.5°$ と変化する。赤道面、黄道面を基準面とすると、昇交点経度はそれぞれ$3° \sim 5°$、$86° \sim 114°$ の間を振動し、軌道傾斜角は $22.8° \sim 23.6°$、$1.2° \sim 2.0°$ と変化する。図３において、赤道の極をP、黄道面の極をK、不変面の極

をＩ、木星の軌道面の極をＪとする。軌道面の極Ｊは不変面の極Ｉの回りを回転するが、赤道の極Ｐや黄道の極Ｋに対しては $(\Delta\Omega_{JP})$、$(\Delta\Omega_{JK})$ の範囲で振動する。このような例は母惑星の J_2 と太陽摂動の影響を受ける衛星の運動を記述する場合にも生じ、基準面の選び方で、昇交点経度と軌道傾斜角は大きく変わる場合がある。

2.3 地球から見て惑星が曜日と同じ順に並ぶ日はあるか？

スカイウオッチャー（１９９８年２月号）に福岡県の山添氏が地球から見て惑星が１週間の曜日（日、月、火、水、木、金、土）と同じ順に並ぶ日を見付けたという記事があった。視点を地球にした時、太陽の回りを回る惑星の運動がどう見えるかの例として考えてみた。図４は２０００年から１０年間の月と惑星の離角である。ＤＥ４０５を用い１６００年から２２００年の６００年間で太陽に対する惑星の離角の大きさが曜日の順番と同じになる時を計算した。土、金、木、水、火、月、日と並ぶ日は１５回でその内土星の離角が１８０度以下になるのは３例であった。また、日、月、火、水、木、金、土と並ぶ日は１３回でその内土星の離角が１８０度以下になるのは２例であった。山添氏の見付けた日は２０９８年６月２９日で、太陽から土星までの全ての惑星が７８度に入っており、この状態が約１日半続く条件の良い日であった。

year	month	date	hour	Sat. Saturn	Fri. Venus	Thurs. Jupiter	Wed. Mercury	Tues. Mars	Mon. Moon	Sun. Sun
1957	8	25	12	95.8	34.5	31.5	23.1	9.0	0.3	0
2053	10	11	22	139.6	46.6	21.5	21.1	1.6	0.4	0
2098	6	29	12	77.3	43.8	43.1	23.5	21.7	5.8	0

year	month	date	hour	Sun. Sun	Mon. Moon	Tues. Mars	Wed. Mercury	Thurs. Jupiter	Fri. Venus	Sat. Saturn
1667	5	22	22	0	0.5	0.9	10.4	37.9	43.5	119.9
2105	4	4	0	0	10.3	19.8	25.5	30.0	43.0	118.7

Table 1. The elongations for the planets form in sequence of a day of the week.

3 まとめ

一つの現象を表現する場合、座標系の選び方により、簡単に表現出来る場合と、見掛け上非常に複雑になり、問題の本質が解らなくなる場合がある。考えている問題に対して、現象を簡潔に表現でき、問題を簡単に説明出来る表現法は何かを十分検討して採用すべきである。また、見慣れた現象でも視点を変えれば、別の現象として面白い結果が潜んでいる可能性もある。

4 参考文献

山添富雄：スカイウオッチャー,1998年2月号,46

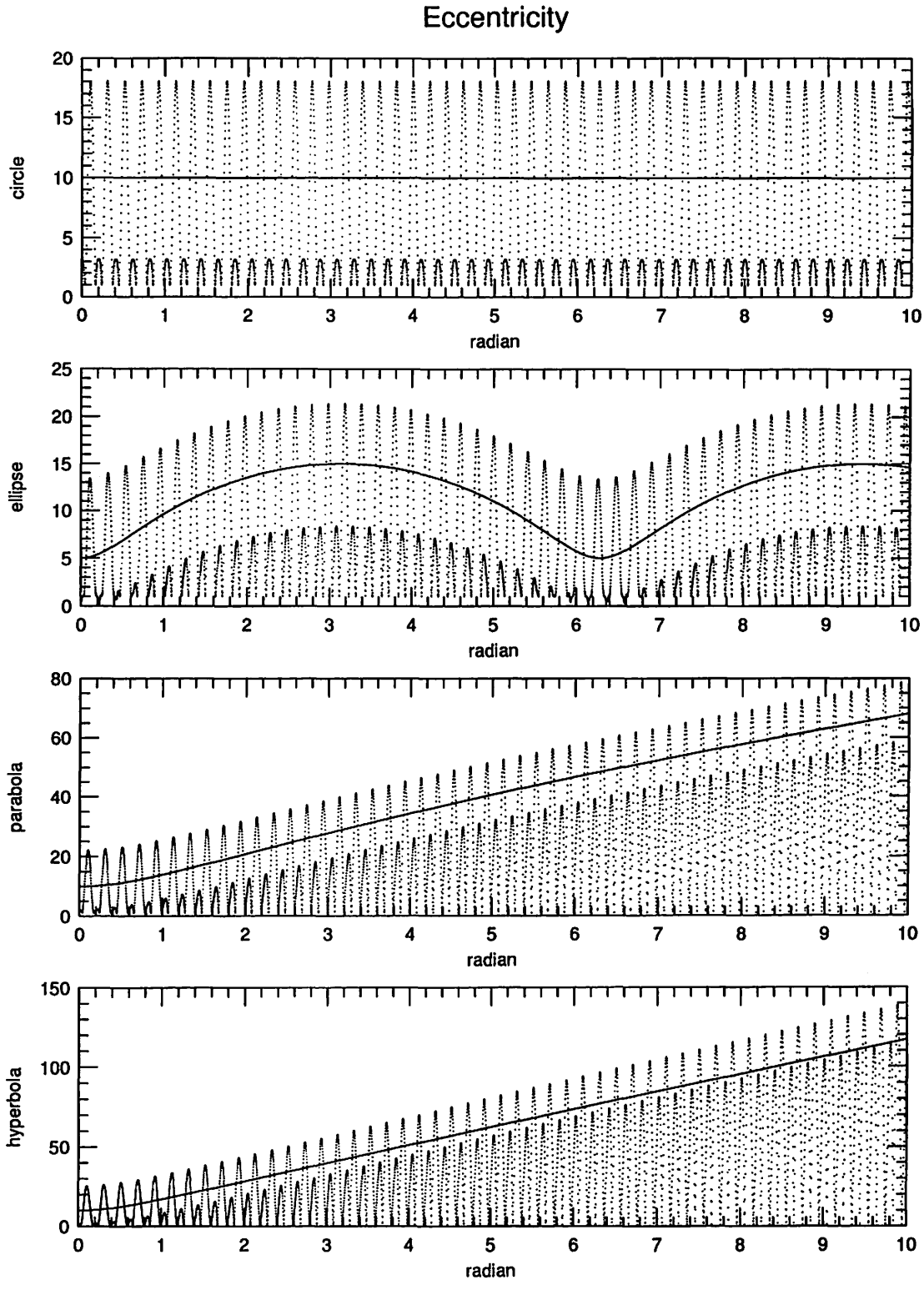

Figure 1. Eccentricities of conic section referred to the coordinates system which rotates uniformly. Solid lines are r/a_0.

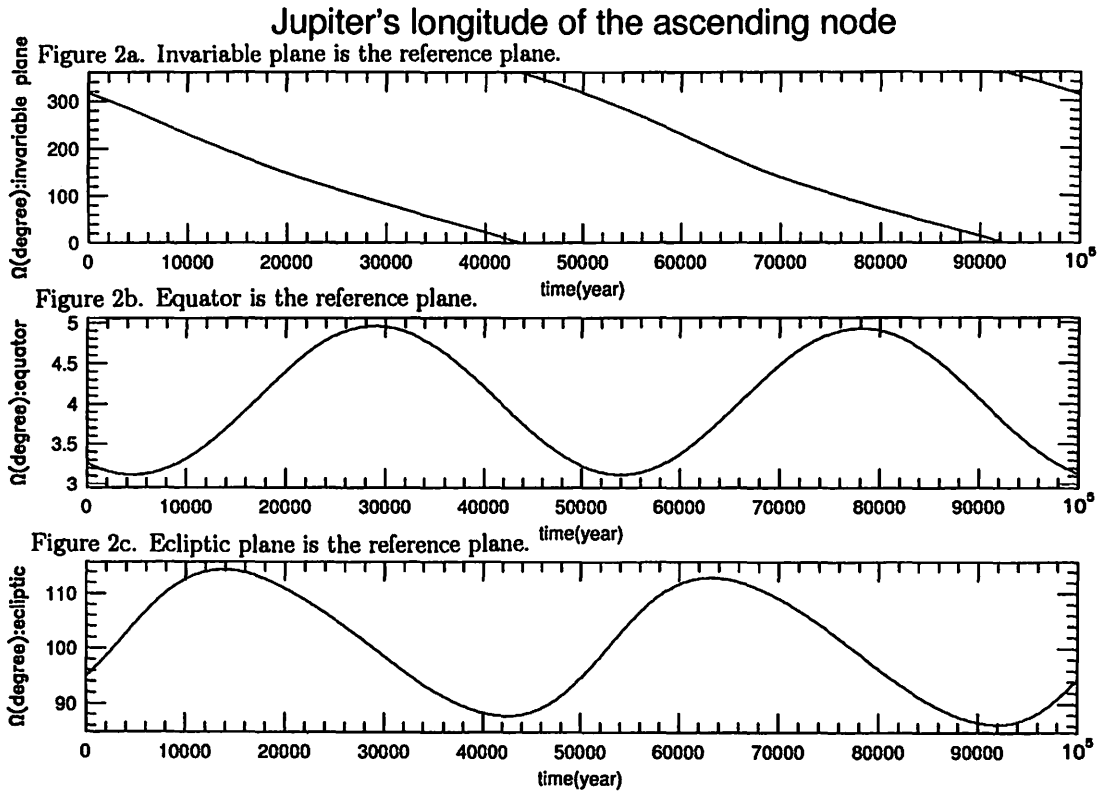

Figure 2. Jupiter's longitude of the ascending node.
The reference planes in figure 2a, 2b and 2c are invariable plane, equator and ecliptic plane, respectively.

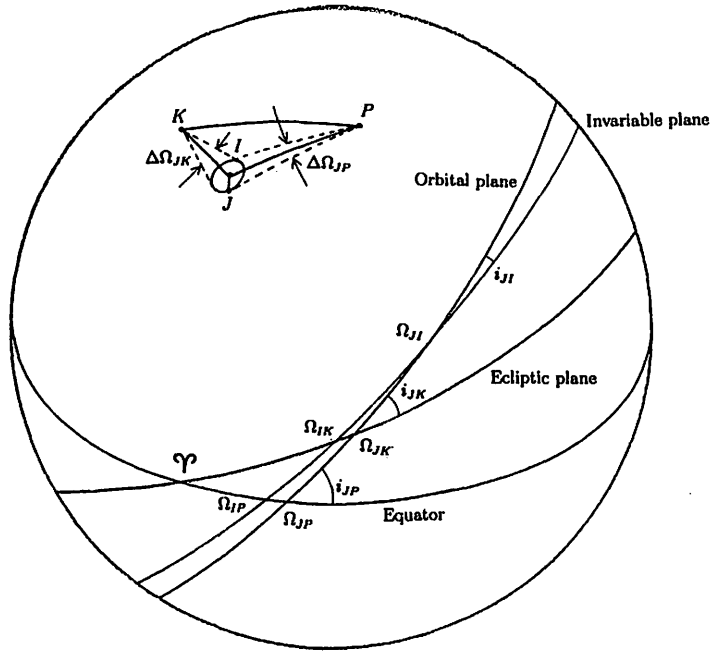

Figure 3. The inclinations, the longitudes of ascending node and the poles of the equator, ecliptic, invariable and orbital planes.

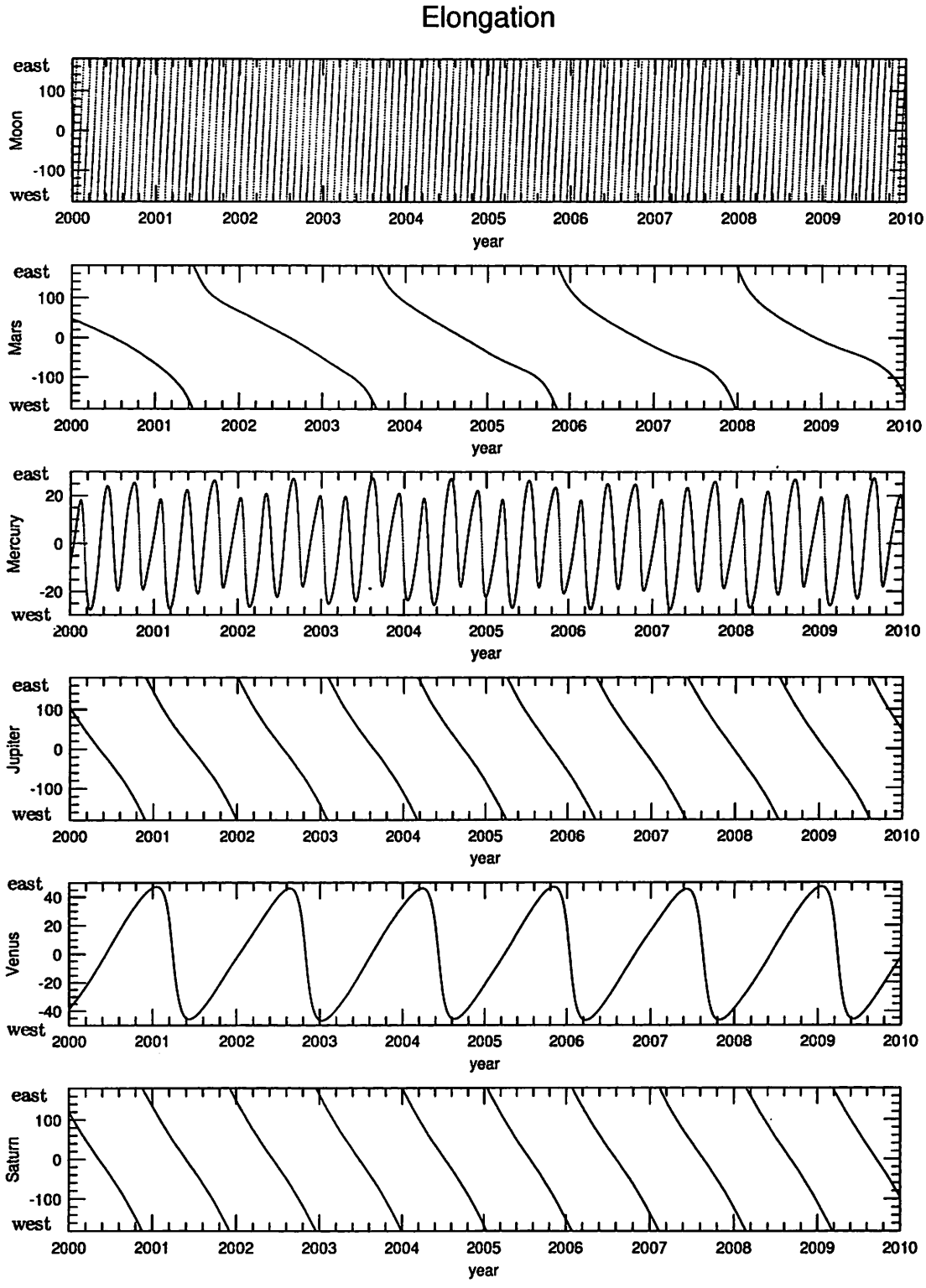

Figure 4. The elongations for the Moon and planets for ten years.

天文学者からの質問192
192 questions from astronomers

谷川清隆・伊藤孝士
Kiyotaka Tanikawa and Takashi Ito

astroQA@exodus.mtk.nao.ac.jp

192 questions of astronomers which they want to know the answers are listed. They are the replies to our questionnaire to the astronomers in Japan, "What do you want to know, and how are you doing to know that?". The list of questions are used on the open-house day of National Astronomical Observatory, Mitaka, 1997. It is still upgraded on our website.

この質問集は平成九年度の国立天文台三鷹一般公開日企画「質問コーナー」の客寄せのために作製されたものです。かつては一般公開日の名物企画だった質問コーナーもこの数年はマンネリを極め、沈滞という形容を地で行く救いようのない廃れようでした。そこで私達は発想を転換し、客の質問を待つのではなく、天文学者自身が今もっとも質問したいこと—知りたいことは何なのかについてアンケートを行い、回答をまとめた冊子を作って配布しました。その結果、質問コーナーは近年まれに見る異常なほどの盛況を呈し、大成功を収めることができました。これに気を良くした私達は更に多くの天文学者の考えを掲載するため、日本天文学会の公式メーリングリスト tennet の上にも同様なアンケートを流しました。その結果回答された項目数は 192 個に達しました。次のページからは、「私は○○○について知りたい。だから□□□□□をやっている」という形式で 192 個の疑問とそれに対する取り組みが並んでいます。多くの天文学者の生の考えをなるべく伝えるために、回答された原文をほとんど無修正で掲載しています。外国語には邦訳を付加しました。

回答を送っていただいた皆様にはこの場を借りて深く感謝いたします。tennet のメールとしては以下の三通を参照してください。最新の回答集は http://exodus.mtk.nao.ac.jp/に於いて参照できます。また、この回答集は近日中に天文月報にも掲載される予定です。

```
Message-Id:  <199711140347.MAA32332@exodus.mtk.nao.ac.jp> ([tennet 543])
Message-Id:  <199711180919.SAA26944@exodus.mtk.nao.ac.jp> ([tennet 550])
Message-Id:  <199801260201.LAA17887@exodus.mtk.nao.ac.jp> ([tennet 611])
```

なお、無記名や匿名での回答、公序良俗に著しく反すると当方で判断した回答については掲載を見合わせています。予め御了承ください。

天文学者って何考えてるの?

天文学者からの質問192

1. わたしは (太陽という身近な星で)「太陽フレア」という突発的な磁気エネルギー解放が起こるメカニズムを理解したい。

   だからまず、太陽フレアの結果起こるプラズマの熱化過程 (こちらの方が観測しやすい) を理解しようと、フレアの流体計算を行い、観測と比較しながら熱化過程のシナリオを考察している。

2. わたしは星生成のメカニズムを理解したい。

   だから赤外線観測装置を開発して観測的研究をしている。

3. 私は、一般相対論の効果 (重力レンズ) を直接観測したい。

   だからいま (超高精度角分解能を実現できる) 光赤外干渉計を開発している。

4. 私は恒星や惑星系の誕生過程を明らかにしたい.

   そのために最先端の観測設備で新しい観測をしたい.
   そのためにすばる望遠鏡の赤外性能を良くするための
   技術開発や基礎実験をしている.
   (書類書きもしている, ですが.)

5. 私は宇宙の塵を調べたい (惑星や生命のもとになるので)

   だから, すばる望遠鏡に積もる地球の塵を払う仕事をする

6. わたしは宇宙の雲を調べたい (分子雲が星の生まれる現場なので)

   だから, 大望遠鏡の鏡が曇らないよう工夫をしている

7. わたしは彗星の起源を理解したい。

   そのために、彗星や関連する天体の観測研究を行っている。

8. 私は「宇宙の膨張が止まるかどうか」を知りたい。

   だから、「VLBI 観測で減速定数の計測」を行っています。

9. わたしは星形成を理解したい。

   だから星形成の材料となる分子雲がいかに作られるかを物理法則を使って理論的に説明しようとしている。

10. わたしは今までよく見ることができなかった宇宙の現象を見たい.

    だから光赤外干渉計を作っている.

11. I want to understand the stellar populations in barred galaxies.
    (わたしは棒状銀河内の星の種族を理解したい.)

    So, for the present, I am studying their chemical composition and trying to interpret their chemical evolution.
    (だからいまのところ棒状銀河の化学組成を調べ, 化学進化を理解しようとしている.)

12. I want to understand if the basic idea of homogeneity and isotropy of Big Bang theory can be justified by light element abundances observed at high redshifts and in halo population II stars.
    (ビッグバン理論の一様性と等方性という基本的発想が高赤方変位天体や銀河ハローの種族 II 星で観測される軽元素の存在量から正当化されるかどうか理解したい.)

    So, now I am investigating the spectral line formation processes in turbulent media to estimate quantitatively the spread of the abundances caused by correlation effects in random velocity fields.
    (だからいま, わたしは乱流媒質中のスペクトル線形成を調べ, ランダムな速度場内の相関効果に起因する存在量の広がりを定量的に見積もっている.)

13. Watakusi wa hosi fu to AGNs jets wo riyu ga wakaritai.
    (わたしは星風と AGN ジェットの原因を理解したい.)

Ima, watasi wa riron to sugaku MHD sitsiumontati ga kenkyu-site iru.
(いま, わたしは理論的にまた数学的に MHD の問題を研究している.)

---

14. わたしは、銀河系全体にひろがる星間分子雲の地図をつくりたい。

だから、電波望遠鏡をチリのアンデス山中に置いて、日本からは見えない南の天の川を観測している。

---

15. わたしはどのように、地球やほかの太陽系の惑星ができたのかを理解したい.

だから今は特に質量が大きい木星型の惑星が生まれる過程を、計算機を使って数値シミュレーションを行う事で調べている.

---

16. 私は恒星系の振動現象を理解したい.

だから数値シミュレーションや振動の解析をしている.

---

17. I want to understand Where we are and Why we are there.
(我々がどこにいるのか, またなぜそこにいるのか理解したい.)

So, for the present, I am investigating the evolution of galaxies.
(だからいまわたしは銀河の進化を研究している.)

---

18. わたしは銀河系内のガスの性質を理解したい。

だから電波望遠鏡を使って、銀河系のいろいろな場所のガスを観測している。

---

19. わたしは、宇宙の塵に阻まれてこれまであまり奥深くまで見えなかった活動現象 (星生成活動、活動銀河核など) を理解したい。

だから赤外線の観測装置開発と観測を行なっている。

---

20. I'm interested in the furthest objects ever seen, the so called QSOs.
私は、何よりも遠方にある天体 (クエーサ) に興味を持っています。

At present, I'm doing model calculations of QSOs.
現在は、クエーサのモデル計算に取り掛かっています。

---

21. 天王星と冥王星の横倒し自転、金星の逆行自転、木星・土星・海王星の衛星の逆行公転の起源を知りたい。

講義等でこの話題を取り上げ、この問題にチャレンジする学生を探している。

---

22. I just interested in some general properties of motion of asteroids and Nereid.
(わたしは小惑星やネレイドの運動の一般的性質に興味があります.)

For the present I'm trying to construct a semi-analytical theory of motion for the latter.
(いまのところネレイドの運動の半解析的理論を作っています.)

---

23. 私は銀河の進化過程を知りたい。

そこで、QSO 吸収線系の電離状態や化学進化について、理論計算結果と観測を比較、シナリオを検討している。また、観測データを自給自足するため、すばる望遠鏡の高分散分光器の開発に参加している。

---

24. わたしは重力波で宇宙を眺めてみたい.

だから重力波検出用のレーザー干渉計 (TAMA300) を開発している.

---

25. わたしは星がものを放出するしくみを理解したい.

だからいまいろいろな星の赤外スペクトルの特徴を調べている.

---

26. わたしは小さい恒星が質量放出を起こす過程を理解したい.

だからいま球状星団の晩期型星の赤外観測をしている.

---

27. わたしは銀河のもつ多様な性質の因果関係を理解したい。

そのために多数の銀河のデータの収集及び統計解析を行なっている。

---

28. 私は宇宙の中で銀河がいつ誕生し、どのような道を歩んできたかを理解したい。

だから楕円銀河・銀河群・銀河団における重元素の起源を調べ、宇宙の各階層の化学進化の研究をしている。

---

29. わたしはいま大質量星周辺の物理状態を理解したい。

だからいま近赤外光分散分光器を開発して、観測している。

---

30. わたしはニュートン力学で宇宙を説明したい。

だからわたしはニュートン力学で説明できる現象ばかり追いかけている。

---

31. わたしは地球の起源と進化の必然性を理解したい。

だからいま惑星形成の数値シミュレーションを行っている。

---

32. 私は宇宙の起源と生命の起源、その進化と互いの関連を理解したい。

だからいま、宇宙の起源と多少とも関わりのあることをしている。

---

33. 私は、宇宙を理解したい。

けれど、難しいから、その一部分だけ研究している。

---

34. 私は、まだ誰も見たことのない微小な小惑星の分布を知りたい。

これをスバル望遠鏡で観測するべく、シミュレーションなど、色々準備を進めています。

---

35. 私は宇宙を理解したい。

だからマッチョを調べている。

---

36. I want to understand the motion of a close binary system.
(私は近接連星の運動を理解したい.)

So, for the present, I am doing to study the effects of the disturbing forces of the system (e.g. tide, rotation, drag, radiation pressure, ...).
(だからいま私はこの系に働く摂動力の効果 (たとえば, 潮汐, 自転, ガス抵抗, 放射圧など) を調べています.)

---

37. もっと広く遠くを見たい.

で、広視野撮像装置をつくってま.

---

38. 私は時間的にも光度的にも、いつ変光するか予測出来ない「不規則型変光星のカオス的振る舞い」を調べたい。

だから、世界中から過去に観測されたこれらの星のデータを集め、時系列解析、パワースペクトル等による解析法を駆使し、「不規則型変光星の振る舞いの中に秘められた規則性の有無を探る」ための観測と研究を行っております。

---

39. わたしは太陽系についてもっと詳しく知りたい。

だから彗星の観測をしています。

---

40. わたしは、銀河系に分布するX線プラズマや星間ガスの起源や運動を理解したい。

だから、今のところは計算機で数値シミュレーションをしている。将来は、観測の役に立ちたい。

---

41. 私は宇宙の過去、現在、未来を知りたい。

だから遠方の天体と近方の天体の構造をVSOPを用いて調べ、宇宙の膨張する速度を調べている。

---

42. 私は銀河の形成と進化の過程を理解したい。

そのために、銀河の光度進化および化学進化を理論的に計算し、それを観測と比較する研究を行なっている。同時に、この結果を用いて宇宙論パラメータに制限を与えるテストについても研究している。

---

43. わたしは引力で相互作用する多体系のカオスを理解したい.

だからいま三体問題の運動を計算機シミュレーションで観測している.

---

44. わたしは 太陽からはるか遠方にある「エッジワース・カイパーベルト」について探究したい.

だからいま 太陽からわずかな距離にある地球上で数値計算と観測準備に情熱を燃やしている.

---

45. Yo estoy interesado en entender cómo se formaron las galaxias.
(私は銀河がどのようにできたか、に興味があります.)

Para tal propósito es necesario estudiar las poblaciones estelares de las galaxias de tipo temprano (elípticas y lenticulares), en particular conocer los principales parámetros que caracterizan dichas poblaciones, como son el contenido metálico, la edad, la proporción entre estrellas enanas y gigantes y si los distintos elementos químicos se encuentran en las proporciones distintas a las de nuestro entorno solar.
(だから早期型銀河 (たとえば楕円銀河や S0 銀河) の星の種族を調べる必要があります. 私はとくに種族の特徴となる金属量, 年齢, 矮星と巨星の存在比などのパラメータを決めることに興味があり, 太陽近傍の金属量と違っているかどうかを知ろうとしています.)

---

46. わたしはあらゆる元素がどこからやってきたか知りたい。

だからいま新星、超新星などによる元素合成を調べている。

---

47. わたしは宇宙をもっとはっきり見たい。

だから地球大気のゆらぎを補正する補償光学 (AO) を作っている。

---

48. 私は銀河がどうやってできたかを知りたい。

だからすばる望遠鏡を作っている。

---

49. わたしは人類の未来について知りたい。

だから、地球外文明の存在に興味を持っているが、いま何もしていない。

---

50. わたしは宇宙の始めの様子を知りたい。

だから、それが観測できる手段である重力波検出法の開発を進めている。

---

51. わたしは銀河の中心核の活動の様子や、周辺の物理状態を理解したい.

だからいま銀河の中心核のまわりのガスやプラズマを観測している.

---

52. 私は生命の起源を知り, 宇宙生命の可能性を研究したい.

従って電波望遠鏡による分光観測によって星間物質中の有機物を探している.

---

53. 私は自分の体を作っている元素の起源を知りたい.

だから星の大気や星周物質の組成を可視光や赤外線分光観測によって調べている.

---

54. 私は地球以外に植民する可能性を探りたい.

だから系外惑星の探査をするため高分解能の観測装置を作ろうとしている.

---

55. 私は宇宙で一番小さい星 (恒星) を発見したい. それは褐色矮星の最も小さいものだろう.

だから赤外線で高分解能の観測をしようとしている.

---

56. 私は原始惑星系円盤の組成と星間物質との関連を知りたい.

だから彗星と星間雲について分光観測を行い, 組成や変成の状態を調べようとしている.

---

57. わたしは「宇宙でなぜジェットが噴出しているか」を理解したい.

だからいま「電磁流体力学の方程式」をこねくり回している.

---

58. わたしは「宇宙になぜブラックホールがあるのか」を理解したい.

これはいたずら好きの神様が宇宙に落し穴を掘ったのでにゃかな.
神様のなかにもドジなのがいて落ちちゃったかも.

---

59. 私たちの大先輩である江戸幕府の天文方が、西洋の天文学をいかに苦労して吸収しようとしたかを知りたい。

だから、私も苦労して天文方の古文書を判読しています。

---

60. わたしはすべての経験科学をつくる方法をつくりたい。

だからいま認識方程式を作っている。

---

61. わたしは円盤を理解したい。

計算機の中で円盤を作って調べています。

---

62. 私は2つの恒星が、お互いの共通重心の周りを運動する事によって起こる星食関係を利用して、恒星の大気構造をしらべたい。

だから、測光観測や偏光観測を協同研究者と行っている。

---

63. 私は初期の銀河や宇宙を知りたい。

だからいま遠方の天体を研究している。

---

64. わたしは、天文現象のすべてを予報したい。

だから、いろいろな天体の位置と運動を調べている。

---

65. 私は、新しい装置の "目" で、まだ見ぬ宇宙の姿を見てみたい。

だから、すばる望遠鏡用観測装置の開発をしています。

---

66. わたしは、太陽フレアの発生機構を理解したい。

だからいまX線コロナ・ループの時間変化を調べている。

---

67. わたしはダークマターが何で説明できるかを理解したい.

だから褐色わい星の研究をしている.

---

68. わたしは宇宙の化学分析からその生成と進化を理解したい.

だから分光学の研究を進めている。

---

69. わたしは星の外層大気構造を理解したい。

だからISO (赤外線宇宙望遠鏡) などで星の赤外線観測を行なっている。

---

70. わたしは「宇宙には地球のような惑星がどれくらいたくさんあるのか? どのような物理条件がそろえば地球ができるのか?」を理解したい.

だからいま「惑星系の形成過程」を「理論計算および、太陽系や生まれたばかりの星の観測」を行なってしらべている。

---

71. わたしは太陽系の起源を知りたい.

だから太陽系の始源天体の観測的研究を行っている.

---

72. わたしは太陽系天体がどのような物質からできているかを知りたい.

だから太陽系の小天体の物質科学的研究を行っている.

---

73. わたしは惑星地球の起源を知りたい。

だから惑星科学的見地から地球科学を研究している.

---

74. わたしは、天文や物理を記述する数学をあみだした人々の思考過程を理解したい。

だから、いつか科学史を勉強したいが、今そこまで手が広げられない。

---

75. わたしは惑星系の誕生過程を理解したい。

だから惑星形成の母体となる星周円盤の進化を調べている。

---

76. 私は、この宇宙がどこから来たのか、何なのか、どこへ行くのかを理解したい。

だから、今 原始宇宙の手がかりとなる AGN, Quasar の研究を進め、この宇宙の運命を決める宇宙論パラメータの手がかりを探っています。手がかりを増やすために、いろいろな波長域でのスペクトルを解析しています。

77. 私は、愛と友情の真実を確かめるために宇宙の果てを探っている。

と思ったら、人生の果てが見えてきたような気がするが、まだ真実はつかめていない。人生は希望に満ちていることを観測したい。

78. I am interested to understand how the different elements (oxygen, iron etc) that compose the various objects in the universe came into being,
(私は宇宙のさまざまな天体を構成する異なる元素 (酸素, 鉄等) がどのように生まれたのか知りたい.)

that is why I am studying stellar nucleosynthesis (the sequences of nuclear reactions taking place in hot stellar interiors during the various phases in the lives of stars); we know that almost all elements, except the lightest ones, are produced by stars.
(だから私は星の中での元素合成 (星の一生の間に星の内部の高温部分で起こる連鎖核反応) を調べている. 軽元素を除くほとんどの元素が星の内部で作られたことがわかっている.)

79. 私は、活動銀河核の謎を解明したい。

だから、太陽フレアの研究をしている。

80. 私達人間はなぜこうして存在しているのだろう。
私達のまわりの花や鳥、この地球はどうやって生まれてきたのだろう。
夜空に輝く星ぼし、その集団である銀河、そして
そもそもこの宇宙は、どうしてできたのだろう。

どうしたら、この問に答えられるでしょう。
判らない。でも天文の研究をします。

81. わたしは恒星の内部を観測的に理解したい.

だから恒星の振動を調べている.

82. わたしは口径 8m の「すばる」望遠鏡を使って宇宙の元素の歴史や原始天体 (銀河) の形成過程を観測したい。

だから高分散分光器を製作している。

83. すばるの高分散分光器の性能を完全に引き出したい.

だから高精度の視線速度 (1cm/s) の計測で恒星の惑星系を探したい。

84. 私の人生は、なぜ、どうして、このように陰惨で暗澹たるものに
落ち込んでしまったのか。その縁 (えにし) を知りたい。

だが、それを知ったからと言って人生をやり直せるわけでもあるまい。
それでも私は問い続ける。
あの時あの場で私はどうしてあのようにしか振舞うことができなかったのか?
どうしてあの時もう一歩踏み出して勇気を振り絞ることができなかったのか?
どうしてあの場で今一歩踏み堪える力を持つことができなかったのか?
その答を探しながら屍のように生きる日々。
もしも居られるなら神よ、私に平安を与えたまえ。

宇宙の研究は私にとって、再生への希求そのものである。

85. 宇宙の果てで、星が生まれはじめた直後の、若い銀河をみつけたい。

巨大電波干渉計を地球上でいちばん空気の澄んだところに建設すべく、南米はアンデス山脈の標高 5000m にある砂漠地帯を放浪している。

86. さまざまな銀河の中心核に潜むブラックホールの「食生活」について知りたい。

ブラックホールの「主食」であると思われる星間ガスを、野辺山の電波干渉計でくわしく調べている。

87. 銀河にも「派手な人」「地味な人」いろいろなタイプがいるのはなぜか知りたい。

銀河を形づくる星を生み出す母胎 (高密度ガス) がどうなっているのか、野辺山の電波干渉計で観測している。

88. 空気があっても、ゆらゆらと像がボケない、シャープな電波画像が欲しい。

ゆらゆらと像をボカす原因の「水蒸気」がリアルタイムで測定できるように、高精度の大気放射量測定装置を作っている。

89. 月は地球の子供、兄弟あるいは他人という色々な説がある。わたしは月と地球の本当の関係を知りたい。

だからその鍵となる月中心核の大きさを知るために月の重力を人工衛星をつかって測ろうと計画している。そのために2003年の月探査周回衛星計画に向けて機器の開発や計算機プログラムの開発を行っている。

---

90. 西日本の大地に働いている東西方向の圧縮力が一昨年の兵庫県南部地震を引き起こした。なぜこんな力が日本に働いているかを知りたい。

私はその原因はインドのユーラシア大陸への衝突にともなって東アジアの陸塊が東へ毎年1～2センチづつ押し出されているせいだろうとにらんでいる。それを証明するため天然の電波星や人工衛星の電波を使って西南日本の大地の動きと中国や韓国の大地の動きの関係を調べている。

---

91. あるはずなのにどうしても観測できない地震(silent earthquake)をとらえたい。

地震がみえない原因は断層運動がゆっくりすぎて地面が揺れないせいであろうと私は考えている。だから私は地面の揺れを観測する地震計ではなく、天体観測によってゆっくりした地面の動きを観測してそのしっぽをつかまえようと思っている。

---

92. 私は地球の内部構造と中で起こっている運動を知りたい.

だから超伝導重力計の国際観測網を作り,観測する.

---

93. 私は、人類が宇宙へ進出するのは自然が我々に課した責務だと考えている。

だから、そのための基礎となる宇宙の知識を広めるために日夜天文学を研究している。

---

94. 私は、自分が知っていることを他人に伝えるのが好きである。

だから、自分が天文学の研究で得た知識を人々に知らせるために広報活動にも力を入れている。

---

95. 私は、人類が宇宙進出するに当たって、そのガイドマップを作りたいと思っている。

だから、宇宙のどこでどのような星がどのようにできるのかを調べるために、銀河系や銀河での星間分子ガスの様子を調べている。

---

96. 私は、昔から地図を見て、そこがどのようなところか想像するのが好きだった。

だから、いままで誰も見たことがない場所の地図を作るために、天体の観測をして、「天体の地図」を作っている。

---

97. 私は、いろいろなところへ出かけるのが好きである。特に、「探検」がしてみたい。しかし、地球上はもはや探検し尽くされてしまった。

だから、宇宙を探検するために、天文学の研究を行ない、想像の上での探検を行なっている。

---

98. 私は太陽系外に人類が居住可能な惑星があるのかどうかに関心がある。

だから、ドレークの式で示される因子を確定するために、星の周りで惑星がどのようにできるのかの手掛かりを電波を使って探している。

---

99. 私は手軽に天体のデータを扱えるソフトウェアを使いたいが、思うようなものが手近にない。

だから、自分で、希望に合う天体データ処理用ソフトウェアを作っている。

---

100. 私は機械が動くのを見るのが好きである。

だから、望遠鏡を動かすためのソフトウェアを作っている。

---

101. 宇宙パラメータを測定したい。研究者になりたい。

だから今MAGNUMプロジェクトをやっている。

---

102. 私は、どうして世界が $f = ma$ という微分方程式で構成されているのかを知りたい。

しかしこれは物理学だけでは解決できそうにないので、いずれは出家して仏陀の教えの中からその理由を見い出すつもりである。天網恢恢疎にして漏らさず。呵呵!

---

103. わたしは星の生まれる所の詳細な構造を理解したい.

だからいま国内VLBIネットワークを使って水メーザーの観測研究をしている.

---

104. わたしは我々の銀河系の本当の姿(形と運動)を理解したい.

だからいまVERA計画実現に向けて準備をしている.

---

105. わたしは膨張宇宙の中で銀河がどうやって形成されるのか理解したい。

だから、銀河の観測データを調べたり、銀河形成のモデルを考えたりしている。

---

106. わたしは、Saha and Tremaine (1992, *Astron. J.*, **104**, 1633 1640, Symplectic integrators for solar system dynamics) の1636ページ左段の(19a)(19b)式の次のパラグラフにある記載 "Since $\hat{\boldsymbol{J}}$ is fixed in the surrogate system ($\hat{H}$), and $\boldsymbol{J}$ is fixed in the real system (H), ..." の真意が図りかねるので、これを明解にしたい。

なぜなら、"fixed" を『不動の、一定した』という意味だと思えば、正準変換を行う以前の変数である$\hat{\boldsymbol{J}}$や$\boldsymbol{J}$は周期項を含んでいるのだから、これらは明らかに "fixed" ではない。従って、上記で用いられている$\hat{\boldsymbol{J}}$, $\boldsymbol{J}$は、本来は短周期成分に関して平均化された変数$\hat{\boldsymbol{J}}^*$, $\boldsymbol{J}^*$を意味しているはずだからである。

---

107. 銀河はどのように生まれてくるのだろう。

銀河誕生のシミュレーションをしている。

---

108. わたしは宇宙プラズマがなぜ爆発するかを理解したい.

だからいま人工衛星や電波望遠鏡を使って太陽フレアを観測している.

---

109. わたしは他人があっと驚く性能の望遠鏡を実現したい.

だから「ようこう」衛星の硬X線望遠鏡を提案・設計した.
(ほぼ目標を達成できた。次は何にチャレンジしようかな?)

---

110. わたしは クェーサーなどの活動銀河核が、太陽の1兆倍ものエネルギーをどのように作りだし、光速の90%を越えるジェットをどのように加速しているのか、また、これらの天体がどのようにして生まれるのか を理解したい.

だからいま VSOP(電波天文衛星「はるか」) を使って、若いクェーサーの中心核を精密に調べる観測 をしている.

---

111. わたしは全宇宙の大きさを正確に測りたい。わたしは天文学を精密科学にしたい。わたしは楽しい天文学をやりたい。

だからVLBIを天文の装置にしようと大変苦労している。

---

112. わたしは10年スケールの気候変動のメカニズムを理解したい.

だからいま, 地球表面上の水の質量移動によって生じる極運動を計算し, 地球回転の立場から見た, 海洋と大陸間に存在する10年スケールの水循環について研究している.

---

113. わたしは日本において, 地球温暖化に伴う海面上昇のシグナルを検出したい.

だからいま, 検潮所の地殻変動を精密に監視するGPS測位の精度向上のため, GPS測位の大きな測定誤差要因である水蒸気の動態について研究している.

---

114. 私は宇宙の構造を理解したい。

だからたくさんのデータを集めたデータベースを作っている。

---

115. わたしは、日本地図を描くがごとく、私たちの銀河系の精密な三次元立体地図を作りたい。

だからいま、「宇宙の灯台」とも言うべき宇宙メーザーを見て、どうしたらそれらの位置と距離を正確に測定できるのかを、研究している。

---

116. わたしは、予測できない未知の天体現象を自分で見つけてみたいと思っている。

だからいま、国立天文台水沢観測センター10m電波望遠鏡での観測に使用する電波分光計を立ち上げている。なかなか立ち上がらなくていらいらするが、毎日夜ぐっすり眠っている。

---

117. 私は将来、国立天文台の台長になりたい。

そのために研究のみではなく、日頃の政治活動も抜かりなく行っている。
ちなみに、天文台長を退官したら文部省の審議官になるつもりである。

---

118. わたしは電波を使って未知の天体を発見したい。

だから人類として究極の電波望遠鏡を作りたい。そのために現在南米チリの 5000m 高地でさまざまな調査をしたり、装置の検討を行っている。

---

119. わたしは宇宙の仕組みと今後の進化を理解したい.

だからいま天体の形成過程を研究している.

---

120. わたしは、何でもいいから誰も見たことがないような変なモノを観測してみたい。

だからすばるの初期に使う観測装置を製作している。

---

121. わたしは宇宙がどのようにでき、銀河が作られ、星が生まれ、惑星ができ、生命が発生したのかを理解したい.

だから銀河が生まれる様子や銀河の赤ちゃん (原始銀河) また惑星系の赤ちゃん (原始惑星系) を調べている.

---

122. わたしは「LMSA」を使って原始銀河や宇宙のはてを観測したい.

だからその計画の実現のために、計画の立案、推進、装置の開発を行っている。

---

123. わたしは、地球がどこまで理想的な弾性体であるかを知りたい。

だから、長周期の潮汐現象を調べている。

---

124. わたしは、海面が本当に上昇しているのか知りたい。三陸のリアス式海岸が今でも沈降し続けているのか知りたい。

だから、海面の高さを測る検潮所の位置変化を、GPS と VLBI を使って見張っている。

---

125. わたしは、地球の内部の流体核と固体核の動きを知りたい。

だから、重力計を使って微細な重力加速度の変化を観測している。

---

126. わたしは小惑星というものが何であるかを理解したい。

だからその軌道進化を調べるためにいろいろな計算をしている。

---

127. わたしはカオスの本質およびその扱い方を理解したい。

だから膨大な量の数値計算をしている。

---

128. わたしは太陽系の起源や太陽系外の惑星系の形成過程を理解したい。

だから、いつか本格的に惑星系形成について勉強したいが、まだ小惑星についての解析に留まっている。

---

129. わたしは、アインシュタインの一般相対性理論が正しいかどうか確かめたい。

だから、一般相対性理論から予言される重力波を見つけるための装置 (TAMA300) を開発している。

---

130. わたしは、電磁波では見ることのできない宇宙の姿を観てみたい。

だから、重力波検出装置の感度を高めるために日夜奮闘している。

---

131. わたしは、宇宙の始まりを重力波を通して直接観てみたい。

だから、ちょっと難しいものがあるかもしれないとは思いながらも、重力波検出装置の感度をより一層高めるために粉骨砕身の努力をしている。

---

132. わたしは宇宙ではどういう環境で分子が作られるのかを知りたい。

だからいろんな分子を観測して、分子雲の化学組成と物理状況の関係について研究している。

---

133. I wish to understand the univserse and cosmology.
(宇宙と宇宙論を理解したい.)

For that purpose, I study quasars and brown dwarfs. Comprendes!?
(そのためにクエーサーと褐色矮星を調べている. わかるかな!?)

---

134. I want to understand if one can undestand what have not been understood yet.
(まだ理解されていないことを理解できるようになるのかどうか理解したい.)

But now I am thinking if I really understand what, I thought, I understood.
(けれど, 理解したと思ったことを本当に理解しているのだろうかと考えている.)

---

135. Now I want to understand what I want to understand.
(自分が何を理解したいのか理解したい.)

That is why, now I am doing everything I can to understand what I have to understand to understand what I want to understand.
(だから, 自分が理解したいことを理解するためには何を理解すればよいかを理解するためにあらゆることをしている.)

---

136. 私は、地球外にも存在しているはずであろう生命はどのようなものか、太陽以外の恒星の周りにはどのような惑星がめぐっているのかに興味をおぼえる。また宇宙から地球を眺めてもみたい。

だから、というわけではないが(そこまで具体的ではないという意味で)、天文の世界にやってきたが、太陽を経由して今は地球大気観測の装置開発を行っている (超伝導受信機を用いたサブミリ波帯による観測装置)。この経験を生かして、上記の仕事にいつか取り組む日がくるかもしれないことを漠然と想像しながら、日々の仕事に励んでいる。"しかし常にそうであるように、現実はもっと奇怪なものになるかもしれない。(by A. C. Clarke)"

---

137. 私は、惑星間空間擾乱の原因を知りたい。

だからいま Coronal Mass Ejection (コロナ質量放出) の研究をしている。

---

138. わたしはダークマターの正体をしりたい.

だから手始めに低質量星の寄与を評価するため、近赤外線で広域深探査するためのカメラを製作している.

---

139. 宇宙の大きさ年令を知りたい。

高感度のミリ波受信機を作っている。

---

140. わたしは宇宙ジェットの起源を知りたい。

とりあえず、そのために私はブラックホールと宇宙磁場を研究しています。

---

141. 私は、宇宙の大規模構造がどうなっているかを知りたい。

だから今、銀河団を見つける新しい方法を考えている。

---

142. 私は人間を理解したい。

だからいま宇宙と女性を研究している。

---

143. 私は、スーパーコンピューターを使うよりもずっと速く計算をしなければならない。

だからいま、スーパーコンピュータより速い専用計算機を自分で作っている。
でも大変である。誰か手伝わない? お金くれるだけでもいいけど。

---

144. わたしはエコシシステムとしての銀河の形成と進化の過程を理解したい。

だから球状星団と衛星銀河の系の形成の研究をしている。

---

145. わたしは宇宙の始まりから現在の姿に至るまでの過程を物理学として理解したい。

だから今、宇宙の大規模構造の進化、銀河の進化を特に環境効果という側面から観測、理論の両方のアプローチを用いて研究している。

---

146. わたしは宇宙の歴史を理解したい.

だからいま恒星物理学の勉強と球状星団の研究の準備をしている.

---

147. わたしは自分をとりまく宇宙という自然を多くの人に意識してもらいたい.

だからいま博物館で天文教育活動をしている.

---

148. I want to understand how do spiral galaxies live.
(私は渦巻銀河の生態を知りたい.)

So I am working now on the problem what makes spiral arms so stable.
(だから何が渦巻の腕をこんなにも丈夫にしているか調べている.)

---

149. 私は、半規則的変光星の表面で何が起こっているかを知りたい。

だからいま、偏光観測を行っている。

---

150. 私は、炭素星の進化上の位置を理解したい。

だからいま、分光観測を細々と行っているが、遅々として進まない。

---

151. 私は、小・中・高校・一般社会で天文分野がどのように教えられているかに興味を持っている。

だからいま、本や雑誌での天文分野の記述を少しずつ調べている。

---

152. わたしは銀河がかつてどこからきて、今どうなっていて、この先どこへゆくのかを理解したい。

だから今、土曜日曜も休まずに毎日片道一時間半かけて大学まで通い、指導教官に怒られながら論文を書いたり、徹夜して書いたプロポーザルをリジェクトされたり、発表会でボロボロになったり、研究室の人と議論して不勉強を晒したりしつつ、いろんな人に助けてもらいながら望遠鏡を使って銀河を観測して、少しずつ手探りで銀河とお近づきになろうとするかたわら、パソコンやワークステーションで遊んだり、友達と酒を飲んで騒いだり、本屋でマンガを立ち読みしたり、季節季節の風花雪月を愛でたり、という大学院生生活を送っています。

---

153. わたしは天文学(者)と社会がどうお付き合いすればいいのかを知りたい。

だから今、お気に入りのCDをかけて、チョコレートを食べながらアンケートに答えている。(アンケートの回答を考えているうちにチョコレートはなくなってしまったが)

---

154. 私は、表面温度が約6000度である我らが母なる恒星(ほし)の上空に、どうして200万度もの薄い大気が広がっているのかを理解したい。でも、理論を作るのには自分は不向きだと思っている。

だから、可視光・電波・X線など、いろいろな波長の光で得られる情報を総合して、大気の物理状態の時間と場所による違いを観測的にできるだけ詳しく決定し、理屈を考えるための材料を提供しようと努力している。

---

155. 私は、天文学者と呼ばれる職業に就きたい。

だから、天文学の学べる大学院に進んで、その時点で一番面白そうだった分野についての勉強を始め、何か貢献をしたいと努力を続けている。

---

156. 私は宇宙の大きさを測りたい。

だから少しずつ観測装置を買い集めている。

---

157. わたしは宇宙の雲がどのようにして恒星や惑星になったかを知りたい。

だから家族を家に残して、観測所に出張し、データを取っている。

---

158. わたしは、天文学という素晴らしい学問を多くの人に知ってもらいたい。

だから大学の授業を真面目にやっているが、なかなか素晴らしさが伝わらない。

---

159. わたしは、天文学の研究者を増やしたい。

だから眠たい会議にも出席して、他分野の人の理解を得ようとしているが、成果はあがらない。

---

160. 私は、観測ではわからないことについて知りたい。

だから理論的に研究している。

---

161. 私は、自分の能力の限界を知りたい。

だから人がやらない難しい問題を研究している。

---

162. 私は最後のフロンティアである宇宙について知りたい。

だから誰もやったことののないことを勇敢に研究したい。

---

163. 私は銀河の進化を人とは違った観点から研究したい。

だから銀河進化をカオスの視点から研究している。

---

164. わたしは 自分の不完全、中途半端な心、意識とは何かを理解したい。

だから今、たまたまほんの偶然で(もしかしたら大きく道を誤って)天体現象に関する研究をしている。

---

165. 私は、いずれ地球人は宇宙へ進出して進化していくべきものと考える。

よって、宇宙の高エネルギー粒子線環境とそれが生体に与える影響に関して研究を行なっている。

---

166. 私は、根っからの楽天主義者で人類の長期の存続を信じている。即ち、銀河系のどこかには知的生命体が同時に存在すると思う。

よって、これを探査するために、稼動時間に余裕のある大型パラボラアンテナを利用して「通信実験」を行なうべきと思うが、まだなにもしていない。

---

167. 私は地球の生命がどこからきてどこへいくのか知りたい。

だから宇宙の研究をする。

---

168. わたしはまだ誰もが見たことのない星誕生の有り様を見てみたい.

だからいま、なかなか通らないけど、そのための観測プロポーザルを書いている.

---

169. わたしはかつての自分のように星を眺めて感動する人々を増やしたい.

だからいま、教室で天文学を教え、寒いのに屋外で学生の相手をしている.

---

170. わたしは世界がカオスであることを知っている。けれどどれくらいカオスなのか知らない。

だから街の雑踏の中で、人々が尻から出す見えない糸の絡まり具合を想像して考え込んでいる。

---

171. 私は、宇宙とは何か、宇宙はどんな歴史をもち、将来どうなるかを知りたい。

それを知る手がかりとして、現在、銀河の形成と進化を研究している。

---

172. わたしは地球の近くに来る可能性のある天体に興味があります。

だから、その天体を観測して、位置を測ったり、天体力学を使って軌道を計算したりしています。

---

173. 私は、いろいろな星のまわりの塵やガスの物理状態を理解したい。

だから、私は今、そのような塵やガスによって散乱された光を偏光装置を使って調べている。

---

174. 私は様々な銀河の中心部を詳しく分析し、そこで起こっていることを理解したい。

だから、代表的な銀河の中心部の、世界で最高の解像度を持つデータを解析している。

---

175. I want to understand the intricate structure of spacetime.
(私は時空の入り組んだ構造を理解したい)

So, for the present, I am trying to contribute to the effort for the detection of gravitational waves.
(だから今、重力波を検出する試みに貢献しようとしている)

---

176. I want to understand what are there in the sky above.
(私は頭上の空に何があるのか知りたい)

So, for the present, I am trying to detect gravitational waves which brings information of heavenly objects to me.
(だから今、天上の物体の情報をもたらす重力波を検出しようとしている)

---

177. わたしは、銀河のタイプの違いを生じる銀河形成のメカニズムを理解したい。

だから今、銀河のタイプによる基本構造の違いを調べている。

---

178. わたしは、自分の生まれた宇宙がどうなっているか知りたい。
だから、最新のX線観測データを用いて銀河団を研究している。

179. 天体からやってくる光の彩をこの目で見たい。
ただそのためにせっせと分光器を作っている。

180. わたしは宇宙ジェットの発生機構を理解したい。
だから今ブラックホール磁気圏の研究をしている。

181. わたしはパルサー星雲の構造を理解したい。
だから今パルサー風と磁場の構造を調べている。

182. わたしは宇宙における生命の起源・進化を理解したい。
だけど今何も勉強していない。

183. わたしは真の宇宙像を理解したい。
だから超高感度の検出器を開発研究している。

184. わたしは来る21世紀に人類が繰り出すべき宇宙世界の現実 を理解したい。
だから今、その第一歩となる太陽圏、太陽系の真実を明らかにしようと観測を行なっている。

185. 私は、太陽風のダイナミックスを理解したい。
だから、人工天体が観測できない広大な惑星間空間を短時間に観測できる惑星間空間シンチレーションの方法で太陽風を観測している。

186. 私は銀河の進化を理解したい。
だから原始ガス雲の熱的進化を調べている。

187. 私は、古代人が星空の下で何を思ったか知りたい。
だから今、天文学を学び、今年、天文学史の研究を始める。

188. わたしは赤くて大きな星がどんなものなのかを理解したい。
だから赤色巨星の放出した物質の痕跡を調べている。

189. 私は、誕生したばかりの楕円銀河を発見したい。
だから今 ASTRO-F (IRIS) にのせるカメラをつくっている。

190. 私は「天体現象における普遍性のある力学過程」を理解したい。
だから今「相対論的プラズマ流の構造形成の研究」をしている。

191. 私は『すばる』望遠鏡で宇宙の物質の進化を調べたい。
だから、大型の高分散分光器 (HDS) 作製に参加している。

192. どうして化学特異星が出来たのか、理解したい。
だから、岡山天体物理観測所でこれらの星のスペクトルを観測して元素組成解析をしている。

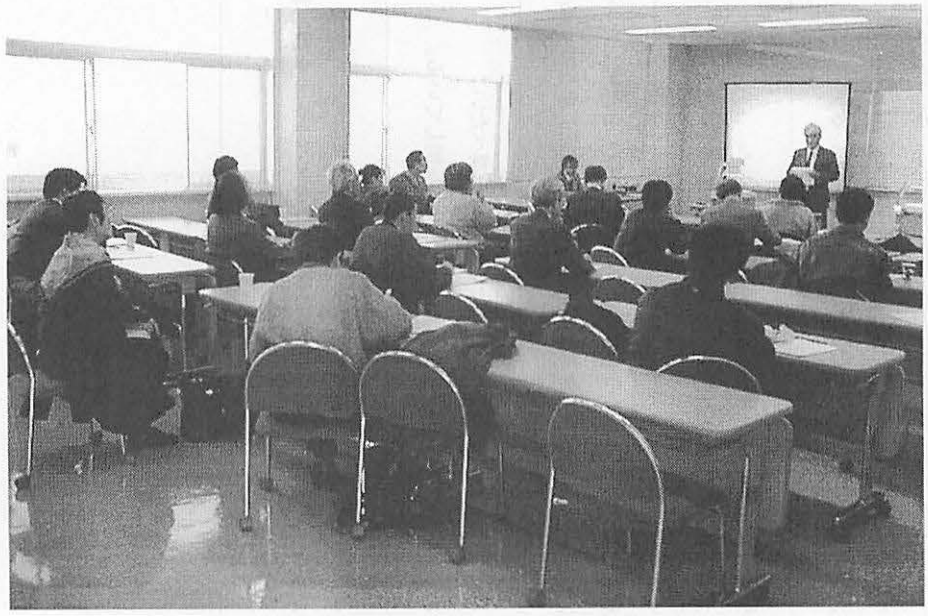

古在由秀先生による特別講演
「天体力学研究会の30年」
1998年3月6日　於 総研大葉山キャンパス

日本の近代天文学の始まりや，天体力学の発展へと導いた著名な研究者について講演をしていただいた。

天体力学研究会の歴史は，巻末にある付録の「過去の集録の目次」を参照のこと。

目次で見る天体力学研究会の歴史

The History of *Celestial Mechanics Symposiums* with Tables of Contents

布施 哲治
総合研究大学院大学 ／ 国立天文台
181-8588 三鷹市大沢 2-21-1

Tetsuharu Fuse
Department of Astronomical Science, Graduate University for Advanced Studies, Mitaka, Tokyo 181-8588

E-mail tetsu@pluto.mtk.nao.ac.jp

Abstract

This "*Celestial Mechanics Symposium*" is the 30th anniversary. We review the history of "*Celestial Mechanics Symposiums*" with the tables of contents in past proceedings.

1 Source of information about the Symposiums

過去の天体力学研究会のことを調べる最良の方法は，集録を見ることである。そこで，国立天文台の木下宙氏，畑中至純氏，平山智啓氏，中井宏氏らに協力していただき，過去の集録などを見せていただいた[1]。なお，本集録の巻末に付録として，これら集録の目次を載せてある。

2 Summary

集録の目次などをもとにして，それぞれの回の「開催日」,「開催場所」,「世話人」,「講演数」を表 1 にまとめてみた。なお今回 (第 30 回) の講演数には，今回初の試みである**ポスターセッション**も含めている。また図 1 は，表 1 中の各回ごとの講演数の変化を示しており，時代と共に増加している様子がわかる。このような集録は，(第 6 回を除いた) 第 5 回より出版され，第 19 回からは毎年異なる色のカラー表紙となった。第 1 ～ 3 回と第 6 回は集録がないため，当時の案内状をもとにしている (図 2)。第 4 回については，いずれの資料が見つからなかった。さらに，現在では「天体力学研究会」という呼び名も，第 1 回から第 3 回までは「**天体力学勉強会**」と呼ばれおり，また「小惑星について (第 1 回)」,「天体力学に於ける電子計算機の利用 (第 2 回)」,「n 体問題 (第 3 回)」とテーマが決まっていたことが案内状からわかる (図 2)。

[1] 国立天文台・三鷹の図書室にも，過去の集録は保管されている.

Table 1 : The No., date, place, organizer(s) and number of assembly of "Celestial Mechanics Symposiums". The '?' means that there is not any information about them.

第 回	開催日	開催場所	世話人	講演数
1	1967 年 7 月 7-8 日	東京天文台	竹内・古在・堀	?
2	1968 年 7 月 5-6 日	京都大学	古在	7
3	1969 年 11 月 21-22	水沢緯度観測所	古在	5
4	?	?	?	?
5	1972 年 1 月 27-28 日	東京大学	古在・木下	15
6	1972 年 11 月 26-27 日	東北大学	堀	9
7	1973 年 12 月 3-4 日	京都御車会館	堀・湯浅	9
8	1975 年 2 月 12-13 日	東京天文台	堀・湯浅	10
9	1976 年 2 月 22-23 日	京都堀川会館	堀・湯浅	13
10	1977 年 2 月 24 日	東京天文台	堀・湯浅	8
11	1978 年 1 月 23-24 日	東京天文台	堀・湯浅	10
12	1979 年 1 月 25-26 日	京都堀川会館	堀・湯浅	14
13	1980 年 2 月 14-15 日	東京天文台	堀・湯浅	11
14	1981 年 1 月 26-27 日	東北大学	堀・湯浅	16
15	1982 年 2 月 22-23 日	東京天文台	堀・湯浅	16
16	1983 年 2 月 24-25 日	京都産業大学	堀	16
17	1984 年 2 月 1-2 日	東京天文台	堀・木下・吉田	16
18	1985 年 1 月 29-30 日	近畿大学	古在・堀・木下・湯浅	20
19	1986 年 2 月 14-15 日	明石市立天文科学館	木下・中井	21
20	1987 年 2 月 12-13 日	東京大学山上会	木下・中井・吉川	23
21	1987 年 12 月 17-18 日	京都産業大学	木下・吉川	23
22	1989 年 1 月 30-31 日	国立天文台	木下・吉田	22
23	1989 年 12 月 20-21	京都産業大学	木下・吉田	24
24	1991 年 1 月 22-23 日	国立天文台	木下・吉田	23
25	1992 年 12 月 21-22	国立天文台	木下・中井	22
26	1994 年 1 月 12-13 日	国立天文台	木下・中井	27
27	1995 年 1 月 10-11 日	国立天文台	木下・中井	26
28	1996 年 1 月 29-30 日	国立天文台	木下・中井	28
29	1997 年 1 月 28-29 日	国立天文台	木下・中井	34
30	1998 年 3 月 4-6 日	総研大葉山	福島・伊藤・布施	33

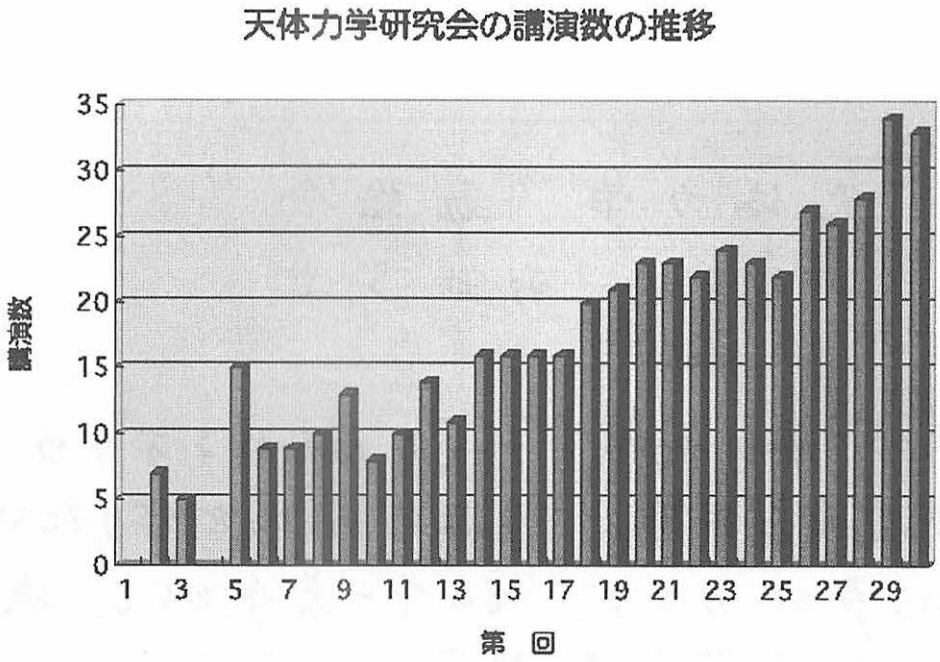

Figure 1: The change of number of the speakers at the each symposium.

図 3 は，第 2 回の天体力学勉強会のプログラムである (図中のプログラムの上にあるタイトルは,「天体力学研究会」となっている)。講演数が少なかったことから，時間的にゆとりがあったようである。本集録の目次を見てわかる通り，今回も講演数は非常に多かったが，より深い議論ができるよう，講演時間は一人当たりおよそ 40 分を確保した。

今回の研究会の案内は，時代を反映し (一部の方を除いて) 電子メールで行なわれた。第 1 回天体力学勉強会などの案内は，懐かしい「青刷り」の案内状であった (図 2)。

なお，研究会についての他の情報源としては，国立天文台の畑中至純氏による，第 2 回と第 3 回の研究会の報告が天文月報にある (畑中 1968,1970)。

3 the 50th ?

今回は，第 30 回という節目であることから，過去の集録をもとに,「天体力学研究会」を振り返ってみた。20 年先の**第 50 回**の折には，再び集録から 50 年間の歴史を振り返ってみたい。

References

第 1 - 3, 6 回 天体力学勉強会 案内状.
第 5, 7 - 29 回 天体力学研究会 集録.
畑中至純, 天文月報 61, 237, 1968.
畑中至純, 天文月報 63, 46, 1970.

"天体力学　勉強会"

お知らせ

天体力学に興味を持って居られる方々の研究連絡を密接にするための場を作りたいという声がおこり、その第一着手として次のような勉強会を計画致しました。

テーマは「小惑星について」

講演者と題目は未定ですが、広瀬、秋山、古在、堀、竹内氏らにお願いしたいと思っています。

その他、講演希望の方がありましたら東京天文台係まで至急お知らせ下さい。

広い範囲の方々の御参加を歓迎します。

6月19日

東京天文台

竹内・古在・堀

Figure 2: The circular of the 1st symposium (Jun. 19, 1967).

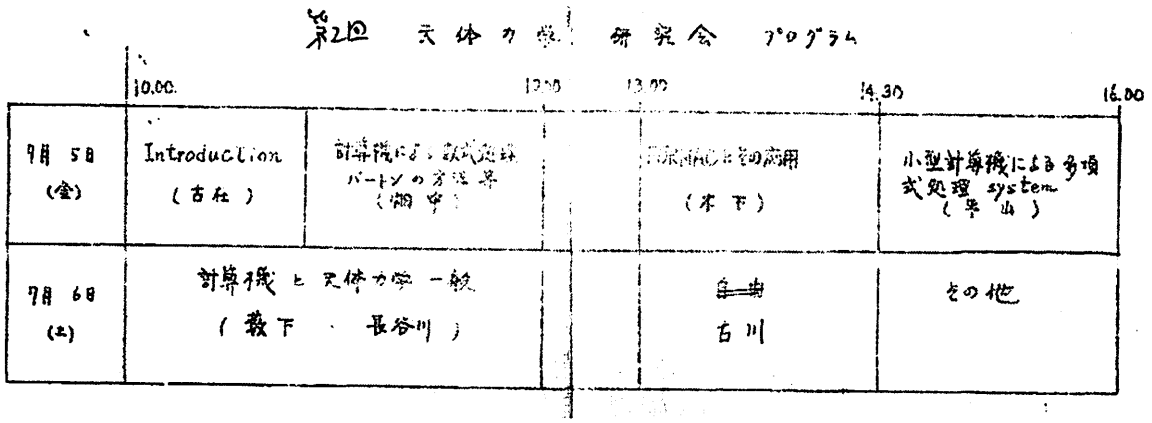

第2回 天体力学研究会 プログラム

	10:00	12:00	13:00	14:30 16:00
7月5日 (金)	Introduction (古在)	計算機による数式処理 パートンの方法等 (畑中)	FORMAC とその応用 (木下)	小型計算機による多項式処理 System (平山)
7月6日 (土)	計算機と天体力学一般 (藪下・長谷川)		自由 古川	その他

Figure 3: The time table of the 2th symposium (Jul. 5-6, 1968).

第 4 回の研究会について，情報をお持ちでしたら，**布施**まで御連絡下さい。

付　　録

天体力学研究会

過去の集録の目次

第５回　～　第29回　（第６回を除く）

「目次で見る天体力学研究会の歴史」（布施哲治）

第5回

目　　次

第7回

目　　次

第8回

目　　次

第9回

目　　次

第10回

目　　次

第11回

目　　次

第12回

目　次

第13回

目　　次

第14回

目　　次

第15回

目　　次

第16回

目　次

第17回

目　　次

第18回

目　　次

第 19 回

TABLE OF CONTENTS

第20回

目　次

＊本研究会は昭和６１年度科研費総合Ｂ「位置天文学の高精度観測方式の総合的検討」（代表者：土屋淳　東京天文台助教授　課題番号61306004）からの補助を得て開かれたものである。

第21回

目　　次

＊本研究会は、昭和６２年度科研費総合Ａ「地球回転データの物理的解釈」（代表者：岡本功、水沢緯度観測所、課題番号62302013）、および京都産業大学からの補助を得て開かれたものである。

第22回

目　　次

第23回

目　　次

第24回

目　次

第25回

目次

第 26 回

目次

第 27 回

目次

第 28 回

目次

第 29 回

目次

Proc. 30th Symposium on Celestial Mechanics

第30回 惑星力学 講演集